Universitat Autònoma de Barcelona

Functionalized Silica Nanoparticles for Catalysis, Nanomedicine and Rare Earth Metal Recycling

Hao Li

UAB

DOCTORAL THESIS

Functionalized Silica Nanoparticles for Catalysis, Nanomedicine and Rare Earth Metal Recycling

Hao Li

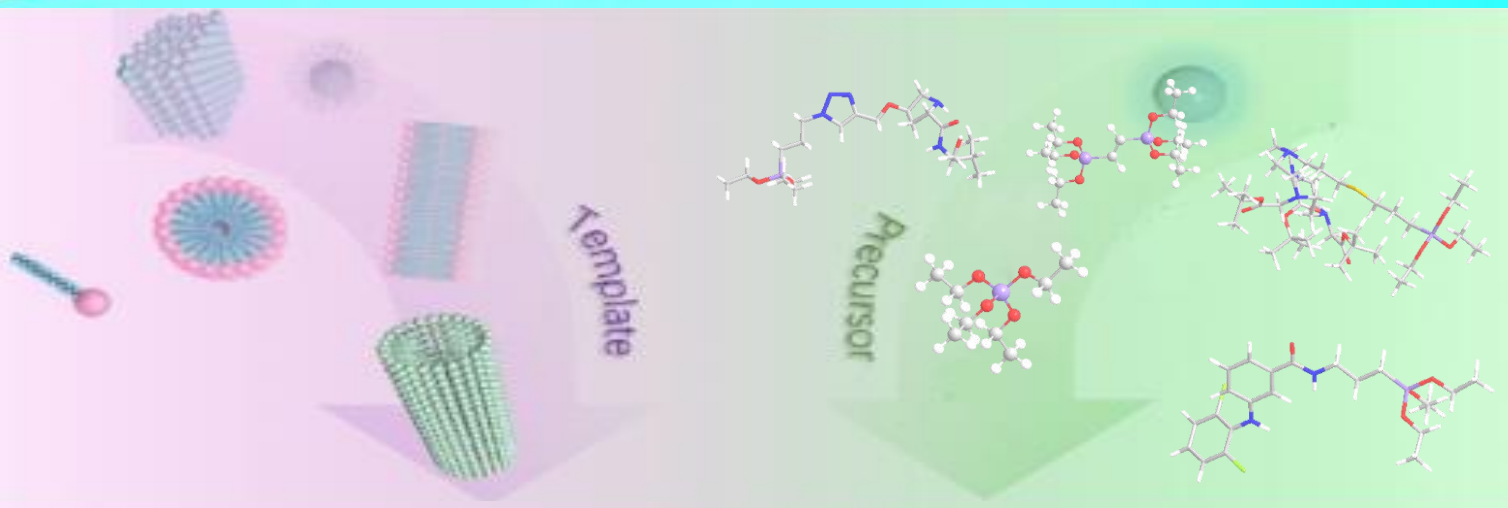

Non-porous NPs | MSNs | MONs | PMO NPs | MNPs

Applications

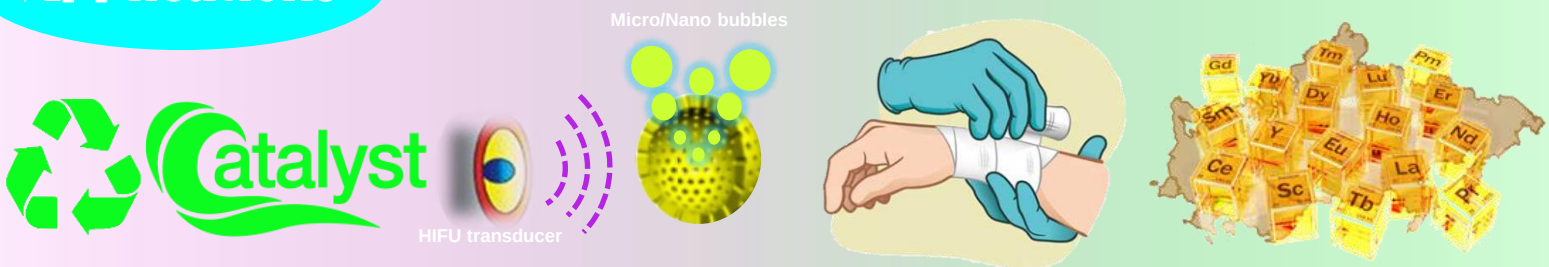

Recyclable catalyst | HIFU Responsive Agents | Anti-Inflammatory | Rare earth metal recycling

Supervisor

Prof. Roser Pleixats

Universitat Autònoma de Barcelona

2020, Spain

UNIVERSITAT AUTÒNOMA DE BARCELONA

Doctoral School

Faculty of Science

Department of Chemistry

Functionalized Silica Nanoparticles for Catalysis, Nanomedicine and Rare Earth Metal Recycling

Hao Li

Supervisor:

Prof. Roser Pleixats i Rovira

PhD in Chemistry

Doctoral Thesis, 2020

UNIVERSITAT AUTÒNOMA DE BARCELONA

Doctoral School

Faculty of Science

Department of Chemistry

Functionalized Silica Nanoparticles for Catalysis, Nanomedicine and Rare Earth Metal Recycling

Dissertation submitted for the degree of

Doctor

Hao Li

Supervisor:

Prof. Roser Pleixats i Rovira

Full professor of Organic Chemistry

Universitat Autònoma de Barcelona

Cerdanyola del Vallès, Barcelona. 1st, June, 2020

About the Author

My name is Hao Li, I was born in Anhui Province, China. I obtained the B.S. degree in 2011 from *Anhui Normal University* (P. R. of China), and then joined *Shanghai Institute of Organic Chemistry, Chinese Academy of Sciences* as a research assistant in Professor Xue-Long Hou's group. In 2013, I was admitted to the co-cultivation program of *Shanghai University* (P. R. of China) and the *Shanghai Institute of Organic Chemistry* (SIOC) and received the M.S. degree under the supervision of Prof. Xue-Long Hou and Prof. Bing Xu in 2016. Since September 2016, I have been a Ph.D. student under the supervision of Prof. Roser Pleixats in *Universitat Autònoma de Barcelona* (Spain). From October 2019 to January 2020 I worked in *Institut Charles Gerhardt Montpellier*, France, as a visiting scholar, under the supervision of Prof. Jean-Olivier Durand. My research involves synthesis and applications of chiral ligands in asymmetric catalysis, and silica-based nanomaterials for catalysis, biomedical applications and metal recycling.

About the Supervisor

Prof. Roser Pleixats received her PhD from the *Universitat Autònoma de Barcelona* (UAB) in 1984, under the supervision of Prof. Marcial Moreno Mañas. After a postdoctoral stay at the *Université des Sciences et Techniques du Languedoc* (USTL) in Montpellier with Prof. R. J. P. Corriu and E. Colomer, she returned to UAB where she became Associate Professor in 1991 and Full Professor of Organic Chemistry in 2004. She has been assistant coordinator of the degree in Chemistry, Vice-Dean of the Faculty of Sciences and coordinator of the PhD program in Materials Science. Her current research interests focus on metal nanoparticles and organosilica-based (nano)materials for catalysis and biomedical applications.

to my family, supervisors, my friends and alma maters

ACKNOWLEDGMENTS

Time is a bird forever on the wing. For the past four years, I really had a fulfilling life here. Not only have I met many knowledgeable professors, but also truthful friends. I would like to express my great gratitude towards all those who have offered me sincere assistance in the four years.

First and foremost, my hearty thanks go to my supervisor-Professor Roser Pleixats (Department of Chemistry, Universitat Autònoma de Barcelona, Spain), who has given insightful suggestions and constant encouragement both in my study and in my life. Without her enlightening suggestions and instructions, it would be a tough task for me to finish my thesis.

Secondly, I would like to sincerely thank Professor Jean-Olivier Durand (Institut Charles Gerhardt Montpellier, France) for giving me two visit chances to his laboratory and friendly guidance on research projects during my stages in Montpellier. I am also greatly indebted to Dr. Xavier Cattoën (Institut Néel Grenoble, France), Dr. Patrick Midoux and Dr. Chantal Pichon (Centre of Molecular Biophysics, France), Dr. Mathilde Menard (Institut Charles Gerhardt Montpellier, France) and Prof. Gulaim Seisenbaeva (Swedish University of Agricultural Sciences, Sweden) for their help in our research work.

I would also like to thank all my colleagues in our group, Prof. Adelina Vallribera, Dr. Albert Granados, Guillem Fernández. Thanks to all the colleagues in the lab, Dr. Jordi Salabert, Dr. Enrico Faggi, Marc Villabona, Kevin Reyes, Laura Parejo, Carolina Gascó. Thanks to Prof. Jordi Hernando, Prof. Rosa María Sebastián and other professors in the Organic Chemistry unit.

Many thanks to other collaborators and persons in charge of the UAB Services, Prof. Ester Fernández (Departament de Biologia Cel·lular, Fisiologia i Immunologia, Faculty of Veterinary of UAB), Dr. Míriam Pérez and Dr. Pau Nolis (NMR), Dr. Emma Rossinyol (TEM), Dr. Martí de Cabo (SEM), Dr. Angel Álvarez (P-XRD), Dr. Maria Jesús Ibarz (MS).

Last my thanks would go to my beloved family for their loving considerations and great confidence in me all through these years, especially my parents, they gave me life and raised me as an adult. My growth is inseparable from their love. What regrets me most is that when I want to repay my father, he went to heaven early. I also owe my sincere gratitude to my friends and my fellow classmates who gave me their help and time in listening to me and helping me work out my problems during the difficult course of the thesis.

Most sincere thanks to my wife-Yang. In my busy work, she raised the burden of the family so that I had no worries. With her love I was full of strength daily to perform the research work. Thanks to my baby-Amy, you brought me endless joy. When I see you, the heavy study and work pressure disappears. Whenever I see you, all stress can be turned into motivation.

To all, again, thank you very much.

Hao Li

FINANCIAL AND TECHNICAL SUPPORT

We gratefully acknowledge China Scholarship Council for the predoctoral scholarship (CSC scholarship, No. 201606890025), and the financial support for the research project of CNRS (France), Ministerio de Economía, Industria y Competitividad (MINECO) of Spain (Projects CTQ2014-53662-P and CTQ2016-81797-REDC), Ministerio de Ciencia, Innovación y Universidades (MCIU) of Spain (Project RTI2018-097853-B-I00 and RED2018-102387-T), and DURSI-Generalitat de Catalunya (Project SGR2017-0465).

We acknowledge as well the technical support from *Servei d'Anàlisi Química de la UAB, Servei de Ressonància Magnètica Nuclear de la UAB*, *Servei de Microscòpia de la UAB, Servei de Difracció de Raigs X de la UAB, Institut de Ciència dels Materials de Barcelona (ICMAB-CSIC), Institut Català de Nanociència i Nanotecnologia (ICN2), Servei de Llengües de la UAB, Doctoral School of UAB, Department of Chemistry of UAB, Institut Charles Gerhardt Montpellier (CNRS), Centre of Molecular Biophysics (CNRS), Swedish University of Agricultural Sciences and University of Montpellier*.

TABLE OF CONTENTS

PUBLICATIONS

The results obtained in this Thesis have been reported in the following publications:

- **H. Li**, M. Pérez-Trujillo, X. Cattoën, R. Pleixats,* Recyclable mesoporous organosilica nanoparticles derived from proline-valinol amides for asymmetric organocatalysis, *ACS Sustainable Chem. Eng.* **2019**, *7*, 14815. DOI: 10.1021/acssuschemeng.9b02838
- **H. Li**, C. Gascó, A. Delalande, C. Charnay, L. Raehm, P. Midoux, C. Pichon, R. Pleixats,* J. -O. Durand,* Periodic Mesoporous Organosilica Nanoparticles with BOC group, towards HIFU responsive agents. *Molecules* **2020**, *25*, 974. DOI: 10.3390/molecules25040974
- **H. Li**, L. Raehm, C. Charnay, J. -O. Durand,* R. Pleixats,* Preparation and Characterization of Novel Mixed Periodic Mesoporous Organosilica Nanoparticles. *Materials* **2020**, *13*, 1569. DOI: 10.3390/ma13071569
- **H. Li**, A. Granados,* E. Fernández,* R. Pleixats,* A. Vallribera,* Anti-inflammatory cotton fabrics and silica nanoparticles with potential topical medical applications. *ACS Appl. Mater. Interfaces* **2020**, DOI: 10.1021/acsami.0c06629

Other future articles:

- **H. Li**, A. Vardanyan, C. Charnay, L. Raehm, R. Pleixats,* G. Seisenbaeva,* J. -O. Durand,* Synthesis of cyclen and ethenylene-based periodic mesoporous organosilica nanoparticles, metal (II) adsorption studies. In preparation. **2020**
- **H. Li**, M. Menard, G. Seisenbaeva, R. Pleixats,* J. -O. Durand,* Functionalization of iron oxide core-shell silica nanoparticles for heavy rare earth elements recovery from wastewater. In preparation. **2020**.

ACADEMIC ACTIVITY

During my PhD thesis, I have attended five international congresses, Jornades Doctorals activity each year, one project meeting, one workshop, and one talent meeting (four oral presentations and six posters).

- XXXVI Reunión BIENAL de la Real Sociedad Española de QUÍMICA, 24-29 June, 2017 Sitges, Spain (as a volunteer)
  Poster: Kinetic Resolution of 5-Substituted Cyclohexenols by Palladium-Catalyzed Asymmetric Redox-Relay Heck Reaction
- The Xth International School on Organometallic Chemistry "Marcial Moreno Mañas", 5-8 July, 2017 Ciudad Real
  Poster: Studies Toward the Preparation of Mesoporous Organosilica Nanoparticles for Biomedical Applications
- The XIth International School on Organometallic Chemistry "Marcial Moreno Mañas", 6-8 June, 2018 Oviedo, Spain
  Oral Presentation and Poster: Functionalized Mesoporous Silica Nanoparticles as Recyclable Organocatalysts for Asymmetric Aldol Reaction
- The XIIth International School on Organometallic Chemistry "Marcial Moreno Mañas", 12-14 June, 2019, Castellón, Spain
  Oral presentation and Poster: Cotton Fabrics and Mesoporous Silica Nanoparticles Functionalized with Anti-Inflammatory Drugs for Medical Applications
- XXth International Sol-Gel Conference, 25-30 August, 2019, St. Petersburg, Russia.
  Poster: Mesoporous organosilica nanoparticles derived from proline-valinol amides as recyclable catalysts for asymmetric aldol reaction
- AEROGEL WORKSHOP, Sunday, 25th of August, St. Petersburg, Russia
- 3rd Project Consortium Meeting of the ERA-MIN2 project “MetRecycle” 28 November, 2019, Montpellier, France
- "Novena Edició de les Jornades Doctorals 2019" 22-24, May, 2019, Department of Chemistry, UAB, Cerdanyola, Spain
  Oral presentation and Poster: Functionalized mesoporous silica nanoparticles for catalytic and biomedical applications
- The 7th Jiangsu University (JSU) Forum for High-level Overseas Talents, 27-29, December, 2019, Jiangsu, China
  Oral presentation: Application of Functionalized Silica Nanoparticles

ABBREVIATIONS

$[\alpha]^{T}_{\lambda}$:	Specific optical rotation
Ac_2O:	acetic anhydride
AcOH:	acetic acid
Adsor.:	adsorption
anh.:	anhydrous
Anti-Inf.:	anti-inflammatory
aq.:	aqueous
Ar:	aryl
atm:	atmosphere
ATR (IR):	Attenuated Total Reflectance
Bn:	benzyl
Boc:	*tert*-butoxycarbonyl
b.p.:	boiling point
BTEB:	bis-triethoxysilylbenzene
BTEE:	1,2-bis(triethoxysilyl)ethane
BTSE:	1,2-bis(triethoxysilyl)ethylene
BET:	Brunauer-Emmett-Teller
BJH:	Barrett-Joyner-Halenda
cat.:	catalyst
Cbz:	benzyloxycarbonyl
$CDCl_3$:	deuterated chloroform
C dots:	cornell dots
CH_3CN:	acetonitrile
CMC:	critical micellar concentration
^{13}C-NMR:	13-Carbon Nuclear Magnetic Resonance
conc.:	concentrated
CP-MAS:	Cross-Polarization Magic Angle Spinning
CTAB:	cetyltrimethylammonium bromide
CP-MAS:	Copper-catalysed azide-alkyne cycloadditions
Cy:	cyclohexyl
Δ:	heating
d (NMR):	doublet
DCA:	dichloroacetic acid
DCC:	*N*,*N*'-dicyclohexylcarbodiimide
DCM:	dichloromethane
dd (NMR):	double doublet
δ (NMR):	chemical shift
Desor.:	desorption
DIPEA:	diisopropylethylamine
DiClfen:	diclofenac
DLS:	Dynamic Light Scattering
DMA:	dimethylacetamide
DMAP:	*N,N'*-dimethyl-4-aminopyridine
DMF:	dimethylformamide
DMPA:	2,2-dimethoxy-1,2-diphenyl-ethanone
DMSO:	dimethyl sulfoxide
DOX:	doxorubicin hydrochloride
DPTA:	diethylenetriaminepentaacetic acid
dq (NMR):	double quartet
dr:	diastereomeric ratio
DSC:	Differential Scanning Calorimetry
dt (NMR):	double triplet
EA:	elemental analysis
EDTA:	ethylenediaminetetraacetic acid
ee:	enantiomeric excess
equiv.:	equivalent
er:	enantiomeric ratio
ESI:	Electrospray Ionization
Et_3N:	triethylamine
EtO:	ethoxy
Et_2O:	diethyl ether
EtOAc:	ethyl acetate
EtOH:	ethanol
Exp.:	experiment
FAS:	fluorinated alkyl silanes
$\emptyset_{pore}$:	pore size
Fe_3O_4 NCs:	iron oxide nanocrystals
FTIR:	Fourier-transform infrared spectroscopy
GC:	Gas Chromatography
GC-MS:	Gas Chromatography with Mass spectrometry detector
H_{Ar}:	aromatic hydrogen
HMDS:	hexamethyldisilazane
HIFU:	High-intensity focused ultrasound
^{1}H-NMR:	Proton Nuclear Magnetic Resonance
HMPA:	hexamethylphosphoramide
HR-MS:	High Resolution Mass Spectrometry
HREE:	heavy rare earth element

HSAB: Hard-Soft Acid Base
Ibup: ibuprofen
ICP: Inductively Coupled Plasma
Im: imidazole
IMes: Imidazole Mesityl
^{i}Pr: isopropyl
^{i}PrOH: isopropanol
LREE: light rare earth element
J (NMR): coupling constant
KHDMS: potassium bis(trimethylsilyl)amide
KO^{t}Bu: potassium *tert*-butoxide
λ: wavelength
lit.: literature
LDV: Laser Doppler Velocimetry
M: molar
m (a NMR): multiplet
m: *meta*
MCM-41: Mobil Composition of Matter No. 41
m-CPBA: *meta*-Chloroperoxybenzoic acid
min: minutes
Me: methyl
MeO: methoxy
MeOH: methanol
Mes: Mesityl
mol%: molar percentage
m.p.: melting point
MONs: mesoporous organosilica nanoparticles
MS: Mass Spectrometry
MSNs: mesoporous silica nanoparticles
MsCl: methanesulfonyl chloride
MW: molecular weight
NFSI: *N*-Fluorobenzenesulfonimide
NLDFT: Non local density functional theory
NMs: nanomaterials
NPs: nanoparticles
v (IR): frequency
o: *orto*
OTf: trifluoromethanesulfonyl
p: *para*
PBS: Phosphate-buffered saline
PMO: periodic mesoporous organosilica
PMP: *p*-methoxyphenyl
Prot.: protective group
p-TSA/TsOH: *p*-toluenesulfonic acid
p-XRD: Powder X-Ray Diffraction
q (NMR): quartet
quint (NMR): quintuplet
®: registered brand
REE: rare earth element
R_f: retention factor
ROM: Ring-Opening Metathesis
ROMP: Ring-Opening Metathesis Polymerization
r.t.: room temperature
s (NMR): singlet
Salicyl: salicylic acid
S_{BET}: surface area measured by BET
SEM: Scanning electron microscopy
SSNMR: Solid State Nuclear Magnetic Resonance
t (NMR): triplet
TBAF: tetrabutylammonium fluoride
TBAB: tetra-*n*-butylammonium bromide
TBOS: tetrabutoxysilane
TBTA: *tris*-(benzyltriazolylmethyl)amine
^{t}Bu: *tert*-butyl
TCP: 4,5,6,7-tetrachorophthalyl
TEM: Transmission electron microscopy
TEOS: tetraethoxysilane
TFA: trifluoroacetic acid
THP: tetrahydropyranyl
TGA: thermogravimetry
TMSCl: trimethylchlorosilane
TLC: Thin Layer Chromatography
TMOS: tetramethoxysilane
TMS: trimethylsilyl
TBDMS: *tert*-butyldimethylsilyl
TBDPS: *tert*-butyldiphenylsilyl
THF: tetrahydrofuran
TPOS: tetrapropoxysilane
Ts: tosyl
TS: transition state
μW: microwave
V_{pore}: pore volume
w/w: weight percentatge

ABSTRACT

During the last decade, silica nanoparticles have found applications in catalysis, water purification, biomedical, agricultural and industrial fields… due to their unique chemical and physical characteristics, such as high surface area, excellent biocompatibility, good thermal, mechanical and chemical stability, adjustable pore size and shape, enriched surface silanol groups with easy surface modification. Our research in this thesis has been focused on the preparation and characterization of various types of novel functionalized silica nanoparticles, as well as their application in catalysis, biomedicine and rare earth elements recovery.

Novel mesoporous silica nanoparticles derived from mono- and bis-silylated proline-valinol amides were prepared and used as recyclable catalysts for the asymmetric aldol reaction with high activity and selectivity. These nanomaterials can be successfully recovered and reused for up to six runs (**Chapter 2**). Conversely, our efforts in the preparation of recyclable organosilica nanoparticles as chiral catalysts or ligands for the enantioselective α-trifuoromethylation and α-fluorination of carbonyl compounds were not successful (**Chapter 2**).

A series of mixed periodic mesoporous organosilica nanoparticles possessing Boc and *tert*-butyl ester groups were prepared as potential high intensity focused ultrasound (HIFU) responsive agents. These nanomaterials were expected to release CO_2 and/or isobutene from the temperature-sensitive COO^tBu group. However, Boc group was found to be quite stable and could not be removed under HIFU conditions at 80 ºC, requiring the addition of acid. The concept is nevertheless promising for future contrast agents for HIFU based therapies (**Chapter 3**).

Non-steroidal anti-inflammatory drugs such as ibuprofen and diclofenac were grafted to silica nanoparticles through an amide functional group for potential application in ointment and cream topical formulations. Furthermore, coating of cotton fabrics with these functionalized silica nanoparticles provided hydrophobic fabrics for potential topical cutaneous applications in dressings intended to treat chronic wounds. The corresponding anti-inflammatory drug is released in situ by the selective enzymatic cleavage of the amide bond in the presence of proteases (**Chapter 4**).

Two functionalized magnetic core-shell mesoporous silica nanoparticles containing cyclen moieties were prepared as novel adsorbents for the specific and selective recovery of different rare earth (REs) ions from wastewater (**Chapter 5**).

CHAPTER 1

GENERAL INTRODUCTION TO SILICA NANOPARTICLES

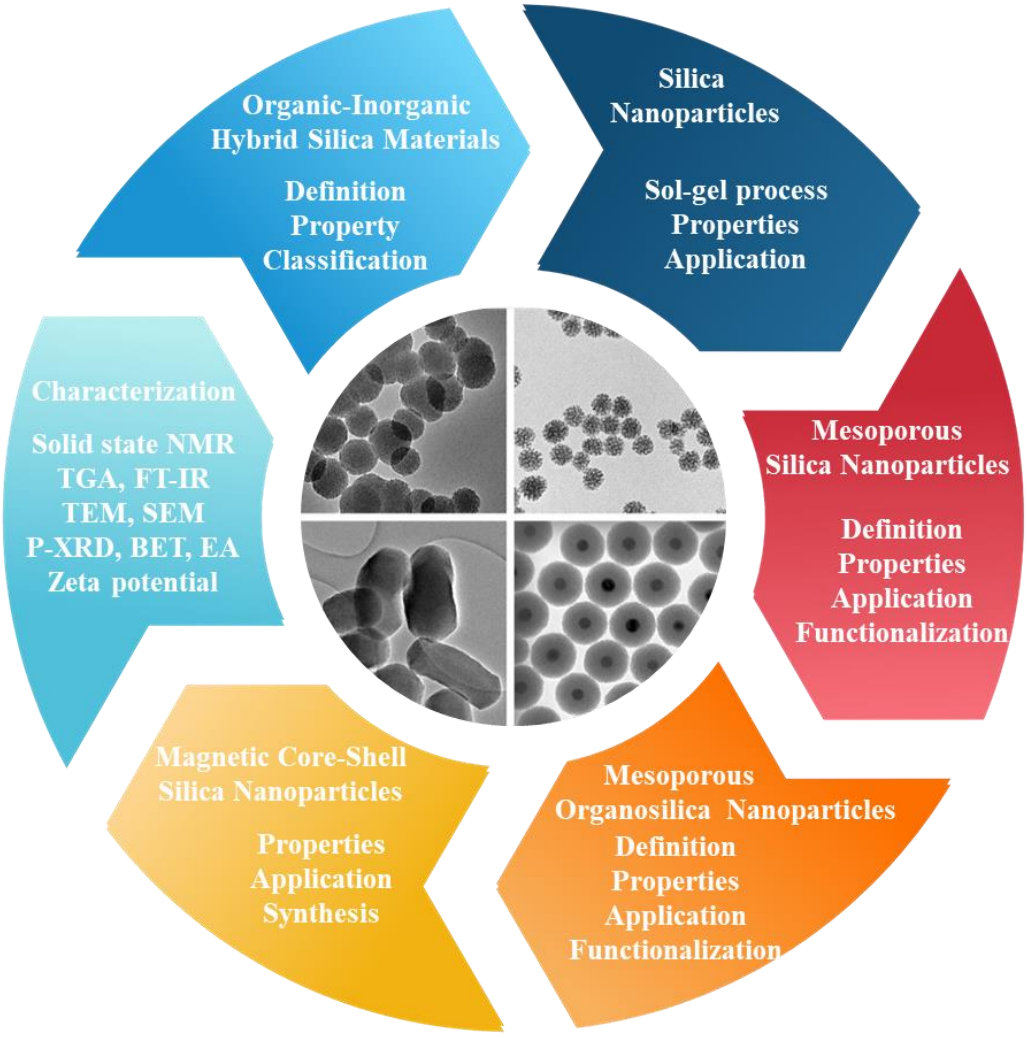

CHAPTER 1

GENERAL INTRODUCTION TO SILICA NANOPARTICLES

1.1 Introduction

Silica, also known as silicon dioxide, is an oxide of silicon with the chemical formula SiO_2, most commonly found in nature as quartz and in various living organisms.[1] It is one of the most abundant components of the earth's crust found in nature, which occurs either in crystalline or amorphous forms.[2] It has a three-dimensional network structure, the Si atom shows a tetrahedral coordination, consisting of four oxygen atoms surrounding a central Si atom, built up by packing [SiO_4] units, and a bulk structure that terminates at the surface in two different ways, that is with oxygen on the surface through siloxane groups (≡Si—O—Si≡) or silanol groups (≡Si — OH). There are three types of silanol groups, namely vicinal (hydrogen-bonded silanols), geminal (two silanol groups attached to the same silicon atom) or isolated (no hydrogen bonds possible) silanol sites, as shown in **Figure 1.1**.[3]

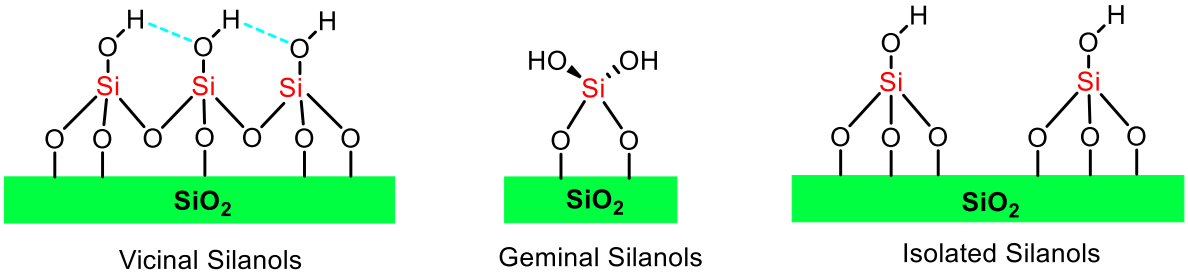

Figure 1.1 Various types of silanol group present on the surface of silica nanospheres

1.2 Organic-inorganic hybrid silica materials

The organic-inorganic hybrid silica materials are one of the most investigated materials in science and technology these years. Many different routes to change the composition and to control the structure of this type of materials were developed in fundamental research and transferred to technological applications. The combination of inorganic with functional organic and biological components have made the hybrid silica materials probably the broadest playground of different disciplines in materials science.[4-5]

Many natural materials consist of inorganic and organic building blocks. In most cases, the inorganic part provides mechanical strength and an overall structure to the natural objects,

while the organic part delivers bonding between the inorganic building blocks and/or the soft tissue, such as bone, or nacre. However, the organic-inorganic hybrid silica materials are not simply physical mixtures.[6] They can be broadly defined as composites with organic and inorganic components, intimately mixed. Indeed, hybrids are either homogeneous system derived from monomers and miscible organic and inorganic components, or heterogeneous systems where at least one of the components' domains has a dimension ranging from some Å to several nanometers.[7]

It is obvious that the properties of these materials are not only the sum of the individual contributions of both phases, but the role of the inner interfaces could be predominant. Hybrid silica materials can be classified based on the possible interactions connecting the inorganic and organic species (**Figure 1.2**). Class I hybrid silica materials are those that show weak interactions between the two phases, such as van der Waals, hydrogen bonding or weak electrostatic interactions. Class II hybrid silica materials are those that show strong chemical interactions between the components such as covalent bonds.[7]

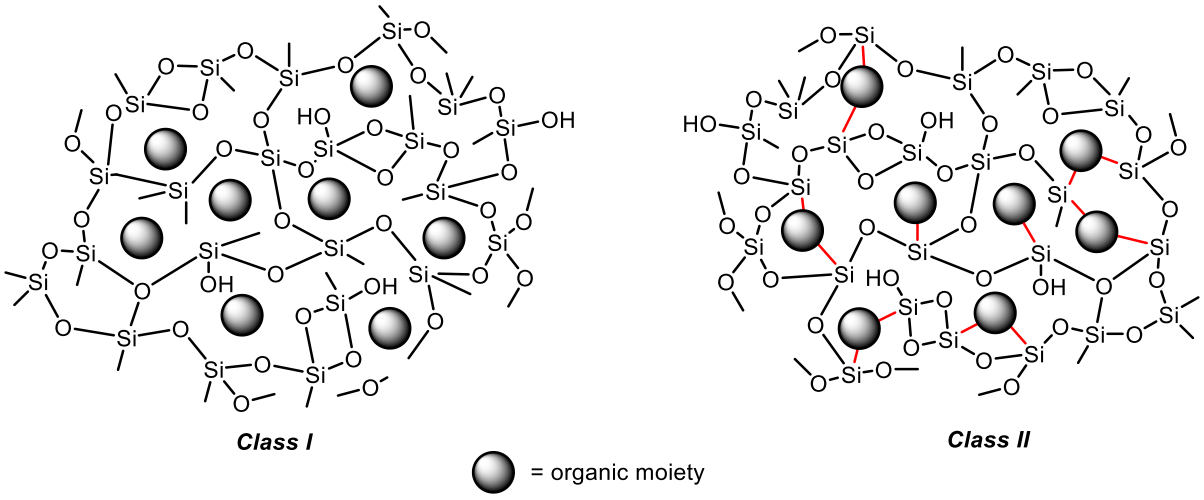

Figure 1.2 Hybrid silica materials classification

1.3 Silica Nanoparticles (Silica NPs)

At the nanoscale, physical, chemical, and biological properties differ from the properties of individual atoms and molecules of bulk matter, providing the opportunity to develop new classes of advanced materials which meet the demands from high-tech applications.[8] Therefore, the design and development of organic-inorganic hybrid silica nanomaterials have captivated the attention of several researchers worldwide. The applications of hybrid silicas

were still limited by the lack of control on the morphology and particle size. The ability to control both the size and morphology of the material and to obtain nano-sized silica particles broadens the spectrum of applications of mesoporous organosilicas and/or improves their performances.

Silica nanoparticles (silica NPs) are fabricated via the condensation of $Si(OR)_4$ to form nanoparticulated materials composed of silicon and oxygen, which are monodisperse with narrow size distributions.[9] During the last decade, silica NPs became the subject of intense research worldwide due to their unique chemical and physical characteristics such as high surface area, excellent biocompatibility, good thermal, mechanical and chemical stability, possibility to adopt various shapes ranging from spheres to rods with tunable diameter, enriched surface silanol groups with easy surface modification, large-scale synthetic availability, and the ability to be used as a shell on different types of inorganic nanoparticles such as iron oxide, gold or lanthanide nanoparticles.

N. M. Khashab and colleagues divided the siliceous nanomaterials family into five broad categories: a) silicon NPs, b) silica NPs, c) organosilica NPs, d) silsesquioxane NPs, and e) inorganically doped mesoporous silica NPs (**Figure 1.3**).[10] Owing to their interesting properties, silica nanoparticles have important applications in catalysis, biomedical, agricultural and industrial fields, water purification…, which made them like magic bullets.[8-11] In 2012, A. Bitar and co-workers highlighted novel uses of silica NPs in the biomedical sector.[12] L. P. Singh and colleagues presented an overview of research progress in the field of the preparation and application of silica NPs using the sol-gel method.[13] V. Shirshahi and M. Soltani discussed the application of silica NPs in molecular imaging.[14] The synthesis, analysis, properties, characterization methods and applications of silica NPs in biomedical imaging, as drug delivery vehicles, in diagnosis and therapeutics were highlighted by M. G. Devi and S. Balachandran in 2016.[15] A. Ramazani and colleagues provided an overview on the synthesis and functionalization of silica NPs and their catalytic applications.[16] Recently, A. Rastogi and co-workers brought together the literature on silica NPs and discussed the impact of them on several aspects of agricultural sciences. They also discussed the future application of silica NPs in plant growth, plant development, and improvement of plant productivity.[17] C. Ramaligam and colleagues reviewed the important applications of silica nanoparticles from the medicine and agricultural fields to the environmental bioremediation.[18]

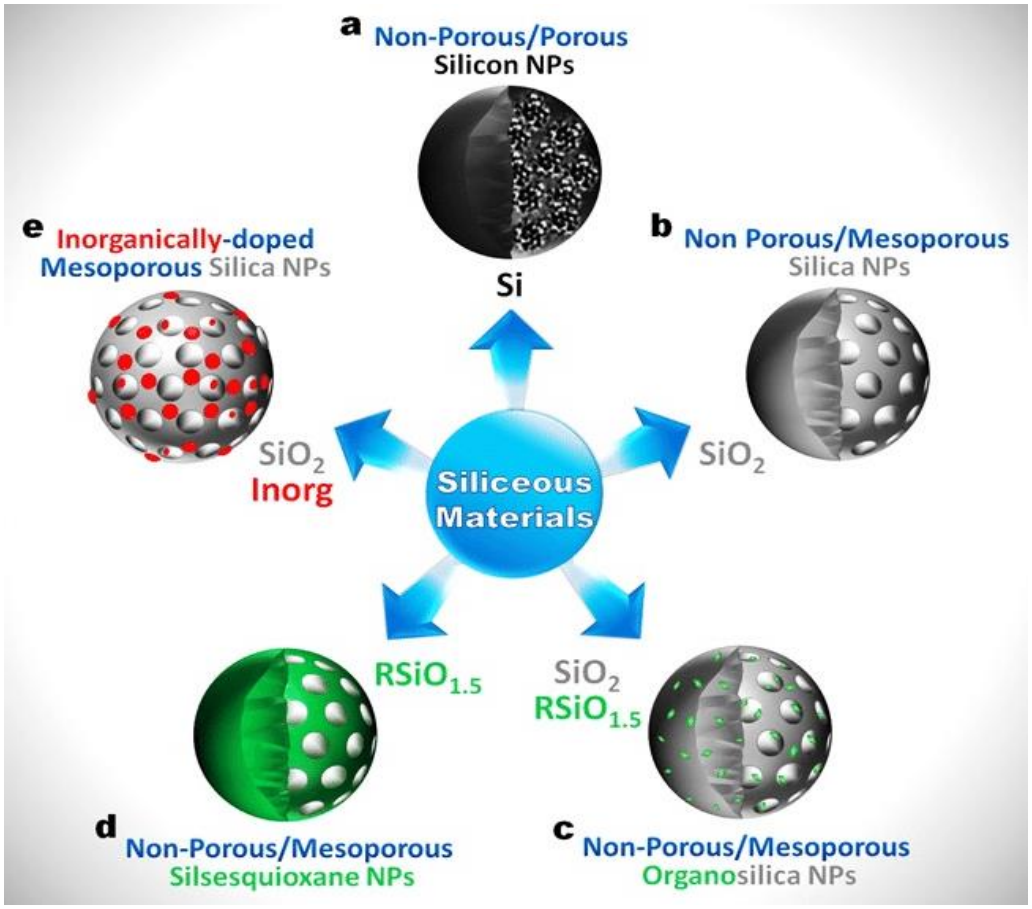

Figure 1.3 Representation of various families of siliceous nanomaterials: a) silicon NPs, b) silica NPs, c) organosilica NPs, d) silsesquioxane NPs, e) inorganically-doped mesoporous silica NPs. Reproduced with permission from Wiley-VCH.[10]

Although many articles have been reported on the potential use of nanoparticles for medical applications, the number of probes translated into human clinical trials is remarkably small. A major challenge of particle probe development and their translation is the elucidation of safety profiles associated with their structural complexity, not only in terms of size distribution and heterogeneities in particle composition, but also their effects on biological activities and the relationship between particle structure and pharmacokinetics. In 2014, a first-in-human clinical trial of ultrasmall inorganic hybrid silica nanoparticles (Cornell dots, C dots) were described in patients with metastatic melanoma for the imaging of cancer by M. S. Bradbury and colleagues.[19] In 2017, they reported the synthesis, characterization, and long-term stability of ultrasmall (<10 nm diameter), dual-modality and integrin targeting silica nanoparticles and the extent to which their surface ligand density differentially modulates key *in vitro* and *in vivo* biological activities in melanoma models over a range of ligands.[20]

During the last decade, remarkable efforts have been made on the investigations for novel processing methodologies to prepare silica NPs, resulting in better control of the size, shape, porosity and significant improvements in the physico-chemical properties. Several techniques have been developed for the synthesis of silica NPs, such as flame spray pyrolysis, hydrothermal method, chemical vapour deposition, micro-emulsion, ball milling, sol-gel method. The first procedure for the preparation of monodisperse spherical silica particles via the hydrolysis of a solution of tetraethylorthosilicate (TEOS) in ethanol at high pH was established by Stöber and colleagues in 1968.[21] Subsequently, Arriagada *et al*. reported a reverse microemulsion strategy for the synthesis of monodisperse silica nanoparticles.[22] The strategy produces silica NPs in the microcavities of reverse micelles through the careful and controlled addition of silicon alkoxides and a suitable catalyst into the medium containing these reverse micelles. The ability to control the size distribution of NPs increases the efficiency of this work. However, there are some serious drawbacks, such as high cost and difficulty in the removal of surfactants from the final products. Some other significant approaches for the synthesis of silica NPs include flame decomposition of metal-organic precursors or chemical vapour condensation via the reaction of silicon tetrachloride with hydrogen and oxygen.[23]

Among all the described techniques, the preparation by the sol-gel method has been the focus of research as the synthesis is straightforward and scalable. It is the most common process to synthesize bulk silica (and also silica NPs with some control of the conditions), which involves the simultaneous hydrolysis and condensation reactions of the precursors. The process typically starts by mixing an alkoxide precursor, such as tetraethoxysilane (TEOS) with a convenient solvent (ethanol, THF, DMF…) and a suitable catalyst at room temperature to give colloidal silanol and siloxane species, oligomers and other small clusters (**Scheme 1.1a**).[24] These clusters condense through further siloxane bridges, then form small particles, and eventually tridimensional networks that entrap the solvent to form a gel. On the macroscopic scale, gelation is the thickening of the initial solution into an elastic solid (gel) which is not fluid. This stage, however, is not the end of the process. During the aging process of the gel, hydrolysis and condensation continue (**Scheme 1.1b**) and the network stiffens restraining the flow of the pore liquid. Although the system seems virtually unchanged, polymerization, coarsening and phase transformation occur. Finally, the gel is dried and, after a thermal or mechanical treatment, the material is obtained as a powder.

(a) Basic principle of the sol-gel process:

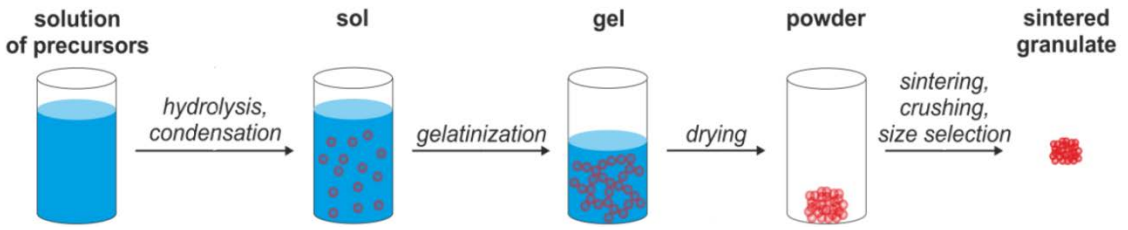

(b) Hydrolysis and condensation reactions:

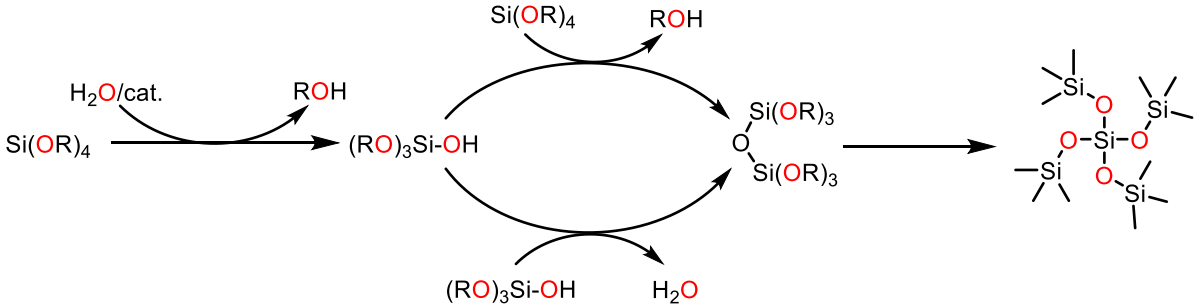

Scheme 1.1 a) Physics and b) chemistry of the sol-gel process

The nucleophilic attack of water to the silicon atom of the tetraalkoxysilane in the first step takes place through different mechanisms, depending on the catalyst used: acidic, basic or nucleophilic (F^-,[25] N-methylimidazole,[26] DMF, *N*,*N*-dimethylaminopyridine).[27] The final properties of the silica material, such as the surface area, strongly depend on the experimental parameters used in the sol-gel process. In the case of silica NPs, basic catalysis is the most commonly used (ammonia, sodium hydroxide) and a cationic surfactant is added if we want to control the porosity, size and monodispersity of the nanomaterial, resulting in mesoporous silica NPs (see **section 1.4**). In the absence of surfactant, non-porous and non-monodisperse particles are obtained. Moreover, small changes in the experimental procedure (temperature, solvent, concentration, stirring, …) can significantly affect the properties of the final silica NPs.

The rates and mechanism for each type of catalyst can be summarized as follows:[13, 27-29]

(1) Acidic catalysis: the nucleophilic attack of water (or silanol) occurs after the reversible protonation of an alkoxy group, leading to pentacoordinate intermediate prone to lose an alcohol molecule (**Scheme 1.2**).[29] The first step in the hydrolysis is the fast protonation on an alkoxide oxygen atom, leading to the development of a positive charge on it. This protonation makes the bond between the silicon center and the attacked oxygen (Si—O) more polarized

and facilitates its breakage for the departure of alcohol leaving group.[30] The rate-controlling step in acid hydrolysis is an S_N2 nucleophilic attack of water oxygen on the silicon from the backside. This latter nucleophilic attack results in the formation of a pentacoordinate reactive intermediate in which the silicon center is partially bonded to both $-OH_2$ and $-OHR$ while the incoming group (attacking water molecule), the silicon center, and the leaving group (departing alcohol molecule) lie on an axis that is perpendicular to the plane in which the silicon center and the other three alkoxide groups lie.[29] The condensation rate and mechanism depend on the pH of the reaction. For instance, the condensation reactions become irreversible at low pH because the solubility of silica and its rate of dissolution are insignificant. The mechanism of condensation under acidic conditions is also depicted in **Scheme 1.2**.[29] The first step is the fast step and is an electrophilic attack of the proton on the oxygen of the silanol group. This attack makes the silanol oxygen positively charged. The second step is the formation of a siloxane bridge (Si-O-Si) via the loss of a hydronium cation (the catalyst) as a result of the condensation between a protonated silanol group with an unprotonated one. Noticeably, the first steps in both hydrolysis and condensation reactions are similar.

The two-step acid promotion for hydrolysis reaction and sol formation mechanism is known as "A_2 sols".[29,31-32] The presence of bulky or long alkyl substituents decreases the rate of the hydrolysis reaction by hindering the Walden inversion of the S_N2 transition state.[33-34] It was also found that the hydrolysis reaction was first-order with respect to water concentration under acidic conditions. Accordingly, an increase in the water to alkoxide ratio resulted in an increase in the rate of hydrolysis. However, the enthalpy of the hydrolysis declined upon increasing the extent of hydrolysis.

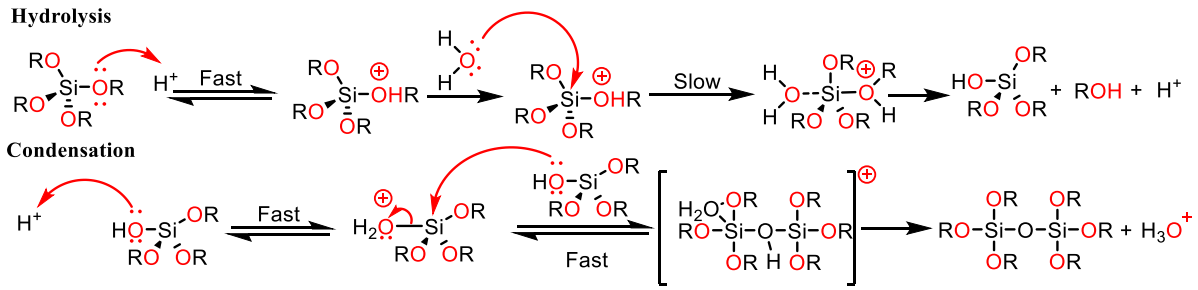

Scheme 1.2 Hydrolysis and condensation of tetraalkoxysilane promoted by acidic catalysis

(2) Basic catalysis: In the presence of hydroxide anions, a nucleophilic attack to the tetraalkoxysilane occurs through an anionic pentacoordinate intermediate, from which an

alkoxide group is eliminated (hydrolysis reactions, **Scheme 1.3**).[17,29] Abstraction of the silanol proton by the hydroxide ion is the first step in the condensation process, leading to the formation of siloxide ion and water. A siloxane linkage is, then, formed through the S_N2 attack of the latter ion on the silicon center of silanol. This step regenerates the hydroxide ion catalyst and is the rate-determining step of the condensation reactions (**Scheme 1.3**). [31-32]

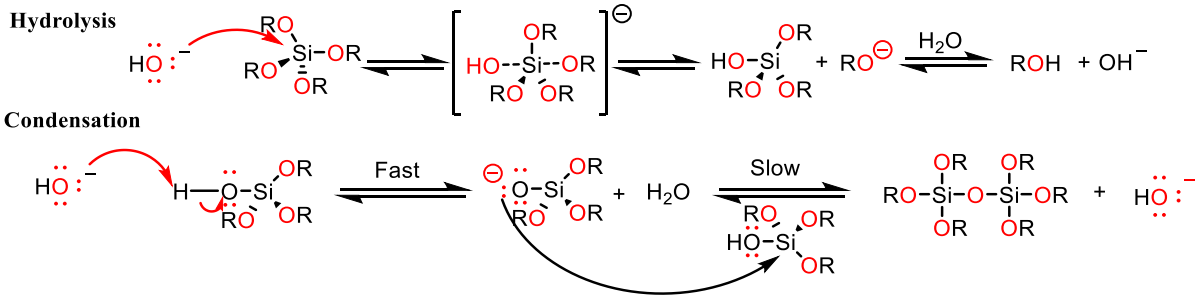

Scheme 1.3 Hydrolysis and condensation of tetraalkoxysilane promoted by basic catalysis

(3) Nucleophilic catalysis: an anionic pentacoordinate intermediate is generated upon the coordination of the nucleophile to the silicon center of a tetraalkoxysilane. Water or silanol then coordinate to this intermediate and form a hexacoordinate transition state, which evolves to give an alcohol, a silanol and to regenerate the catalyst (**Scheme 1.4**).[25-27] Many bases, even the hydroxide anion, can act as nucleophilic catalysts (besides as a base catalyst), although the fluoride anion is one of the most commonly used for bulk organosilicas.

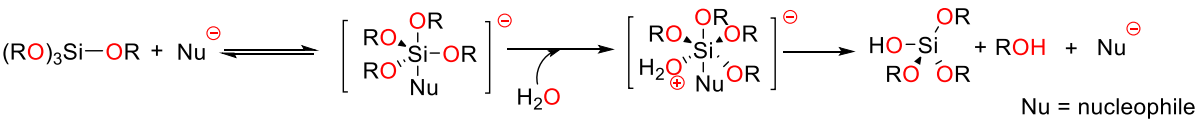

Scheme 1.4 Hydrolysis of tetraalkoxysilane promoted by nucleophilic catalysis

Most inorganic alkoxides hydrolyze and condensate very rapidly even in the absence of catalyst. In contrast, the hydrolysis of alkoxysilanes is so slow that it requires the addition of either an acid or base catalyst (**Figure 1.4**).

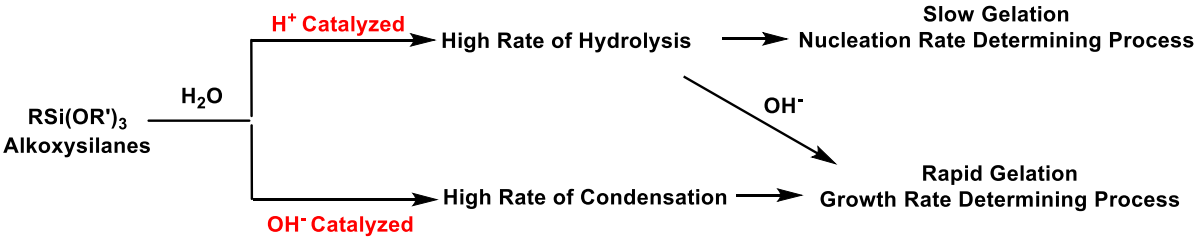

Figure 1.4 Effect of catalyst on hydrolysis and condensation.

When an acid catalyst is employed, the rate-controlling step is the particle nucleation and the fast step is the hydrolysis. This fact leads to the production of more linear-like networks with less siloxane bonds and high concentrations of silanol groups, and hence, minimally branched polymeric species. On the other hand, the gelation process by base catalyst is faster than with acid catalyst, the growth of the particles is rate determining and prevents the quick aggregation of sol particles resulting in highly dense materials with fewer silanol groups in the overall network (**Figure 1.4**).[31-32]

The rates of both the hydrolysis and condensation reactions depend strongly on the pH parameter as shown in **Figure 1.5**.[31-32,35-36] For instance, at pH $\approx$ 7, molecular hydrolysis takes place at a slow rate, while molecular condensation occurs at a fast one. This inverse relationship between the rates of the hydrolysis and condensation reactions controls both the kinetics of the reaction and the ultimate network structure.

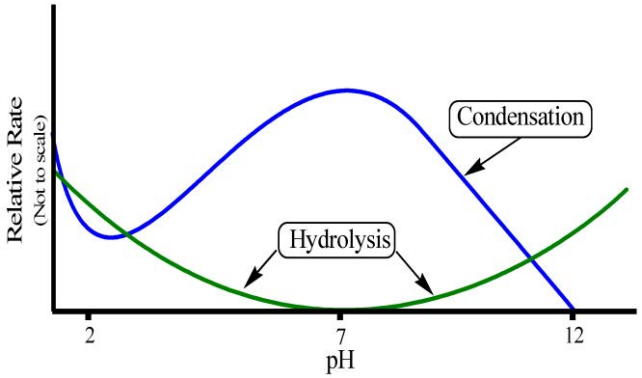

Figure 1.5 Effect of pH on hydrolysis and condensation rates. Reproduced with permission from MDPI.[28]

The linear or branched geometry of the oligomers is directed by inductive effects: positive pentacoordinate silicon atoms (intermediates in the acidic catalysis) are more stabilized by OR (R = Me, H) groups than by O-Si groups (OR more electron donor than OSi), so this will favor the formation of cations at the extremities of the chains, thus linear chains are preferentially formed (anisotropic growth). Conversely, negative Si atoms formed under basic or nucleophilic catalysis are destabilized by electron donor OR groups, and less destabilized by less electron donor OSi groups. So central negative Si are preferred, thus branched chains are easily formed (isotropic growth, spherical form) (**Scheme 1.5**). For this reason, silica nanoparticles are synthesized in basic/nucleophilic medium (NaOH, NH_3,…).

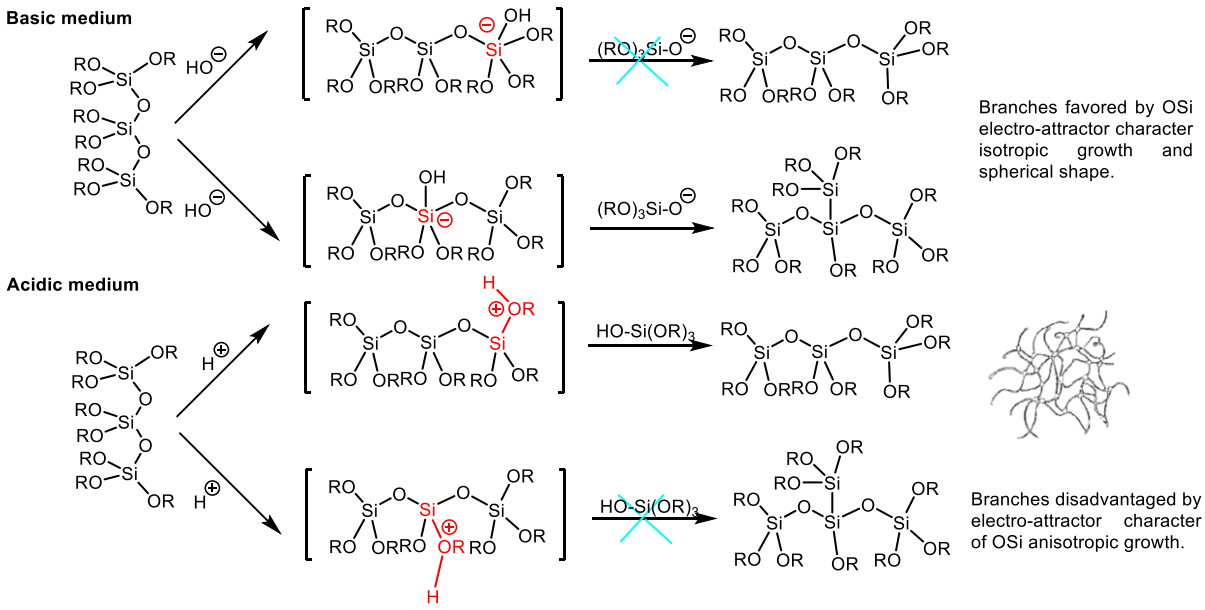

Scheme 1.5 The linear or branched geometry of the oligomers

Microemulsion is another method for the preparation of silica NPs with adjustable size and distribution properties. Schulman and colleagues first used microemulsions for the synthesis of ultrafine silica NPs.[37] Microemulsions are water in oil (w/o) or oil in water (o/w) nanodispersed colloids that are stabilized by a surfactant film.[36] These thermodynamically stable dispersions are like nanoreactors, which can be used to perform chemical reactions and synthesize nanomaterials. In microemulsions, the surfactant molecules align themselves to form spherical aggregates in the continuous phase. The silica NPs grow inside the water droplet of a w/o microemulsion, catalyzed by the base-assisted hydrolysis of silicon alkoxide. A typical reverse micelle system is shown in **Figure 1.6**.[38] The main character of this method is the production of special nanoparticles in such nanoreactors by suitable control of the effective parameters.[39] The major limitations associated with this approach are high cost and difficulty in removal of surfactants in the final products. Arriagada *et al*. reported the synthesis of silica NPs through the controlled hydrolysis of tetraethoxysilane in a non-ionic surfactant/ammonium hydroxide/cyclohexane reverse micellar system.[40]

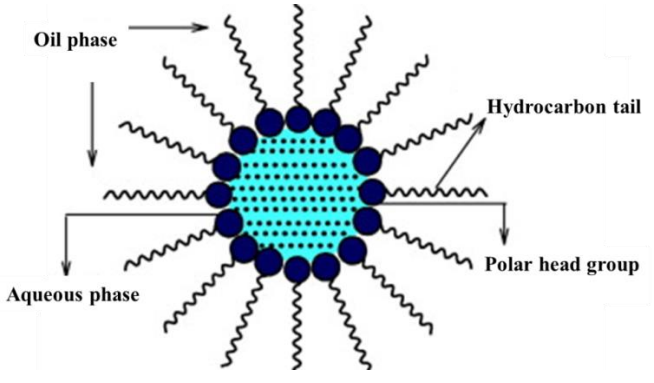

Figure 1.6 A typical reverse micelle system. Reproduced with permission from Elsevier.[38]

1.4 Mesoporous silica nanoparticles (MSNs) and functionalized MSNs

Porous materials are materials with pores (cavities, channels or interstices). The characteristics of a porous material vary depending on the size, arrangement and shape of the pores, as well as the porosity (the ratio of the total pore volume relative to the apparent volume of the material) and composition of the material itself. Porous materials have attracted the attention of the researchers for their varied applications, such as optical, electrochemical sensors, adsorption, biomedicine, catalysis.... which are due to their high surface areas and large pore volumes.[5] Depending on the predominant pore size, the porous materials are classified by IUPAC into three classes: (a) microporous with pore diameters less than 2.0 nm, (b) mesoporous with pore diameters between 2.0 and 50 nm, (c) macroporous with pore diameters greater than 50 nm (**Figure 1.7**).[41]

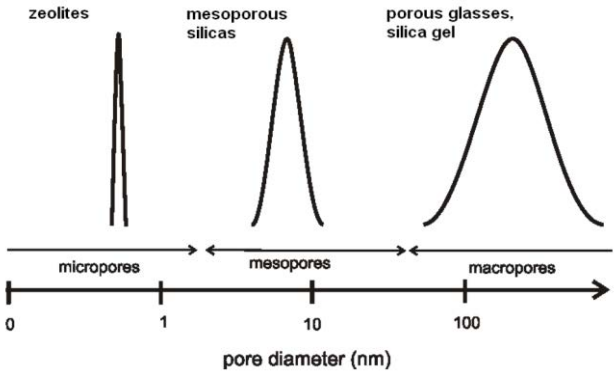

Figure 1.7 Pore diameter ranges according to IUPAC

In **Figure 1.7**, three representative classes of silica materials with micro-, meso- and macropores are depicted. Well known members of the microporous materials are the zeolites, which have pore sizes in the range of 0.2-1.0 nm, they provide excellent catalytic properties by virtue of their crystalline aluminosilicate network. Typical mesoporous materials include some kinds of silica and alumina that have similarly-sized mesopores. Mesoporous oxides of niobium, tantalum, titanium, zirconium, cerium and tin have also been reported. However, the flagship of mesoporous materials is mesoporous carbon, which has direct applications in energy storage devices.[42] Mesoporous carbon has porosity within the mesopore range and this significantly increases the specific surface area. Another very common mesoporous material is activated carbon, which is typically composed of a carbon framework with both mesoporosity and microporosity depending on the conditions under which it was synthesized.

It is well known that materials with controlled and periodically ordered mesopores provide opportunities for reaction or interaction with varieties of molecules that cannot access the

smaller micropores of zeolites. Therefore, many applications of mesoporous materials as catalysts, separation agents, sensing materials, and adsorbents have been reported in the past few years. However, their applications are still limited in some cases by the relatively small pore sizes. Thus, mesoporous materials with larger pores and well-defined pore structure remain an active and demanding research area.

Mesoporous silica nanoparticles (MSNs) are silica-based nano-sized materials which contain hundreds of empty channels (mesopores) arranged in a 2D network of honeycomb-like porous structure.[43] They have attracted substantial attention in recent years due to their advantageous structural properties, such as high surface area, large pore volume, tunable particle size and pore diameter, tunable pore structures, physicochemical stability, uniform mesoporosity, flexible morphology, the possibility to specifically functionalize the inner pore system and/or the external particle surface, excellent biocompatibility and biodegradation. They also present excellent physicochemical, thermal, and mechanical stability.[43-46] These highly attractive features make MSNs a promising and widely applicable platform for catalysis application,[16,47-48] functional material application (thermal energy storage,[49-50] adsorption,[51-54] polymer filler,[55-56] optical devices,[57-59]…) and diverse biomedical application[60-65] (imaging,[66-68] biosensors,[45,69-71] drug delivery,[72-81] cancer therapy,[82-87]…).

In the past two decades, great progress has been made in the synthesis of MSNs. Lin and colleagues have discussed different synthetic methodologies to prepare well-dispersed MSNs in a review in 2013, including fast self-assembly, soft and hard templating and a modified Stöber method.[88] Most commonly, they are prepared using a surfactant templated sol-gel method. The synthesis of MSNs can be achieved by various adjustments of synthesis conditions, including the pH of the reaction mixture, the characteristics of surfactants or copolymers used, as well as the concentrations and the sources of silica.[88]

As we have mentioned in the synthesis of silica NPs, MSNs can also be obtained by hydrolysis and condensation of tetraalkoxysilanes (sol-gel process). In order to obtain mesoporous structure, surfactants such as cetyltrimethylammonium bromide (CTAB) should be used. In the case of a CTAB templating, at a concentration of surfactant above the critical micellar concentration (CMC), individual CTAB molecules form positively charged micelles in which the hydrophobic tails of the surfactants “hide” from the aqueous solution. At concentrations higher than the CMC, spherical micelles became cylindrical, and at even higher concentrations, hexagonal packings of these cylindrical micelles are formed on scales of a few hundred of nanometers. The medium in which silanes and organosilanes hydrolyze

and condense is thus favoring a templating effect since negatively charged silanes (≡Si—O—) are attracted to positively charged CTAB ($-N^+(CH_3)_3$) micellar packings. Using an analogy with the construction of Romans aqueducts, the micelles acted as the wooden structures which are used to support the aqueduct stones during the construction. However, the synthesis of MSNs usually starts well below the CMC of CTAB, so with individual CTA^+ cations. It is the formation of CTA^+ - silanolate (individual or condensed) ion pairs, with CMC much lower than that of CTA^+, Br^- that allows the formation of the micellar assemblies. When only a silica precursor was used, such as tetraethoxysilane (TEOS), the resulting nanomaterials will be MSNs.[62]

In order to improve the chemical and physical properties, MSNs can be chemically functionalized by post-synthetic grafting[89] or by co-condensation with the required functionalized silylated compounds.[90] Post-synthetic grafting is the most popular approach for covalently incorporating organic functionalities onto the mesoporous material. It is a post-synthesis method, which refers to the subsequent modification of the inner surfaces of mesostructured silica phases with organic groups. This method is based on a condensation reaction between a given trialkoxysilane $(R'O)_3SiR$, or less frequently, chlorosilanes $ClSiR_3$ or silazanes $HN(SiR_3)_2$, and the free silanol and geminal silanol groups on the silica surface (**Scheme 1.6**).[89] In principle, functionalization with a variety of organic groups can be realized in this way by variation of the organic residue **R**.

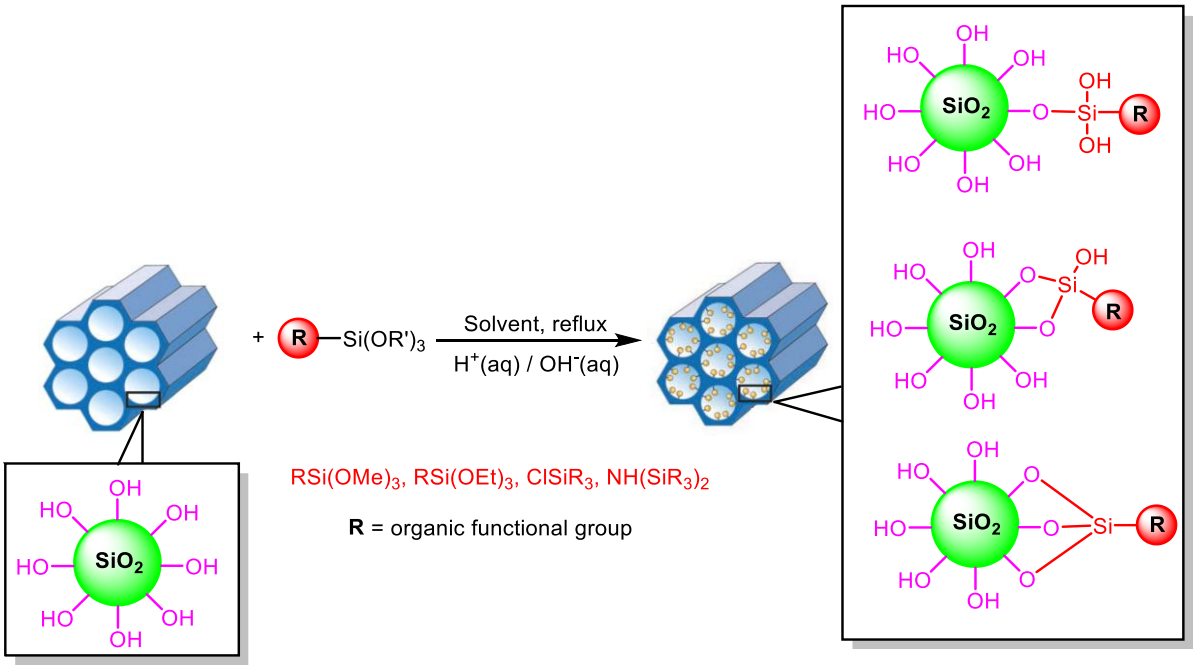

Scheme 1.6 Post-synthetic functionalization of mesoporous pure silica nanoparticles with terminal organosilanes of the type $(R'O)_3SiR$.

This method of modification has the advantage that, under the synthetic conditions used, the mesostructure of the starting silica phase is usually retained, whereas the lining of the walls is accompanied by a reduction in the porosity of the hybrid material (albeit depending upon the size of the organic residue and the degree of occupation).[91] If the organosilanes react preferentially at the pore openings during the initial stages of the synthetic process, the diffusion of further molecules into the center of the pores can be impaired, which can in turn lead to a nonhomogeneous distribution of the organic groups within the pores and a lower degree of occupation. In extreme cases (e.g., with very bulky grafting species), this can lead to complete closure of the pores (pore blocking).[92]

Alternatively, MSNs can be functionalized via the co-condensation method which is a directly synthesizing nanoparticles method (one-pot synthesis method).[87] In this approach, the desired terminal trialkoxyorganosilane $(R'O)_3SiR$ (R' is typically OEt or OMe, R is an organic group) is co-condensed with tetraalkoxysilanes [$(R'O)_4Si$ (TEOS or TMOS)] in the presence of structure-directing agents leading to materials with organic residues anchored covalently to the pore walls during the nanoparticle synthesis (**Scheme 1.7**).[92-93] If no template is added, dense non-porous functionalized silica nanoparticles are obtained.

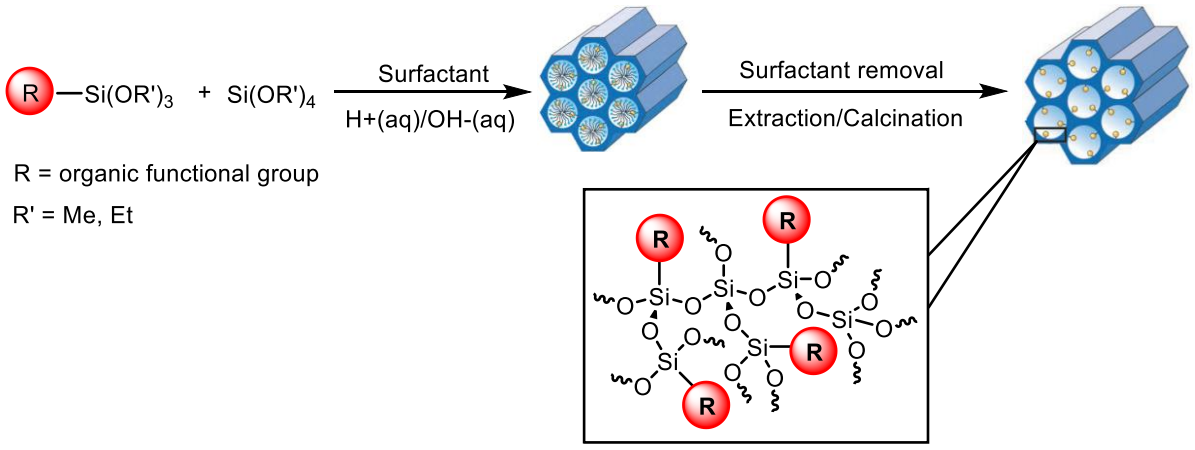

Scheme 1.7 Co-condensation method for the preparation of mesoporous organosilica nanoparticles, according to Fröba.[92]

In the post-grafting method the distribution of functional groups generally are inhomogeneous, while the co-condensation method typically resulted into homogeneously distributed organic groups on the entire inner pore surfaces of nanoparticles with no pore blockage or shrinkage problems.[94] Another advantage of co-condensation method is the easy controlling of the particle morphology in the final mesoporous silicate[95-96] that is closely related to the biomineralization process in nature. However, the co-condensation method also

has a number of disadvantages: in general, the degree of mesoscopic order of the products decreases with increasing concentration of $(R'O)_3SiR$ in the reaction mixture, which ultimately leads to totally disordered products. Consequently, the content of organic functionalities in the modified silica phases does not normally exceed 40 mol%. Furthermore, the proportion of terminal organic groups that are incorporated into the pore-wall network is generally lower than would correspond to the starting concentration of the reaction mixture. These observations can be explained by the fact that an increasing proportion of $(R'O)_3SiR$ in the reaction mixture favors homocondensation reactions at the cost of cross-linking co-condensation reactions with the silica precursors. The tendency towards homocondensation reactions, which is caused by the different hydrolysis and condensation rates of the structurally different precursors, is a constant problem in the co-condensation method and the homogeneous distribution of different organic functionalities in the framework cannot be guaranteed. Moreover, an increase in loading of the incorporated organic groups can lead to a reduction in the pore diameter, pore volume, and specific surface areas. A further, purely methodological disadvantage that is associated with the co-condensation method is that care must be taken not to destroy the organic functionality during removal of the surfactant, which is why commonly only extractive methods can be used, and calcination is not suitable in most cases.[92] The co-condensation procedure with complex molecules remains thus a challenging task for the preparation of organically modified silica nanoparticles. The combination of both synthetic approaches has afforded multifunctional platforms with a wide variety of applications.

1.5 Mesoporous organosilica nanoparticles (MONs)

Mesoporous organosilica nanoparticles (MONs), as a new type of organic-inorganic hybrid mesoporous nanomaterials, are obtained by inserting a certain kind of organic groups into the framework of mesoporous silica nanoparticles (MSNs) at the molecular level.[97-100] It is highly desirable to integrate the advantages of organic and inorganic nanosystems into one novel nanoplatform,[100-104] which potentially overcomes incomplete utilization of the surface area, showing super additive effects for benefiting various downstream applications.[105-106] For example, Shi's group reported the large scale fabrication of monodispersed MONs with a framework incorporating physiologically active thioether bonds, controllable nanostructure, composition and morphology, which provided the material foundation for exploring the versatile biomedical applications of organosilica nanosystems.[107] Significantly, the as-

synthesized MONs of less than 50 nm in particle size exhibit significantly faster biodegradation as compared to traditional MSNs, and more importantly, unique reduction-responsive biodegradation behavior. The reductive microenvironment triggered biodegradation of MONs enables the concurrent reduction-responsive anticancer drug releasing from MONs. Also encouragingly, the MONs as drug nanocarriers show high biocompatibility, and endow the MONs-based drug delivery systems with significantly enhanced antitumor effect and largely diminished systemic side effect to normal tissues and organs. Based on the facile fabrication of MONs with controllable key structure/composition/morphology parameters, and its unique reduction responsive biodegradation behavior and high performance for drug delivery, these MONs are expected to show greater potentials for clinical translation as compared to traditional MSNs.[107] In 2018, Yue and co-workers systematically compared disulfide-based mesoporous organosilica nanoparticles (ss-MONs) with MSNs with regard to endocytosis, drug release, cytotoxicity, and therapeutic effect.[108] MSNs and ss-MONs with equal morphology and size were designed and used to payload doxorubicin hydrochloride (DOX) for liver cancer chemotherapy. The ss-MONs showed considerable degradability in the presence of glutathione and performed comparably to MSNs on biocompatibility measures, including cytotoxicity and endocytosis, as well as in drug- loading capacity. Notably, DOX-loaded ss-MONs exhibited higher intracellular drug release in cancer cells and better anticancer effects in comparison with DOX-loaded MSNs. Hence, the ss-MONs may be more desirable carriers for a highly efficient and safe treatment of cancer.[108] These MONs based on the intrinsic features of the integrated organic fragments can provide specific physicochemical properties and performances.[109-111] They exhibit significantly improved stability and biological behaviors under physiological conditions.[98,102,110,112-118] Therefore, MONs are envisioned to be one of the most prosperous nanomaterials over next decade that could be utilized for many applications such as catalysis,[102,117-118] drug/gene delivery,[104,119-121] adsorption,[123] biosensing,[124] molecular imaging[100,125] waste water treatment[126] and other biomedical applications.[107,127-128]

Unlike traditional MSNs, the mesoporous frameworks of MONs are based on the homogeneous integration of organic (organic bridged silsesquioxanes) and inorganic (tetraethoxysilane) groups.[99,129-131] However, because of the lower rate of hydrolysis and condensation of organic-bridged silsesquioxanes than tetraethoxysilane, control over the nanostructure, morphological uniformity, size distribution, porosity and compositions of

MONs is quite challenging.[131-132] The synthetic approaches developed for MSNs have also been applied to MONs. The evolution of the chemical-bonding micro environment of silica nanoparticles was changed from a pure "—Si—O—Si—" (MSNs) to "—Si—R—Si—" (MONs) framework. As shown in **Scheme 1.8**, they are obtained by the condensation of a bridged silsesquioxane with tetraethoxysilane in the presence of surfactant and the appropriate catalyst. Properly speaking, we should name them as doped MSNs. If all the precursors involved in the condensation are bridged silsesquioxanes, a new type of MONs will be formed, which are periodic mesoporous organosilica nanoparticles (PMO NPs or PMONs). The following section is focused on this kind of nanoparticles.

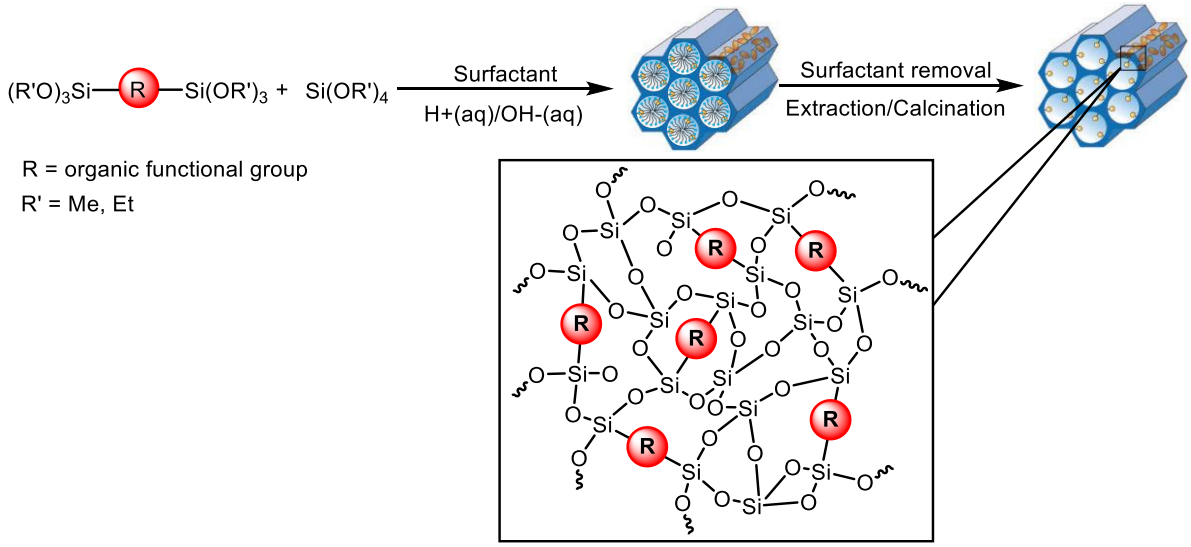

Scheme 1.8 Co-condensation method for mesoporous organosilica nanoparticles (MONs or doped MSNs).

1.6 Periodic mesoporous organosilica nanoparticles (PMO NPs or PMONs)

Periodic mesoporous organosilicas (PMO), one of the most advanced organic-inorganic hybrid silica materials, have attracted much attention from research groups since they were firstly reported in 1999.[133-135] PMO materials are obtained by the sol-gel process from organo-bridged alkoxysilanes in the presence of structure-directing agents. A large number of PMOs have been developed over the past years, providing a wide variety of applications, such as adsorption,[136-141] catalysis,[142-148] light-harvesting,[149-150] electronics,[151-153] drug release studies in simulated biological media,[78,154-158] chromatography,[159] enzyme immobilization,[160-161] bactericides.[162-163]

In recent years, some groups have focused on the research of PMOs and many excellent reviews have been published. Ozin and co-workers discussed the history of the discovery and

development of PMOs, emphasizing the most important advances regarding their compositions and structures, morphologies and properties in 2005.[164] After that, Fröba,[92] Jaroniec,[165] Fujita and Inagaki,[166] Lin,[167] Ozin,[160] Inagaki and co-workers,[168] and Corma[169] published some excellent reviews about PMOs researches. In 2013, Van Der Voort and co-workers provided a comprehensive overview of these materials, discussing their functionalities, morphology and applications.[170] One year later, Park and co-workers also published a comprehensive overview for the advanced applications of PMOs.[171]

Although a wide variety of bulk PMO materials has been reported, reaching the nanoscale for such materials is much more challenging and has been less studied. In a recent review article by Croissant, Durand and Khashab in 2015, the authors describe the synthetic strategies for the preparation of nanoscaled PMO materials (PMON), and their applications in catalysis and nanomedicine. The remarkable assets of the PMO structure are also detailed, and insights are provided for the preparation of more complex PMO nanoplatforms.[103]

PMO (nano)materials (bulk PMO and PMON) are fundamentally unique because they have several advantages, such as robust porous organic-inorganic framework,[172] porous channels,[171] tunable pore size organization,[168,173] biocompatibility,[100] and the highest organic content in the nanomaterial.[174] Moreover, the functionalization of inner and outer surface allows the modulation of the properties and enable dispersability in aqueous or organic solvents.[136] The hydrophilicity and hydrophobicity of the pores is also adjustable.[110,175] The PMONs may be degraded under certain conditions when specific functional groups sensitive to acid-base, redox, photochemical, or biochemical reactions are present in the structure of the organic framework.[176] The post-modification of the organic fragment is also possible by classical organic chemistry.[177-178] Especially in nanomedicine, properties of PMO NPs such as low hemolytic behavior,[112] increased biocompatibility and higher loading capacities, tunable physico-chemistry of the pores and designed biodegradability,[179] are particularly important when compared to mesoporous silica nanoparticles.

Similarly to MSNs, PMO nanomaterials are synthesized in the presence of surfactants that act as templates, but from different starting silylated precursors. The incorporation of organic groups as bridging components directly and specifically into the pore walls by the use of disilylated organosilica precursors allow us to prepare a new generation of silica nanoparticles which combine the advantages of organic and inorganic units while

overcoming their intrinsic disadvantages accordingly.[62,103,144,166,179] These new NPs were named periodic mesoporous organosilica nanoparticles (PMO NPs or PMONs).

The first bulk PMO materials were prepared by Inagaki and co-workers in 1999 from 1,2-bis(trimethoxysilyl)ethane in the presence of structure directing agents under basic conditions, showing surface areas of 750 and 1170 m^2g^{-1}.[134] In the same year, the group of Ozin reported the synthesis of a material exhibiting a surface area of about 640 m^2g^{-1} from 1,2-bis(triethoxysilyl)ethane.[133] Stein and colleagues published a similar work, with the same precursor and surfactant, but they obtained a material with a very high surface area of 1200 m^2g^{-1} and a low long-range order.[135]

In general, bulk PMO and PMO NPs are obtained via hydrolysis of bridged organosilica precursor of the $(R'O)_3Si\text{-}R\text{-}Si(OR')_3$ type in the presence of some structure-directing agents like block copolymers or surfactants (**Scheme 1.9**).[160,180-184] In that way, the organic groups were located within the channel walls of the resulting (nano)material as bridges between the Si centers.[168,185-186]

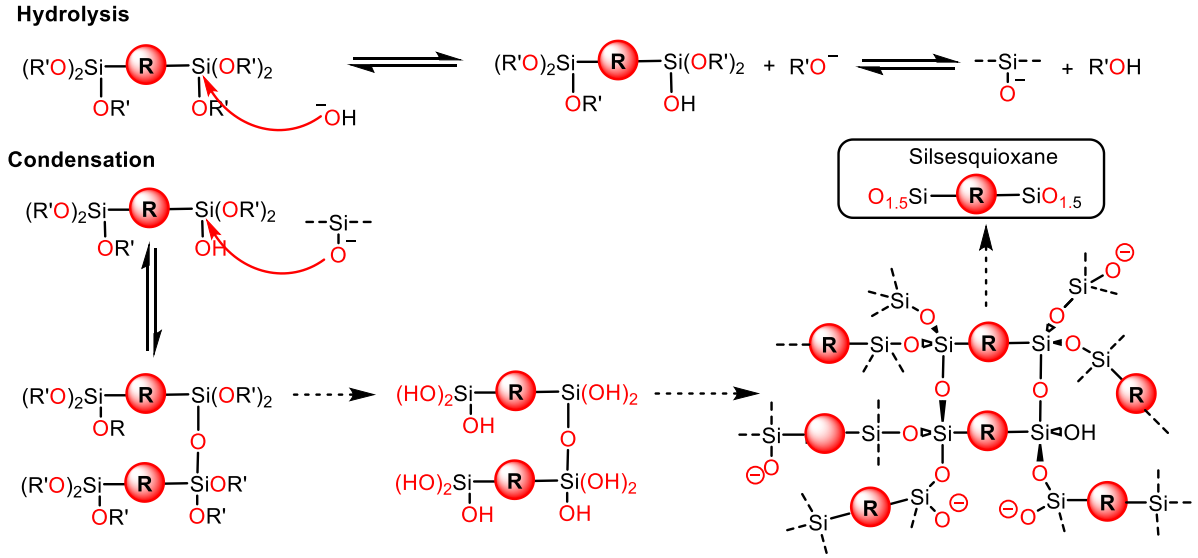

Scheme 1.9 Hydrolysis and condensation of bridged silsesquioxanes.

If there is only one bridged organosilica precursor, pure PMO NPs can be formed. If there is more than one bridged organosilica precursor with different functional groups, then functionalized PMO NPs will be obtained with two different functionalities in the framework wall (**Scheme 1.10**).

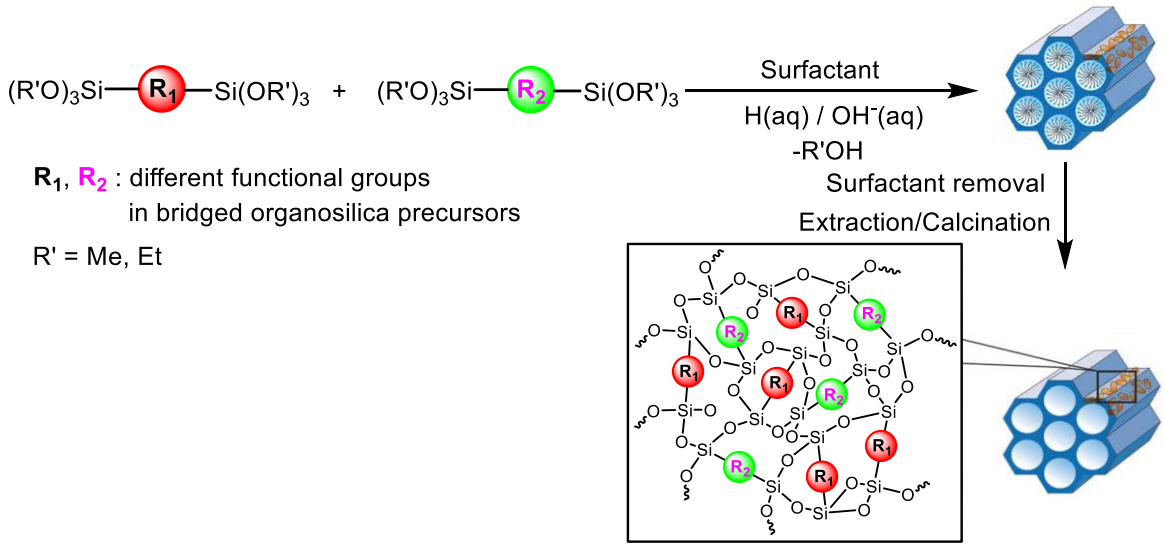

Scheme 1.10 General synthetic pathway to PMO NPs formed from two different disilylated organic bridging units.

Unlike MSNs, the porous frameworks of PMONs are based on organic functional groups covalently linking siloxane domains.[187] It is noteworthy to mention that there is a common confusion in the scientific literature between PMO nanomaterials and organically-modified mesoporous silica nanoparticles (**Figure 1.8**).[188] Strictly, PMO NPs would refer to the nanomaterials formed exclusively from organo-bridged alkoxysilanes in the presence of template. When tetraethyl orthosilicate (TEOS) is also added to the templated sol-gel process, doped MSN (also named MON) will be obtained. However, some authors do not make this distinction

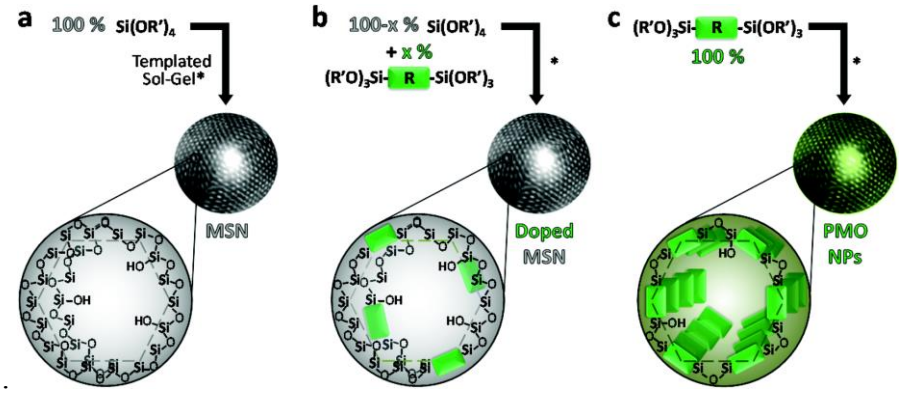

Figure 1.8 Schematic representation of a) **MSN**, b) organically-doped **MSN**, and c) **PMO NPs**. Reproduced with permission from the Royal Society of Chemistry.[188]

Specifically, the synthesis of PMO at the nanoscale level needs to consider the careful control of a range of conditions, such as the reaction temperature, reaction time, pH, solvent, precursors, optimized reactants ratio, catalyst, mixing method and stirring speed. The

experimental conditions control the template-silica interactions, the silica condensation rate, the assembly kinetics and, thus, the nucleation and growth rates.[88,92,189-190]

More importantly, different types of PMO NPs can be obtained through templating strategies. Among them, spherical NPs, nanorods, nanofibers, and multipodal NPs are the most important and most interesting PMONs (**Figure 1.9**).

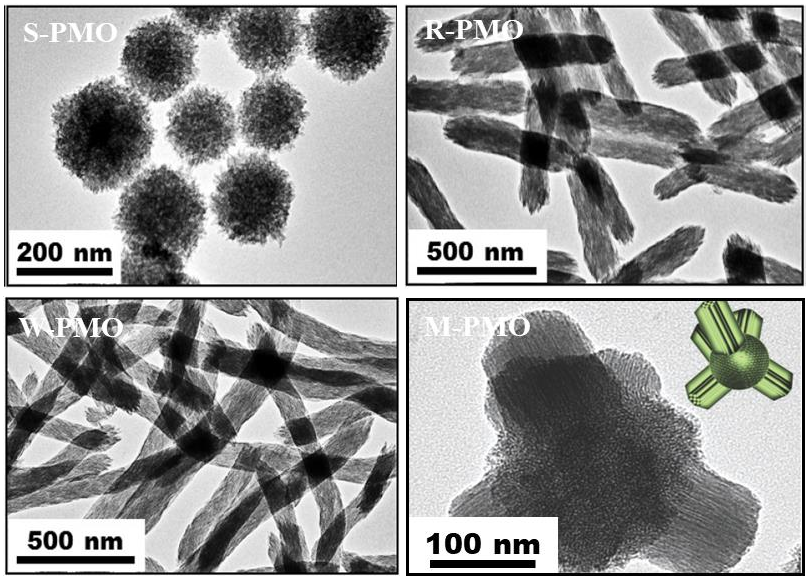

Figure 1.9 TEM images of different types of PMO NPs: a) Nanospheres (S-PMO),[168] b) Nanorods (R-PMO), [168] c) Nanowires (W-PMO),[168] d) Multipodal PMO (M-PMO).[123]

The first PMO NPs with a hollow spherical morphology (HPMON) were prepared from 1,2-bis(trimethoxysilyl)ethane by using the FC-4 fluorocarbon surfactant [$C_3F_7O(CFCF_3CF_2O)_2$–$CFCF_3CONH(CH_2)_3^-N^+(C_2H_5)_2CH_3,I^-$] and the cetyltrimethylammonium bromide (CTAB) cationic surfactant as co-structure directing agents.[191] Moreover, by varying the FC-4 over CTAB ratio, the shell thickness of the HPMO NPs could be tuned, while non-hollow PMO microspheres were obtained by using only the CTAB surfactant. The procedure followed to obtain phenylene-bridged PMO nanospheres was based on co-templating by a poly(ethylene oxide)-poly(DL-lactic acid-*co*-glycolic acid)-poly(ethylene oxide) triblock copolymer and the FC-4 surfactant.[192] It was interesting that the authors found these two surfactants were immiscible, the shell was templated by FC-4, and the core by the poly-lactic acid based polymer.[192] If only the Pluronic P123 block copolymer (without FC-4) was used as template, hollow silica nanospheres were obtained instead of the expected PMO material.[193] Later, a variety of PMO nanospheres with different organic bridged linkers, such as methylene, ethylene, ethynylene and phenylene were reported by scientists.[112,193-194] Nanorods and

nanofibers attracted a lot of scientists' attention as a very important class of PMO NPs. In 2005, Lu and colleagues used Pluronic P123 triblock copolymer as a structure-directing agent to first control the synthesis of ethylene bridged PMO nanorods.[195] Jaroniec and colleagues then described the controlled synthesis of ethylene-phenylene wide microrods with coil-like morphology by using 1,2-bis(triethoxysilyl)ethane (BTEE) and 1,4-bis(triethoxysilyl)benzene (BTEB) as organosilica precursors, and a Pluronic P123 poly(ethylene oxide)-poly(propylene oxide)-poly(ethylene oxide) (PEO-PPO-PEO) triblock copolymer template.[196] In 2009, P. Mohanty and K. Landskron used the trisilylated octaethoxy-1,3,5-trisilapentane as precursor with P123 surfactant, and among different nano-objects, PMO nanorods and nanofibers were obtained with an adjustable aspect ratio from 2:1 to 20:1 by varying the concentration of the precursor.[197-198] Later on, methylene-, ethenylene, and phenylene-bridged PMO helical fibers were reported using CTAB and (S)-β-citronellol as templating agents.[199] The sizes could be tuned to obtain nanorods depending on the precursor used. Later, in some research works CTAB was used as the only template to prepare bridged PMO nanorods.[110,173] Interestingly, Khashab's group reported the first controlled syntheses of *para*-phenylene-bridged PMONs with various morphologies, from nanospheres to nanorods and nanowires, with CTAB as a structure directing agent by adjusting the organic co-solvents.[106] A unique multipodal PMON with phenylene-bridged cores and ethenylene-bridged pods was designed by Durand and colleagues, which was prepared in a one-pot two-step process via NaOH catalysis in CTAB-templated aqueous media.[123] While the sole condensation of the 1,4-bis(triethoxysilyl)benzene or 1,2-bis-(triethoxysilyl)ethylene precursor produced phenylene- and ethenylene-bridged PMO nanospheres and nanorods, respectively, the subsequent addition of the ethenylene precursor into a solution of freshly-prepared phenylene-bridged NPs generated multipodal nano-objects.

Although the development of PMOs (and PMONs) have prompted great interest in the material sciences,[168-170] owing to their specific composition and function, the synthesis of PMOs and PMONs with large and flexible organic bridging groups within the mesoporous wall remains a challenge.[186] The applications are nearly unlimited and the interest in these straightforward materials is still growing year after year. For example, pioneering works in drug,[100-101,110,113,200-201] gene[202] and protein[160] delivery, catalysis, [100,118,139] separation,[141,203] and energy[204] have demonstrated the superior properties of PMOs when compared to organosilica analogues. The synthesis and development of new functional PMOs at the nanoscale level (PMONs) are very meaningful, especially in developing more applications in nanomedicine.

1.7 Magnetic core-shell silica nanoparticles

Initially, scientists studied the single nanoparticles because they improved the properties compared with the bulk materials. Later, they found that heterogeneous, composite or sandwich colloidal semiconductor particles have better efficiency than their corresponding single particles.[205-206] During this period, core-shell nanoparticles were proposed. With the advancement of characterization technology, different core-shell nanostructures have been studied. The definition of core-shell nanomaterials has now been extended to nanomaterials with different boundary materials (fully or partially covering the internal components). Depending on the type of materials used for their synthesis, core-shell nanoparticles can be classified into two categories: organic and inorganic.[207] In order to be more precise, four categories of nanoparticles can be described: (i) inorganic/inorganic core-shell nanoparticles; (ii) inorganic/organic core-shell nanoparticles; (iii) organic/inorganic core-shell nanoparticles; (iv) organic/organic core-shell nanoparticles. Herein, we mainly focused on inorganic/organic core-shell nanoparticles, especially magnetic cores coated with functionalized silica NPs. During the last decades, magnetic nanoparticles have attracted much attention for a wide range of applications,[208-229] such as in biomedicine (treatment of cancer, imaging, guided drug delivery, controlled release or thermal treatment…),[210-222] catalysis (oxidation, hydrogenation, C-C coupling, reduction, olefin metathesis…),[223-224] biotechnology (bioseparation, biosensing,…)[221,223,225-226] and functional materials (energy storage devices, photoelectrochemical water splitting, recovery of metals from waste water, …).[227-228]

The first step in the synthesis of magnetic core-shell silica nanoparticles is the preparation of iron oxide nanoparticle cores. In recent years, significant research has been developed around the synthesis of magnetic core-shell silica nanoparticles and its optimization leading to shape-controlled, stable and monodispersed nanoparticles. A comparison of the synthesis methods is given in **Figure 1.10**.[229] Briefly, iron oxide NPs can be synthesized by the following three methods: (1) Physical methods: these are elaborated procedures which suffer from the inability to control the size of particles in the nanometer range.[230] (2) Chemical methods: these methods are simple, tractable, and efficient, in which the size, composition, and even the shape of the NPs can be managed.[231] Iron oxides can be synthesized through the coprecipitation of Fe^{2+} and Fe^{3+} by the addition of a base.[232] The size, shape, and composition of iron NPs synthesized through chemical methods depend on the type of salt used, Fe^{2+}/Fe^{3+} ratio, pH, and ionic strength.[221] (3) Biological methods.[233] Each method has its own

advantages and disadvantages. Physical methods are easy to perform, but controlling the particle size is difficult, while in wet chemical preparation, particle size can be somewhat controlled by adjusting the conditions. The chemical methods include electrochemical method, sol-gel method, supercritical fluid method, hydrothermal method, chemical co-precipitation, sonochemical decomposition method, flow injection method, and use of nanoreactors, which give access to high quality iron oxide NPs. However, in all these techniques, aqueous medium is a most efficient pathway to obtain the iron magnetic NPs. It has been demonstrated that the particle size as well as the polydispersity of the NPs could be tailored by changing the associated factors such as Fe^{2+}/Fe^{3+} ratio,[232,234] base (NaOH, $NH_3 \cdot H_2O$, CH_3NH_2…) and ionic strength ($N(CH_3)_4^+$, $CH_3NH_3^+$, NH_4^+, Na^+, Li^+, and K^+).[18] Some other factors also have an influence on the size of the NPs, such as the stirring rate, temperature, inlet of nitrogen gas, agitation, pH, and reactants ratio.[235] Biological methods ensure low cost, reproducibility, high yield, and scalability, but are time-consuming.[236] The chemical synthetic routes dominate among these three methods. As shown in **Figure 1.10**, one quarter of iron oxide nanoparticles are synthesized by co-precipitation, followed by hydrothermal and microemulsion methods.

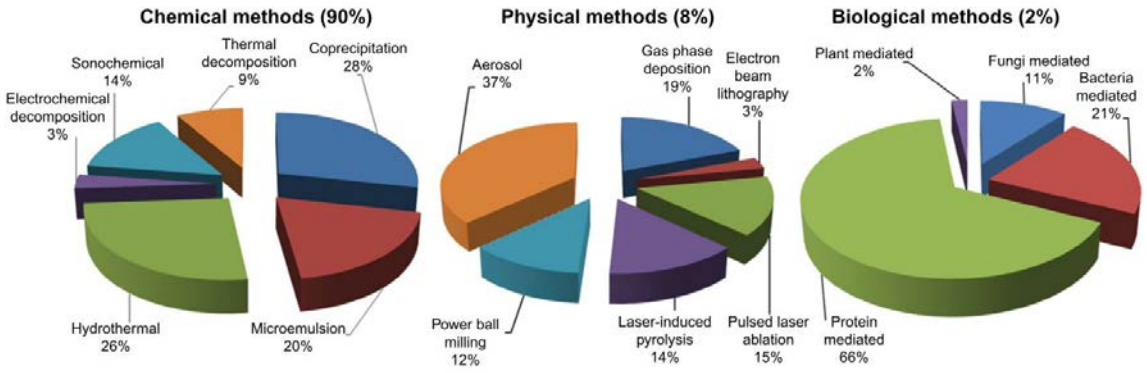

Figure 1.10 A comparison of the synthesis of magnetic iron oxide NPs by three different routes. Reproduced with permission from the Dove Press.[229]

The most common method to obtain Fe_3O_4 (magnetite) or γ-Fe_2O_3 (maghemite) nanoparticles is by co-precipitation.[237] This method consists of mixing ferric (Fe^{3+}) and ferrous (Fe^{2+}) ions in a 1:2 molar ratio in highly basic or acidic solutions. The type of iron source, reaction temperature, pH and other parameters can affect the size and shape of the NPs.

The microemulsion method involves the use of water droplets as nanoreactors in the continuous phase (oil) in the presence of surfactant molecules. More specifically, iron

precursors can be precipitated as iron oxide in the water phase located in the center of the micelles. Iron oxides do not precipitate in the organic phase, because the iron precursors are unreactive in this phase.[238-239] Surfactants are used both as the precipitating agent and the capping agent.[240] However, despite their use, the produced NPs are aggregated and in most cases they require several stabilization treatments.

Hydrothermal synthesis is the oldest method reported for the synthesis of magnetite, and consists of heating an iron precursor with a high vapor pressure (usually 0.3 to 4 MPa) in an aqueous medium. Compared with other processes, this technology can provide better crystallinity.[241-242] There are two approaches depending on whether a particular surfactant is used: sonochemical synthesis and thermal decomposition. In the sonochemical synthesis process, a high-energy ultrasonication creates acoustic cavitations, which can provide localized heat with a temperature of about 5000 K. At high temperatures, the formation and growth of nuclei and the implosive collapse of bubbles can take place. The advantages of this method are the monodispersity of NPs combined with the variety of shapes. However, the main drawback is the scale of the synthesis, as this is only aimed for small-scale production. On the other hand, the thermal decomposition method consists in the decomposition of $Fe(cup)_3$ (cup = *N*-nitrosophenylhydroxylamine), $Fe(acac)_3$ (acac = acetylacetonate) or $Fe(CO)_5$ in the organic solution phase and then oxidation to form high quality monodispersed iron oxide NPs. However, higher temperatures are required, followed by complicated operations using toxic and expensive iron complexes. It is worth noting that the iron oxide NPs obtained by thermal decomposition method are usually dispersed in nonpolar solvents.

Each method has its advantages and disadvantages. Among them, co-precipitation is still the main method for the synthesis. The numerous advantages overcome certain disadvantages. This synthetic route provides a convenient scale-up strategy with low cost and high NPs concentration in the final dispersion. The conditions used are mild and the process can be carried out in water without any surfactant. The only disadvantage, which is high polydispersity in size, can be ignored, because the NPs can be sorted by adjustments in the synthetic protocol.

Magnetic NPs are very sensitive to oxidation and agglomeration because of their magnetic nature,[208] and they also exhibit high chemical reactivity as well as strong magnetic dipole interactions, which lead to their poor stability. When oxidized, thin oxide layer generally form on the surface of the particles, which changes their properties dramatically. Natural

agglomeration of these particles into larger clusters also restricts the use of such nanoparticles in various applications.[243-244] In order to overcome these problems, several encapsulation procedures have been proposed. Silica coating has particular advantages in various carriers for coatings and shells. Theoretically and experimentally, a silica shell provides better chemical and thermal stability to magnetic NPs by establishing equilibrium between the attractive and repulsive forces. Silica-based magnetic nanoparticles have the following attractive features: (i) sufficient binding strength between the active species and magnetic support to enable recycling; (ii) good chemical inertness of the magnetic support; (iii) high saturation magnetization to facilitate magnetic separation; (iv) soft ferromagnetism for redispersion; (v) low cost, ready availability, mechanical robustness and straightforward synthesis; (vi) a quasi-homogeneous dispersion can be achieved.

Almost all the silica-based core-shell NPs are synthesized using sol-gel chemistry, historically known as the Stöber method (**Figure 1.11**).[21] This wet chemical method entails the hydrolysis and subsequent condensation of silicon alkoxides or silicon halides in alcohol, water or a mixture thereof in the presence of a base catalyst, such as ammonia, to afford uniform colloidal microspheres. The Si-OR bonds hydrolyze readily with water to form Si-OH groups. These silanol groups can then condense with each other to form polymeric structures with very stable siloxane Si-O-Si bonds. This allows surface treatment, coupling and assembling of very dissimilar surfaces chemically, as between inorganic and organic materials. Both particle size and distribution are important parameters in the synthesis and subsequent applications of nanoparticles. The increase in particle size, for example, leads to the decrease of the specific area. However, these important factors can be controlled by selectively choosing the reaction media and the physical parameters of the reaction such as temperature, reactant concentration and pH of the media.

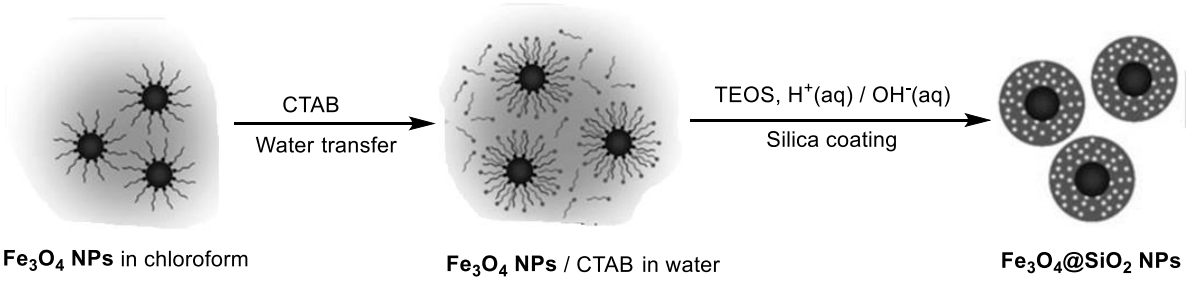

Figure 1.11 Schematic representation of the synthetic procedure for magnetite/mesoporous silica core-shell

The effect of pH on the particle size depends mainly on the reaction mechanism involved. This is especially true when H^+ or OH^- ions are directly involved in the reaction. In the case of the sol-gel process, the condensation step can be realized either in basic or acidic medium. When the pH of the reaction is acidic, the condensation reaction is slower than the hydrolysis reaction, leading to the formation of microporous gel containing the nanoparticles. On the other hand, in basic conditions the silicates grow around Fe_3O_4 germs, as the Fe_3O_4 serve as nuclei for the NPs formation. In addition, the catalyst's quantity, H^+ or OH^- ions, is a key parameter for the shell formation. A shell of silica nanoparticles is readily formed when the amount of catalyst is high enough during the synthesis. A low quantity of catalyst can cause problems in the homogeneity of the silica shell.

The amount of organosilanes has an impact on the mean size of the silica shell, and hence, on the size of the core-shell NP. Insufficient quantity of precursor can affect the colloidal stability of the dispersion, by not reaching a total coverage of iron oxide NPs. During this process, a form of rosary is created with connecting iron oxide NPs and not distinct core-shell NPs.

The nature of the synthesis medium can also have a significant effect on the quality of the synthesized core-shell NPs. In order to have enough electrostatic repulsion, the medium must be relatively polar. The sol-gel synthesis is carried out in a mixture of water/ethanol with every solvent contributing to the synthesis. Water can affect different parameters during the synthesis if the volume is not ideally adjusted. As a solvent with high dielectric constant, it stabilizes the core-shell MNPs and facilitates the individual coverage of each iron oxide NP separately. When the quantity is too low, aggregation is observed, leading to micrometric sized nanoparticles. Indeed, the quantity of water is proportional to the concentration of iron oxide NPs introduced; if one of them is increased, the other should follow this augmentation. However, it is important to mention that a high amount of water increases the speed of hydrolysis of organosilanes, as mentioned before. A high speed of hydrolysis can evoke the condensation of organosilanes in bulk, thus the formation of pure silica particles can occur. The addition of ethanol can assist in solving this problem by decreasing the speed of the hydrolysis.

An important advantage of silica coating over iron oxide nanoparticles is the well-known surface chemistry and broad spectrum of functional groups for modifying the silica surface to give the desired properties. Surface functionalization allows control over the interactions

between the NPs and various chemical systems, which is essential for the effective utilization of these nanomaterials for different applications. The functionalization of magnetic core-shell silica nanoparticles can be performed in a similar way as we have described for the functionalization of MSNs. There are two main methods: a) incorporation of functional groups *via* sol-gel methodology, b) surface functionalization, which includes b1) post-grafting (the reaction of an organosilane or organic molecule directly with the silanol groups on the surface); b2) post-modification (chlorination of the silica surface followed by reaction of the Si-Cl bonds with an appropriate functional molecule/reactant; modification of a previously grafted organic molecule containing a functional group by a suitable organic reaction).

1.8 Characterization methods

The range of characterization methods used in the analysis of the composition, the molecular and nanometric structure as well as the morphological parameters of silica nanoparticles is quite large. It is very important to explain different analytical techniques of silica nanoparticles, because some of them are not commonly used in the general organic chemistry, but they are helpful to understand the activity of the functionalized silica materials.[245] Chemical analyses can provide the information about the amount of organic fragments loaded in the material. Physical parameters such as surface area, pore size distribution, material morphology or texture are very important in catalysis, as they affect the reagent and product diffusion or the accessibility of the catalytic center. The following is a brief summary of different methods generally used for characterization of silica nanoparticles: X-ray diffraction, nitrogen physisorption, scanning electron microscopy (SEM) and transmission electron microscopy (TEM) are used to investigate the porous structure and the morphology of the nanomaterials. Additionally, dynamic light scattering (DLS) is employed to investigate silica nanoparticles regarding their size and agglomeration behavior. Furthermore, zeta potential measurements are used to investigate the surface properties of the silica nanoparticles. Infrared spectroscopy (IR) gives detailed information about the chemical bonding of the nano-structured materials. Thermogravimetric analysis (TGA) evaluates the number of organo-functionalities introduced in the materials. Solid-state NMR spectroscopy has significantly advanced the understanding of stationary phase materials by providing complementary information on chemically modified surfaces.

1.8.1 Solid state ^{13}C CP MAS and ^{29}Si CP MAS NMR spectroscopy

By combining cross polarization with magic angle rotation, a high-resolution spectrum of a rigid solid can be obtained, which is called cross polarization magic angle rotation (CP MAS) technology. The ^{29}Si CP MAS NMR spectroscopy confirms the covalent bond between silicon and the organic component and gives information about the degree of condensation in the silica nanoparticles. During the sol-gel process, a great variety of silicon species is formed containing different numbers of Si-O-Si bonds (**Figure 1.12**). These species lead to structures giving signals with different chemical shifts in the ^{29}Si CP MAS spectrum depending on the substitution pattern around the silicon atom **(Figure 1.13)**.

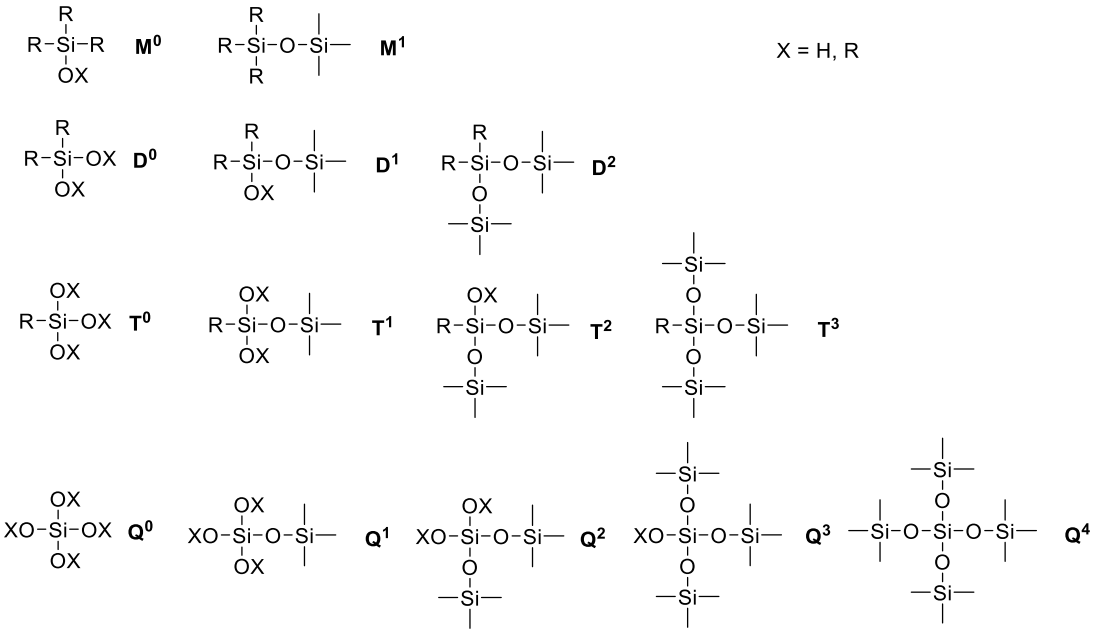

Figure 1.12 Silicon environments and their corresponding label in the ^{29}Si CP MAS NMR spectroscopy

In the ^{29}Si CP MAS NMR spectrum, signals are divided into four categories: M, D, T and Q. The categorie M represents monofunctional silicon coming from monoalkoxysilanes, D denotes the silicon species derived from dialkoxysilanes, T implies units stemming from trialkoxysilanes, and Q stands for those derived from tetralkoxysilanes. In addition, numeric superindices are used to indicate the degree of condensation. For instance, the superindex “0” means no condensation occurred, and “1” implies only one alkoxy group has condensed, “2” suggests two alkoxy groups have condensed and so on. The nature of the organic moiety (alkyl, aryl, …) or the catalyst used in the sol-gel process can also affect the chemical shift.

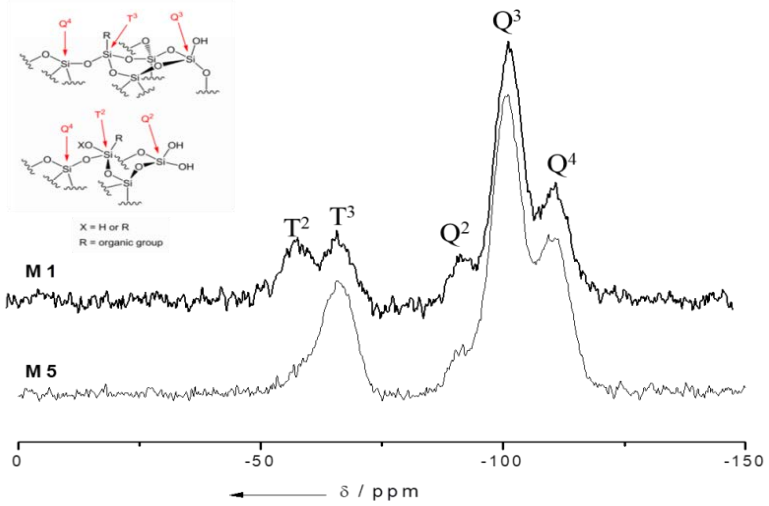

Figure 1.13 Example of ^{29}Si CP MAS NMR of mesoporous silica nanoparticles **M1** and **M5** (see ***Chapter 2***)

The ^{13}C CP MAS NMR spectroscopy is quite useful to check that the organic functionality has been loaded in the organosilica nanoparticles. It is similar with the common ^{13}C NMR of the silylated monomer in solution, but the peak shape becomes broader (**Figure 1.14**). It provides qualitative information for the identification of organic functional groups. Unlike the spectrum recorded in solution, signals of different carbon atoms easily overlap.

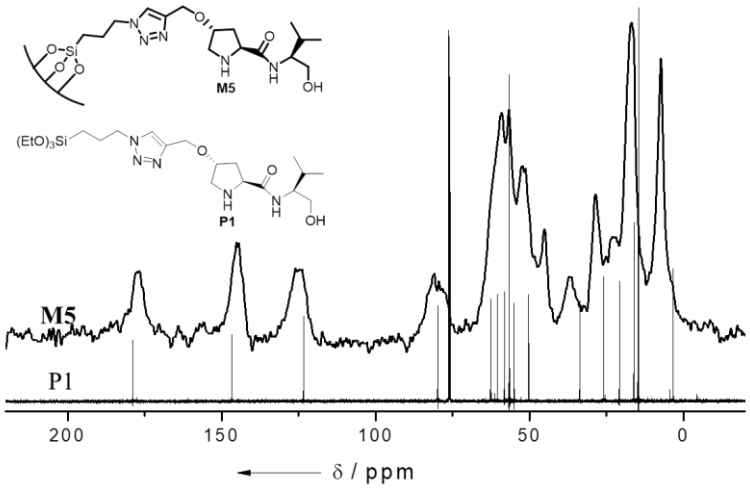

Figure 1.14 Comparison of ^{13}C NMR of precursor **P1** and ^{13}C CP MAS NMR of material **M5** (see ***Chapter 2***)

It must be considered that solid state ^{13}C and ^{29}Si NMR suffer from low sensitivity.[246] Functionalized silicon sites T^n are too diluted to be readily observed in the ^{29}Si CP MAS NMR in some cases. Generally, for high dilution of the organic component in the organosilica nanoparticles (tetraalkoxysilane/organotrialkoysilane ratio higher than 10), the spectrum provides mainly information about the Q^n and the proton-rich sites (Si-OH). The

^{13}C CP MAS NMR suffers from similar drawbacks and therefore for the high dilution of organic component, little evidence of the organic moiety incorporation is often obtained.

1.8.2 Elemental analysis

Elemental analysis is a process where a sample of some material is analyzed for its elemental and sometimes isotopic composition. It can be qualitative (determining which elements are present), and it can be quantitative (determining how much of each are present). The carbon, hydrogen, heteroatoms (nitrogen, sulfur, chlorine, bromine or iodine) contained in the materials can be analyzed by combustion. The amount of other elements such as silicon or metals can be determined by inductively coupled plasma (ICP), atomic absorption or atomic emission analyses. The theoretical and experimental contents can be considerably different, and frequently less organic functionality than expected is loaded in the organosilica nanoparticles. This may be caused by the fact that the hydrolysis rate is lower for organotrialkoxysilanes with respect to tetraalkoxysilanes. Within the group of tetraalkoxysilanes, the hydrolysis rate decreases in the following order: tetramethoxysilane (TMOS) > tetraethoxysilane (TEOS) > tetrapropoxysilane (TPOS) > tetrabutoxysilane (TBOS). The degree of condensation also contributes to the difference between theoretical and experimental values. The discrepancy may also come from traces of surfactant or residual high-boiling point solvent in the material. Therefore, the content of the organic precursor in the organosilica nanoparticles can be ascertained by elemental analysis of the characteristic elements. In our work, the loading of the catalyst and anti-inflammatory drug has been determined by elemental analysis of nitrogen.

1.8.3 Fourier Transform Infrared spectroscopy (FTIR)

Fourier transform infrared spectroscopy (FTIR) is an important technique used to obtain an infrared spectrum of absorption of the materials.[247] It allows the qualitative identification of the functional groups (such as carbonyl, nitrile, sulfonyl, isonitrile, amine, azide) present within the sample and offers the potential to study the properties of the chemical bonds in a molecule by exciting vibrational transitions.[248-250] However, the use of this technique is limited to the organosilica nanoparticles with low organic fragment dilution in the inorganic framework. When the ratio tetraalkoxysilane/organosilane is higher than 10, the IR spectrum is dominated by Si-O-Si vibration bands (around 1000 cm^{-1}), surface adsorbed water and silanol species (3500-3200 cm^{-1}).[251]

1.8.4 Surface area analysis

Surface area is a physical property that impacts the quality and character of solid phase materials. Materials with identical physical dimensions may exhibit entirely different performance profiles based on variations in the physical surface area of the materials. Surface area measurement is an important analysis used in many industries for catalysts, zeolites, MOFs, batteries, absorbents, artificial bone, pharmaceuticals, metal powders. Gas adsorption-desorption analysis is commonly used for surface area measurements, the average pore size and the pore size and pore volume distributions of a variety of different solid materials. *Adsorption* is the process in which atoms or molecules are weakly bound to the surface of a solid and form a layer at the interface. Its counterpart, *desorption* denotes the reverse process, in which the number of adsorbed atoms or molecules decreases.

N_2-sorption analyses are performed at 77 K from thoroughly degassed samples. The adsorption isotherm is built by adding controlled doses of nitrogen gas on the cold sample and monitoring the corresponding relative pressure in the surrounding environment (p/p^0, p^0 represents the saturation pressure of the nitrogen at the temperature of the measurement). When p/p^0 reaches 1, spontaneous liquefaction of N_2 occurs. Under these conditions, consecutive molecular layers of nitrogen can be adsorbed on the solid surface. In a monolayer adsorption mode, all the adsorbed molecules are in contact with the surface layer of the sample, whereas in a multilayer adsorption, the adsorption space accommodates more than one layer of molecules, so that not all adsorbed molecules are in direct contact with the surface layer of the sample. The surface area of a given sample, such as organosilica nanoparticles, may be calculated based on the adsorbed amount of nitrogen from monolayer adsorption.

The graphic representing the relationship, at constant temperature, between the amount adsorbed and the equilibrium pressure of the gas is known as *the adsorption-desorption isotherm.*[252] In some cases, a hysteresis loop appears when adsorption and desorption curves do not coincide. In 1940, S. Brunauer, L. S. Deming, W. E. Deming and F. Teller classified isotherms in five different types.[253] In 1985, the international Union of Pure and Applied Chemistry (IUPAC) expanded this classification to six types. [254-255] However, over the past 30 years various new characteristic types of isotherms have been identified and shown to be closely related to particular pore structures. M. Thommes and colleagues refined the original

IUPAC classification of physisorption associated hysteresis loops.[261] The updated classification of physisorption isotherms is shown in **Figure 1.15**.[256-258]

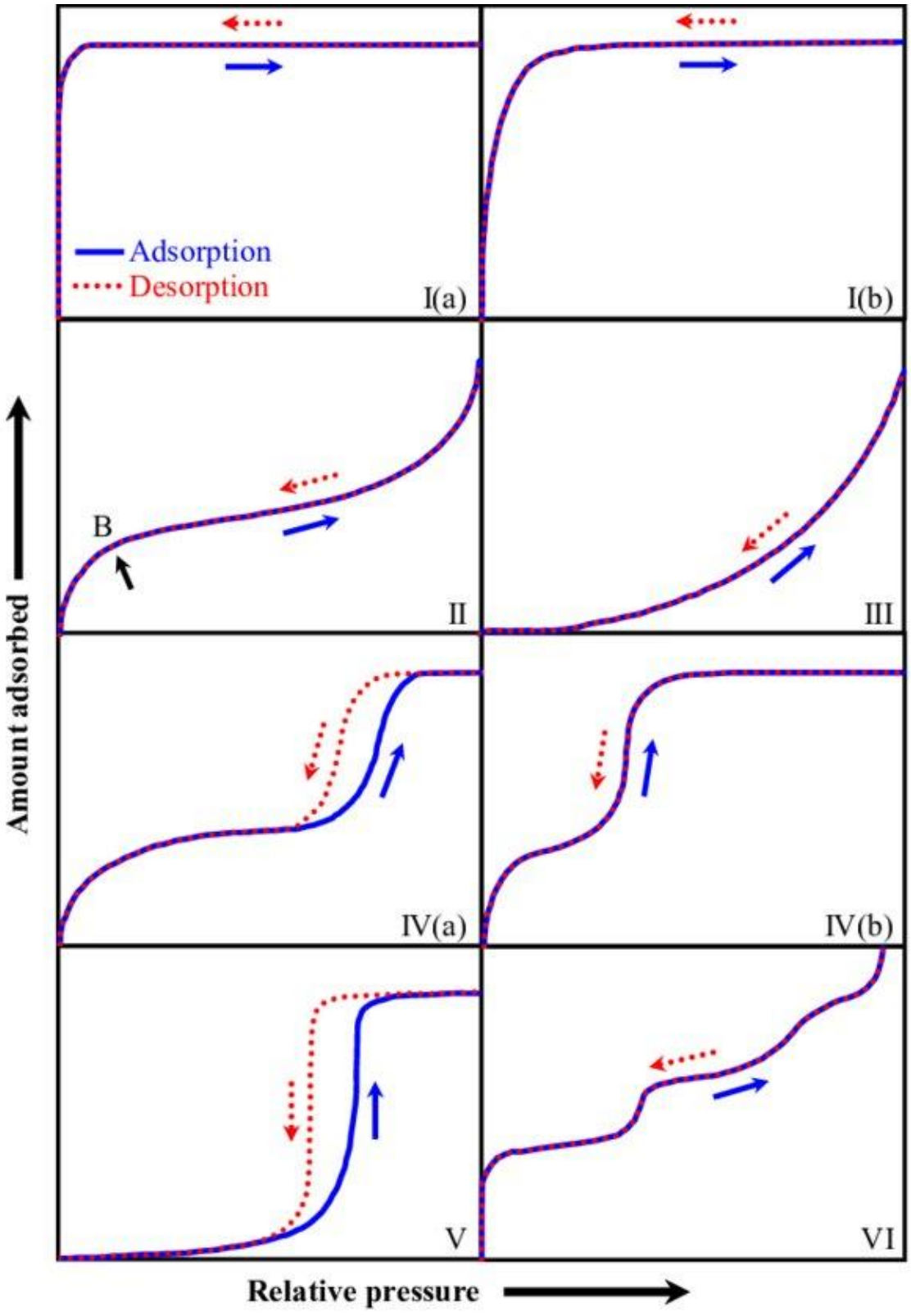

Figure 1.15 Physisorption isotherms classification (©2015 IUPAC, B symbolizes monolayer formation).[256-25]

Reversible *Type I* isotherms are given by microporous solids having relatively small external surfaces (such as some activated carbons, molecular sieve zeolites and certain porous oxides). A *Type I* isotherm is concave to the p/p^0 axis and the amount adsorbed approaches a limiting value. This limiting uptake is governed by the accessible micropore volume rather than by the internal surface area. A steep uptake at very low p/p^0 is due to enhanced adsorbent-adsorptive interactions in narrow micropores (micropores of molecular dimensions), resulting in micropore filling at very low p/p^0. For nitrogen and argon adsorption at 77 K and 87 K, *Type I (a)* isotherms are given by microporous materials having mainly narrow micropores (of width < ~1 nm); *Type I (b)* isotherms are found with materials having pore size distributions over a broader range including wider micropores and possibly narrow mesopores (< ~2.5 nm). Reversible *Type II* isotherms are given by the physisorption of most gases on nonporous or macroporous adsorbents. The shape is the result of unrestricted monolayer-multilayer adsorption up to high p/p^0.[259] Some mesoporous materials also give this adsorption curve, where a monolayer adsorption is observed at low relative pressure and saturation at high relative pressure, but without hysteresis loop. The interaction between adsorbate and adsorbent is strong. Point B represents the beginning of the almost linear middle section of the isotherm. It is often taken to indicate the stage at which monolayer coverage is complete and multilayer adsorption is about to begin. If the knee is sharp, point B usually corresponds to the completion of monolayer coverage. A more gradual curvature (i.e., a less distinctive point B) is an indication of a significant amount of overlap of monolayer coverage and the onset of multilayer adsorption. The thickness of the adsorbed multilayer generally appears to increase without limit when $p/p^0 = 1$. Type *III* isotherms are observed in systems with weak adsorbate-adsorbent interactions. Type *III* isotherm is not common, it is convex to the x axis over its entire range.[259-260] It also indicates unrestricted multilayer formation process. It forms because lateral interactions between adsorbed molecules are strong in comparison to interactions between the adsorbent surface and adsorbate. In contrast to a *Type II* isotherm, the amount adsorbed remains finite at the saturation pressure ($p/p^0 = 1$). *Type IV* isotherms are given by mesoporous adsorbents (such as many oxide gels, industrial adsorbents and mesoporous molecular sieves). The adsorption behaviour in mesopores is determined by the adsorbent-adsorptive interactions and also by the interactions between the molecules in the condensed state. In this case, the initial monolayer-multilayer adsorption on the mesopore walls, which takes the same path as the corresponding part of a *Type II* isotherm, is followed by pore condensation. Pore condensation is the phenomenon whereby a gas condenses to a liquid-like phase in a pore at a pressure p less than the saturation pressure p^0 of the bulk

liquid.[261-262] A typical feature of *Type IV* isotherms is a final saturation plateau, of variable length (sometimes reduced to a mere inflexion point). In the case of a Type *IV* (a) isotherm, capillary condensation is accompanied by hysteresis. This occurs when the pore width exceeds a certain critical width, which is dependent on the adsorption system and temperature (for nitrogen and argon adsorption in cylindrical pores at 77 K and 87 K, respectively, hysteresis starts to occur for pores wider than ~ 4 nm).[261,263] With adsorbents having mesopores of smaller width, completely reversible Type IVb isotherms are observed. In principle, Type *IV* (b) isotherms are also given by conical and cylindrical mesopores that are closed at the tapered end. In the low p/p^0 range, the *Type V* isotherm shape is very similar to that of *Type III* and this can be attributed to relatively weak adsorbent-adsorbate interactions. At higher p/p^0, molecular clustering is followed by pore filling. For instance, *Type V* isotherms are observed for water adsorption on hydrophobic microporous and mesoporous adsorbents. The reversible stepwise *Type VI* isotherm is representative of layer-by-layer adsorption on a highly uniform nonporous surface. The step-height now represents the capacity for each adsorbed layer, while the sharpness of the step is dependent on the system and the temperature. Amongst the best examples of *Type VI* isotherms are those obtained with argon or krypton at low temperature on graphitized carbon blacks.

In our work, focus will be placed on Type I and Type IV isotherms which are associated with adsorption in microporous (containing pores < 2 nm in width) and mesoporous (containing pores 2-50 nm in width) materials respectively. Furthermore, we will focus on nitrogen at 77 K isotherms, which are widely used in industrial and research settings for surface area and pore size characterization. For structural characterization of primarily macroporous materials (containing pores > 50 nm in width), alternative techniques, such as mercury porosimetry, should be considered.[264]

Some silica materials show adsorption isotherms as a combination of *types* I-VI. The micropores existing in some mesoporous materials can be recognized in type IV isotherms, resulting in a higher adsorption at low relative pressure. The hysteresis appearing in the multilayer range of isotherms is generally associated with capillary condensation in mesoporous structures. This phenomenon occurs when the gas is first adsorbed in pores, where it can condense to the liquid state upon enough gas supply. Many different shapes of hysteresis loops have been reported, but the main types are shown in **Figure 1.16**. Types H1, H2(a), H3 and H4 were identified in the original IUPAC classification of 1985, [254-255] which

is now extended in the light of more recent findings. Each of these six characteristic types are closely related toparticular features of the pore structure and underlying adsorption mechanism.[256]

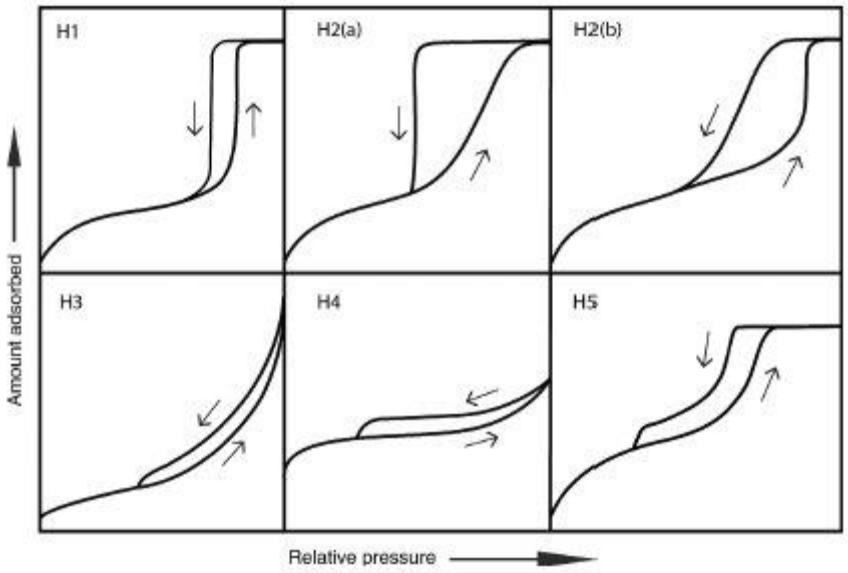

Figure 1.16 Types of hysteresis loops according to the IUPAC.

The type H1 loop is found in materials which exhibit a narrow range of uniform mesopores, as for instance in templated silicas, such as MCM-41, MCM-48, SBA-15, some controlled pore glasses and ordered, mesoporous carbons. Usually, network effects are minimal, and the steep, narrow loop is a clear sign of delayed condensation on the adsorption branch. However, type H1 hysteresis has also been found in networks of ink-bottle pores where the width of the neck size distribution is comparable to the width of the pore/cavity size distribution (e.g., 3DOm carbons[261]). Hysteresis loops of type H2 are given by more complex pore structures in which network effects are important. The very steep desorption branch, which is a characteristic feature of H2(a) loops, can be attributed either to pore-blocking/percolation in a narrow range of pore necks or to cavitation-induced evaporation. H2(a) loops are for instance given by many silica gels, some porous glasses (e.g., vycor) as well as some ordered mesoporous materials (e.g., SBA-16 and KIT-5 silicas). The type H2(b) loop is also associated with pore blocking, but the size distribution of neck widths is now much larger. Examples of this type of hysteresis loops have been observed with mesocellular silica foams and certain mesoporous ordered silicas after hydrothermal treatment. There are two distinctive features of the type H3 loop: (i) the adsorption branch resembles a type II isotherm (ii) the lower limit of the desorption branch is normally located at the cavitation-induced p/p^0.

Loops of this type are given by non-rigid aggregates of plate-like particles (e.g., certain clays) but also if the pore network consists of macropores which are not completely filled with pore condensate. The H4 loop is somewhat similar, but the adsorption branch is now a composite of types I and II, the more pronounced uptake at low p/p^0 being associated with the filling of micropores. H4 loops are often found with aggregated crystals of zeolites, some mesoporous zeolites, and micro-mesoporous carbons. Although the type H5 loop is unusual, it has a distinctive form associated with certain pore structures containing both open and partially blocked mesopores (e.g., plugged hexagonal templated silicas). As already indicated, the common feature of H3, H4 and H5 loops is the sharp step-down of the desorption branch. Generally, this is located in a narrow range of p/p^0 for the particular adsorptive and temperature (e.g., at $p/p^0 \sim 0.4$-0.5 for nitrogen at temperatures of 77 K).

The curve shape gives information about the pore size (p/p^0 from the hysteresis point) and the pore volume (the area limited by adsorption and desorption curves). There are several mathematical transformations which have been developed to calculate the specific surface from the adsorption isotherm data. The most common models are named after their developers: Langmuir (Langmuir isotherms) and Brunauer-Emmett-Teller (BET isotherms).[265-266]

The Langmuir interpretation is the simplest characterization method and is based on the approximations that (i) the adsorption is leading at most to monolayer formation, (ii) the surface is uniform and (iii) all binding sites are equal. Furthermore, the ability of a molecule to bind at a specific surface site is independent of the occupancy of neighboring binding sites (no interactions between adsorbed molecules). The Langmuir equation is shown as **Equation 1.1**.

$$\frac{n}{n_m} = \frac{K \cdot p}{1 + K \cdot p}$$

Equation 1.1 Langmuir equation n: amount of adsorbate, n_m: capacity of one monolayer, p: pressure, $K = k_{ad}/k_{de}$

Brunauer-Emmett-Teller (BET) analysis is the most widely used method that provides precise specific surface area evaluation of materials by nitrogen multilayer adsorption measured as a function of relative pressure using a fully automated analyser.[266] This technique encompasses external area and pore area evaluations to determine the total specific surface area in m^2/g

yielding important information in studying the effects of surface porosity and particle size in many applications. However, the BET method is not suitable to measure the microporous materials. The BET equation can be expressed as follows (**Equation 1.2**).[266-267]

$$\frac{n}{n_m} = \frac{C \cdot \frac{p}{p^0}}{(1 - \frac{p}{p^0})(1 + C - \frac{p}{p^0})}$$

Equation 1.2 BET equation n: amount of adsorbate, n_m: capacity of one monolayer, C: BET constant, p: equilibrium pressure, p^0: saturation vapor pressure of adsorbate

Sorption data are further applicable to determine the pore volume and the pore size distribution of an analyzed sample. This method is based on the change of physical properties of gas molecules when being adsorbed in a porous material. The pore size distribution function is a very important characteristic of porous materials. The thermodynamic relation between the reduced pore radius r_k and the relative vapor pressure p/p^0 is described by Kelvin's equation (**Equation 1.3**).

$$RT \ln \frac{p^0{}_k}{p_0} = -\frac{2\gamma V_m}{r_c}$$

Equation 1.3 Kelvin equation R: gas constant, T: temperature, $p^0{}_k$: equilibrium pressure, p^0: saturation vapor pressure, γ: surface tension, V_m: molar volume, r_c: reduced radium

Kelvin's equation frequently leads to inexact results as it tends to underestimate the pore size. An enhancement by Barrett-Joyner-Halenda (BJH) corrects the Kelvin radius r_k by including the thickness t of the monolayer which is already adsorbed to the sample surface.[16] BJH analysis is widely utilized to determine pore area and specific pore volume using adsorption and desorption techniques.[268] However, this method is limited, as it disregards the impact of surface curvature on the formation of the film, it is only derived for cylindrical pores, it assumes formation of homogenous films and it does not explicitly account for surface forces between the film and the surface. Due to these limitations the BJH method is known to underestimate the pore size, especially for small pores. An approach which combines density functional theory (DFT) with the grand canonical Monte Carlo (GCMC) simulation method is frequently applied and usually gives the most exact results. In order to obtain the equilibrium density profile via DFT, the corresponding grand potential is minimized for a pore system in equilibrium with a bulk phase. The function contains terms describing attractive as well as

repulsive solid-fluid and fluid-fluid interactions. Hypothetically, two different DFT methods exist, but in contrast to the applied non-local density functional theory (NLDFT) the local density functional theory (LDFT) is not applicable for narrow pores. The reason is that it cannot characterize short-range correlations inside the pores.[269] NLDFT in combination with Monte Carlo simulations quite reliably describes the local fluid structure near curved solid walls.

1.8.5 Electron Microscopy

Electron Microscopy is a powerful tool for obtaining high resolution images of silica nanoparticles. The material morphology can be studied by Scanning Electron Microscopy (SEM) and Transmission Electron Microscopy (TEM).

Scanning electron microscopy (SEM) can provide the particle morphology of the material by scanning the surface of a sample with a focused beam of electrons. The electron beam is scanned in a raster scan pattern, and the beam's position is combined with the detected signal to produce an image. It can achieve resolution better than 1 nanometer. A high magnification microscope can use a focused scanned electron beam to produce high-resolution images of a specimen. The X-rays emitted are characteristic for the elements in the top few μm of the sample. After the primary electron beam interacts with the sample, ionized atoms can relax by electron shell-to-shell transitions, which lead to either X-ray emission or Auger electron ejection. Images obtained by SEM provide information on the physical properties of hybrid materials including surface topography, texture, particle shape, size of material and composition.[270] **Figure 1.17** shows examples of SEM images of different types of silica nanoparticles prepared in this work.

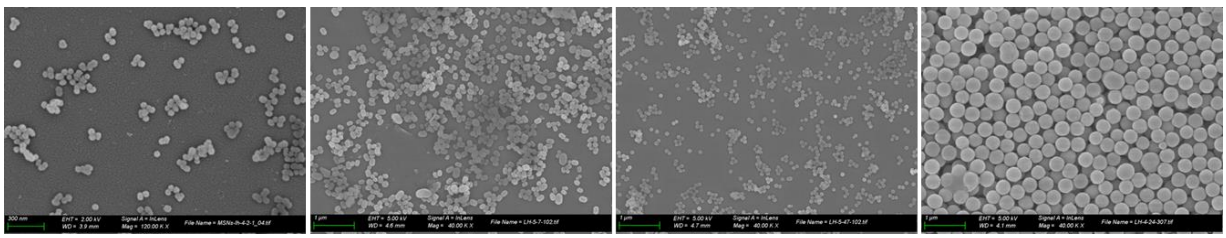

Figure 1.17 SEM images of different silica nanoparticles

SEM can make several types of signals, which include secondary electrons, back scattered electrons, characteristic X-rays and light (cathodoluminescence). All these signals come from the beam of electrons striking the surface of the specimen and interacting with the sample at

or near its surface. The most common SEM mode is detection of secondary electrons emitted by atoms excited by the electron beam. It can produce very high-resolution images of the sample surface, revealing details about 1 to 5 nm in size. Due to the way these images are created, SEM micrographs have a very large depth of focus yielding a characteristic three-dimensional appearance useful for understanding the surface structure of the sample. Characteristic X-rays are the second most common imaging mode for SEM. X-rays are emitted when the electron beam removes an inner shell electron from the sample, causing a higher energy electron to fill the shell and give off energy. These characteristic X-rays are used to identify the elemental composition of the sample. Back-scattered electrons (BSE), which come from the sample, may also be used to form an image. BSE images are often used in analytical SEM along with the spectra made from the characteristic X-rays as clues to the elemental composition of the sample.

For conventional imaging, SEM requires that specimens be conductive for the electron beam to scan the surface and that the electrons have a path to ground. All samples are generally mounted on some sort of holder. Nonconductive solid specimens are coated with a layer of conductive material. An ultrathin coating of electrically conducting material such as gold, gold/palladium alloy, platinum, tungsten or graphite is deposited on the sample either by low vacuum sputter coating or by high vacuum evaporation. This is done to prevent the accumulation of static electric charge on the specimen during electron irradiation. Another reason for coating, even when there is more than enough conductivity, is to improve contrast and resolution, a situation most common when using samples with low atomic number.

The spatial resolution of the SEM techniques depends on various parameters, most of them are instrument related. Typically, modern full-sized SEM provide resolution between 1 and 20 nm, whereas desktop systems can provide a resolution of 30 nm or more, which is much lower than that of transmission electron microscopy (TEM), but SEM has some advantages compared with TEM. For example, a quite large area of the specimen can be imaged, bulk materials can be used as samples and, as mentioned, a variety of analytical modes is available for measuring the composition and nature of the specimen.

Transmission electron microscopy (TEM) is a microscopy technique in which a beam of electrons is transmitted through a specimen to form an image. With this technique, mesoporous channels located inside the material can be seen in the structured materials, as

well as their structural organization.[271] **Figure 1.18** shows examples of TEM images of different types of silica nanoparticles that our research focused on.

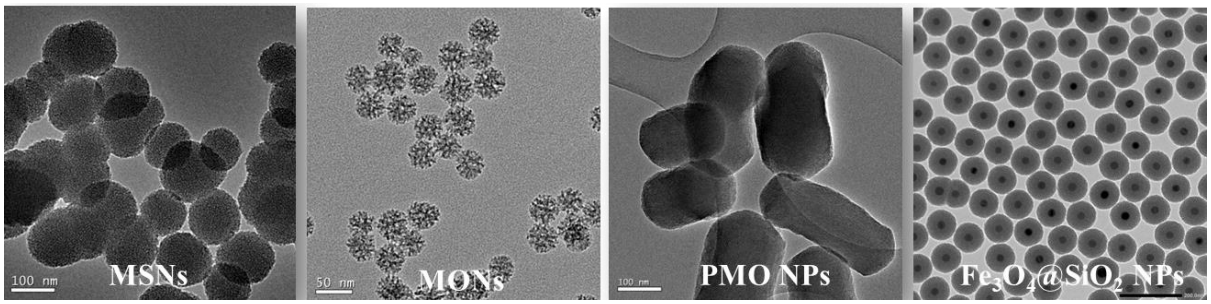

Figure 1.18 TEM images of different types of silica nanoparticles

Transmission electron microscopy (TEM) images are produced by focusing a beam of electrons onto a very thin specimen which is partially transmitted by those electrons and carries information about the inner structure of the specimen. The image is recorded by hitting a fluorescent screen, photographic plate, or light sensitive sensor such as a CCD camera. The latter has the advantage that the image may be displayed in real time on a monitor or computer.

It is often difficult in TEM to receive details of a sample because of low contrast, which is based on the weak interaction with the electrons. Particularly, samples that have a high content of organic components often reveal this problem, which can be partially overcome by using stains such as heavy metal compounds. The dense electron clouds of the heavy atoms interact strongly with the electron beam. However, sometimes the organic components of the sample are not detected because they decompose in the electron beam; this can be avoided using cryogenic microscopy, which keeps the specimen at liquid nitrogen or liquid helium temperatures (cryo-TEM).[272]

Further information about the sample can be obtained by analytical TEM. For example, the elemental composition of the specimen can be determined by analyzing its X-ray spectrum or the energy-loss spectrum of the transmitted electrons. Additionally, if the material observed is crystalline, diffraction patterns are obtained that give information about the crystal orientation and very powerful instruments can even investigate the crystal structure.Modern high-resolution TEM (HRTEM) can go down to a resolution <100 pm. One of the major limitations of TEM is the extensive sample preparation, which makes TEM analysis a relatively time-consuming process with a low throughput of samples.

1.8.6 Powder X-ray Diffraction (P-XRD)

The powder X-ray diffraction (P-XRD) is a rapid analytical technique which can be performed to characterize nanostructures and to gain information about the crystallinity of the investigated material. Additionally, the size of the nanomaterials, information about the pore structure, pore width and pore wall thickness can be obtained.[273] The P-XRD technique can measure the organization of the mesoporous silica materials. It obtains the diffraction pattern of the material and then plots the intensity relative to the detector angle 2θ. Under irradiation, the interaction of the repeating planes of a sample with an incident beam is described by Bragg's law (**Equation 1.4** and **Figure 1.19**).[274]

$$\text{Sin } \theta = n \lambda/2d$$

Equation 1.4 Bragg's law θ: the angle between the incident beam and the plane, n: the integer, λ: the incident beam wavelength, d: the spacing between atom layers

The distance between planes can be determined from the incident and the measured dispersion angles. Normally, P-XRD plot represent the intensity I with respect to a parameter called q, which is calculated as follow $q = 4 \pi \text{Sin } \theta / \lambda$. The relationship between q and d is the following: $q = 2\pi/d$.

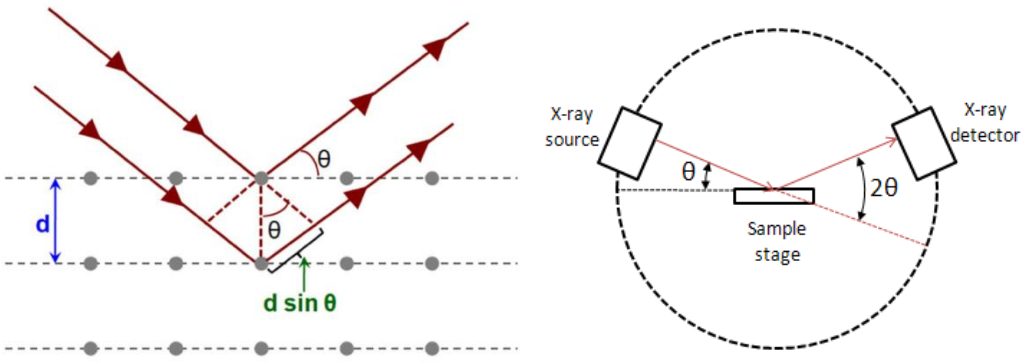

Figure 1.19 Schematic representation of Bragg's law

When a material is organized, well-defined peaks can be observed in the plot and from their pattern (**Figure 1.20**), it is possible to know the type of organization (hexagonal, lamellar, cubic, worm-like, …). On the other hand, amorphous materials do not allow obtaining clear signals.

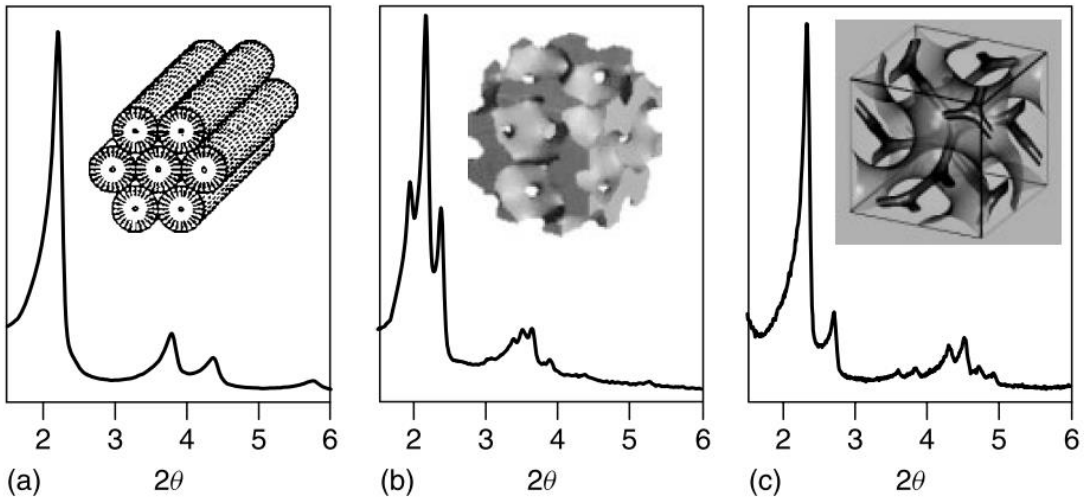

Figure 1.20 Examples of powder X-ray diffraction patterns obtained for ordered mesoporous silica mesophases, shown with their pore topology. (a) MCM-41 with p6mm symmetry; (b) SBA-1 with $Pm\bar{3}n$ symmetry; (c) MCM-48 with $Ia\bar{3}d$ symmetry.

Small-angle X-ray scattering (SAXS) is a technique where the source for the scattering of the X-rays is the inhomogeneities in the sample within the nanometer range. It is useful to withdraw information on the network microstructure, regarding the morphology of the sample.[275] SAXS patterns are recorded at very low angles (typically < 3-5 °). In this angular range, information about the shape and size of the inhomogeneities (for example, clusters or nanoparticles in an organic matrix) and their distances is obtained. Furthermore, pores can also be defined as inhomogeneities, therefore, SAXS is also used to characterize regularly ordered porous materials. The resolution of SAXS experiments is strongly dependent on the equipment. The highest resolution is obtained at beamlines at synchrotrons.

In general, X-ray diffraction peaks for mesoporous silica materials appear in the low-angle range as the pore diameter is rather large in comparison to interatomic distances; therefore, small angle X-ray scattering (SAXS) ranging from 2θ = 0.1-10 ° is used. X-ray radiation is emitted from a metal source, typically copper, with a characteristic wavelength (Cu-Kα is 1.54182 Å).[276] In order to obtain monochromatic X-ray radiation for X-ray diffraction measurements, monochromators or blocking filters are used.[277] The wavelength of the monochromatic X-rays is in the Ångstrøm range, which is the same order of magnitude as interatomic distances in solids.

1.8.7 Thermogravimetric analysis (TGA)

Thermogravimetric analysis (TGA) is a widely used method of thermal analysis in which changes in physical and chemical properties of materials are measured as a function of increasing temperature (with constant heating rate), or as a function of time (with constant temperature and/or constant mass loss). TGA can provide information about physical phenomena, such as second-order phase transitions, including vaporization, sublimation, absorption and desorption. Besides, it can provide information about chemical phenomena, including chemisorption, desolvation (especially dehydration), decomposition, and solid-gas reactions, such as oxidation or reduction.[278] TGA is commonly employed with respect to hybrid materials and silica nanoparticles to investigate the thermal stability (degradation temperatures), the amount of inorganic component, which usually stays until the end of the measurement due to its high thermal resistance, and the level of absorbed moisture or organic volatiles in these materials. Typically, TGA plots show the weight lost in relation to the temperature. Typical ranges that can be distinguished are the loss of moisture and absorbed solvents up to 150 °C, the decomposition of organic components between 300 °C and 500 °C. Usually the measurements are carried out under air or an inert gas.[279] In this technique, a thermogravimetric (TG) curve is recorded, in which the mass is plotted as a function of temperature (T) or time (t) during heating process. The nature of the organic moiety decides the choice of the experimental parameters like the gradient of temperature (typically 5-10 °C/min) or the analyzing atmosphere (air, argon).

Differential scanning calorimetry (DSC) is a thermoanalytical technique in which the difference in the amount of heat required to increase the temperature of a sample and a reference with a well-defined heat capacity is measured as a function of temperature. Both the sample and reference are maintained at nearly the same temperature throughout the experiment. Generally, the temperature program for a DSC analysis is designed in such a way that the sample holder temperature increases linearly as a function of time. The reference sample should have a well-defined heat capacity over the range of temperatures to be scanned.[280]

1.8.8 Dynamic Light Scattering analyses (DLS)

Dynamic light scattering (DLS) is a valuable tool to determine the size of particles and molecules in solution as well as to investigate solution dynamics.[281-282] This technique is highly valuable for the analysis of nanometer-sized particles, typically with diameters between 1-1000 nm. DLS is also referred to as photon correlation spectroscopy (PCS) or quasi-elastic light scattering (QELS).[283] It mainly analyzes time fluctuations by intensity or photon autocorrelation function.

The Brownian motion, which is a random movement of the particles in a liquid caused by constant collisions, is highly correlated to the particle size. Therefore, the particles in solution are in constant, random movement and the interparticle distance changes constantly, and so do the conditions for constructive and destructive interference of scattered light. This results in a time-dependent intensity fluctuation of the scattered light. Since the diffusion of larger particles is slower than that of smaller particles, the intensity of the scattered light will change more slowly for larger particles and aggregates. During DLS measurements, these changes in intensity are recorded over a distinct time and can be evaluated afterwards (**Figure 1.21**).

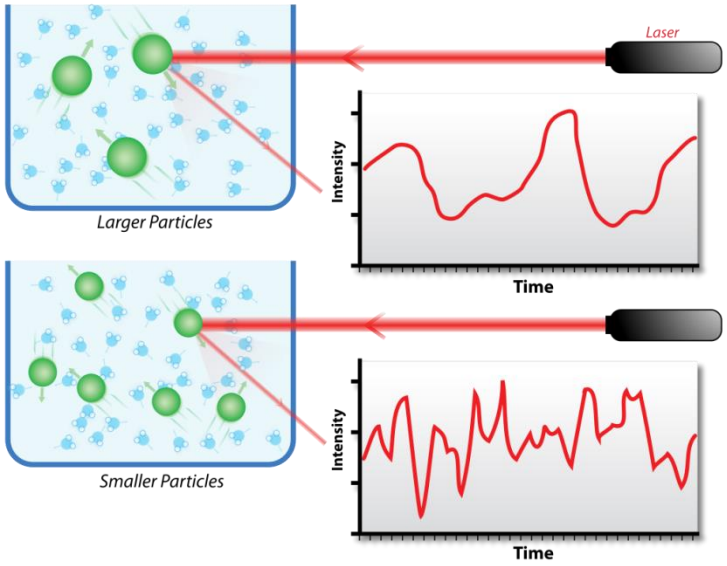

Figure 1.21 Hypothetical dynamic light scattering of two samples: Larger particles on the top and smaller particles on the bottom

DLS measures the hydrodynamic diameter *d(H)* which is a value that is related to the diffusion properties of a particle in a liquid. The translational diffusion coefficient D depends on diverse parameters, including the ionic strength of the suspension, the texture of the

particle surface, and the shape of the particles. Correlation analysis is used to calculate the diffusion coefficient, which is associated with the hydrodynamic diameter of colloidal spherical particles via the Stokes-Einstein equation (**Equation 1.5**):

$$d\,(H) = \frac{kT}{3\pi\eta\,D}$$

Equation 1.5 Stokes-Einstein equation, *d(H)* is the hydrodynamic diameter, *D* is the translational diffusion coefficient, *k* is the Boltzmann's constant, *T* is the temperature, η is the viscosity.

1.8.9 Zeta potential

Zeta potential determination is a significant characterization technology of silica nanoparticles to estimate the surface charge, which can be employed for understanding the physical stability of nanosuspensions (**Figure 1.22**).[284] A large positive or negative value of zeta potential of silica nanoparticles indicate good physical stability of nanosuspensions due to electrostatic repulsion of individual particles. **Table 1.1** shows the level of stability with respect to the zeta potential values.[285] In general, nanoparticles with zeta potential absolute values greater than 30 mV (which can be positive or negative) have high degrees of stability as for they have sufficient repulsive force for physical colloidal stability. On the other hand, a small zeta potential absolute value (positive or negative) can result in particle aggregation and flocculation due to the van der Waals attractive forces between particles, leading to physical instability.[286-288] Along with zeta potential values, other factors such as material properties, presence of surfactants, and solution chemistry also affect the physical stability of obtained nanosuspensions.

Table 1.1 Stability behaviour of a colloid depending on zeta potential

Zeta potential (mV)	Stability behavior
0 to ±5	Rapid coagulation or flocculation
±10 to ±30	Incipient instability
±30 to ±40	Moderate stability
±40 to ±60	Good stability
⩾ ±60	Excellent stability

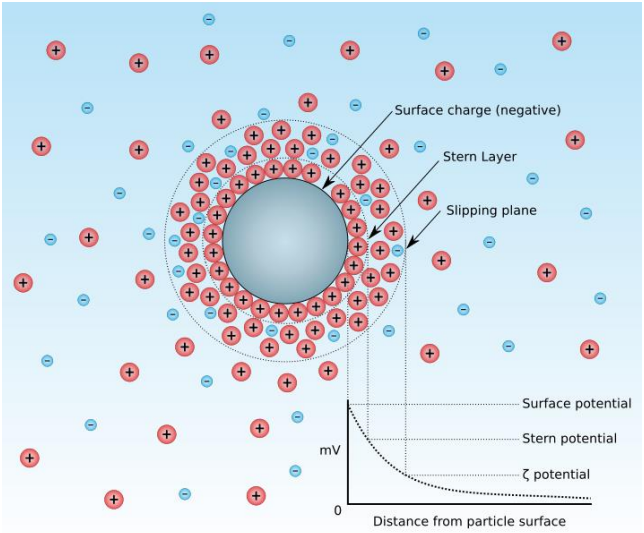

Figure 1.22 Diagram showing the ionic concentration and potential difference as a function of distance from the charged surface of a particle suspended in a dispersion medium.

It is important to consider that the magnitude of the charge on the nanoparticle surface depends on the solution pH.

In order to measure the zeta potential of a sample, an electric field is applied across the dispersion and the electrophoretic mobility is observed. Particles inside the dispersion that possess a zeta potential will migrate towards the electrode of opposite charge whereby the migration velocity is proportional to the magnitude of the zeta potential. Using the technique of laser Doppler anemometry, this velocity within the dispersion is measured. An incident laser beam striking one of the moving particles causes a frequency or phase shift that is recorded as the particle mobility. This mobility is transformed into zeta potential with the application of an appropriate theory together with the input of the dispersant's viscosity. The Henry equation (**Equation 1.6**) describes the relation between the electrophoretic mobility and the zeta potential.

$$U_E = \frac{2\,\varepsilon\xi\,f(k\alpha)}{3\eta}$$

Equation 1.6 Henry equation. U_E is the electrophoretic mobility, ε is the dielectric constant of the sample, ζ is the zeta potential, $f(k\alpha)$ is the Henry function, η is the vsosity.

Specifically, to obtain the electrophoretic mobility, the velocity of the particles is determined by Laser Doppler Velocimetry (LDV).[289] The LDV applies an electrical field of known strength across the capillary cell which contains the colloidal particle solution. A shift in

frequency is observed when the laser light (633 nm) passes the sample, determined by the velocity of the particles. Henry´s function is commonly set to $f(k\alpha) = 1.5$, according to Smoluchowski´s approximation, which is frequently used for particles larger than 200 nm and when the electric double layer is very thin compared to the particle diameter. Hückel's approximation uses $f(k\alpha) = 1.0$, this is frequently used for small particles in organic solvents.

1.9 Thesis outline

In this work, we focused on the elaboration of silica-based nanoparticles for various applications in catalysis, nanomedicine and environmental remediation:

a) functionalized mesoporous silica nanoparticles for catalysis (**Chapter 2**)

b) (periodic) mesoporous organosilica nanoparticles for high intensity focused ultrasound-based therapies (**Chapter 3**)

c) functionalized silica nanoparticles for topical anti-inflammatories (**Chapter 4**)

d) magnetic core-shell mesoporous silica nanoparticles for rare earth elements recovery from wastewater (**Chapter 5**).

1.10 References

1. R. K. Iler, *The Chemistry of Silica*, New York: Wiley. **1979**.
2. D. Napierska, L. C. Thomassen, D. Lison, J. A. Martens, P. H. Hoet, *Part. Fibre Toxicol.* **2010**, *7*, 39.
3. R. K. Sharma, S. Sharma, S. Dutta, R. Zboril, M. B. Gawande, *Green Chem.* **2015**, *17*, 3207.
4. G. Kickelbick, *Hybrid Mater.* **2014**, *1*, 39.
5. C. Sanchez, B. Julián, P. Belleville, M. Popall, *J. Mater. Chem.* **2005**, *15*, 3559.
6. C. Sanchez, P. Gómez-Romero, Functional Hybrid Materials, Wiley VCH, Weinheim, **2004**.
7. C. Sanchez, F. Ribot, *New J. Chem.* **1994**, *18*, 1007.
8. K. J. Klabunde, R. M. Richards, *Nanoscale Materials in Chemistry*, Second Edition, New York: Wiley. **2009**.
9. I. Ab Rahman1, V. Padavettan, *J. Nanomater.* **2012**, Article ID 132424, **DOI:** 10.1155/2012/132424.
10. J. G. Croissant, Y. Fatieiev, N. M. Khashab, *Adv. Mater.* **2017**, *29*, 1604634.
11. E. Pérez Mayoral, E. Soriano, V. Calvino-Casilda, M. L. Rojas-Cervantes, R. M. Martín-Aranda, *Catalysis Today* **2017**, *285*, 65.
12. A. Bitar, N. M. Ahmad, H. Fessi, A. Elassari, *Drug Discovery Today* **2012**, *17*, 1147.
13. L. P. Singh, S. K. Bhattacharyya, R. Kumar, G. Mishra, U. Sharma, G. Singh, S. Ahalawat, *Adv. Colloid Interface Sci.* **2014**, *214*, 17.
14. V. Shirshahi, M. Soltani, *Contrast Media Mol. Imaging* **2015**, *10*, 1.
15. M. G. Devi, S. Balachandran, *Int. J. Adv. Res. Sci. Eng. Technol.* **2016**, *4*, 249.
16. A. Ramazani, P. A. Asiabi, H. Aghahosseini, F, Gouranlou, *Curr. Org. Chem.* **2017**, *21*, 908.
17. A. Rastogi, D. K. Tripathi, S. Yadav, D. K. Chauhan, M. Živčák, M. Ghorbanpour, N. I. El-Sheery, M. Brestic, *3 Biotech* **2019**, *9*, 90.
18. P. Gh Jeelani, P. Mulay, R. Venkat, C. Ramalingam, *Silicon* **2019**, **DOI:** 10.1007/s12633-019-00229-y.
19. E. Phillips, O. Penate-Medina, P.B. Zanzonico, R. D. Carvajal, P. Mohan, Y. Ye, J. Humm, M. Gönen, H. Kalaigian, H. Schöder, H. W. Strauss, S. M. Larson, U. Wiesner, M. S. Bradbury, *Sci. Transl. Med.* **2014**, *6*, 260ra149.
20. F. Chen, K. Ma, M. Benezra, L. Zhang, S. M. Cheal, E. Phillips, B. Yoo, M. Pauliah, M. Overholtzer, P. Zanzonico, S. Sequeira, M. Gonen, T. Quinn, U. Wiesner, M. S. Bradbury, *Chem. Mater*. **2017**, *29*, 8766.
21. W. Stöber, A. Fink, E. Bohn, *J. Colloid Interface Sci.* **1968**, *26*, 62.
22. K. Osseo-Asare, F. J. Arriagada, *Colloids Surf.* **1990**, *50*, 32.
23. L. Singh, S. Agarwal, S. Bhattacharyya, U. Sharma, S. Ahalawat, *Nanomater. Nanotechnol.* **2011**, *1*, 44.
24. S. Pilz, H. Najafi, M. Ryser, V. Romano, *Fibers* **2017**, *5*, 24.
25. M. Cypryk, B. Gostyński, M. Pokora, *New J. Chem.* **2019**, *43*, 15222.
26. H. Valizadeh, M. Amiri, F. Hosseinzadeh, *Dyes and Pigments* **2012**, *92*, 1308.
27. R. J. P. Corriu, D. Leclerq, *Angew. Chem. Int. Ed.* **1996**, *35*, 1421.
28. ALOthman Z. A. *Materials* **2012**, *5*, 2874.
29. L. L. Hench, J. K. West, *Chem. Rev.* **1990**, *90*, 33.
30. A. Julbe, C. Balzer, J. M. Barthez, C. Guizard, A. Larbot, L. Cot, *J. Sol-Gel Sci.Tech.***1995**, *4*, 89.

31. C. Brinker, G. Scherer, Sol-Gel Science: The Physics and Chemistry of Sol-Gel Processing. Academic Press, Inc.: New York, **1990**.
32. C. J. Brinker, *Adv. Chem. Ser.* **1994**, *234*, 361.
33. L. Mercier, T. J. Pinnavaia, *Adv. Mater.* **1997**, *9*, 500.
34. X. Feng, G. E. Fryxell, L. Q. Wang, Y. A. Kim, J. Liu, K. M. Kemner, *Science* **1997**, *276*, 923.
35. L. V. Ng, P. Thompson, J. Sanchez, C. W. Macosko, A. V. McCormick, *Macromolecules* **1995**, *28*, 6471.
36. J. Wen, G. L. Wilkes, *Chem. Mater.* **1996**, *8*, 1667
37. T. Hoar, J. Schulman, *Nature* **1943**, *152*, 102
38. M. A. Malik, M. Y. Wani, M. A. Hashim, *Arab. J. Chem.* **2012**, *5*, 397.
39. M.A. Lopez-Quintela, *Curr. Opin. Colloid Interface Sci.* **2003**, *8*, 137.
40. F. J. Arriagada, K. Osseo-Asare, *J. Colloid Interface Sci.* **1999**, *211*, 210.
41. K. S. W. Sing, D. H. Everett, R. A. W. Haul, L. Moscou, R. A. Pierotti, J. Rouquerol, T. Siemieniewska, *Pure Appl. Chem.* **1985**, *57*, 603.
42. A. Eftekhari, Z. Y. Fan, *Mater. Chem. Front.* **2017**, *1*, 1001.
43. D. Douroumis, I. Onyesom, M. Maniruzzaman, J. Mitchell, *Criti. Rev. Biotechnol.* **2013**, *33*, 229.
44. M. Vallet-Regi, A. Rámila, R. P. Del Real, J. Pérez-Pariente, *Chem. Mater*. **2001**, *13*, 308e311.
45. I. I. Slowing, B. G. Trewyn, S. Giri, V. S.-Y. Lin, *Adv. Funct. Mater.* **2007**, *17*, 1225.
46. K. Möller, T. Bein, *Chem. Mater.* **2017**, *29*, 371e388.
47. Cheng-Yu Lai, *J. Thermodyn. Catal.* **2013**, *51*, 1000e124.
48. R. K. Sharma, S. Sharma, S. Dutta, R. Zboril, M. B. Gawande, *Green Chem.* **2015**, *17*, 3207.
49. S. Mothahar, N. Nikkam, A. A. Alemrajabi, R. Khodabandeh, M. S. Toprak, M. Muhammed, *Int. Commun. Heat Mass.* **2014**, *56*, 114.
50. R. A. Mitran, D. Berger, C. Munteanu, C. Matei, *J. Phys. Chem. C.* **2015**, *119*, 15177.
51. A. Popat, J. Liu, Q. H. Hu, M. Kennedy, B. Peter, G. Q. Lu, S. Z. Qiao, *Nanoscale* **2012**, *4*, 970.
52. J. Chen, Y. Sheng,Y. H. Song, M. Q. Chang, X. T. Zhang, L.Cui, D. Y. Meng, H. Zhu, Z. Shi, H. F. Zou, *ACS Sustainable Chem. Eng.* **2018**, *6*, 3533.
53. S. Kachbouri, N. Mnasri, E. Elaloui, Y. Moussaoui, *J. Saudi Chem. Soc.* **2018**, *22*, 405.
54. X. L. Yan, J. F. Meng, X. Y. Hu, R. Feng, M. Zhou, *J. Sol-Gel Sci. Tech.* **2019**, *89*, 617
55. N. Suzuki, M. Barakat Zakaria Hegazy, Y. -D. Chiang, K. C.-W Wu, Y. Yamauchi, *Phys. Chem. Chem. Phys.* **2012**, *14*, 7427.
56. M. Conradi, *Mater. Technol.* **2013**, *47*, 285.
57. C. H. Lee, S. H. Cheng, Y. J. Wang, Y. C. Chen, N. T. Chen, J. Souris, C. T. Chen, C. Y. Mou, C. S. Yang, L. W. Lo, *Adv. Funct. Mater.* **2009**, *19*, 215.
58. J. Moghal, J. Kobler, J. Sauer, J. Best, M. Gardener, A. A. R. Watt, G. Wakefield, *ACS Appl. Mater. Interfacess* **2012**, *4*, 854.
59. S. Kumari, P. D.Sahare, *J. Mater. Sci. Technol.* **2013**, *29*, 742.
60. Z. X. Li, J. C. Barnes, A. Bosoy, J. F. Stoddart, J. I. Zink, *Chem. Soc. Rev.* **2012**, *41*, 2590.
61. R. Narayan, U. Y. Nayak, A. M. Raichur, S. Garg, *Pharmaceutics* **2018**, *10*, 118
62. J. G. Croissant, Y. Fatieiev, A. Almalik, N. M. Khashab, *Adv. Healthcare Mater.* **2018**, *7*, 1700831.
63. M. Manzano, M. Vallet-Regí, *Chem. Commun.* **2019**, *55*, 2731.

64. S. Jafari, H. Derakhshankhah, L. Alaei, A. Fattahi, B. S. Varnamkhasti, A. A. Sabourty, *Biomed. Pharmacother* **2019**, *109*, 1100.
65. D. Tarn, C. E. Ashley, M. Xue, E. C. Carnes, J. I. Zine, C. J. Brinker, *Acc.Chem. Res*. **2013**, *46*, 792.
66. J. M. Rosenholm, C. Sahlgren, M. Linden, *Curr. Drug Targets* **2011**, *12*, 1166.
67. J. L. Vivero-Escoto, R. C. Huxford-Phillips, W. B. Lin, *Chem. Soc. Rev.* **2012**, *41*, 2673.
68. F. Carniato, L. Tei, M. Botta, *Eur. J. Inorg. Chem.* **2018**, 4936.
69. B. G. Trewyn, S. Giri, I. I. Slowinga, V. S.-Y. Lin, *Chem. Commun.* **2007**, 3236.
70. S. S. Pillai, H. Yukawa, D. Onoshima, V. Biju, Y. Baba, *Nano Hybrids and Composites*, **2018**, *19*, 55.
71. G. Valenti, E. Rampazzo, S. Bonacchi, L. Petrizza, M. Marcaccio, M. Montalti, L. Prodi, F. Paolucci, *J. Am. Chem. Soc.* **2016**, *138,* 15935.
72. C. Y. Lai, B. G. Trewyn, D. M. Jeftinija, K. Jeftinija, S. Xu, S. Jeftinija, V. S.-Y. Lin, *J. Am. Chem. Soc.* **2003**, *125*, 4451.
73. J. Lu, M. Liong, J. I. Zink, F. Tamanoi, *Small* **2007**, *3*, 1341.
74. E. Ruiz-Hernández, A. Baeza, M. Vallet-Regí, *ACS Nano.* **2011**, *5*, 1259.
75. F. Q. Tang, L. L. Li, D. Chen, *Adv. Mater.* **2012**, *24*, 1504.
76. C. Argyo, V. Weiss, C. Bräuchle, T. Bein, *Chem. Mater.* **2014**, *26*, 435.
77. Y. Wang, Q. F. Zhao, N. Han, L. Bai, J. Li, J. Liu, E. Che, L. Hu, Q. Zhang, T. Y. Jiang, S. L. Wang, *Nanomedicine: NBM.* **2015**, *11*, 313.
78. S. Giret, M. Wong Chi Man, C. Carcel, *Chem. Eur. J.* **2015**, *21*, 13850.
79. J. G. Croissant, Y. Fatieiev, A. Almalik, N. M. Khashab, *Adv. Healthcare Mater.* **2017**, *7*, 1700831.
80. W. Chen, C. A. Glackin, M. A. Horwitz, J. I. Zink, *Acc.Chem. Res*. **2019**, *52*, 1531.
81. M. Manzano, M. Vallet-Regí, *Adv. Funct. Mater.* **2019**, 1902634.
82. J. Lu, M. Liong, Z. X. Li, J. I. Zink, F. Tamanoi, *Small* **2010**, *6*, 1794.
83. Y. Feng, N. Panwar, D. J. H. Tng, S. C. Tjin, K. Wang, K. -T. Yong, *Coord. Chem. Rev.* **2016**, *319*, 86.
84. L. B. de Oliveira Freitas, L. de Melo Corgosinho, J. Araújo Quintão Arantes Faria, V. M. dos Santos, J. Magalhães Resende, A. Soares Leal, D. Assis Gomes, *Micropor. Mesopor. Mat.* **2017**, *242*, 271e283.
85. M. J. Xuan, J. X. Shao, J. Zhao, Q. Li, L. R. Dai, J. B. Li, *Angew. Chem. Int. Ed.* **2018**, *57*, 6049
86. T. T. Li, S. X. Shi, S. Goel, X. Shen, X. X. Xie, Z. Y. Chen, H. X. Zhang, S. Li, X. Qin, H. Yang, C. H. Wu, Y. Y. Liu, *Acta Biomater.* **2019**, *89*, 1.
87. D. Fahima, *Curr. Med. Chem.* **2019**, **DOI**: 10.2174/0929867325666180501101044.
88. S. H. Wu, C. Y. Mou, H. P. Lin, *Chem. Soc. Rev.* **2013**, *42*, 3862.
89. C. Théron, A. Gallud, C. Carcel, M. Gary-Bobo, M. Maynadier, M. Garcia, J. Lu, F. Tamanoi, J. I. Zink, M. Wong Chi Man, *Chem. Eur. J.* **2014**, *20*, 9372.
90. N. Moitra, P. Trens, L. Raehm, J.-O. Durand, X. Cattoën, M. Wong Chi Man, *J. Mater. Chem.* **2011**, *21*, 13476.
91. R. Anwander, C. Palm, J. Stelzer, O. Groeger, G. Engelhardt, *Stud. Surf. Sci. Catal.* **1998**, *117*, 135.
92. F. Hoffmann, M. Cornelius, J. Morell, M. Fröba, *Angew. Chem. Int. Ed.* **2006**, *45*, 3216.
93. I. I. Slowing, J. L. Vivero-Escoto, B. G. Trewyn, V. S. Y. Lin, *J. Mater. Chem.* **2010**, *20*, 7924.
94. S. Huh, J. W. Wiench, B. G. Trewyn, S. Song, M. Pruski, V. S. Y. Lin, *Chem. Commun.* **2003**, 2364.
95. G. A. Ozin, *Chem. Commun.* **2000**, 419.

96. H. Yang, N. Coombs, G. A. Ozin, *Nature* **1997**, *386*, 692.
97. B. Karimi, D. Elhamifar, J.H. Clark, A.J. Hunt, *Chem. Eur J.* **2010**, *16*, 8047
98. Y. Chen, J. Shi, *Adv. Mater.* **2016**, *28*, 3235.
99. J. E. Lee, N. Lee, T. Kim, J. Kim, T. Hyeon, *Acc. Chem. Res.* **2011**, *44*, 893.
100. Y. Chen, Q. Meng, M. Wu, S. Wang, P. Xu, H. Chen, Y. Li, L. Zhang, L. Wang, J. Shi, *J. Am. Chem. Soc.* **2014**, *136*, 16326.
101. J. Croissant, D. Salles, M. Maynadier, O. Mongin, V. Hugues, M. Blanchard-Desce, X. Cattoën, M. Wong Chi Man, A. Gallud, M. Garcia, M. Gary-Bobo, L. Raehm, J.-O. Durand, *Chem. Mater.* **2014**, *26*, 7214.
102. M. Waki, Y. Maegawa, K. Hara, Y. Goto, S. Shirai, Y. Yamada, N. Mizoshita, T. Tani, W. J. Chun, S. Muratsugu, M. Tada, A. Fukuoka, S. Inagaki, *J. Am. Chem. Soc.* **2014**, *136*, 4003.
103. J. G. Croissant, X. Cattoën, M.Wong Chi Man, J.O. Durand, N.M. Khashab, *Nanoscale* **2015**, 7, 20318.
104. M. Wu, Q. Meng, Y. Chen, Y. Du, L. Zhang, Y. Li, L. Zhang, J. Shi, *Adv. Mater.* **2015**, *27*, 215.
105. P. Huang, Y. Chen, H. Lin, L. Yu, L. Zhang, L. Wang, Y. Zhu, J. Shi, *Biomaterials* **2017**, *125*, 23.
106. Y. Fatieiev, J.G. Croissant, K. Alamoudi, N.M. Khashab, *Chem. Plus. Chem.* **2017**, *82*, 631.
107. L. D. Yu, Y. Chen, H. Lin, W. X. Du, H. R. Chen, J. L. Shi, *Biomaterials* **2018**, *161*, 292.
108. J. Yue, S. Z. Luo, M. M. Lu, D. Shao, Z. Wang, W. F. Dong, *Chem. Biol. Drug Des.* **2018**, *92*, 1435.
109. D. Shen, J. Yang, X. Li, L. Zhou, R. Zhang, W. Li, L. Chen, R. Wang, F. Zhang, D. Zhao, *Nano Lett.* **2014**, *14*, 923.
110. J. Croissant, X. Cattën, M. Wong Chi Man, A. Gallud, L. Raehm, P. Trens, M. Maynadier, J.-O. Durand, *Adv. Mater.* **2014**, *26*, 6174.
111. Z. Wang, D. Wang, Z. Qian, J. Guo, H. Dong, N. Zhao, J. Xu, *ACS Appl. Mater. Interfaces* **2015**, *7*, 2016
112. C. Urata, H. Yamada, R. Wakabayashi, Y. Aoyama, S. Hirosawa, S. Arai, S. Takeoka, Y. Yamauchi, K. Kuroda, *J. Am. Chem. Soc.* **2011**, *133*, 8102.
113. X. Qian, W. Wang, W. Kong, Y. Chen, *RSC Adv.* **2014**, *4*, 17950.
114. Y. Fatieiev, J. G. Croissant, S. Alsaiari, B. A. Moosa, D. H. Anjum, N. M. Khashab, *ACS Appl. Mater. Interfaces* **2015**, *7*, 24993.
115. N. Lu, Y. Tian, W. Tian, P. Huang, Y. Liu, Y. Tang, C. Wang, S. Wang, Y. Su, Y. Zhang, J. Pan, Z. Teng, G. Lu, *ACS Appl. Mater. Interfaces* **2016**, *8*, 2985.
116. J. Wu, Y. Liu, Y. Tang, S. Wang, C. Wang, Y. Li, X. Su, J. Tian, Y. Tian, J. Pan, Y. Su, H. Zhu, Z. Teng and G. Lu, *ACS Appl. Mater. Interfaces* **2016**, *8*, 17927.
117. J. Gao, X. Zhang, S. Xu, F. Tan, X. Li, Y. Zhang, Z. Qu, X. Quan, J. Liu, *Chem. Eur J.* **2014**, *20*, 1957.
118. J. Liu, H.Q. Yang, F. Kleitz, Z.G. Chen, T. Yang, E. Strounina, G. Q. M. Lu, S.Z. Qiao, *Adv. Funct. Mater.* **2012**, *22*, 591.
119. M. Wu, Y. Chen, L. Zhang, X. Li, X. Cai, Y. Du, L. Zhang, J. Shi, *J. Mater. Chem. B* **2015**, *3*, 766.
120. Z. Teng, X. Su, Y. Zheng, J. Zhang, Y. Liu, S. Wang, J. Wu, G. Chen, J. Wang, D. Zhao, G. Lu, *J. Am. Chem. Soc.* **2015**, *137*, 7935.
121. S. Rahmani, J. Budimir, M. Sejalon, M. Daurat, D. Aggad, E.Vives, L. Raehm, M. Garcia, L. Lichon, M. Gary-Bobo,J. -O.Durand, C. Charnay, *Molecules* **2019**, *24*, 332.
122. M. Dang, W. Li, Y. Y. Zheng, X. D. Su, X. B. Ma, Y. L. Zhang, Q. Q. Ni, J. Tao, J. J. Zhang, G. M. Lu, Z. G. Teng, L. H. Wang, *J. Mater. Chem. B* **2017**, *5*, 2625.

123. J. Croissant, X. Cattoen, M. Wong Chi Man, P. Dieudonne, C. Charnay, L. Raehm, J. -O. Durand, *Adv. Mater.* **2015**, *27*, 145.
124. J. J. Zhang, X. F. Wang, J. Wen, X. D. Su, L. X. Weng, C. Y. Wang, Y. Tian, Y. L. Zhang, J. Tao, P. Xu, G. M. Lu, Z. G. Teng, L. H. Wang, *Biomater. Sci.* **2019**,*7*, 4790.
125. L. Zhang, S.Z. Qiao, Y.G. Jin, Z.G. Chen, H.C. Gu, G.Q. Lu, *Adv. Mater.* **2008**, *20*, 805.
126. S. Yang, S. S. Chen, J. Fan, T. T. Shang, D. L. Huang, G. D. Li, *J. Colloid Interface Sci.* **2019**, *554*, 565.
127. Z. Zhou, R.N. Klupp Taylor, S. Kullmann, H. Bao, M. Hartmann, *Adv. Mater.* **2011**, *23*, 2627.
128. B. W. Yang, Y. Chen, J. L. Shi, *Mater. Sci. Eng. R* **2019**, *137*, 66.
129. Q. He, J. Shi, *J. Mater. Chem.* **2011**, *21*, 5845.
130. B. Karimi, F.K. Esfahani, *Chem. Commun.* **2011**, *47*,10452.
131. Z. Teng, S. Wang, X. Su, G. Chen, Y. Liu, Z. Luo, W. Luo, Y. Tang, H. Ju, D. Zhao, G. Lu, *Adv. Mater.* **2014**, *26*, 3741.
132. A. B. D. Nandiyanto, S. G. Kim, F. Iskandar, K. Okuyama, *Micropor. Mesopor. Mater.* **2009**, *120*, 447.
133. T. Asefa, M. J. MacLachlan, N. Coombs, G. A. Ozin, *Nature* **1999**, *402*, 867.
134. S. Inagaki, S. Guan, Y. Fukushima, T. Ohsuna, O. Terasaki, *J. Am. Chem. Soc.* **1999**, *121*, 9611.
135. B. J. Melde, B. T. Holland, C. F. Blanford, A. Stein, *Chem. Mater.* **1999**, *11*, 3302.
136. E. De Canck, I. Ascoop, A. Sayari, P. Van Der Voort, *Phys. Chem. Chem. Phys.* **2013**, *15*, 9792.
137. S. Martens, R. Ortmann, F. J. Brieler, C. Pasel, Y. J. Lee, D. Bathen, M. Fröba, *Z. Anorg. Allg. Chem.* **2014**, *640*, 632.
138. R. O. Otero, D. Esquivel, M. A. A. Ulibarri, C. S. Jiménez-Sanchidrián, F. J. Romero-Salguero, J. M. Fernández, *Chem. Eng. J.* **2013**, *228*, 205.
139. J. Gao, X. Zhang, S. Xu, F. Tan, X. Li, Y. Zhang, Z. Qu, X. Quan, J. Liu, *Chem. Eur. J.* **2014**, *20*, 1957.
140. W. R. Grüning, G. Siddiqi, O. V. Safonova, C. Copéret, *Adv. Synth. Catal.* **2014**, *356*, 673.
141. M. Ide, E. De Canck, I. Van Driessche, F. Lynen, P. Van Der Voort, *RSC Adv.* **2015**, *5*, 5546.
142. J. A. Melero, J. Iglesias, J. M. Arsuaga, J. Sainz-Pardo, P. de Frutos, S. Blazquez, *J. Mater. Chem.* **2007**, *17*, 377.
143. Q. Yang, J. Liu, L. Zhang, C. Li, *J. Mater. Chem.* **2009**, *19*, 1945.
144. P. Kumar,V. V. Guliants, *Micro. Meso. Mater.* **2010**, *132*, 1.
145. B. Karimi, F. Kabiri Esfahani, *Chem. Commun.* **2011**, *47*, 10452.
146. B. Karimi, H. M. Mirzaei, A. Mobaraki, *Catal. Sci. Technol.* **2012**, *2*, 828.
147. P. Borah, X. Ma, K. T. Nguyen, Y. Zhao, *Angew. Chem. Int. Ed.* **2012**, *51*, 7756.
148. M. Waki, N. Mizoshita, Y. Maegawa, T. Hasegawa, T. Tani, T. Shimada, S. Inagaki, *Chem. Eur. J.* **2012**, *18*, 1992.
149. S. Inagaki, O. Ohtani, Y. Goto, K. Okamoto, M. Ikai, K.-I. Yamanaka, T. Tani, T. Okada, *Angew. Chem. Int. Ed*. **2009**, *48*, 4042.
150. H. Takeda, Y. Goto, Y. Maegawa, T. Ohsuna, T. Tani, K. Matsumoto, T. Shimada, S. Inagaki, *Chem. Commun.* **2009**, 6032.
151. N. Mizoshita, M. Ikai, T. Tani, S. Inagaki, *J. Am. Chem. Soc.* **2009**, *131*, 14225.
152. N. Mizoshita, T. Tani, H. Shinokubo, S. Inagaki, *Angew. Chem. Int. Ed.* **2012**, *124*, 1182.
153. M. Ikai, Y. Maegawa, Y. Goto, T. Tani, S. Inagaki, *J. Mater. Chem. A*, **2014**, *2*, 11857.

154. C. X. Lin, S. Z. Qiao, C. Z. Yu, S. Ismadji, G. Q. Lu, *Micropor. Mesopor. Mater.* **2009**, *117*, 213.
155. H. Y. Wu, F. K. Shieh, H. M. Kao, Y. W. Chen, J. R. Deka, S. H. Liao, K. C. W. Wu, *Chem. Eur. J.* **2013**, *19*, 6358.
156. D. Aggad, C. Mauriello-Jimenez, S. Dib, J. G. Croissant, L. Lichon, D. Laurencin, S. Richeter, M. Maynadier, S. K. Alsaiari, M. Boufatit, L. Raehm, M. Garcia, N. M. Khashab, M. Gary-Bobo, J. -O. Durand, *ChemNanoMat* **2018**, *4*, 46.
157. J. J. Zhang, L. X. Weng, X. D. Su, G. M. Lu, W. F. Liu, Y. X. Tang, Y. L. Zhang, J. Wen, Z. G. Teng, L. H. Wang, *J. Colloid Interf. Sci.* **2018**, *513*, 214.
158. N. Ž. Knežević, S. Djordjević, V. Kojić, D. Janaćković, *Inorganics* **2019**, *7*, 16.
159. V. Rebbin, R. Schmidt, M. Fröba, *Angew. Chem. Int. Ed.* **2006**, *45*, 5210.
160. W. Wang, J. E. Lofgreen, G. A. Ozin, *Small* **2010**, *6*, 2634.
161. M. Khademy, B. Karimi, S. Zareian, *ChemistrySelect* **2017**, *2*, 9953.
162. J. Gehring, B. Trepka, N. Klinkenberg, H. Bronner, D. Schleheck, S. Polarz, *J. Am. Chem. Soc.* **2016**, *138*, 3076.
163. A. Birault, E. Molina, G. Toquer, P. Lacroix-Desmazes, N. Marcotte, C. Carcel M. Katouli, J. R. Bartlett, C. Gérardin, M. Wong Chi Man, *ACS Appl. Bio Mater.* **2018**, *1*, 1787.
164. B. Hatton, K. Landskron, W. Whitnall, D. Perovic, G. A. Ozin, *Acc. Chem. Res.* **2005**, *38*, 305.
165. M. Jaroniec, *Nature* **2006**, *442*, 638.
166. Fujita, S., Inagaki, S. *Chem. Mater.* **2008**, *20*, 891.
167. H. S. Xia, C. H. (Clayton). Zhou, D. S. Tong, C. X. Lin, *J. Porous Mater.* **2010**, *17*, 225.
168. N. Mizoshita, T. Tani, S. Inagaki, *Chem. Soc. Rev.* **2011**, *40*, 789.
169. U. Díaz, D. Brunel, A. Corma, *Chem. Soc. Rev.* **2013**, *42*, 4083.
170. P. Van Der Voort, D. Esquivel, E. D. Canck, F. Goethals, I. V. Driessche, F. J. Romero-Salguero, *Chem. Soc. Rev.* **2013**, *42*, 3913.
171. S. S. Park, M. S. Moorthy, C. S. Ha, *NPG Asia Materials* **2014**, *6*, e96.
172. A. S. Manchanda, M. Kruk, *Micropor. Mesopor. Mater.* **2016**, *222*, 153.
173. K. Qian, F. Liu, J. Yang, X. Huang, W. Gu, S. Jambhrunkar, P. Yuan, C. Yu, *RSC Adv.* **2013**, *3*, 14466.
174. J. G. Croissant, X. Cattoën, J. O. Durand, M. Wong Chi Man, N. M. Khashab, *Nanoscale* **2016**, *8*, 19945
175. A. Noureddine, P. Trens, G. Toquer, X. Cattoën, M. Wong Chi Man, *Langmuir* **2014**, *30*, 12297.
176. A. Corma, U. Díaz, M. Arrica, E. Fernández, Í. Ortega, *Angew. Chem. Int. Ed.* **2009**, *48*, 6247.
177. K. Bürglová, A. Noureddine, J. Hodačová, G. Toquer, X. Cattoën, M. Wong Chi Man, *Chem. Eur. J.* **2014**, *20*, 10371.
178. A. C. Gomes, M. A. Lourenço, S. M. Bruno, P. Ferreira, A. A. Valente, M. Pillinger, I. S. Gonçalves, *J. Organomet. Chem.* **2014**, *751*, 501
179. X. Du, X. Li, L. Xiong, X. Zhang, F. Kleitz, S. Z. Qiao, *Biomaterials* **2016**, *91*, 90.
180. Y. Liang, M. Hanzlik, R. Anwander, *J. Mater. Chem.* **2006**, *16*, 1238.
181. S. Fujita, S. Inagaki, *Chem. Mater.* **2008**, *20*, 891.
182. N. Mizoshita, T. Tani, S. Inagaki, Chem. Soc. Rev. **2011**, *40*, 789.
183. N. Li, J. G. Wang, H. J. Zhou, P. C. Sun, T. H. Chen, *Chem. Mater.* **2011**, *23*, 4241.
184. G. Yasutomo, O. Kentaro, I. Shinji, *Bull. Chem. Soc. Jpn.* **2005**, *78*, 932.

185. R. J. P. Corriu, *Angew. Chem., Int. Ed.* **2000**, *39*, 1376.
186. K. J. Shea, D. A. Loy, *Chem. Mater.***2001**, *13*, 3306.
187. S. Li, B. A. Moosa, J. G. Croissant, N. M. Khashab, *Angew. Chem., Int. Ed.* **2015**, *127*, 6908.
188. A. Noureddine, L. Lichon, M. Maynadier, M. Garcia, M. Gary-Bobo, J. I. Zink, M. Wong Chi Man, X. Cattoën, *Nanoscale* **2015**, *7*, 11444.
189. W. J. Hunks, G. A. Ozin, *J. Mater. Chem.* **2005**, *15*, 3716.
190. S. S. Park, C. S. Ha, *Chem. Rec.* **2006**, *6*, 32.
191. H. Djojoputro, X. F. Zhou, S. Z. Qiao, L. Z. Wang, C. Z. Yu, G. Q. Lu, *J. Am. Chem. Soc.* **2006**, *128*, 6320.
192. E. B. Cho, D. Kim, M. Jaroniec, *Micropor. Mesopor. Mater.* **2009**, *120*, 252.
193. J. Liu, S. Bai, H. Zhong, C. Li, Q. Yang, *J. Phys. Chem. C* **2010**, *114*, 953.
194. B. Guan, Y. Cui, Z. Ren, Z.-a. Qiao, L. Wang, Y. Liu, Q. Huo, *Nanoscale* **2012**, *4*, 6588.
195. S. Z. Qiao, C. Z. Yu, W. Xing, Q. H. Hu, H. Djojoputro, G. Q. Lu, *Chem. Mater.* **2005**, *17*, 6172.
196. E.-B. Cho, D. Kim, M. Jaroniec, *J. Phys. Chem. C* **2008**, *112*, 4897.
197. P. Mohanty, K. Landskron, *Nanoscale Res. Lett.* **2009**, *4*, 169.
198. P. Mohanty, K. Landskron, *Nanoscale Res. Lett.* **2009**, *4*, 1524.
199. M. Zhang, Y. Li, L. Bi, W. Zhuang, S. Wang, Y. Chen, B. Li, Y. Yang, *Chin. J. Chem.* **2011**, *29*, 933.
200. C. Mauriello-Jimenez, J. Croissant, M. Maynadier, X. Cattoen, M. Wong Chi Man, J. Vergnaud, V. Chaleix, V. Sol, M. Garcia, M. Gary-Bobo, L. Raehm, J.-O. Durand, J. *Mater. Chem. B* **2015**, *3*, 3681.
201. X. Qian, W. Wang, W. Kong, Y. Chen, *J. Nanomater.* **2014**, Article ID: 972475. DOI: 10.1155/ 2014/972475.
202. C.M. Jimenez, D. Aggad, J. G. Croissant, K. Tresfield, D. Laurencin, D. Berthomieu, N. Cubedo, M. Rossel, S. Alsaiari, D. H. Anjum, R. Sougart, M. A. Roldan-Gutierrez, S. Richeter, E. Oliviero, L. Raehm, C. Charnay, X. Cattoën, S. Clément, M. Wong Chi Man, M. Maynadier, V. Chaleix, V. Sol, M. Garcia, M. Gary-Bobo, N .M. Khashab, N. Bettache, J. -O. Durand, *Adv. Funct. Mater.* **2018**, *28*, 1800235.
203. Y. Wei, X. Li, R. Zhang, Y. Liu, W. Wang, Y. Ling, A. M. El-Toni, D. Zhao, *Sci. Rep.* **2016**, *6*, 20769.
204. M. Sasidharan, K. Nakashima, N. Gunawardhana, T. Yokoi, M. Ito, M. Inoue, S.-i. Yusa, M. Yoshio, T. Tatsumi, *Nanoscale* **2011**, *3*, 4768.
205. H. C. Youn, S. Baral, J. H. Fendler, *J. Phys. Chem.* **1988**, *92*, 6320.
206. A. Henglein, *Chem. Rev.***1989**, *89*, 1861.
207. R. G. Chaudhuri, S. Paria, *Chem. Rev.* **2012**, *112*, 2373.
208. D. L. Huber, *Small* **2005**, *1*, 482.
209. J. Gao, H. Gu, B. Xu, *Acc. Chem. Res.* **2009**, *42*, 1097.
210. R. Hao, R. Xing, Z. Xu, Y. Hou, S. Gao, S. Sun, *Adv. Mater.* **2010**, *22*, 2729.
211. N. Lee, D. Yoo, D. Ling, M. H. Cho, T. Hyeon, J. Cheon, *Chem. Rev.* **2015**, *115*, 10637.
212. M. L. Bruschi, L. A. Sica de Toledo, *Magnetochemistry* **2019**, *5*, 50.
213. S. Sabale, P. Kandesar, V. Jadhav, R. Komorek, R. K. Motkuri, X. Y. Yu, *Biomater. Sci.* **2017**, *5*, 2212.
214. D. S. Ling, N. Lee, T. Hyeon, *Acc. Chem. Res.* **2015**, *48*, 1276.
215. W. Wu, Z. H. Wu, T. Yu, C. Z. Jiang, W. S. Kim, *Sci. Technol. Adv. Mater.* **2015**, *16*, 023501.
216. S. M. Dadfar, K. Roemhild, N. I. Drude, S. von Stillfried, R. Knüchel, F. Kiessling, T. Lammers, *Adv. Drug Deliv. Rev.* **2019**,*138*, 302.

217. M. Magro, D. Baratella, E. Bonaiuto, J. de A. Roger, F. Vianello, *Curr. Med. Chem.* **2018**, *25*, 540.
218. M. Saeed, W. Z. Ren, A. Q. Wu, *Biomater. Sci.* **2018**, *6*, 708.
219. S. Palanisamy, Y. M. Wang, *Dalton Trans.* **2019**, *48*, 9490.
220. M. Mahmoudi, S. Sant, B. Wang, S. Laurent, T. Sen, *Adv. Drug Deliv. Rev.* **2011**, *63*, 24.
221. S. Laurent, D. Forge, M. Port, A. Roch, C. Robic, L.V. Elst, R. N. Muller, *Chem Rev.* **2008**, *108*, 2064.
222. Widder, K. J.; Senyei, A. E.; Scarpelli, D. G. *Exp. Biol. Med.* **1978**, *158*, 141.
223. A. H. Lu, E. L. Salabas, F. Schueth, *Angew. Chem. Int. Ed.* **2007**, *46*, 1222.
224. E. A. Campos, D. V. B. S. Pinto, J. I. S. Olivira, E. C. Mattos, R. C. L. Dutra, *J. Aerosp. Technol. Manag.* **2015**, *7*, 267.
225. I. S. Lee, N. Lee, J. Park, B. H. Kim, Y. W. Yi, T. Kim, T. K. Kim, I. H. Lee, S. R. Paik, T. Hyeon, *J. Am. Chem. Soc.* **2006**, *128*, 10658.
226. J. B. Haun, T. J. Yoon, H. Lee, R. Weissleder, *Wiley Interdiscip. Rev. Nanomed. Nanobiotechnol.* **2010**, *2*, 291.
227. L. Ling, X. Y. Huang, W. X. Zhang, *Adv. Mater.* **2018**, *30*, 1705703.
228. P. Tartaj, M. P. Morales, T. Gonzalez-Carreño, S. Veintemillas-Verdaguer, C. J. Serna, *Adv. Mater.* **2011**, *23*, 5243.
229. A. Ali, H. Zafar, M. Zia, I. Haq, A. R. Phull, J. S. Ali, A. Hussain, *Nanotechnol. Sci. Appl.* **2016**, *9*, 49.
230. B. R. Cuenya, *Thin Solid Films.* **2010**, *518*, 3127.
231. W. Wu, Q. He. C. Jiang. *ChemInform.* **2009**, *40*, i.
232. S. Wu, A. Sun, F. Zhai, J. Wang, W. H. Xu, Q. Zhang, A. A. Volinsky, *Mater. Lett.* **2011**, *65*, 1882.
233. K. B. Narayanan, N. Sakthivel, *Adv Colloid Interface Sci.* **2010**, *156*, 1.
234. T. A. ElBayoumi, V. P. Torchilin, V. Weissig, Liposomes: Methods and Protocols, Volume 1: Pharmaceutical Nanocarriers**.** **2010**.
235. J. Xu, H. B. Yang, W. Y. Fu, K. Du, Y. M. Sui, J. J. Chen, Y. Zeng, M. H. Li, G. T. Zou, *J. Magn. Magn. Mater.* **2007**, *309*, 307.
236. K. B. Narayanan, N. Sakthivel, *Adv Colloid Interface Sci.* **2010**, *156*, 1.
237. R. Massart, *IEEE Transactions on Magnetics* **1981**, *17*, 1247.
238. K. Inouye, R. Endo, Y. Otsuka, K. Miyashiro, K. Kaneko, T. Ishikawa, *J. Phys.Chem.* **1982**, *86*, 1465.
239. B. W. Müller, R. H. Müller, *J. Pharm. Sci.* **1984**, *73*, 919.
240. J. Vidal-Vidal, J. Rivas, M. A. López-Quintela, *Colloids Surf., A Physicochem. Eng. Asp.* **2006**, *288*, 44.
241. S. Giri, S. Samanta, S. Maji, S. Ganguli, A. Bhaumik, *J. Magn. Magn. Mater.* **2005**, *285*, 296.
242. X. Hu, J. C. Yu, J. Gong, *J. Phy.Chem. C* **2007**, *111*, 11180.
243. S. Wei, Q. Wang, J. Zhu, L. Sun, H. Lin, Z. Guo, *Nanoscale* **2011**, *3*, 4474.
244. I. Robinson, L. D. Tung, S. Maenosono, C. Wälti, N. T. K. Thanh, *Nanoscale* **2010**, *2*, 2624.
245. A. Corma, *Chem. Rev.* **1995**, *95*, 559.
246. M. Lelli, D. Gajan, A. Lesage, M. A. Caporini, V. Vitzthum, P. Miéville, F. Héroguel, F. Rascón, A. Roussey, C. Thieuleux, M. Boualleg, L. Veyre, G. Bodenhausen, C. Coperet, L. Emsley, *J. Am. Chem. Soc.* **2011**, *133*, 2104.
247. P. R. Griffiths, J. A. de Hasseth, J. D. Windfordner, *Fourier Transform Infrared Spectrometry (2nd ed.),* Wiley, **2007**.

248. J. Hollas, *Modern Spectroscopy (4th ed.),* Wiley, **2004**.
249. C. Brundle, C. Evans, S. Wilson, *Encyclopedia of Materials Characterization: Surfaces, Interfaces, Thin Films.* **1992**, Butterworth-Heinemann Limited.
250. M. Hesse, H. Meier, B. Zeeh, *Spektroskopische Methoden in der Organischen Chemie*. Thieme Georg Verlag, **2005**.
251. Z. Sassi, J. C. Bureau, A. Bakkali, *Vibrational Spectroscopy*, **2002**, *28*, 251.
252. J. U. Keller, R. Staudt, *Gas adsorption equilibria. Experiment methods and adsorptive isotherm,* Springer, **2005**.
253. S. Brunauer, L. S. Deming, W. E. Deming, E. Teller, *J. Am. Chem. Soc.*,**1940**, *62*, 1723.
254. K. S. W. Sing, D. H. Everett, R. A. W. Haul, L. Moscou, R. A. Plerotti, J. Rouquérol, T. Siemieniewska, *Pure Appl. Chem.* **1985**, *4*, 603.
255. Z. Y. Ryu, J. T. Zheng, M. Z. Wang, B. J. Zhang, *Carbon*, **1999**, *37*, 1257.
256. M. Thommes, K. Kaneko, A.V. Neimark, J. P. Olivier, F. Rodriguez-Reinoso, J. Rouquerol, K. S. W. Sing, *Pure Appl. Chem.* **2015**, *87*, 1051.
257. F. Sotomayor, K. A. Cychosz, M. Thommes, *Acc. Mater. Surf. Res.* **2018**, *3*, 34.
258. Md. M. Rahman, M. Muttakin, A. Pal, A. Z. Shafiullah, B. B. Saha, *Energies* **2019**, *12*, 4565.
259. M. Muttakin, S. Mitra, K. Thu, K. Ito, B. B. Saha, *Int. J. Heat Mass Transf.* **2018**, *122*, 795.
260. K. C. Ng, M. Burhan, M. W. Shahzad, A. B. Ismail, *Surface. Sci. Rep.* **2017**, *7*, 10634.
261. M. Thommes, K. A. Cychosz. *Adsorption* **2014**, *20*, 233.
262. P. A Monson, *Micropor. Mesopor. Mater.* **2012**, *160*, 47.
263. J. Landers, G. Y. Gor, A. V. Neimark, *Colloid. Surfaces A: Physicochem. Eng. Aspects* **2013**, *437*, 3.
264. J. Rouquerol, G. Baron, R. Denoyel, H. Giesche, J. Groen, P. Klobes, P. Levitz, A. V. Neimark, S. Rigby, R. Skudas, K. Sing, M. Thommes, K. Unger, *Pure Appl. Chem.* **2011**, *84*, 107.
265. I. Langmuir, *J. Am. Chem. Soc.* **1916,** *38*, 2221.
266. S. Brunauer, P. H. Emmett, E. Teller, *J. Am. Chem. Soc.* **1938**, *60*, 309.
267. P. W. Atkins, *Physikalische Chemie*, Wiley-VCH, **2001**.
268. E. P. Barrett, L. G. Joyner, P. P. Halenda, *J. Am. Chem. Soc.* **1951**, *73*, 373.
269. S. Lowell, J. E. Shields, M. A. Thomas, M. Thommes, *Characterization of Porous Solids and Powders: Surface Area, Pore Size and Density.* Springer, **2006**.
270. Debbie J. Stokes, *Principles and Practice of Variable Pressure Environmental Scanning Electron Microscopy (VP-ESEM)*. Chichester: **2008**, John Wiley & Sons. ISBN 978-0470758748.
271. D. B. Williams, C. B. Carter, *Transmission Electron Microscopy (2nd ed.),* Springer, **2009**.
272. Z. Li, M. L. Baker, W. Jiang, M. K. Estes, B. V. Prasad, *Journal of Virology*., **2009**, *83*, 1754.
273. P. J. Fratzl, *Appl. Crystallogr.* **2003**, *36*, 397.
274. S. E. Dann, *Reactions and Characterization of SOLIDS.* Royal Society of Chemistry, **2002**.
275. Z. Sassi, J. C. Bureau, A. Bakkali, *Vibrational Spectroscopy*, **2002**, *28*,251.
276. B. D. Cullity, S. R. Stock, *Elements of X-Ray Diffraction*. Prentice Hall, **2001**.
277. Y. Waseda, E. Matsubara, K. Shinoda, *X-Ray Diffraction Crystallography: Introduction, Examples and Solved Problems*. Springer, **2011**.
278. A. W. Coats, J. P. Redfern, *Analyst*, **1963**, *88*, 906.

279. G. Kickelbick, Hybrid Materials. *Synthesis, Characterization, and Applications.* Wiley-VCH, **2007**.
280. B. Wunderlich*, Thermal Analysis*, *New York*: *Academic Press*, **1990**, 137.
281. B. J. Berne, R. Pecora, *Dynamic Light Scattering.* Courier Dover Publications, **2000**.
282. R. Pecora, *Dynamic Light Scattering: Applications of Photon Correlation Spectroscopy*, Plenum Press, **1985**.
283. K. Kalantar-Zadeh, B. Fry, *Nanotechnology-Enabled Sensors*, Springer, **2008.**
284. J. Jiang, G. Oberdörster, P. Biswas, *J. Nanoparticle Res.* **2009**, *11*, 77.
285. A. Kumar, C. K. Dixit, "Methods for characterization of nanoparticles". *Advances in Nanomedicine for the Delivery of Therapeutic Nucleic Acids*. **2017**, 43-58.
286. M. Jumaa, B.W. Müller, *Int. J. Pharm.* **1998**, *163*, 81.
287. R. J. Hunter, *Zeta Potential in Colloid Science: Principles and Applications.* Academic Press, **2013**.
288. R. Shah, D. Eldridge, E. Palombo, I. Harding, *J. Phys. Sci.* **2014**, *25*, 59.
289. Malvern Intruments, Zetasizer Nano Series - User Manual, **2004**.

CHAPTER 2

FUNCTIONALIZED MESOPOROUS SILICA NANOPARTICLES AS RECYCLABLE CHIRAL CATALYSTS

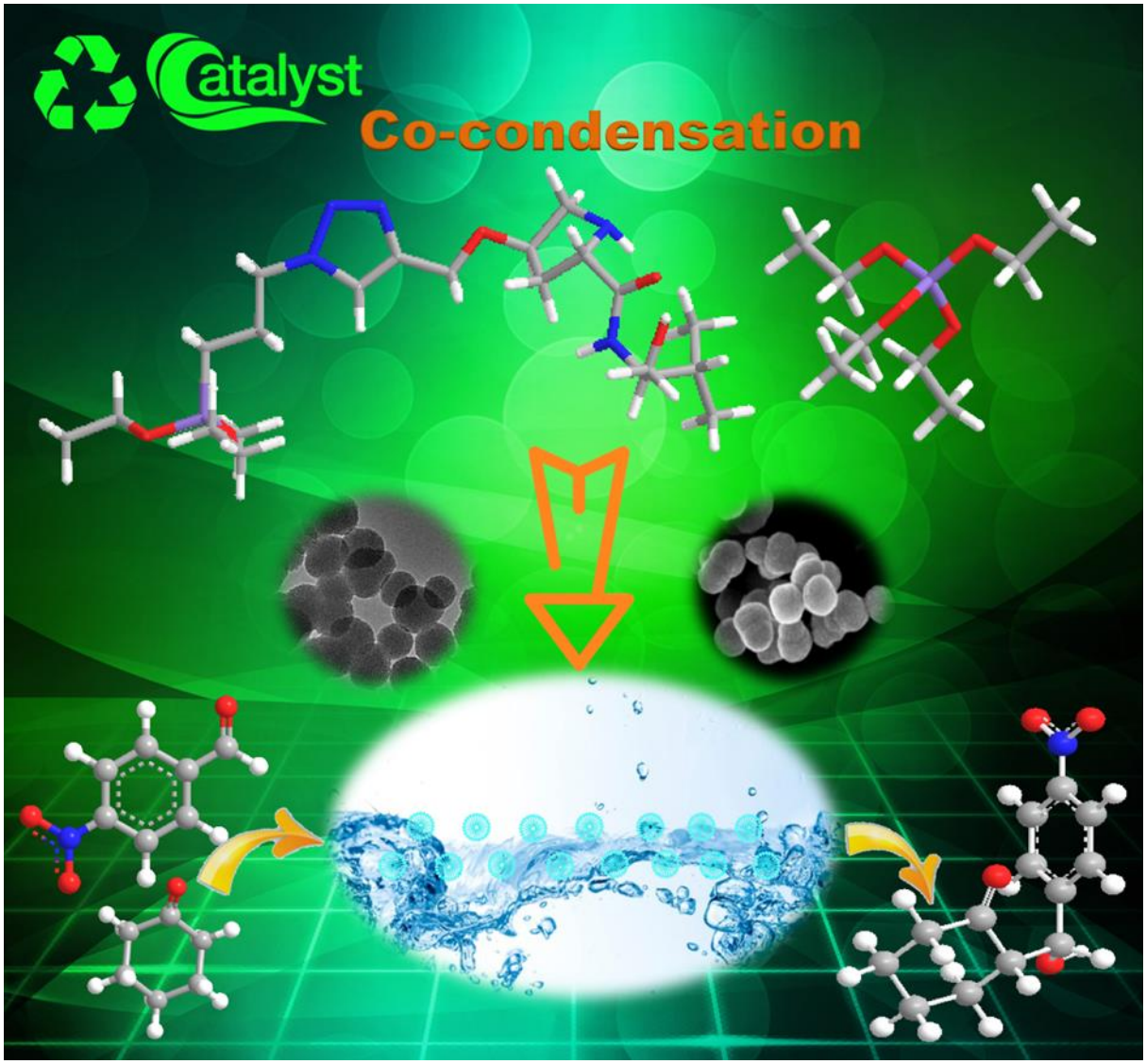

H. Li, M. Pérez-Trujillo, X. Cattoën, R. Pleixats,* Recyclable mesoporous organosilica nanoparticles derived from proline-valinol amides for asymmetric organocatalysis. *ACS Sustainable Chem. Eng.* **2019**. *7*(17): 14815-14828. DOI: 10.1021/acssuschemeng.9b02838

CHAPTER 2

FUNCTIONALIZED MESOPOROUS SILICA NANOPARTICLES AS RECYCLABLE CHIRAL CATALYSTS

2.1 Introduction

Mesoporous silica materials benefit from unique features that have attracted substantial interest for their use as catalyst-immobilization matrices. These features include high surface area, chemical, thermal, and mechanical stability, highly uniform pore distribution and tunable pore size, high adsorption capacity, and an ordered porous network for free diffusion of substrates and reaction products.[1] In the field of catalysis, a simple strategy to facilitate easy recovery and recycling of the catalyst is the attachment of the catalytic moiety in a solid inorganic polymeric support. The formation of organic-inorganic hybrid silica materials is attractive as a means to achieve supported catalysts, as they combine the advantages of a silica matrix with the properties of the organic or organometallic moiety. However, the applications for bulk mesoporous organosilicas are still limited by the lack of control of the morphology and particle size. The ability to obtain nanosized silica particles in a controlled manner broadens the spectra of applications[2-7] and improves the performances of these nanomaterials with unique properties. Thus, in recent years, MSNs have been considered attractive as catalysts support due to properties such as well-defined crystalline structure, large surface areas, uniform pore sizes, excellent thermal and mechanical stability, highly acidic sites in the protonated form and the presence of silanol groups on the surface, which allow the incorporation of a wide variety of functionalities.[8-10] Their nanometric size provides the advantages of an enhanced surface over volume ratio and a shorter pore length, thus easier diffusion in the case of mesoporous MCM-41 silica nanoparticles. Their short channels can act as the solid supports for highly accessible active sites in catalysis. In contrast to insoluble mesoporous organosilicas in micrometer or larger dimensions, well-suspended stable solutions of mesoporous organosilica nanoparticles can provide higher reaction rates in catalytic processes.[11]

In spite of the potential of organically modified MSNs, they have scarcely been applied in organocatalysis. Most of the examples involve simple achiral organocatalysts for aldol,[12-14] Knoevenagel,[15-16] and Henry condensations,[17-19] Michael additions,[20] cyanosilylation[12] and

Diels-Alder[21] reactions, conversion of cellulose to 5-hydroxymethylfurfural,[22] synthesis of tetrasubstituted imidazoles by a four component reaction,[23] selective formation of enol lactones and δ-keto esters from chromene and formic acid,[24] and one-pot three-component synthesis of 2-aminochromene derivatives.[16] As far as the asymmetric organocatalysis is concerned, only chiral imidazolidinones on mesoporous silica nanoparticles obtained by post-synthesis procedures have been described for stereoselective Diels-Alder cycloadditions.[25-26]

The enantioselective production of compounds has been a core subject of scientists' research, and asymmetric catalysis is one of the most direct and efficient ways to achieve enantioselective synthesis. Therefore, asymmetric organocatalysis becomes one of the major challenges in the modern organic chemistry.[27-34] Compared with enzymatic catalysis and metal catalysis, organocatalysis is generally considered to be an environmentally benign synthetic methodology with appealing green chemistry features regarding the type of catalyst involved (nontoxic, readily available, low cost，low sensitivity to moisture and oxygen，stable and easy to handle). These advantages confer a huge direct benefit in the production of pharmaceutical intermediates.[35-41] Many chemists are currently focusing on how to further improve its efficiency, stereoselectivity and applicability in practical applications. To this end, catalyst immobilization has been well explored in the development of recyclable organocatalysts as it is also typically practiced in its counterpart fields, enzymatic catalysis and metal catalysis.[42-46] Indeed, immobilized chiral organocatalysts can be easily recovered and reused and, in a number of cases, the immobilization may lead to enhanced activity and enantioselectivity.

In recent years, a series of immobilized organocatalysts have been developed for asymmetric organic reactions. The supports mainly used for covalent attachment of organocatalysts include organic polymers, solid acids, ionic liquids, magnetic nanoparticles and silica-based materials (**Figure 2.1**).[47] Another strategy involves the entrapment of organocatalysts into clay materials (montmorillonites and layered double hydroxides)).[48] In addition, dendrimers[49-50] and supramolecular hosts[51] are also promising and viable supports for organocatalysts.

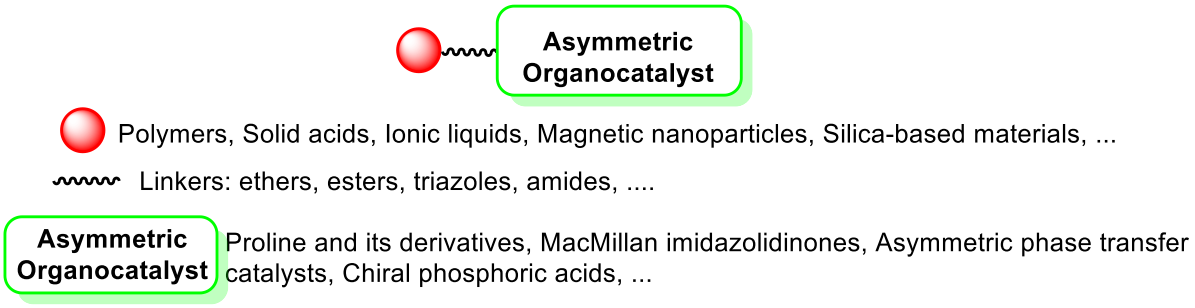

Figure 2.1 Supported asymmetric organocatalysts

In some cases, significant enhancement of efficiency and stereoselectivity can be obtained with a judicious selection of the immobilization strategy and supports. Unfortunately, some supported catalysts can only be recovered and reused for a limited number of runs. Moreover, multi-step synthesis is often required to achieve catalyst immobilization, and in most cases significant structural perturbations to the parent catalyst backbone are inevitable. Therefore, the development of supported organocatalysts with direct impact in real synthetic applications remains a challenging goal of great interest for the chemical community. Ideally, catalyst immobilization strategy should provide: 1) minimal synthetic modification and structural perturbations to the parent catalysts; 2) a facile catalyst linkage that allows for combinatorial screening; 3) a synergistic support to achieve optimal activity and selectivity. To this end, noncovalent immobilization represents one of the viable approaches to be further explored.

Homogeneous catalysts offer a great number of important advantages over their heterogeneous counterparts. Specifically, all catalytic sites are accessible because the catalyst is usually found in solution. Furthermore, it is often possible to tune the chemoselectivity, regioselectivity and/or stereoselectivity of the catalyst. Compared with heterogeneous catalysts, the main disadvantage of homogeneous catalysts is the difficulty to separate the final products from the catalyst and the reaction solvent.[52] This problem arises mainly because some homogeneous catalysts are thermally sensitive, and the most common separation method for relatively volatile liquid catalysts, distillation, requires high temperatures. Other conventional processes such as chromatography or extraction can also result in catalyst loss.[52-53] In any case, the separation is tedious and time-consuming. In contrast with metal-based catalytic processes, the organocatalyzed reactions require higher catalyst loadings (up to 30% molar), which not only represents a large amount, especially for multigram scale applications, but also a drawback in the purification of products. In addition,

the preparation of chiral organic catalysts of a certain structural complexity may involve several steps.

Taking into account the previously mentioned considerations, catalyst recovery and recycling remain a scientific challenge of economic and environmental relevance. Although separation techniques such as organic solvent nanofiltration[54-55] and membrane nanofiltration,[56-57] have been developed, some of the catalyst recovery technologies are not economically viable in industrial applications. Therefore, the recycling of the catalyst through simple operations and its reuse during processing is very important. Currently, one of the most widely used strategies to this purpose consists in immobilizing the homogeneous catalyst on an insoluble support.[44-45,58-62] Moreover, the recovery and reuse are facilitated because the filtration at the end of the reaction allows an easy separation and the organic products are obtained with lower contamination without time-consuming chromatography.

The choice of the support is quite relevant. On the one hand, supported catalysts are often sterically hindered and hence less accessible than their non-supported counterparts. Actually, the immediate surroundings of the active site can strongly affect the stereochemical approach of the reagents. On the other hand, a higher density of catalytic sites can be translated into higher activity, but this is not a general rule.[61,63-65] There are two main general approaches on immobilized organocatalysts: covalently supported and non-covalently supported catalysts (**Figure 2.2**).[45] In the first case, the organocatalysts have been covalently anchored to a soluble (such as PEG, dendrimers, …)[66-68] or insoluble (such as mesostructured silica MCM-41, cross-linked polystyrene, magnetite, …)[69-73] support. But in any case, the solubility properties must allow an easy separation. Indeed, by changing some environmental conditions such as solvent polarity or reaction temperature, the advantages of homogeneous and heterogeneous systems can be coupled. In the second case, the organocatalysts have been adsorbed (e.g. onto IL-modified SiO_2), dissolved (e.g. polyelectrolytes), included (e.g. β-CD) or linked by electrostatic interactions (e.g. PS/SO_3H, LDH) in several supports.

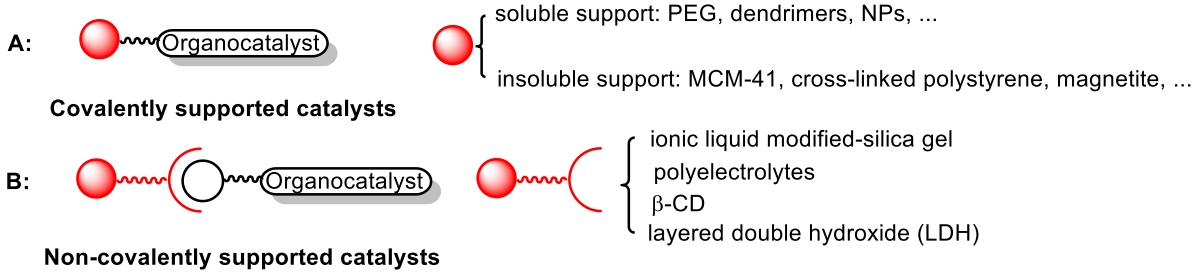

Figure 2.2 General approaches for supported organocatalysts

Supported organic catalysts have been the subject of some review articles over the past two decades.[43,60-61,74-75] Our group has contributed to this field by the development of silica supported recyclable organocatalysts. Dr. Montserrat Trilla prepared hybrid silica materials containing imidazolium and dihydroimidazolium salts from monosilylated and disilylated monomers in 2009 (**Figure 2.3**).[63] These materials are good recyclable catalysts for the Knoevenagel condensation between active methylene compounds and aromatic aldehydes in solvent-free conditions, providing a green and sustainable route to electrophilic trisubstituted alkenes. The immobilized catalysts show higher activities for this transformation than other related homogeneous bis-imidazolium salts.

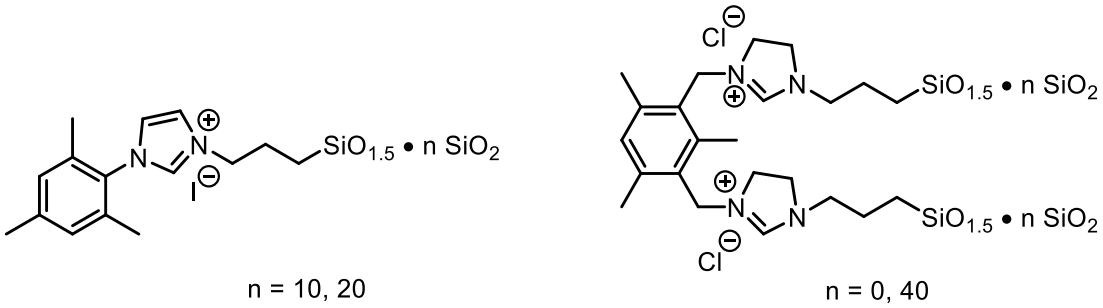

Figure 2.3 Hybrid silica materials containing imidazolium and dihydroimidazolium salts

Dr. Amàlia Monge-Marcet reported an hybrid silica material derived from a bis-silylated prolinamide by sol-gel methodology, which has been applied as a supported recyclable asymmetric organocatalyst in aldol and Michael reactions in 2011 (**Figure 2.4**).[76] This material exhibits performances similar to those of similar homogeneous organocatalysts.

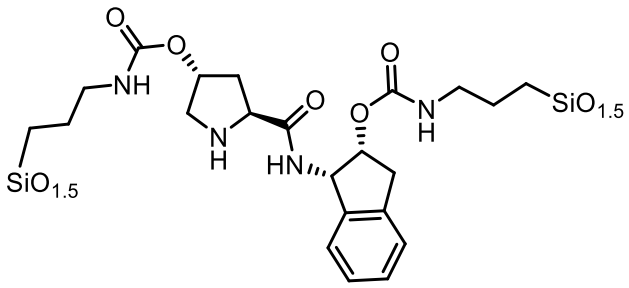

Figure 2.4 Hybrid silica material derived from a bis-silylated prolinamide

After that, Dr. Amàlia Monge-Marcet also prepared several silica-supported materials derived from a monosilylated prolinamide both by grafting and by sol-gel co-condensation (**Figure 2.5**).[77] These materials were used as recyclable catalysts in direct aldol reactions under simple and green conditions (water as solvent, absence of an acid co-catalyst, room temperature).

Good recyclabilities are observed without the need for catalyst regeneration, with enantioselectivities (ee up to 92%) higher than that of the parent homogeneous catalysts.

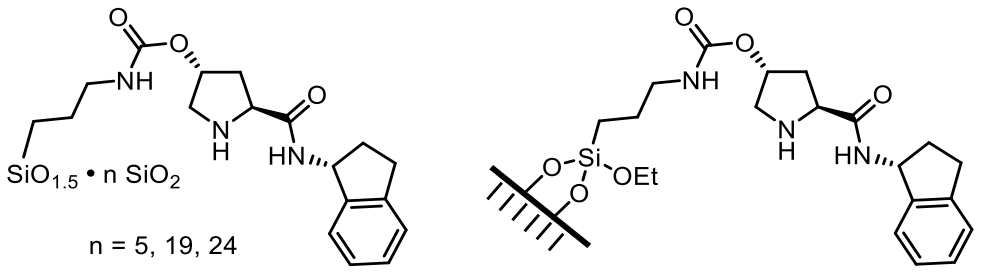

Figure 2.5 Silica-supported materials derived from a monosilylated prolinamide

Dr. Wusheng Guo reported the preparation of silica-immobilized iodoarenes by the sol-gel methodology from mono- and disilylated monomers and their catalytic performance in the α-tosyloxylation of aliphatic ketones, using m-CPBA as a stoichiometric oxidant, achieving from moderate to good isolated yields (**Figure 2.6**). The recyclability of the supported catalysts by a simple filtration was also investigated.[78]

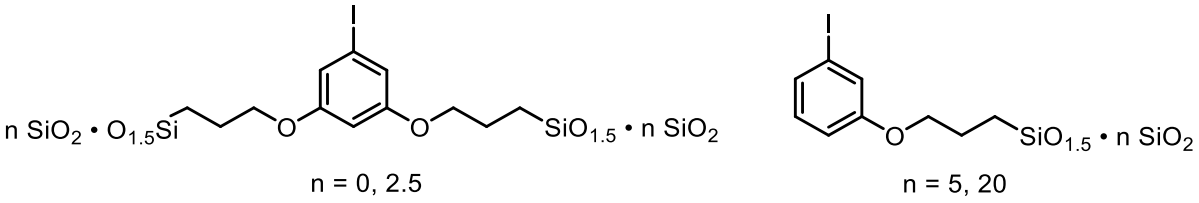

Figure 2.6 Silica-immobilized iodoarenes for α-tosyloxylation of aliphatic ketones

Dr. Meritxell Ferré prepared several hybrid silica materials by sol-gel cogelification and grafting methods from chiral mono-silylated proline sulphonamide precursors in 2016 (**Figure 2.7**).[79] The catalytic performances and reusability of these hybrid silica materials have been evaluated in direct intermolecular asymmetric aldol reactions between ketones and aromatic aldehydes and in a Robinson annulation using simple and green conditions (water, room temperature). Good conversions and recyclability, and from moderate to good diastereo- and enantioselectivities have been achieved. This is the first report on the preparation of sol-gel derived proline sulphonamides and the use of these hybrid silica materials as immobilized recyclable organocatalysts.[79]

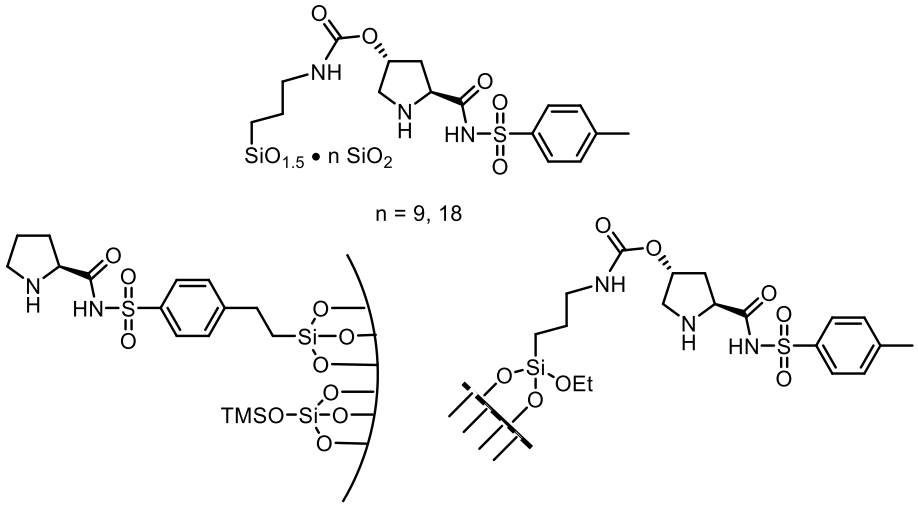

Figure 2.7 Hybrid silica materials from mono-silylated proline sulphonamides for aldol reaction

In spite of the results previously achieved, it is still necessary and meaningful to undertake further research on chiral organocatalysts that can be recycled and reused. In this work, we have focused on mesoporous silica nanoparticles as support because, as stated before, they have been scarcely investigated in asymmetric organocatalysis. We decided to study the direct asymmetric aldol reaction considering that there was no report of asymmetric induction on this process catalyzed by functionalized mesoporous silica nanoparticles.

2.2 Mesoporous silica nanoparticles derived from proline-valinol amides as recyclable organocatalysts for asymmetric aldol reaction

2.2.1 Asymmetric direct aldol reaction

The aldol reaction is a carbon-carbon bond forming process between two carbonyl compounds which results in the formation of β-hydroxy carbonyl compounds. Since the discovery of the aldol reaction by Wurtz in 1872,[80] it has become one of the most important topics in modern catalytic synthesis, and one of the most studied synthetic types in the field of asymmetric organic catalysis. It is also one of the most widely used methods to access complex organic molecules in a stereoselective fashion.[81-87] **Scheme 2.1** shows the direct catalytic asymmetric aldol process and issues of selectivity. There are numerous challenges such as issues of chemo-, regio-, diastereo-, and enantioselectivity in the aldol reation.[88] Development of catalytic methods, which avoid the production of stoichiometric by-products while maintaining the high levels of control available from stoichiometric processes, provides an atom economical alternative for this important transformation.[89]

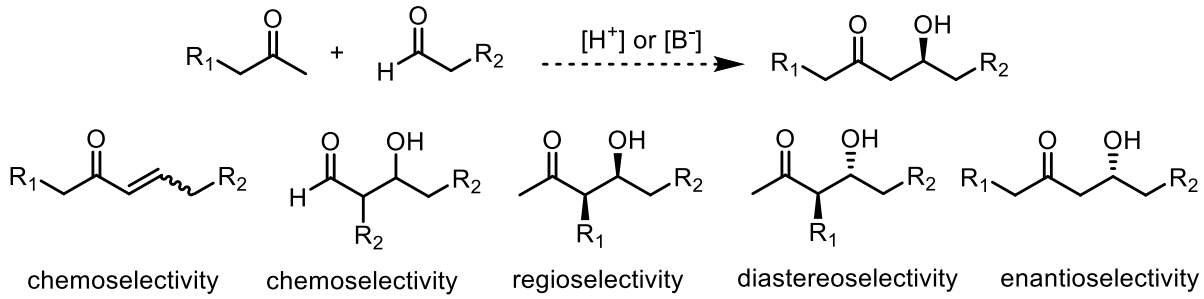

Scheme 2.1 The direct catalytic asymmetric aldol reaction and issues of selectivity.

In 1971, the first report of a direct asymmetric aldol reaction catalyzed by a small molecule was the Hajos-Parrish-Eder-Sauer-Wiechert cyclization (**Scheme 2.2**).[90-91] The intramolecular aldol reaction on triketone **2** to give the cyclized product **3** in excellent yield and enantioselectivity proceeded with only 3 mol% of L-proline **1**. Since then, amino acids such as L-proline and others are particularly appealing catalysts for the aldol reaction, due to their natural abundance and low cost.

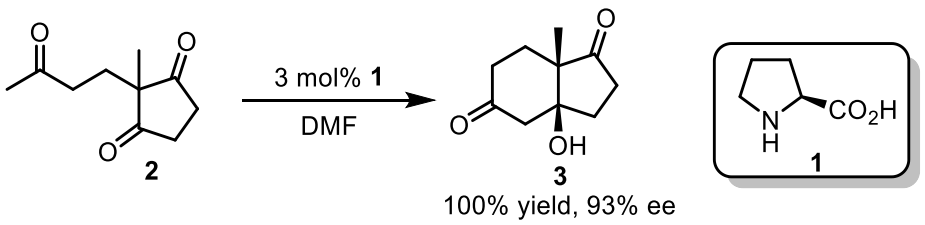

Scheme 2.2 Hajos-Parrish-Eder-Sauer-Wiechert aldol reaction

In 2000, List and colleagues described the first intermolecular proline-catalyzed direct aldol reaction (**Scheme 2.3**).[92] The treatment of aldehydes with 20-30 mol% of **1** in a 4:1 DMSO:acetone solution gave the desired aldol adducts **4**. Whereas aromatic and branched aliphatic aldehydes gave the highest yields and enantioselectivity, α-unbranched aldehydes were less successful substrates, giving low yields and moderate enantioselectivity.[93] Two years later, List and colleagues extended the substrates to ketones other than acetone. However, a large excess of these ketones were required (acting as co-solvent) and the reaction was limited to cyclohexanone, cyclopentanone and some simple short chain acyclic ketones.[94]

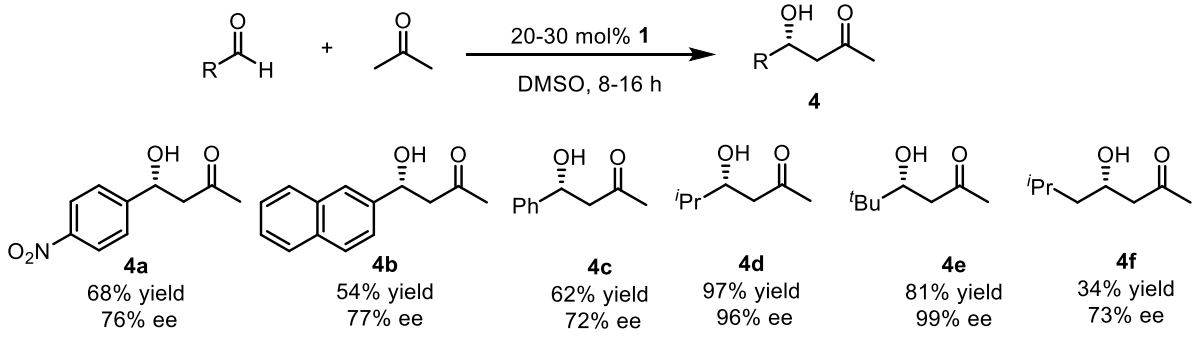

Scheme 2.3 The first intermolecular proline-catalyzed direct aldol reaction

Subsequently, some research groups developed a series of more reactive catalysts, which were proline derivatives, for direct aldol reaction. Some of the common modifications of the proline structure were aimed at increasing the hydrophobicity to improve the solubility in organic solvents. The modification of the carboxylic acid group to obtain a variety of other hydrogen-bonding groups, such as amide and thioamide, has also been investigated. Other trends include adding sterically bulky substituents and other stereocenters to enhance the enantioselectivity.

The amino acid L-proline and other proline derivatives have been used as organocatalysts for enantioselective aldol reactions via an enamine pathway, often enabling the reactions to be

performed in water as a sustainable medium. The generally accepted mechanism for a typical α-functionalization of carbonyl compound such as an aldol reaction starts with the enamine formation **A**. This step is followed by the addition of the enamine to a carbonyl (or other electrophile), which is activated by the carboxylic acid of proline through hydrogen-bond formation **B**. Finally, the hydrolysis of the iminium ion **C** affords the final product and regenerates the chiral catalyst **1** (**Scheme 2.4**).[82]

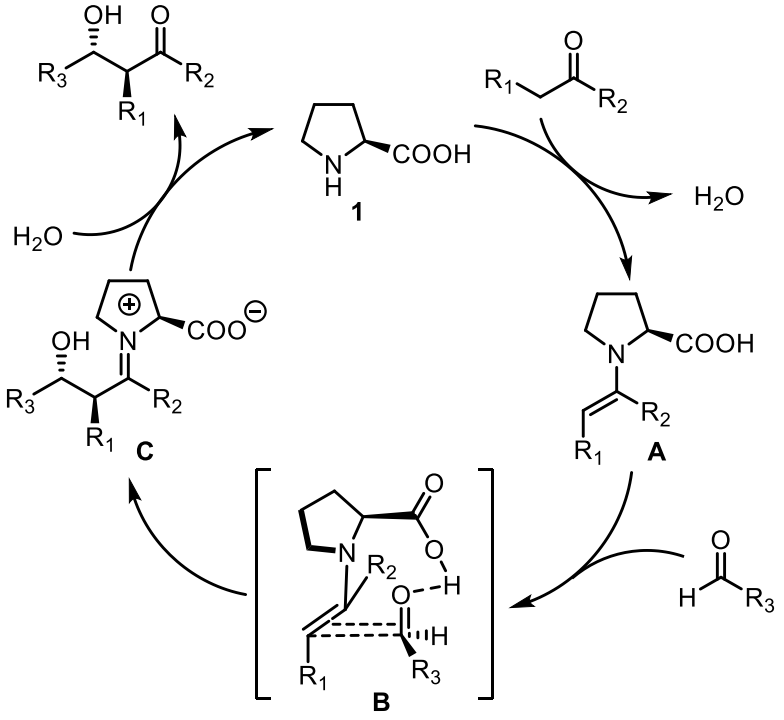

Scheme 2.4 List-Houk model mechanism of intermolecular proline-catalyzed aldol reaction.

Among other derivatives, we should mention L-proline derived amide **5.** In 2003, Tang and colleagues first reported that **5** (20 mol%) catalyze the direct asymmetric aldol reaction of acetone with aldehydes, up to 93% ee being obtained for aromatic aldehydes and up to 99% ee for aliphatic aldehydes (**Scheme 2. 5**).[95]

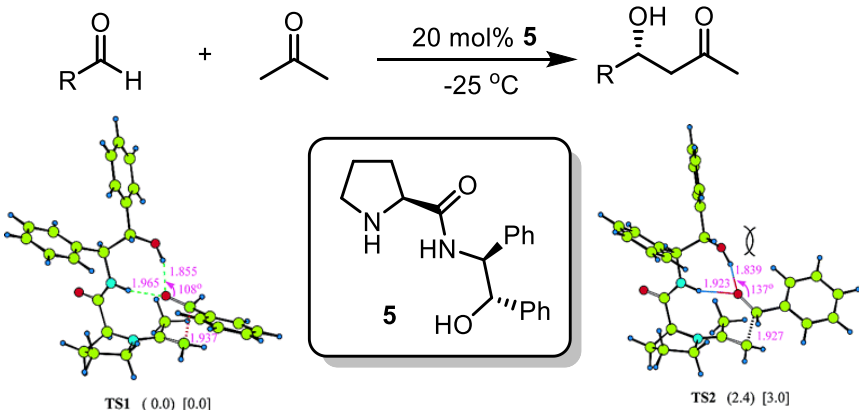

Scheme 2.5 L-proline derived amide **5** as catalyst for direct asymmetric aldol reaction

As shown in **Scheme 2.5**, the best transition structures for the reaction of benzaldehyde with acetone are similar to those with proline as the catalyst, except that here both the amide and the hydroxyl groups are hydrogen-bonded with the aldehyde. The hydroxyl group appears to be the better hydrogen-bond donor as indicated by the shorter hydrogen bond. The two phenyl groups of the catalyst are in equatorial positions. **TS1**, which leads to the formation of the major product observed experimentally, is found to be much more stable than **TS2**. The phenyl group of benzaldehyde in **TS1** does not have steric interactions with anything. On the other hand, the phenyl group of benzaldehyde in **TS2** has a severe steric interaction with the hydroxyl group (H- - -H distance is only about 2.14 Å). The C=O- - -H(O) angle must open up to reduce the steric interaction. The theoretical study of transition states demonstrates that the hydroxyl group of the organocatalyst is involved in the stereo discrimination.[95] These results suggest a new strategy for designing of new class of organocatalysts for direct asymmetric aldol reactions because several chiral sources contain multi-hydrogen bond donors. In 2009, Singh and colleagues found that the "hydrophobic effect" plays also a significant role in the direct aldol reaction.[96] Thus, the structural features of the organocatalyst play a crucial role in obtaining high optical purity of aldol adducts in an aqueous medium. Moreover, the role of water in increasing the rate and enantioselectivity of the reaction has been illustrated.[92]

A novel dipeptide derivative based on the proline catalysis concept and double hydrogen bonding activation was described by Li and co-workers in 2009 (**Scheme 2.6**). They found that proline-valinol thioamide **6** exhibits excellent activity and stereoselectivity for direct aldol reactions in the presence of acid additive.[97]

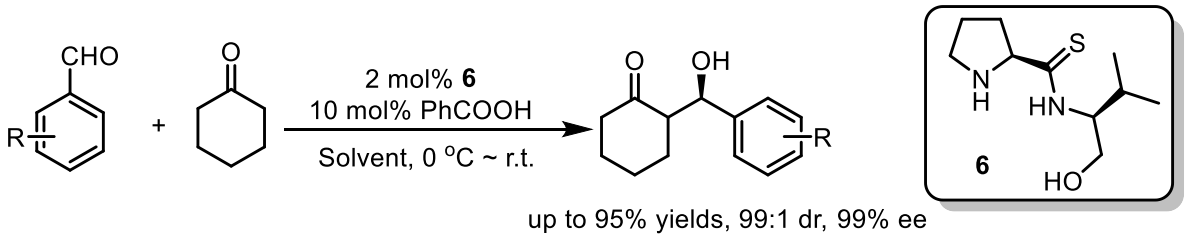

Scheme 2.6 Direct aldol reaction catalyzed by proline-valinol thioamide **6**

In the last 15 years, the direct asymmetric aldol reaction has experienced an exponentially growing development and is widely used in the synthesis of drugs, natural products, and other useful intermediates. Several review articles have been published related to organocatalysis in asymmetric aldol reaction.[81-82,94,98-113] Although the organocatalysts for this process have many striking features, several drawbacks should be mentioned. Some of these catalytic systems suffer from poor solubility in conventional solvents, others require high catalyst loading, and the separation and recovery of the homogeneous catalysts remain tedious. The immobilization of organocatalysts on organic as well as inorganic supports may allow lower catalyst loading, improved selectivity, easy separation of the catalyst and recyclability. Several types of polymers, dendrimers, silica materials, ionic liquids, polyethyleneglicols (PEG), and cyclodextrines have been identified as good supports to overcome partly these boundaries. A series of supported organocatalysts have been used for asymmetric aldol reaction.[86,114-117]

In our opinion, studies for the new highly active, stereoselective and highly recyclable organocatalysts are always desirable and important. Based on the research of our group, we decided to focus our attention on functionalized mesoporous silica nanoparticles as recyclable catalysts for the direct asymmetric aldol reactions. We chose proline-valinol amides/thioamides as organocatalysts.

2.2.2 Objectives

Based on the precedents mentioned before, following our studies on recyclable organocatalysts based on sol-gel methodologies, and going a step further from bulk insoluble organosilicas to dispersible nanosized materials, our objectives in this part of the thesis were as follows:

a) The preparation of functionalized mesoporous silica nanoparticles derived from mono- and bis-silylated proline-valinol amide and proline-valinol thioamide precursors. For this purpose, we first planned the synthesis of these silylated precursors (**Figure 2.8**). Then, we aimed to the preparation of several mesoporous silica nanoparticles derived from these precursors by post-grafting and co-condensation methods.

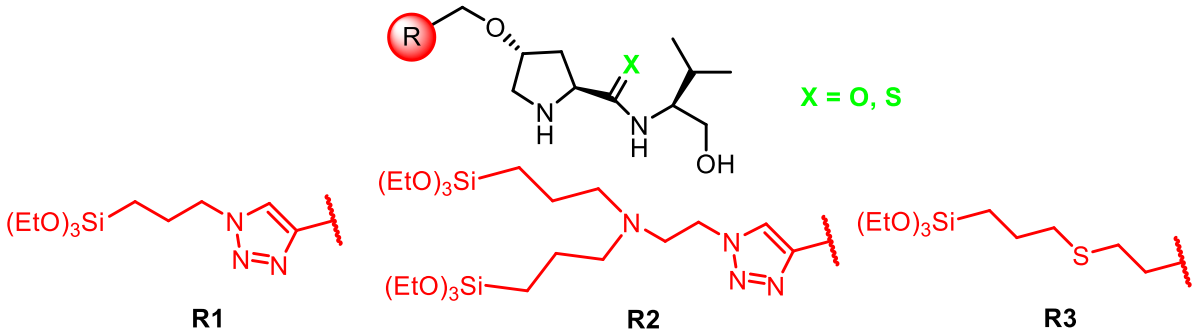

Figure 2.8 Silylated proline-valinol amides/thioamides for functionalized mesoporous silica nanoparticles

b) The characterization of all these new materials with appropriate techniques, such as elemental analysis, ^{13}C and ^{29}Si CP MAS solid state NMR, electron microscopy, nitrogen-sorption measurements, dynamic light scattering, zeta-potential, infrared spectroscopy and powder X-ray diffraction.

c) The assay of these functionalized mesoporous silica nanoparticles as chiral recyclable organocatalysts in direct asymmetric aldol reactions (inter- and intramolecular versions) (**Scheme 2.7**).

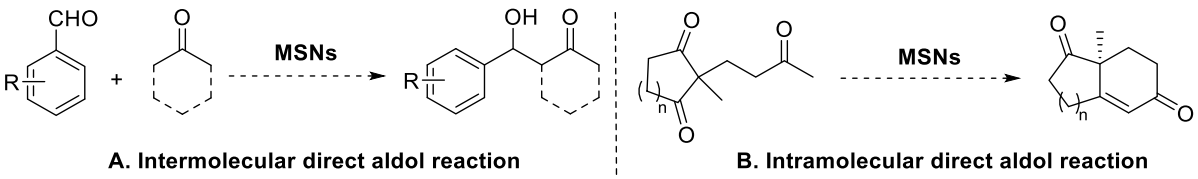

Scheme 2.7 Inter- and intramolecular direct aldol reactions with functionalized MSNs

2.2.3 Results and Discussion

2.2.3.1 Synthesis of silylated proline-valinol amides

Following our objectives, we pursued the preparation of different mesoporous silica nanoparticles derived from mono- and bis-silylated proline-valinol amides in order to evaluate and compare the performances of the supported organocatalysts in terms of efficiency and selectivity. Therefore, we first designed the silylated precursors **P1** and **P2** (**Figure 2.9**).

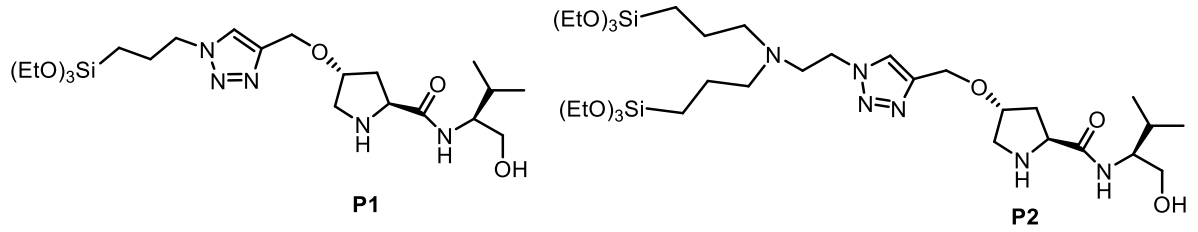

Figure 2.9 Monosilylated proline-valinol amide **P1** and bis-silylated proline-valinol amide **P2**

The retrosynthetic analysis for the precursor **P1** is depicted in **Scheme 2.8**. The treatment of a suitable hydroxyl containing *N*-protected proline **7** with propargyl bromide will provide **8**, which could be then reacted with L-valinol to form proline-valinol amide **9**. The desired silylated precursor would then be obtained by copper-catalyzed alkyne-azide cycloaddition reaction (CuAAC)[164-165] of the alkyne with the silylated azide **10** followed by a final step of amine deprotection in **11**. The retrosynthetic analysis for **P2** would be similar, but using the appropriate disilylated azide in the CuAAC reaction.

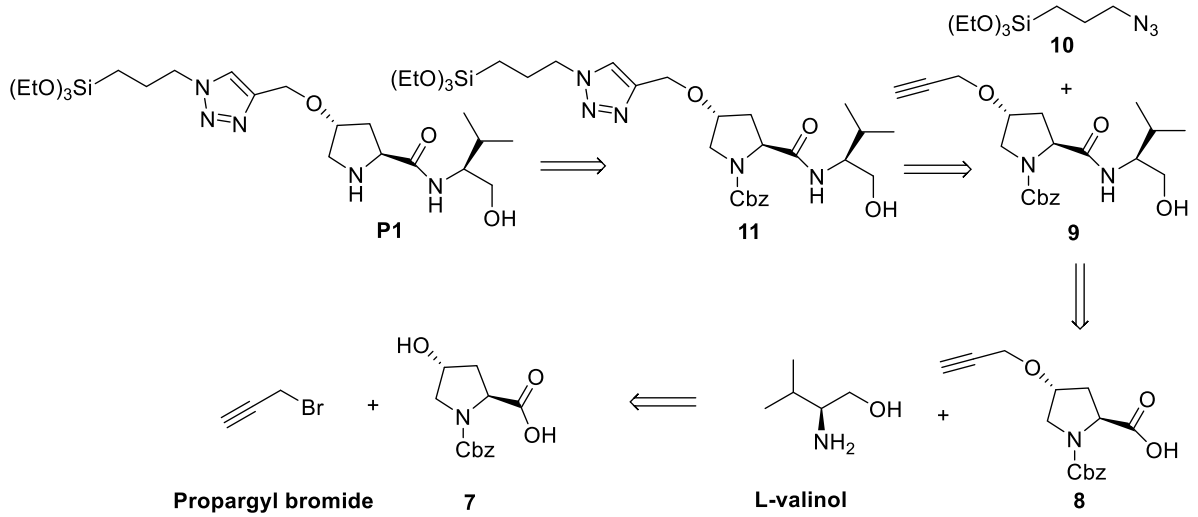

Scheme 2.8 Retrosynthetic analysis of silylated proline-valinol amide **P1**

Based on this retrosynthetic analysis, we first synthesized the mono-silylated precursor **P1.** The synthesis of intermediate **8** was undertaken starting from commercially available *Cbz*-protected 4-hydroxy-(*S*)-proline **7 (Scheme 2.9)** following a two-step procedure developed by Fache and colleagues in 2003.[120] The double propargylation of **7** with excess of propargyl bromide in the presence of NaH in anhydrous DMF provided **12** in 81% yield. Subsequent hydrolysis of the ester by using NaOH in MeOH afforded the free acid **8** in 93% isolated yield after acidic work-up.

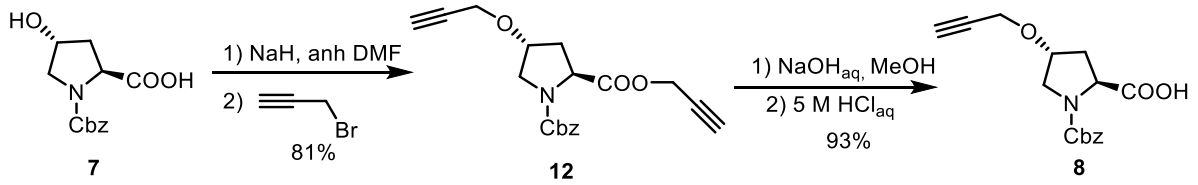

Scheme 2.9 Synthesis of *Cbz*-protected proline **8** following the procedure by Fache and colleagues

Pozzi and colleagues described in 2009 a direct synthetic route to alkoxyprolines.[121] Following this procedure, *Cbz*-protected 4-hydroxy-(*S*)-proline **7** was transformed into the corresponding dianion with NaH in a mixture of dimethyl sulfoxide and tetrahydrofuran (1:16 v/v), which experienced monoalkylation with propargyl bromide to give the proline **8** in a single step in 88% yield and with complete stability of the stereogenic center (**Scheme 2.10**).

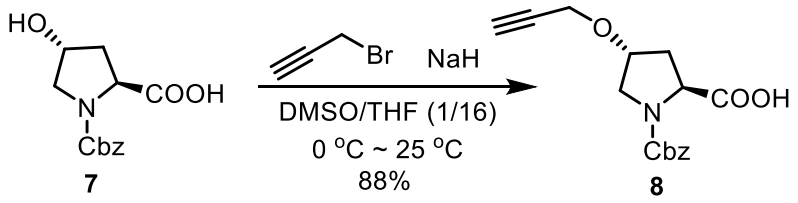

Scheme 2.10 Synthesis of *Cbz*-protected proline **8** following the procedure by Pozzi and colleagues

The amide **9** was obtained in 94% yield, through the intermediacy of a mixed anhydride, by reaction with L-valinol in the presence of triethylamine (**Scheme 2.11**). Then, a copper-catalyzed alkyne-azide cycloaddition reaction (CuAAC)[118-119] of the alkyne **9** with (3-azidopropyl)triethoxysilane **10** under anhydrous conditions[122] provided quantitatively the dipeptide **11**. The best results in our case were obtained with the use of CuI and tris(benzyltriazolylmethyl)amine (TBTA) in the presence of Et_3N in dry THF at 60 ºC for 16 h. After the work-up, the pure organosilane **11** was obtained in quantitative yield by washing the crude mixture with anhydrous pentane several times. Finally, the silylated precursor **P1**

was achieved in 96% yield by removal of the protecting group through hydrogenolysis (3 atm H_2, 10% wt Pd/C, 60 ºC, overnight) (**Scheme 2.11**).

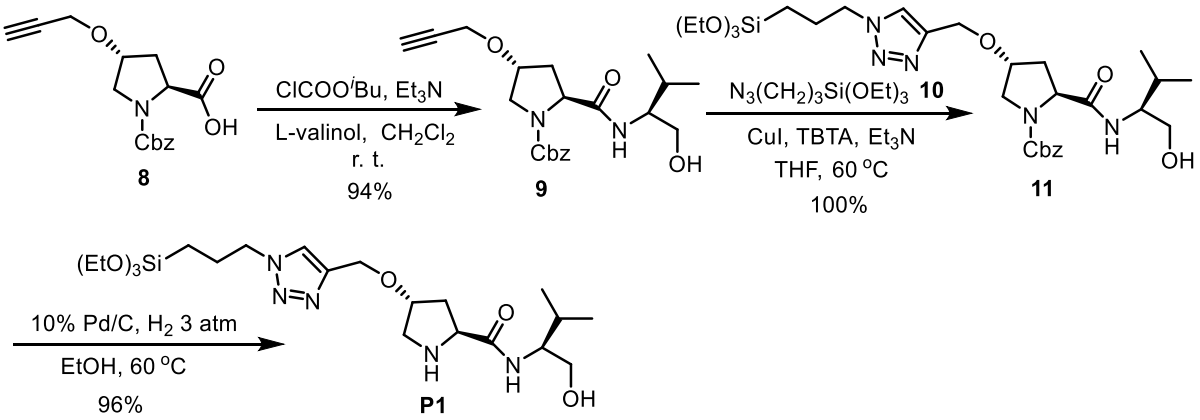

Scheme 2.11 Synthesis of the mono-silylated precursor **P1**

In a similar manner, **P2** was efficiently synthesized by the click reaction between the alkyne **9** and the disilylated azide **13**[123] followed by amine deprotection in **14** (65 % overall yield from **9**) (**Scheme 2.12**).

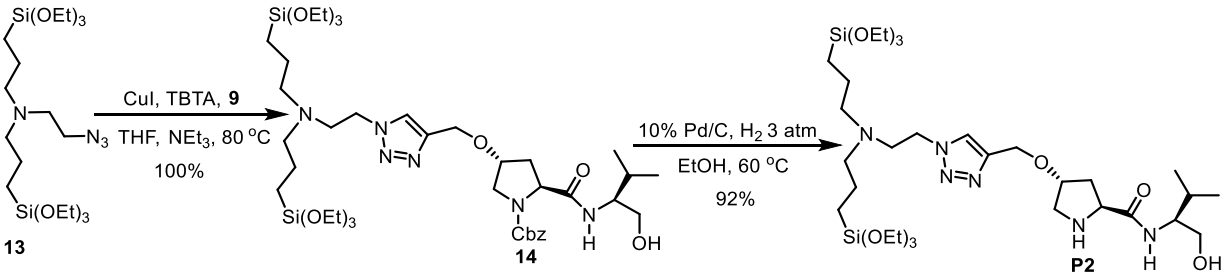

Scheme 2.12 Synthesis of the bis-silylated precursor **P2**

The silylated compounds **P1** (**Figure 2.10a**) and **P2** (**Figure 2.10b**) were fully characterized by ^{1}H and ^{13}C NMR spectroscopy. The performance of 1D and 2D NMR experiments (1D ^{1}H, 2D ^{1}H,^{1}H-COSY, ^{1}H,^{1}H-TOCSY, ^{1}H,^{1}H-NOESY, ^{1}H,^{13}C-HSQC and ^{1}H,^{13}C-HMBC) and the coordinated analysis of the resulting spectra allowed the complete characterization of the molecules (collaboration with Míriam Pérez, from the NMR Service of UAB) .

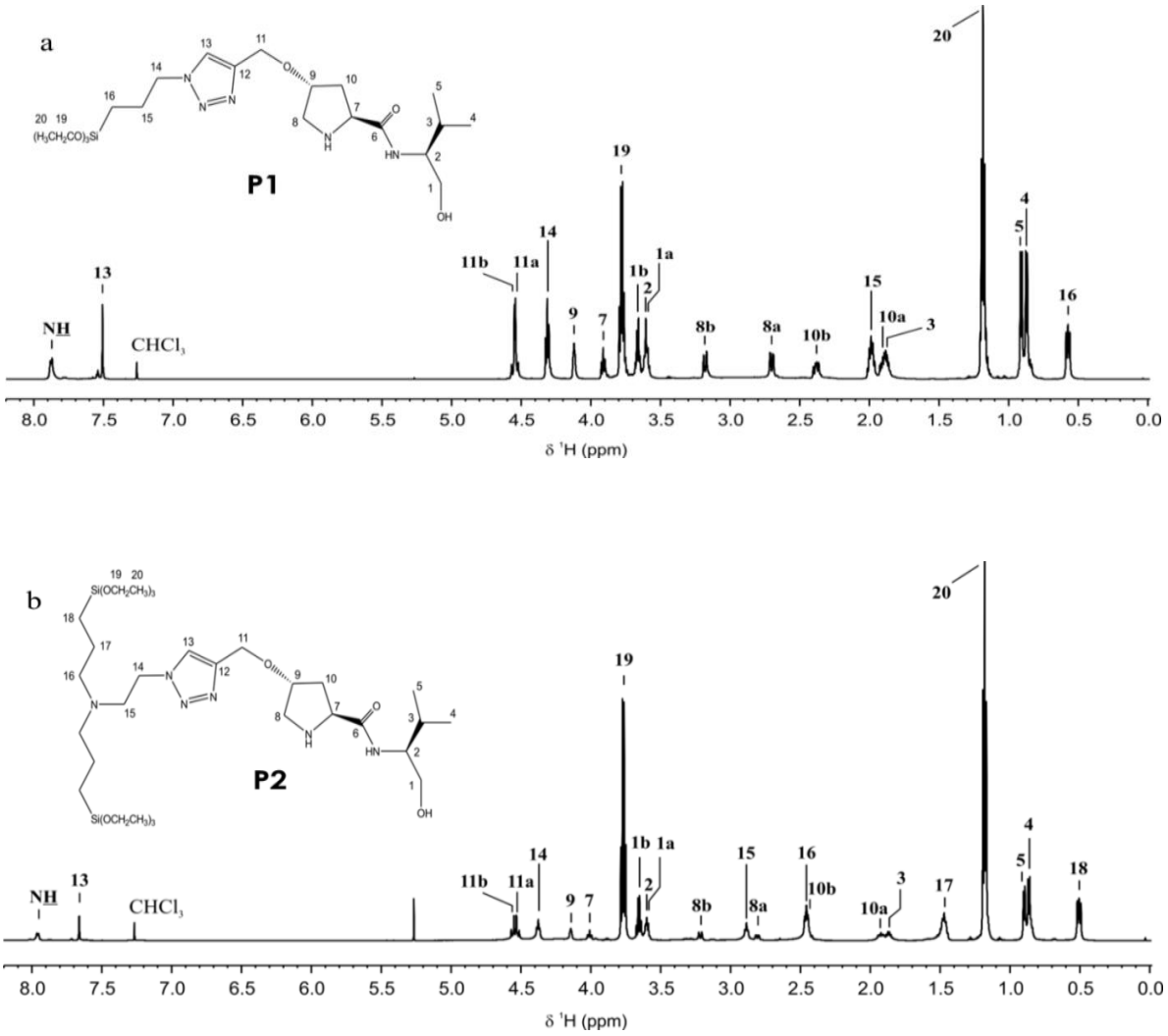

Figure 2.10 Assigned ^{1}H-NMR spectra corresponding to **P1** (a) and **P2** (b). Spectra acquired at 298.0 K and at a magnetic field of 600 MHz.

Results from 2D NMR correlations, such as TOCSY, NOESY and HMBC, confirmed both structures. Also, peak integrations were in accordance with them. The full ^{1}H and ^{13}C characterizations of **P1** and **P2** are collected in **Table 2.1**.

Table 2.1 ^{1}H and ^{13}C NMR chemical shifts and H-H *J* couplings of precursors **P1** and **P2**

	P1			**P2**		
	^{1}H		**^{13}C**	**^{1}H**		**^{13}C**
Id	**δ (^{1}H)** [ppm]	**(mult.,* $J_{H,H}$)** [Hz]	**δ (^{13}C)** [ppm]	**δ (^{1}H)** [ppm]	**(mult.,* $J_{H,H}$)** [Hz]	**δ (^{13}C)** [ppm]
1a	3.604	m	64.36	3.596	m	64.94
1b	3.659	m	"	3.647	m	"
2	3.605	m	57.03	3.598	m	57.36
3	1.883	m	29.05	1.865	m	29.00
4	0.869	d, $^{3}J_{4\text{-}3}$ = 6.8	18.34	0.861	d, $^{3}J_{4\text{-}3}$ = 6.7	18.49
5	0.907	d, $^{3}J_{5\text{-}3}$ = 6.8	19.72	0.895	d, $^{3}J_{5\text{-}3}$ = 6.7	19.65
6	-		175.77	-		176.01
7	3.910	t, $^{3}J_{7\text{-}10}$ = 8.0	60.00	4.007	t, $^{3}J_{7\text{-}10}$ = 8.4	59.88
8a	2.702	dd, $^{2}J_{8a\text{-}8b}$ = 12.7 $^{3}J_{8a\text{-}9}$ = 3.4	52.49	2.804	dd, $^{2}J_{8a\text{-}8b}$ = 12.8 $^{3}J_{8a\text{-}9}$ = 2.5	52.44
8b	3.177	d, $^{2}J_{8b\text{-}8a}$ = 12.7	"	3.212	d, $^{2}J_{8b\text{-}8a}$ = 12.8	"
9	4.119	m (br)	80.72	4.139	m (br)	80.67
10a	1.903	m	36.63	1.915	m	36.46
10b	2.382	m	"	2.434	m	"
11a	4.533	d, $^{2}J_{11a\text{-}11b}$ = 12.1	62.20	4.519	d, $^{2}J_{11a\text{-}11b}$ = 11.8	62.09
11b	4.554	d, $^{2}J_{11b\text{-}11a}$ = 12.1	"	4.555	d, $^{2}J_{11b\text{-}11a}$ = 11.8	"
12	-		144.82	-		144.47
13	7.502	s	122.55	7.656	s	123.27
14	4.312	t, $^{3}J_{14\text{-}15}$ = 7.0	52.53	4.373	t, $^{3}J_{14\text{-}15}$ = 6.3	48.91
15	1.985	m	24.27	2.884	t, $^{3}J_{15\text{-}14}$ = 6.3	54.17
16	0.571	m	7.59	2.454	t, $^{3}J_{16\text{-}17}$ = 7.3	57.06
17	-		-	1.468	m	20.32
18	-		-	0.503	m	7.81
19	3.777	q, $^{3}J_{20\text{-}19}$ = 7.0	58.60	3.766	q, $^{3}J_{20\text{-}19}$ = 7.0	58.38
20	1.182	t, $^{3}J_{19\text{-}20}$ = 7.0	18.51	1.178	t, $^{3}J_{19\text{-}20}$ = 7.0	18.33

* s (Singlet), d (doublet), t(triplet), dd (doublet of doublets), m (multiplet), br (broad).

The obtention of precursor **P3** was envisaged through a thiol-alkene click reaction between the suitable alkene and (3-mercaptopropyl)triethoxysilane. The attempted synthesis is summarized in **Scheme 2.13**. First, the selective allylation of hydroxyl group of *Cbz*-protected 4-hydroxy-(*S*)-proline **7** to give the proline derivative **15** was performed following the methodology reported by Pozzi[121] and that we had successfully applied in the case of

propargylation. The proline-valinol amide **16** was prepared from **15** in 96% yield, through the intermediacy of a mixed anhydride, by reaction with L-valinol in the presence of triethylamine in dichloromethane at room temperature. The mixture of **16** and (3-mercaptopropyl)triethoxysilane was irradiated at 365 nm using 2,2-dimethoxy-1,2-diphenylethanone (DMPA) as initiator, and the desired compound **17** was obtained in quantitative yield.[124]

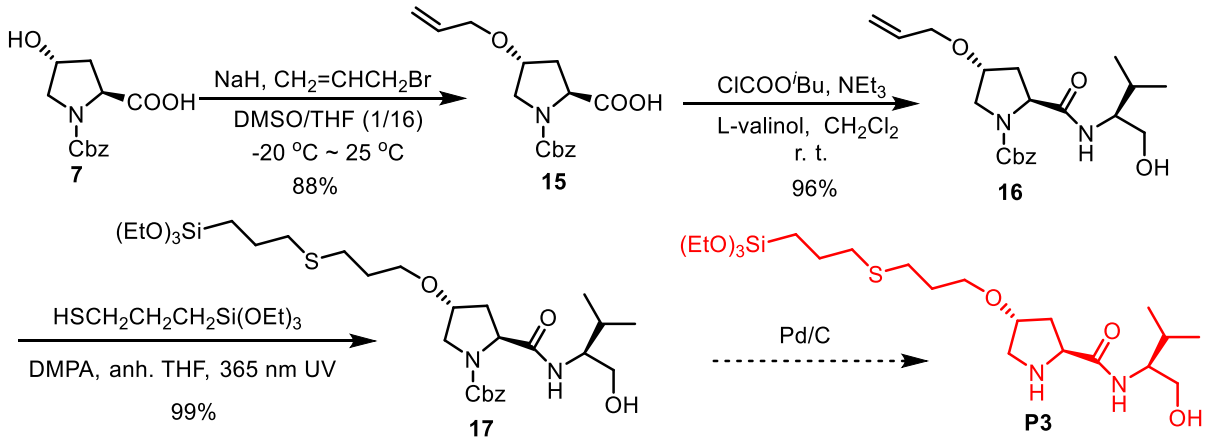

Scheme 2.13 Attempted synthesis of monosilylated precursor **P3**

Finally, we tried to deprotect the amino group under different conditions (**Table 2.2**). The attempts to remove the *Cbz* group were unsuccessful even if the reaction temperature was raised or the amount of catalyst was increased or different reducing systems were used (3 atm H_2 and Pd/C; cyclohexene and Pd/C) (**Scheme 2.13**). We suspect that the presence of sulfur atom may deactivate the Pd/C catalyst.[125-129] Unfortunately, we finally did not obtain the precursor **P3** and we were not allowed to use it for the preparation of organosilica nanoparticles.

Table 2.2 Investigation of deprotection reaction in **17** to afford **P3**

Entry	Reaction conditions	Result
1	Pd/C (20 mol% Pd , H_2, 3 atm, 50 °C	No reaction
2	Pd/C (20mol % Pd), H_2, 3 atm, 60 °C	No reaction
3	Pd/C (40 mol% Pd), H_2, 3 atm, 60 °C	No reaction
4	Pd/C (20 mol% Pd), cyclohexene, 80 °C	No reaction

2.2.3.2 Attempts to prepare a proline-valinol thioamide

Gryko reported in 2005 that the replacement of the amide group with the thioamide functionality has a beneficial effect on both the yield and the stereoselectivity of the aldol addition.[130] Nájera and co-workers also demonstrated in 2008 that prolinethioamides containing an aminoindane ring in their structure were more efficient organocatalysts in the aldol reaction than their prolinamide analogues.[131-132] Moreover, as we have mentioned before, Li and colleagues developed a novel thioamide-type dipeptide derivative based on the proline catalysis concept and double hydrogen bonding activation and examined its applications in the organocatalytic asymmetric aldol reaction. High yields and excellent enantioselectivities and diastereoselectivities were obtained by using only 2 mol% catalyst (see **6** in **Scheme 2.6**).[97] This may arise from the higher acidity of the thioamide NH group relative to the amide NH functionality.[133]

In 2011, Gryko and colleagues also further confirmed that the replacement of the amide group with more acidic thioamide functionality has a beneficial effect on both the yield and the stereoselectivity by a comparative study on the catalytic activity of prolinamides and their respective thioamides. In prolinethioamides, the NH becomes a better hydrogen bond donor, which is crucial for the efficacy of the catalyst, but also steric factors influence the stereochemical outcome of the aldol reaction. Furthermore, since L-prolinamides and thioamides bear a terminal hydroxyl group, the enantioselectivity can be tuned through the configuration and the electronic and steric nature of the α-substituent.[134]

As the homogeneous proline-valinol thioamides provided higher activities and selectivities than the corresponding amides, we were very interested in the synthesis of silylated proline-valinol thioamide precursors for the preparation of mesoporous organosilica nanoparticles by both post-grafting and co-condensation methods.

The synthesis strategy envisaged for the monosilylated thioamide precursor **P4** (**Scheme 2.14**) started from the already prepared proline-valinol amide **9** (see previous **Scheme 2.11**), which could then be converted into proline-valinol thioamide **18** by treatment with Lawesson's reagent. In order to avoid the destruction of hydroxyl group in the formation of proline-valinol thioamide with Lawesson's reagent, we chose TBDMS (*tert*-butyldimethylsilyl) as hydroxyl protecting group. The reaction of **9** with TBDMSCl in the presence of Et_3N gave **18** in 97% yield (**Scheme 2.14**), which was subsequently treated with Lawesson's reagent in

THF, the thioamide **19** being obtained in 53% yield. The deprotection of the TBDMS group was done with the gentle methodology developed by Kim,[135] in which HCl is generated *in situ* from 1-chloroethyl chloroformate in MeOH. The proline-valinol thioamide **20** was obtained in 55% isolated yield. At this moment, we proceeded with the preparation of the silylated azide **21** under copper-catalyzed alkyne-azide cycloaddition reaction (**Scheme 2.14**).

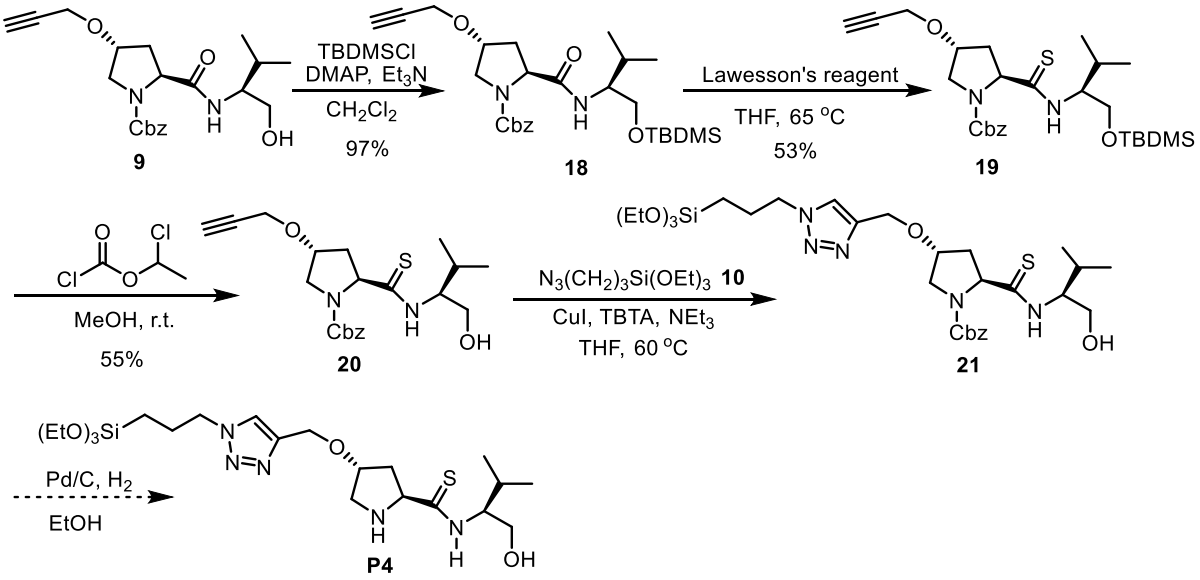

Scheme 2.14 Attempted synthesis of the monosilylated thioamide precursor **P4**

In contrast to the amide analog **9**, we found that alkyne **20** reacted sluggishly with the azide **10** and the reaction was not complete. Therefore, we used the crude mixture to test the deprotection. The *Cbz* group was also found very difficult to remove by hydrogenolysis (H_2 3 atm and Pd/C), probably due to the presence of sulfur atom in the molecule as we had observed in compound **17**.

Unfortunately, all our efforts to achieve the corresponding silylated thioamide precursor **P4** were unsuccessful. For this reason, we decided to focus on **P1** and **P2** precursors and prepare and test the nanomaterials derived from these efficiently synthesized silylated amides.

2.2.3.3 Preparation of mesoporous silica nanoparticles derived from proline-valinol amides

From the precursors **P1** and **P2**, six different functionalized mesoporous silica nanoparticles were prepared by sol-gel co-condensation methodology and by grafting on mesostructured silica nanoparticles of **MCM-41** type[136] and **M0**.[137] The MSN of MCM-41 type were prepared[136] under basic conditions (NaOH) in the presence of a cationic template (CTAB) and showed a regular hexagonal array of uniform channels (**Scheme 2.15a**). **M0** nanoparticles were obtained[137] in a buffer solution of pH 7 with a mixture of cationic and nonionic surfactants (CTAB and Brij-56) resulting in a more disordered wormlike mesostructure (**Scheme 2.15b**).

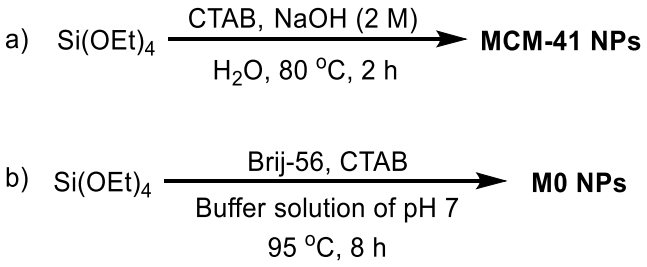

Scheme 2.15 Preparation of **MCM-41** NPs and **M0** NPs

Specifically, **M1** and **M2** were synthesized by anchoring the precursors **P1** and **P2**, respectively, to MCM-41 MSN under standard conditions (**Scheme 2.16a**). Similarly, **M3** and **M4** were prepared in analogous manner by grafting **P1** and **P2** to **M0** MSN, respectively (**Scheme 2.16b**). Finally, materials **M5** and **M6** were obtained by co-condensation of precursors **P1** and **P2** with tetraethyl orthosilicate (TEOS) using Brij-56 and hexadecyltrimethylammonium bromide (CTAB) as templates, in an analogous manner to **M0**. They were synthesized in an aqueous buffer solution of pH 7 from mixtures with the molar ratios Brij-56 : CTAB : TEOS : $\mathbf{P_n}$: H_2O = 1 : 20 : 160 : 16 : 120000. The final solution was stirred at 95 ºC for 8 h (**Scheme 2.16c**) and then the nanoparticles were collected by centrifugation (13500 rpm) at room temperature. The surfactants were removed from the obtained solid by treatment with an ethanolic solution of NH_4NO_3 and then the resulting material was washed successively with ethanol, Mili-Q water and ethanol.

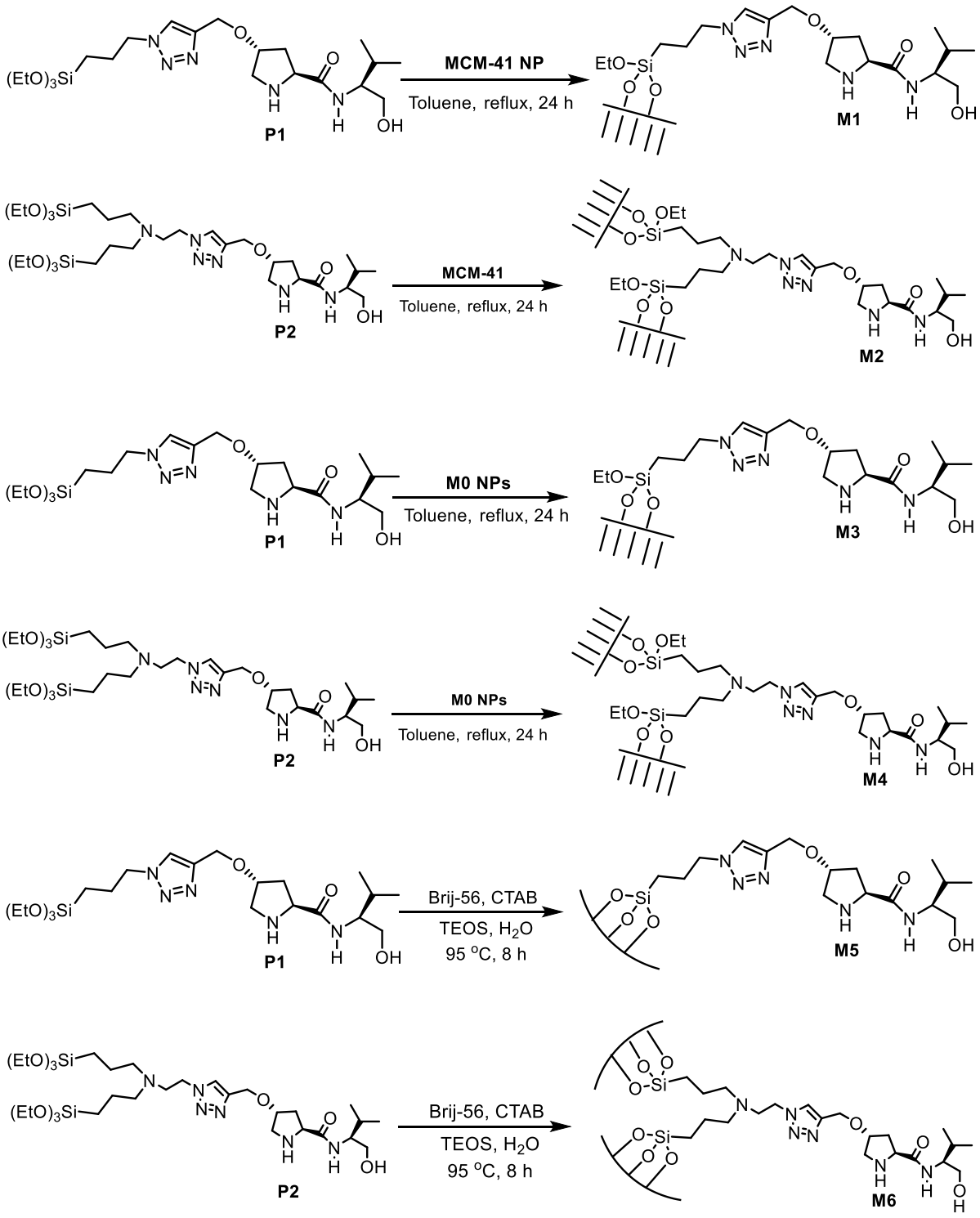

Scheme 2.16 Preparation of mesoporous silica nanoparticles **M1-M6.**

2.2.3.4 Characterization of functionalized mesoporous silica nanoparticles M1-M6 and the parent MCM-41 and M0 nanoparticles

The functionalized mesoporous silica nanoparticles were characterized by ^{13}C and ^{29}Si CP MAS solid state NMR, elemental analysis, transmission electron microscopy (TEM), scanning electron microscopy (SEM), nitrogen-sorption measurements, dynamic light scattering (DLS), zeta-potential, infrared spectroscopy (IR) and powder X-ray diffraction (*p*-XRD) (with the collaboration of Xavier Cattoën from Intitut Néel in Grenoble). Some physical data of **M1-M6** and parent **MCM-41** and **M0** are given in **Table 2.3**.

Table 2.3 Some physical data of **M1-M6** and parent MSNs **(MCM-41** and **M0).**

Mat.	N_2-sorption measurements			N content	Cat. Loading	Particle size (nm)		Zêta potential
	S_{BET} (m^2g^{-1})	V_{pore} (cm^3g^{-1})[a]	$\emptyset_{pore}$ (nm)[b]	Exp. (%)[c]	(mmol g^{-1})[d]	TEM	DLS	(mV)
MCM-41 NPs	1097	0.79	2.7	-	-	-	112	-25
M0	332	0.29	3.1	-	-	75±8	102	-25
M1	682	0.29	2.6	5.43	0.78	-	nd[e]	nd[e]
M2	477	0.21	2.5	5.84	0.69	-	80	49
M3	183	0.14	3.0	3.33	0.48	84±10	150	25
M4	177	0.13	3.0	3.07	0.37	78±7	135	40
M5	135	0.09	2.5	5.71	0.82	107±10	170	20
M6	16	0.02	-	6.70	0.80	-	nd[e]	nd[e]

[a] Determined from the uptake at saturation at p/p° = 0.8. [b] Diameter determined by NLDFT. [c] Experimental value of N content according to the elemental analysis. [d] mmol proline-valinol amides g^{-1} material calculated from the N elemental analysis. [e] Aggregated nanoparticles.

We present in **Figure 2.11** the TEM and SEM images, and *p*-XRD diffraction patterns of **MCM-41** and **M0 NPs**. We can notice that the obtained **MCM-41** shows quite well ordered hexagonal arrays of mesopores. The **M0** has a spherical morphology with a uniform size but less ordered than **MCM-41**. The *p*-XRD pattern of **MCM-41** at 2θ angles from 1.5° to 6° exhibit a characteristic intense (100) peak and two obvious (110) and (200) reflections at 2θ = 2.3°, 3.9°, 4.4°, respectively. The strong peak (100) directly point out the presence of MCM-41 structure, and the two weak peaks (110) and (200) can be indexed to the P6 mm space group, indicating a hexagonal mesostructured material with a high degree of long range ordering of the structure. In contrast, the *p*-XRD of **M0** only shows broad signals indicative of a disordered mesostructure.

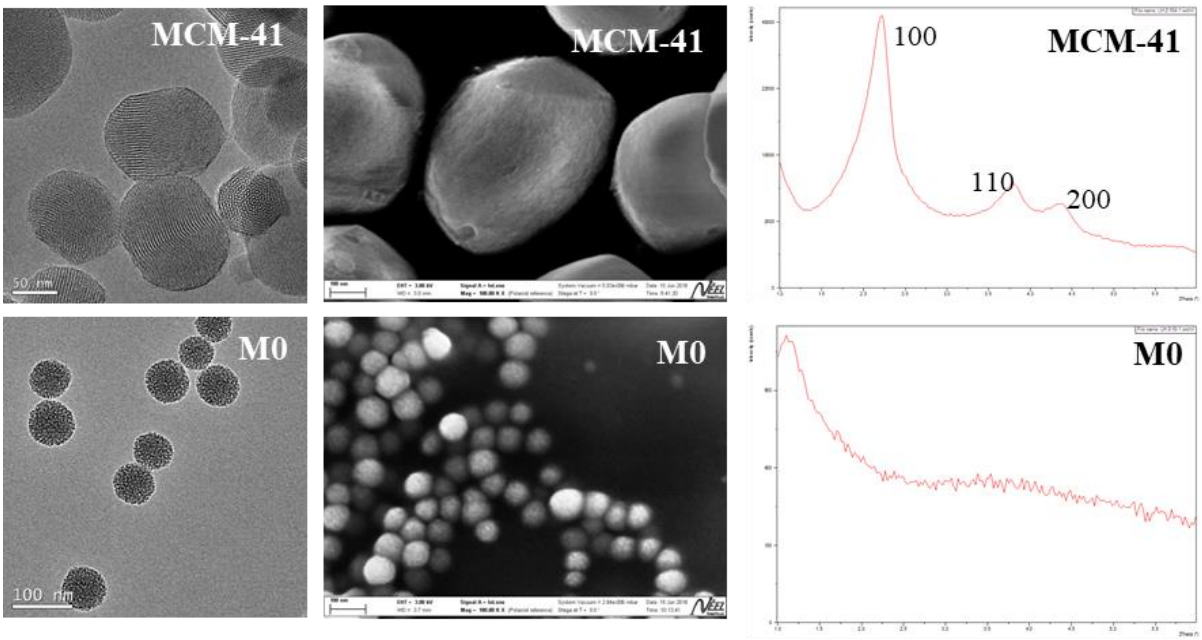

Figure 2.11 TEM and SEM images, and *p*-XRD diffraction patterns of **MCM-41** and **M0**

The materials **M1-M6** were first investigated by electron microscopies, to confirm their nanosize. **M1** and **M2** obtained from **MCM-41** NPs by grafting, preserve the initial rod-like morphology with lengths from 100 to 600 nm. The TEM images display the typical parallel channels throughout the rods in all three cases. Similarly, **M3** and **M4**, obtained from **M0**, preserve the initial spherical morphology, with diameters around 80 nm. The TEM images clearly indicate the presence of pores, though they are not organized as in **MCM-41**. Interestingly, the synthesis of **M5** by co-condensation with 10 mol% of the elaborated organosilane **P1** yielded spherical NPs uniform in size (110 nm), with the same type of porosity as for **M0**, as seen by TEM. However, the same synthesis from the bis-silylated precursor **P2** afforded aggregated nano-objects **M6** with no visible porosity (**Figure 2.12**). These results are also supported by SEM as well as by DLS analyses. Selected SEM of **M1** and **M5** are shown in **Figure 2.12**.

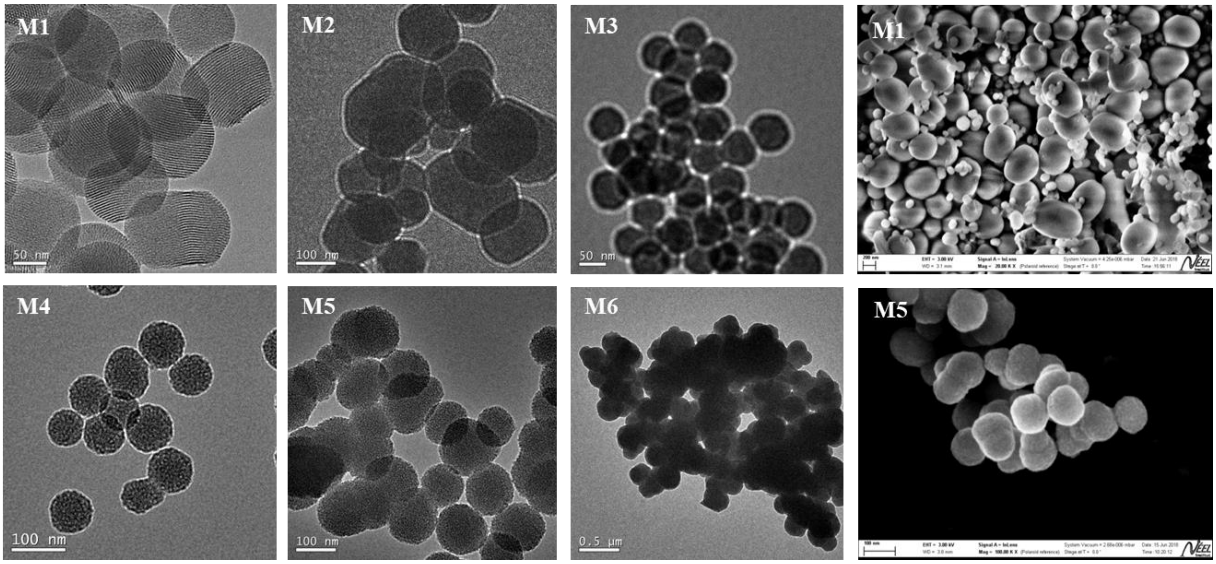

Figure 2.12 TEM images of **M1-M6** and selected SEM images of **M1** and **M5**

The porosity of the materials was probed by N_2-sorption experiments: for **M1** and **M2**, prepared by grafting from **MCM-41**, the surface area and pore volumes were significantly reduced compared to the parent MSNs whereas the pore diameter was only slightly decreased, in agreement with what is usually observed. The specific surface areas and pore volumes for the **M0**-derived materials **M3** and **M4** are significantly lower (surface areas from 330 to 180 m^2/g after grafting, **Table 2.3**). The surface area of **M5** obtained by co-condensation was 135 m^2/g. Except for **M6**, which is not porous, all materials display isotherms typical of mesoporous materials with small pores (no hysteresis) (**Figure 2.13**). Indeed, the pore diameters of all these materials lie in the range 2.5-3.0 nm. The contribution of micropores is negligible for all materials except **M5**, which displays ca 40 m^2/g of microporous surface area. The *p*-XRD analyses only showed an organized porosity for the **MCM-41**-derived materials **M1** and **M2**, typical for a hexagonal 2D symmetry with a sharp Bragg peak (1,0) and the two first harmonics ((1,1) and (2,0)). The broad pattern observed for **M0** and related materials (**M3** and **M4** from grafting and **M5** from co-condensation) is typical for porous materials with no organization of pores, and is even not detected for **M6**, which is in agreement with its very low porosity (**Figure 2.14)**.

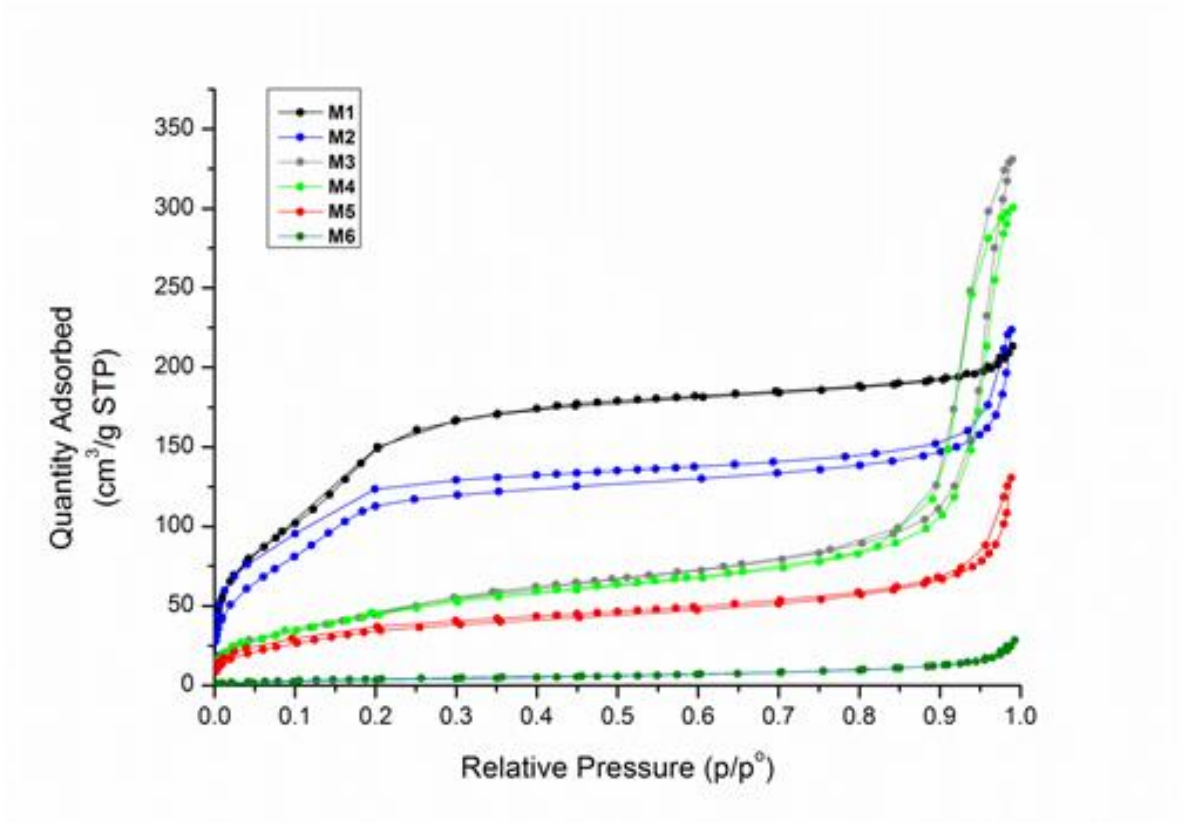

Figure 2.13 N_2-sorption isotherms of **M1-M6**

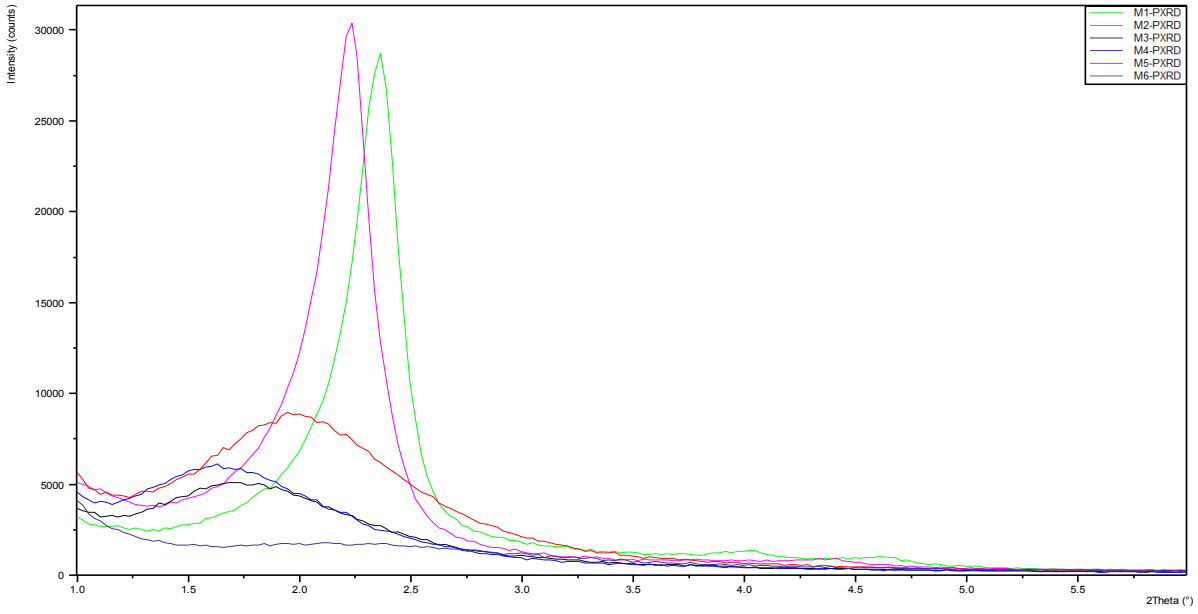

Figure 2.14 *p*-XRD of **M1-M6**

The presence of the organic ligand in the nanomaterials was ensured by the solid-state NMR spectra (^{29}Si and ^{13}C). The ^{29}Si CP MAS NMR spectra (**M1**, **M3**, **M5**, **M6**) showed two groups of chemical shifts: T units from -59 to -69 ppm resulting from the organosilanes **P1**

and **P2**, and Q units ranging from -93 to -113 ppm formed from TEOS, as exemplified by the ^{29}Si CP MAS NMR spectrum of **M1** and **M5** (**Figure 2.15** bottom). Indeed, the presence of T signals suggested that the integrity of the Si-C bond was maintained during the formation of the nanomaterial, which was also confirmed by the ^{13}C solid state NMR spectrum with the strong signal at 8 ppm (**Figure 2.15** top). The superposition of the ^{13}C spectra of **P1** in solution and of **M5** shows a good similarity between the two spectra, suggesting thereby the integrity of the organic skeleton. For both **M1** (grafting) and **M5** (co-condensation) the ^{29}Si NMR display mostly T^2 (-58 ppm) and T^3 (-67 ppm) environments, which confirms the strong anchoring of the organic frameworks within the silica network by two or three Si-O-Si linkages.

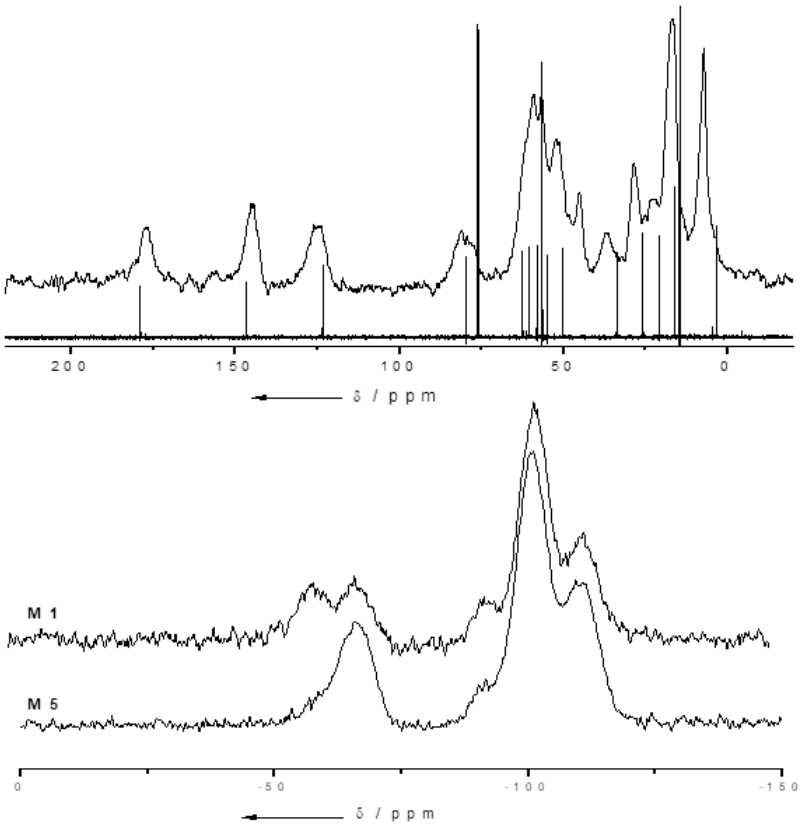

Figure 2.15 ^{13}C NMR spectra of **M5** and **P1** (top) and ^{29}Si CP MAS spectra of **M1** and **M5** (bottom)

The catalyst loading was inferred from the nitrogen elemental analysis (**Table 2.3**), with **M5** presenting the highest loading (0.82 mmol g^{-1}). Finally, the dispersibility of the NPs was checked in dilute NaCl aqueous solution. Except for **M1** that was not easily dispersible, the NPs were moderately aggregated after dispersion at 1 mg/mL. The zeta potential ζ evolved from ca -25 mV at pH 7 for the pure silica samples MCM-41 and **M0**, in agreement with an

isoelectric point of ca 3.5 for silica, to positive values for the functional materials which display amino groups that are protonated at pH 7. Indeed, the ζ potential was *ca* +25 mV when precursor **P1** was grafted or co-condensed and *ca* +45 mV when precursor **P2** was employed. This agrees with the higher density in amino groups in materials derived from **P2** (two amino groups in its structure) compared to **P1** (one amino group), which results in more protons attached to the surface of the NPs at neutral pH (**Table 2.3**).

It is worth to mention that **M5** is the first nanosized chiral organocatalyst obtained by co-condensation procedures.

2.2.3.5. Catalytic activity and recyclability of mesoporous silica nanoparticles derived from proline-valinol amides

2.2.3.5.1 Catalytic tests of functionalized mesoporous silica nanoparticles in the direct aldol reaction between *p*-nitrobenzaldehyde 22a and cyclohexanone 23a

The activity of the mesoporous silica nanoparticles **M1**-**M6** derived from proline-valinol amides was then evaluated via a typically used benchmark reaction for the direct asymmetric aldolisations, the reaction between *p*-nitrobenzaldehyde **22a** and cyclohexanone **23a** to give aldol **24aa** as a diastereomeric mixture. We first undertook a screening of reaction conditions (catalytic nanomaterial, solvent, temperature, reaction time) using a 10 mol% of catalyst, an excess of ketone and a 2 M concentration of aldehyde, as summarized in **Table 2.4**. Initial experiments performed with **M1** in water at room temperature and at 0 ºC gave full conversion in 6 and 8 h, respectively (entries 1 and 2 of **Table 2.4**). Thus, lower temperature resulted in a slight decrease of the reaction rate, but the selectivity was improved up to an anti/syn ratio of 89/11 and an enantiomeric ratio (er) for the major anti isomer of 91/9. We next examined the effect of solvent with the same catalyst **M1** and an initial temperature of 0 ºC. We observed a very significant decrease in the conversion and selectivity with the use of tetrahydrofuran, acetonitrile, ethyl acetate, toluene, dimethylformamide and dimethylsulfoxide (entries 3-8 of **Table 2.4**). The reaction which performed in brine at 0 ºC (entry 9 of **Table 2.4**) gave a similar selectivity to that of entry 2, but the reaction was much slower than in distilled water. Under neat conditions at the same temperature, a clear deleterious effect was found in both the reactivity and asymmetric induction (entry 10 of **Table 2.4**). The catalytic tests with the other nanoparticles **M2**-**M6** were then performed with a 10 mol% loading in water at 0 ºC (entries 11-15 of **Table 2.4**). The best result was obtained

with **M5**, for which a full conversion was achieved after 11 h (*dr* 89/11, er_{anti} 92/8, entry 14 of **Table 2.4**). The next step was to determine the influence of the catalyst loading on the aldol reaction with **M5** in water at 0 ºC (5 and 15 mol%, entries 16-17 of **Table 2.4** compared with 10 mol% of entry 14). Whereas the reaction rate was affected as expected, the diastereo- and enantioselectivity did not change significantly. Finally, we have found that the addition of 10% of benzoic acid as co-catalyst to **M5** and **M1** slightly improves the enantioselectivity, but has a deleterious effect on the reaction rate (compare entries 18 and 19 with entries 14 and 2 in **Table 2.4**). In any case, it appears that the materials derived from the monosilylated precursor **P1** showed better performance than those derived from the disilylated **P2.** The two points of attachment of the catalytic moiety to the matrix in the case of materials **M2**, **M4** and **M6** probably induce less flexibility to this moiety, limiting the right approach to the reactants for an optimal activity and selectivity.

For a better comparison between the performances of homogeneous and heterogeneous catalysts, the reaction between **22a** and **23a** was also carried out with the monosilylated precursor **P1**, in spite of the risk of a slow hydrolysis of the triethoxysilyl group in water (entries 20-21 of **Table 2.4**). In the absence of acid co-catalyst a reaction time between 12 and 24 h was needed for complete conversion (no control was performed during the night) to obtain the diastereomeric mixture **24aa** with lower selectivity (*dr* = 76/24; er_{anti} = 79/21, entry 20 of **Table 2.4**) than with the heterogeneous catalyst **M1** (entry 2 of **Table 2.4**). The reaction rate and enantioselectivity of **P1** were improved by the addition of benzoic acid to achieve the same values as with **M1**, although the diastereoselectivity was somewhat lower (reaction time = 8 h, *dr* = 82/18, er_{anti} = 91/9, entry 21 of **Table 2.4**).

As mentioned before, the use of organosilica nanoparticles should reduce the problems of diffusion and low reaction rates encountered with bulk organosilicas. The reaction times required for complete conversion in this aldol reaction with **M1** and **M5** compete well with those found for an homogeneous proline-valinol thioamide (5 mol% cat, 10 mol% PhCOOH, water, 0 ºC to rt, 8 h, 94% yield),[97] with the added advantage over the homogeneous organocatalyst that there is no need of acid co-catalyst in our experiments to accelerate the reaction. Moreover, faster reaction rates are observed here than with silica-supported prolinamides (10 mol% cat, water, 7-24 h at rt for 99% conversion, and 6 d at 5 ºC for 80% conversion)[77] and prolinsulphonamides (10 mol% cat, water, rt, 4 d for 99% conversion).[79]

Table 2.4 Screening of the reaction conditions for asymmetric aldol reaction between *p*-nitrobenzaldehyde **22a** and cyclohexanone **23a**.

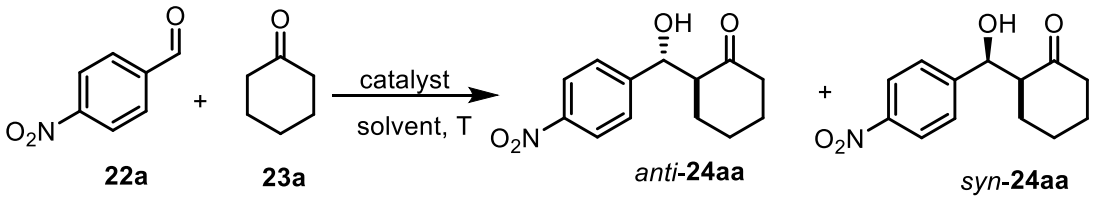

Entry	Solvent[b]	M	T[c] [°C]	t [h]	yield[d] [%]	dr[e] [anti/syn]	er_{anti}[f]	er_{syn}[f]
1	H_2O	**M1**	r.t.	6	>99	86/14	88/12	76/24
2	H_2O	**M1**	0	8	>99	89/11	91/9	80/20
3	THF	**M1**	0~r.t.	24	16	75/25	61/39	55/45
4	CH_3CN	**M1**	0~r.t.	24	39	87/13	88/12	76/24
5	EtOAc	**M1**	0~r.t.	52	80	83/17	70/30	51/49
6	Toluene	**M1**	0~r.t.	52	60	85/15	77/23	66/34
7	DMF	**M1**	0~r.t.	64	19	78/22	80/20	70/30
8	DMSO	**M1**	0~r.t.	96	31	70/30	78/22	67/33
9	neat	**M1**	0	24	49	83/17	54/46	68/32
10	Brine	**M1**	0	31	>99	87/13	91/9	76/24
11	H_2O	**M2**	0	24	>99	85/15	89/11	74/26
12	H_2O	**M3**	0	16	>99	85/15	81/19	65/35
13	H_2O	**M4**	0	26	90	87/13	82/18	71/29
14	H_2O	**M5**	0	11	>99	89/11	92/8	82/18
15	H_2O	**M6**	0	48	>99	84/16	88/12	73/27
16[g]	H_2O	**M5**	0	26	>99	90/10	93/7	81/19
17[h]	H_2O	**M5**	0	8	>99	89/11	91/9	82/18
18[i]	H_2O	**M5**	0	22	>99	88/12	95/5	79/21
19[i]	H_2O	**M1**	0	29	>99	86/14	96/4	76/24
20	H_2O	**P1**	0	16	>99	76/24	79/21	57/43
21[i]	H_2O	**P1**	0	8	>99	82/18	91/9	60/40

[a] Reaction conditions: Molar ratio of **22a/23a/M** = 10:50:1. [b] Solvent (0.5 mL/mmol of **22a**). [c] r.t. (room temperature, 22-25 °C); 0~r.t. represents the first twelve hours at 0 °C, and then at room temperature. [d] Isolated yield. e Determined by ^{1}H-NMR spectroscopy. [f] Determined by chiral HPLC (Daicel Chiralpak AD-H column, flow 1.0 mL/min, 254 nm, n-Hexane/iPrOH 95/5). [g] Molar ratio of **11a/23a/M** = 20:100:1. [h] Molar ratio of **22a/23a/M** = 20:100:3. [i] 10 mol% benzoic acid as co-catalyst.

2.2.3.5.2 Catalytic tests of functionalized mesoporous silica nanoparticles in the direct aldol reaction between *p*-nitrobenzaldehyde 22a and acetone 23b

In order to compare the heterogeneous catalysts with the homogeneous proline-valinol amide, we conducted the aldol reaction between *p*-nitrobenzaldehyde **22a** and acetone **23b** (5 equiv) in water at 0 ºC (10 mol% of **M1**) to give the corresponding aldol product **24ba** in quantitative yield after 10 h with an *ee* of 46% (entry 1 of **Table 2.5**). In the case of the homogeneous proline-valinol amide **25**[97] the same reaction was not performed in water, but in DMSO at 0 ºC (10 mol% of catalyst) furnishing the aldol product in only 43% yield after 12 h with 55% *ee* (entry 8 of **Table 2.5**). If benzoic acid was used as a co-catalyst with homogeneous proline-valinol amide **25**, the *ee* increased to 70% with 85% yield (entry 10 of **Table 2.5**). Thus, our catalyst in aqueous conditions reacts faster than the homogeneous one in dimethylsulfoxide, and the enantioselectivity remains moderate in both cases. Other mesoporous silica nanoparticles were tested in the reaction, in all cases the aldol product was obtained in higher yields but moderate *ee* values (entries 2-6 of **Table 2.5**). Even if benzoic acid was used as a co-catalyst, the *ee* value of the product was not improved, but the reaction time was extended (entry 7 vs entry 1, **Table 2.5**).

Table 2.5 Catalytic performance of **M1-M6** in the direct aldol reaction of *p*-nitrobenzaldehyde with acetone

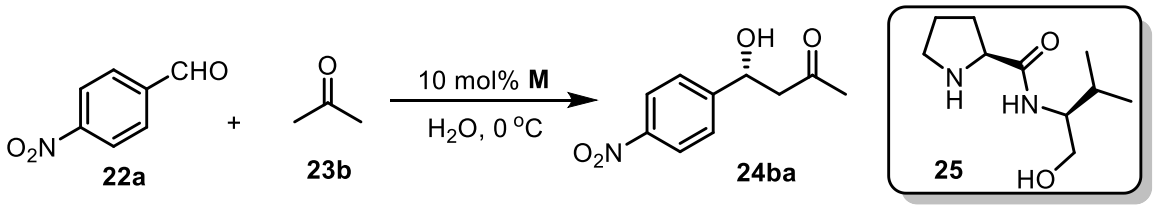

Entry	Solvent[b]	Catalyst	t [h]	yield [%][c]	ee [%][d]
1	H_2O	**M1**	10	> 99	46
2	H_2O	**M2**	21	> 99	42
3	H_2O	**M3**	14	> 99	42
4	H_2O	**M4**	21	> 99	40
5	H_2O	**M5**	12	> 99	44
6	H_2O	**M6**	44	> 99	32
7[e]	H_2O	**M1**	48	> 99	44
8	DMSO	**25**	12	43	55
9[f]	DMSO	**25**	12	89	52
10[e]	DMSO	**25**	8	85	70

[a] Reaction conditions: molar ratio of **22a/23b/M** = 10 : 50 : 1. [b] Solvent (0.5 mL/mmol of **22a**). [c] Isolated yield. [d] Determined by chiral HPLC (Daicel Chiralpak AD-H column, flow 1 mL/min, 254 nm, Hexane/iPrOH 95/5). [e]10 mol% benzoic acid as co-catalyst. [f] molar ratio of **22a/23b/M** = 5 : 25 : 1.

2.2.3.5.3 Catalytic tests of functionalized mesoporous silica nanoparticles in the direct aldol reaction between *p*-nitrobenzaldehyde 22a and cyclopentanone 23c

Cyclopentanone **23c** was also tested as a nucleophile in the direct asymmetric aldol reaction with *p*-nitrobenzaldehyde **22a** (**Table 2.6**). With the decrease in the ring size of the cyclic ketone, a clear reduction of the diastereoselectivity was observed, the *syn*-diastereomer being slightly favored in this case. Unfortunately, the enantioselectivity in both diastereoisomeric anti/syn products was not high. Compared with cyclohexanone, the reactivity of cyclopentanone is significantly lower and longer reaction times are required to complete the reaction, although with all the materials we could achieve 99% yield of the diastereoisomeric mixture.

Table 2.6 Catalytic performance of **M1-M6** in the direct aldol reaction of *p*-nitrobenzaldehyde with cyclopentanone

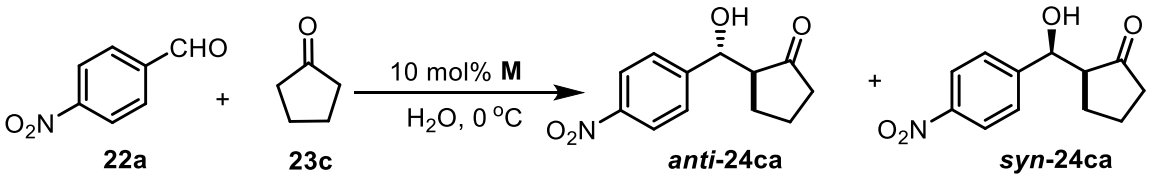

22a **23c** ***anti*-24ca** ***syn*-24ca**

Entry	Catalyst	t [h]	yield [%][b]	dr [anti/syn][c]	er_{anti}[d]	er_{syn}[d]
1	**M1**	45	> 99	40/60	78/22	66/34
2	**M2**	63	> 99	39/61	73/27	68/32
3	**M3**	37	> 99	39/61	66/34	62/38
4	**M4**	64	> 99	35/65	64/36	63/37
5	**M5**	24	> 99	36/64	71/29	62/38
6	**M6**	96	> 99	34/66	72/28	63/37

[a] Reaction conditions: molar ratio of **22a/23c/M** = 10 : 50 : 1; 0.5 mL water/mmol of **22a**). [b] Isolated yield. [c] Determined by ^{1}H-NMR spectroscopy. [d] Determined by chiral HPLC (Daicel Chiralpak AD-H column, flow 1 mL/min, 254 nm, Hexane/iPrOH 95/5).

2.2.3.5.4 Substrate scope for direct asymmetric aldol reaction

On the basis of the optimal conditions (see section 2.2.3.5.1), we chose **M1** and **M5** as the best catalysts to examine the substrate scope of the aldol reaction of **23a** with a variety of aromatic aldehydes **22a-i** (**Table 2.7**) in water, at 0 ºC, with an amount of catalyst of 10 mol%, in the absence of any co-catalyst. **M3** was also considered as catalyst for extending the scope. The corresponding aldol products **24** were obtained in high isolated yields (from 71 to >99 %) with good to excellent *anti/syn* diastereoselectivity (*dr* from 81/19 to 90/10) and enantioselectivity for the major *anti* isomer (*er* from 81/19 to 95/5).

Table 2.7 Direct asymmetric aldol reactions between aromatic aldehydes **22** and ketones **23** to give aldols **24** with **M1**, **M3** and **M5**

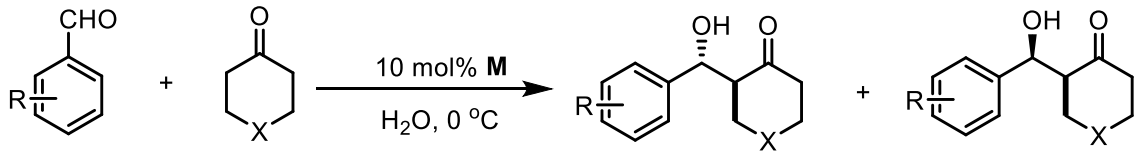

22 **23** *anti*-**24xy** *syn*-**24xy**

22a: R = 4-NO_2 **22f**: R = 4-Br **23a**: X = CH_2
22b: R = 2-NO_2 **22g**: R = 2-Cl **23d**: X = O
22c: R = 2,4-NO_2 **22h**: R = 2,4-Cl
22d: R = 4-Cl **22i**: R = 4-CF_3
22e: R = 4-F

x = a, d ; y = a-i

Entry	22	23	24xy[b]	M	t [h]	yield[c] [%]	dr[d] [anti/syn]	er_{anti}[e]	er_{syn}[e]
1	**22a**	**23a**	**24aa**	**M1**	8	>99	89/11	91/9	80/20
2	**22a**	**23a**	**24aa**	**M5**	11	>99	89/11	92/8	82/18
3	**22a**	**23a**	**24aa**	**M3**	14	>99	85/15	81/19	65/35
4	**22b**	**23a**	**24ab**	**M1**	25	96	90/10	92/8	n.d.[f]
5	**22b**	**23a**	**24ab**	**M5**	30	97	90/10	94/6	n.d.[f]
6	**22b**	**23a**	**24ab**	**M3**	26	97	87/13	89/11	n.d.[f]
7	**22c**	**23a**	**24ac**	**M1**	54	94	86/14	90/10	78/22
8	**22c**	**23a**	**24ac**	**M5**	52	94	87/13	93/7	80/20
9	**22c**	**23a**	**24ac**	**M3**	56	94	87/13	89/11	78/22
10	**22d**	**23a**	**24ad**	**M1**	54	76	87/13	93/7	71/29
11	**22d**	**23a**	**24ad**	**M5**	60	71	86/14	95/5	60/40
12	**22e**	**23a**	**24ae**	**M1**	30	81	86/14	91/9	64/36
13	**22e**	**23a**	**24ae**	**M5**	48	75	87/13	92/8	74/26
14	**22f**	**23a**	**24af**	**M1**	48	97	90/10	92/8	75/25
15	**22f**	**23a**	**24af**	**M5**	48	89	87/13	93/7	82/18
16	**22g**	**23a**	**24ag**	**M1**	24	97	85/15	93/7	76/24
17	**22g**	**23a**	**24ag**	**M5**	22	96	88/12	94/6	83/17
18	**22g**	**23a**	**24ag**	**M3**	24	95	87/13	91/9	75/25
19	**22h**	**23a**	**24ah**	**M1**	24	97	81/19	92/8	n.d.[f]
20	**22h**	**23a**	**24ah**	**M5**	24	98	84/16	95/5	n.d.[f]
21	**22h**	**23a**	**24ah**	**M3**	30	95	83/17	91/9	n.d.[f]
22	**22i**	**23a**	**24ai**	**M1**	22	>99	88/12	91/9	75/25
23	**22i**	**23a**	**24ai**	**M5**	28	>99	89/11	94/6	82/18
24	**22i**	**23a**	**24ai**	**M3**	36	>99	84/16	91/9	64/36
25	**22a**	**23d**	**24da**	**M1**	9	>99	88/12	90/10	75/25
26	**22a**	**23d**	**24da**	**M5**	12	>99	89/11	95/5	81/19
27	**22a**	**23d**	**24da**	**M5**	10	>99	90/10	93/7	70/30

[a] Molar ratio **22/23/M** = 10:50:1; water, 0 °C; 0.5 mL of water/mmol of **22**. [b] In the numbering of **24xy**, **x** refers to the starting ketone and **y** to the starting aldehyde. [c] Isolated yield. [d] Determined by ^{1}H NMR spectroscopy. [e] Enantiomeric ratio determined by chiral HPLC (Daicel Chiralpak AD-H and OD-H columns). [f] Not determined.

The reaction with *p*-nitrobenzaldehyde **22a** provided the highest reaction rates (entries 1-3, **Table 2.7**). Lower reactivity was found for *o*-nitrobenzaldehyde **22b** (entries 4-6, **Table 2.7**) and 2,4-dinitrobenzaldehyde **22c** (entries 7-9, **Table 2.7**), probably due to steric hindrance of the *ortho*-substituent. The selectivity was also good for aldehydes bearing halogen groups in *para* and/or *ortho* position (entries 10-21 in **Table 2.7**). Curiously, 2-chlorobenzaldehyde **22g** provided higher yields than 4-chlorobenzaldehyde **16d** (compare entries 16-17 with entries 10-11 in **Table 2.7**). Also *p*-trifluoromethylbenzaldehyde **22i** furnished excellent yields and selectivities with all the tested catalysts (entries 22-24 in **Table 2.7**). To increase the scope of the methodology, the aldol reaction was also extended to 4-oxotetrahydropyran **23d** which also gave the aldol product in excellent yield with satisfying diastereo- and enantioselectivities (entries 25-27 in **Table 2.7**). Unfortunately, less reactive aromatic aldehydes bearing strong electron-donating groups such as *p*-methoxy- resulted in the failure of the reaction. The order of the performance of the materials would be **M1** > **M5** > **M3** with respect to the reaction rates, although we have observed differences on this order depending on the substrate. We should also consider that the reaction times were not optimized in all cases (control was not performed during the night). Regarding the selectivity, the order would be **M5** > **M1** ≥ **M3**, but sometimes the differences in the selectivity were not very significant. Curiously, whereas **M3** gave lower *dr* and *er* for **24aa** (entry 3, **Table 2.7**), the enantioselectivities with this catalyst were improved for other substrates (entries 6, 9, 18, 21, 24, 27 of **Table 2.7**). Taking all that into account, a simple rationalization of the different performances of the materials does not seem feasible. These results proved that we have developed a robust nanocatalytic system, which can be applied to a variety of substrates. It was found that the aromatic aldehydes bearing an electron-withdrawing group were very active due to the electrophilicity of the substrates.

2.2.3.5.5 Recycling experiments with M1 and M5 in the model aldol reaction

After the scope investigation, we tested the reusability of **M1** (10 mol%) in the aldol reaction between **22a** and **23a** performed in water at 0 ºC for 8 h (optimized conditions in section 2.2.3.5.1). The recycling procedure consisted in the addition of ethyl acetate to the crude mixture, centrifugation to separate the nanoparticles and decantation of the supernatant to isolate the product. To our delight, we found that the activity, diastereo- and enantioselectivity were maintained up to five consecutive cycles (**Table 2.8**).

Table 2.8 Recycling of **M1** in the asymmetric aldol reaction between *p*-nitrobenzaldehyde **22a** and cyclohexanone **23a** in water**.**

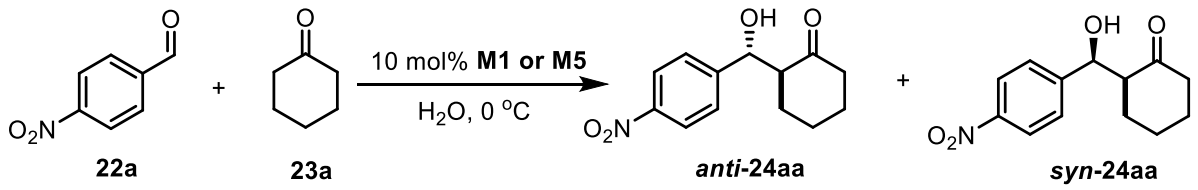

Cycle	Catalyst	t [h]	yield [%][b]	dr [anti/syn][c]	er_{anti} [%][d]	er_{syn} [%][d]
1	**M1**	8	> 99	89/11	90/10	80/20
2	**M1**	8	> 99	88/12	89/11	80/20
3	**M1**	8	> 99	89/11	90/10	80/20
4	**M1**	8	> 99	89/11	91/9	80/20
5	**M1**	8	> 99	89/11	91/9	81/19

[a] Molar ratio **22a/23a/M1** = 10:50:1; 0.5 mL of water/mmol of **22a**, 0 ºC. [b] Isolated yield of the diastereomeric mixture of **24aa**. [c] Determined by ^{1}H NMR spectroscopy. [d] Enantiomeric ratio determined by chiral HPLC (Daicel Chiralpak AD-H column).

The reusability of **M5** has also been successfully achieved in the same aldol reaction. The yield, diastereomeric and enantiomeric ratios in six consecutive runs are shown in **Figure 2.16**.

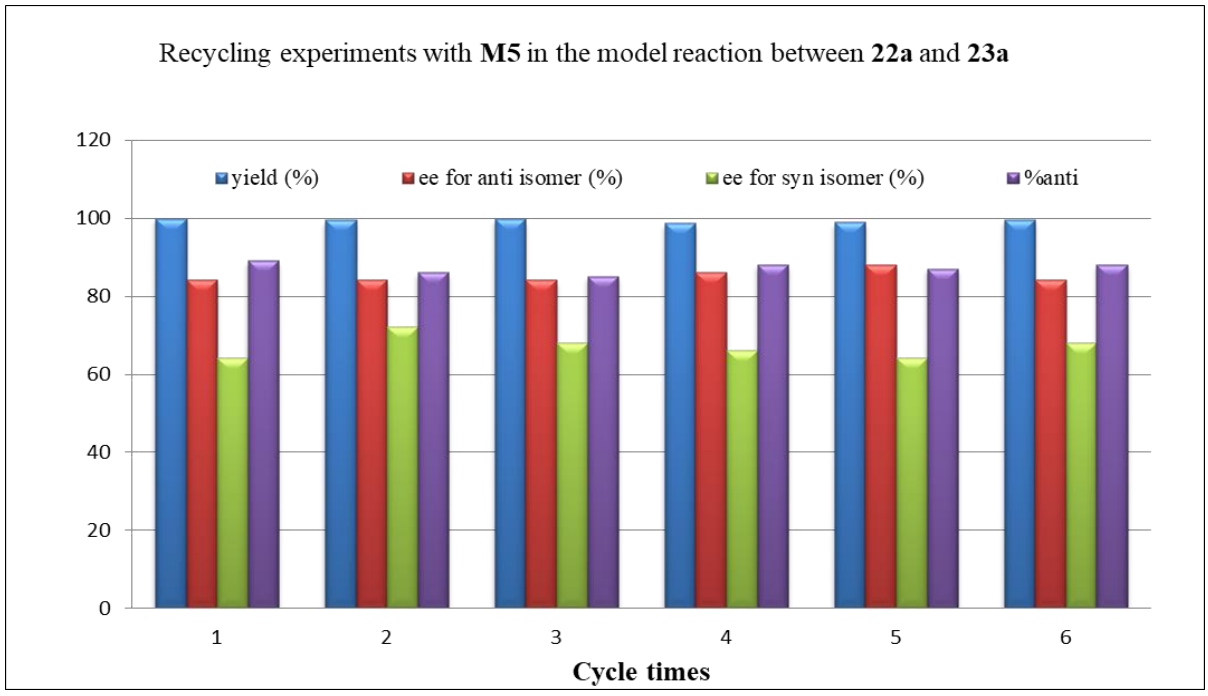

Figure 2.16 Recycling of **M5** in the asymmetric aldol reaction between *p*-nitrobenzaldehyde **22a** and cyclohexanone **23a** in water.

Because some organosilicas may experience deactivation or changes in characteristic functional groups after the performance of catalytic tests,[14,138] TEM, *p*-XRD, IR and elemental analysis of **M1** and **M5** were performed after the catalytic cycles to assure no significant changes in the catalysts occurred. The *p*-XRD of the recovered materials is shown in **Figure 2.17**. For both **M1** and **M5**, there is no obvious change between the fresh and reused catalyst. The IR spectra of the recovered materials were recorded (after a first and a fifth cycle of **M1** and after the first and sixth cycle of **M5**), no significant differences appeared between the fresh and reused nanomaterials (**Figure 2.18**). The TEM images of both **M1** and **M5** recovered after the reaction further confirmed the stability of the catalysts (**Figure 2.19**). The elemental analysis demonstrated that the initial amount of 0.8 mmol g^{-1} for **M1** was maintained after the fifth cycle. Unfortunately, the low amounts of catalysts used in the recycling experiments made difficult the suitable recording of a ^{13}C-CP MAS NMR spectra of the materials after a catalytic test. In short, no significant changes between fresh and reused catalysts were found by comparison of *p*-XRD, TEM, FT-IR, and elemental analysis.

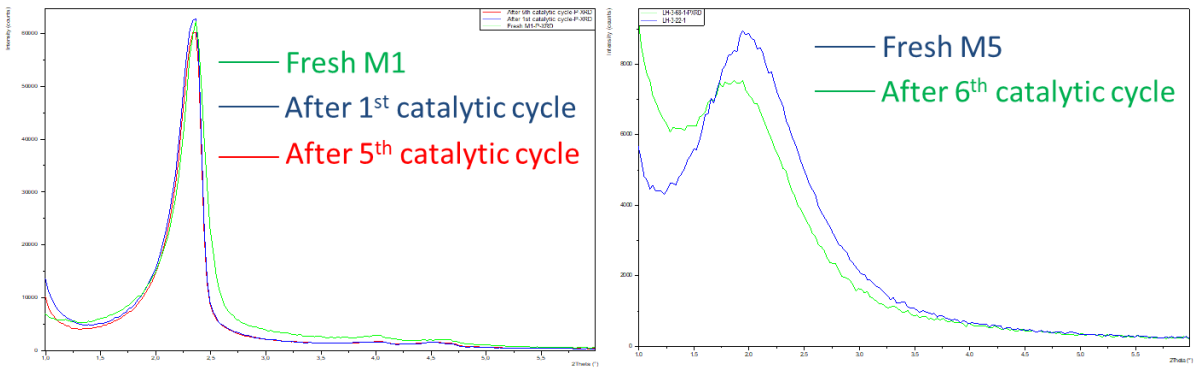

Figure 2.17 *p*-XRD of **M1** and **M5** (fresh and reused)

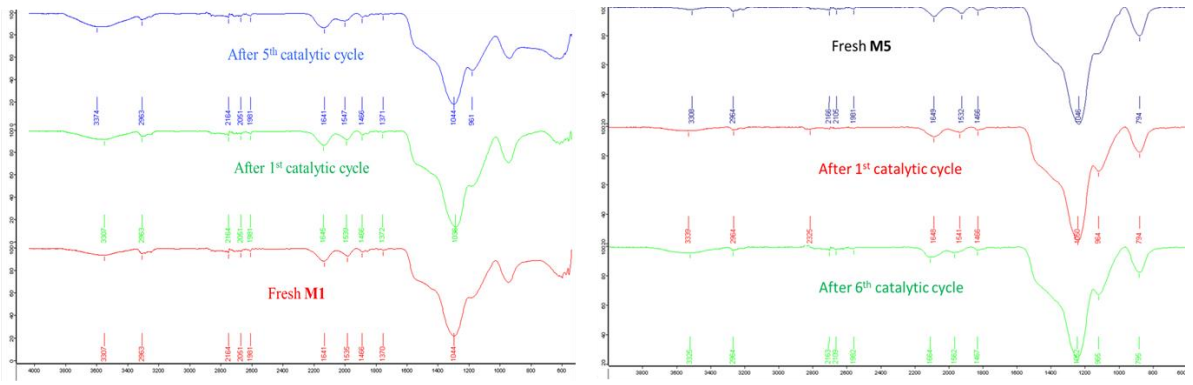

Figure 2.18 FT-IR spectra of **M1** and **M5** (fresh catalyst and reused one)

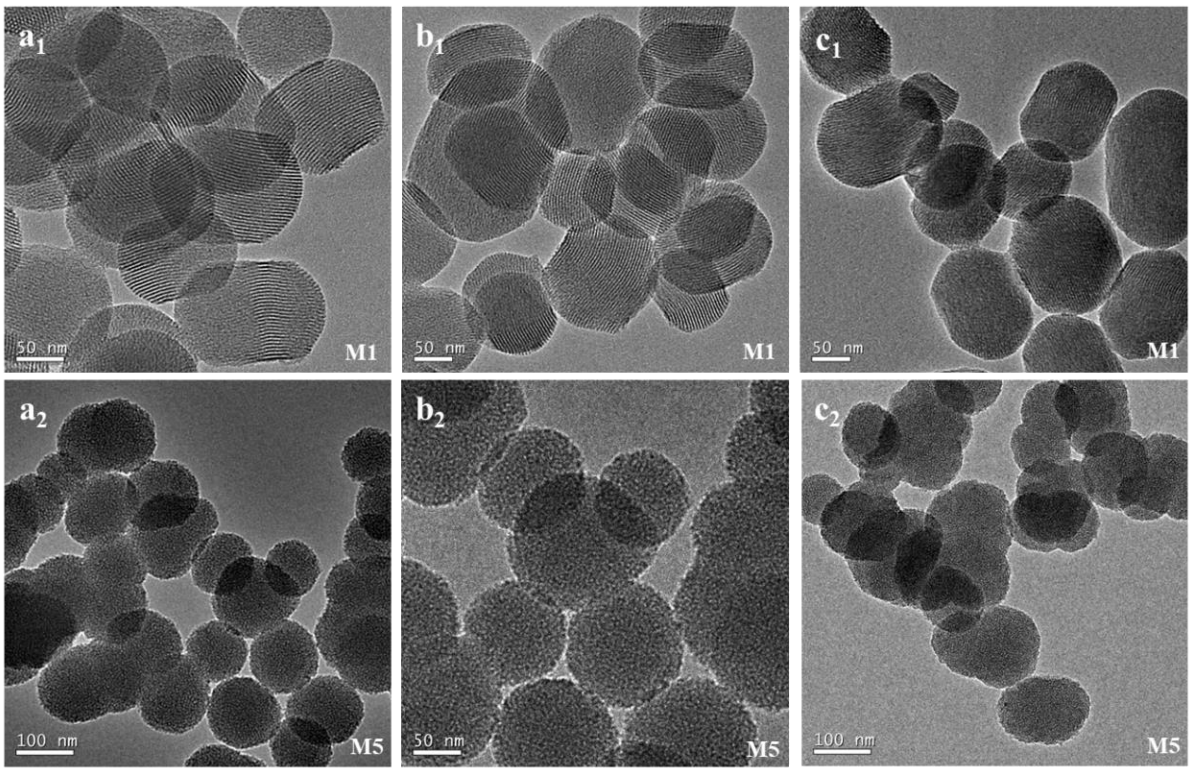

Figure 2.19 TEM images**:** a_1) Fresh **M1**, b_1) after 1st catalytic cycle **M1**, c_1) after 5th catalytic cycle **M1**; a_2) Fresh **M5**, b_2) after 1st catalytic cycle **M5**, c_2) after 6th catalytic cycle **M5**.

2.2.3.5.6 Kinetic studies of the direct asymmetric aldol reaction of aldehyde 22a with cyclohexanone 23a catalyzed by M1

In order to know more about the reaction, we carried out some kinetic experiments. The variation of yield, diastereo- and enantioselectivity with the reaction time has been studied for the reaction between **22a** and **23a** with **M1** (10 mol%) as catalyst in water at 0 ºC (**Figure 2.20a**). Along the reaction time, the yield of **24aa** exhibited a Langmuir type increase,[139] reaching almost the maximum at 7 h. The *dr* remained constant after 3 h of reaction and the *ee* held almost the same values along the time. A pseudo-first order kinetics plot was found (**Figure 2.20b**) by following the variation of the concentration of limiting aldehyde **22a** along the reaction time,[140] with an observed rate constant of 0.48 ± 0.02 h^{-1}.

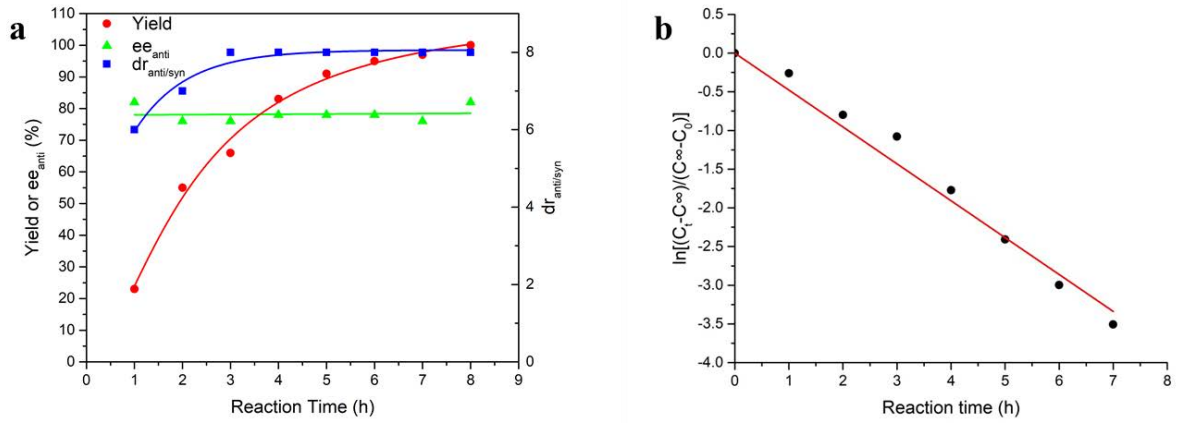

Figure 2.20 a) Variation of yield of **24aa**, *dr* and *ee* of product with reaction time in the direct asymmetric aldol reaction of aldehyde **22a** with cyclohexanone **23a** catalyzed by **M1**. Reaction conditions: molar ratio **22a**/**23a**/**M1** = 10:50:1; 0.5 mmol **22a**, 0.25 mL of water, 2.5 mmol **23a**, 0 ºC. b) Pseudo first order kinetic plot of the model aldol reaction between **22a** and **23a** catalyzed by **M1**. $C_\infty = 0$, final concentration of **9a**, at infinite time; C_t = concentration of **22a** at given time t; C_0 = initial concentration of **22a**, at t = zero time. $R^2 = 0.99$. Yield of **24aa** and C_t of **22a** were determined by ^{1}H NMR spectroscopy.

As previously pointed out, the proposed mechanism for the aldol reaction with the proline-valinol amides and thioamides is based on the proline catalysis concept and double hydrogen bonding activation of the electrophilic aldehyde (by the NH and the OH groups).[97] The reaction begins with the condensation of the cyclohexanone with the amine fragment of the proline derived organocatalyst to form a nucleophilic enamine, which would attack the aldehyde to give, after hydrolysis, the desired aldol product.[141] The enantioselection would arise from the positioning of the aldehyde via the double hydrogen bonding through the NH and OH groups of the proline-valinol amide moiety. From the previously mentioned experiments, it is clear that the reaction with the heterogeneous catalyst benefits from the acidic silanol groups on the surface of the organosilica nanoparticles, which play the role of co-catalyst. However, the Si-OH groups might also have a deleterious effect on the selectivity, competing with the NH and/or OH groups of the organocatalyst for the positioning of the aldehyde. In view of the comparison between **P1** and **M1**, this interference does not seem to be very important in our case, but might modulate the selectivity depending on the material and the substrate.

2.2.3.5.7 Catalytic performance of M1 and M5 in the intramolecular aldol reaction

Finally, the catalytic performance of functionalized mesoporous silica nanoparticles **M1** and **M5** were also assayed for the intramolecular aldol reaction with triketone **26** in water at room temperature (**Scheme 2.17**). In this particular reaction, the use of 10 mol% *p*-nitrobenzoic acid as additive and column chromatography of the reaction crude mixture were required to achieve Wieland-Miescher ketone **27** in good isolated yields with moderate enantiselectivity.

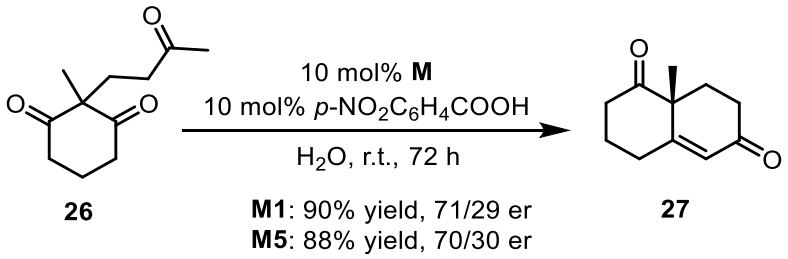

Scheme 2.17 Intramolecular aldol reactions catalyzed by **M1** and **M5**

All these results proved that we have developed robust nanocatalytic systems, which can be applied to a variety of substrates. We should emphasize that the developed procedure is very simple and environmentally friendly (aqueous medium, 0 ºC, no acid co-catalyst, relatively low loadings of the nanocatalyst, easy separation and recycling of the catalyst).

2.2.4 Conclusions

In summary, we have prepared mesoporous silica nanoparticles derived from mono- and bis-silylated proline-valinol amides **P1** and **P2**. The action of these dipeptide derivatives relies on the proline catalysis concept (enamine pathway) and double hydrogen bonding activation. The linking between the organocatalytic moiety and the silylated group was built through a copper-catalyzed azide-alkyne cycloaddition reaction (CuAAC) under anhydrous conditions. For the preparation of the nanomaterials, we have used both a grafting procedure to previously synthesized mesoporous silica nanoparticles (MSNs) and a co-condensation method with TEOS in a buffered neutral medium with Brij-56/CTAB as templates. *To the best of our knowledge, this is the first report on the obtention of functionalized mesoporous silica nanoparticles by co-condensation procedures with a chiral precursor of a certain structural complexity*. The functionalized mesoporous silica nanoparticles **M1-M6** have been fully characterized by elemental analysis, ^{29}Si and ^{13}C CP MAS NMR spectroscopy, TEM, SEM, N_2-sorption measurements, DLS, zeta-potential, IR and p-XRD. We have then evaluated their activity and recyclability as catalysts in the asymmetric aldol reaction between several aromatic aldehydes **22a-i** and the six-membered cyclic ketones **23a,d** to afford efficiently aldols **24** as an *anti/syn* diastereomeric mixture with good diastereo- and enantiomeric ratios (up to dr 90/10 and er 96/4). Acetone **23b** and cyclopentanone **23c** were found to be less reactive than the six-membered ketones and gave poor selectivities. The best catalysts were **M1** derived from grafting of the monosilylated **P1** to MSNs of MCM-41 type and **M5** synthesized from **P1** by co-condensation (TEOS:**P1**=10:1). The optimized protocol for the organocatalyzed aldol reaction is simple and environmentally friendly. The reaction takes place in water at 0 ºC, no acid co-catalyst is needed, relatively low loadings of the nanocatalyst (5-10 mol%) are required, the catalyst is easily recovered by centrifugation and decantation, avoiding chromatographic separation. ***M1** has been recycled up to five runs with no loss of activity and selectivity*. ***M5** has also been recycled up to six runs.* Finally, the intramolecular asymmetric aldol reaction with triketone **26** was successfully catalysed by **M1** and **M5** obtaining good yields but moderate enantioselectivity. The use of organosilica nanoparticles decreases the problems of diffusion and low reaction rates encountered with bulk organosilicas. *To the best of our knowledge, this is the first report of asymmetric induction on the direct aldol reaction achieved by mesoporous silica nanoparticles derived chiral organocatalysts.*

2.2.5 Experimental section

2.2.5.1 General information

Nuclear Magnetic Resonance (NMR) spectroscopy was performed at the *Servei de Ressonància Magnètica Nuclear* of the *Universitat Autònoma de Barcelona* (UAB). The ^{1}H and ^{13}C NMR spectra in solution were recorded on Bruker DPX-360 or Bruker Avance-II 600 spectrometers, operating at ^{1}H NMR frequencies of 360.13 and 600.13 MHz respectively, and at 298.0 K of temperature. 1D ^{1}H and 2D $^{1}H,^{1}H$-COSY, $^{1}H,^{1}H$-TOCSY, $^{1}H,^{1}H$-NOESY, $^{1}H,^{13}C$-HSQC, and $^{1}H,^{13}C$-HMBC experiments were performed using standard Bruker pulse sequences and acquired under routine conditions. All the spectra were calibrated using the residual solvent signal ($CHCl_3$, δ_H, 7.26 and δ_C, 77.16 ppm). Chemical shift data were expressed in ppm and coupling constant (*J*) values in Hz. The multiplicity of peaks was abbreviated as s (singlet), d (doublet), t (triplet), q (quartet) and dd (doublet of doublets). The ^{29}Si and ^{13}C CP-MAS NMR spectra were obtained from a Bruker AV400WB, the repetition time was 5 seconds with contact times of 5 milliseconds.

Infra-red spectra (IR) spectroscopy was recorded with a Bruker Tensor 27 spectrometer using a Golden Gate ATR module with a diamond window.

Specific rotation values ($[\alpha]_D$) were obtained at 20 ºC in a JASCO J-175 polarimeter at 589.6 nm and they are given in 10^{-1} deg cm^2 g^{-1}

Mass-spectrometry (MS): Low- and high-resolution mass spectra were obtained by direct injection of the sample with electrospray techniques in a Hewlett-Packard 5989A and *microTOF-Q* instruments respectively.

Elemental analysis (EA) of C, N and H were performed using Flash 2000 Organic Elemental analyser of Thermo Fisher Scientific with BBOT as an internal standard.

From the *Servei d'Anàlisi Química* of the *Universitat Autònoma de Barcelona* the following experimental data were acquired: IR, $[\alpha]_D$, MS and EA.

Transmission Electron Microscopy (TEM) analyses were performed in the *Servei de Microscòpia* of UAB on a JEM-2011 Electron Microscope 200 Kv.

Powder X-ray diffraction (p-XRD) was performed in the *Servei de Difracció de Raigs X* of UAB with X'Pert Power from PANalytical (45Kv/40 mA, K_α 1.5419 Å with a cooper anode).

Field Effect Scanning Electron Microscopy (FESEM), **Dynamic Light Scattering (DLS) and Zeta potential** were obtained from the *Institut Néel* in Grenoble. DLS analyses were performed using a Vasco Kin instrument from Cordouan Technologies. Zeta potential measurements were performed on a Wallis instrument from Cordouan Technologies. Field emission scanning electron microscope (FESEM) images were obtained with a Zeiss Ultra+ scanning electron microscope. The NPs in powder form were deposited on doped silicon wafers with carbon tape for observation without metallization. A voltage of 3 kV was used at a working distance of 3 mm.

The enantiomeric ratio (*er*) of the products was determined by chiral stationary phase HPLC (chiral columns Daicel Chiralpak AD-H and OD-H) with a Waters 2960 instrument using a UV photodiode array detector in our group.

The surface areas were determined by the Brunauer-Emmet-Teller (BET) method from N_2 adsorption-desorption isotherms obtained with a Micromeritics ASAP2000 analyzer, which belongs to *Institut de Ciència dels Materials de Barcelona (ICMAB)* after degassing samples for 30 h at 55 °C under vacuum. The pore diameter distribution was calculated by Non-Local Density Functional Theory (NLDFT) method (carbon slit-pore model for N_2 sorption at 77 K).

Thin-Layer Chromatography (TLC) was performed using 0.25 mm plates (Alugram Sil G/UV_{254}).

Chromatographic purifications were performed under N_2 pressure on Scharlau silica gel 60, 0.04-0.06 mm for flash chromatography, which had a particle size of 230-400 mesh.

Others: When required, experiments were carried out with standard high vacuum and Schlenk techniques. Dry toluene was purchased from Merck. Dry solvents and reagents were obtained following standard procedures: triethylamine was distilled over CaH_2, CH_3CN was dried by molecular sieves, THF and pentane were from solvent-processing equipment (*PureSolv*, Innovative Technology).

2.2.5.2 Preparation of silylated precursors P1 and P2

2.2.5.2.1 Synthesis of (3-azidopropyl)triethoxysilane[142]

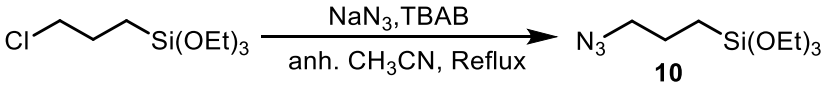

In a 100 mL Schlenk was added tetra-*n*-butylammonium bromide (1.29 g, 4.0 mmol), NaN_3 (1.95 g, 30.0 mmol) and (3-chloropropyl)triethoxysilane (4.82 g, 20.0 mmol) in dry acetonitrile (60 mL). The mixture was stirred under reflux and argon atmosphere for 48 hours. Then the solvent was removed under reduced pressure. The crude mixture was then diluted in Et_2O (60 mL), the suspension was filtered and the solid washed with Et_2O (2 × 30 mL). The solvent was removed from the combined filtrates, the product was obtained as a pure and colorless liquid (4.51 g, 91% yield). **^{1}H NMR (360 MHz, $CDCl_3$) δ (ppm):** 3.83 (q, *J* = 7.2 Hz, 6H), 3.26 (t, *J* = 7.2 Hz, 2H), 1.75-1.67 (m, 2H), 1.23 (t, *J* = 7.2 Hz, 9H), 0.70-0.65 (m, 2H); **^{13}C NMR (91 MHz, $CDCl_3$)** δ **(ppm):** 58.5, 53.8, 22.7, 18.3, 7.6.

2.2.5.2.2 Synthesis of N-(2-azidoethyl)-3-(triethoxysilyl)-N-(3-(triethoxysilyl)propyl)propan-1-amine, 13

Synthesis of 2-azidoethanol[143]

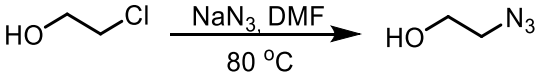

To a stirred solution of 2-chloroethanol (15.00 g, 186.3 mmol) in DMF (50 ml) was added sodium azide (16.96 g, 260.8 mmol). The mixture was heated to 80°C under stirring for 64 h. Then, the mixture was allowed to cool to room temperature, the solid was filtered out, water was added (60 mL) to the filtrate and it was extracted with ethyl acetate (100 mL × 3). The organic extracts were combined and washed with water (80 mL × 3). The organic phase was then dried over anhydrous sodium sulfate, filtered and the solvent removed under reduced pressure. The final product was obtained as a colorless liquid (14.8 g, 91%). **^{1}H NMR (360 MHz, $CDCl_3$) δ (ppm):** 3.77 (t, *J* = 7.2 Hz, 2H), 3.44 (t, *J* = 7.2 Hz, 2H), 2.02 (br s, 1H).

Synthesis of 2-azidoethyl 4-methylbenzenesulfonate[143]

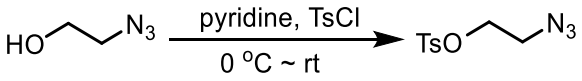

To a stirred solution of 2-azidoethanol (3.48 g, 40.0 mmol) in dry pyridine (20 mL) at 0°C was added *p*-toluenesulfonyl chloride (11.44 g, 60.0 mmol). This stirred mixture was allowed to warm to room temperature and left for 3 h. Then, the mixture was cooled to 0°C and diluted with diethyl ether (100 ml). Aqueous hydrochloric acid solution (2 M, 15 mL) was slowly added and the reaction mixture stirred vigorously for 5 min. The aqueous phase was separated and extracted with diethyl ether (3 x 100 mL). The organic extracts were combined, dried over anhydrous sodium sulfate and concentrated under reduced pressure. The resulting residue was purified by flash column chromatography on silica gel with hexane/ EtOAc = 3:1 to afford a colorless liquid (7.14 g, 74% yield). **^{1}H NMR (360 MHz, $CDCl_3$) δ (ppm):** 7.83 (d, *J* = 7.2 Hz, 2H), 7.38 (d, *J* = 7.2 Hz, 2H), 4.16 (t, *J* = 7.2 Hz, 2H), 3.49 (t, *J* = 7.2 Hz, 2H), 2.46 (s, 3H).

Synthesis of 1-azido-2-iodoethane[143]

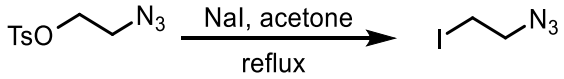

A mixture of 2-azidoethyl 4-methylbenzenesulfonate (10.37 g, 43.0 mmol) and sodium iodide (11.99 g, 79.99 mmol) in acetone (120 ml) was heated at reflux for 18 h. The reaction mixture was then allowed to cool to room temperature and concentrated at reduced pressure. Water (80 mL) was added to the residue and the product extracted with ethyl acetate (3 x 150 mL). The organic extracts were combined, dried over anhydrous sodium sulfate and concentrated under reduced pressure. The final product was obtained as yellow oil (6.74 g, 80% yield). **^{1}H NMR (360 MHz, $CDCl_3$) δ (ppm):** 3.66 (t, *J* = 7.2 Hz, 2H), 3.25 (t, *J* = 7.2 Hz, 2H).

Synthesis of *N*-(2-azidoethyl)-3-(triethoxysilyl)-*N*-(3-(triethoxysilyl)propyl)propan-1-amine, 13 [82]

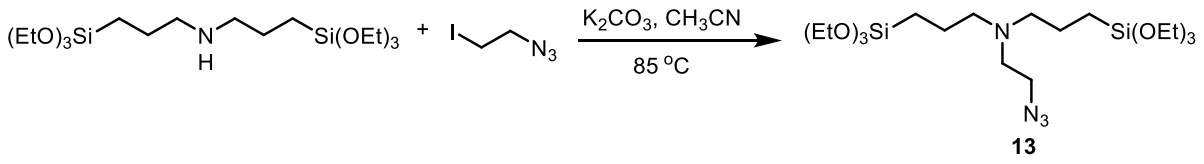

13

A mixture of bis(triethoxysilylpropyl)amine (6.39 g, 15.0 mmol), 1-azido-2-iodoethane (2.95 g, 15.0 mmol) and potassium carbonate (4.15 g, 46.0 mmol) in dry acetonitrile (60 mL) was stirred overnight at 85 ^{o}C in a sealed tube. After the mixture was concentrated, anhydrous pentane was added, then the solution was filtered and the filtrate was concentrated, the pure product was obtained as a yellow liquid (6.97 g, 94% yield). **^{1}H NMR (360 MHz, $CDCl_3$) δ (ppm):** 3.83 (q, *J* = 7.2 Hz, 12H), 3.26 (t, *J* = 7.2 Hz, 2H), 2.66 (t, *J* = 7.2 Hz, 2H), 2.46 (t, *J* = 7.2 Hz, 4H), 1.61-1.51 (m, 4H), 1.23 (t, *J* = 7.2 Hz, 18H), 0.60 (t, *J* = 7.2 Hz, 4H); **^{13}C NMR (91 MHz, $CDCl_3$) δ (ppm):** 58.3, 57.3, 53.4, 49.5, 20.4, 18.3, 7.8.

2.2.5.2.3 Synthesis of 1-benzyl 2-(prop-2-yn-1-yl) (2*S*,4*R*)-4-(prop-2-yn-1-yloxy)pyrrolidine-1,2-dicarboxylate, 12[120]

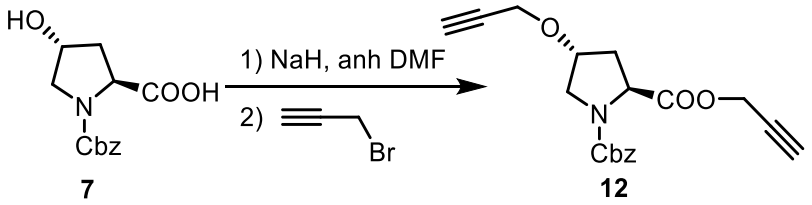

7 **12**

A solution of *N*-Cbz-Hydroxy-L-proline **7** (5.36 g, 20.0 mmol) in dry DMF (40 mL) at 0 °C under nitrogen was treated with NaH (2.08 g of 60% dispersion in oil, corresponding to 1.25 g of NaH, 52.0 mmol). After stirring for 30 min, propargyl bromide solution (7.40 g of 80 wt.% in xylene, corresponding to 5.95 g of propargyl bromide, 52.0 mmol) was added with a syringe and the solution was stirred at room temperature overnight. After addition of water (30 mL), 5M HCl (aq) was added until the pH value reached 2. The solution was then extracted with Et_2O (3 × 60 mL) and dried over anhydrous Na_2SO_4. After evaporation of the solvent, the pure product was isolated from the residue by flash column chromatography on silica gel with hexane/EtOAc = 3:2 to afford a colorless oil (6.12 g, 81% yield). **$[\alpha]_D^{20}$** = -48 ^{o} (*c* 0.01, CH_2Cl_2). **^{1}H NMR (360 MHz, $CDCl_3$) (mixture of rotamers) δ (ppm):** 7.36-7.29 (m, 5+5H), 5.20-5.03 (m, 2+2H), 4.83-4.69 (m, 1+1H), 4.57-4.45 (m, 2+2H), 4.35 (br s, 1+1H), 4.17-4.11 (m, 2+2H), 3.80-3.76 (m, 1H), 3.73-3.65 (m, 1+2H), 2.49-2.43 (m, 3+3H), 2.17-2.10 (m, 1+1H). **^{13}C NMR (91 MHz, $CDCl_3$) (mixture of rotamers) δ (ppm):** 171.8, 171.6, 154.8, 154.2, 136.4, 136.3, 128.5, 128.5, 128.1, 128.0, 127.9, 127.9, 79.1, 76.7, 75.6, 75.3, 75.0, 67.3, 57.8, 57.6, 56.4, 52.7, 52.5, 51.7, 51.6, 36.5, 35.2.

2.2.5.2.4 Synthesis of (2*S*,4*R*)-1-((benzyloxy)carbonyl)-4-(prop-2-yn-1-yloxy)pyrrolidine-2-carboxylic acid, 8

Method 1: [120]

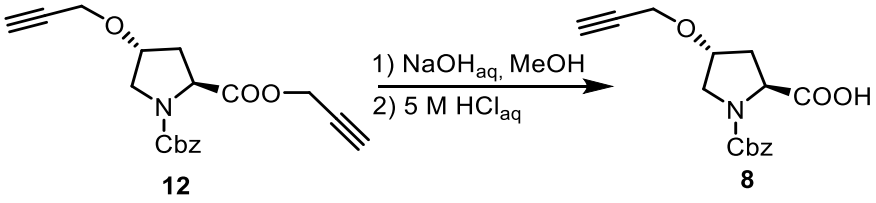

To a stirred solution of **12** (6.13 g, 18.0 mmol) in MeOH (25.0 mL), a solution of NaOH (2.16 g, 54.0 mmol) in water (16.0 mL) was added and the reaction mixture was allowed to stir at room temperature for 24 h. After addition of water (20.0 mL), the pH was adjusted at 10 by addition of 5M HCl (aq) and the reaction mixture was washed with Et_2O (3 × 30 mL). This ethereal phase was discarded. The pH of the aqueous phase was then adjusted to 4 with 5M HCl (aq) and the solution extracted with EtOAc (3 × 60 mL). The organic phase was dried over anhydrous Na_2SO_4 and after evaporation of the ethyl acetate and purification by flash-chromatography with hexane/EtOAc = 8:1, the pure product was obtained as colorless oil (5.09 g, 93% yield).

Method 2: [121]

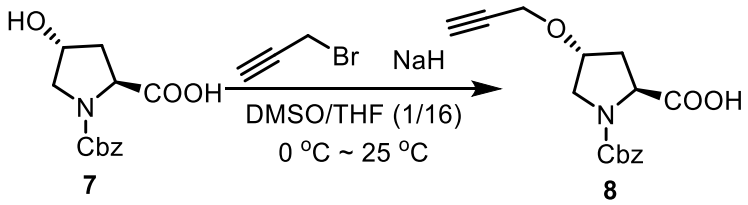

To a flame-dried three-necked round bottom flask was placed NaH (3.12 g of 60% in mineral oil, corresponding to 1.87 g of NaH, 78.0 mmol) under $N_{2,}$ then the flask was cooled to 0 °C and a solution of **7** (8.04 g, 30.0 mmol) in a mixture of anhydrous THF (62 mL) and DMSO (5.0 mL) was slowly added by syringe. The heterogeneous mixture was stirred for 30 min at 0ºC. Then, a solution of propargyl bromide (11.15 g of 80 wt. % in xylene, corresponding to 8.92 g of propargyl bromide, 75.0 mmol) in THF (18.0 mL) was added by syringe. The reaction mixture was stirred at room temperature until **7** was completely consumed (TLC monitoring, 18 h). The reaction was then quenched with water (60.0 mL) and the pH was

adjusted to 4 with 10% aqueous solution of $KHSO_4$. The crude solution was extracted with AcOEt (3 × 120 mL). The organic layer was washed with brine (3 × 60 mL), dried over Na_2SO_4, and the solvent was evaporated under vacuum. The acid **8** was isolated by flash column chromatography on silica gel with EtOAc/MeOH = 9:1 to afford colorless oil (8.01 g, 88 % yield). **$[\alpha]_D^{20}$** = -66 ° (*c* 0.01, CH_2Cl_2). **^{1}H NMR (360 MHz, $CDCl_3$) (mixture of rotamers) δ (ppm):** 10.96 (s, 1H), 7.36-7.24 (m, 5H), 5.20-5.07 (m, 2H), 4.52-4.44 (m, 1H), 4.34-4.33 (m, 1H), 4.20-4.08 (m, 2H), 3.79-3.61 (m, 2H), 2.50-2.38 (m, 2H), 2.26-2.14 (m, 1H). **^{13}C NMR (91 MHz, $CDCl_3$) (mixture of rotamers) δ (ppm):** 177.7, 176.5, 155.6, 154.5, 136.2, 136.1, 128.4, 128.2, 128.0, 127.6, 79.1, 79.1, 76.3, 75.6, 75.2, 67.7, 67.4, 58.0, 57.5, 56.5, 56.5, 51.7, 51.6, 36.6, 35.1.

2.2.5.2.5 Synthesis of benzyl (2*S*,4*R*)-2-(((*S*)-1-hydroxy-3-methylbutan-2-yl)carbamoyl)-4-(prop-2-yn-1-yloxy)pyrrolidine-1-carboxylate, 9[97]

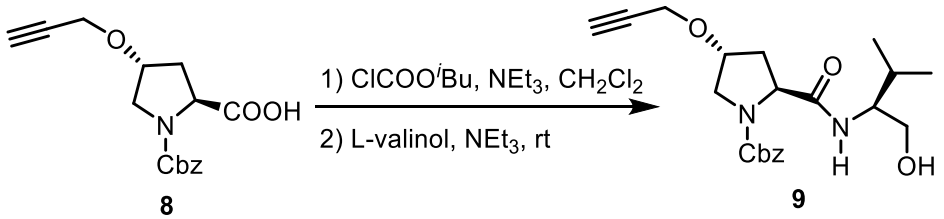

To a stirred solution of **8** (7.58 g, 25.0 mmol) in CH_2Cl_2 (20 mL), Et_3N (5.20 mL, d = 0.73 g/mL, 37.5 mmol) was slowly added at 0 °C. After the solution had been stirred for 10 min, isobutyl chloroformate (3.93 g, 28.75 mmol) was added dropwise to the reaction mixture at 0 °C. After the solution had been stirred for an additional 20 min at 0 °C, Et_3N (3.99 mL, d = 0.73 g/mL, 28.75 mmol) and L-valinol (2.97 g, 28.75 mmol) in CH_2Cl_2 (10 mL) were added to the reaction mixture. The reaction mixture was then warmed up to room temperature and it was stirred at room temperature overnight. The reaction was quenched by addition of 1M HCl and diluted with CH_2Cl_2 (80 mL), the organic phase was washed with H_2O (3 × 30 mL), brine (2 × 30 mL) and dried over anhydrous Na_2SO_4, filtered, and then concentrated under reduced pressure. Purification was accomplished by recrystallization (CH_2Cl_2/hexane) to give the final product as a white solid (9.12 g, 94% yield). **$[\alpha]_D^{20}$** = -70 ° (*c* 0.01, CH_2Cl_2). **^{1}H NMR (360 MHz, $CDCl_3$) (mixture of rotamers) δ (ppm):** 7.34-7.31 (m, 5H), 6.81 (s, 1H), 5.19-5.10 (m, 2H), 4.46-4.36 (m, 2H), 4.14 (s, 2H), 3.91-3.43 (m, 5H), 2.84 (s, 1H), 2.49-2.43 (m, 2H), 2.21-2.11 (m, 1H), 1.88-1.69 (m, 1H), 0.89-0.79 (m, 6H). **^{13}C NMR (91 MHz, $CDCl_3$) (mixture of rotamers) δ (ppm):** 171.9, 156.3, 136.1, 128.6, 126.3, 127.9, 79.3, 76.6,

74.9, 63.9, 59.5, 57.7, 56.5, 51.8, 33.9, 28.9, 19.5, 18.5. **IR (film) (cm^{-1})**: 3415.4, 3256.6, 2958.3, 1649.9, 1556.7, 1427.5, 1176.5, 1073.6, 943.1, 811.2, 645.4. **MS (ESI) m/z:** 411.2, 390.2, 389.2, 371.2, 345.2, 214.1; **HRMS (ESI) m/z** $[M + Na]^+$ calcd for $C_{21}H_{28}N_2O_5Na$: 411.1890, found: 411.1898.

2.2.5.2.6 Preparation of benzyl (2*S*,4*R*)-2-(((*S*)-1-hydroxy-3-methylbutan-2-yl)carbamoyl)-4-((1-(3-(triethoxysilyl)propyl)-1*H*-1,2,3-triazol-4-yl)methoxy)pyrrolidine-1-carboxylate, 11

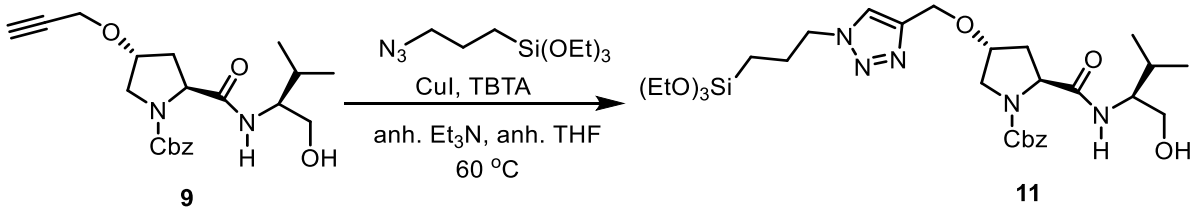

To a dry, 100 mL Schlenk flask equipped with a stir bar and under nitrogen atmosphere, CuI (11.4 mg, 0.06 mmol), TBTA (31.86 mg, 0.06 mmol) and anhydrous THF (30 mL) were added. The resulting mixture was stirred for 30 min, then **9** (1.17 g, 3.0 mmol), (3-azidopropyl)triethoxysilane (741.4 mg, 3.0 mmol) and anhydrous Et_3N (1.5 mL, 0.73 g/mL, 10.8 mmol) were added by using a syringe. The resulting mixture was stirred at 60 ºC (N_2 atmosphere) until **9** was fully consumed (14 h, reaction monitored by TLC). Then, the solvent was evaporated under reduced pressure and the residue was washed with anhydrous pentane to provide the pure product as colorless oil (1.90 g, 100 % yield). $[\alpha]_D^{20}$ = -48 º (*c* 0.01, CH_2Cl_2). **^{1}H NMR (600 MHz, $CDCl_3$) (mixture of rotamers) δ (ppm):** 7.51 (s, 1H), 7.34-7.27 (m, 5H), 6.78 (s, 1H), 5.29-5.12 (m, 2H), 4.63-4.59 (m, 2H), 4.54 (br s, 1H), 4.34-4.30 (m, 3H), 3.82 (q, *J* = 6 Hz, 6H), 3.74-3.58 (m, 5H), 2.45 (br s, 1H), 2.24(br s, 1H), 2.04-1.99 (m, 2H), 1.88-1.72 (m, 1H), 1.21(t, *J* = 6 Hz, 9H), 0.89-0.79 (m, 6H), 0.62-0.59 (m, 2H), NH and OH were not detected; **^{13}C NMR (151 MHz, $CDCl_3$) (mixture of rotamers) δ (ppm):** 171.9, 156.4, 144.5, 136.3, 128.6, 128.3, 128.0, 122.6, 76.4, 67.6, 63.8, 62.8, 59.7, 58.6, 57.7, 52.6, 34.3, 29.0, 24.3, 22.4, 19.6, 18.4, 14.1, 7.6. **IR (film) (cm^{-1})**: 3307.4, 2970.9, 1685.1, 1415.8, 1353.4, 1072.6, 955, 767.7, 697.0. **MS (ESI) m/z:** 658.3 $[M + Na]^+$, 637.3, 636.3 $[M + H]^+$, 590.3, 553.3, 531.3, 413.3, 301.1, 148.9; **HRMS (ESI) m/z** $[M + Na]^+$ calcd for $C_{30}H_{49}N_5O_8SiNa$: 658.3243, found: 658.3231.

2.2.5.2.7 Preparation of (2*S*,4*R*)-*N*-((*S*)-1-hydroxy-3-methylbutan-2-yl)-4-((1-(3-(triethoxysilyl)propyl)-1*H*-1,2,3-triazol-4-yl)methoxy)pyrrolidine-2-carboxamide, P1

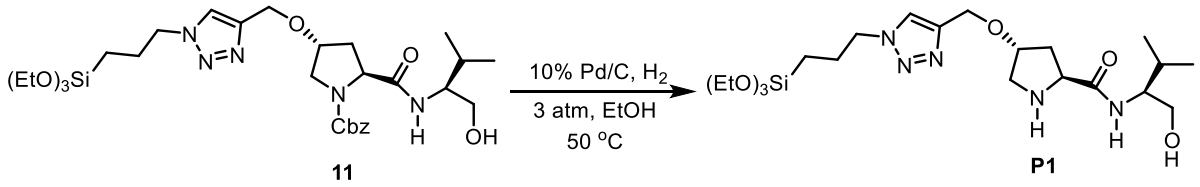

A mixture of **11** (1.27 g, 2.0 mmol) and 425.7 mg of 10% Pd/C (0.4 mmol Pd, 20 mol%) in 20 mL of absolute ethanol was hydrogenated at 50 ºC under 3 atm pressure for 6 h. The mixture was filtered through Celite® 545, and the solvent from filtrate evaporated at reduced pressure to afford the final product **P1** as a colorless oil (962 mg, 96% yield). $[\alpha]_D^{20}$ = -26 º (*c* 0.01, CH_2Cl_2). **^{1}H NMR (600 MHz, $CDCl_3$) δ (ppm):** 7.88 (d, *J* = 7.2 Hz, 1H), 7.50 (s, 1H), 4.55 (d, *J* = 12.1 Hz, 1H), 4.53 (d, *J* = 12.1 Hz, 1H), 4.31 (t, *J* = 7.0 Hz, 2H), 4.12 (br s, 1H), 3.91 (t, *J* = 8.0 Hz, 1H), 3.78 (q, *J* = 7.0 Hz, 6H), 3.66-3.61 (m, 3H), 3.18 (d, *J* = 12.7 Hz, 1H), 2.70 (dd, *J* = 12.7 and 3.4 Hz, 1H), 2.38 (m, 1H), 1.99 (m, 2H), 1.90 (m, 1H), 1.88 (m, 1H), 1.18 (t, *J* = 7.0 Hz, 9H), 0.91 (d, *J* = 6.8 Hz, 3H), 0.87 (d, *J* = 6.8 Hz, 3H), 0.57 (m, 2H), NH and OH were not detected; **^{13}C NMR (151 MHz, $CDCl_3$) δ (ppm):** 175.5, 144.7, 122.3, 80.7, 64.2, 62.1, 59.9, 58.8, 56.9, 52.4, 52.4, 36.5, 29.0, 24.1, 19.7, 18.4, 18.3, 7.7. **IR (film) (cm^{-1})**: 3324.5, 2927.2, 1649.0, 1519.0, 1072.3, 954.6, 783.3, 679.6. **MS (ESI) m/z:** 502.3 $[M+H]^+$, 479.3, 465.3, 452.9, 413.3; **HRMS (ESI) m/z** $[M+H]^+$ calcd for $C_{22}H_{44}N_5O_6Si$: 502.3055, found: 502.3055.

2.2.5.2.8 Preparation of benzyl (2*S*,4*R*)-4-((1-(2-(bis(3-(triethoxysilyl)propyl)amino)ethyl)-1*H*-1,2,3-triazol-4-yl)methoxy)-2-(((*S*)-1-hydroxy-3-methylbutan-2-yl)carbamoyl)pyrrolidine-1-carboxylate, 14

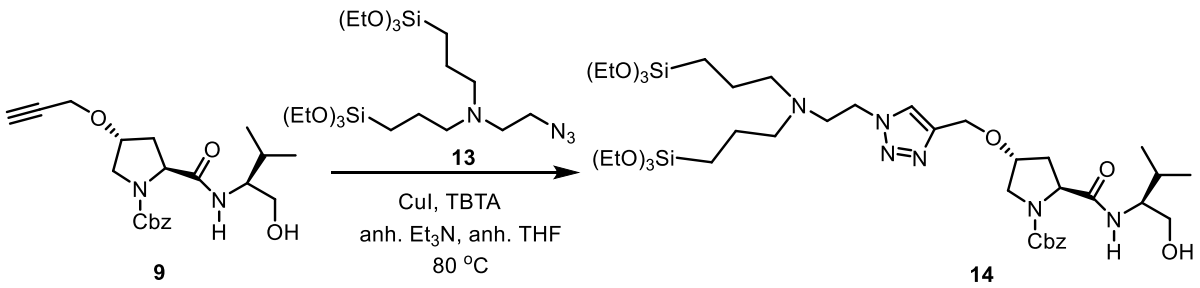

To a dry 50 mL Schlenk flask equipped with a stir bar and under nitrogen atmosphere, CuI (7.6 mg, 0.04 mmol), TBTA (21.20 mg, 0.04 mmol) and anhydrous THF (10 mL) were added.

The resulting mixture was stirred for 30 min. This solution was transferred to another dry 50 mL Schlenk flask, equipped with a reflux condenser and under nitrogen atmosphere, containing a solution of **9** (777 mg, 2.0 mmol) in anhydrous THF (10 mL). Then, a mixture of *N*-(2-azidoethyl)-3-(triethoxysilyl)-N-(3-(triethoxysilyl)propyl)propan-1-amine **13** (989.6 mg, 2.0 mmol) and anhydrous Et_3N (1.0 mL, 0.73 g/mL, 7.2 mmol) was added by using a syringe. The resulting mixture was stirred at 80 ºC (N_2 atmosphere) until **9** was fully consumed (16 h, TLC monitoring). Then, the solvent was evaporated under reduced pressure and the residue was washed with anhydrous pentane to provide the pure product **14** as colorless oil (1.77 g, 100 % yield). **$[\alpha]_D^{20}$** = -34 º (*c* 0.01, CH_2Cl_2). **^{1}H NMR (360 MHz, $CDCl_3$) (mixture of rotamers) δ (ppm):** 7.62 (s, 1H), 7.34 (br s, 5H), 6.71 (br, 0.61H), 6.07 (br s, 0.18H), 5.17-5.08 (m, 2H), 4.60 (s, 2H), 4.45-4.29 (m, 4H), 3.83 (q, *J* = 7.2 Hz , 12H), 3.74-3.59 (m, 4H), 2.88 (t, *J* = 7.2 Hz, 2H), 2.48-2.44 (m, 4H), 2.20 (br s, 1H), 1.87-1.83 (m, 1H), 1.50-1.46 (m, 4H), 1.21 (t, *J* = 7.2 Hz, 18H), 0.87 (t, *J* = 7.2 Hz, 6H), 0.56-0.51 (m, 4H), OH was not detected; **^{13}C NMR (91 MHz, $CDCl_3$) (mixture of rotamers) δ (ppm):** 171.9, 156.4, 144.1, 136.2, 128.5, 128.2, 127.9, 123.3, 77.3, 67.5, 63.8, 62.6, 59.6, 58.4, 57.7, 57.0, 54.2, 51.8, 48.9, 34.2, 28.9, 20.3, 19.5, 18.3, 7.8. **IR (film) (cm^{-1})**: 3308.1, 2927.1, 1702.4, 1542.0, 1415.4, 1292.9, 1220.4, 1072.7, 952.9, 767.6, 697.0. **MS (ESI) m/z:** 883.5 $[M + H]^+$, 861.0, 847.0, 553.3, 453.3, 413.3; **HRMS (ESI) m/z** $[M + H]^+$ calcd for $C_{41}H_{75}N_6O_{11}Si_2$: 883.5027, found: 883.5019.

2.2.5.2.9 Preparation of (2*S*,4*R*)-4-((1-(2-(bis(3-(triethoxysilyl)propyl)amino)ethyl)-1*H*-1,2,3-triazol-4-yl)methoxy)-*N*-((*S*)-1-hydroxy-3-methylbutan-2-yl)pyrrolidine-2-carboxamide, P2

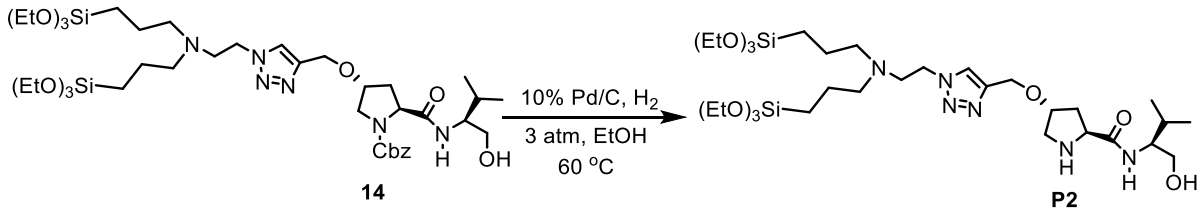

A mixture of **14** (1.79 g, 2.0 mmol) and 425.7 mg of 10% Pd/C (0.4 mmol Pd, 20 mol%) in 20 mL of absolute ethanol was hydrogenated at 60 ºC under 3 atm pressure for 48 h. The mixture was filtered through Celite® 545, and the solvent from filtrate evaporated at reduced pressure to afford the final product as a colorless oil (1.38 mg, 92% yield). **$[\alpha]_D^{20}$** = -12 º (*c* 0.01, CH_2Cl_2). **^{1}H NMR (600 MHz, $CDCl_3$) δ (ppm):** 7.96 (d, *J* = 7.8 Hz, 1H), 7.66 (s, 1H),

4.56 (d, *J* = 11.8 Hz, 1H), 4.52 (d, *J* = 11.8 Hz, 1H), 4.37 (t, *J* = 6.3 Hz, 2H), 4.14 (br, 1H), 4.01 (t, *J* = 8.4 Hz, 1H), 3.77 (q, *J* = 7.0 Hz, 12H), 3.67-3.58 (m, 3H), 3.21 (d, *J* = 12.8 Hz, 1H), 2.88 (t, *J* = 6.3 Hz, 2H), 2.80 (dd, *J* = 12.8 and 2.5 Hz, 1H), 2.47-2.41 (m, 5H), 1.92 (m, 1H), 1.87 (m, 1H), 1.47 (m, 4H), 1.18 (t, *J* = 7.0 Hz, 18H), 0.90 (d, *J* = 6.7 Hz, 3H), 0.86 (d, *J* = 6.7 Hz, 3H), 0.50 (m, 4H), OH was not detected; **^{13}C NMR (91 MHz, $CDCl_3$) δ(ppm):** 176.0, 144.5, 123.3, 80.7, 64.9, 62.1, 59.9, 58.4, 57.4, 57.1, 54.2, 52.4, 48.9, 36.5, 29.0, 20.3, 19.7, 18.5, 18.3, 7.8. **IR (film) (cm^{-1})**: 3323.7, 2927.2, 1655.3, 1522.7, 1388.8, 1099.9, 1072.9, 952.8, 769.8. **MS (ESI) m/z:** 749.5 $[M + H]^+$, 618.4, 551.3, 452.3, 413.7, 375.2, 259.2; **HRMS (ESI) m/z** $[M + H]^+$ calcd for $C_{33}H_{69}N_6O_9Si_2$: 749.4659, found: 749.4656.

2.2.5.2.10 Synthesis of (2*S*,4*R*)-4-(allyloxy)-1-((benzyloxy)carbonyl)pyrrolidine-2-carboxylic acid, 15[121]

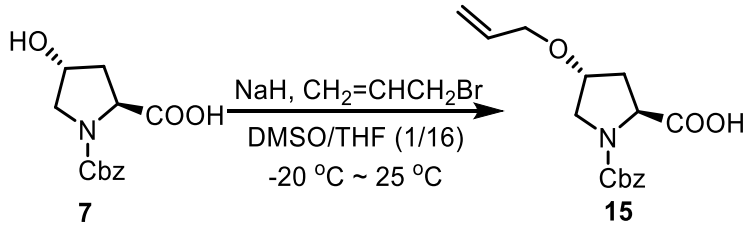

To a flame-dried three-necked round bottom flask was added NaH (1.56 g of 60% in mineral oil, 39.0 mmol) under N_2 and the flask was cooled to -20 °C. Then, a solution of *N*-Cbz-4-hydroxyproline (4.02 g, 15.0 mmol) in a mixture of anhydrous THF (15.0 mL) and DMSO (1.5 mL) was slowly added by syringe. The temperature was then raised to reach 0 °C and the heterogeneous mixture was stirred for 30 mins. The temperature was reduced again to -20 °C and a solution of 3-bromo-1-propene (4.54 g, 37.5 mmol) in THF (9.0 mL) was added by syringe. The reaction mixture was stirred at room temperature until the starting material was completely consumed (TLC analysis, 15 h). The reaction was then quenched with water (30.0 mL) and the pH was adjusted to 4 with 10% aqueous solution of $KHSO_4$ (ca. 15.0 mL). The crude mixture was extracted with AcOEt (3 × 60 mL). The organic layer was washed with brine (2 × 20 mL), dried over anhydrous Na_2SO_4, and the solvent was evaporated under vacuum. The product was isolated by flash column chromatography on silica gel with EtOAc/MeOH = 9:1 to afford a colorless oil (4.04 g, 88 % yield). **^{1}H NMR (360 MHz, $CDCl_3$) δ (ppm):** 8.84 (br s, 1H), 7.36-7.28 (m, 5H), 5.91-5.81 (m, 1H),5.29-5.11 (m, 4H), 4.54-4.48 (m, 1H), 4.17-4.11 (m, 1H), 4.11-3.96 (m, 2H), 3.65-3.62 (m, 2H), 2.40-2.16 (m, 2H).

2.2.5.2.11 Synthesis of benzyl (2*S*,4*R*)-4-(allyloxy)-2-(((*S*)-1-hydroxy-3-methylbutan-2-yl)carbamoyl)pyrrolidine-1-carboxylate, 16

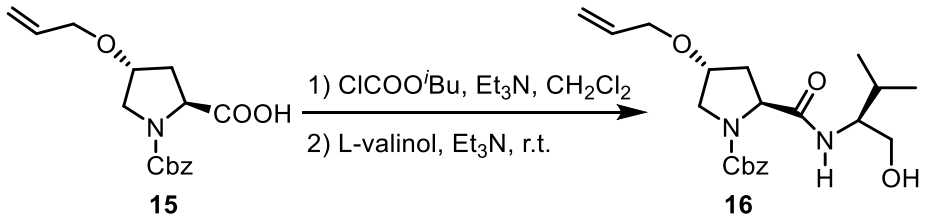

To a stirred solution of **15** (3.88 g, 12.7 mmol) in CH_2Cl_2 (20 mL), Et_3N (2.64 mL, 0.73 g/mL, 19.05 mmol) was slowly added at 0 °C. After the solution had been stirred for 10 min, isobutyl chloroformate (2.00 g, 14.61 mmol) was added dropwise to the reaction mixture at 0 °C. After the solution had been stirred for an additional 20 min at 0 °C, a solution of Et_3N (2.03 mL, 14.61 mmol) and L-valinol (1.51 g, 14.61 mmol) in CH_2Cl_2 (3 mL) was added. Then the reaction mixture was warmed up to room temperature and it was stirred overnight. The reaction was quenched by addition of 1M HCl and diluted with CH_2Cl_2 (60 mL), the organic phase was washed with H_2O (3 × 20 mL), brine (2 × 20 mL) and dried over anhydrous Na_2SO_4, filtered, and then concentrated under reduced pressure. Purification was accomplished by recrystallization (CH_2Cl_2/hexane) to give the final product as a white solid (4.74 g, 96% yield). **^{1}H NMR (360 MHz, $CDCl_3$) δ (ppm):** 7.35-7.26 (m, 5H), 6.77 (br s, 1H), 5.92-5.81 (m, 1H), 5.28-5.14 (m, 4H), 4.44 (t, J = 7.2 Hz, 1H), 4.18-4.11 (m, 1H), 3.98-3.84 (m, 2H), 3.67-3.56 (m, 5H), 2.43 (br s, 1H), 2.17 (br s, 1H), 1.84-1.72 (m, 1H), 0.97-0.79 (m, 6H). **^{13}C NMR (91 MHz, $CDCl_3$) δ (ppm):** 172.7, 156.2, 136.2, 134.3, 128.5, 128.2, 127.9, 117.3, 75.9, 70.2, 67.5, 63.4, 59.8, 58.1, 52.5, 34.4, 28.9, 19.2. **MS (ESI) m/z:** 413.3 $[M + Na]^+$, 391.2, 373.2, 348.2, 347.2, 216.1, 149.0; **HRMS (ESI) m/z** $[M + Na]^+$ calcd for $C_{21}H_{30}N_2O_5Na$: 413.2047, found: 413.2047.

2.2.5.2.12 Preparation of benzyl (2*S*,4*R*)-2-(((*S*)-1-hydroxy-3-methylbutan-2-yl)carbamoyl)-4-(3-((3-(triethoxysilyl)propyl)thio)propoxy)pyrrolidine-1-carboxylate, 17

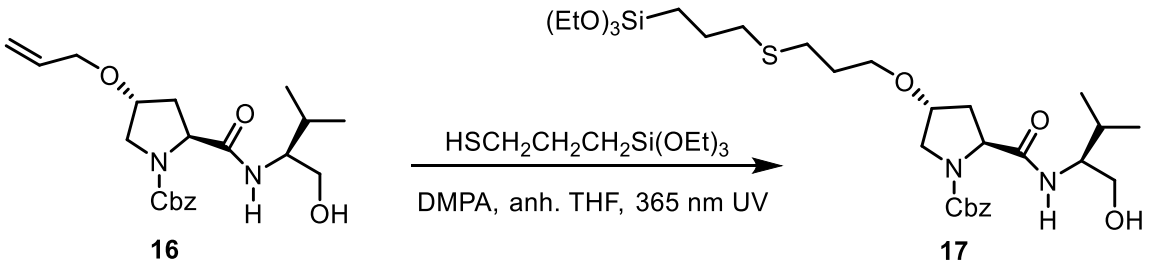

16 17

In a 50 mL Schlenk tube under nitrogen, benzyl (2*S*,4*R*)-4-(allyloxy)-2-(((*S*)-1-hydroxy-3-methylbutan-2-yl)carbamoyl)pyrrolidine-1-carboxylate **16** (781 mg, 2.0 mmol) and 2,2-dimethoxy-1,2-diphenylethanone (102.5 mg, 0.4 mmol) were dissolved in anhydrous THF (20.0 mL). Then (3-mercaptopropyl)triethoxysilane (500.8 mg, 2.1 mmol) was added and the stirred mixture was irradiated with a UV lamp at 365 nm under argon atmosphere until **16** was fully consumed (TLC monitoring, 20 h). Then, the solvent was removed under reduced pressure and the residue was washed with anhydrous pentane, obtaining the pure product as colorless oil (1.25 g, 99% yield). **^{1}H NMR (360 MHz, $CDCl_3$) δ (ppm):** 7.36-7.31 (m, 5H), 5.20-5.10 (m, 2H), 4.43 (t, *J* = 7.2 Hz, 1H), 4.11 (br s, 1H), 3.82 (q, *J* = 7.2 Hz, 6H), 3.66-3.48 (m, 6H), 2.72 (br s, 1H), 2.55-2.49 (br s, 4H), 2.41 (br s, 1H), 2.14 (br s, 1H), 1.85-1.76 (m, 2H), 1.71-1.64 (m, 2H), 1.22 (t, *J* = 7.2 Hz, 9H), 0.87 (t, *J* = 7.2 Hz, 6H), 0.73 (t, *J* = 7.2 Hz, 2H). **MS (ESI) m/z:** 651.3 $[M + Na]^+$, 629.3, 583.3, 537.2, 475.2, 413.3, 149.0; **HRMS (ESI) m/z** $[M + Na]^+$ calcd for $C_{30}H_{52}N_2O_8SSiNa$: 651.3106, found: 651.3105.

2.2.5.2.13 Preparation of benzyl (2*S*,4*R*)-2-(((S)-1-((*tert*-butyldimethylsilyl)oxy)-3-methylbutan-2-yl)carbamoyl)-4-(prop-2-yn-1-yloxy)pyrrolidine-1-carboxylate, 18

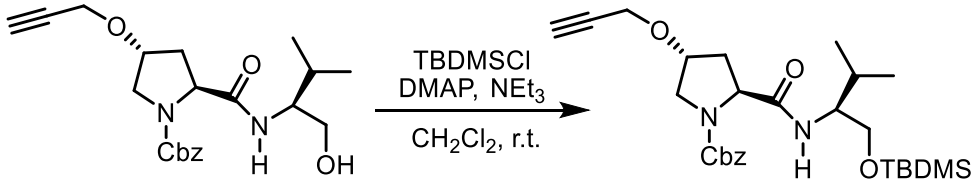

9 18

To a stirred solution of **9** (3.88 g, 10 mmol) in anhydrous CH_2Cl_2 (120 mL), Et_3N (1.6 mL, 11.5 mmol), TBDMSCl (1.80 g, 11.9 mmol) and DMAP (122.2 mg, 1.0 mmol) were added in this order at 0 ^oC. The reaction mixture was stirred at room temperature for 44 h. The reaction

mixture was diluted with CH_2Cl_2 and washed with saturated aqueous $NaHCO_3$, saturated aqueous NH_4Cl and water. The organic layer was dried over anhydrous Na_2SO_4, filtered, and the solvent was removed under reduced pressure. The resulting residue was purified by flash chromatography (hexane/EtOAc = 2:1) to give the product as a yellow oil (4.86 g, 97% yield). **$[\alpha]_D^{20}$** = -65 ° (*c* 0.03, CH_2Cl_2). **^{1}H NMR (360 MHz, $CDCl_3$) δ (ppm):** 7.34-7.31 (m, 5H), 6.78 (d, *J* = 7.2 Hz, 1H), 5.23-5.02 (m, 2H), 4.44-4.37 (m, 2H), 4.13-4.09 (m, 2H), 3.71-3.38 (m, 5H), 2.56-2.42 (m, 2H), 2.23-1.12 (m, 1H), 1.91-1.68 (m, 1H), 0.89-0.79 (m, 15H), 0.04 (s, 6H). **^{13}C NMR (91 MHz, $CDCl_3$) δ (ppm):** 170.6, 156.0, 136.4, 128.5, 128.1, 127.9, 74.8, 67.4, 62.8, 60.4, 59.3, 56.6, 55.8, 51.4, 33.9, 28.7, 25.9, 21.1, 19.6, 18.4, 14.2, -5.5.

2.2.5.2.14 Preparation of benzyl (2*S*,4*R*)-2-(((*S*)-1-((tert-butyldimethylsilyl)oxy)-3-methylbutan-2-yl)carbamothioyl)-4-(prop-2-yn-1-yloxy)pyrrolidine-1-carboxylate, 19

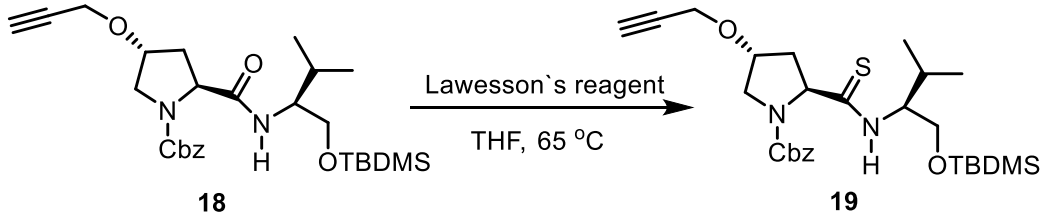

A mixture of **18** (1.005 g, 2 mmol) and Lawesson's reagent (485.4 mg, 1.2 mmol) in anhydrous THF (20 mL) was heated at 65 ℃ overnight under an argon atmosphere. After removal of the solvent under reduced pressure the resulting residue was purified by flash chromatography (hexane/EtOAc = 10:1) to afford compound **19** as a colorless oil (546 mg, 53% yield). **^{1}H NMR (360 MHz, $CDCl_3$) δ (ppm):** 8.57 (br s, 1H), 7.36 (br s, 5H), 5.17-5.12 (m, 2H), 4.45-4.36 (m, 2H), 4.13-4.11 (m, 2H), 4.00-3.41 (m, 5H), 2.76-2.42 (m, 2H), 2.32 (br s, 1H), 1.83-1.53 (m, 1H), 0.95-0.88 (m, 15H), 0.04 (s, 6H).

2.2.5.2.15 Preparation of benzyl (2*S*,4*R*)-2-(((*S*)-1-hydroxy-3-methylbutan-2-yl)carbamothioyl)-4-(prop-2-yn-1-yloxy)pyrrolidine-1-carboxylate, 20

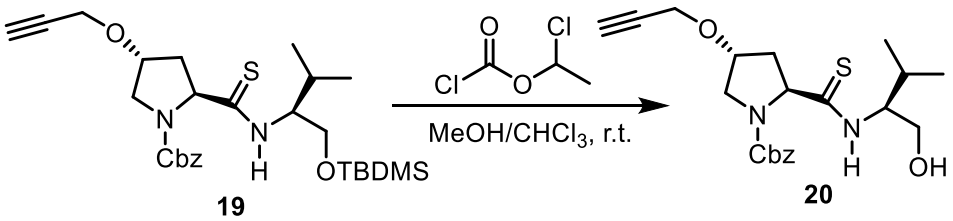

In a 25 mL round bottom flask, **19** (508 mg, 0.98 mmol) was dissolved in a mixture of MeOH/$CHCl_3$ (16 mL, 1/1 v/v) at room temperature. To this solution, 1-chloroethyl chloroformate (280 mg 1.96 mmol) was added slowly and the mixture was stirred overnight at room temperature. When TLC showed no starting compound the volatiles were removed under reduced pressure. The residue was purified by flash chromatography using hexane/AcOEt = 1/1 as eluent. Compound **20** was isolated as a colorless oil (217 mg, 55% yield). **^{1}H NMR (360 MHz, $CDCl_3$) δ (ppm):** 8.28 (br s, 1H), 7.36-7.34 (m, 5H), 5.14 (br s, 2H), 4.88 (br s, 1H), 4.39 (br s, 2H), 4.16-4.11 (m, 2H), 3.83 (br s, 1H), 3.61 (br s, 2H), 2.75-2.44 (m, 2H), 2.04-1.96 (m, 2H), 1.60 (s, 1H), 1.26 (br s, 1H), 0.96-0.89 (m, 6H).

2.2.5.2.16 Preparation of benzyl (2*S*,4*R*)-2-(((*S*)-1-hydroxy-3-methylbutan-2-yl)carbamothioyl)-4-((1-(3-(triethoxysilyl)propyl)-1*H*-1,2,3-triazol-4-yl)methoxy) pyrrolidine-1-carboxylate, 21

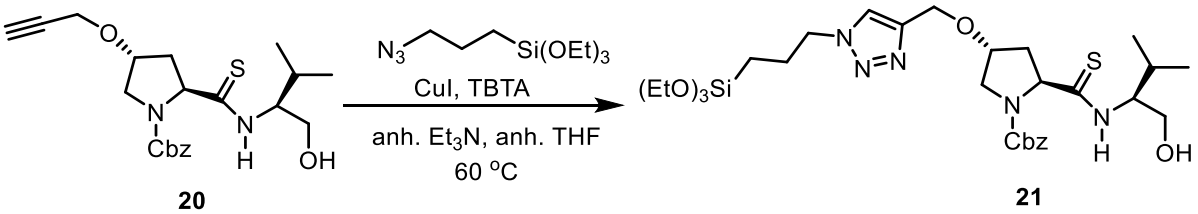

To a dry, 10 mL Schlenk flask equipped with a stir bar and under nitrogen atmosphere, CuI (1.62 mg, 0.0085 mmol), TBTA (4.53 mg, 0.0085 mmol) and anhydrous THF (5 mL) were added. The resulting mixture was stirred for 30 min, then a mixture of **20** (172 mg, 0.425 mmol), (3-azidopropyl)triethoxysilane (105.1 mg, 0.425 mmol) and anhydrous Et_3N (212 μL) was added by using a syringe. The resulting mixture was stirred at 60 ºC (N_2 atmosphere); 64 hours later, there was still some starting material **20** (reaction monitored by TLC). At this point, the solvent was evaporated under reduced pressure and the residue was washed with anhydrous pentane to provide the crude product as colorless oil (267.2 mg). From HNMR, the crude product was a mixture of the starting material and the final product. We used the crude mixture for next step directly.

2.2.5.3 Preparation of mesoporous silica nanoparticles derived from proline-valinol amides

2.2.5.3.1 Preparation of mesoporous MCM-41 silica nanoparticles[136]

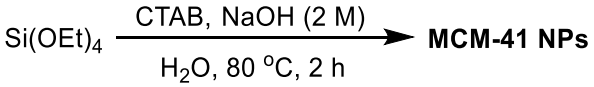

In an open 250 mL round bottom flask without reflux condenser was placed a solution of cetyltrimethylammonium bromide (CTAB, 315 mg, 0.86 mmol) in Mili-Q water (150 mL). Then a solution of 2 M NaOH (1.1 mL, 2.2 mmol) was added, causing the pH to increase to above 12 and inducing the complete dissolution of CTAB. The mixture was stirred at 1000 rpm at 80 °C while stirring to create a homogeneous solution. Tetraethyl orthosilicate (TEOS, 1.4 mL, 6.28 mmol) was added to the solution dropwise. The condensation process was conducted for two hours at 80 °C under stirring. The suspension was cooled to room temperature while stirring and the NPs were collected by centrifugation (13500 rpm at 25°C for 45 mins). In order to remove the surfactant, 20 mL of an alcoholic solution of ammonium nitrate [NH_4NO_3, 6 g/L in 96% EtOH] was added to each tube. The tubes were sonicated for 30 min at 50 °C, then cooled and centrifuged (30 min at 135000 rpm at 25 °C), the supernatant was discarded. This NH_4NO_3 washing was performed 3 times. Each solid in the tubes was washed successively with 96% ethanol, Mili-Q water, 96% ethanol using the same protocol (30 min at 50 °C sonication, centrifugation). The final product was dried for few hours under vacuum at room temperature. The MCM-41 silica nanoparticles were obtained as a white solid (296 mg). **BET:** S_{BET} = 1097 m^2/g, V_{pore} = 0.79 cm^3g^{-1}, $\emptyset_{pore}$ = 2.7 nm. **IR (ATR) ν (cm^{-1}):** 3432.1, 1043.7, 959.4, 879.5, 796.0.

2.2.5.3.2 Preparation of mesoporous M0 silica nanoparticles[137]

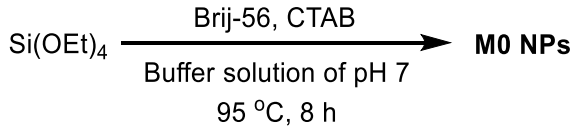

MSNs were synthesized in an aqueous buffer solution of pH 7 from a mixture with the following molar ratios: Brij-56:CTAB:TEOS:H_2O = 7:20:160:120,000. Initially, CTAB (911 mg, 2.50 mmol) and Brij-56 (597.6 mg, 0.875 mmol) were dissolved in the buffer solution, prepared from KH_2PO_4 (857.5 mg, 6.3 mmol) and NaOH (145 mg, 3.625 mmol) in H_2O (270

mL, 15000 mmol), under vigorous stirring and heating at 95 ºC. When the solution became homogeneous, TEOS (4.17 g, 20 mmol) was added slowly. The reaction was maintained for 8 hours under stirring at 95ºC. The suspension was cooled to room temperature while stirring and the NPs were collected by centrifugation (13500 rpm at 25 °C for 45 mins). In order to remove the surfactant, 20 mL of an alcoholic solution of ammonium nitrate [NH_4NO_3, 6 g/L in 96% EtOH] was added to each tube, sonicated for 30 min at 50 °C, then cooled and centrifuged (30 min at 13500 rpm at 25 °C), the supernatant was discarded. This NH_4NO_3 washing was performed 3 times. Each solid in the tubes was washed successively with 96% ethanol, Mili-Q water, 96% ethanol using the same protocol (30 min at 50 °C sonication, centrifugation). The final product was dried for few hours under vacuum at room temperature. The **M0 NPs** were obtained as a white solid (940 mg). **BET:** S_{BET} = 332 m^2/g, V_{pore} = 0.29 cm^3g^{-1}, $\emptyset_{pore}$ = 3.1 nm. **IR (ATR) ν (cm^{-1}):** 2925.8, 1044.1, 966.0, 797.3, 621.3.

2.2.5.3.3 Preparation of functionalized mesoporous silica nanoparticles M1

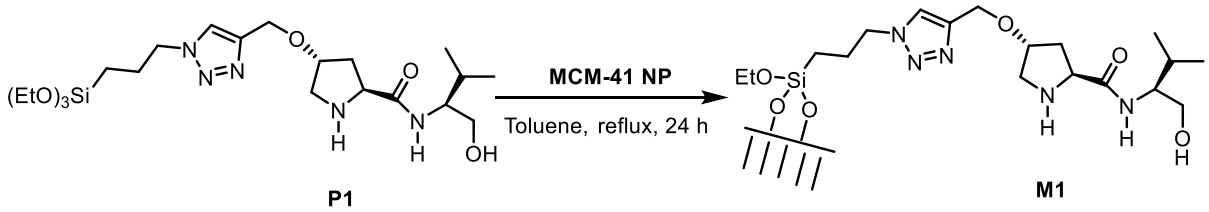

In a 250 mL round bottom flask equipped with a Dean-Stark apparatus, compound **P1** (401.3 mg, 0.8 mmol) and mesostructured silica nanoparticles MCM-41 (480.6 mg, 8 mmol) were refluxed in dry toluene (80 mL) for 24 h. After this time, the suspension was centrifuged (12000 rpm at 25 °C for 45 min). The solid was washed successively with ethanol (3 × 20 mL) and acetone (2 × 20 mL) (30 min at 50 °C sonication, 30 min for centrifugation), then dried under vacuum and finally crushed to give the grafted material **M1** as a white solid (450 mg). **EA:** 5.43% N, 17.74% C, 2.95% H (0.78 mmol prolinamide/g material). **BET:** S_{BET} = 682 m^2/g, V_{pore} = 0.29 cm^3g^{-1}, $\emptyset_{pore}$ = 2.6 nm. **IR (ATR) ν (cm^{-1}):** 3322.7, 1648.4, 1534.5, 1055.8, 960.6, 796.4. **^{13}C CP MAS NMR (100.6 MHz) *δ*:** 177.1, 144.8, 125.0, 80.3, 60.2, 57.8, 52.6, 36.9, 29.8, 24.8, 17.7, 17.0, 7.9; **^{29}Si CP MAS NMR (79.5 MHz) *δ* (ppm)::** -60 (T^2), -68 (T^3), -93 (Q^2), -103 (Q^3), -113 (Q^4).

2.2.5.3.4 Preparation of functionalized mesoporous silica nanoparticles M2

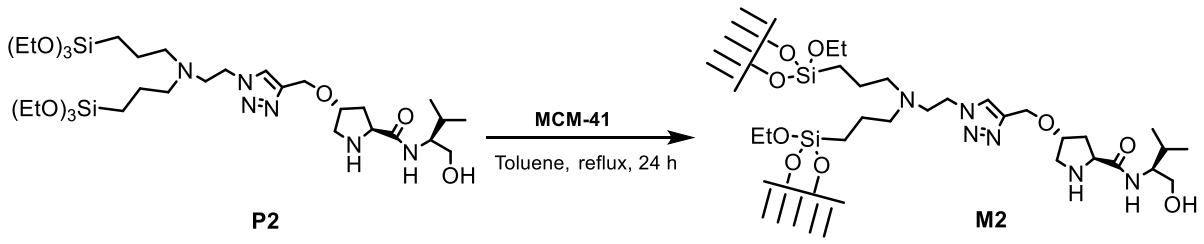

In a 250 mL round bottom flask equipped with a Dean-Stark apparatus, compound **P2** (599.3 mg, 0.8 mmol) and mesostructured silica nanoparticles MCM-41 (480.6 mg, 8 mmol) were refluxed in dry toluene (80 mL) for 24 h. After this time the suspension was centrifuged (12000 rpm at 25 °C for 45 min). The solid was washed successively with ethanol (3 × 20 mL) and acetone (2 × 20 mL), (30 min at 50 °C sonication, 30 min for centrifugation), then dried under vacuum and finally crushed to give the grafted material **M2** as a white solid (620 mg). **EA:** 5.84% N, 21.76% C, 3.63% H (0.69 mmol prolinamide/g material). **BET:** S_{BET} = 477 m^2/g, V_{pore} = 0.21 cm^3g^{-1}, $\emptyset_{pore}$ = 2.5 nm. **IR (ATR) ν (cm^{-1}):** 3320.0, 2923.3, 1655.0, 1531.3, 1464.3, 1221.3, 1050.5, 794.8. **^{13}C CP MAS NMR (100.6 MHz) δ (ppm):** 176.2, 145.3, 124.1, 79.0, 58.2, 29.9, 17.3, 9.6.

2.2.5.3.5 Preparation of functionalized mesoporous silica nanoparticles M3

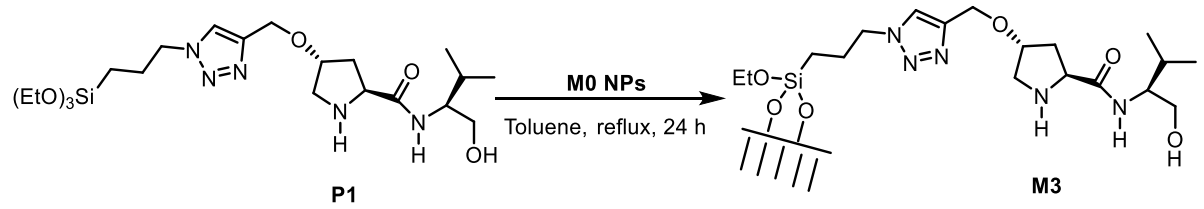

In a 250 mL round bottom flask equipped with a Dean-Stark apparatus, compound **P1** (634 mg, 1.26 mmol) and mesostructured silica nanoparticles **M0 NPs** (759.2 mg, 12.6 mmol) were refluxed in dry toluene (120 mL) for 24 h. After this time, the suspension was centrifuged (12000 rpm at 25 °C for 45 min). The solid was washed successively with ethanol (3 × 20 mL) and acetone (2 × 20 mL) (30 min at 50 °C sonication, 30 min for centrifugation), then dried under vacuum and finally crushed to give the grafted material **M3** as a white solid (760 mg). **EA:** 3.33% N, 15.63% C, 2.76% H (0.48 mmol prolinamide/g material). **BET:** S_{BET} = 183 m^2/g, V_{pore} = 0.14 cm^3g^{-1}, $\emptyset_{pore}$ = 3.0 nm. **IR (ATR) ν (cm^{-1}):** 2925.4, 1654.3, 1529.6, 1466.5, 1050.1, 795.5. **^{13}C CP MAS NMR (100.6 MHz) δ (ppm):** 176.8, 145.3, 126.0, 80.9, 67.9, 58.2, 53.9, 30.1, 23.1, 17.6, 8.7; **^{29}Si CP MAS NMR (79.5 MHz) δ (ppm):** -60 (T^2), -69 (T^3), -95 (Q^2), -103 (Q^3), -113 (Q^4).

2.2.5.3.6 Preparation of functionalized mesoporous silica nanoparticles M4

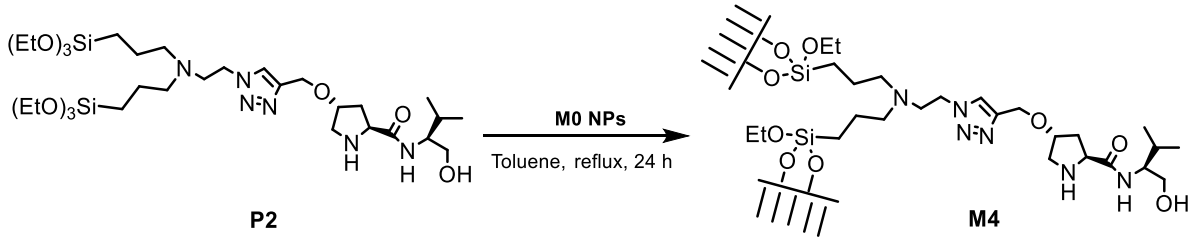

In a 250 mL round bottom flask equipped with a Dean-Stark apparatus, compound **P2** (943.9 mg, 1.26 mmol) and mesostructured silica nanoparticles **M0 NPs** (759.2 mg, 12.6 mmol) were refluxed in dry toluene (120 mL) for 24 h. After this time the suspension was centrifuged (12000 rpm at 25 °C for 45 min). The solid was washed successively with ethanol (3 × 20 mL) and acetone (2 × 20 mL) (30 min at 50 °C sonication, 30 min for centrifugation), then dried under vacuum and finally crushed to give the grafted material **M4** as a white solid (718 mg). **EA:** 3.07% N, 15.60% C, 2.80% H (0.37 mmol prolinamide/g material**). BET:** S_{BET} = 177 m^2/g, V_{pore} = 0.13 cm^3g^{-1}, $\emptyset_{pore}$ = 3.0 nm. **IR (ATR) ν (cm^{-1}):** 2926.2, 1655.6, 1529.2, 1467.2, 1048.8, 794.6. **^{13}C CP MAS NMR (100.6 MHz) δ (ppm):** 176.7, 144.8, 127.8, 80.4, 67.1, 57.9, 53.9, 30.1, 23.0, 17.4, 8.2.

2.2.5.3.7 Preparation of functionalized mesoporous silica nanoparticles M5

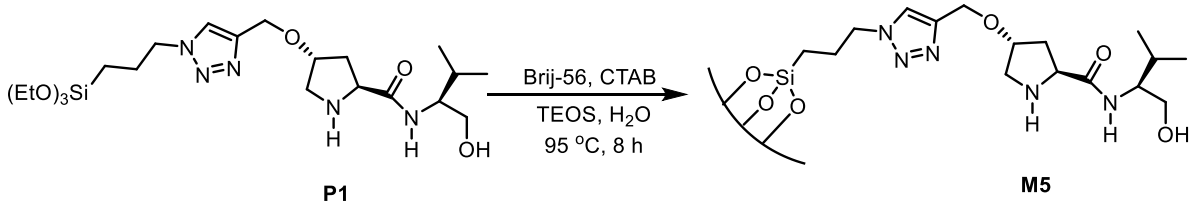

MSNs were synthesized in an aqueous buffer solution of pH 7 from a mixture with the following molar ratios: Brij-56:CTAB:TEOS:**P1**:H_2O = 7:20:160:16:120,000. Initially, CTAB (455.5 mg, 1.25 mmol) and Brij-56 (298.8 mg, 0.438 mmol) were dissolved in the buffer solution, prepared from KH_2PO_4 (428.8 mg, 3.15 mmol) and NaOH (72.5 mg, 1.81 mmol) in H_2O (135 mL, 7500 mmol), under vigorous stirring (1000 rpm) and heating at 95 ºC. When the solution became homogeneous, a mixture of TEOS (2.08 g, 10 mmol) and **P1** (501.7 mg, 1 mmol) was added slowly. The reaction was maintained for 8 hours under stirring at 95ºC. The suspension was cooled to room temperature while stirring and the NPs were collected by centrifugation (13500 rpm at 25 °C for 45 mins). In order to remove the surfactant, the samples were then treated three times with a solution of NH_4NO_3 (6 g/L in 96% EtOH), and washed three times with 96% ethanol, Mili-Q water, 96% ethanol, respectively.

The treatment with NH_4NO_3 and the following steps were identical as those described for the **M0 NPs**. The material **M5** was obtained as a white solid (541 mg). **EA:** 5.71% N, 17.22% C, 3.04% H (0.82 mmol prolinamide/g material). **BET:** S_{BET} = 135 m^2/g, V_{pore} = 0.09 cm^3g^{-1}, $\emptyset_{pore}$ = 2.5 nm. IR (ATR) ν (cm^{-1}): 3308.4, 2963.8, 1649.2, 1532.2, 1466.1, 1046.3, 794.3. **^{13}C CP MAS NMR (100.6 MHz) δ (ppm):** 176.8, 144.7, 125.7, 81.7, 59.9, 58.0, 52.2, 46.1, 38.1, 29.6, 26.2, 24.2, 17.9, 8.5; **^{29}Si CP MAS NMR (79.5 MHz) δ (ppm):** -59 (T^2), -69 (T^3), -94 (Q^2), -103 (Q^3), -113 (Q^4).

2.2.5.3.8 Preparation of functionalized mesoporous organosilica nanoparticles M6

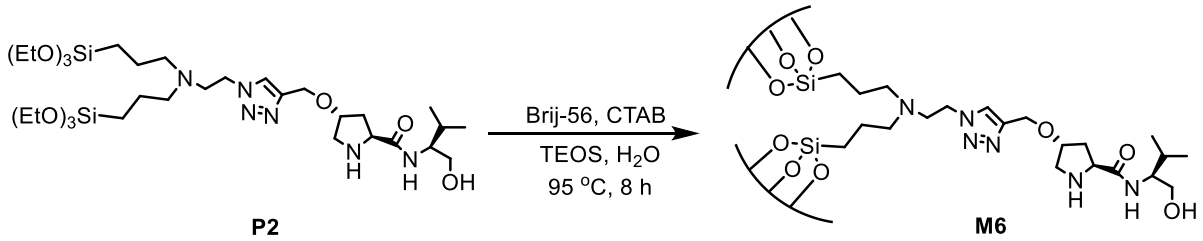

MSNs were synthesized in an aqueous buffer solution of pH 7 from a mixture with the following molar ratios: Brij-56:CTAB:TEOS:**P2**:H_2O = 7:20:160:16:120,000. Initially, CTAB (456 mg, 1.25 mmol) and Brij-56 (299 mg, 0.438 mmol) were dissolved in the buffer solution, prepared from KH_2PO_4 (429 mg, 3.15 mmol) and NaOH (73 mg, 1.81 mmol) in H_2O (135 mL, 7500 mmol), under vigorous stirring (1000 rpm) and heating at 95 ºC. When the solution became homogeneous, a mixture of TEOS (2.08 g, 10 mmol) and **P2** (749.1 mg, 1 mmol) was added slowly. The reaction was maintained for 8 hours under stirring at 95ºC. The suspension was cooled to room temperature while stirring and the NPs were collected by centrifugation (13500 rpm at 25 °C for 45 mins). In order to remove the surfactant, the samples were then treated three times with a solution of NH_4NO_3 (6 g/L in 96% EtOH), and washed three times with 96% ethanol, Mili-Q water, 96% ethanol, respectively. Treatment with NH_4NO_3 and the following steps were identical as those described for the **M0 NPs**. The material **M6** was obtained as a white solid (1.26 g). **EA:** 6.70% N, 19.89% C, 3.64% H (0.80 mmol prolinamide/g material). **BET:** S_{BET} = 16 m^2/g, V_{pore} = 0.02 cm^3g^{-1}, $\emptyset_{pore}$ = - nm. **IR (ATR) ν (cm^{-1}):** 3386.5, 1640.4, 1541.9, 1466.7, 1048.2, 789.0, 711.7. **^{13}C CP MAS NMR (100.6 MHz) δ (ppm):** 174.1, 144.6, 126.4, 78.9, 58.2, 36.1, 29.4, 19.9, 19.0, 9.9; **^{29}Si CP MAS NMR (79.5 MHz) δ (ppm):** -59 (T^2), -68 (T^3), -93 (Q^2), -103 (Q^3), -113 (Q^4).

2.2.5.4 Typical procedure for catalytic test in asymmetric aldol reaction with functionalized mesoporous silica nanoparticles

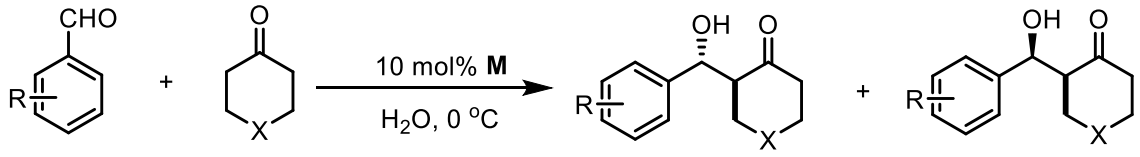

22 **23** *anti*-**24xy** *syn*-**24xy**

22a: R = 4-NO_2 **22f**: R = 4-Br **23a**: X = CH_2
22b: R = 2-NO_2 **22g**: R = 2-Cl **23d**: X = O
22c: R = 2,4-NO_2 **22h**: R = 2,4-Cl
22d: R = 4-Cl **22i**: R = 4-CF_3
22e: R = 4-F

x = a, d ; y = a-i

In a vial, cyclic ketone (2.5 mmol), mili-Q water (250 μL) and the supported catalyst **M** (10 mol%, 0.05 mmol) were stirred together for 20 min at 0 ºC. After this time, the aldehyde (0.5 mmol) was added and the mixture was stirred until TLC showed complete consumption of the aldehyde. Then the crude mixture was diluted with EtOAc (10 mL) and centrifuged (4000 rpm, 15 min). The solid catalytic material resulting from the centrifugation was washed several times with EtOAc (3 × 10 mL) and the combined supernatants were concentrated under vacuum. From this residue, the conversion, the *anti/syn* ratio of the diastereomeric mixture and *er* were determined. The solid catalytic material that had been collected by centrifugation and washed with EtOAc was then dried under vacuum and directly used in the next cycle.

Spectroscopic and chromatographic data for aldol compounds *anti*-24

2-(Hydroxy-(4-nitrophenyl)methyl)cyclohexan-1-one, ***24aa***[131]

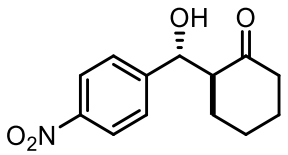

^{1}H NMR (360 MHz, $CDCl_3$) δ (ppm): 8.22 (d, *J* = 7.2 Hz, 2H), 7.52 (d, *J* = 7.2 Hz, 2H), 4.90 (dd, *J* = 7.2 and 3.6 Hz, 1H), 2.62-2.55 (m, 1H), 2.52-2.48 (m, 1H), 2.41-2.32 (m, 1H), 2.15-2.08 (m, 1H), 1.85-1.81 (m, 1H), 1.70-1.54 (m, 3H), 1.44-1.35 (m, 1H); **^{13}C NMR (91 MHz, $CDCl_3$) δ (ppm):** 214.8, 148.3, 147.6, 127.9, 123.6, 74.0, 57.2, 42.7, 30.7, 27.6, 24.7. **HPLC:** Daicel Chiralpak AD-H column, flow 1 mL/min, 254 nm, n-hexane/i-PrOH 95/5, *syn*

isomer: t_{major} = 43.90 min, t_{minor} = 35.77 min; *anti* isomer: t_{major} = 67.00 min, t_{minor} = 49.31 min.

2-(Hydroxy-(2-nitrophenyl)methyl)cyclohexan-1-one, ***24ab***[144]

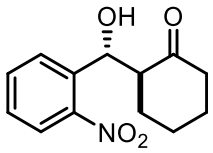

Purification by flash chromatography on silica gel with hexane/AcOEt (3/1) as eluent, white solid. **^{1}H NMR (360 MHz, $CDCl_3$) δ (ppm):** 7.86 (d, *J* = 7.2 Hz, 1H), 7.78 (d, *J* = 7.2 Hz, 1H), 7.64 (t, *J* = 7.2 Hz, 1H), 7.43 (t, *J* = 7.2 Hz, 1H), 5.43 (d, *J* = 7.2 Hz, 1H), 4.18 (br s, 1H), 2.79-2.71 (m, 1H), 2.50-2.43 (m, 1H), 2.38-2.29 (m, 1H), 2.12-2.04 (m, 1H), 1.87-1.83 (m, 1H), 1.78-1.53 (m, 4H); **^{13}C NMR (91 MHz, $CDCl_3$) δ (ppm):** 215.0, 148.1, 136.6, 133.1, 129.0, 128.4, 124.1, 69.8, 57.3, 42.8, 31.1, 27.8, 25.0. **HPLC:** Daicel Chiralpak AD-H column, flow 1 mL/min, 254 nm, n-hexane/i-PrOH 90/10, *syn* isomer: t_{major} = 13.49 min, t_{minor} = 11.59 min; *anti* isomer: t_{major} = 21.18 min, t_{minor} = 23.16 min.

2-(Hydroxy-(2,4-dinitrophenyl)methyl)cyclohexan-1-one, ***24ac***[145]

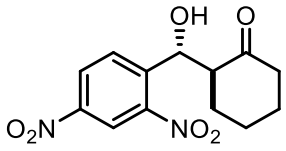

Purification by flash chromatography on silica gel with hexane/AcOEt (2/1) as eluent, white solid**. ^{1}H NMR (360 MHz, $CDCl_3$) δ (ppm):** 8.75 (d, *J* = 2.2 Hz, 1H), 8.48 (dd, *J* = 7.2 and 3.6 Hz, 1H), 8.08 (d, *J* = 7.2 Hz, 1H), 5.52 (t, *J* = 5.8 Hz, 1H), 4.30 (d, *J* = 7.2 Hz, 1H), 2.76-2.71 (m, 1H), 2.48-2.44 (m, 1H), 2.36-2.28 (m, 1H), 2.15-2.11 (m, 1H), 1.92-1.56 (m, 5H); **^{13}C NMR (91 MHz, $CDCl_3$) δ (ppm):** 214.5, 148.2, 147.0, 143.9, 131.0, 127.1, 119.9, 70.2, 56.9, 42.9, 31.4, 27.7, 25.0. **HPLC:** Daicel Chiralpak AD-H column, flow 1.2 mL/min, 254 nm, n-hexane/i-PrOH 92/8, *syn* isomer: t_{major} = 20.46 min, t_{minor} = 26.44 min; *anti* isomer: t_{major} = 36.42 min, t_{minor} = 32.61 min.

2-((4-Chlorophenyl)(hydroxy)methyl)cyclohexan-1-one, ***24ad***[146]

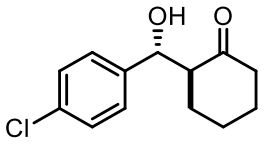

Purification by flash chromatography on silica gel with hexane/AcOEt (4/1) as eluent, white solid. **^{1}H NMR (360 MHz, $CDCl_3$) δ (ppm):** 7.33-7.31 (m, 2H), 7.27-7.24 (m, 2H), 4.77 (dd, *J* =7.2 and 3.6 Hz, 1H), 4.00 (d, *J* = 3.6 Hz, 1H), 2.59-2.45 (m, 2H), 2.40-2.31 (m, 1H), 2.13-2.06 (m, 1H), 1.82-1.78 (m, 1H), 1.71-1.48 (m, 3H), 1.34-1.21 (m, 1H); **^{13}C NMR (91 MHz, $CDCl_3$) δ (ppm):** 215.4, 139.5, 133.6, 128.5, 128.4, 74.1, 57.4, 42.7, 30.7, 27.7, 24.7. **HPLC:** Daicel Chiralpak AD-H column, flow 0.5 mL/min, 221 nm, n-hexane/i-PrOH 90/10, *syn* isomer: t_{major} = 22.24 min, t_{minor} = 19.16 min; *anti* isomer: t_{major} = 33.96 min, t_{minor} = 29.49 min.

2-((4-Fluorophenyl)(hydroxy)methyl)cyclohexan-1-one, ***24ae***[144]

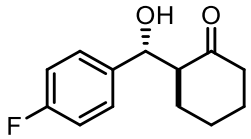

Purification by flash chromatography on silica gel with hexane/AcOEt (4/1) as eluent, white solid. **^{1}H NMR (360 MHz, $CDCl_3$) δ (ppm):** 7.31-7.27 (m, 2H), 7.06-7.01 (m, 2H), 4.79 (dd, *J* =7.2 and 3.6 Hz, 1H), 4.00 (d, *J* = 3.6 Hz, 1H), 2.57-2.47 (m, 2H), 2.39-2.35 (m, 1H), 2.09-2.07 (m, 1H), 1.82-1.78 (m, 1H), 1.68-1.53 (m, 3H), 1.30-1.26 (m, 1H); **^{13}C NMR (91 MHz, $CDCl_3$) δ (ppm):** 215.5, 128.7, 128.6, 115.4, 115.1, 74.1, 57.5, 42.7, 30.8, 27.7, 24.7. **HPLC:** Daicel Chiralpak AD-H column, flow 0.5 mL/min, 254 nm, n-hexane/i-PrOH 90/10, *syn* isomer: t_{major} = 21.60 min, t_{minor} = 18.95 min; *anti* isomer: t_{major} = 31.80 min, t_{minor} = 28.58 min.

2-((4-Bromophenyl)(hydroxy)methyl)cyclohexan-1-one, ***24af***[146]

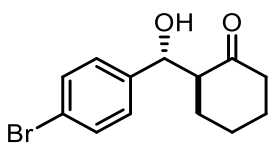

Purification by flash chromatography on silica gel with hexane/AcOEt (5/1) as eluent, white solid. **^{1}H NMR (360 MHz, $CDCl_3$) δ (ppm):** 7.49 (d, *J* = 10.8 Hz, 2H), 7.21 (d, *J* = 7.2 Hz, 2H), 4.77 (dd, *J* =7.2 and 3.6 Hz, 1H), 4.00 (d, *J* = 3.6 Hz, 1H), 2.59-2.46 (m, 2H), 2.40-2.31 (m, 1H), 2.13-2.05 (m, 1H), 1.82-1.78 (m, 1H), 1.72-1.49 (m, 3H), 1.36-1.23 (m, 1H); **^{13}C NMR (91 MHz, $CDCl_3$) δ (ppm):** 215.3, 140.0, 131.5, 128.7, 121.7, 74.2, 57.3, 42.7, 30.7, 27.7, 24.7. **HPLC:** Daicel Chiralpak AD-H column, flow 0.5 mL/min, 221 nm, n-hexane/i-PrOH 90/10, *syn* isomer: t_{major} = 23.82 min, t_{minor} = 20.18 min; *anti* isomer: t_{major} = 37.94 min, t_{minor} = 32.52 min.

2-((2-Chlorophenyl)(hydroxy)methyl)cyclohexan-1-one, ***24ag***[131]

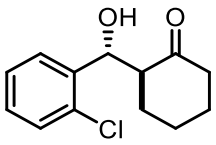

^{1}H NMR (360 MHz, $CDCl_3$) δ (ppm): 7.56-7.54 (m, 1H), 7.35-7.29 (m, 1H), 7.24-7.19 (m, 1H), 7.43 (t, *J* = 7.2 Hz, 1H), 4.04 (d, *J* = 7.2 Hz, 1H), 2.72-2.65 (m, 1H), 2.49-2.45 (m, 1H), 2.38-2.32 (m, 1H), 2.11-2.07 (m, 1H), 1.90-1.82 (m, 1H), 1.75-1.52 (m, 4H); **^{13}C NMR (91 MHz, $CDCl_3$) δ (ppm):** 215.3, 139.0, 133.0, 129.2, 128.7, 128.2, 127.2, 70.4, 57.6, 42.7, 30.4, 27.8, 24.9. **HPLC:** Daicel Chiralpak AD-H column, flow 1 mL/min, 254 nm, n-hexane/i-PrOH 95/5, *syn* isomer: t_{major} = 10.26 min, t_{minor} = 9.92 min; *anti* isomer: t_{major} = 19.44 min, t_{minor} = 17.01 min.

2-((2,4-Dichlorophenyl)(hydroxy)methyl)cyclohexan-1-one, ***24ah***[144]

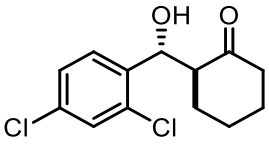

^{1}H NMR (360 MHz, $CDCl_3$) δ (ppm): 7.51 (d, *J* = 7.2 Hz, 1H), 7.36 (d, *J* = 3.6 Hz, 1H), 7.31-7.27 (m, 1H), 5.30 (d, *J* = 7.2 Hz, 1H), 4.06 (br s, 1H), 2.66-2.59 (m, 1H), 2.49-2.45 (m, 1H), 2.38-2.29 (m, 1H), 2.12-2.08 (m, 1H), 1.90-1.83 (m, 1H), 1.73-1.56 (m, 4H); **^{13}C NMR (91 MHz, $CDCl_3$) δ (ppm):** 215.1, 137.8, 133.8, 133.5, 129.2, 128.9, 127.6, 70.1, 57.5, 42.7, 30.4, 27.8, 24.9. **HPLC:** Daicel Chiralpak OD-H column, flow 1 mL/min, 220 nm, n-hexane/i-PrOH 95/5, *syn* isomer: not determined; *anti* isomer: t_{major} = 11.47 min, t_{minor} = 14.70 min.

2-(Hydroxy-(4-(trifluoromethyl)phenyl)methyl)cyclohexan-1-one, ***24ai***[147]

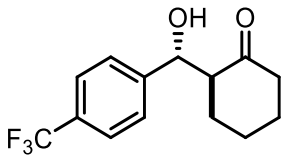

^{1}H NMR (360 MHz, $CDCl_3$) δ (ppm): 7.62 (d, *J* = 7.2 Hz, 2H), 7.45 (d, *J* = 7.2 Hz, 2H), 4.86 (d, *J* =7.2 Hz, 1H), 4.01 (br s, 1H), 2.63-2.56 (m, 1H), 2.51-2.46 (m, 1H), 2.41-2.31 (m, 1H), 1.89-1.78 (m, 1H), 1.75-1.48 (m, 3H), 1.39-1.25 (m, 1H); **^{13}C NMR (91 MHz, $CDCl_3$) δ (ppm):** 215.1, 145.0, 130.2 (q, *J* = 32.8 Hz), 127.4, 125.4 (q, *J* = 3.6 Hz), 122.6 (q, *J* = 318 Hz), 74.3, 57.3, 42.7, 30.8, 27.7, 24.7. **HPLC:** Daicel Chiralpak AD-H column, flow 0.5 mL/min, 221 nm, n-hexane/i-PrOH 90/10, *syn* isomer: t_{major} = 16.67 min, t_{minor} = 14.50 min; *anti* isomer: t_{major} = 26.39 min, t_{minor} = 21.45 min.

4-Hydroxy-4-(4-nitrophenyl)butan-2-one, ***24ba***[97]

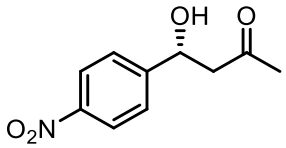

^{1}H NMR (360 MHz, $CDCl_3$) δ (ppm): 8.23 (d, *J* = 10.8 Hz, 2H), 7.55 (d, *J* = 7.2 Hz, 2H), 5.28 (dd, *J* = 3.6, 7.2 Hz, 1H), 3.58 (br s, 1H), 2.92-2.79 (m, 2H), 2.22 (s, 3H); **^{13}C NMR (91 MHz, $CDCl_3$) δ (ppm):** 208.6, 149.9, 126.4, 123.8, 68.9, 67.8, 51.5, 42.9, 30.7. **HPLC:** Daicel Chiralpak AS column, flow 1 mL/min, 254 nm, n-hexane/i-PrOH 85/15, t_{major} = 20.10 min, t_{minor} = 30.91 min.

2-(Hydroxy(4-nitrophenyl)methyl)cyclopentan-1-one, ***24ca***[131]

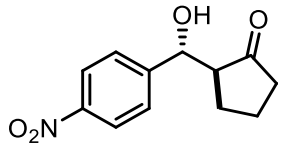

^{1}H NMR (360 MHz, $CDCl_3$) δ (ppm): 8.23 (d, *J* = 10.8 Hz, 2H), 7.53 (t, *J* = 10.8 Hz, 2H), 5.42 (br, 0.6H syn), 4.86 (d, *J* = 10.8Hz, 0.4H anti), 2.51-2.33 (m, 3H), 2.18-2.16 (m, 1H), 2.04-1.95 (m, 2H). **^{13}C NMR (62.5 MHz, $CDCl_3$) δ (ppm):** 222.0, 219.5, 150.0, 148.3, 146.9, 130.5, 127.0, 126.1, 123.6, 123.4, 123.3, 74.1, 70.1, 55.8, 54.8, 38.7, 38.3, 32.5, 26.5, 26.5, 22.1, 20.1, 19.4. **HPLC:** Daicel Chiralpak AD-H column, flow 1 mL/min, 254 nm, n-

hexane/i-PrOH 95/5, *syn* isomer: t_{major} = 37.79 min, t_{minor} = 27.26 min; *anti* isomer: t_{major} = 48.86 min, t_{minor} = 46.86 min.

3-(Hydroxy-(4-nitrophenyl)methyl)tetrahydro-4H-pyran-4-one, ***24da***[132]

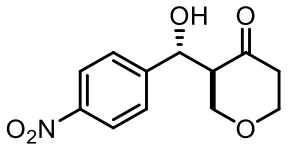

^{1}H NMR (360 MHz, $CDCl_3$) δ (ppm): 8.24 (d, *J* = 7.2 Hz, 2H), 7.50 (d, *J* = 7.2 Hz, 2H), 5.00 (d, *J* = 7.2 Hz, 1H), 4.23-4.18 (m, 1H), 3.83 (br s, 1H), 3.79-3.70 (m, 2H), 3.48-3.42 (m, 1H), 2.92-2.86 (m, 1H), 2.73-2.64 (m, 1H), 2.56-2.48 (m, 1H); **^{13}C NMR (91 MHz, $CDCl_3$) δ (ppm):** 209.3, 147.8, 147.4, 127.5,126.4, 123.9, 123.7, 71.3, 69.8, 68.4, 57.6, 42.9. **HPLC:** Daicel Chiralpak AD-H column, flow 1 mL/min, 254 nm, n-hexane/i-PrOH 80/20, *syn* isomer: t_{major} = 16.45 min, t_{minor} = 14.53 min; *anti* isomer: t_{major} = 23.95 min, t_{minor} = 20.25 min.

Synthesis of 2-methyl-2-(3-oxobutyl)cyclohexane-1,3-dione[131]

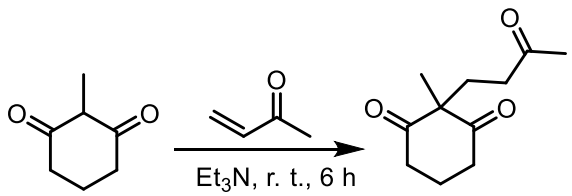

26

To the 2-methylcyclohexane-1,3-dione (1.26 g, 10.0 mmol) in a standard glass vial (10 mL) with a stirring bar was added methyl vinyl ketone (0.77 g, 11.0 mmol) followed by Et_3N (14 µL, 0.726 g/cm^3, 0.1 mmol). The initial thick suspension slowly became more fluid as the solid slowly dissolved to give a yellow solution. After 6 h the mixture was absorbed onto silica gel and purified by flash chromatography (hexane/EtOAc = 2:1) to give the corresponding triketone (1.85 g, 94% yield). **^{1}H NMR (360 MHz, $CDCl_3$) δ (ppm):** 2.76-2.59 (m, 4H), 2.34 (t, *J* = 7.2 Hz, 2 H), 2.10-1.90 (m, 7H), 1.24 (s, 3H).

General procedure for the catalytic tests in intramolecular aldol reaction with M1 and M5

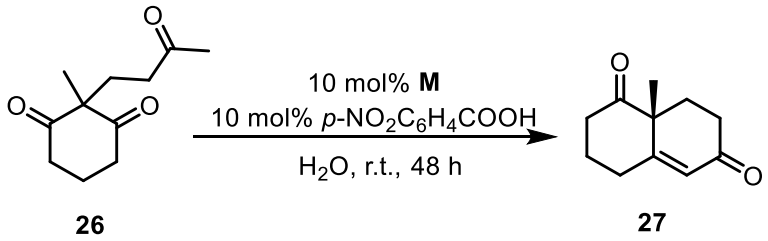

26 **27**

A mixture of 2-methyl-2-(3-oxobutyl)cyclohexane-1,3-dione **26** (98 mg, 0.5 mmol), water (250 μL, 0.5 mL/mmol of **26**), *p*-nitrobenzoic acid (8.36 mg, 0.05 mmol) and MSNs (10 mol%, 0.05 mmol) were stirred in a vial at room temperature until ^{1}H-NMR showed complete conversion of triketone. Then the crude mixture was diluted with EtOAc (10 mL) and centrifuged (4000 rpm). The solid catalytic material resulting from the centrifugation was washed several times with EtOAc (3 × 10 mL) and the combined supernatants were concentrated under vacuum. After flash chromatography of the residue on silica gel using hexane/AcOEt (solvent gradient, from 7/1 to 1/2), the final product was obtained as a pale yellow oil (80.4 mg, 90% yield).[131] **^{1}H NMR (360 MHz, $CDCl_3$) δ (ppm):** 5.85 (s, 1H), 2.76-2.66 (m, 2H), 2.52-2.43 (m, 4H), 2.19-2.08 (m, 5H), 1.76-1.65 (m, 1H), 1.45 (s, 3H); **^{13}C NMR (91 MHz, $CDCl_3$) δ (ppm):** 211.09, 198.35, 165.83, 125.87, 50.61, 37.68, 33.62, 31.77, 29.67, 23.29, 22.92. **HPLC:** Daicel Chiralpak IC column, flow 1 mL/min, 254 nm, n-hexane/i-PrOH 90/10, t_{major} = 41.58 min, t_{minor} = 36.74 min.

2.3 Studies towards the preparation of recyclable organosilica nanoparticles as chiral catalysts or ligands for the enantioselective α-trifluoromethylation and α-fluorination of carbonyl compounds.

2.3.1 Asymmetric α-trifluoromethylation and α-fluorination of carbonyl compounds

Fluorine is one of the most venerable elements in pharmaceuticals and agrochemicals, as well as in materials science, because an organic molecule bearing one or more fluorine atoms can often change its chemical and biological behaviour, such as the acidity or basicity of neighboring groups, dipole moment, and properties such as lipophilicity, metabolic stability, and bioavailability.[148-151] In general, fluorinated organic compounds have unique properties such as higher stability, higher electronegativity, and water and oil resistancy, which are potentially beneficial in terms of the development of novel pharmaceutical agents and advanced materials. Recent evidence has shown that approximately 20% of pharmaceuticals and 30-40% of agrochemicals on the market contain at least one fluorine atom.[152-153] Almost all domains of society are impacted by fluorine chemistry. Particularly in the past decade, a combination of the increasing importance of fluorine-containing molecules and the successful development of bench stable, commercially available fluorine sources has brought the expansion of fluorine chemistry into the mainstream organic synthesis community.[154] This has resulted in an acceleration in the development of new fluorination methods and consequently in methods for the asymmetric introduction of fluorine or fluorine containing groups. However, the special properties of fluorine (the most oxidizing, the most electronegative element (Pauling electronegativity, 4.0), a small ionic radius (1.33 Å), it forms easily a strong hydrogen bond),[155] often make the synthesis of fluorine-containing compounds a complex task, especially when the synthesis of target compounds requires an enantiocontrolled methodology. Asymmetric fluorination and trifluoromethylation reactions are two of the major straightforward operations for the construction of fluorine-containing molecules. As with the incorporation of the fluorine atom, the introduction of the trifluoromethyl (CF_3) group into organic molecules can substantially alter their properties. As with fluorine, the prevalence of CF_3 groups in pharmaceuticals and agrochemicals coupled with the development of new trifluoromethylating reagents also has led to a recent surge in the development of asymmetric trifluoromethylation.

Since the beginning of the 21st century, chemists have developed many methods to incorporate fluorine into organic molecules by making carbon-fluorine (C-F) and carbon-trifluoromethyl (C-CF_3) bonds on both aromatic rings and aliphatic chains via nucleophilic,

electrophilic and radical reactions (in some cases in diastereo- and/or enantioselective manner).[154,156-176] These new bond-forming reactions can be efficient means to access the desired organic molecules that are not readily synthesized using traditional fluorination chemistry. The development of suitable catalysts for these reactions has beneficially influenced the progress of modern fluorination.

Herein, we have only chosen two typical chiral organocatalysts or chiral ligands for both asymmetric fluorination and trifluoromethylation reactions for discussion, because our research efforts have been focused on these catalysts. In 2005, MacMillan and co-workers reported the use of an imidazolidinone dichloroacetate for α-fluorination of linear aldehydes with *N*-fluorobenzenesulfonimide (NFSI) to achieve excellent enantioselectivity in THF/^{i}PrOH (**Scheme 2.18**).[177] In fact, the dichloroacetic acid (DCA) salt of imidazoline **28** was able to catalyze the reaction with only 20 mol% loading. The authors found that the addition of 10% ^{i}PrOH as cosolvent generally improved enantiocontrol and efficiency, although the origin of this effect is not clear. This reaction shows a broad scope of functional group (olefins, esters, carbamates, amines, aryl rings and sterically demanding substituents) tolerance, but α-branched aldehydes were not mentioned, probably due to the poor enantioselectivity. They also evaluated the effect of the catalyst loading on reaction efficiency and they found that the amount of catalyst can be decreased until 2.5 mol% without loss of enantioselectivity. They identified NFSI as a reagent that might participate in the requisite closed transition state via sulfone-proton bonding and concomitant fluorine/enamine activation (**Scheme 2.18**).

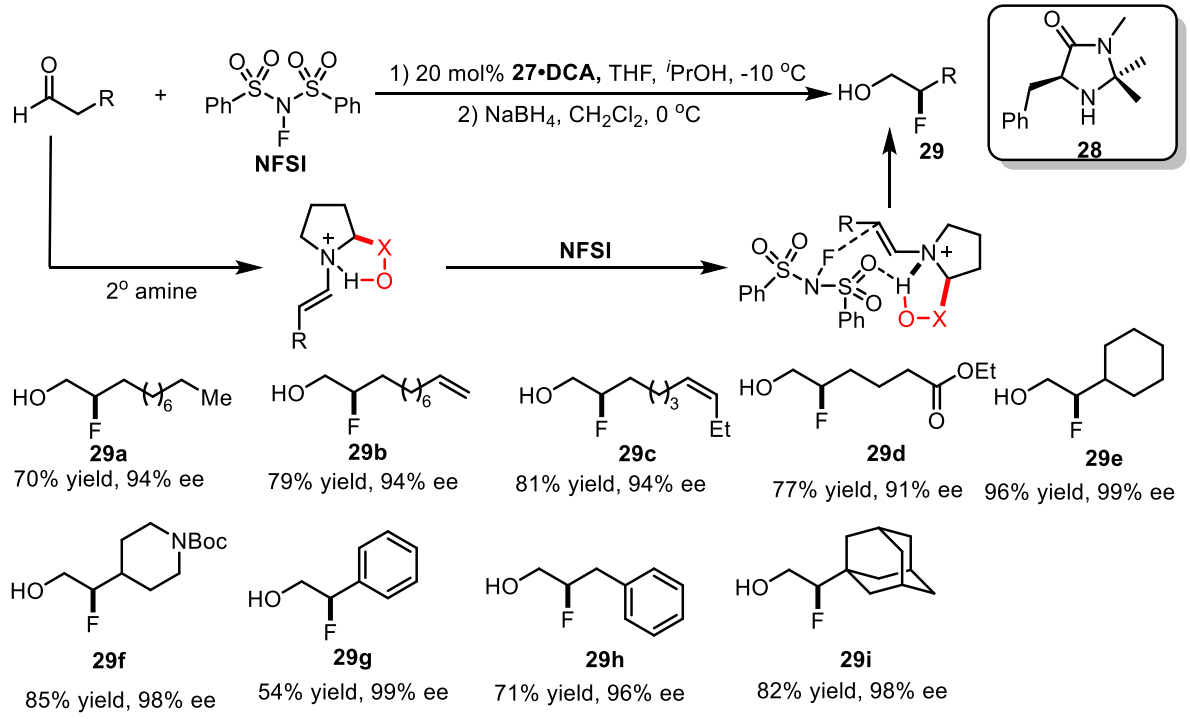

Scheme 2.18 The first direct enantioselective α-fluorination of aldehydes reported by MacMillan et al.

In the same year, Barbas III and colleagues also described that MacMillan's first-generation catalyst **28** in stochiometric amounts can promote the **α**-fluorination of linear aldehydes with NFSI (**Scheme 2.19**).[178]

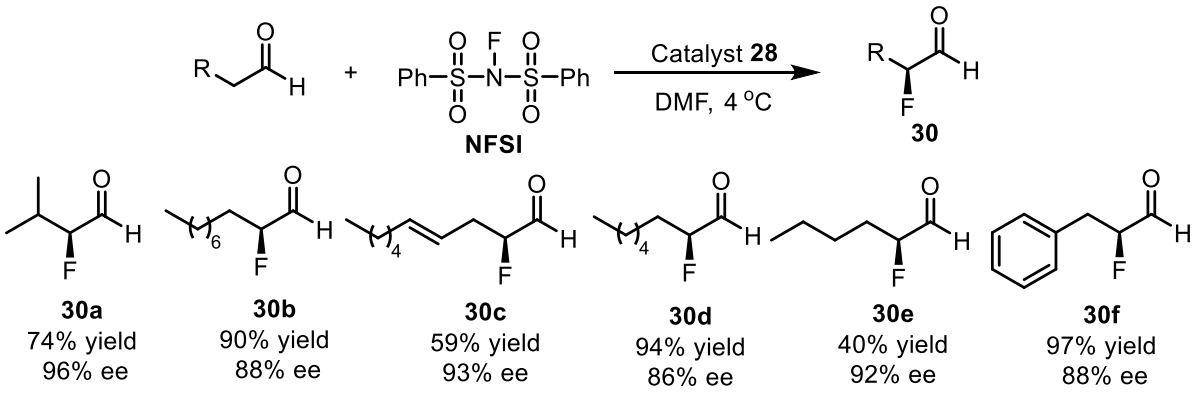

Scheme 2.19 α-Fluorination of aldehydes reported by Barbas III and colleagues

In 2010, Allen and MacMillan reported the enantioselective α-trifluoromethylation of aldehydes using the commercially available trifluoromethylating Togni's reagent with the MacMillan's first-generation imidazolidinone **28•TFA** salt and copper(I) chloride as catalytic system (**Scheme 2.20**).[179]

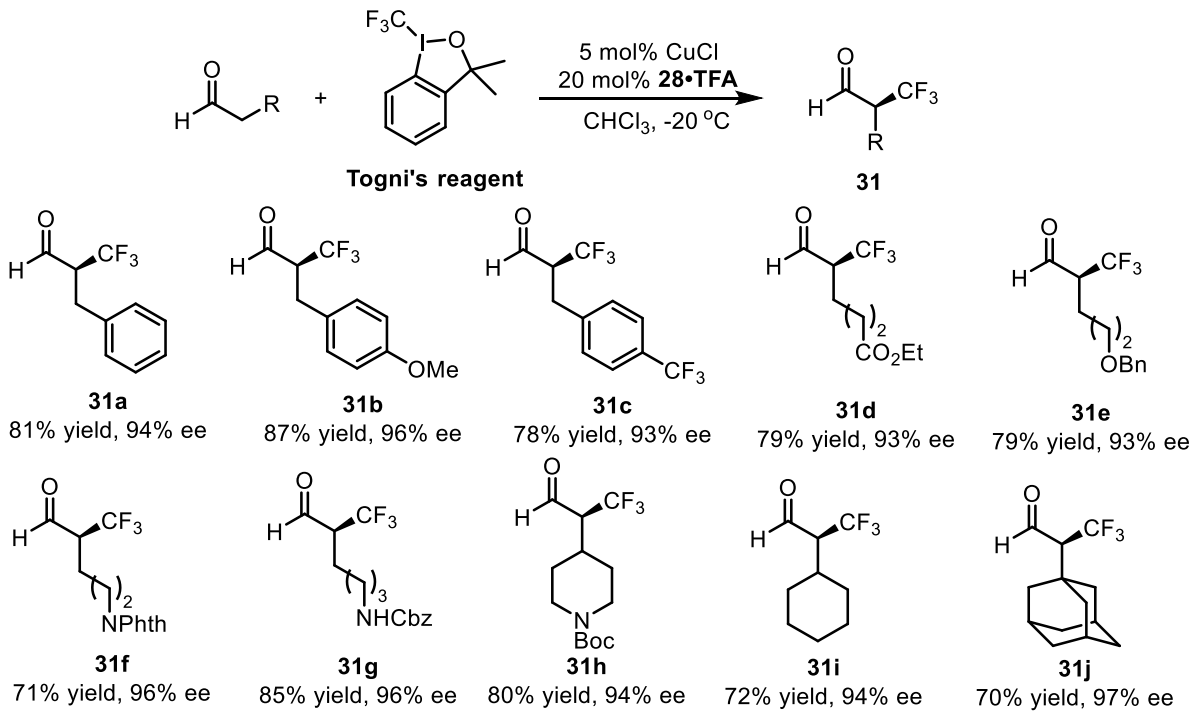

Scheme 2.20 α-Trifluoromethylation reported by Allen and MacMillan.

They envisioned that Togni's reagent should undergo Lewis acid-catalyzed bond cleavage to generate the highly electrophilic iodonium salt **32**. At the same time, condensation of the amine catalyst with an aldehyde substrate should generate a chiral enamine **33** that is sufficiently π-electron-rich to participate in an enantioselective C-I bond formation via a closed-shell pathway. The resulting λ^3-iodane species **34** was envisaged to undergo reductive elimination with stereoretentive alkyl transfer, thus forming the aryl iodide **35** and the new C-CF_3 bond in **36**, although a single electron transfer mechanism cannot be completely ruled out for this latter sequence. Hydrolysis of **36** would then release the amine catalyst and the desired enantioenriched α-trifluoromethyl aldehyde product **31** (**Scheme 2.21**).[179] A range of Lewis acidic metals provided conversion and enantioenrichment, but CuCl proved to be the most effective and a range of substituted aldehydes were demonstrated to be active.

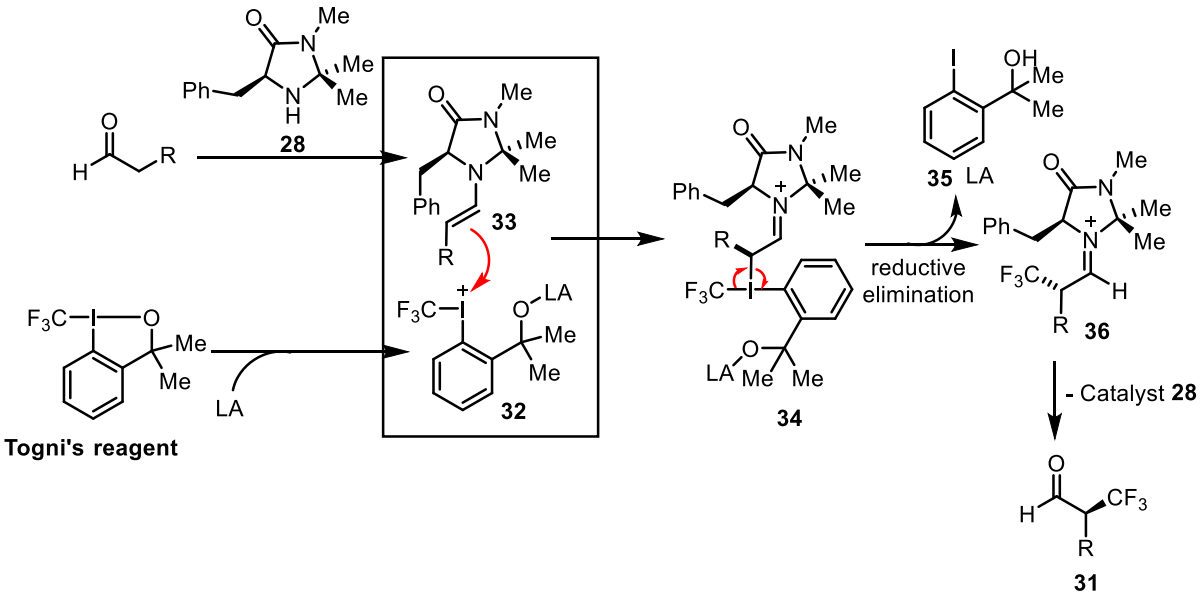

Scheme 2.21 Mechanism proposed by MacMillan and co-workers.

On the other hand, Gade and co-workers described in 2011 the synthesis of a new class of chiral tridentate *N*-donor pincer ligands, bis(oxazolinyl-methyldiene)isoindolines (boxmi) (**Scheme 2.22**).[180] These tridentate N-donor pincer ligands **37** are conveniently prepared from readily available phthalimides by Wittig coupling with ethyl (triphenylphosphoranylidene)acetate to afford the ligand backbone with ester groups, which can be subsequently condensed with chiral amino alcohols to give the corresponding ligands after cyclization.

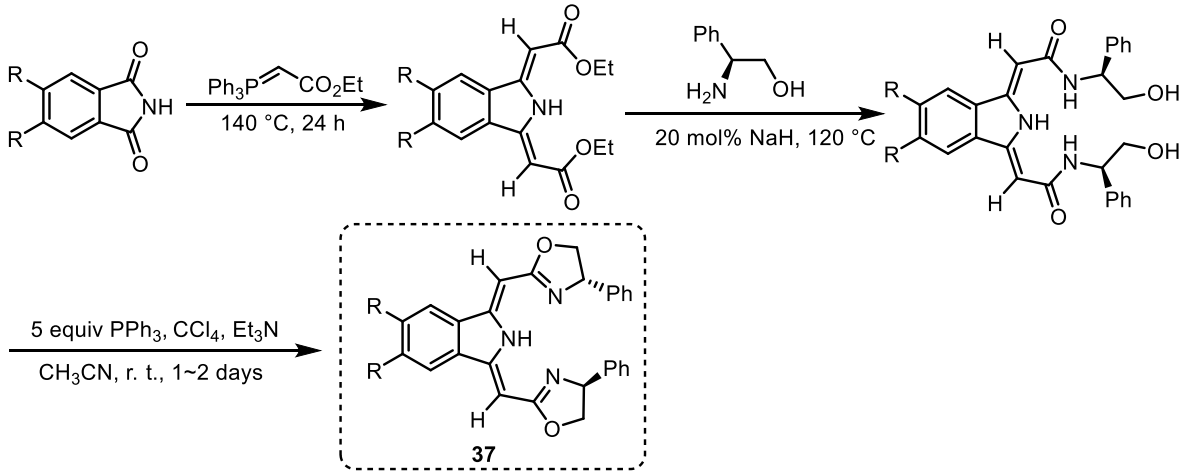

Scheme 2.22 Synthesis of Boxmi ligands **37**

These chiral ligands were subsequently applied in the Ni(II)-catalyzed enantioselective fluorination of oxindoles and β-ketoesters with NFSI to afford the corresponding products in

excellent yields with enantioselectivities of up to 99% ee. They can synthesize the *N*-Boc-protected MaxiPost™ which is an effective opener of maxi-K channels and a potential agent for the treatment of stroke[181-182] in 90% yield with >99% ee (**Scheme 2.23**).[180]

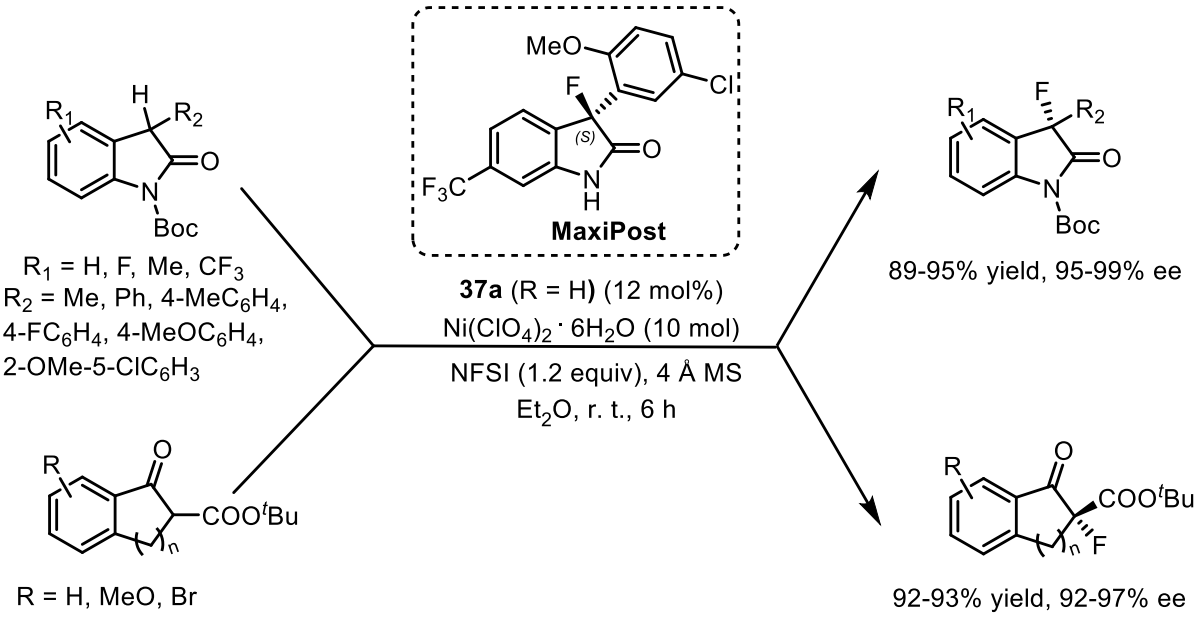

Scheme 2.23 Nickel-(*S*,*S*)-Ph-boxmi catalyzed enantioselective electrophilic fluorination.

One year later, Gade and colleagues developed an efficient protocol for enantioselective trifluoromethylation of cyclic β-ketoesters using "CF_3 reagents" via Cu-boxmi catalysis (**Scheme 2.24**).[183] This method was efficiently applied to a panel of cyclic five- and six-membered ring β-ketoesters such as indanone and cyclopentanone derivatives as well as tetralone-derived *tert*-butyl β-ketoesters or cyclohexanone-derived *tert*-butyl esters. In addition, the transformation demonstrated large functional group tolerance and the outcome of the reaction showed very high enantioselectivity.

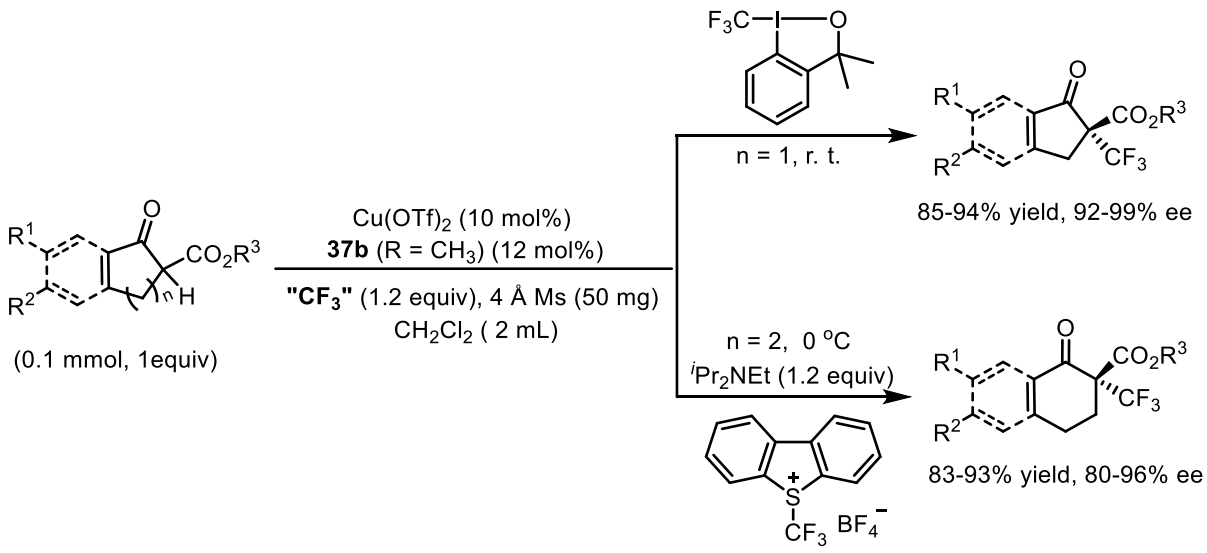

Scheme 2.24 Enantioselective electrophilic trifluoromethylation of β-ketoesters.

Recently, our colleagues in the research group have developed lanthanum(III) triflate with chiral PyBOX-type C_2-symmetric ligands for the enantioselective α-trifluoromethylation of β-oxo esters[184] and europium(III) triflate with (*S*,*R*)-ind-pybox as pre-catalyst for the highly enantioselective α-fluorination of alkyl 1-oxo-indanecarboxylates.[185]

So far, significant progress has been made in the development of the asymmetric fluorination and trifluoromethylation reactions in recent years. More efforts still need to be made in the discovery of alternative, more efficient, cheap, and easy to handle sources of fluorine and fluorinated reagents to offer new perspectives in the construction of organofluorine compounds. *Also importantly, the exploration of recyclable catalysts for the enantioselective α-fluorination or α-trifluoromethylation reactions remains a challenge because, at the best of our knowledge, no precedents exist on the immobilization of the mentioned chiral catalytic systems for these reactions*

2.3.2 Objectives

According to the previous introduction, we decided to prepare organosilica nanoparticles derived from MacMillan imidazolidinones and bis(oxazolinylmethylidene)isoindoline (boxmi) ligands in order to test them as recyclable catalysts in enantioselective fluorination and trifluoromethylation reactions (with the addition of the corresponding metal salt when required as explained in ***Section* 2.3.1**). In this way, our detailed objectives with respect to the synthesis of the nanomaterials are as follows:

In principle, MacMillan's imidazolidin-4-ones offer two different sites for attachment to a solid support: the amide nitrogen and the aryl residue at the stereogenic center. We aimed to explore both of them as connecting points for silylation (see the two monosilylated precursors **P5** and **P6** in **Figure 2.21**). Then mesoporous silica nanoparticles derivem from them will be prepared by grafting and/or co-condensation methods.

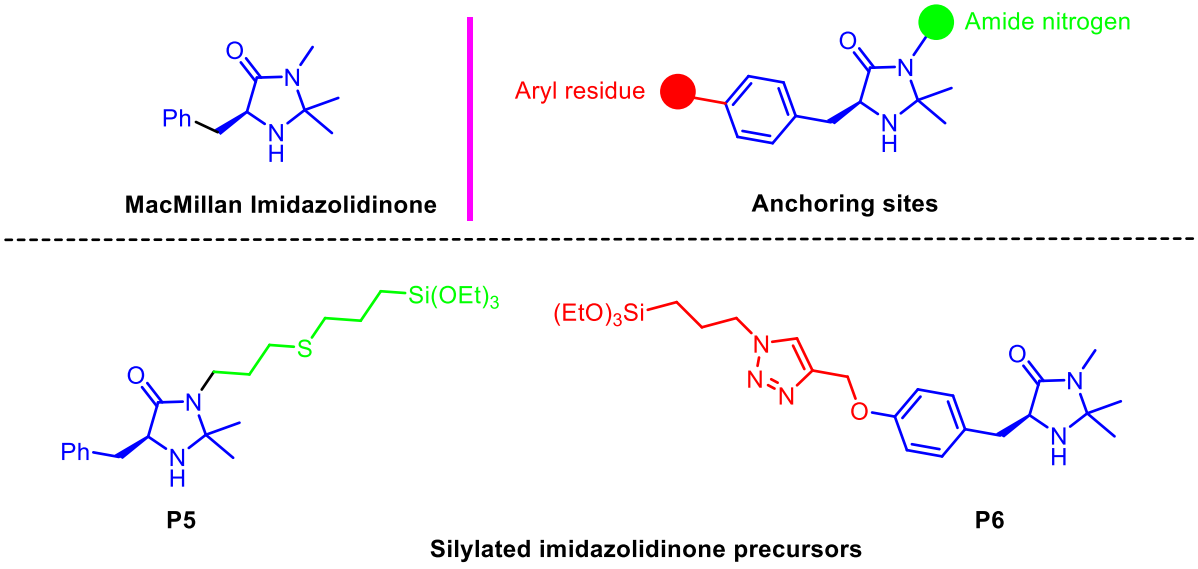

Figure 2.21 Silylated imidazolidinone precursors for functionalized MSNs

The silylation of the boxmi ligand on the aromatic ring was decided in order the support to be as far away as possible of the catalytic moiety (the tridentate *N*-donor center that will coordinate to the copper or nickel). In that way, the effect of the immobilization on the reactivity and selectivity should be minimized. The synthesis of the monosilylated precursor **P7** shown in **Figure 2.22** was envisaged. Then functionalized mesoporous silica nanoparticles will be prepared from it by grafting and/or co-condensation methods.

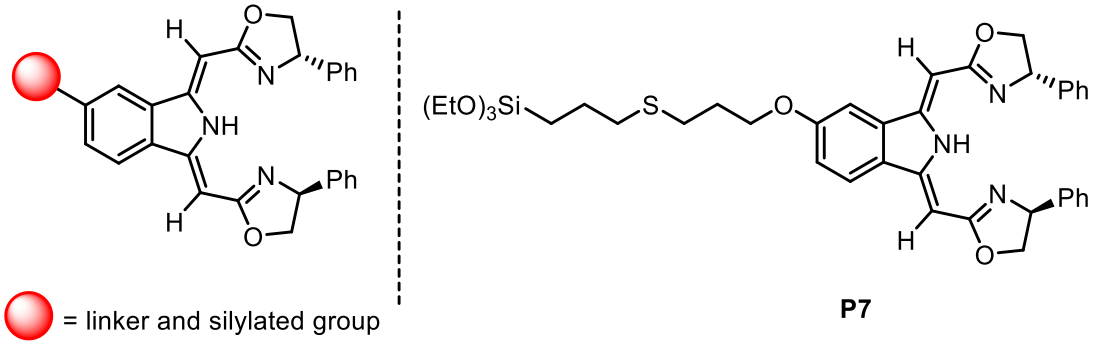

Figure 2.22 Silylated bis(oxazolinylmethylidene)isoindoline (boxmi) ligand for MSNs

2.3.3 Results and Discussion

2.3.3.1 Synthesis of the silylated imidazolidinone precursors

The synthesis of the monosilylated precursor **P5** is summarized in **Scheme 2.25**. The condensation of allyl amine with (*S*)-phenylalanine methyl ester hydrochloride **38** followed by an acid-catalyzed reaction of the resulting **39** with acetone afforded imidazolidinone **40** in 90% yield after one chromatographic purification.[186] The versatile thiol-alkene click reaction of **40** with (3-mercaptopropyl)triethoxysilane at room temperature under irradiation at 365 nm using 2,2-dimethoxy-1,2-diphenylethanone (DMPA) as initiator, provided the desired **P5** in 95% yield after flash column chromatography.

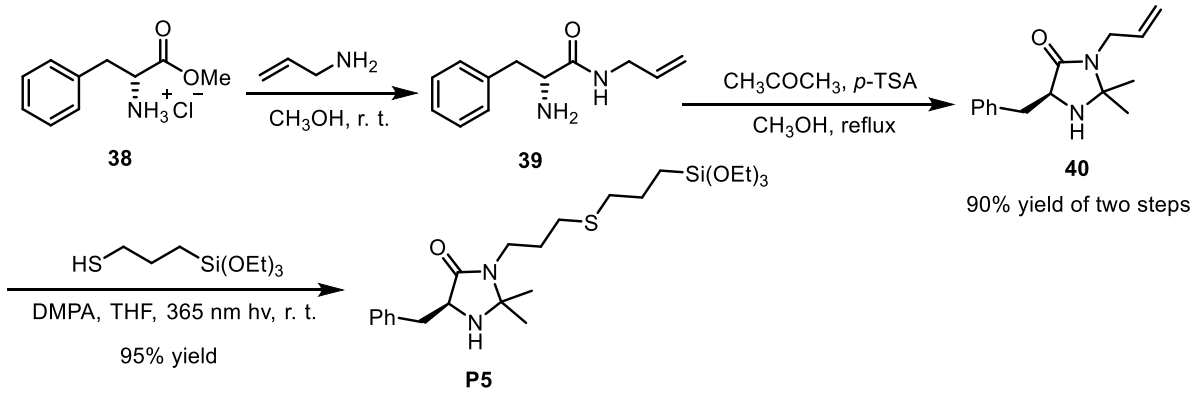

Scheme 2.25 Synthesis of silylated imidazolidinone precursor **P5**

Another option is offered by the use of (*S*)-tyrosine instead of (*S*)-phenylalanine to generate an imidazolidinone already equipped with a properly located and chemically suitable handle for the hetereogenization process. Thus, we started from (*S*)-tyrosine methyl ester hydrochloride **41**, which was readily prepared from commercially available L-tyrosine by treatment with thionyl chloride in methanol. Imidazolidinone **43** was easily obtained in 77%

yield by formation of the corresponding *N*-methyl amide **42** and subsequent treatment with acetone.[187-188] Reaction of **43** with propargyl bromide in DMF in the presence of NaH allowed us to introduce the carbon-carbon triple bond[187] and obtain **44**, which was subjected to copper-catalyzed azide-alkyne dipolar cycloaddition with azide **10** to give the precursor **P6** (**Scheme 2.26**).

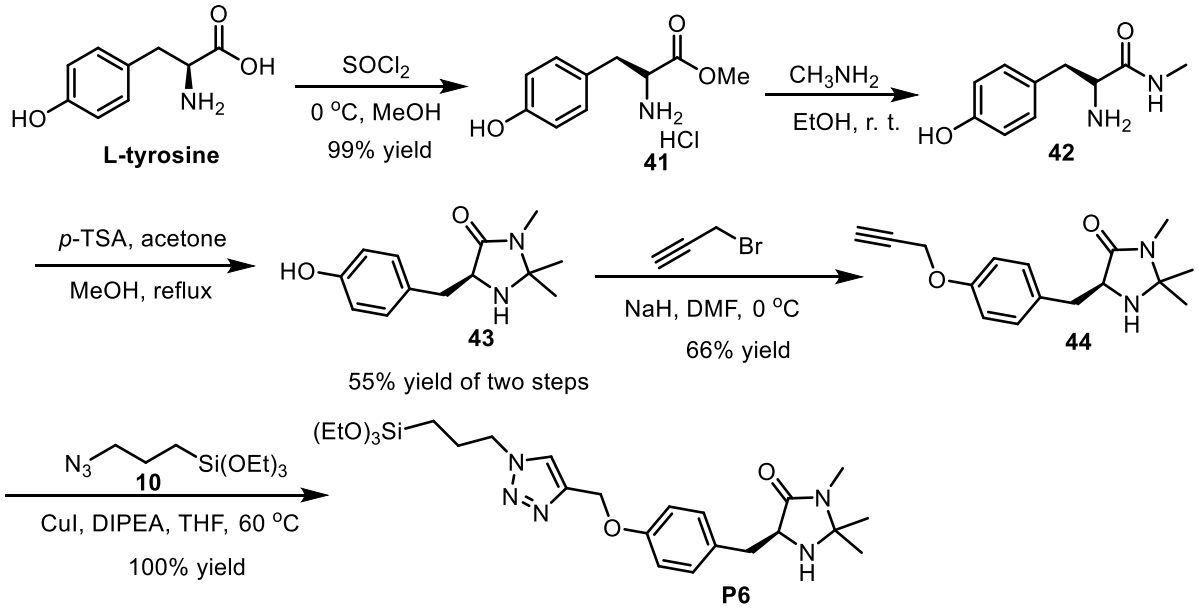

Scheme 2.26 Synthesis of silylated imidazolidinone precursor **P6**

2.3.3.2 Attempted synthesis of the silylated bis(oxazolinylmethylidene)isoindoline (boxmi) ligand

The bis(oxazolinylmethylidene)isoindoline ligand **53** was prepared in eight steps starting from comercially available 4-hydroxyphthalic acid **45** (**Scheme 2.27**). First, the two carboxylic acid groups were protected by methyl esterification,[190] and then the hydroxyl group of **46** was subjected to allylation reaction to obtain compound **47**.[191] Ester hydrolysis was carried out under basic conditions to obtain, after acidic work-up, a free dicarboxylic acid **48**,[191] which undergoes self-condensation in refluxing acetic anhydride to offer the phtalic anhydride **49**.[192] Then the phatalimide **50** was obtained by treatment of **49** with urea at 150 ℃.[193] The backbone of the pincer ligand **51** was prepared from **50** according to improved Wittig procedures.[180,194-195] Compound **52** was synthesized in high yield by melting **51** with the corresponding amino alcohol in the presence of a catalytic amount of NaH,[196-197] and the desired compound **53** was obtained from **52** using a Ph_3P/CCl_4 /Et_3N cyclization protocol.[198]

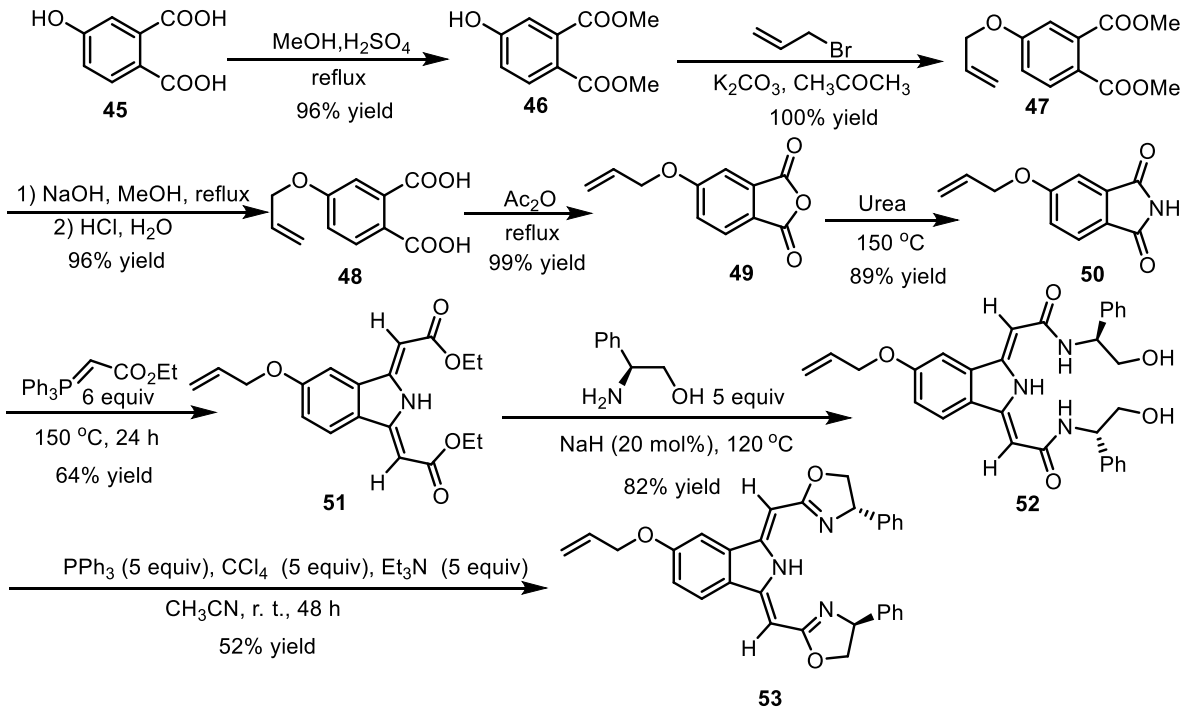

Scheme 2.27 Synthesis of bis(oxazolinylmethylidene)isoindoline ligand **53**

The final step was the introduction of a silylated moiety in compound **53** to afford the precursor **P7**. Many trials have been made, but unfortunately, we did not get the final silylated monomer which was required for the formation of the organosilica nanoparticles. First, the thiol-alkene click reaction was used as a synthetic strategy and compound **53** was reacted with (3-mercaptopropyl)triethoxysilane at room temperature under irradiation at 365 nm using 2,2-dimethoxy-1,2-diphenylethanone (DMPA) as initiator.[83] The ^{1}H NMR analysis of the crude mixture confirmed that the addition of thiol did not take place on the right olefinic moiety, but the disilylated product **54** was formed (**Scheme 2.28**).

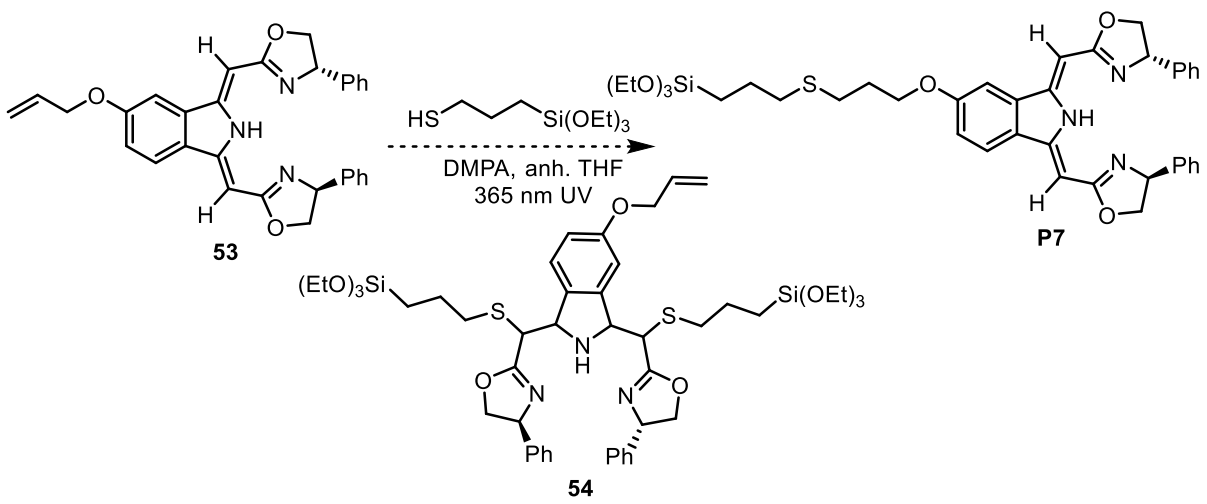

Scheme 2.28 Attempt to prepare **P7** by thiol-alkene click reaction

Then, the hydrosilylation of the alkene **53** was tested as alternative strategy to functionalize the carbon-carbon-double bond of the allyloxy group. We performed the reaction under several conventional reported procedures, with trimethoxysilane or triethoxysilane as reagents (**Table 9**). Unfortunately, the final precursors **P8**/**P9** were not obtained in any case.

Table 2.9 Several conventional reported procedures tested for the hydrosilylation of compound **52**

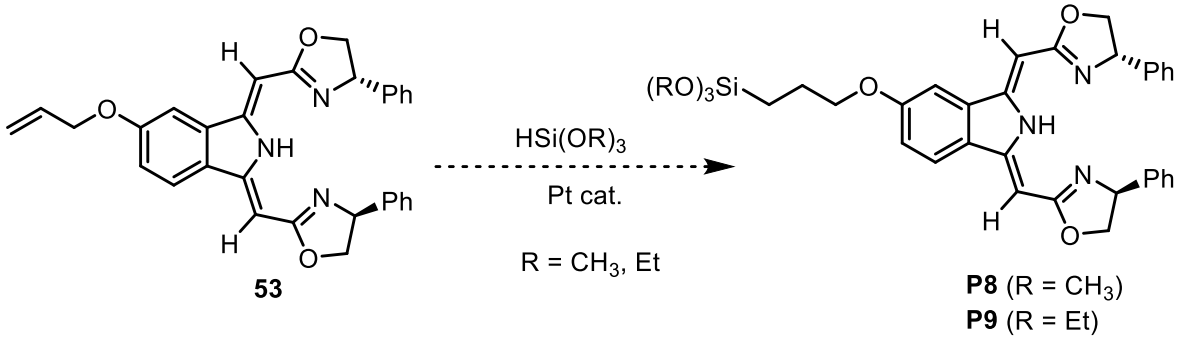

53

P8 (R = CH_3)
P9 (R = Et)

Entry	Reaction conditions	Result
1	Karstedt cat., $HSi(OEt)_3$, anh. THF, room temperature	No reaction
2	Karstedt cat., $HSi(OEt)_3$, anh. THF, 50 °C	No reaction
3	Karstedt cat., $HSi(OEt)_3$, neat, 80 °C	No reaction
4	Karstedt cat., $HSi(OCH_3)_3$, anh. CH_3CN, room temperature	No reaction
5	Karstedt cat., $HSi(OCH_3)_3$, anh. CH_3CN, 50 °C	No reaction
6[199]	Pt NPs, $HSi(OEt)_3$, neat, 90 °C	No reaction

At this point of the project, we tested the hydrosilylation of the alkene with the more reactive trichlorosilane, followed by treatment with anhydrous ethanol and Et_3N, a method that had previously given good results with other substrates.[200-202] When compound **53** was submitted to these conditions, a complex mixture was obtained (**Scheme 2.29**).

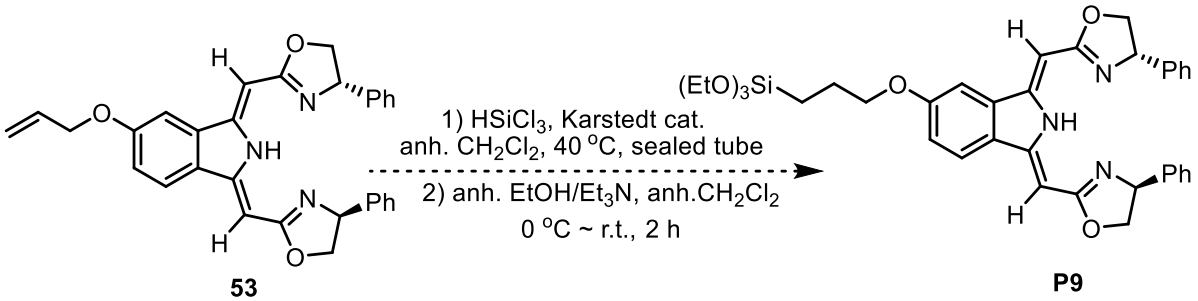

53 **P9**

Scheme 2.29 Attempted hydrosilylation of **53** with trichlorosilane

2.3.3.3 Preparation of mesoporous organosilica nanoparticles derived from MacMillan imidazolidinone

We first selected the precursor **P6** to prepare mesoporous organosilica nanoparticles. The material **M7** was prepared by co-condensation with tetraethyl orthosilicate (TEOS), using Brij-56 and hexadecyltrimethylammonium bromide (CTAB) as templates,[203] in an aqueous buffer solution of pH 7 from mixtures with the molar ratios Brij-56 : CTAB : TEOS : **P6** : H_2O = 1 : 20 : 160 : 16 : 120000. The final solution was stirred at 95 ºC for 8 h (**Scheme 2.30**) and then the nanoparticles were collected by centrifugation (13500 rpm) at room temperature. The surfactants were removed from the obtained solid by treatment with an ethanolic solution of NH_4NO_3 and then the resulting material was washed successively with ethanol, Mili-Q water and ethanol.

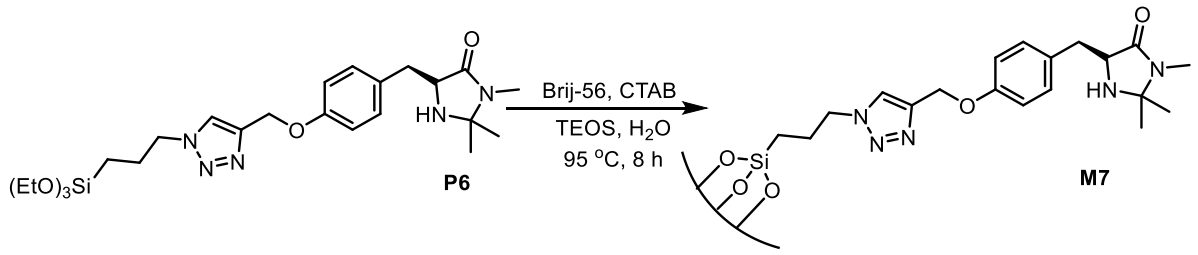

Scheme 2.30 Preparation of **M7** derived from the precursor **P6**

The functionalized mesoporous silica nanoparticles **M7** were characterized by transmission electron microscopy (TEM), elemental analysis and infrared spectroscopy (IR). The TEM images clearly indicate the presence of pores and spherical nanoparticles were obtained ranging from 150 nm to 200 nm (**Figure 2.23**). From IR, the band with a shift of the carbonyl to 1672 cm-1 showed the presence of the organic moiety of **P6** in the material. A broad band between 1200-1000 cm^{-1} (γSi-O-Si) characteristic of a well-condensed material was observed (**Figure 2.24**). The catalyst loading was inferred from the nitrogen elemental analysis (0.92 mmol g^{-1}).

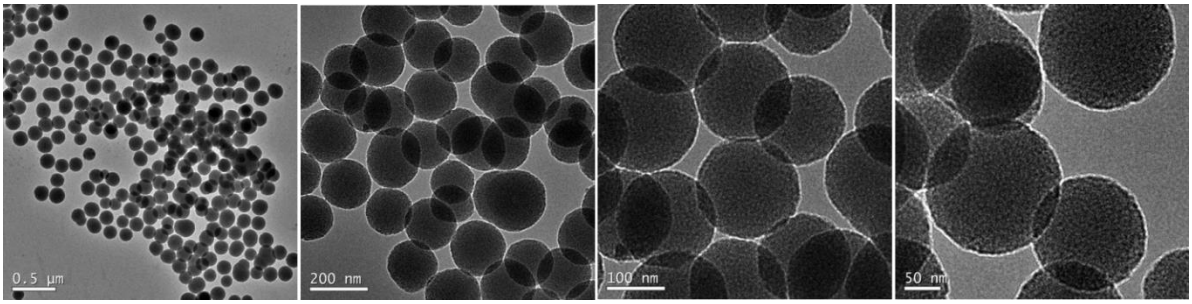

Figure 2.23 TEM images of **M7** at different magnification

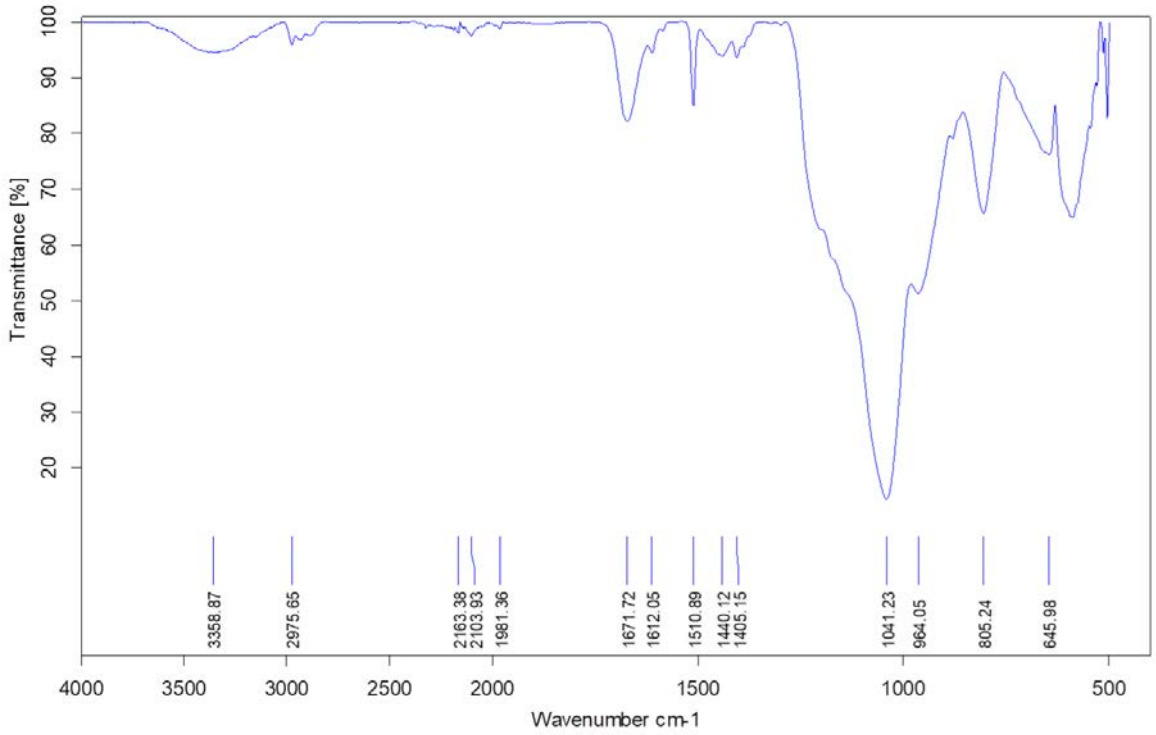

Figure 2.24 IR of **M7**

Due to the failure of the catalytic tests with this material **M7** (see *Section* **2.3.3.4**) we did not proceed to further characterize the material and we did not use the precursor **P5** to prepare functionalized mesoporous organosilica nanoparticles.

2.3.3.4 Investigation on the catalytic performance of organosilica nanoparticles derived from MacMillan imidazolidinone in the α-fluorination and trifluoromethylation reactions

The activity of the functionalized mesoporous silica nanoparticles **M7** was then evaluated in the α-fluorination of the β-ketoester *tert*-butyl 1-oxo-indanecarboxylate, **55**, with NFSI under the conditions reported by Barbas III and colleagues (**Scheme 31**).[178] We found that with our supported catalyst the product **56** was afforded in a 90% yield but as a racemic mixture. The catalyst **M7** can be recovered and reused on a second run with 85% yield (ee = 0). In order to know why there is no enantioselectivity, we performed some blank experiments. When the fluorine source NFSI was not added, the product was not generated. Unexpectedly, the reaction in the presence of NSFI, but in the absence of **M7** as catalyst, had a conversion of 57% after 24 hours. Thus, **M7** only speeds up the reaction, but it is not capable to induce enantioselectivity.

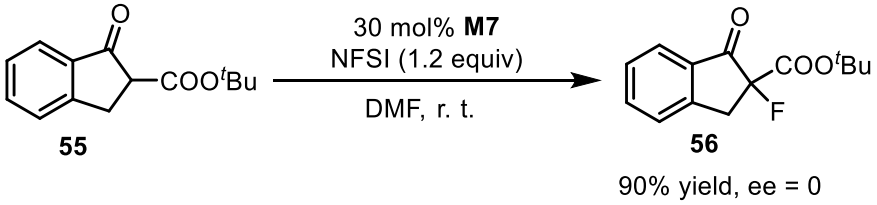

Scheme 2.31 α-fluorination of *tert*-butyl 1-oxo-indanecarboxylate **55** by **M7**

Next, we tested the α-trifluoromethylation of *tert*-butyl 1-oxo-indanecarboxylate **55** with the Togni reagent using the reaction conditions reported by Allen and MacMillan to produce compound **57** (**Scheme 2.32**).[179] Unfortunately, in this case there was no reaction at all.

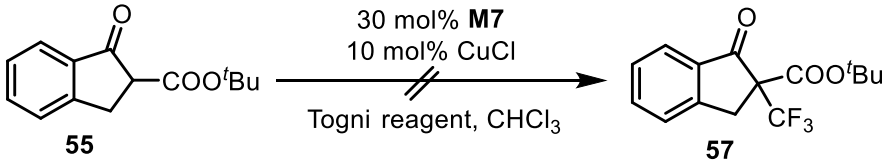

Scheme 2.32 Attempted α-Trifluoromethylation of *tert*-butyl 1-oxo-indanecarboxylate **54** by **M7**

Based on the α-trifluoromethylation reaction of aldehydes by Togni reagent reported by Allen and MacMillan in 2010,[179] we tested 3-phenylpropanal **58** as substrate and **M7** as supported catalyst in the presence of CuCl, but the α-trifluoromethylated product **59** was not obtained (**Table 2.10**).

Table 2.10 Attempted α-trifluoromethylation of 3-phenylpropanal under catalysis by **M7**

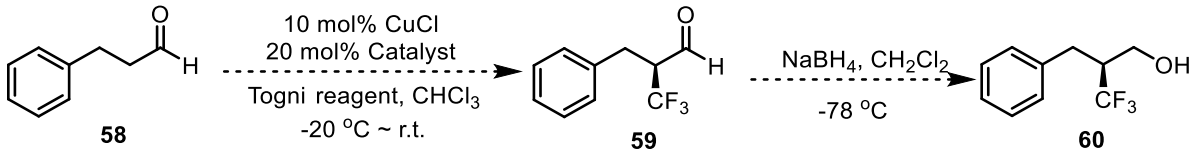

Entry	Catalyst	Result
1	**M7**	No reaction
2	**M7 •TFA** salt	No reaction
3	**M7** and TFA	No reaction

2.3.4 Conclusions

In this part, we have prepared organosilica nanoparticles derived from a MacMillan imidazolidinone (catalyst **M7),** which was used as a supported catalyst for some fluorination and trifluoromethylation reactions. Unfortunately, we did not succeed in our purposes, either there was no reaction or no asymmetric induction. On the other hand, we have undertaken the preparation of monosilylated bis(oxazolinylmethylidene)isoindoline (boxmi) ligands (**P8** / **P9**), but we encountered difficulties in the last step of the synthetic route, the introduction of the $Si(OR)_3$ group on the carbon-carbon double bond of the allyloxy moiety of compound **53**. Both the click thiol-ene addition and alkene hydrosilylation were used as synthetic strategies. In the first case, the selectivity of the reaction failed, and in the second case, the substrate was found to be unreactive. For this reason, we could not proceed to the preparation of the corresponding functionalized mesoporous silica nanoparticles as supported ligands for trifluoromethylation and fluorination reactions.

2.3.5 Experimental section

2.3.5.1 General information

All the information is given in ***Section* 2.2.5.1**.

2.3.5.2 Preparation of silylated precursors

2.3.5.2.1 Synthesis of silylated imidazolidinone precursor P5

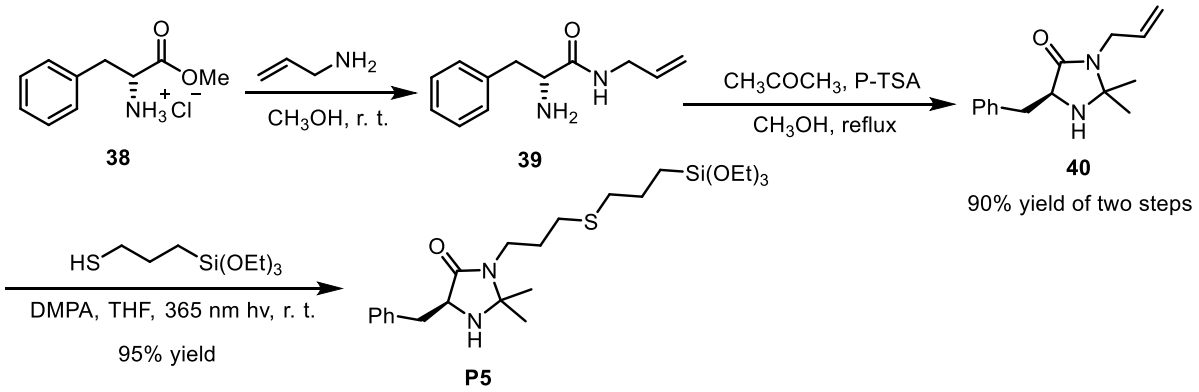

Synthesis of compound (*S*)-40.[186] To a stirred solution of allylamine (6.2 mL, 83.4 mmol) in dry CH_3OH (6.0 mL) kept under nitrogen, (*S*)-phenylalanine methyl ester hydrochloride (6.0 g, 27.8 mmol) was added in one portion. The mixture was stirred for 24 h at room temperature. The solvent was then evaporated under vacuum. The resulting pale yellow solid was suspended in Et_2O, then the solution was concentrated under vacuum; this process was repeated several times. The final product was dissolved in CH_3OH (15 mL) and acetone (25 mL), and *p*-TSA (90 mg, 0.47 mmol) was added. The mixture was refluxed for 24 h and concentrated under vacuum to afford the crude product **40** that was purified by flash chromatography with a hexane/EtOAc (1:1) mixture as eluent. The pure product was isolated in 90% overall yield. **^{1}H NMR (360 MHz, $CDCl_3$): δ (ppm)**: 7.33-7.18 (m, 5H), 5.78-5.68 (m, 1H), 5.09-5.02 (m, 2H), 4.00-3.82 (m, 1H), 3.78 (*t*, *J* = 7.2 Hz, 1H), 3.72-3.63 (m, 1H), 2.89-2.83 (m, 2H), 1.26 (s, 3H), 1.15 (s, 3H).

Synthesis of the precursor P5. In a 50 mL Schlenk tube under nitrogen, compound **40** (488.7 mg, 2.0 mmol) and 2,2-dimethoxy-1,2-diphenylethanone (102.5 mg, 0.4 mmol) were dissolved in anhydrous THF (10.0 mL). Then (3-mercaptopropyl)triethoxysilane (500.7 mg, 2.1 mmol) was added and the stirred mixture was irradiated with a UV lamp at 365 nm under argon atmosphere overnight. Then, the solvent was removed under reduced pressure and the residue was washed with anhydrous pentane several times, the pure product was obtained as colorless oil (965 mg, 100% yield). **^{1}H NMR (360 MHz, $CDCl_3$) δ (ppm)**: 7.42-7.19 (m, 5H),

5.83-5.68(m, 1H), 4.04 (d, *J* = 3.6 Hz, 1H), 3.85 (q, *J* = 7.2 Hz, 6H), 3.19-3.12 (m, 2H), 2.58-2.52(m, 2H), 1.78-1.70 (m, 4H), 1.42-1.29 (m, 4H), 1.26-1.16 (m, 15H), 0.75 (t, *J* = 7.2 Hz, 2H).

2.3.5.2.2 Synthesis of silylated imidazolidinone precursor P6

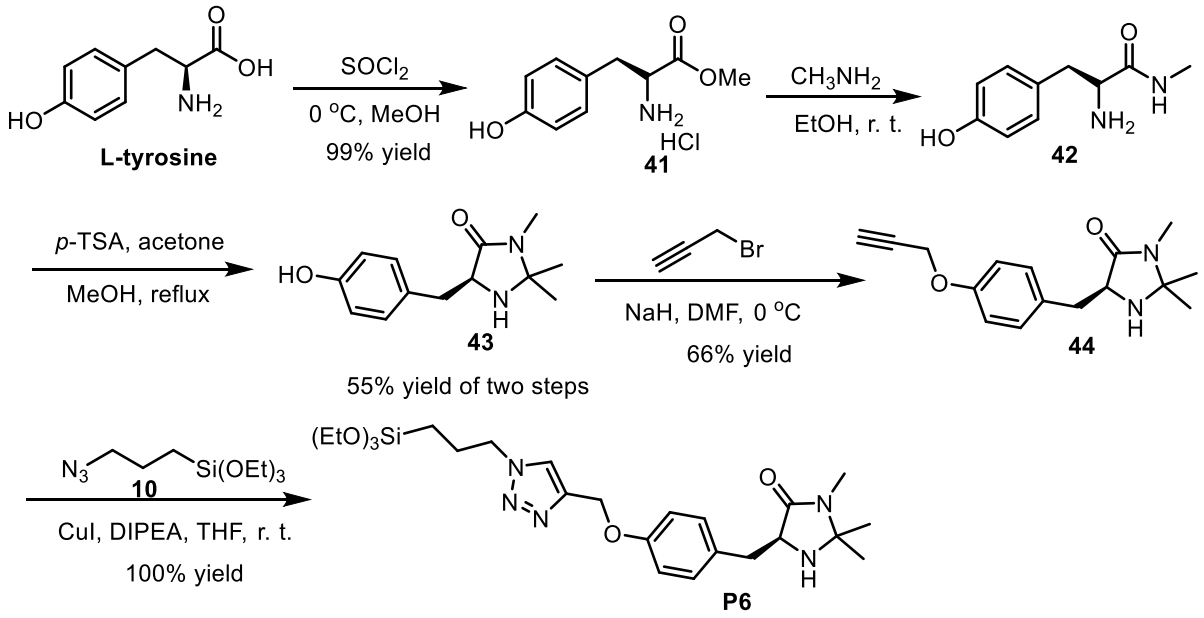

Synthesis of compound 41.[187] To a suspension of L-tyrosine in ice-cooled dry methanol, thionyl chloride (10 mL) was added dropwise. After the solution was stirred at room temperature overnight, the solvent was removed under reduced pressure to give quantitatively (*S*)-tryrosine methyl ester hydrochloride **41** as white solid (6.31 g, 99% yield). **^{1}H NMR (360 MHz, D_2O) δ (ppm)**: 7.15 (d, *J* = 7.2 Hz, 2H), 6.89 (d, *J* = 10.8 Hz, 2H), 4.33 (t, *J* = 7.2 Hz, 1H), 3.81 (s, 3H), 3.26-3.10 (m, 2H).

Synthesis of compound 43.[188] (*S*)-tryrosine methyl ester hydrochloride **41** (3.48 g, 15.0 mmol) was added in one portion to a stirred solution of methylamine (4.66 g, 150.0 mmol) in ethanol (150 mL). The mixture was stirred at room temperature for 24 h. Then, the solvent was removed under vacuum, the residue was suspended in Et_2O and then concentrated, and the process was repeated several times to remove the excess of methylamine. The amide **42** was used directly in the next step without further purification. Thus, the resulting crude yellow product **42** was dissolved in methanol (45 mL) and acetone (15 mL), *p*-TSA (90 mg, 0.47 mmol) was added and the mixture was heated under reflux for 24 h, then concentrated under vacuum. The residue was purified by silica gel column chromatography (CH_2Cl_2:MeOH = 15:1) to afford the product **43** (2.51 g, 55% yield of two steps). **^{1}H NMR**

(360 MHz, $CDCl_3$) δ (ppm): 7.03 (d, *J* = 7.2 Hz, 2H), 6.74 (d, *J* = 7.2 Hz, 2H), 3.77 (t, *J* = 7.2 Hz, 1H), 3.02-3.00 (m, 2H), 2.75 (s, 3H), 1.27 (s, 3H), 1.17 (s, 3H), NH and OH were not detected.

Synthesis of compound 44.[189] A solution of **43** (2.40 g, 10.24 mmol) in 20 mL of dry DMF was slowly added to a suspension of NaH (454.8 mg, 11.37 mmol, 60% dispersion in mineral oil) in 10 mL of dry DMF at 0 ^{o}C under Ar atmosphere. Then propargyl bromide (1.69 g, 11.37 mmol, 80% in toluene) was added dropwise. The resulting brown mixture was allowed to stir at room temperature overnight. The reaction was quenched with 100 mL of water; the mixture was extracted with diethyl ether (3 × 160 mL). The combined organic layers were washed with water and brine, dried with anhydrous sodium sulfate, filtered and concentrated under reduced pressure. The residue was purified by silica gel column chromatography (CH_2Cl_2/CH_3OH, v/v = 50:1) to afford **44** as an orange solid (1.85 g, 66%). **^{1}H NMR (360 MHz, $CDCl_3$) δ (ppm)**: 7.17 (d, *J* = 7.2 Hz, 2H), 6.92 (d, *J* = 7.2 Hz, 2H), 4.66 (d, *J* = 3.6 Hz, 2H), 3.75 (t, *J* = 7.2 Hz, 1H), 3.11-2.95 (m, 2H), 2.75 (s, 3H), 2.51-2.50 (m, 1H), 1.26 (s, 3H), 1.17 (s, 3H).

Synthesis of precursor P6. To a solution of **44** (1.53 g, 4.66 mmol) in dry THF (20 mL) was added CuI (17.75 mg, 0.09 mmol) and DIPEA (1.54 mL, 9.32 mmol) under nitrogen atmosphere. Then (3-azidopropyl)triethoxysilane (1.15 g, 4.66 mmol) was added by using a syringe. The resulting mixture was stirred at 60 ºC (Argon atmosphere) until **44** was fully consumed (44 h, reaction monitored by TLC). Then, the solvent was evaporated under reduced pressure and the residue was washed with anhydrous pentane several times. The pure product was obtained as colorless oil (2.40 g, 100% yield). **^{1}H NMR (360 MHz, $CDCl_3$) δ (ppm)**: 7.63 (br s, 1H), 7.16 (d, *J* = 7.2 Hz, 2H), 6.93 (d, *J* = 7.2 Hz, 2H), 5.17 (s, 2H), 4.36 (t, *J* = 7.2 Hz, 2H), 3.83-3.75 (m, 7H), 3.08-2.97 (m, 2H), 2.75 (s, 3H), 2.05-1.98 (m, 2H), 1.26-1.16 (m, 15H), 0.60 (t, *J* = 7.2 Hz, 2H).

2.3.5.2.3 Synthesis of bis(oxazolinylmethylidene)isoindoline ligand 53

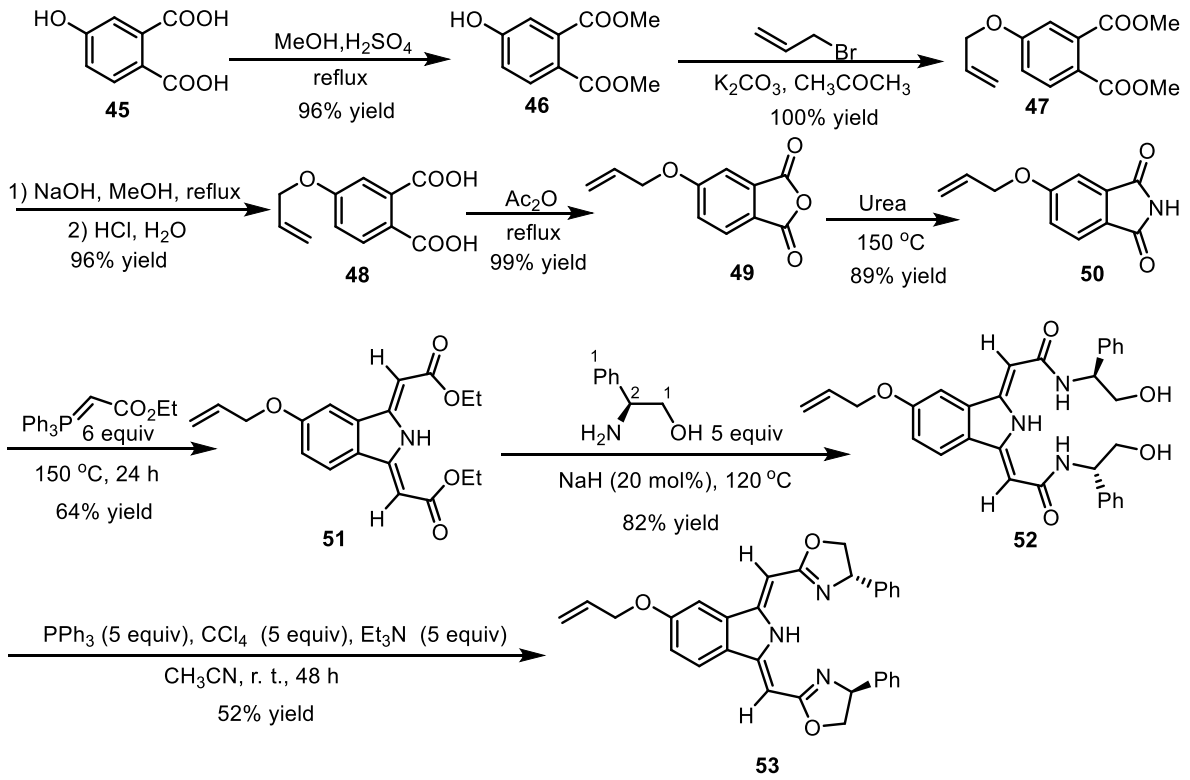

Synthesis of compound 46.[190] A solution of 4-hydroxy-phthalic acid **45** (4.8 g, 26.35 mmol) and 0.74 ml concentrated sulfuric acid (95-98%) in 50 ml of methanol is heated under reflux overnight. The methanol is evaporated and the residue was purified by a flash column chromatography with CH_2Cl_2:MeOH = 20:1, the pure product **46** was obtained as orange solid (5.31 g, 96% yield). **^{1}H NMR (360 MHz, $CDCl_3$) δ (ppm)**: 7.76 (d, *J* = 7.2 Hz, 1H), 7.01 (br s, 1H), 6.94-6.92 (m, 1H), 6.62 (s, 1H), 3.91 (s, 3H), 3.86 (s, 3H).

Synthesis of compound 47.[191] A solution of **46** (5.29 g, 25.09 mmol) in acetone (30 mL) was added dropwise to a suspension of ally1 bromide (3.64 g, 30.11 mmol) and K_2CO_3 (4.16 g, 30.11 mmol) in acetone (30 mL) at 50 °C. The stirred reaction mixture was heated for 15 h, then filtered and the solvent evaporated to give **47** as an orange oil (6.27 g, 100% yield). **^{1}H NMR (360 MHz, $CDCl_3$) δ (ppm)**: 7.81 (d, *J* = 7.2 Hz, 1H), 7.08 (br s, 1H), 7.02-6.98 (m, 1H), 6.08-5.97 (m, 1H), 5.44-5.30 (m, 2H), 4.60 (d, *J* = 3.6 Hz, 2H), 3.91 (s, 3H), 3.87 (s, 3H).

Synthesis of compound 48.[191] A solution of **47** (6.27 g, 25.0 mmol) and NaOH (2.5 g, 62.5 mmol) in methanol (50 mL) was heated at reflux overnight. After the solvent was removed,

the reaction mixture was dissolved in water. This aqueous solution was washed with diethyl ether and acidified with 1M HCI (pH < 4). Extractive workup with diethyl ether afforded **48** as an orange solid (5.33 g, 96%). **^{1}H NMR (360 MHz, DMSO-d$_6$) δ (ppm)**: 7.75 (d, *J* = 10.8 Hz, 1H), 7.11-7.08 (m, 2H), 6.07-6.00 (m, 1H), 5.43-5.27 (m, 2H), 4.67 (d, *J* = 3.6 Hz, 2H).

Synthesis of compound 49.[192] The diacid **48** (5.33 g, 23.99 mmol) was heated under reflux in acetic anhydride (40 mL) for 15 h. The volatile components were evaporated (with liquid-N_2 to cold) and then toluene was added to the remaining residue and evaporated (remove residual acetic acid or anhydride). This process was repeatedfour times and the final product **49** was obtained as an orange solid (4.85 g, 99% yield). **^{1}H NMR (360 MHz, acetone-d$_6$) δ (ppm)**: 8.00-7.97 (m, 1H), 7.55-7.54 (m, 2H), 6.17-6.09 (m, 1H), 5.52-5.33 (m, 2H), 4.88-4.86 (m, 2H).

Synthesis of compound 50.[193] A mixture of **49** (4.94 g, 24.19 mol) and urea (726.5 mg, 12.10 mmol) was added to *o*-xylene (8 mL), the mixture was stirred at 150 °C for 2 h and then allowed to cool to room temperature. The pure product **50** was obtained as an orange solid (4.35 g, 89% yield) after recrystallization with EtOAc. **^{1}H NMR (360 MHz, CDCl$_3$) δ (ppm)**: 7.92 (s, 1H), 7.78 (d, *J* = 7.2 Hz, 1H), 7.34 (d, *J* = 3.6 Hz, 1H), 7.27-7.21 (m, 1H), 6.09-6.00 (m, 1H), 5.48-5.35 (m, 2H), 4.68 (d, *J* = 7.2 Hz, 2H); **^{13}C NMR (91 MHz, CDCl$_3$) δ (ppm)**: 167.9, 163.9, 135.2, 131.8, 125.4, 124.6, 121.0, 118.8, 108.8, 69.5. **MS (ESI) m/z**: 133.1, 149.0, 186.1, 187.1, 204.1, 205.1, 219.1, 226.1; **HRMS (ESI) m/z** $[M + Na]^+$ calcd for $C_{11}H_9O_3N$+Na: 226.0475, found: 226.0471.

Synthesis of compound 51.[180] Compound **50** (203.2 mg, 1.0 mmol) and (carbethoxymethylene)triphenylphosphorane (2.09 g, 6.0 mmol) were mixed in a Schlenk tube under argon. Then the solid mixture was stirred at 150 ^{o}C for 24 h. The crude product was directly purified by column chromatography (n-hexane/ethyl acetate 12:1) to obtain the desired product **51** as colorless solid (221 mg, 64%). **^{1}H NMR (360 MHz, CDCl$_3$) δ (ppm)**: 11.42 (s, 1H), 7.58 (d, *J* = 7.2 Hz, 1H), 7.14 (br s, 1H), 7.09 (d, *J* = 7.2 Hz, 1H), 6.07-6.04 (m, 1H), 5.57 (s, 1H), 5.53 (s, 1H), 5.45 (dd, *J* = 14.4, 3.6Hz, 1H), 5.35 (dd, *J* = 10.8, 3.6Hz, 1H), 4.63-4.61 (m, 2H), 4.32-4.28 (m, 4H), 1.58-1.33 (m, 6H); **^{13}C NMR (91 MHz, CDCl$_3$) δ (ppm)**: 168.5, 168.3, 161.0, 150.9, 150.8, 136.5, 132.4, 127.4, 122.7, 118.6, 118.3, 106.3, 87.0, 86.3, 69.3, 60.1, 60.0, 14.51, 14.49. **MS (ESI) m/z**: 252.1, 298.1, 299.1, 344.1; **HRMS (ESI) m/z** $[M + H]^+$ calcd for $C_{19}H_{21}O_5N$+H: 344.1492, found: 344.1488.

Synthesis of compound 52.[180] Compound **51** (343.4 mg, 1.0 mmol) and (S)-2-amino-2-phenyl-1-ethanol (686.0 g, 5.0 mmol) were mixed and melted in a Schlenk tube under argon. The solid mixture was then rapidly heated to 120 ^{o}C in a preheated oil bath. NaH (60%, 8.0 mg, 0.2 mmol) was added to the resulting mixture, and the reaction mixture was stirred at 120 ºC under slightly reduced pressure for 7 h.The reaction mixture turned brown and became highly viscous. After subsequent cooling to ambient temperature, the crude product was directly purified by column chromatography (dichloromethane/methanol from 40:1 to 10:1) to obtain the desired product **52** as a dark solid (431 mg, 82% yield). **^{1}H NMR (360 MHz, $CDCl_3$) δ (ppm)**: 7.65-7.63 (m, 1H), 7.41-7.09 (m, 12H), 6.13-6.05 (m, 1H), 5.75 (s, 1H), 5.69 (s, 1H), 5.50-5.28 (m, 2H), 5.06 (br s, 2H), 4.65-4.64 (m, 2H), 3.81-3.72 (m, 4H), NH and OH were not detected; **^{13}C NMR (91 MHz, $CDCl_3$) δ (ppm)**: 170.3, 170.0, 162.2, 149.2, 141.9, 141.8, 137.8, 134.4, 129.4, 128.3, 128.1, 123.3, 119.2, 118.0, 106.9, 89.5, 88.6, 70.3, 66.5, 56.7. **MS (ESI) m/z**: 161.1, 221.1, 256.1, 298.1, 338.1, 389.1, 435.2, 526.2; **HRMS (ESI) m/z** $[M + H]^+$ calcd for $C_{31}H_{31}O_5N_3$+H: 526.2336, found: 526.2326.

Synthesis of compound 53.[180] PPh_3 (870.8 mg, 3.32 mmol), Et_3N (336.0 mg, 3.32 mmol), and CCl_4 (510.7 mg, 3.32 mmol) were added to a solution of **52** (348.7 mg, 0.663 mmol) in MeCN (15 mL). The reaction mixture was stirred at room temperature. After completion of the reaction (monitored by TLC, 48 h), water (100 mL) was added and the resulting mixture was extracted with CH_2Cl_2 (120 mL × 3). The combined organic phase was dried over anhydrous Na_2SO_4. The solvent was removed under reduced pressure, and the crude product was purified by flash chromatography on silica gel (hexane/ethyl acetate 4:1) to give **53** as colorless oil (170.1 mg, 52.4% yield). **^{1}H NMR (360 MHz, $CDCl_3$) δ (ppm)**: 11.79 (s, 1H), 7.61-7.58 (m, 1H), 7.29-7.05 (m, 12H), 6.10-6.03 (m, 1H), 5.65 (s, 1H), 5.61 (s, 1H), 5.48-5.26 (m, 4H), 4.67-4.62 (m, 4H), 4.05-4.02 (m, 2H); **MS (ESI) m/z**: 298.1, 375.2, 475.4, 478.2, 490.2; **HRMS (ESI) m/z** $[M + H]^+$ calcd for $C_{31}H_{27}O_3N_3$+H: 490.2125, found: 490.2115.

2.3.5.3 Preparation of functionalized mesoporous silica nanoparticles M7

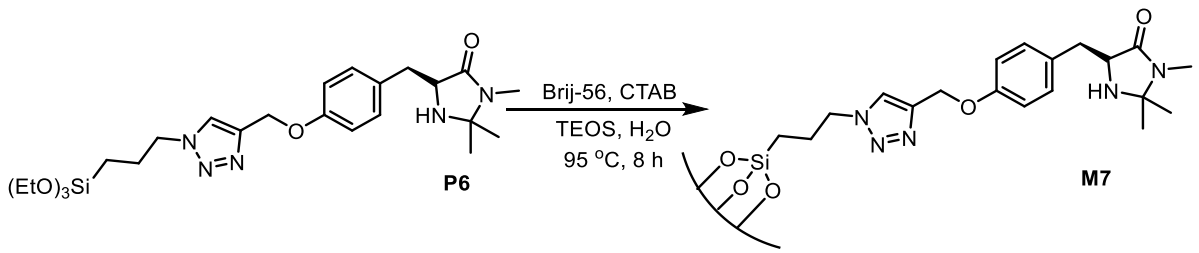

MSNs were synthesized in an aqueous buffer solution of pH 7 from a mixture with the following molar ratios: Brij-56:CTAB:TEOS:**P6**:H_2O = 7:20:160:16:120,000. Initially, CTAB (455.5 mg, 1.25 mmol) and Brij-56 (298.8 mg, 0.438 mmol) were dissolved in the buffer solution (prepared from KH_2PO_4 (428.8 mg, 3.15 mmol) and NaOH (72.5 mg, 1.81 mmol) in H_2O (135 mL, 7500 mmol)), under vigorous stirring (1000 rpm) and heating at 95 ºC. When the solution became homogeneous, a mixture of TEOS (2.08 g, 10 mmol) and **P6** (519.7 mg, 1 mmol) was added slowly. The reaction was maintained for 8 hours under stirring at 95ºC. The suspension was cooled to room temperature while stirring and the NPs were collected by centrifugation (13500 rpm at 25 °C for 45 mins). In order to remove the surfactant, 20 mL of an alcoholic solution of ammonium nitrate [NH_4NO_3, 6 g/L in 96% EtOH] was added to each tube, sonicated for 30 min at 50 °C, then cooled and centrifuged (30 min at 135000 rpm at 25 °C), the supernatant was discarded. This NH_4NO_3 washing was performed 3 times. Each solid in the tubes was washed successively with 96% ethanol, Mili-Q water, 96% ethanol using the same protocol (30 min at 50 °C sonication, centrifugation). The final product was dried for few hours under vacuum at room temperature. The material **M7** was obtained as a white solid (873 mg). **EA:** 6.42% N, 22.09% C, 3.38% H (0.92 mmol imidazolidinonee/g material). **IR (ATR) ν (cm^{-1})**: 3358.9, 2975.7, 1671.7, 1510.9, 1041.2, 964.1, 805.2, 646.0.

2.3.5.4 General procedure for the α-fluorination of carbonyl compounds

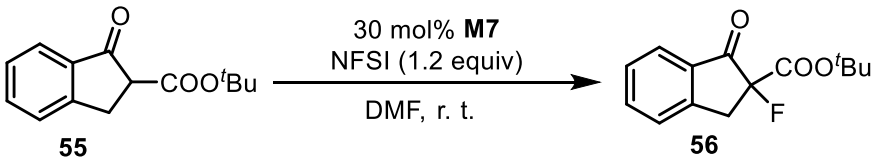

55 56

The substrate (23.23 mg, 0.1 mmol) and the catalyst **M7** (33 mg, 30 mol%) were placed in a tube and DMF (0.2 mL) was added. The mixture was stirred at room temperature for 10 min, then NFSI (37.84 mg, 0.12 mmol) was added and the reaction mixture was stirred at room temperature until complete conversion of the substrate. Then the mixture was centrifuged. The liquid supernatant was added to an aqueous NH_4Cl solution and extracted with EtOAc (5 mL). The recovered solid catalyst was washed with EtOAc (5 mL) and isolated by centrifugation. The combined organic phases were dried over anhydrous sodium sulfate and the solvent was evaporated. The residue was purified by a flash column chromatography, the pure product was obtained as colorless oil.

2.3.5.5 General procedures for the α-trifluoromethylation of carbonyl compounds

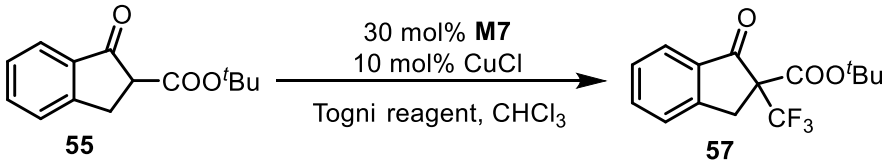

55 57

To a schlenk tube, the substrate (22.23 mg, 0.1 mmol) and CuCl (1.0 mg, 0.1 mmol), the supported catalyst **M7** (33.0 mg, 0.3 mmol) and Togni reagent (21.8 mg, 0.2 mmol) were added. Then, the air was removed and changed with N_2 by a three pump-and-fill cycles. Then, $CHCl_3$ (0.5 mL) was added and the mixture was stirred at room temperature for 24 hour. CH_2Cl_2 was added and filtered, the filtrate was extracted with CH_2Cl_2 and concentrated in vacuo. The crude product was obtained as colorless oil and analysed by proton NMR.

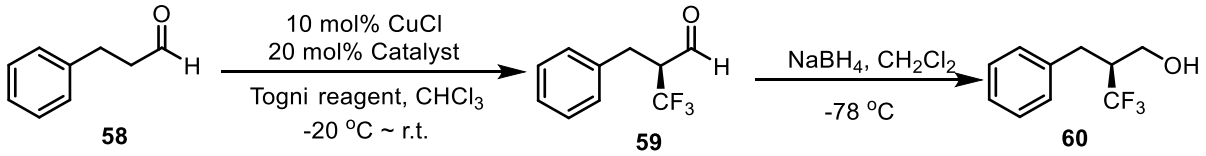

58 59 60

To a schlenk tube, CuCl (3.0 mg, 0.03 mmol), the supported catalyst **M7** (130.0 mg, 0.12 mmol) and Togni reagent (200 mg, 0.6 mmol) were added. Then, the air was removed and changed with N_2 by a three pump-and-fill cycles. The schlenk tube was placed in a bath at -20 °C and degassed $CHCl_3$ (1.35 mL) was added to the mixture. Then, the substrate (160 μL, 1.2 mmol) was added and the mixture was stirred at - 20 °C for 24 hour. At this point, the mixture was cooled to -78 °C and diluted with cold CH_2Cl_2 (2.0 mL), $NaBH_4$ (230 mg, 6 mmol) was added to reduce the aldehyde to the corresponding alcohol, followed by cold MeOH (1.0 mL). The reaction mixture was stirred for one hour at this temperature. The solution was transferred to cold aqueous NH_4Cl solution at 0 °C. The resulting solution was warmed to room temperature, CH_2Cl_2 was added and filtered, the filtrate was extracted with CH_2Cl_2 and concentrated in vacuo. The crude product was obtained as colorless oil and analysed by proton NMR.

2.4 References

1. C. Y. Lai, *J. Thermodyn Catal.* **2013**, *5,* 1.
2. M. Manzano, M. Vallet-Regí, *Chem. Commun.* **2019**, *55*, 2731.
3. I. I. Slowing, J. L. Vivero-Escoto, B. G. Trewyn, V. S. Y. Lin, *J. Mater. Chem.* **2010**, *20*, 7924.
4. M. V. Ambrogio, C. R. Thomas, Y. Zhao, J. I. Zink, J. F. Stoddart, *Acc. Chem. Res*. **2011**, *44*, 903.
5. N. Chen, S. Cheng, J. S. Souris, C. Chen, C. Mou, L. Lo, *J. Mater. Chem. B* **2013**, *1*, 3128.
6. J. G. Croissant,; X. Cattoën, M. Wong Chi Man, J.-O. Durand, N. M. Khashab, *Nanoscale* **2015**, *7*, 20318.
7. E. Yamamoto, K. Kuroda, *Bull. Chem. Soc. Jpn.* **2016**, *89*, 501.
8. Y. Wan, D. Zhao, *Chem. Rev.* **2007**, *107*, 2821.
9. F. Hoffmann, M. Cornelius, J. Morell, M. Fröba, *Angew. Chem. Int. Ed.* **2006**, *45*, 3216.
10. A. Stein, B. J. Melde, R. C. Schroden, *Adv. Mater.* **2000**, *12*, 1403.
11. S. H. Wu, C. Y. Mou, H. P. Lin, *Chem. Soc. Rev.* **2013**, *42*, 3862.
12. S. Huh, H. T. Chen, J. W. Wiench, M. Pruski, V. S. Y. Lin, *Angew. Chem. Int. Ed.* **2005**, *44*, 1826.
13. S. Shylesh, A. Wagner, A. Seifert, S. Ernst, W. R. Thiel, *Chem. Eur. J*. **2009**, *15*, 7052.
14. K. Kandel, S. M. Althaus, C. Peeraphatdit, T. Kobayashi, B. G. Trewyin, M. Pruski, I. I. Slowing, *J. Catal*. **2012**, *291,* 63.
15. F. Zhu, X. Sun, F. Lou, L. An, P. Zhao, *Cat. Lett*. **2015**, *45*, 1072.
16. P. Cruz, Y. Pérez, I. del Hierro, *Eur. J. Inorg. Chem*. **2018**, 4206.
17. Y. Huang, B. G. Trewyin, H. T. Chen, V. S. Y. Lin, *New J. Chem.* **2008**, *32*, 1311.
18. Y. Huang, S. Xu, V. S. Y. Lin, *Angew. Chem. Int. Ed.* **2011**, ***50***, 661.
19. A. T. Dickschat, F. Behrends, M. Bühner, J. Ren, M. Weiβ, H. Eckert, A. Studer, *Chem. Eur. J*. **2012**, *18*, 16689.
20. A. Puglisi, R. Annunziata, M. Benaglia, F. Cozzi, A. Gervasini, V. Bertacche, M. C. Sala, *Adv. Synth. Catal*. **2009**, *351*, 219.
21. H. T. Chen, B. Trewyin, J. Wiench, M. Pruski, V. Y. Lin, *Top. Catal*. **2010**, *53,* 187.
22. W. H. Peng, Y. Y. Lee, C. Wu, K. C. W. Wu, *J. Mater. Chem*. **2012**, *22*, 23181.
23. S. Ray, P. Das, A. Bhaumik, A. Dutta, C. Mukhopadhyay, *Appl. Catal. A*, **2013**, *458*, 183.
24. P. Das, S. Ray, P. Bhanja, A. Bhaumik, C. Mukhopadhyay, *ChemCatChem* **2018**, *10*, 2260.
25. A. Puglisi, M. Benaglia, R. Annunziata, V. Chiroli, R. Porta, A. Gervasini, *J. Org. Chem*. **2013**, *78*, 11326.
26. R. Porta, M. Benaglia, V. Chiroli, F. Coccia, A. Puglisi, *Isr. J. Chem*. **2014**, *54*, 381.
27. H. U. Blaser, *Chem. Commun.* **2003**, 293.
28. A. Berkessel, H. Gröger, Asymmetric Organocatalysis: From Biomimetic Concepts to Applications in Asymmetric Synthesis, Wiley-VCH, Weinheim, Germany, **2005**.
29. Dalko, P. I., Ed. Enantioselective Organocatalysis: Reactions and Experimental Procedures; Wiley-VCH: Weinheim, Germany, **2007**.
30. B. List, Asymmetric organocatalysis, Springer, **2009**.
31. E. N. Jacobsen, D. W. C. MacMillan, *PNAS* **2010**, *107*, 20618
32. O. I. Kolodiazhnyi, Asymmetric Synthesis in Organophosphorus Chemistry: Synthetic Methods, Catalysis, and Applications, Wiley-VCH, **2017**.

33. H. Pellissier, *Curr. Org. Chem.* **2018**, *21*, 323.
34. A. Ding, M. Meazza, H. Guo, J. W. Yang, R. Rios, *Chem. Soc. Rev.* **2018**, *47*, 5946.
35. R. Marcia de Figueiredo, M. Christmann, *Eur. J. Org. Chem*. **2007**, *2007*, 2575.
36. J. Alemán, S. Cabrera, *Chem. Soc. Rev.* **2013**, *42*, 774.
37. D. L. Hughes, *Org. Process Res. Dev.* **2018**, *22*, 574.
38. A. Ricci, *ISRN Org. Chem.* **2014**, 531695, **DOI** : 10.1155/2014/531695.
39. B. M. Sahoo, B. K. Banik, *Curr. Organocatal.* **2019**, *6*, 92.
40. A. Carlone, L. Bernardi, *Phys. Sci. Rev.***2019**, **DOI** : 10.1515/psr-2018-0097.
41. F. G. Adly, A. Ghanem, *Catalysts* **2019**, *9*, 775.
42. D. E. De Vos, I. F. J. Vankelecom, P. A. Jacobs, Chiral Catalyst Immobilization and Recycling, Wiley-VCH Verlag GmbH, D-69469, Weinheim, **2000**.
43. F. Cozzi, *Adv. Synth. Catal.* **2006**, *348*, 1367.
44. M. Benaglia, *New J. Chem.* **2006**, *30*, 1525.
45. M. Gruttadauria, F. Giacalone, R. Noto, *Chem. Soc. Rev.* **2008**, *37*, 1666.
46. K. Ding, Y. Uozumi, (eds) Handbook of Asymmetric Heterogeneous Catalysis, Wiley-VCH, Weinheim, **2008**.
47. W. Zhang, B. W. Cue Jr, Green Techniques for Organic Synthesis and Medicinal Chemistry, First Edition. John Wiley & Sons, Ltd, **2012**.
48. T. Mitsudome, K. Nose, T. Mizugaki, K. Jitsukawa, K. Kaneda, *Tetrahedron Lett.* **2008**, *49*, 5464.
49. Z. J. Wang, G. J. Deng, Y. Li, Y. M. He, W. J. Tang, Q. H. Fan, *Org. Lett.* **2007**, *9,* 1243.
50. Y. Y. Wu, Y. Z. Zhang, M. L. Yu, G. Zhao, S. W. Wang, *Org. Lett.* **2006**, *8*, 4417.
51. Z. X. Shen, J. M. Ma, Y. H. Liu, C. J. Jiao, M. Li, Y. W. Zhang, *Chirality* **2005**, *7*, 556.
52. I. R. Shaikh, *J. Catal.* **2014**, 402860, **DOI:** 10.1155/2014/402860.
53. D. J. Cole-Hamilton, *Science* **2003**, *299*, 1702.
54. J. Dreimann, P. Lutze, M. Zagajewski, A. Behr, A. Górak, A. J. Vorholt, *Chem. Eng. Process. Process Intensif.* **2015**, *99*, 124.
55. D. Nair, S. S. Luthra, J. T. Scarpello, L. S. White, L. M. Freitas dos Santos, A. G. Livingston, *Desalination*, **2002**, *147*, 301.
56. J. Fang, R. Jana, J. A. Tunge, B. Subramaniam, *Appl. Catal. A Gen.* **2011**, *393*, 294.
57. L. Ge, B. Wu, Q. Li, Y. Wang, D. Yu, L. Wu, J. Pan, J. Miao, T. Xu, *J. Membr. Sci*. **2016**, *498*, 192.
58. A. Zamboulis, N. Moitra, J. J. E. Moreau, X. Cattoen, M. Wong Chi Man, *J. Mater. Chem.* **2010**, *20*, 9322.
59. T. E. Kristensen, T. Hansen, *Eur. J. Org. Chem.* **2010**, 3179.
60. A. Corma, H. García, *Adv. Synth. Catal.* **2006**, *348*, 1391.
61. M. Benaglia, A. Puglisi, F. Cozzi, *Chem. Rev.* **2003**, *103*, 3401.
62. P. A. Jacobs, Chiral Catalyst Immobilization and Recycling, ed. D. E. De Vos, I. F. Vankelecom, WILEY-VCH: Weinheim, **2000**.
63. M. Trilla, R. Pleixats, M. Wong Chi Man, C. Bied, *Green Chem.* **2009**, *11*, 1815.
64. S. Iimura, K. Manabe, S. Kobayashi, *Org. Biomol. Chem.* **2003**, *1*, 2416.
65. P. L. Anelli, F. Montanari, S. Quici, *J. Org.Chem.* **1986**, *51*, 4910.
66. L. Gu, Y. Wu, Y. Zhang, G. Zhao, *J. Mol. Catal. A: Chem.* **2007**, *263*, 186.
67. M. Benaglia, M. Cinquini, F. Cozzi, A. Puglisi, G. Celentano, *J. Mol. Catal. A: Chem.* **2003**, 204-205, 157.

68. M. Benaglia, M. Cinquini, F. Cozzi, A. Puglisi, G. Celentano, *Adv. Synth. Catal.* **2002**, *344*, 533.
69. T. E. Kristensen, K. Vestli, A. Fredriksen, F. K. Hansen, *Org. Lett.* **2009**, *11*, 2968.
70. E. A. Prasetyanto, S. C. Lee, S. E. Park, *Chem. Commun.* **2008**, 1995.
71. M. Gruttadauria, F. Giacalone, A. Mossuto Marculescu, R. Noto, *Tetrahedron Lett.* **2007**, *48*, 255.
72. D. Font, C. Jimeno, M. A. Pericàs, *Org. Lett.* **2006**, *8*, 4653.
73. K. Kondo, T. Yamano, K. Takemoto, *Makromol. Chem.* **1985**, *16*, 1781.
74. L. C. Branco, A. M. Faisca Phillips, M. M. Marques, S. Gago, P. S. Branco, Recent Advances in Sustainable Organocatalysis, In *Recent Advances in Organocatalysis*; Karame, I., Srour, H., Eds.; InTech: Rijeka, Croatia, **2016**, 141-182. ISBN 978-953-51-2673-7. **DOI:** 10.5772/64279.
75. M. P. van der Helm, B. Klemm, R. Eelkema, *Nature Rev. Chem.* **2019**, *3*, 491.
76. A. Monge-Marcet, X. Cattoën, D. A. Aloso, C. Nájera, M. Wong Chi Man, R. Pleixats, *New J. Chem.* **2011**, *35*, 2766.
77. A. Monge-Marcet, R. Pleixats, X. Cattoën, M. Wong Chi Man, D. A. Aloso, C. Nájera, *Green Chem*. **2012**, *14*, 1601.
78. W. Guo, A. Monge-Marcet, X. Cattoën, A. Shafir, R. Pleixats, *React.Funct. Polym.* **2013**, *73*, 192.
79. M. Ferré, X. Cattoën, M. Wong Chi Man, R. Pleixats, *Chemistryselect* **2016**, *1*, 6741.
80. A. Wurtz, *Bull. Soc. Chim. Fr.* **1872**, *17*, 436.
81. G. Guillena, C. Nájera, D. J. Ramón, *Tetrahedron: Asymmetry* **2007**, *18*, 2249.
82. B. M. Trost, C. S. Brindle, *Chem. Soc. Rev.* **2010**, *39*, 1600.
83. J. Mlynarshi, S. Baś, *Chem. Soc. Rev.* **2014**, *43*, 577.
84. S. Mandal, S. Mandal, S. K. Ghosh, A. Ghosh, R.Saha, S.Banerjee, B. Saha, *Synth. Commun.* **2016**, *46*, 1327.
85. Y. Yamashita, T. Yasukawa, W. -J. Yoo, T. Kitanosono, S. Kobayashi, *Chem. Soc. Rev.* **2018**, *47*, 4388.
86. G. D. Yadav, Deepa, S. Singh, *ChemistrySelect* **2019**, *4*, 5591.
87. M. M. Heravi, V. Zadsirjan, M. Dehghani, N. Hosseintash, *Tetrahedron: Asymmetry* **2017**, *28*, 587.
88. R. Mahrwald, Modern Aldol Reactions, ed. Wiley-VCH, Berlin, **2004**.
89. B. M. Trost, *Science* **1991**, *254*, 1471.
90. Z. G. Hajos, D. R. Parrish, German Pat. DE 2102623, **1971**.
91. U. Eder, G. R. Sauer, R. Wiechert, German Pat. DE 2014757, **1971**.
92. B. List, R. A. Lerner and C. F. Barbas, III, *J. Am. Chem. Soc*. **2000**, *122*, 2395.
93. B. List, P. Pojarliev, C. Castello, *Org. Lett.* **2001**, *3*, 573.
94. B. List, *Tetrahedron* **2002**, *58*, 5573.
95. Z. Tang, F. Jiang, L. T. Yu, X. Cui, L. Z. Gong, A. Q. Mi, Y. Z. Jiang, Y. D. Wu, *J. Am. Chem. Soc.* **2003**, 125, 5262.
96. M. R. Vishnumaya, V. K. Singh, *J. Org. Chem.* **2009**, *74*, 4289.
97. B. Wang, G. H. Chen, L. Y. Liu, W. X. Chang, J. Li, *Adv. Synth. Catal*. **2012**, *14*, 2441.
98. M. Bhanushali, C. G. Zhao, *Synthesis* **2011**, 1815.
99. M. M. Heravi, S. Asadi, *Tetrahedron:Asymmetry* **2012**, *23*, 1431.
100. V. Bisai, A. Bisai, V. K. Singh, *Tetrahedron* **2012**, *68*, 4541.
101. B. Alcaide, P. Almendros, *Eur. J. Org. Chem.* **2002**, 1595.
102. B. Alcaide, P. Almendros, *Angew. Chem. Int. Ed.* **2003**, *42*, 858.

103. S. Mukherjee, J. W. Yang, S. Hoffmann, B. List, *Chem. Rev.* **2007**, *107*, 5471.
104. W. Notz, F. Tanaka, C. F. Barbas, *Acc. Chem. Res.* **2004**, *37*, 580.
105. H. Wennemers, *Chimia* **2007**, *61*, 276.
106. C. Palomo, M. Oiarbide, J. M. Garcia, *Chem. Soc. Rev.* **2004**, *33*, 65.
107. J. Seayad, B. List, *Org. Biomol. Chem.* **2005**, *3*, 719.
108. D. W. C. MacMillan, *Nature* **2008**, *455*, 304.
109. C. F. Barbas III, *Angew. Chem. Int. Ed.* **2008**, *47*, 42.
110. D. Enders, C. Grondal, M. R. M. Huttl, *Angew. Chem. Int. Ed.* **2007**, *46*, 1570.
111. B. List, *Synlett* **2001**, 1675.
112. B. List, *Chem. Commun.* **2006**, 819.
113. M. Benaglia, G. Celentano, F. Cozzi, *Adv. Synth. Catal.* **2001**, *343*, 171.
114. R. Somanathan, L. Z. Flores-Lopez, D. Chevez, M. Parra-Hake, G. Aguirre, *Curr. Top. Catal.* **2012**, *10,* 1.
115. P. Upadhyay, V. Srivastava. *Curr. Organocatalysis* **2016**, *3,* 243.
116. N. A. Brunelli, C. W. Jones, *J. Catal.* **2013**, *308*, 60.
117. Y. B. Huang, W. Zhang, *Green Process. Synth.* **2013**, *2*, 603.
118. V. V. Rostovtsev, L. G. Green, V. V. Fokin, K. B. Sharpless, *Angew. Chem. Int. Ed*. **2002**, *41*, 2596.
119. M. Meldal, C. W. Tornøe, *Chem. Rev*. **2008**, *108*, 2952.
120. F. Fache, O. Piva, *Tetrahedron: Asymmetry* **2003**, *14*, 139.
121. V. Mihali, F. Foschi, M. Penso, G. Pozzi, *Eur. J. Org. Chem.* **2014**, 5351.
122. K. Bürglová, N. Moitra, J. Hodacová, X. Cattoën, M. Wong Chi Man, *J. Org. Chem.* **2011**, *76*, 7326.
123. K. Bürglová, A. Noureddine, J. Hodacová, G. Toquer, X. Cattoën, M. Wong Chi Man, *Chem. Eur. J.* **2014**, *20*, 10371.
124. K. L. Killops, L. M. Campos, C. J. Hawker, *J. Am. Chem. Soc.* **2008**, *130*, 5062.
125. T. C. Xiao, L. D. An, *Catal. Lett*. **1992**, *12*, 287.
126. O. V. Yurkina, A. V. De Vekki, Y. L. Kraev, *Pet. Chem.* **2004**, *44*, 160.
127. Q. F. Zhang, J. H. LÜ, L. Ma, C. S. Lu, W. Liu, X. N. Li, *Chin. J. Chem. Eng.* **2013**, *21*, 622.
128. T .Y. Xu, Q. F. Zhang, D. H. Jiang, Q. X. Liang, C. S. Lu, J. Cen, X. N. Li, *RSC Adv.* **2014**, *4*, 33347.
129. M. D. Argyle, C. H. Bartholomew, *Catalysts* **2015**, *5*, 145.
130. D. Gryko, R. Lipin'ski, *Adv. Synth. Catal.* **2005**, *347*, 1948.
131. D. Almaşi, D. A. Alonso, C. Nájera, *Adv. Synth. Catal.* **2008**, *350*, 2467.
132. D. Almaşi, D. Alonso, A. N. Balaguer, C. Nájera, *Adv. Synth. Catal.* **2009**, *351*, 1123.
133. F. G. Bordwell, D. J. Algrim, J. A. Jr. Harrelson, *J. Am. Chem. Soc.* **1988**, *110*, 5903. (pKa CH_3CONH_2 = 25.5; pKa CH_3CSNH_2 = 18.5, values in DMSO)
134. D. Gryko, M. Chromiński, D. J. Pielacińska, *Symmetry* **2011**, *3*, 265.
135. C. E. Yeom, Y. J. Kim, S. Y. Lee, Y. J. Shin, M. Kim, *Tetrahedron* **2005**, *61*, 12227.
136. C. Théron, A. Gallud, C. Carcel, M. Gary-Bobo, M. Maynadier, M. Garcia, J. Lu, F. Tamanoi, J. I. Zink, M. Wong Chi Man, *Chem. Eur. J*. **2014**, *20*, 9372.
137. Q. J. He, X. Z. Cui, F. M. Cui, L. M. Guo, J. L.Shi, *Micropor. Mesopor. Mater.* **2009**, *117*, 609.
138. A. Zamboulis, N. J. Rahier, M. Gehringer, X. Cattoën, G. Niel, C. Bied, J. J. E. Moreau, M. Wong Chi Man, *Tetrahedron:Asymmetry* **2009**, *20*, 2880.
139. Z. An, Y. Guo, L. Zhao, Z. Li, J. He, *ACS Catal*. **2014**, *4*, 2566.

140. D. Kühbeck, J. Bachl, E-M. Schön, V. Gotor-Fernández, D. D. Díaz, *Helv. Chim. Acta* **2014**, *97*, 574.
141. M. Ferré, R. Pleixats, M. Wong Chi Man, X. Cattoën, *Green Chem*. **2016**, *18*, 881.
142. Q. Zhang, H. Su, J. Luo, Y. Y. Wei, *Catal. Sci. Technol.* **2013**, *3*, 235.
143. F. Macleod, S. Lang, J. A. Murphy, *Synlett* **2010**, *4*, 529.
144. Z. Y. Li, Y. Chen, C. Q. Zheng, Y. Yin, L. Wang, X. Q. Sun, *Tetrahedron* **2017**, *73*, 78.
145. X. Zhang, W. S. Zhao, C. K. Qu, L. L. Yang , Y. C. Cui, *Tetrahedron: Asymmetry* **2012**, *23*, 468.
146. J. G. Hernández, E. Juaristi, *J. Org. Chem.* **2011**, *76*, 1464.
147. S. Kotani, S. Hashimoto, M. Nakajima, *Tetrahedron* **2007**, *63*, 3122.
148. D. O'Hagan, D. B. Harper, *Nat. Prod. Rep.* **1994**, *11*, 123.
149. T. Hiyama, Organofluorine Compounds, Chemistry and Applications; Springer-Verlag: Berlin Heidelberg, **2000**.
150. P. Kirsch, Modern Fluoroorganic Chemistry; Wiley-VCH: Weinheim, **2013**.
151. P. Krisch, Ed. Modern Fluoroorganic Chemistry: Synthesis Reactivity, Applications; Wiley: VCH, Weinheim, **2004**.
152. A. M. Thayer, *Chem. Eng. News* **2006**, *84*, 15.
153. J. Wang, M. Sánchez-Roselló, J. L. Aceña, C. del Pozo, A. E. Sorochinsky, S. Fustero, V. A. Soloshonok, H. Liu, *Chem. Rev.* **2013**, *114*, 2432.
154. X. Y. Yang, T. Wu, R. J. Phopps, F. D. Toste, *Chem. Rev.* **2015**, *115*, 826.
155. R. D. Shannon, *Acta. Crystallogr*. **1976**, *32*, 751.
156. C. Babbio, V. Gouverneur, *Org. Biomol. Chem.* **2006**, *4*, 2065.
157. G. K. S. Prakash, P. Beier, *Angew. Chem. Int. Ed.* **2006**, *45*, 2172.
158. P. M. Pihko, *Angew. Chem. Int. Ed.* **2006**, *45*, 544.
159. Y. Hamashima, M. Sodeoka, *Synlett* **2006**, 1467.
160. N. Shibata, T. Ishimaru, S. Nakamura, T. J. Toru, *Fluorine Chem.* **2007**, *128*, 469.
161. V. A. Brunet, D. O' Hagan, *Angew. Chem. Int. Ed.* **2008**, *47*, 1179.
162. J. A. Ma, D. Cahard, *Chem. Rev.* **2008**, *108*, PR1.
163. N. Shibata, S. Mizuta, H. Kawai, *Tetrahedron: Asymmetry* **2008**, *19*, 2633.
164. M. Ueda, T. Kano, K. Maruoka, *Org. Biomol. Chem.* **2009**, *7*, 2005.
165. D. Cahard, X. Xu, C. Couve-Bonnaire, X. Pannecoucke, *Chem. Soc. Rev.* **2010**, *39*, 558.
166. Y. Zheng, J. A. Ma, *Adv. Synth. Catal.* **2010**, *352*, 2745.
167. S. Lectard, Y. Hamashima, M. Sodeoka, *Adv. Synth. Catal.* **2010**, *352*, 2708.
168. N. Shibata, A. Matsnev, D. Cahard, *Beilstein J. Org. Chem.* **2010**, *6*, 65.
169. T. Furuya, A. S. Kamlet, T. Ritter, *Nature* **2011**, *473*, 470.
170. G. Valero, X. Companyó, R. Rios, *Chem. Eur. J.* **2011**, *17*, 2018.
171. A. D. Dilman, V. V. Levin, *Eur. J. Org. Chem.* **2011**, 831.
172. C. Hollingworth, V. Gouverneur, *Chem. Commun.* **2012**, *48*, 2929.
173. Y. Macé, E. Magnier, *Eur. J. Org. Chem.* **2012**, 2479.
174. T. Liang, C. N. Neumann, T. Ritter, *Angew. Chem. Int. Ed.* **2013**, *52*, 8214.
175. V. Bizet, T. Besset, J. A. Ma, D. Cahard, *Cur. Top. Med. Chem.* **2014**, *14*, 901.
176. Y. Zhu, J. L. Han, J. D. Wang, N. Shibata, M. Sodeoka, V. A. Soloshonok, J. A. S. Coello, F. Dean. Toste, *Chem. Rev.* **2018**, *118*, 3887.

177. T. D. Beeson, D. W. C. MacMillan, *J. Am. Chem. Soc.* **2005**, *127*, 8826-8828.
178. D. D. Steiner, N. Mase, C. F. Barbas III, *Angew. Chem. Int. Ed.* **2005**, *44*, 3706.
179. A. E. Allen, D. W. C. MacMillan, *J. Am. Chem. Soc.* **2010**, *132*, 4986.
180. Q. H. Deng, H. Wadepohl, L. H. Gade, *Chem. Eur. J.* **2011**,*17*, 14922.
181. P. Hewawasam, V. K. Gribkoff, Y. Pendri, S. I. Dworetzky, N. A. Meanwell, E. Martinez, C. G. Boissard, D. J. Post-Munson, J. T. Trojnacki, K. Yeleswaram, L. M. Pajor, J. Knipe, Q. Gao, R. Perrone, J. E. Starrett, *Bioorg. Med. Chem. Lett.* **2002**, *12*, 1023.
182. V. K. Gribkoff, J. E. Starrett, S. I. Dworetzky, P. Hewawasam, C. G. Boissard, D. A. Cook, S. W. Frantz, K. Heman, J. R. Hibbard, K. Huston, G. Johnson, B. S. Krishnan, G. G. Kinney, L. A. Lombardo, N. A. Meanwell, P. B. Molinoff, R. A. Myers, S. L. Moon, A. Ortiz, L. Pajor, R. L. Pieschl, D. J. Post-Munson, L. J. Signor, N. Srinivas, M. T. Taber, G. Thalody, J. T. Trojnacki, H. Wiener, K. Yeleswaram, S. W. Yeola, *Nat. Med.* **2001**, *7*, 471.
183. Q. H. Deng, H. Wadepohl, L. H. Gade, *J. Am. Chem. Soc.* **2012**, *134*, 10769.
184. A. Granados, I. Rivilla, F. P. Cossío, A. Vallribera, *Chem. Eur. J.* **2019**, *25*, 8214.
185. A. Granados, P. Sarró, A. Vallribera, *Molecules* **2019**, *24*, 1141.
186. S. Guizzetti, M. Benaglia, J. S. Siegel, *Chem. Commun.* **2012**, *48*, 3188.
187. L. A. Carpino, B. J. Cohen, K. E. Stephens Jr., S. Y. Sadat-Aalaee, J. H. Tien, D. C. Langridge, *J. Org. Chem.* **1986**, *51*, 3732.
188. K. A. Ahrendt, C. J. Borths, D. W. C. MacMillan, *J. Am. Chem. Soc.* **2000**, *122*, 4243.
189. J. Y. Shi, C. A. Wang, Z. J. Li, Q. Wang, Y. Zhang, W. Wang, *Chem. Eur. J.* **2011**, *17*, 6206.
190. R. Sophie, H. Bence, S. Rosario, W. Jerome, *Chem. Eur. J.***2016**, *22*, 11997.
191. M. Inouye, K. Tsuchiya, T. Kitao, *Angew. Chem. Int. Ed. Engl.* **1992**, *31*, 204.
192. A. J. Woodhead, H. Angove, M. G. Carr, G. Chessari, M. Congreve, J. E. Coyle, J. Cosme, B. Graham, P. J. Day, R. Downham, L. Fazal, R. Feltell, E. Figueroa, M. Frederickson, J. Lewis, R. McMenmin, C. W. Murray, M. A. O'Brien, L. Parra, S. Patel, T. Phillips, D. C. Rees, S. Rich, D. M. Smith, G. Tremartha, M. Vinkovic, B. Williams, A. J.A. Woolford, *J. Med. Chem.* **2010**, *53*, 5956.
193. D. H. Bach, J. Y. Liu, W. K. Kim, J. Y. Hong, S. H. Park, D. Kim, S. N. Qin, T. T. T. Luu, H. J. Park, Y. N. Xu, S. K. Lee, *Biorg. Med.Chem*. **2017**, *25*, 3396.
194. W. Flitsch, H. Peters, *Tetrahedron Lett*. **1969**, *10*, 1161.
195. W. Flitsch, H. Peters, *Chem. Ber.* **1970**, *103*, 805.
196. F. Konrad, J. L. Fillol, H. Wadepohl, L. H. Gade, *Inorg. Chem.* **2009**, *48*, 8523.
197. F. Konrad, J. L. Fillol, C. Rettenmeier, H. Wadepohl, L. H. Gade, *Eur. J. Inorg. Chem.* **2009**, 4950.
198. H. Vorbrggen, K. Krolikiewicz, *Tetrahedron Lett.* **1981**, *22*, 4471.
199. G. Fernández, R. Pleixats, *ChemistrySelect* **2018**, *3*, 11486.
200. D. P. Allen, M. Van Wingerden, R. H. Grubbs, *Org. Lett.* **2009**, *11*, 1261.
201. A. Monge-Marcet, R. Pleixats, X. Cattoën, M. Wong Chi Man, *J Molec Catal. A Chem.* **2012**, *357*, 59.
202. M. Ferré, X. Cattoën, M. Wong Chi Man, R. Pleixats, *ChemCatChem* **2016**, *8*, 2824.
203. H. Li, M. Pérez-Trujillo, X. Cattoën, R. Pleixats, *ACS Sustainable Chem. Eng.* **2019**, *7*, 14815.

CHAPTER 3

PREPARATION OF PERIODIC MESOPOROUS ORGANOSILICA NANOPARTICLES FOR APPLICATION IN HIGH-INTENSITY ULTRASOUND FOCUSED BASED THERAPIES

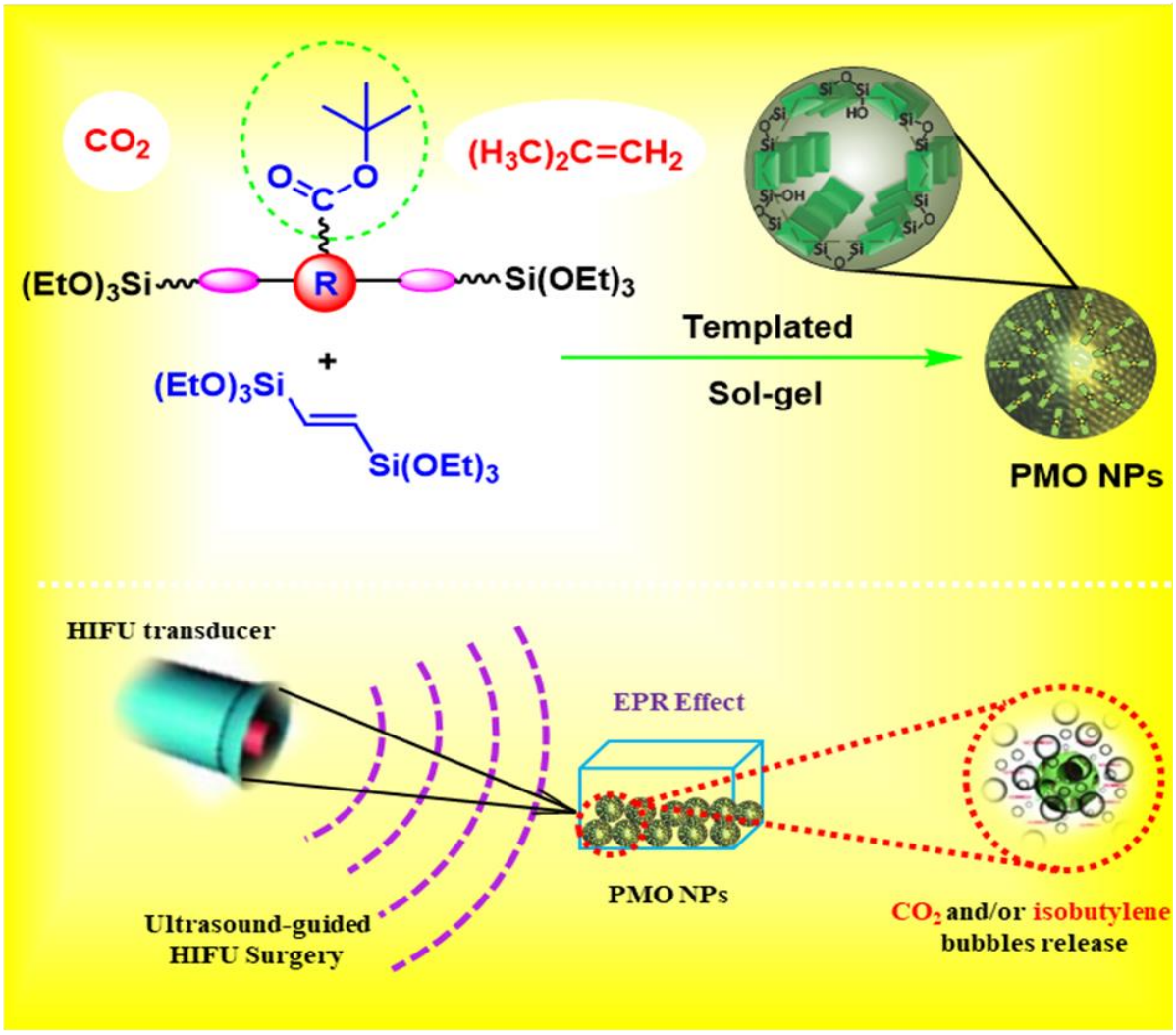

H. Li, C. Gascó, A. Delalande, C. Charnay, L. Raehm, P. Midoux, C. Pichon, R. Pleixats,* J. -O. Durand,* Periodic Mesoporous Organosilica Nanoparticles with BOC group, towards HIFU responsive agents. *Molecules* **2020**, *25*(4): 974. DOI: 10.3390/molecules25040974

H. Li, L. Raehm, C. Charnay, J. -O. Durand,* R. Pleixats,* Preparation and Characterization of Novel Mixed Periodic Mesoporous Organosilica Nanoparticles. *Materials* **2020**, *13*(7): 1569. DOI: 10.3390/ma13071569

CHAPTER 3

PREPARATION OF PERIODIC MESOPOROUS ORGANOSILICA NANOPARTICLES FOR APPLICATION IN HIGH-INTENSITY FOCUSED ULTRASOUND BASED THERAPIES

3.1 Introduction

High intensity focused ultrasound (HIFU), also called focused ultrasound surgery (FUS),[1] is a minimally invasive surgical technique for the thermal ablation of both malignant and benign tumors and cessation of internal bleeding in injured vessels and organs with little damage to the surrounding tissue. It is one of the most promising non-invasive and non-radiative transcutaneous therapeutic modalities for the therapy of cancers and non-neoplastic diseases including breast cancer, liver cancer, pancreas cancer, kidney cancer, prostate cancer, brain cancer, uterine fibroids, etc.[2-11] HIFU has also been used in the treatment of bone tumours[12] and its uses are expanding into new areas such as the treatment of neurological disorders[13] and pain management.[14] This method offers better precision, lower cost, decreased morbidity and mortality rates, and shorter recovery time.[15-16] In HIFU ablation, high intensity ultrasound pulses are concentrated into a cigar-shaped focal zone with millimeter orthogonal resolution.[3,17] At sufficiently high acoustic powers, HIFU can generate a rapid temperature increase (up to 70-80 °C) in the tissue and almost immediately cause the formation of necrotic tissue (**Figure 3.1**).[18-19]

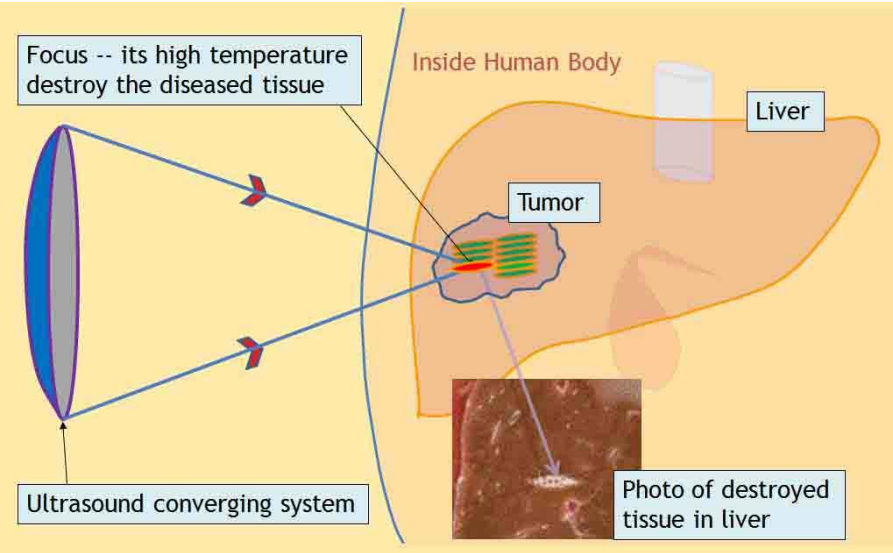

Figure 3.1 The principle of High Intensity Focused Ultrasound (HIFU)

Generally, HIFU is used in conjunction with chemotherapy, radiotherapy and radio-frequency ablation, combining simultaneous imaging and site-specific therapy, consisting in a truly non-invasive treatment that is capable of inducing coagulative necrosis at a precise focal point by thermal effect (ultrasound) monitored during the whole therapy at real time.

Despite of many promising outcomes, there are some limitations for the clinical application of this therapeutic approach because of its relatively low therapeutic resolution and efficacy, making that the treatment results are, often, not ideal. These limitations are due to the high attenuation of the ultrasound intensity with penetration depth. Actually, a solution could be to enhance the acoustic power or the exposition time, however it would increase the risk of side effects, such as skin burns and nerve injury.[16,20-22] It is a great challenge to reduce the normal tissue damage and mitigate the pain of patients receiving HIFU surgery and achieve better therapeutic effects.[23]

In order to overcome these limitations, scientists employ various types of micro- and nano-bubbles,[24] as well as theranostic nanoparticles[25] (which combine therapeutic and diagnostic capabilities) based on biocompatible nano/microparticles that contains synergistic agents used to change the acoustic environment of tissues, increasing the ultrasound energy or enhancing the image to improve monitoring of therapy.[25-35] Theoretically, upon HIFU stimulation, gas bubbles will be generated from the temperature-sensitive compound inside the nanocarrier, dramatically changing the acoustic environment of the tumor for enhanced ultrasound imaging and HIFU ablation. However, such gas-releasing strategy needs the exogenous HIFU pre-stimulation, wherein gas release and HIFU irradiation take place simultaneously without pre-imaging guidance. Organic nanoemulsions (biocompatible polymers, lipids, liposomes) containing a relatively volatile fluorinated compound[36] or a perfluorocarbon gas in its interior[37] have been proposed as contrast agents and synergic agents. The heat produced by HIFU irradiation lead to the release of gas or the vaporization of liquid, forming nanobubbles of gas which then become microbubbles that increase the therapeutic efficiency and/or improve the ultrasound image. However, these organic materials are not robust and stable enough. On the other hand, MSNs, dopped MSNs and PMO NPs offer advantages such as high thermal and chemical stability, excellent biocompatibility/degradability and resistance to the erosion.

In 2016, Min and co-workers developed a new strategy by devising chemical gas (CO_2) generating carbonate copolymer nanoparticles (Gas-NPs), which were clearly distinguished

from the conventional gas-encapsulated micro-sized ultrasound contrast agents. More importantly, Gas-NPs could be readily engineered to strengthen the desirable *in vivo* physicochemical properties for nano-sized drug carriers with higher tumor targeting ability, as well as the high quality of echo properties for tumor-targeted ultrasound imaging. This technology could serve a highly effective platform in building theranostic ultrasound contrast agents with great sophistication and therapeutic applicability in tumor-targeted ultrasound imaging and ultrasound-triggered drug delivery.[38]

In 2017, a multiscale hybrid catalytic nanoreactor has been developed as a tumor-sensitive contrast and synergistic agent for ultrasound-guided HIFU cancer surgery, by integrating dendritic-structured mesoporous organosilica nanoparticles (MONs) and catalase immobilized in the large open pore channels of MONs.[39] Such a hybrid nanoreactor exhibited sensitive catalytic activity toward H_2O_2, facilitating the continuous O_2 gas generation in a relatively mild manner even if incubated with 10 μM H_2O_2, which finally led to enhanced ablation in the tissue-mimicking PAA gel model after HIFU exposure, mainly resulting from intensified cavitation effect. These catalase@MONs could be accumulated within the H_2O_2-enriched tumor region through enhanced permeability and retention (EPR) effect, enabling durable contrast enhancement of ultrasound imaging, and highly efficient tumor ablation under relatively low power of HIFU exposure *in vivo*. Very different from the traditional perfluorocarbon-based contrast and synergistic agent, such an on-demand catalytic nanoreactor could realize the accurate positioning of tumor without HIFU pre-stimulation, and efficient HIFU ablation with a much safer power output which is highly desired in clinical HIFU application.[39] As a summary, these enhancement agents are indeed able to enhance HIFU-associated mechanical effects, providing cavitation nuclei,[40-41] increasing the acoustic attenuation with a consequent temperature rise,[42] reducing the ultrasound intensity and the exposure time required to obtain bioeffects[43] and enhancing the final therapeutic effect.[44]

Hollow periodic mesoporous organosilica nanoparticles (HPMO NPs) are versatile in HIFU synergistic therapy (**Figure 3.2**).[45] HPMO NPs can be transported intravascularly due to their high dispersity and sub-micrometer size. Then, HPMO NPs enter the tumor tissues via the typical enhanced permeability retention (EPR) effect.[46-48] In vitro generated ultrasound can be focused on the tumor tissues based on the tissue penetration capability of ultrasound. The presence of HPMO NPs with unique hollow structures can change the acoustic environment

of tumor tissues to enhance the deposition of ultrasound energy and synergistically improve the HIFU therapeutic efficiency. In 2014, Chen and co-workers used DOX-loaded phenylene-bridged HPMO NPs for *in vivo* HIFU-actuated drug delivery via a photothermal mechanism.[45] They give the first evidence that mesoporous material-based drug delivery nanosystems (e.g., HPMO NPs) can improve the efficiency of focused ultrasound for cancer surgery, which can be further extended for the development of novel HIFU-based therapeutic modalities for more efficient cancer therapy with mitigated side-effects.[45] Moreover, they also used Paclitaxel-loaded HPMO NPs for efficient *in vivo* HIFU-actuated imaging, thanks to the contrast enhancement in ultrasonography image observed after the administration of the NPs.[49] In 2015, phenylene-bridged HPMO NPs were described for the co-delivery of DOX and genes to fight multidrug resistance of cancer cells by Shi's group.[50] A power-dependent HIFU-enhanced release of DOX was also obtained with HPMO NPs designed by co-condensation of phenylene and tetrasulfide based organo-bridged alkoxysilanes.[51] The use of glutathione could also enhance the release of the drug in solution, and *in vitro* and *in vivo* studies showed high anti-cancer efficiencies via HIFU combined therapy.

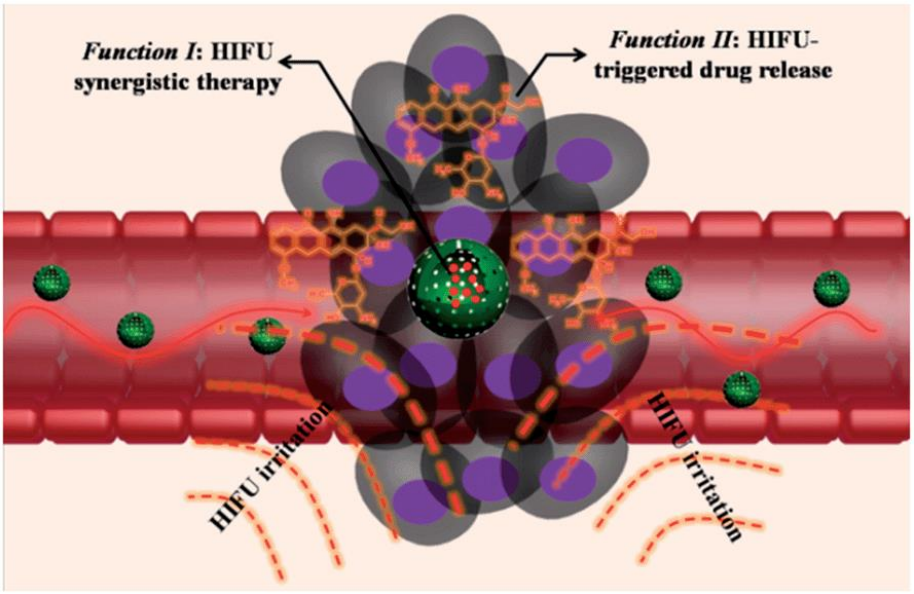

Figure 3.2 Schematic illustration of HPMO NPs-based HIFU synergistic therapy combined with HIFU-triggered drug release. Reproduced with permission from Royal Society of Chemistry.[45]

Therefore, in order to achieve higher efficiency and more safety for HIFU surgery, new gas-releasing strategies are highly desired in order to realize precise pre-imaging guidance and to further reduce the HIFU power output. As mentioned before, some few important results have been achieved based on the combination of PMO NPs and HIFU techniques. We

propose in this thesis a new and challenging gas-releasing strategy, which is based on a series of PMO NPs containing temperature-sensitive *tert*-butyl esters or *N*-Boc groups that can release CO_2 and/or isobutylene upon cleavage under the HIFU power.

3.2 Objectives

Based on the previous introduction, we intended to prepare a series of PMO NPs which contain *tert*-butoxycarbonyl groups to be tested as contrast agents in High Intensity Focused Ultrasound (HIFU) technique. These nanomaterials are expected to release CO_2 and/or isobutene from the temperature-sensitive COO^tBu group (Boc group) under high intensity focused ultrasound conditions. This release would result in the formation of nano/microbubbles that should improve the ultrasound image from HIFU and increase the therapeutic efficacy of the technique. For that purpose, we planned the following specific objectives:

a) The synthesis of disilylated and tetrasilylated precursors containing *tert*-butyl esters or *N*-Boc groups (**Figure 3.3**). Various compounds are envisaged, which differ in the length of the spacer, the functionality (sulfide, carbamate, triazole ring) contained in this spacer, the number of Boc or $CO_2{}^tBu$ groups (1 or 3) present in the molecule and the number of silylated moieties (2 or 4). Our idea was to study the influence of all these structural features on the properties of the nanomaterials derived from these precursors in order to find the best one for our purposes. The increase in the number of silylated functions would be advantageous for obtaining pure PMO NPs and we expected that an increase in the number of Boc/*tert*-butyl ester groups would result in a greater efficiency in the production of microbubbles under HIFU conditions.

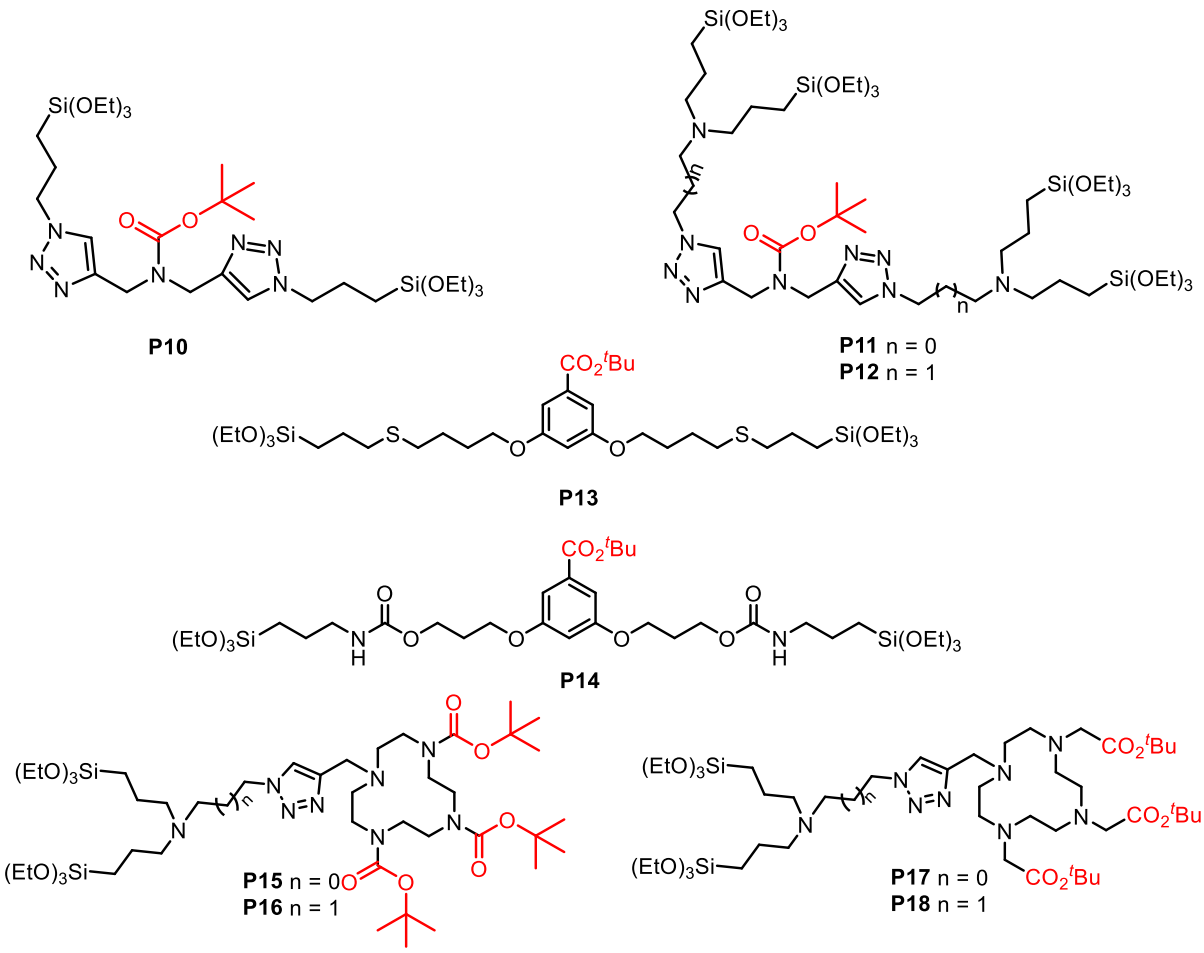

Figure 3.3 Proposed disilylated or tetrasilylated precursors for preparation of PMO NPs

b) The preparation of PMO NPs from these precursors and the characterization of all these new nanomaterials with appropriate techniques, such as ^{13}C CP MAS solid state NMR, electron microscopy, nitrogen-sorption measurements, dynamic light scattering, zeta-potential, infrared spectroscopy and powder X-ray diffraction. .

c) The assay of the prepared nanomaterials in the HIFU technique to verify the formation of nano/microbubbles as a first step to consider these materials as useful candidates for the biomedical application.

3.3 Results and Discussion

In this section, we describe the synthesis of the silylated precursors **P10-P18,** the preparation and characterization of PMO NPs derived from them and the results of HIFU experiments using the as-prepared nanomaterials.

3.3.1 Synthesis of silylated organic precursors containing *tert*-butoxycarbonyl groups

As we have mentioned in the objectives, first we needed to synthesize a series of di- or tetrasilylated organic precursors containing *tert*-butoxycarbonyl groups, either *tert*-butyl esters or Boc-protected amine derivatives. Under the thermal conditions generated *in situ* by high intensity ultrasound irradiation, the PMO NPs derived from these precursors can release CO_2 and/or isobutylene. Cleavage of Boc group on N is generally achieved under acidic conditions (**Scheme 3.1**). However, thermal deprotection has also been described in the literature.[52-55] Some authors reported that *N*-Boc can be removed by heating at 90-100 °C in water to generate CO_2.[56-57]

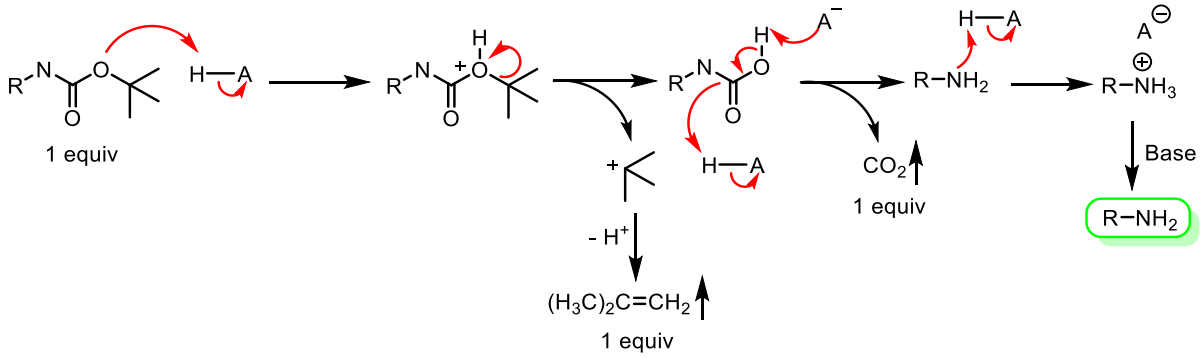

Scheme 3.1 The mechanism of *N*-Boc group cleavage to release CO_2 and isobutylene under acidic conditions.

Similarly, although *tert*-butyl esters are usually hydrolyzed to the corresponding carboxylic acids in aqueous phosphoric acid, thermal cleavage has also been reported with the release of isobutene (**Scheme 3.2**).[58-61]

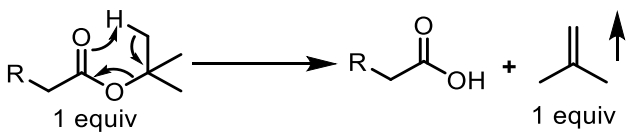

Scheme 3.2 Proposed mechanism for thermal cleavage of *tert*-butyl esters to release isobutylene

3.3.1.1 Synthesis of the silylated organic precursors P10-P12 containing *N*-Boc groups

The three precursors **P10**, **P11** and **P12** can be obtained by a copper-catalyzed azide alkyne cycloaddition (click reaction, CuAAC)[62-63] of the suitable dialkyne with the corresponding silylated azide (**Scheme 3.3**).

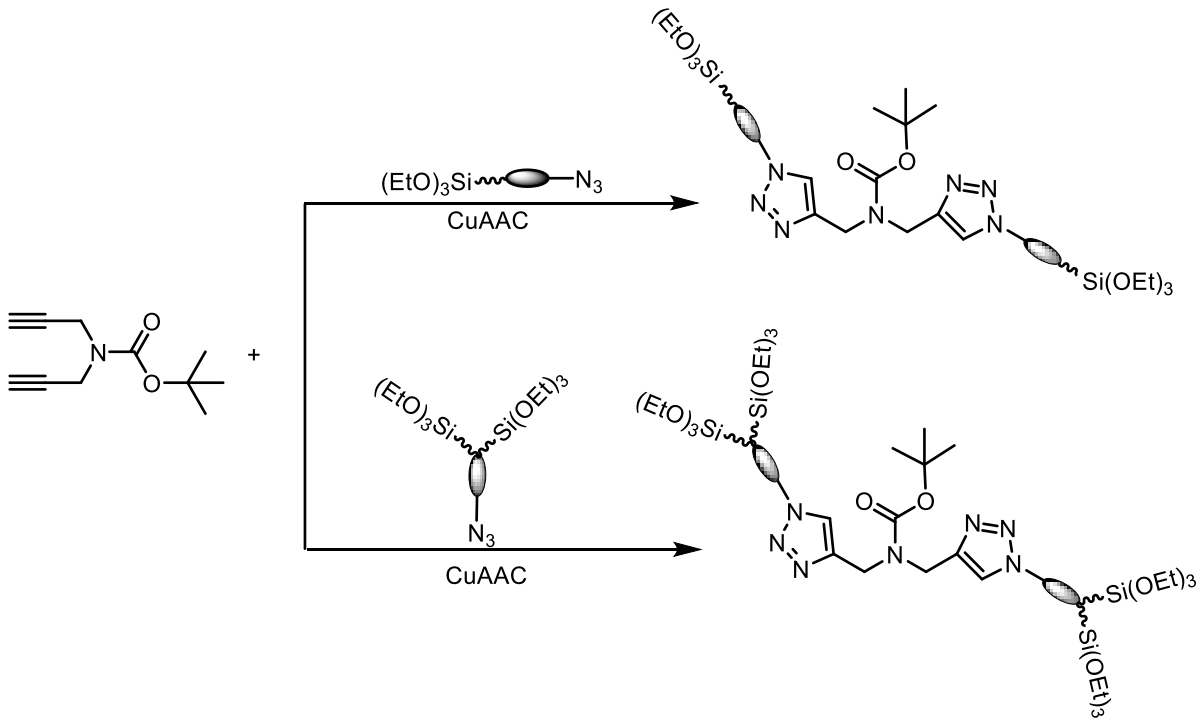

Scheme 3.3 Approach for the synthesis of bridged organosilane precursors by using CuAAC.

N-Boc protection of propargyl amine **61** furnished compound **62** in 91% yield, which was reacted with propargyl bromide in the presence of NaH in anhydrous THF to afford dialkyne **63** in quantitative yield (**Scheme 3.4**).[64]

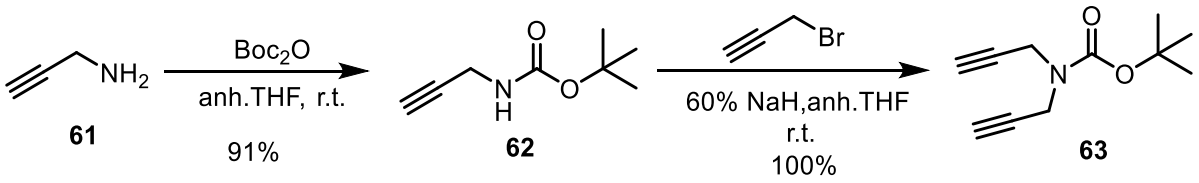

Scheme 3.4 Synthesis of *tert*-butyl di(prop-2-yn-1-yl)carbamate

The disilylated precursor **P10** was obtained by the reaction of dialkyne **63** with (3-azidopropyl)triethoxysilane **10** under copper(I) catalysis under anhydrous conditions.[65] First, the copper catalyst [$CuBr(PPh_3)_3$] was used, but we found that it was difficult to remove it from the crude mixture by washings with different solvents after the reaction. Then, CuI was

chosen as copper source and tris[(1-benzyl-1*H*-1,2,3-triazol-4-yl)methyl]amine (TBTA) as a ligand that stabilizes Cu(I) ions, in a 1:1 mixture of anhydrous Et_3N/anhydrous THF at 50 ºC overnight (**Scheme 3.5**). After the work-up, the disilylated precursor **P10** was obtained in 73% yield. It is worth to point out that this compound was purified by washing with hot anhydrous pentane several times. Part of the compound remains dissolved in pentane, explaining the lower isolated yield.

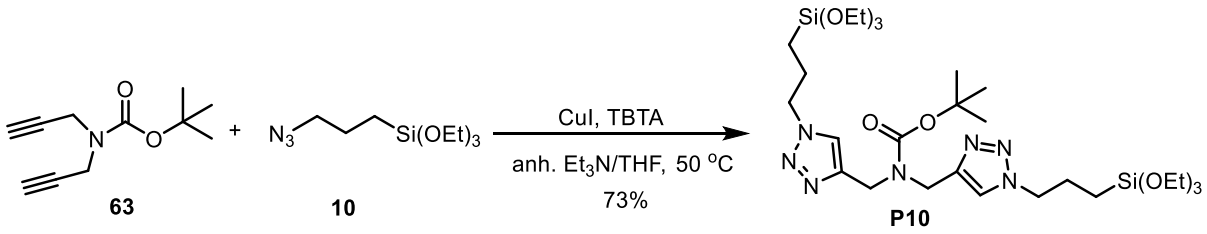

Scheme 3.5 Synthesis of disilylated precursor **P10**

Similarly, the other two silylated precursors **P11** and **P12** were obtained in 96% yield by reacting the corresponding bis(silylated azide) with dialkyne **63** under the same reaction conditions (**Scheme 3.6**).

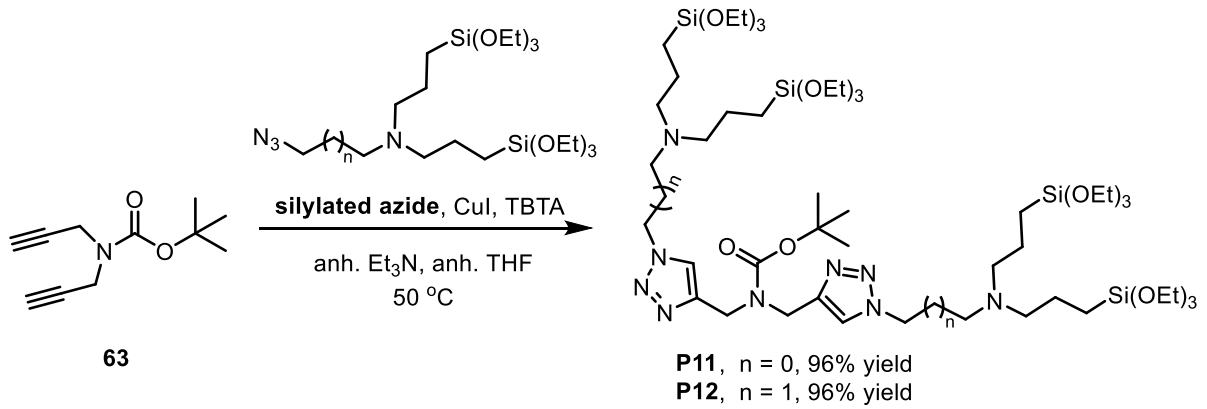

Scheme 3.6 Synthesis of silylated precursors **P11** and **P12**

3.3.1.2 Synthesis of disilylated organic precursors P13-P14 containing *tert*-butyl esters

For the synthesis of **P13** and **P14**, the master student Carolina Gascó in our group had already done some work in the early stage (**Scheme 3.7**). As you can see, the synthetic route starting from 3,5-dihydroxybenzoic acid was quite short, but the efficiency of each step was low or very low. Unfortunately, **P13** was not obtained and only traces of **P14** were observed.[66]

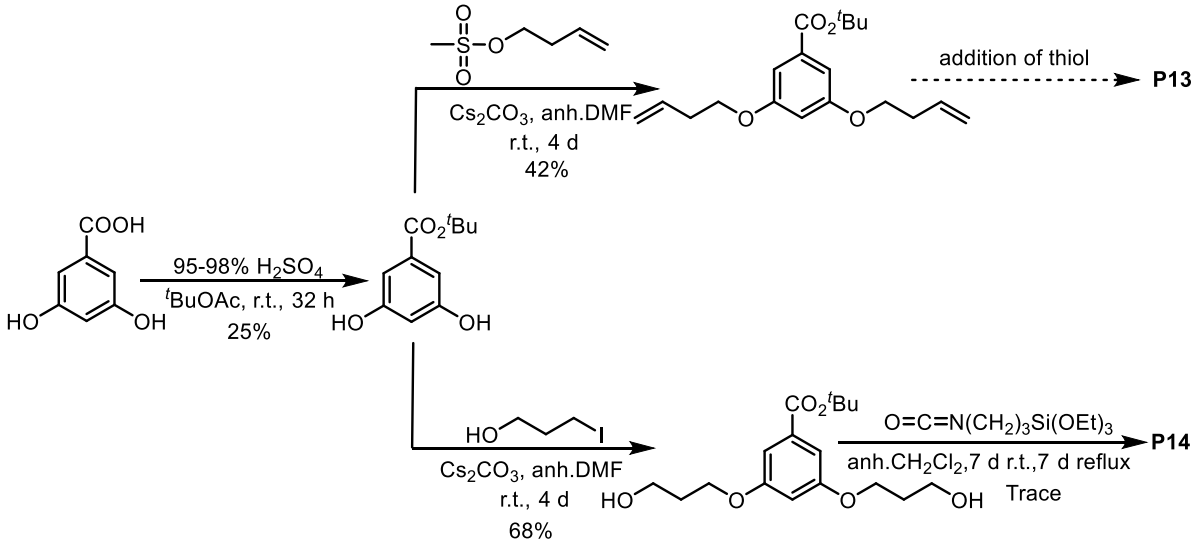

Scheme 3.7 Synthesis of **P13** and **P14** assayed by the master student Carolina Gascó

In order to improve the preparation of these precursors, we redesigned the synthetic route starting with commercial 3,5-dihydroxybenzaldehyde (**Scheme 3.8**). After suitable di-O-alkylation, oxidation of the aldehyde group to the carboxylic acid is required, followed by the formation of *tert*-butyl ester. Finally, we would obtain **P13** and **P14** through the appropriate reactions in each case.

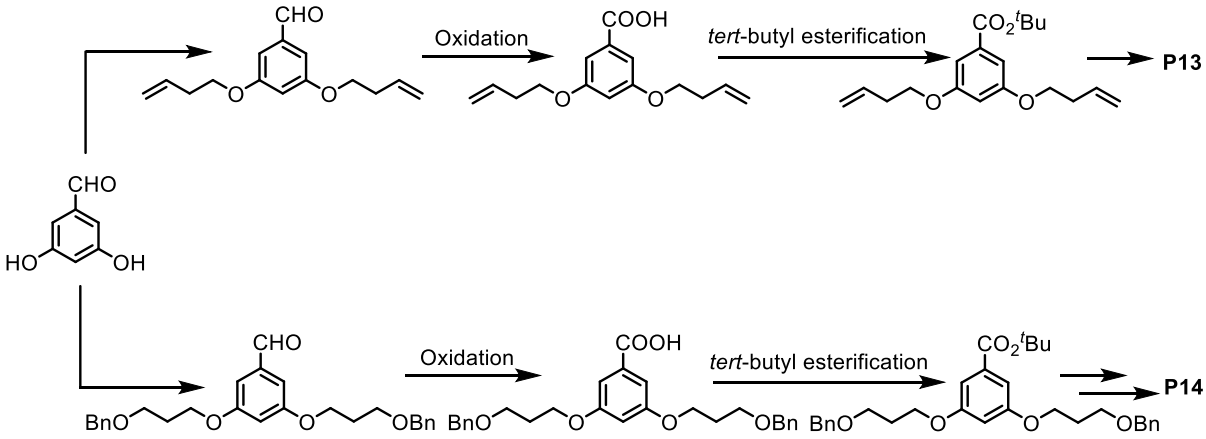

Scheme 3.8 Proposed synthesis for **P13** and **P14** from 3,5-dihydroxybenzaldehyde

For the synthesis of **P13**, we first converted 3-buten-1-ol **64** into but-3-en-1-yl methanesulfonate **65** according to the literature.[67] The dialkylation of 3,5-dihydroxybenzaldehyde **66**, with the mesylate **65**, in the presence of cesium carbonate in DMF at 40 ºC, afforded **67** in 78% isolated yield after chromatographic purification. The

aldehyde **67** was oxidized to the carboxylic acid **68** by using $NaClO_2$, 30% H_2O_2 and NaH_2PO_4 in acetonitrile at room temperature (**Scheme 3.9**).[68]

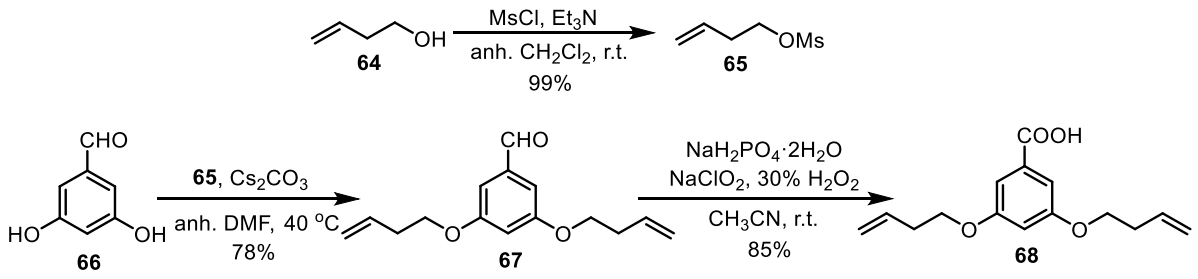

Scheme 3.9 Synthesis of 3,5-bis(but-3-en-1-yloxy)benzoic acid **68**

In principle, the formation of *tert*-butyl esters is a well-known reaction that can be performed under different conditions. We tested three different methods (**Table 3.1**), but in our case the reaction did not succeed under the conditions described in entry 1[69] and entry 2.[70] In both cases, only a small amount of product was formed after a long reaction time, and the starting material was mainly recovered. Fortunately, when we used Boc_2O and 4-dimethylaminopyridine (DMAP) in *tert*-butanol at room temperature, we achieved the ester **69** in 87% isolated yield (entry 3, **Table 3.1**).

Table 3.1 Conditions used for the preparation of *tert*-butyl ester **69**

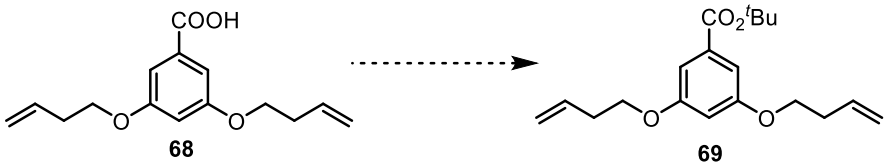

Entry	Reagents	Solvent	Temperature (°C)	Time (h)	Result
1	95-98% H_2SO_4 + ^{t}BuOAc	^{t}BuOAc	r. t.	64	11% yield of **69** 52% recovery of **68**
2	$Cl_3C(C{=}NH)OBu$, $BF_3{\cdot}OEt_2$	CH_2Cl_2	r. t.	96	6% yield of **69** 82% recovery of **68**
3	DMAP, Boc_2O	^{t}BuOH	r. t.	48	87% yield of **69**

Finally, the precursor **P13** was obtained in 70% isolated yield by the versatile thiol-alkene click reaction between dialkene **69** and (3-mercaptopropyl)triethoxysilane under irradiation at 365 nm using 2,2-dimethoxy-1,2-diphenylethanone (DMPA) as initiator (**Scheme 3.10**).[71]

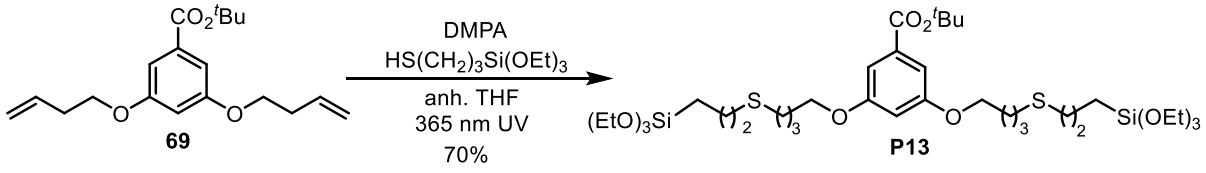

Scheme 3.10 Synthesis of precursor **P13**

For the preparation of precursor **P14**, we first synthesized ((3-iodopropoxy)methyl)benzene **72** (65% overall yield) from the commercially available 1,3-propanediol **70**, through the monobenzylated intermediate **71** (**Scheme 3.11**).[72]

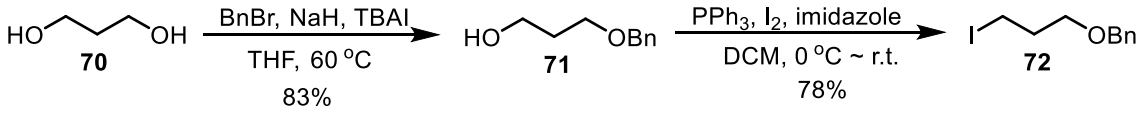

Scheme 3.11 Synthesis of ((3-iodopropoxy)methyl)benzene **22**

Then 3,5-dihydroxybenzaldehyde **66** was dialkylated with the iodide **72** to obtain compound **73**. The next steps were oxidation to the carboxylic acid **74**, formation of *tert*-butyl ester **75**, followed by deprotection of benzylic ethers, leading to the obtention of diol **76** in high yield. Subsequent treatment with the suitable silylated isocyanate provided the disilylated carbamate precursor **P14** (**Scheme 3.12**).

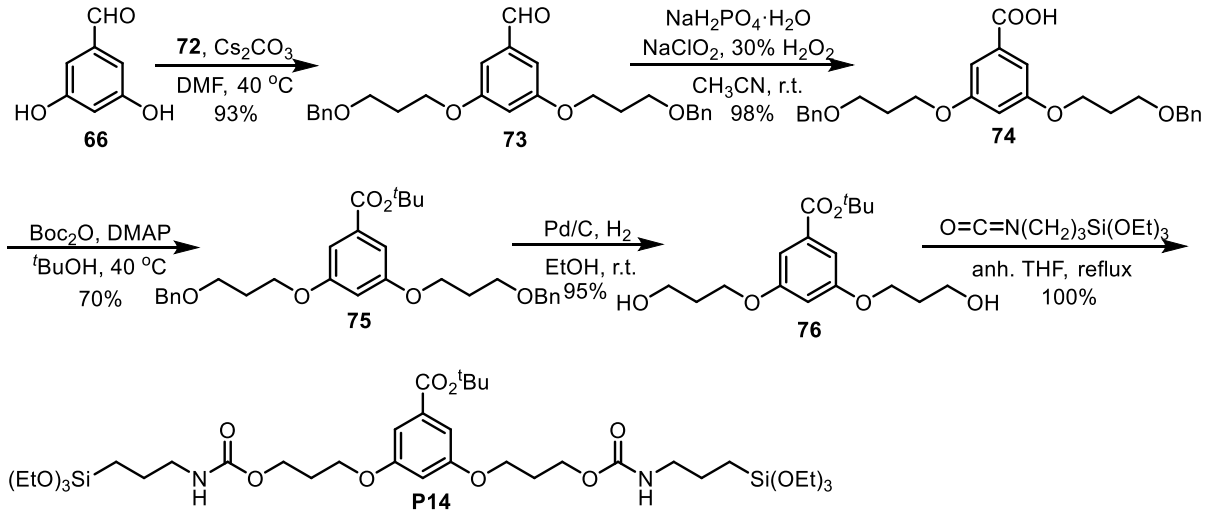

Scheme 3.12 Synthesis of precursor **P14**

3.3.1.3 Synthesis of disilylated organic precursors P15-P18 containing three Boc or *tert*-butyl ester groups

In order to obtain a more significant effect, we designed the following molecules containing multiple Boc or *tert*-butyl ester groups (**Figure 3.4**).

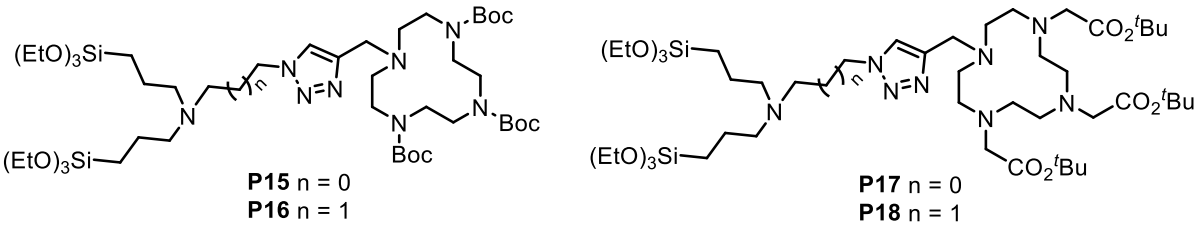

Figure 3.4 The disilylated precursors containing three Boc or *tert*-butyl ester groups

The retrosynthetic analysis of precursors **P15** and **P16** is depicted in **Scheme 3.13**. Commercial cyclen (1,4,7,10-tetraazacyclododecane) could be first reacted with Boc_2O to introduce three Boc groups and then with propargyl bromide to introduce the alkyne moiety. The desired silylated precursors would then be obtained by a copper-catalyzed alkyne-azide cycloaddition reaction (CuAAC)[62-63] of the alkyne function with the corresponding silylated azides.

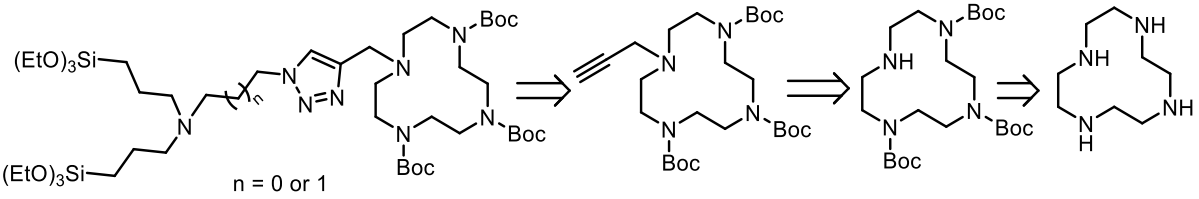

Scheme 3.13 Retrosynthetic analysis of the precursors **P15** and **P16**

The alkyne **79** was obtained in two steps from the commercial cyclen **77** through the *tri*-Boc intermediate **78** following procedures described in the literature (**Scheme 3.14**).[73-74]

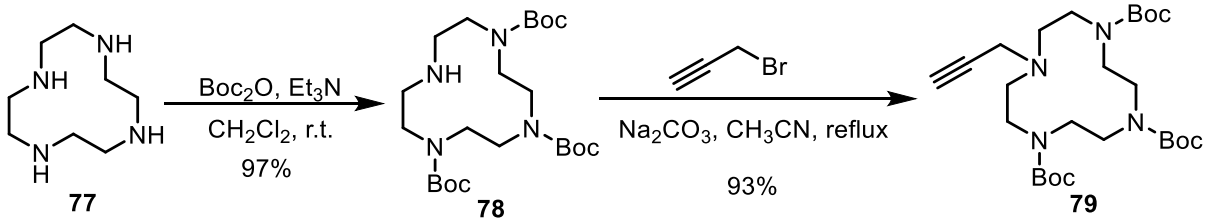

Scheme 3.14 Synthesis of compound **79**

A copper-catalyzed alkyne azide cycloaddition reaction (CuAAC)[62-63] of the alkyne **79** with the corresponding bis-silylated azide, under our previously developed method in anhydrous conditions, provided the disilylated precursors **P15** and **P16** in 93% and 88% isolated yields, respectively (**Scheme 3.15**).

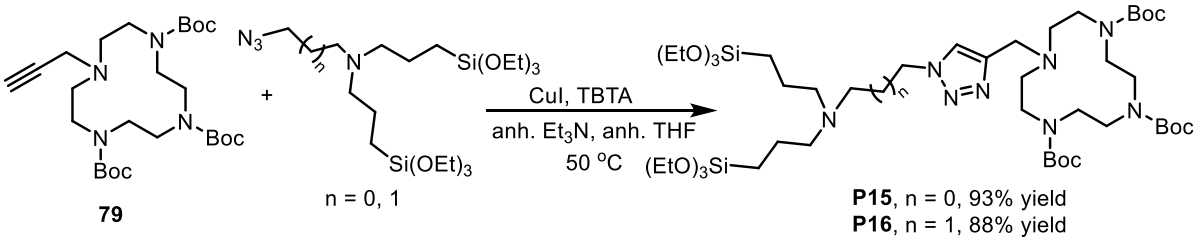

Scheme 3.15 Synthesis of precursors **P15** and **P16**

Compounds **P15** and **P16** (**Figure 3.5**) were fully characterized by ^{1}H and ^{13}C NMR spectroscopy. The complete characterization of the molecules was achieved by the performance of a battery of 1D and 2D NMR experiments (1D ^{1}H, 2D ^{1}H-^{1}H COSY, TOCSY and NOESY, 2D ^{1}H-^{13}C HSQC and HMBC) and the coordinated analysis of the resulting spectra. The assignment of the signals in the ^{1}H NMR spectrum of both compounds is presented in **Figure 3.6**.

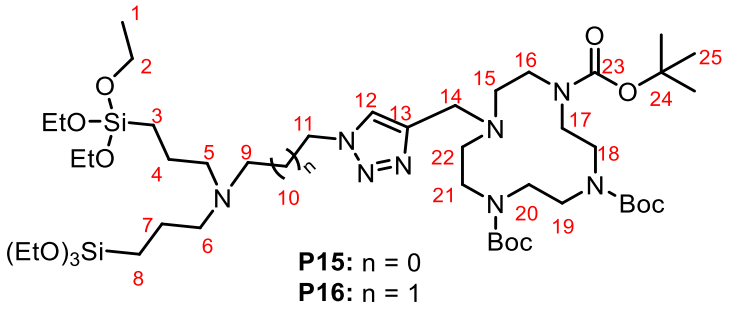

Figure 3.5 Structure of compounds **P15** and **P16**. Numbers assigned to the C atoms.

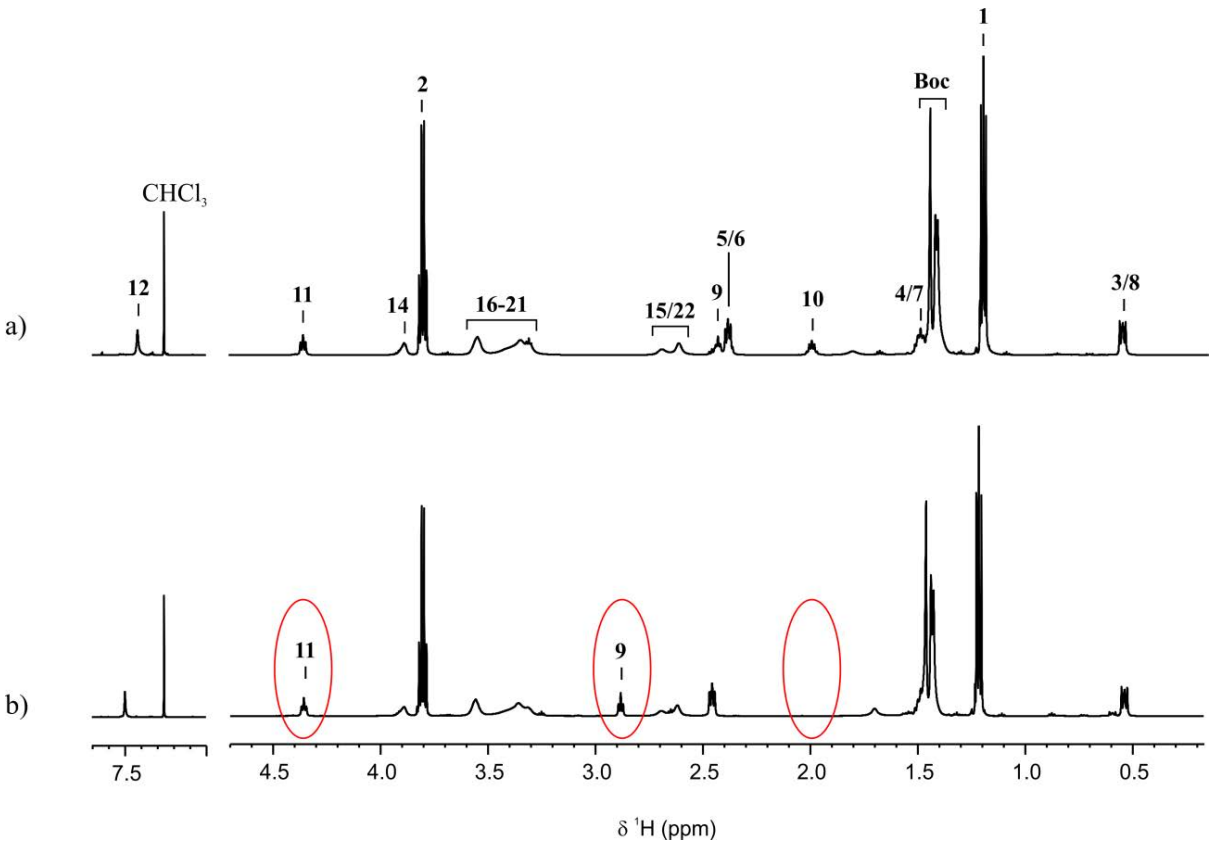

Figure 3.6 Assigned ^{1}H-NMR spectra of samples corresponding to (a) compound **P16** and (b) compound **P15**. Spectra acquired at 298.0 K and at a magnetic field of 600 MHz.

^{1}H-NMR spectra of compounds **P15** and **P16** present some similarities, such as the signals of the cyclen moiety (H15 to H22 peaks); the presence of peaks corresponding to H12 (aromatic peak at 7.42 and 7.50 ppm, respectively) and H14 (broad singlet at 3.89 ppm for both compounds), and signals of protons H1 to H8. As expected, the signal of H11 (triplet at 4.35 ppm for both molecules) is highly deshielded with respect to the original peak of the azide reactant (3.32 ppm in case of the azide with a three carbon chain). The main differences between molecules **P15** and **P16** spectra are the lack of H10 peak in **P15** and the deshielding of H9 signal in **P15** with respect to **P16** (2.88 and 2.44 ppm, respectively), due to the proximity to the triazole ring. Results from 2D NMR correlations, such as TOCSY, NOESY and HMBC, confirmed both structures. Also, peak integrations were in accordance with them. The full ^{1}H and ^{13}C characterization of **P15** and **P16** is collected in **Table 2** (collaboration with Míriam Pérez from the NMR Service at UAB)

Table 3.2 ^{1}H and ^{13}C NMR chemical shifts and H-H *J* couplings of **P15** and **P16**.

	P16			P15		
	^{1}H		^{13}C	^{1}H		^{13}C
Id	**δ (^{1}H)**	**(mult.,* $J_{H,H}$)**	**δ (^{13}C)**	**δ (^{1}H)**	**(mult.,* $J_{H,H}$)**	**δ (^{13}C)**
	[ppm]	[Hz]	[ppm]	[ppm]	[Hz]	[ppm]
1	1.209	t, $^{3}J_{1-2}$ = 7.0	18.46	1.214	t, $^{3}J_{1-2}$ = 7.0	18.41
2	3.803	q, $^{3}J_{2-1}$ = 7.0	58.48	3.802	q, $^{3}J_{2-1}$ = 7.0	58.27
3	0.565	dd, $^{3}J_{3-4}$ = 7.0 $^{3}J_{3-4'}$ = 9.5	8.12	0.537	dd, $^{3}J_{3-4}$ = 7.8 $^{3}J_{3-4'}$ = 9.3	7.92
4	1.502	m	20.36	1.485	m	20.28
5	2.392	t, $^{3}J_{5-4}$ = 7.4	56.98	2.456	t, $^{3}J_{5-4}$ = 7.5	57.18
6	= 5			= 5		
7	= 4			= 4		
8	= 3			= 3		
9	2.437	t, $^{3}J_{9-10}$ = 6.6	51.02	2.881	t, $^{3}J_{9-11}$ = 6.8	54.21
10	2.004	tt, $^{3}J_{10-11}$ = 7.4 $^{3}J_{10-9}$ = 6.6	28.56	X		X
11	4.354	t, $^{3}J_{11-10}$ = 7.4	48.64	4.354	t, $^{3}J_{11-9}$ = 6.8	48.88
12	7.424	s (br)	123.21	7.501	s (br)	123.73
13	-		141.96	-		141.60
14	3.886	s (br)	45.33	3.890	s (br)	45.13
15	[2.70-2.62]	m (br)	[54.5-53.0]	[2.69-2.62]	m (br)	[54.3-53.1]
16	[3.55-3.40]	"	[49.8-47.6]	[3.56-3.31]	"	[50.1-47.5]
17	"	"	"	"	"	"
18	"	"	"	"	"	"
19	"	"	"	"	"	"
20	"	"	"	"	"	"
21	"	"	"	"	"	"
22	=15			=15		
23 (Boc)	-	156.33/155.88/155.53		-	156.33/155.88/155.53	
24 (Boc)	-	79.65/79.54/79.35		-	79.65/79.54/79.35	
25 (Boc)	.455/1.432/1.421	s (br)	28.64	1.460/1.437/1.425	s (br)	28.47

* s (Singlet), d (doublet), t(triplet), dd (doublet of doublets), tt (triplet of triplets), m (multiplet), br (broad).

Next, we aimed to synthesize the disilylated precursors **P17** and **P18** following a similar strategy (**Scheme 3.16**). Thus, the cyclen **77** was treated with three equivalents of *tert*-butyl 2-bromoacetate in the presence of sodium acetate to afford compound **80**,[75] which was reacted with propargyl bromide in acetonitrile at room temperature to give **81**[76] in an overall 54% yield from **77**. Then, the click reaction (CuAAC) between alkyne **81** and the corresponding disilylated azide (n = 1) was carried out under different conditions with the

aim of obtaining the disilylated compound **P18**. For that purpose, both CuI/TBTA and $CuBr(PPh_3)_3$ were used as catalytic systems. Even if the amount of the catalyst was increased from 2 to 4 mol%, or the reaction temperature was raised from 60 to 80 °C, the target product **P18** was not detected (**Table 3.3**). The reaction of **81** with the disilylated azide (n = 0) was not tested because we expected to have the same bad results. The failure of this click reaction was attributed to the complexation of copper to the coordinating **N** sp^3 of the cyclen moiety, inactivating the catalyst.[77] The situation was different in the previous case of alkyne **79** **(scheme 3.15)**, because we had non-coordinating **N** sp^2 in the cyclen moiety.

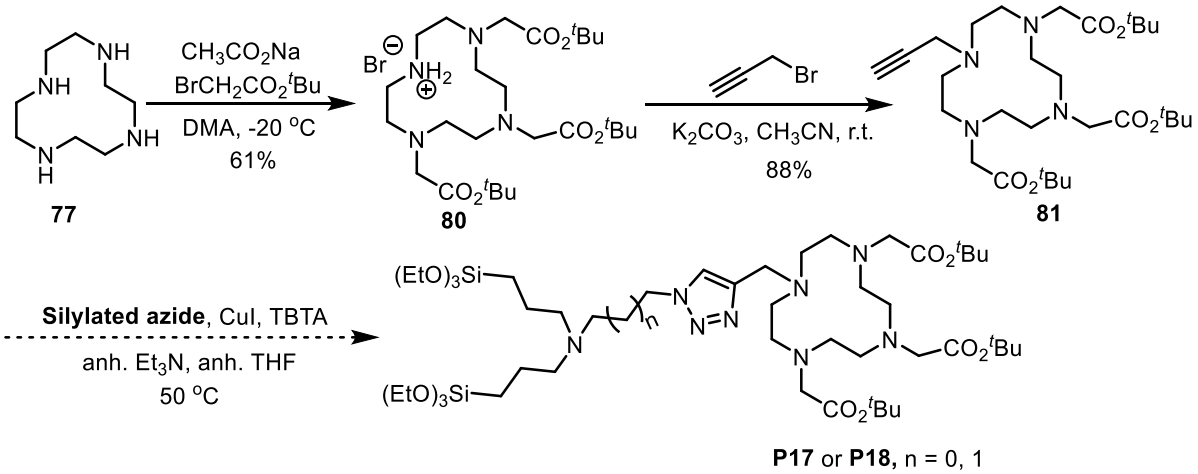

Scheme 3.16 Attempts to synthesize the silylated precursors **P17** and **P18**

Table 3.3 Screening of the CuAAC reaction conditions between **81** and the disilylated azide (n = 1)

Entry	Reaction conditions			Temperature (°C)	Result
	Catalyst	Solvent	Base		
1	2 mol% CuI, TBTA	THF	Et_3N	60	No reaction
2	2 mol% $CuBr(PPh_3)_3$	THF	Et_3N	60	No reaction
3	4 mol% CuI, TBTA	THF	Et_3N	60	No reaction
4	4 mol% $CuBr(PPh_3)_3$	THF	Et_3N	60	No reaction
5	4 mol% CuI, TBTA	THF	Et_3N	80	No reaction
6	4 mol% $CuBr(PPh_3)_3$	THF	Et_3N	80	No reaction

3.3.2 Preparation and characterization of periodic mesoporous organosilica nanoparticles

Generally, PMO materials are obtained by the sol-gel process from organo-bridged alkoxysilanes in the presence of structure directing agents and there are many synthetic protocols for the preparation of nanoscaled PMO materials.[78] Herein, we want to prepare nanomaterials based on ethylene-bridged PMO NPs containing variable proportions of our silylated precursors, with the idea to obtain highly ordered pore structures and typical NP diameters, by using CTAB as a structure-directing agent. According to the method reported by Dr Jean-Olivier Durand in 2014,[79] a series of PMO NPs were synthesized.

3.3.2.1 Preparation and characterization of ethylene-bridged periodic mesoporous organosilica nanoparticles (E PMO NPs)

First, ethylene-based PMO NPs from 100% organic-bridged precursor (*E*)-1,2-bis(triethoxysilyl)ethene (BTSE or **E**) (**E PMO NPs**) were prepared and studied. The synthesis was performed in Mili-Q water with cetyltrimethylammonium bromide (CTAB) as micellar template and sodium hydroxide as catalyst at 80 °C. The template was prepared at this temperature for 50 min with a stirring speed adjusted at 1400 rpm. Then, the sol-gel process was carefully controlled by quick addition of 1,2-bis(triethoxysilyl)ethene (BTSE) and the reaction mixture was stirred for 120 min. Finally, the **E PMO NPs** were collected by centrifugation and the template was removed from the obtained solid by treatment with an ethanolic solution of ammonium nitrate. The resulting solid material was washed successively with ethanol, Mili-Q water and ethanol.

The **E PMO NPs** were characterized by ^{13}C CP MAS solid state NMR, transmission electron microscopy (TEM), nitrogen-sorption measurements, dynamic light scattering (DLS), powder X-ray diffraction (*p*-XRD), infrared spectroscopy (IR) and zeta-potential. ^{13}C CP MAS solid state NMR showed the characteristic signal at 146.3 ppm (C=C). TEM images revealed the presence of 700 nm long nanorods of 200 nm in diameter (**Figure 3.7**). DLS confirmed the nanosize of the materials with average hydrodynamic diameters of 813 nm. Besides, the crystal like 2D-hexagonal porosity visible by TEM was confirmed with the power X-ray diffraction (*p*-XRD) peaks of the hexagonal structure at 2.3, 3.9, and 4.6 degrees (**Figure 3.8a**). FTIR spectroscopy displayed the γ_{Si-C} and $\gamma_{C=C}$ vibration modes at 1193 and 1636 cm^{-1} respectively (**Figure 3.8b**). Importantly, no characteristic peaks of CTAB can be observed,

which confirms that templating surfactant removal is complete after several cycles of washing. The dispersibility of the NPs was checked in Mili-Q water. The NPs were moderately aggregated after dispersion at 1 mg/mL. The ζ potential was *ca* -31.7 mV at pH 7. The nitrogen-sorption measurements resulted in a BET surface area of 798 m^2g^{-1} with a pore diameter of 2.36 nm (BJH method) (see **Figure 3.10** later). The consequence of these consistent results is the reversibility of the adsorption isotherms. Indeed, no hysteresis loop can be observed for materials with pore diameters lower than 4 nm when adsorbing nitrogen at 77.4 K. Using the Kelvin equation, this pore diameter corresponds to the relative pressure of p/p° = 0.42.

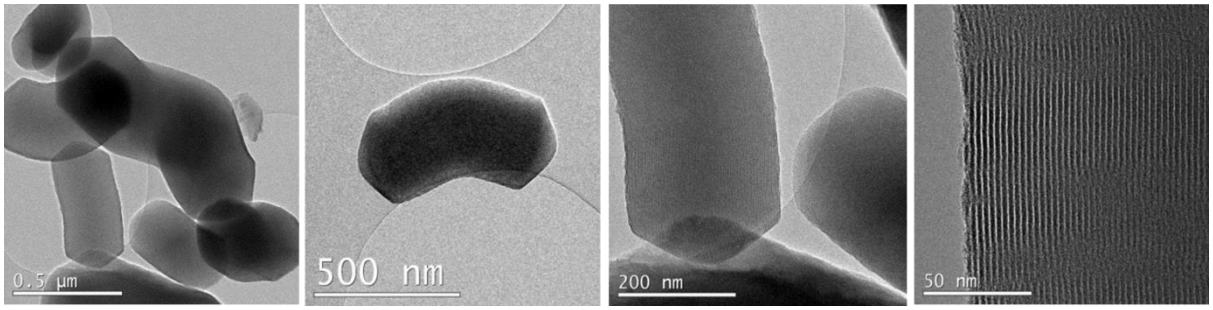

Figure 3.7 TEM images of **E PMO NPs** at different magnification

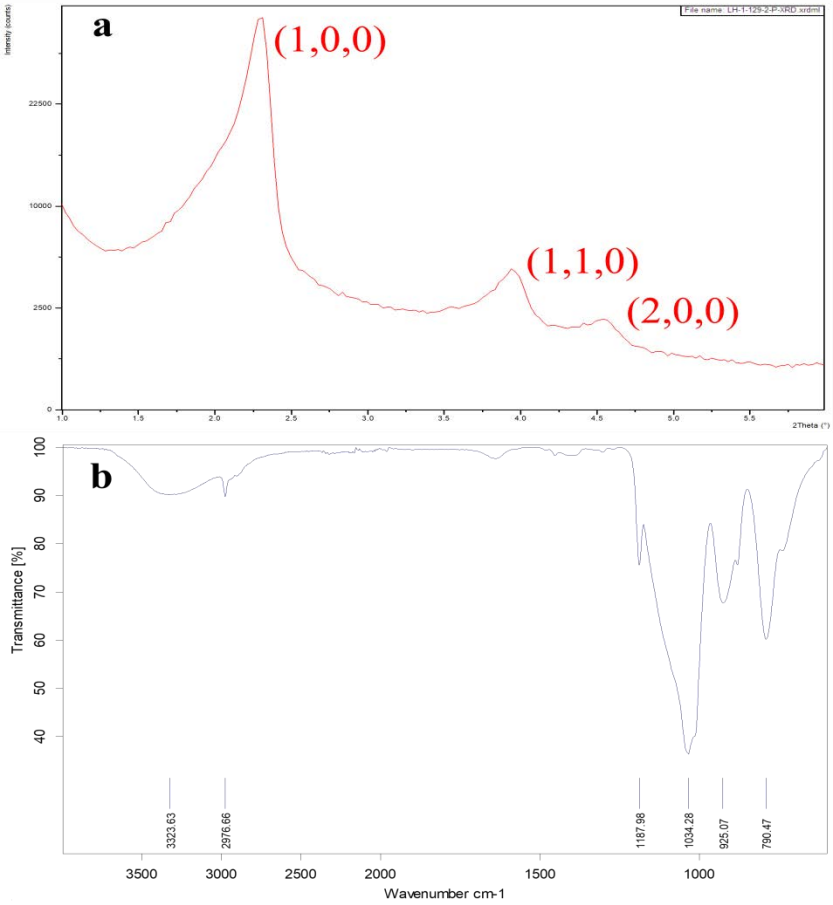

Figure 3.8 a) *p*-XRD and b) FTIR of **E PMO NPs**

3.3.2.2 Preparation and characterization of E-Pn 90/10 PMO NPs and E-Pn 75/25 PMO NPs

Then, a series of mixed **E-Pn PMO NPs** were prepared by mixing the corresponding disilylated precursor and (*E*)-BTSE. The **E-Pn PMO NPs** syntheses were performed for 2 h at 80 °C and 1400 rpm as well, with an initial quick addition of a mixture of (*E*)-BTSE and different amounts of the disilylated precursors. **E-Pn PMO NPs** were collected by centrifugation and the template was removed by washing with an ethanolic solution of ammonium nitrate, the resulting material was washed successively with ethanol, Mili-Q water and ethanol. Herein, two different ratios of **E/Pn** were tested: 90/10, 75/25, in order to study their influence on the NPs size and morphology (**Scheme 3.17**).

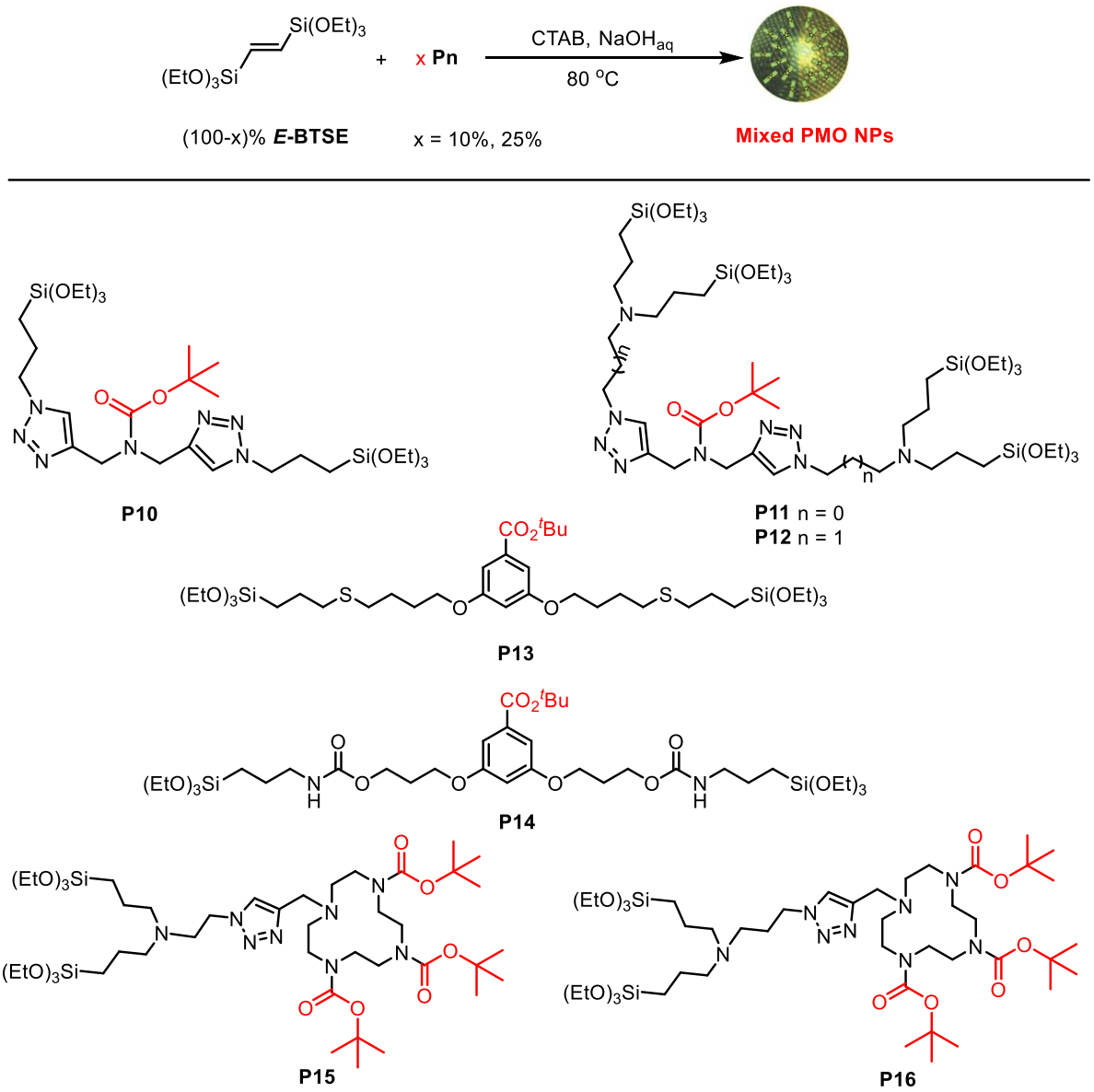

Scheme 3.17 Synthesis of **E-Pn PMO NPs** by mixing the disilylated precursor and (*E*)-BTSE

All the mixed **E-Pn PMO NPs** were characterized by ^{13}C CP MAS solid state NMR, TEM, nitrogen-sorption measurements, DLS, zeta-potential, IR, *p*-XRD, TGA and DSC. Some physical data of **PMO NPs** are given in **Table 3.4**.

Table 3.4 Some physical data of **E-Pn mixed PMO NPs**

Material	N_2-sorption measurements			Particles size (nm)[c]	Zeta potential		TGA[d]
	S_{BET} (m^2g^{-1})	V_{pore} (cm^3g^{-1})[a]	$\emptyset_{pore}$ (nm)[b]		pH	(mV)	
E-P10 90/10 PMO NPs	683	0.48	2.8	447	6.96	-29	78%
E-P11 90/10 PMO NPs	509	0.34	2.7	801	5.92	33	75%
E-P12 90/10 PMO NPs	505	0.36	2.8	479	5.44	36	72%
E-P13 90/10 PMO NPs	973	0.66	2.7	1122	6.80	-31	77%
E-P14 90/10 PMO NPs	696	0.37	2.1	694	6.72	-38	75%
E-P15 90/10 PMO NPs	513	0.36	2.8	520	6.66	39	60%
E-P16 90/10 PMO NPs	492	0.33	2.7	621	6.25	34	68%
E-P10 75/25 PMO NPs	low	nd[e]	nd	507	7.34	-23	67%
E-P11 75/25 PMO NPs	low	nd	nd	513	6.25	20	58%
E-P12 75/25 PMO NPs	low	nd	nd	321	4.86	24	57%
E-P13 75/25 PMO NPs	259	0.17	2.6	742	9.07	-26	67%
E-P14 75/25 PMO NPs	329	0.23	2.7	562	6.85	-42	63%
E-P15 75/25 PMO NPs	162	0.15	3.6	639	6.08	33	53%
E-P16 75/25 PMO NPs	low	nd	nd	463	4.66	41	55%

[a] Determined from the uptake at saturation at p/p° = 0.98. [b] Diameter determined by BJH. [c] Hydrodynamic diameters from DLS. [d] Residual mass;TGA with a heating rate of 10 ºC/min from 30 to 1000 ºC. [e] Not determined.

The morphologies of **E-Pn** were first analyzed by TEM (**Figure 3.9**), and for the majority of the materials rod-like-shape nanoparticles were obtained ranging from 200-300 nm (for **E-P10-12** and **E-P15-16 90/10**) to 500-600 nm (for **E-P13-14 90/10).** For **E-P10** and **E-P11 75/25,** NPs are between 200-300 nm in length**.** For **E-P12 75/25**, smaller nanoparticles (150 nm) were observed. The length of other 75/25 nanoparticles are between 400-600 nm. The hydrodynamic diameters of the nanorods were investigated by DLS (intensity), and the obtained diameters agreed with the sizes determined by TEM (**Table 3.4**). **E-P13 90/10** showed the highest hydrodynamic diameters at about 1418 nm and **E-P12 75/25** showed the smallest hydrodynamic diameters at about 320 nm, the hydrodynamic diameters of other NPs are between 400 nm and 800 nm. The zeta potentials were determined in water (**Table 3.4**). **E-P10 and E-P13-14** showed negative zeta potential in agreement with the presence of $Si\text{-}O^-$ at the surface of the nanorods. The zeta potential of **E-P11-12** and **E-P15-16** were positive because the amino groups of **P11-12** and **P15-16** were protonated below pH 7.

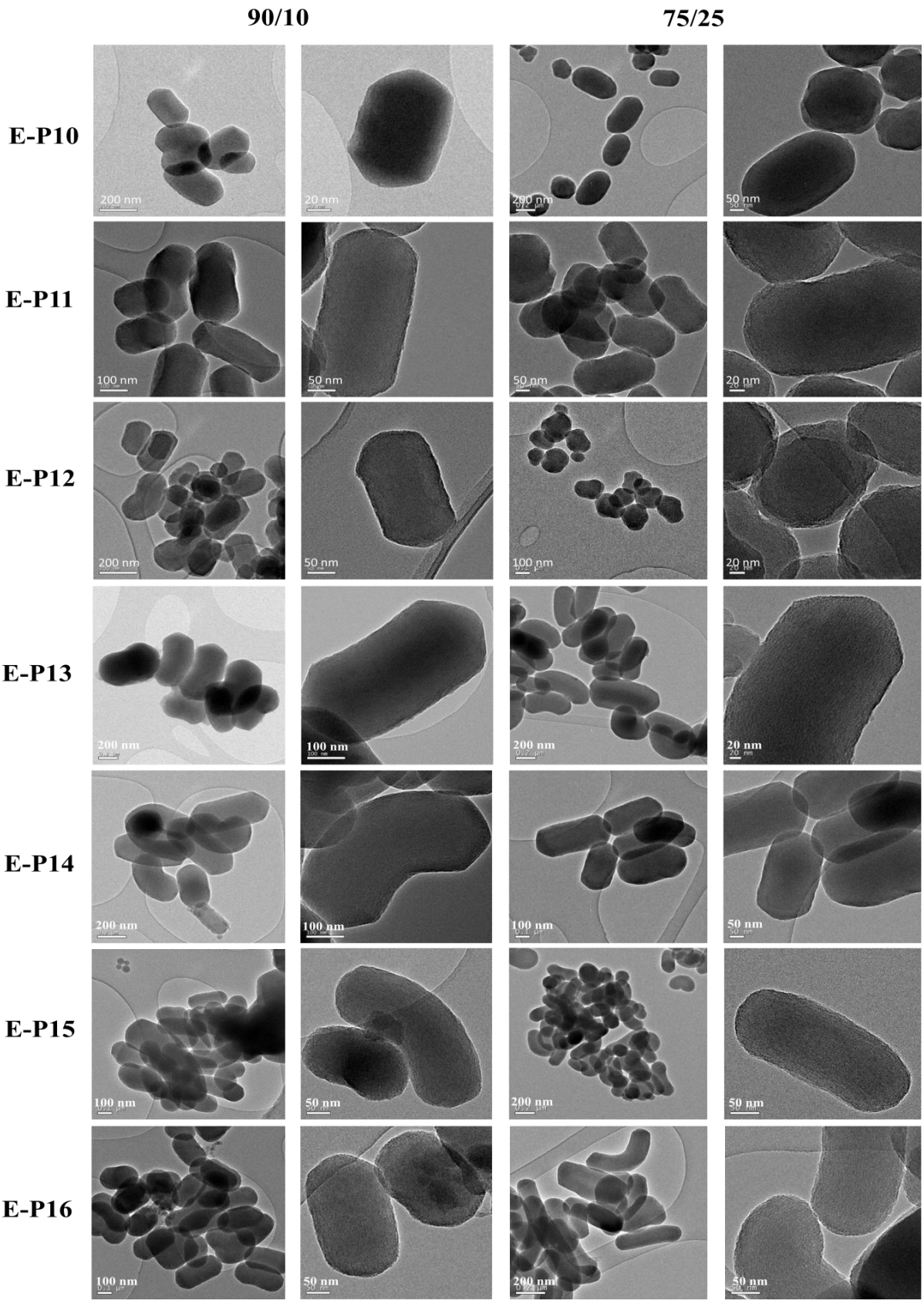

Figure 3.9 TEM images of **E-Pn PMO NPs**, proportion 90/10 and 75/25

The surface area and the porosity of the materials were proved by N_2-sorption experiments (**Table 3.4** and **Figure 3.10**). All the materials showed an isotherm between type I and type IV, between microporous and mesoporous systems. The incorporation of **P10**, **P11** and **P12** at a proportion of 90/10 led to a decrease of specific surface area to 683, 508 and 505 m^2g^{-1}, respectively. Unexpectedly, nanorods from **E-P13** showed a very high specific surface area of 973 m^2g^{-1} with an average small pore size of 2.73 nm. The incorporation of **P14**, **P15** and **P16** at a proportion of 90/10 led also to a decrease of specific surface areas until 695, 513, 491 m^2g^{-1}, respectively, with the corresponding pore sizes of 2.13, 2.82 and 2.67 nm. Note that when increasing the proportion of precursors **Pn** until 25%, materials **E-Pn 75/25** (except for those derived from the *tert*-butyl esters **P13** and **P14**) showed no adsorption of N_2 any more at 78 K, which suggest that the porosity is not accessible to N_2 at this temperature.

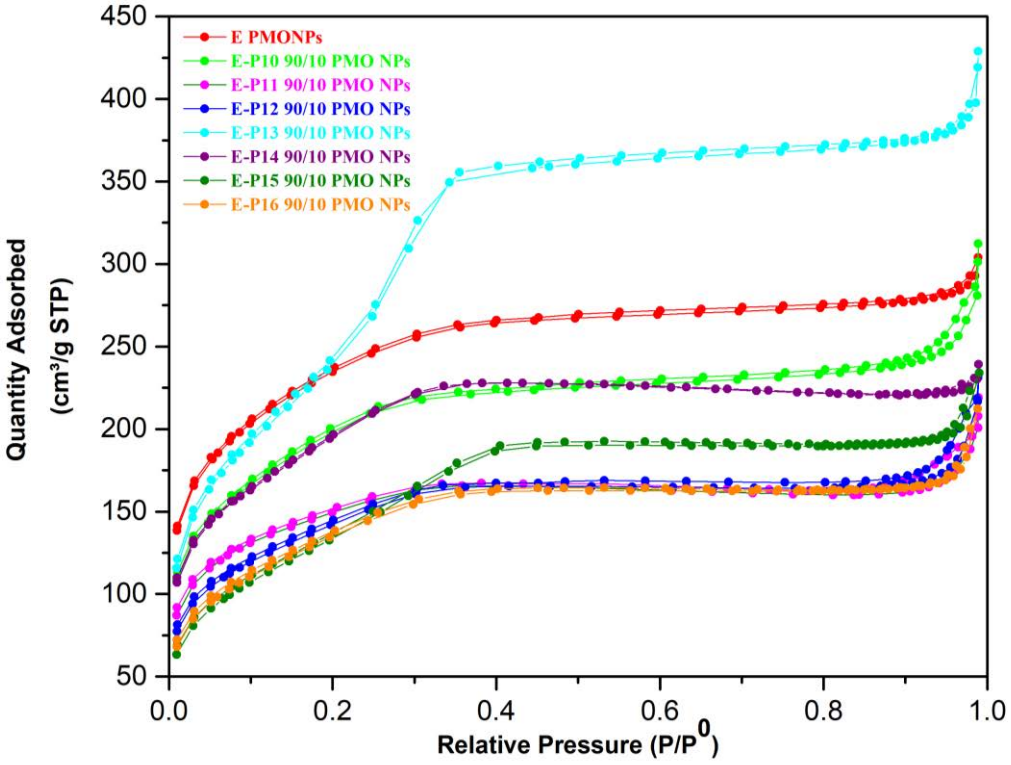

Figure 3.10 N_2-sorption isotherms of **E-BTSE PMO NPs** and different **E-P$_n$** 90/10 **PMO NPs**

Interestingly, small angle X-ray diffraction of nanorods from **E-P13 90/10** showed the d(1,0,0) Bragg peak at 2.2 Θ, with the satellites at d(1,1,0) 4.0 Θ and d(2,0,0) 4.6 Θ, characteristics of a well ordered hexagonal mesoporosity. The other materials are more disordered with a wormlike mesoporosity and a broad non-structured band (**Figure 3.11**).

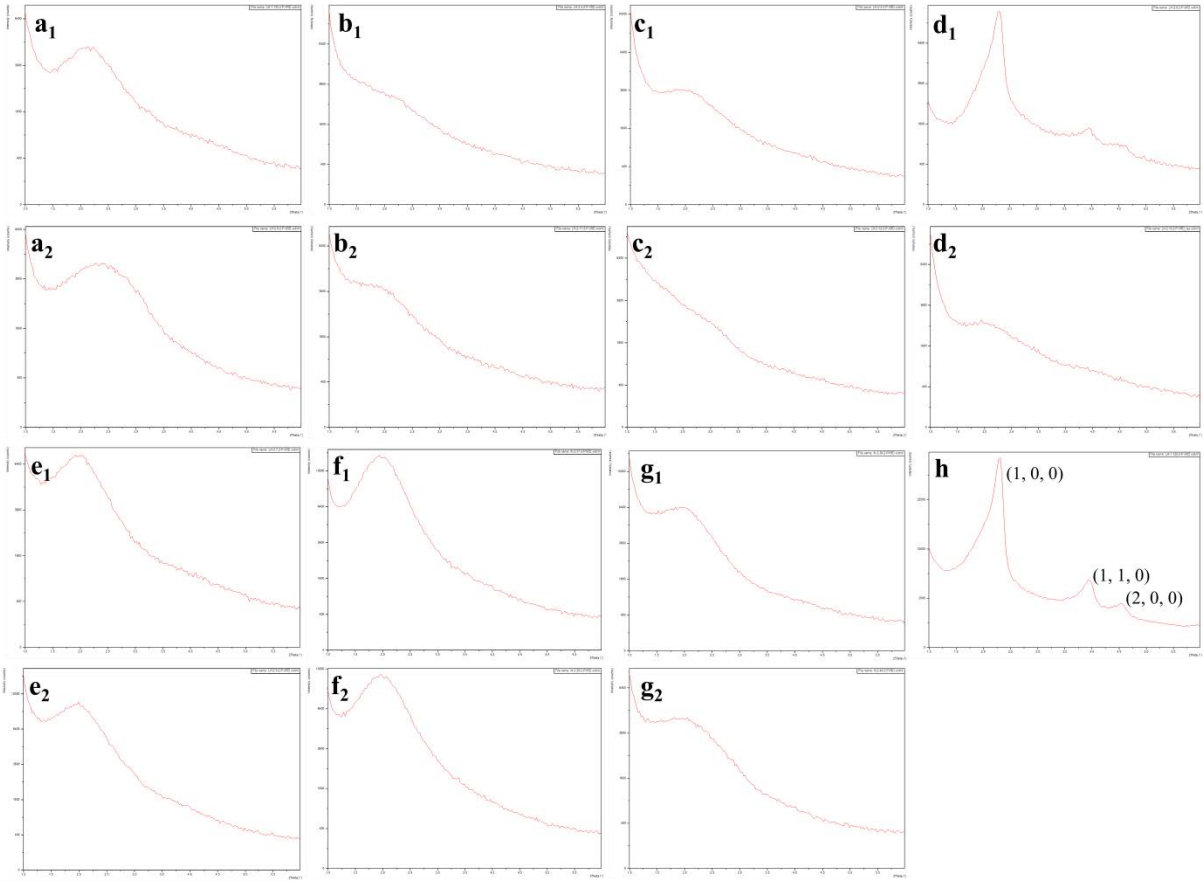

Figure 3.11 *p*-XRD of different **E-Pn PMO NPs:** a_1) **E-P10 90/10**, a_2) **E-P10 75/25**, b_1) **E-P11 90/10**, b_2) **E-P11 75/25**, c_1) **E-P12 90/10**, c_2) **E-P12 75/25**, d_1) **E-P13 90/10**, d_2) **E-P13 75/25**, e_1) **E-P14 90/10**, e_2) **E-P14 75/25**, f_1) **E-P15 90/10**, f_2) **E-P15 75/25**, g_1) **E-P16 90/10**, g_2) **E-P16 75/25**, h) **E PMO NPs**.

FTIR were recorded for all the precursors and materials. A representative example is given in **Figure 3.12** with **P11**, **E-P11 90/10** and **E-P11 75/25**. Precursor **P11** showed the presence of the BOC group at 2973 cm^{-1} (γ_{CH3}), the carbon chains at 2927 and 2883 cm^{-1} (γ_{CH2}), the carbonyl group of the carbamate at 1696 cm^{-1} ($\gamma_{C=O}$), the triazole γ_{CH} at 1457-1386 cm^{-1}, the silicon-oxygen bonds at 1073 cm^{-1} (γ_{Si-O}). All the bands were essentially the same in the materials derived thereof, with a shift of the carbonyl to 1675-1672 cm^{-1} showing a different environment of BOC group in the material. A broad band between 1200-1000 cm^{-1} ($\gamma_{Si-O-Si}$) characteristic of a well-condensed material was also observed. The infrared data of other materials are given in the experimental section (***Section*** 3.3.5.4.2).

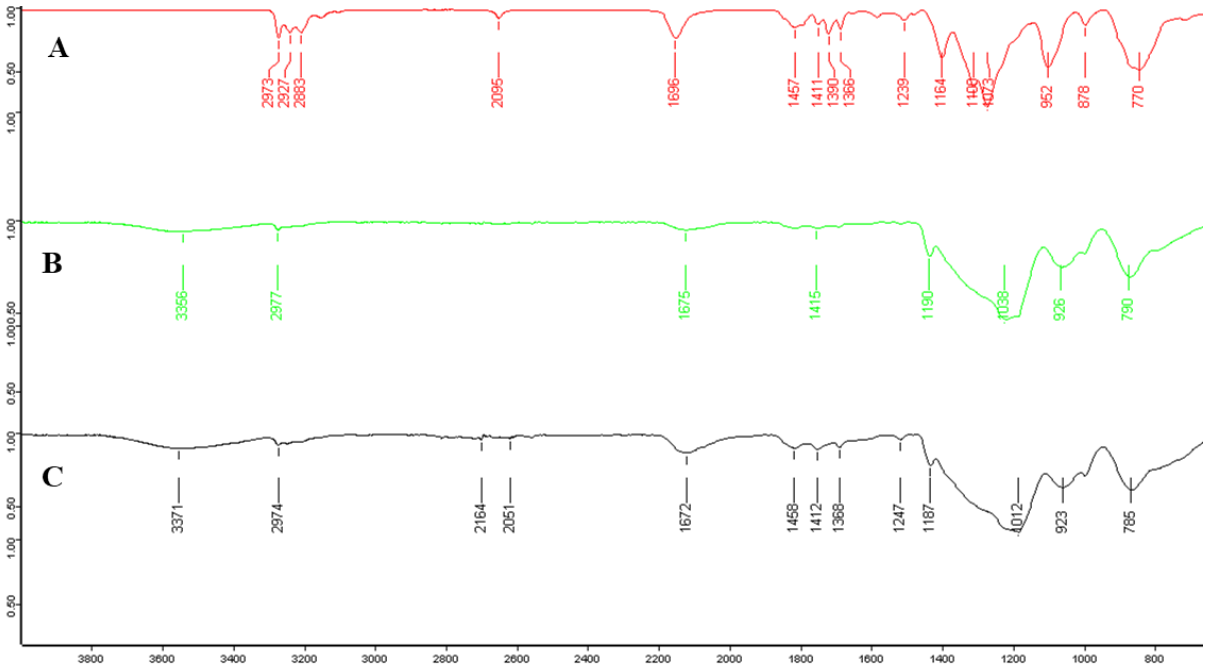

Figure 3.12 FTIR of (**A**) **P11**, (**B**) **E-P11 90/10** and (**C**) **E-P11 75/25**.

The solid state NMR ^{13}C CP MAS spectra of all the samples clearly displayed that the synthesized mixed **PMO NPs** contained the organic skeleton of the precursor (see experimental in ***Section*** 3.3.5.4.2). Here we only present **E-P11 75/25 PMO NPs** as an example. **Figure 3.13a** show the ^{13}C spectra of **P11** in solution. The characteristic signals in ppm are as follows: 155.1 (C=O), 144.4 (C=C, Cq triazole), 123.2 (CH triazole), 80.1 (Cq, ^{t}Bu), 58.2 (CH_2-N, CH_2-triazole), 28.3 (CH_3 ^{t}Bu), 18.2(-CH_2-), 7.7 (CH_2-Si). The spectrum of **E-P11 75/25** (**Figure 3.13b**) show broad signals at about 156 (C=O), 145 (C=C, Cq triazole), 124 (CH triazole), 80 (Cq, ^{t}Bu), 55 (CH_2-N, CH_2-triazole), 29 (CH_3 ^{t}Bu) 22 (-CH_2-), 11 (CH_2-Si). By the superposition of the two spectra, a good match is found in the position of the signals, suggesting thereby the integrity of the organic skeleton.

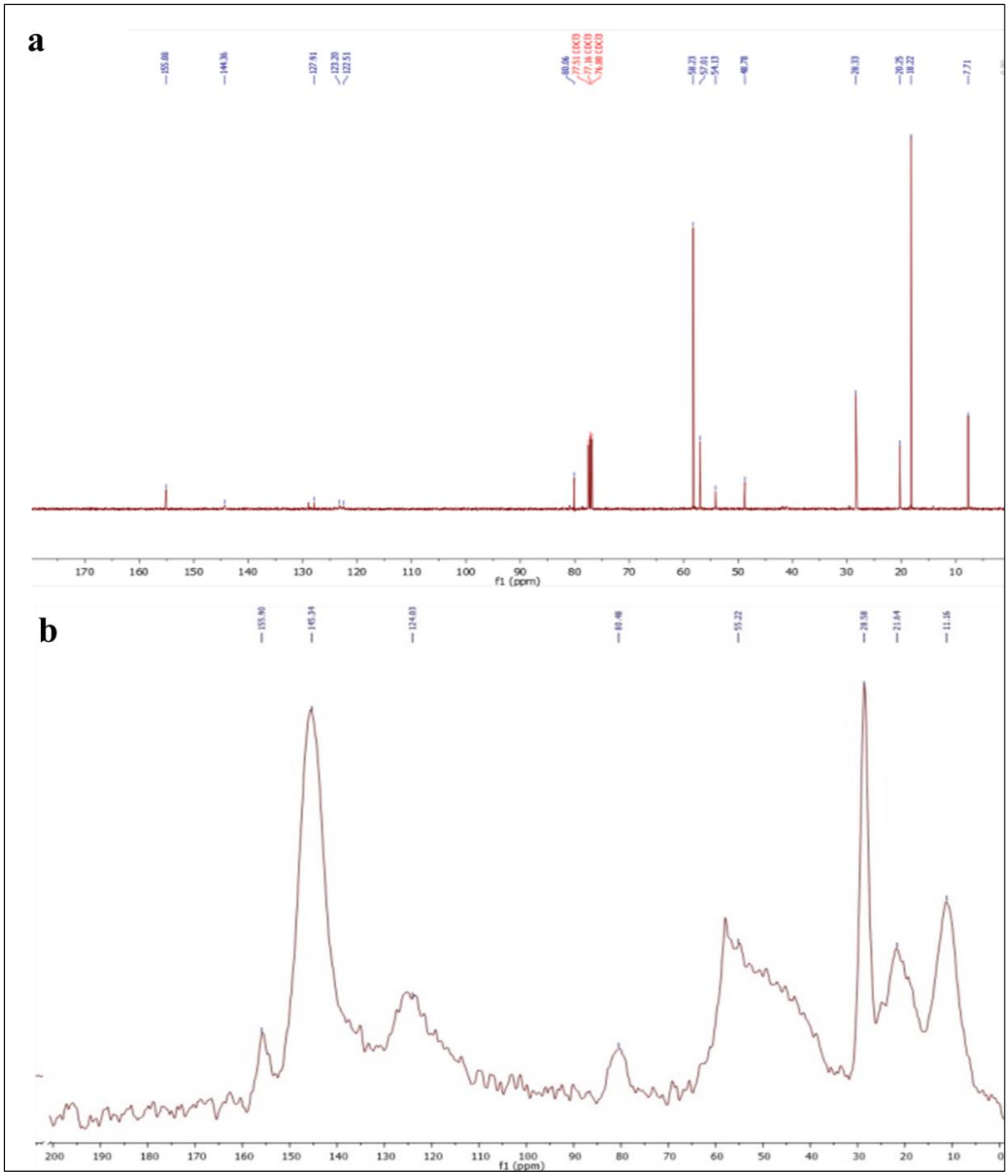

Figure 3.13 a) ^{13}C NMR of **P11** in solution and b) ^{13}C CP-MAS solid-state NMR of **E-P11 75/25**

Finally, TGA analyses of the nanomaterials were performed (**Figure 3.14**). The first loss of mass corresponded to adsorbed water (up to 120 °C). From 150 °C to 220 °C the loss of the *tert*-butoxycarbonyl group was observed. Then, at higher temperatures, the decomposition of the organic part of the material took place. Thus, the BOC group was found to be very stable in the materials in dry solid state as no loss of mass was noticed before 120 °C.

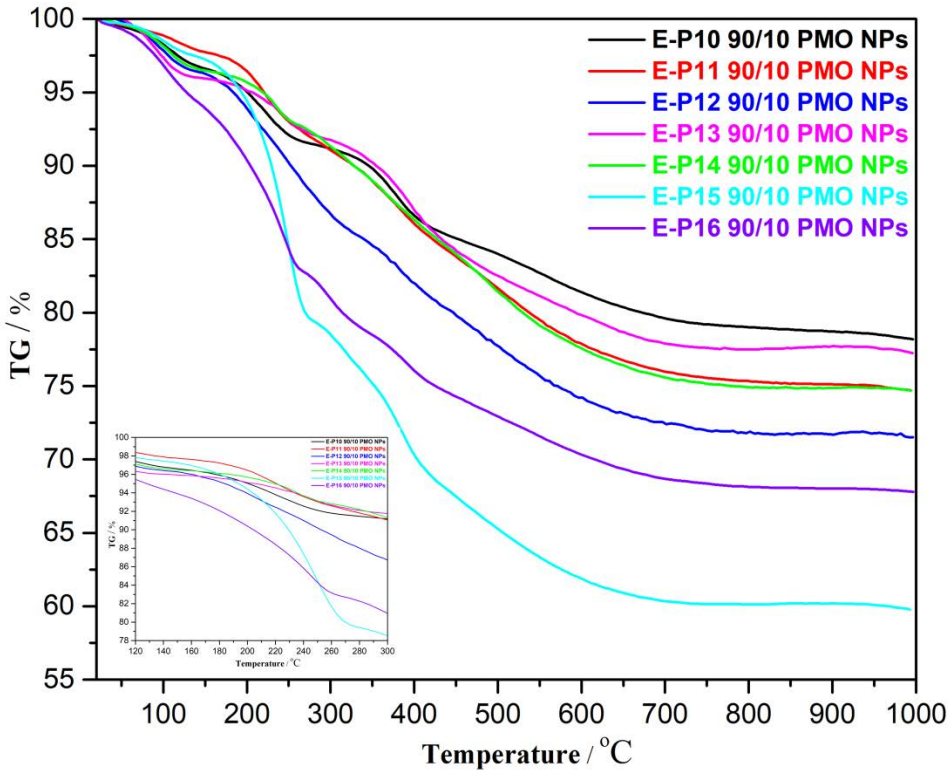

Figure 3.14 TGA of **E-Pn 90/10 PMO NPs**

3.3.2.3 Preparation and characterization of pure P12 PMO NPs and P16 PMO NPs

We then performed the synthesis of some pure **PMO NPs**. For this purpose, **P12** and **P16** were used as the only precursor (no silica source). CTAB was dissolved in aqueous NaOH at 80 °C in highly diluted conditions for 50 min, then the precursor **P12** or **P16** dissolved in EtOH was rapidly added. The condensation mixture was stirred at 80 °C for 24 h, then extraction of CTAB and drying of the sample was performed as explained above for the mixed PMO NPs.

The nanomaterials were analyzed using different techniques. First, TEM images (**Figure 3.15**) showed spherical monodisperse nanoparticles which seem to be composed of sheets of organosilica. Pure **P12 PMO NP**s were clearly porous on TEM images while pure **P16 PMO NPs** were non-porous NPs. N_2 sorption experiments (BET) (**Figure 3.16**) provided a type IV isotherm (mesoporous) for **P12 PMO NP**s and the porosity was determined to be 5.6 nm, with a surface area of 186 m^2g^{-1}. On the other hand, a type III isotherm was obtained for **P16 PMO NPs,** with very low surface area of 20 m^2 g^{-1}. The DLS measurements provided hydrodynamic diameters of 269 nm for pure **P12 PMO NPs** and 217 nm for pure **P16 PMO NPs.** The values of zeta potential (ζ 11 mV, pH 8.9 for **P12 PMO NPs** and ζ 24 mV, pH 7.1

for **P16 PMO NPs**) were positive in agreement with the protonation of nitrogen atoms of tertiary amines. The Boc group of the precursors was not damaged after the condensation reaction as shown by FTIR spectroscopy (**Figure 3.17**) with the carbonyl group observed at 1682 cm^{-1}.

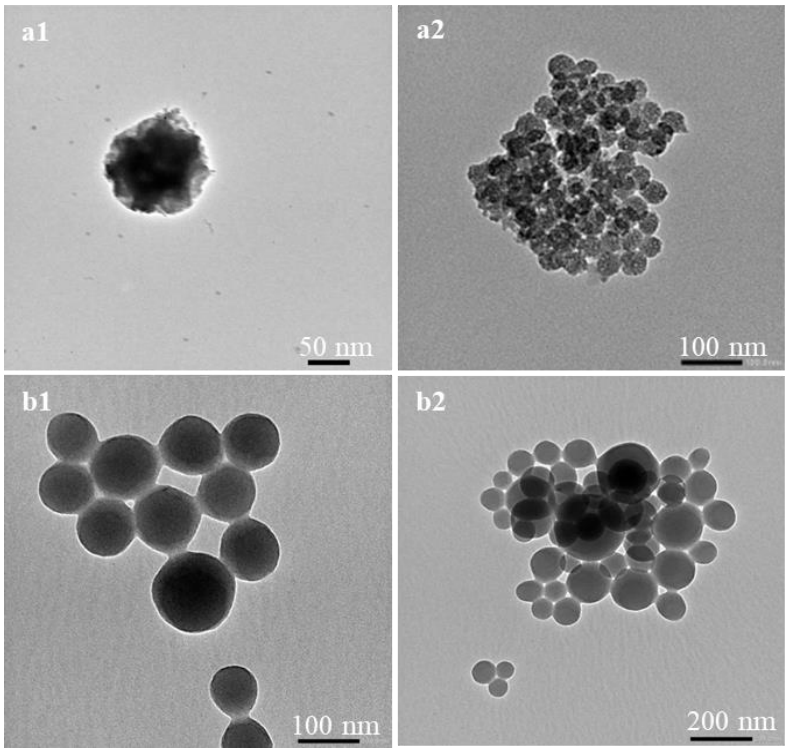

Figure 3.15 TEM images of a1-a2) pure **P12** and b1-b2) **P16 PMO NPs** at different magnification

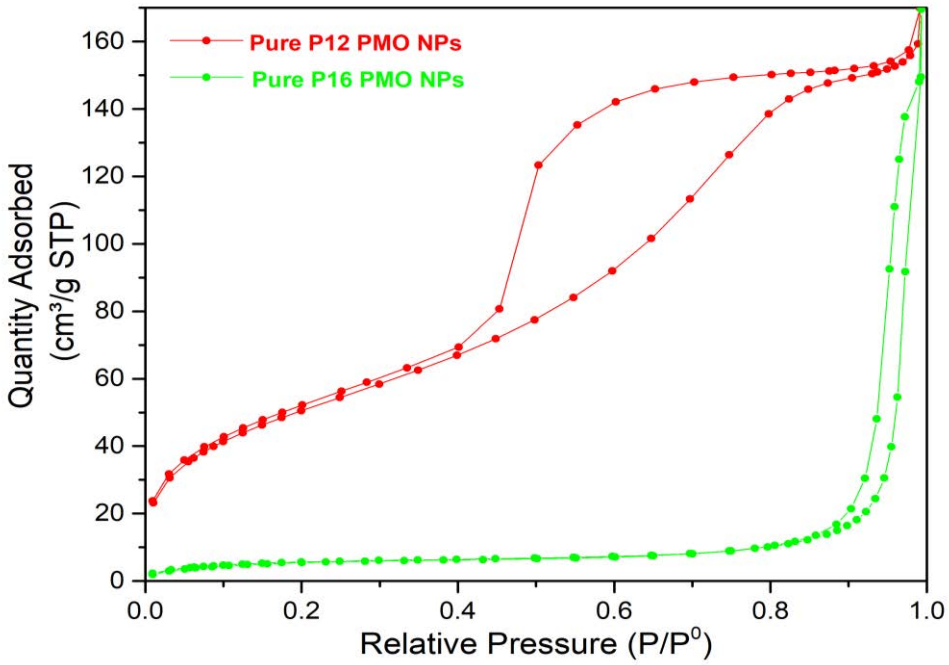

Figure 3.16 N_2 adsorption-desorption experiments (BET) of **Pure P12** and **P16 PMO NPs**

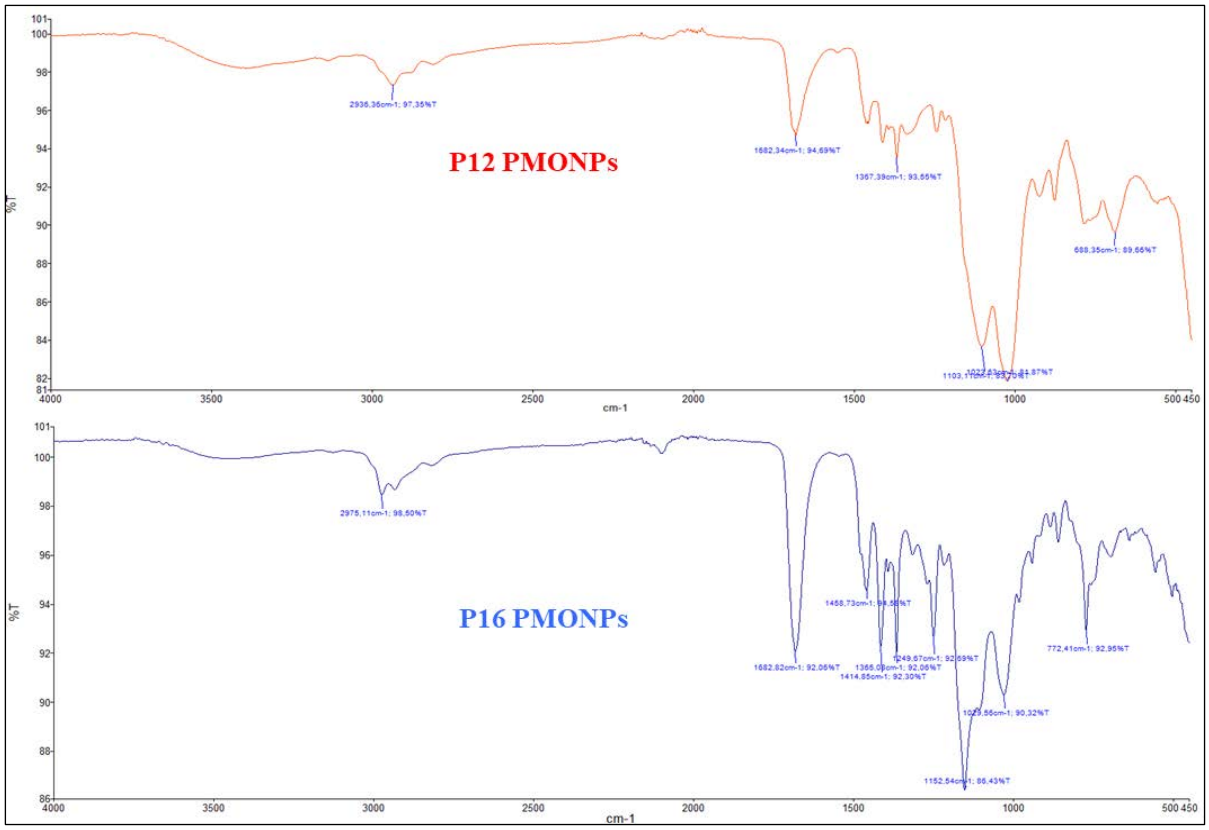

Figure 3.17 FTIR of **P12 PMO NPs and P16 PMO NPs**

From the results obtained, it becomes clear that the structural features of the silylated precursors have an influence on the morphological and textural properties of the nanomaterials (size and shape, specific surface, porosity, degree of organization, …). In any case, the *tert*-butoxycarbonyl group present in the precursors remains in all the nanomaterials. Interestingly, we have found that addition of 10% **P13** to (*E*)-BTSE lead to **mixed P13 PMO NPs** which preserve the well-ordered hexagonal mesoporosity of the parent **(*E*)-BTSE PMO NPs**. The incorporation of a higher amount (25%) of **P13** led to a more disordered nanomaterial (wormlike).

3.3.3 Assay of PMO NPs as High Intensity Focused Ultrasound (HIFU) agents

As we mentioned before, the nanoparticles produced were supposed to release CO_2 and/or isobutene from *tert*-butoxycarbonyl (Boc) group after ultrasonic stimulation. The research of this chapter of the thesis was performed with the cooperation of Dr Jean-Olivier Durand (ICGM, France), in whose laboratory I have made two short stays (1 month and 4 months) and part of the characterization of the nanomaterials. The synthesized PMO NPs have been sent to Dr. Patrick Midoux and Dr. Chantal Pichon (Centre of Molecular Biophysics, France), who performed the HIFU experiments. An OptiCell membrane was used to observe

microbubble formation under ultrasound irradiation (**Figure 3.18a**). The device for ultrasonic stimulation of nanoparticles and observation under the microscope is shown in **Figure 3.18b**.

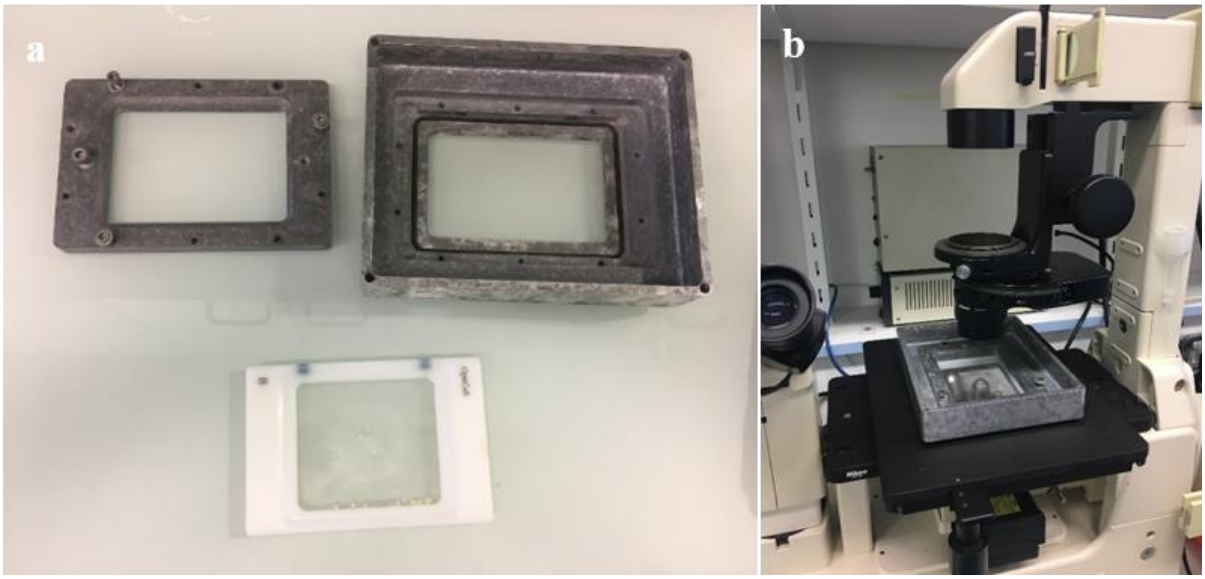

Figure 3.18 a) OptiCell membrane and its support for mounting on the microscope. b) Device for ultrasonic stimulation of nanoparticles and observation under the microscope.

The materials were suspended in PBS buffer (pH 5.5) at a concentration of 10 mg/mL and two different ultrasound stimulation conditions (1MHz PA549 and 5MHz PA629 400 mV CW noPA) were tested. Unfortunately, they did not observe clearly the formation of bubbles. In order to check whether the Boc group was removed or not, we performed an IR analysis on the recovered samples, and we found that there was no difference between the samples before and after the HIFU experiment.

In order to understand the failure of the HIFU experiments, we performed in the laboratory in Montpellier a series of trials. **E-P12 75/25 PMO NPs** was the first material selected to check the release of CO_2 in water under different conditions. It was added (50 mg) to distilled water (10 mL), the mixture was quickly heated to 80 °C or 100 °C and stirred at this temperature for 30 min. The experiments were performed at different pH (7, 5, 3, 1). When the pH was between 3 and 7, we did not observe any bubbles at any temperature. Conversely, at pH 1 and heating at 100ºC we could clearly see the formation of bubbles in the mixture (**Figure 3.19**).

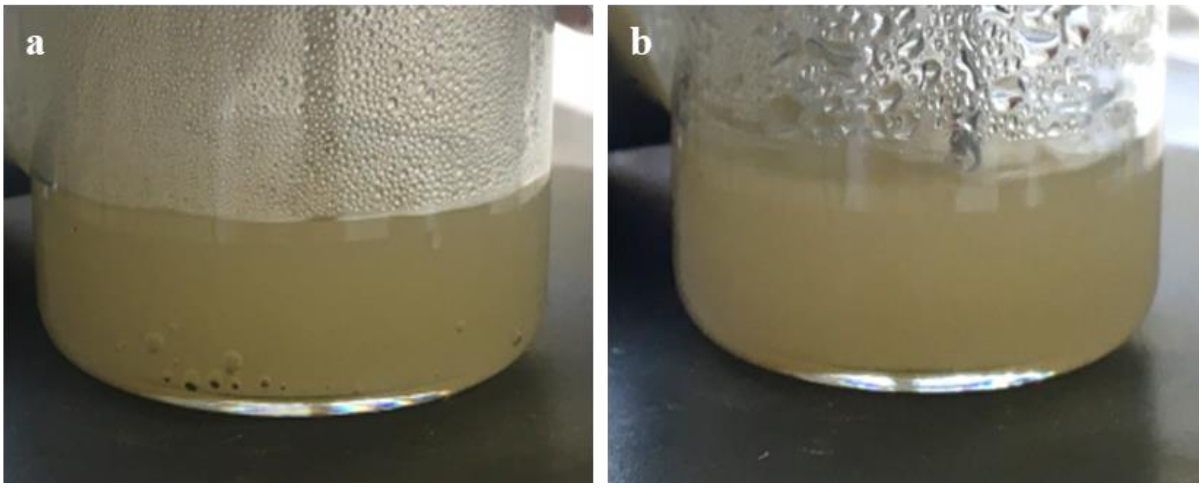

Figure 3.19 Images of **E-P12 75/25 PMO NPs** in water at 100°C and pH 1: **a**) after 5 min and **b**) after 30 min

Moreover, **E-P12 75/25 PMO NPs** recovered from the different experiments were collected by centrifugation and washed with EtOH, then dried for FTIR analyses (**Figure 3.20**). The IR spectrum of the sample treated in acidic water (pH = 1) at 100 °C showed the absence of the characteristic signals of the Boc group (^{t}Bu at 2987 cm^{-1} and C=O at 1680 cm^{-1}). Under the other conditions, the Boc group was still present. These results confirmed the successful released of CO_2 in acidic water at pH 1 at 100 °C after 30 minutes.

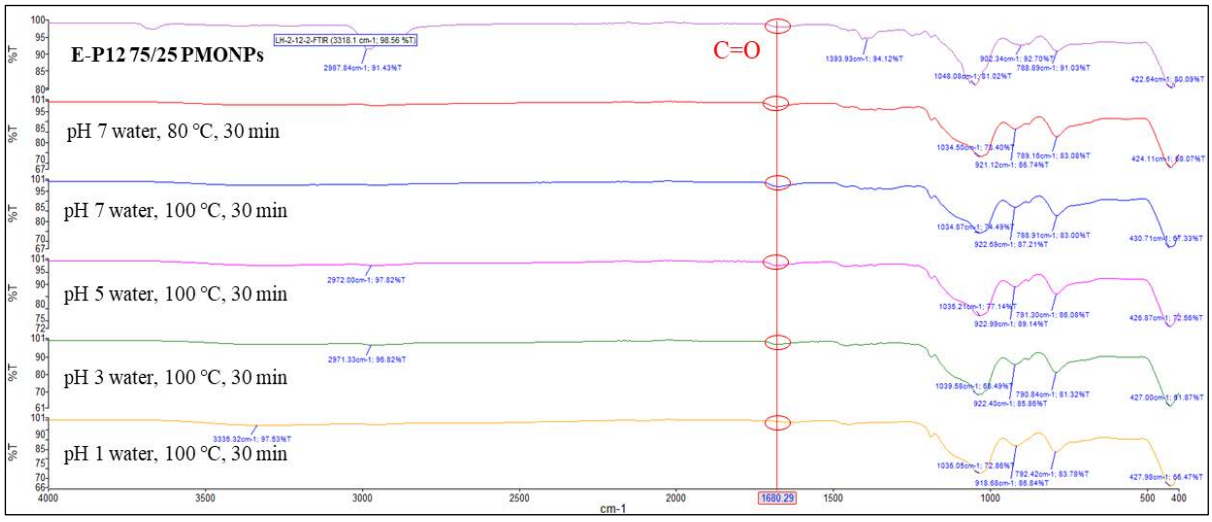

Figure 3.20 FTIR of **E-P12 75/25 PMO NPs** treated under different conditions.

Similarly, the nanomaterial **E-P16 75/25 PMO NPs** was also tested under the same conditions and bubbles were only generated when treated in acidic water (pH 1) at 100 °C. ^{13}C CP-MAS solid-state NMR of the recovered sample confirmed the removal of the Boc group. The characteristic signals (in ppm) at about 155 (C=O), 79 (Cq, ^{t}Bu) and 29 (CH_3 ^{t}Bu)

disappeared (**Figure 3.21**). The FTIR spectrum of the recovered **E-P16 75/25 PMO NPs** (**Figure 3.22**) further corroborate this result.

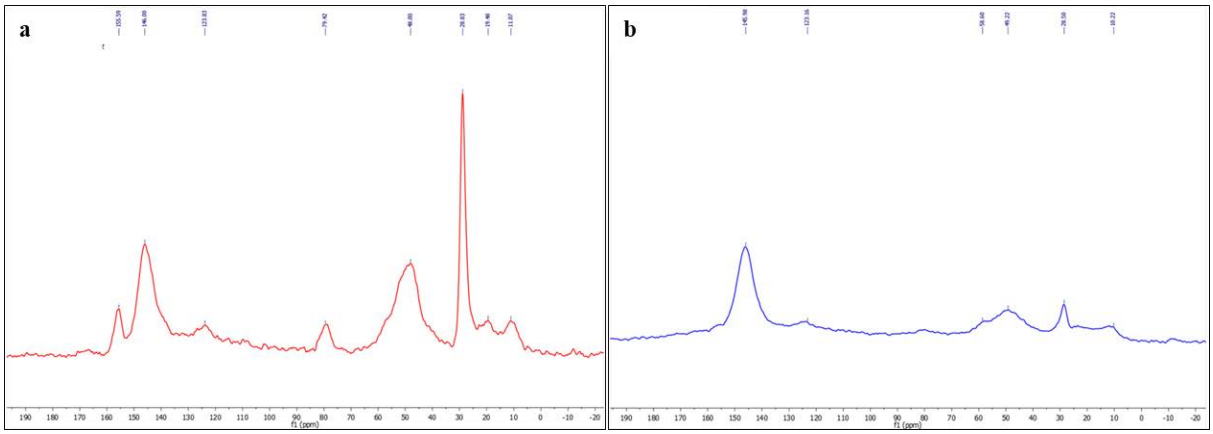

Figure 3.21 ^{13}C CP-MAS solid-state NMR of **E-P16 75/25 PMO NPs**: a) before treatment, b) after heating at 100 ºC in water at pH = 1

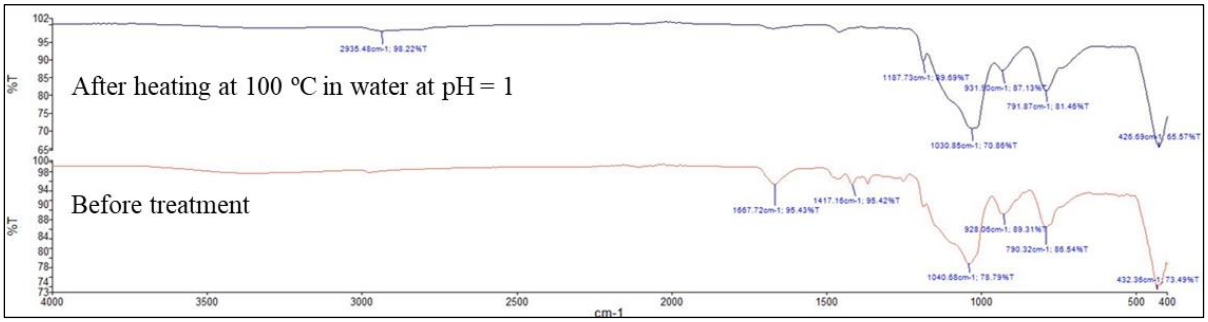

Figure 3.22 FTIR of **E-P16 75/25 PMO NPs** (before and after treatment)

Indeed the electrophilicity of BOC has been shown to strongly influence the reaction rate and reactivity of the cleavage.[87] Therefore, the synthesis of precursor molecules possessing more electrophilic BOC groups can be considered. Another possibility is to introduce carboxylic acid functions in the PMO NPs using triethoxysilanes possessing this function,[88] during the sol-gel procedure, in order to facilitate BOC cleavage in the materials. Moreover, the subsequent hydrolysis of the *tert*-butyl ester groups in the materials derived from **P13** and **P14** would give rise to mixed PMO NPs bearing acidic and coordinating carboxyl groups, which are very relevant for potential applications in nanomedicine for pH-triggered drug delivery[89-90] or in catalysis[91].

3.4 Conclusions

In summary, we have prepared and fully characterized mixed PMO NPs possessing Boc groups as potential HIFU responsive agents. These nanomaterials are expected to release CO_2 and/or isobutene from the temperature-sensitive COO^tBu group (Boc group) under high intensity focused ultrasound conditions. Previously, we have synthesized, through click chemistry (CuAAC reaction), the required silylated precursors (bearing two or four triethoxysilyl groups) presenting *tert*-butyl esters or *N*-Boc groups (**P10** to **P16**). Then, these molecules were co-condensed with (*E*)-bis(triethoxysilyl)ethylene (**BTSE** or **E**) in the presence of CTAB as template under basic catalysis (molar ratios of **E**/**Pn** of 90/10 and 75/25). The obtained nanorods using 10% of the functionalized precursor **Pn** possessed small wormlike mesopores, except for one case (**P13** as precursor) in which the mixed PMO NPs retained the well-ordered hexagonal mesoporosity and exhibited a large BET surface area. When 25% of the precursors **Pn** were used, the nanomaterials were non-porous, except for those derived from the *tert*-butyl esters **P13** and **P14**. Importantly, the Boc group of the precursors **Pn** was not damaged during the sol gel-procedure as shown by FTIR and ^{13}C CPMAS solid-state NMR of the resulting nanomaterials. TGA analyses showed the stability of Boc group inside the materials as no decomposition of this group occurred before 120 °C. Moreover, pure **P12** and **P16 PMO NPs** were also synthesized from the precursors **P12** and **P16** without any other source of silicate. We have found that Boc group was very stable in the nanomaterials as we needed to adjust the pH to 1 to cleave this group in water at 100 °C. We were not able to observe bubbles at pH 5.5 under HIFU stimulation, but the concept is nevertheless promising for future contrast agents for HIFU. In the future, it may be considered to synthesize precursors with more electrophilic Boc groups and introduce carboxylic acid functions in PMO NPs. The mixed PMO NPs bearing acidic and coordinating carboxyl groups resulting from the *tert*-butyl ester hydrolysis would be very relevant for potential applications in catalysis or in nanomedicine for pH-triggered drug delivery.

3.5 Experimental section

3.5.1 General information

The information corresponding to NMR, IR, MS, elemental analysis, TEM and *p*-XRD is given in ***Section* 2.2.5.1**.

^{13}C CP-MAS solid state NMR spectra were obtained from a Varian VNMRS 300 MHz instrument which belongs to the University of Montpellier, the repetition time was 5 seconds with contact times of 5 milliseconds.

Dynamic light scattering (DLS) and **Zeta potential** (ζ) were obtained from the University of Montpellier. DLS analyses were performed using a Cordouan Technologies DL 135 particle size analyzer instrument. Zeta potential measurements were performed on MALVERN Instruments ZETA SIZER Nano series with 1-3 mg samples dispersed in 5 mL of aqueous solution (distilled water or 0.01 M NaCl solution) between pH 4 and 9.

Thermogravimetric analysis (TGA) and differential scanning calorimetry (DSC) were performed at the *Institut de Ciències de Materials de Barcelona* (ICMAB) using a STA 449 F1Netzsch instrument under atmospheric conditions, with a heating rate of 10 ºC/min from 30 to 1000 ºC.

The surface areas were determined by the Brunauer-Emmet-Teller (BET) method from N_2 adsorption-desorption isotherms obtained with a Micromeritics ASAP2020 analyzer which belongs to the University of Montpellier after degassing samples for 12 h at 80 °C under vacuum. The total pore volumes were evaluated by converting the volume adsorbed at p/p^o 0.98 to the volume of liquid adsorbed (single point adsorption total pore volume of pores less than 4000 Å at $p/p° \approx 0.98$). The pore size distributions for **PMO NPs** were determined from the desorption branch using the Barrett-Joyner-Halenda (BJH) method which relies on the Kelvin equation to relate the width of the pores to the condensation pressure.

Others: When required, experiments were carried out with standard high vacuum and Schlenk techniques. Chromatographic purifications were performed under N_2 pressure using 230-400 mesh silica gel (flash chromatography). Dry solvents and reagents were obtained following standard procedures: triethylamine was distilled over CaH_2; DMF, CH_3CN and pyridine were dried by molecular sieves, THF, CH_2Cl_2 and pentane were from solvent

processing equipment (PureSolv, Innovative Technology). Cetyltrimethylammonium bromide (CTAB), sodium hydroxide, ammonium nitrate (NH_4NO_3), and potassium bromide were purchased from Sigma-Aldrich. Absolute ethanol was purchased from Fisher Chemicals and hydrochloric acid from VWR PROLABO.

3.5.2 Synthesis of silylated precursors

3.5.2.1 Synthesis of silylated precursor P10

3.5.2.1.1 Synthesis of *tert*-butyl prop-2-yn-1-ylcarbamate[64]

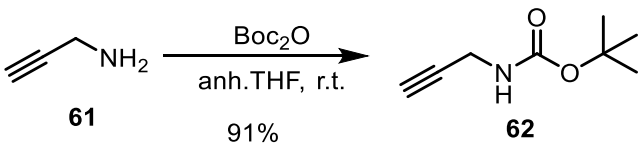

Propargylamine **61** (1.72 g, 31.22 mmol) and di-*tert*-butyl dicarbonate (6.88 g, 31.53 mmol) were dissolved in dry THF (30 mL) and the solution left under continuous stirring at room temperature during 5 hours. After removal of the solvent under reduced pressure, the resulting residue was dissolved in EtOAc (100 mL), washed with H_2O (30 mL × 3) and brine (30 mL). After drying the organic fraction with anhydrous sodium sulphate, the solvent was removed under vacuum obtaining the carbamate **62** as a yellow solid (4.42 g, 91% yield). **^{1}H NMR (360 MHz, $CDCl_3$) δ (ppm)**: 4.70 (br s, 1H), 3.92 (s, 2H), 2.21 (s, 1H), 1.45 (s, 9H).

3.5.2.1.2 Synthesis of *tert*-butyl di(prop-2-yn-1-yl)carbamate[64]

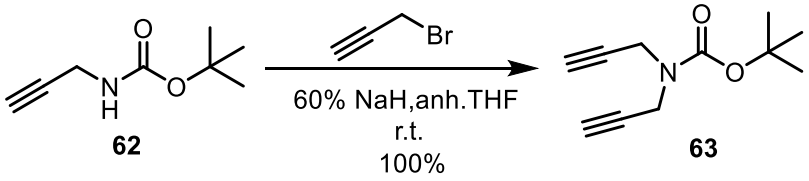

To a stirred solution of *tert*-butyl prop-2-yn-1-ylcarbamate **62** (4.65 g, 30.0 mmol) in dry THF (90.0 mL) was added NaH (1.68 g of 60% dispersion in oil, corresponding to 1.008 g of pure NaH, 42.0 mmol of NaH). The mixture was stirred for 30 min and then propargyl bromide (7.14 g of a 80% solution in toluene, corresponding to 5.712 g of propargyl bromide, 48.0 mmol) was added dropwise. The reaction mixture was stirred at room temperature overnight, and then quenched with saturated aqueous NH_4Cl. The resulting mixture was

extracted with EtOAc (100 mL × 3) and then the combined organic phase was washed with H_2O (60 mL × 3) and brine (60 mL) and dried with anhydrous sodium sulphate. After removing the solvent under vacuum, the pure product **63** was obtained by a flash column chromatography through silica gel eluting with hexane/DCM = 2:1, yellow liquid (5.77 g, 100% yield). **^{1}H NMR (360 MHz, $CDCl_3$) δ (ppm)**: 4.17 (br s, 4H), 2.22 (t, J = 3.6 Hz, 2H), 1.48 (s, 9H); ^{13}C NMR (91 MHz, $CDCl_3$) δ 154.2, 81.1, 78.8, 71.9, 35.1, 28.3.

3.5.2.1.3 Synthesis of *tert*-butyl bis((1-(3-(triethoxysilyl)propyl)-1H-1,2,3-triazol-4-yl)methyl)carbamate, P10

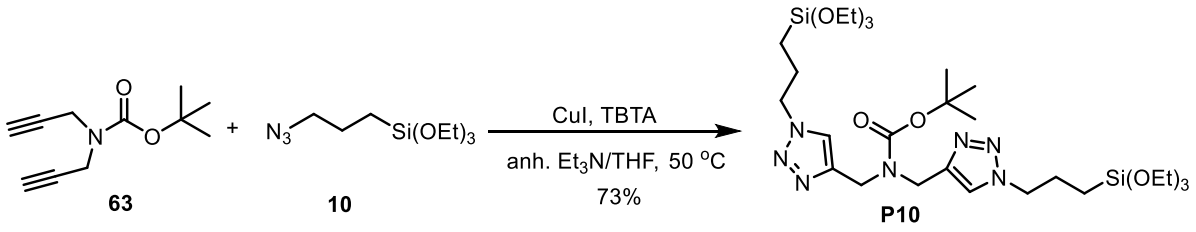

To a dry, 100 mL Schlenk flask equipped with a stir bar and under Argon atmosphere, CuI (7.60 mg, 0.04 mmol), TBTA (21.20 mg, 0.04 mmol) and anhydrous THF (20 mL) were added. The resulting mixture was stirred for 30 min, then (3-azidopropyl)triethoxysilane **10** (988.5 mg, 4.0 mmol), *tert*-butyl di(prop-2-yn-1-yl)carbamate **63** (463.46 mg, 2.4 mmol) and anhydrous Et_3N (1.0 mL, 0.73 g/mL 7.2 mmol) were added by using a syringe. The resulting mixture was stirred at 50 °C (Argon atmosphere) until *tert*-butyl di(prop-2-yn-1-yl)carbamate **63** was fully consumed (16 h, reaction monitored by TLC). Then, the solvent was evaporated under reduced pressure and the residue was washed with cold anhydrous pentane to remove some remaining azide. Hot anhydrous pentane was added to the insoluble fraction to extract the disilylated product, this digestion with hot pentane was repeated several times and the pentane extracts were concentrated under reduced pressure to provide the pure product **P10** as colorless oil (999 mg, 73% yield). **^{1}H NMR (360 MHz, $CDCl_3$) δ (ppm)**: 7.53 (s, 1H), 7.42 (s, 1H), 4.51 (s, 4H), 4.29 (t, J = 7.2 Hz, 4H), 3.78 (q, J = 7.2 Hz, 12H), 2.00-1.96 (m, 4H), 1.42 (s, 9H), 1.17 (t, J = 7.2 Hz, 18H), 0.56 (t, J = 7.2 Hz, 4H); **^{13}C NMR (91 MHz, $CDCl_3$) δ (ppm)**: 155.2, 122.7, 121.9, 80.3, 58.5, 58.4, 52.4, 28.4, 24.2, 18.2, 7.4. **IR (film)** 3132.4, 2973.6, 2927.2, 1692.6, 1390.2, 1163.5, 1073.1, 954.5, 783.2 cm^{-1}. **MS (ESI) m/z**: 688.4, 632.3, 588.3, 558.3; **HRMS (ESI) m/z** $[M + Na]^+$ calcd for $C_{29}H_{57}N_7O_8Si_2Na$: 688.3880, found: 688.3877.

3.5.2.2 Synthesis of silylated precursor P11

Synthesis of tert-butyl bis((1-(2-(bis(3-(triethoxysilyl)propyl)amino)ethyl)-1H-1,2,3-triazol-4-yl)methyl)carbamate, P11

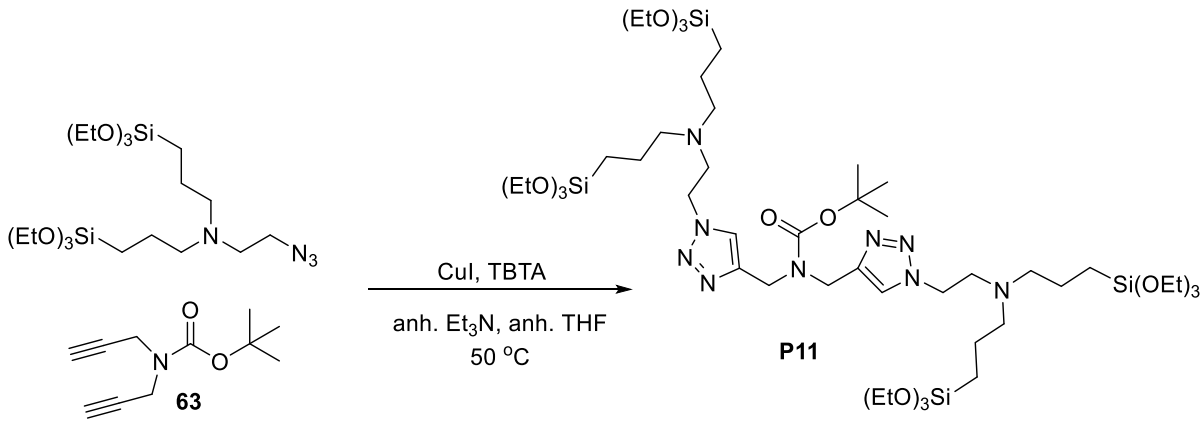

To a dry, 100 mL Schlenk flask equipped with a stir bar and under Argon atmosphere, CuI (7.60 mg, 0.04 mmol), TBTA (21.20 mg, 0.04 mmol) and anhydrous THF (20 mL) were added. The resulting mixture was stirred for 30 min, and then *N*-(2-azidoethyl)-3-(triethoxysilyl)-*N*-(3-(triethoxysilyl)propyl)propan-1-amine (1.98 g, 4.0 mmol), *tert*-butyl di(prop-2-yn-1-yl)carbamate **63** (463.46 mg, 2.4 mmol) and anhydrous Et_3N (1.0 mL, 0.73 g/mL, 7.2 mmol) were added by using a syringe. The resulting mixture was stirred at 50 °C (Argon atmosphere) until *tert*-butyl di(prop-2-yn-1-yl)carbamate was fully consumed (20 h, reaction monitored by TLC). Then, the solvent was partially evaporated under reduced pressure, the remaining solution was filtered through Whatman® membrane filters PTFE (pore size 0.2 μm, diam. 47 mm) and the filtrate evaporated at reduced pressure to afford the final product **P11** as colorless oil (2.27 g, 96% yield). **^{1}H NMR (360 MHz, $CDCl_3$) δ (ppm)**: 7.61 (s, 1H), 7.57 (s, 1H), 4.51 (s, 4H), 4.36 (t, *J* = 7.2 Hz, 4H), 3.80 (q, *J* = 7.2 Hz, 24H), 2.88 (t, *J* = 7.2 Hz, 4H), 2.47 (t, *J* = 7.2 Hz, 8H), 1.53-1.45 (m, 17H), 1.20 (t, *J* = 7.2 Hz, 36H), 0.54 (t, *J* = 7.2 Hz, 8H); **^{13}C NMR (91 MHz, $CDCl_3$) δ (ppm)**: 155.1, 128.9, 127.9, 80.1, 58.2, 57.0, 54.1, 48.8, 28.3, 28.1, 20.2, 18.1, 7.7. **IR (film):** 2972.4, 2927.2, 2882.9, 1695.7, 1457.0, 1389.6, 1164.1, 1073.0, 952.5, 770.1 cm^{-1}. **MS (ESI) m/z**: 1204.7, 1182.7, 688.4, 591.9, 413.3; **HRMS (ESI) m/z** $[M + Na]^+$ calcd for $C_{51}H_{107}N_9O_{14}Si_4Na$: 1204.6906, found: 1204.6894.

3.5.2.3 Synthesis of silylated precursor P12

3.5.2.3.1 Synthesis of 3-azidopropan-1-ol[80]

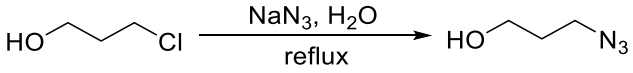

To a stirred solution of NaN_3 (13.00 g, 200 mmol) in H_2O (150 mL) was added 3-chloropropan-1-ol (9.40 g, 100 mmol). The mixture was refluxed for 15 h, then it was allowed to reach room temperature and it was extracted with CH_2Cl_2 (200 mL x 3). The combined organic layers were dried over anhydrous sodium sulfate, filtered and the solvent evaporated to afford 3-azidopropan-1-ol as a colourless liquid (9.31 g, 94% yield). **^{1}H NMR (360 MHz, $CDCl_3$) δ (ppm)**: 3.76 (br s, 2H), 3.45 (t, *J* = 7.2 Hz, 2H), 1.87-1.80 (m, 2H), 1.58 (br s, 1H).

3.5.2.3.2 Synthesis of 1-azido-3-iodopropane[80]

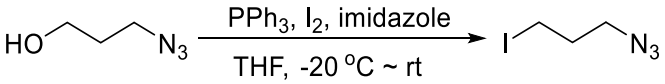

To a vigorously stirred solution of 3-azidopropan-1-ol (9.10 g, 90 mmol) in THF (160 mL) and under argon atmosphere were added PPh_3 (28.33 g, 108 mmol) and imidazole (18.38 g, 270 mmol). The mixture was stirred until total dissolution of the reagents, then it was cooled to -20 ºC and I_2 (29.70 g, 117 mmol) was added in portions. The reaction mixture was stirred at -20 ºC for 10 min, and then allowed to reach room temperature for 30 min. The reaction mixture was spurred into ice-water and a saturated aqueous solution of $NaHCO_3$ (100 mL) was added. A precipitate was formed, which was filtered, and the filtrate was extracted with diethyl ether (3 x 120 mL). The combined organic layers were dried over Na_2SO_4, filtered and the solvent evaporated to afford a residue which was purified by column chromatography on silica gel (hexane/EtOAc = 4/1) to afford a yellow oil (17.27 g, 91% yield). **^{1}H NMR (360 MHz, $CDCl_3$) δ (ppm)**: 3.44 (t, *J* = 7.2 Hz, 2H), 3.25 (t, *J* = 7.2 Hz, 2H), 2.08-2.00 (m, 2H); **^{13}C NMR (91 MHz, $CDCl_3$) δ (ppm)**: 51.47, 32.32, 2.35.

3.5.2.3.3 Synthesis of 3-azido-*N*,*N*-bis(3-(triethoxysilyl)propyl)propan-1-amine[81]

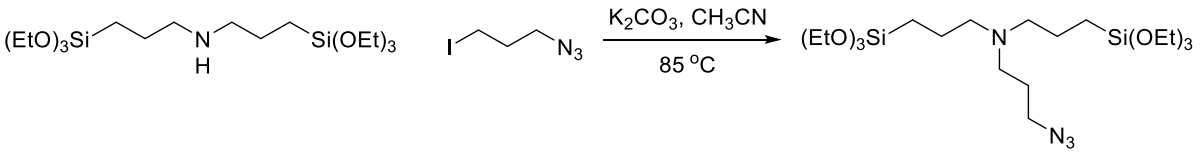

A mixture of bis(triethoxysilylpropyl)amine (12.77 g, 30.0 mmol), 3-iodopropylazide (6.33 g, 30.0 mmol) and potassium carbonate (8.29 g, 60.0 mmol) in acetonitrile (120 mL) was stirred overnight at 85 °C in a sealed tube. The mixture was filtered and the filtrate was concentrated, the final product was obtained as a yellow liquid (1.1 g, 93% yield). **^{1}H NMR (360 MHz, $CDCl_3$) δ (ppm)**: 3.82 (q, *J* = 7.2 Hz, 12H), 3.32 (t, *J* = 7.2 Hz, 2H), 2.47 (t, *J* = 7.2 Hz, 2H), 2.39 (t, *J* = 7.2 Hz, 4H), 1.71-1.67 (m, 2H), 1.54-1.47 (m, 4H), 1.22 (t, *J* = 7.2 Hz, 18H), 0.60-0.55 (m, 4H); **^{13}C NMR (91 MHz, $CDCl_3$) δ (ppm)**: 58.34, 57.13, 50.93, 49.72, 26.84, 20.33, 18.31, 7.96.

3.5.2.3.4 Synthesis of *tert*-butyl bis((1-(3-(bis(3-(triethoxysilyl)propyl)amino)propyl)-1*H*-1,2,3-triazol-4-yl)methyl)carbamate, P12

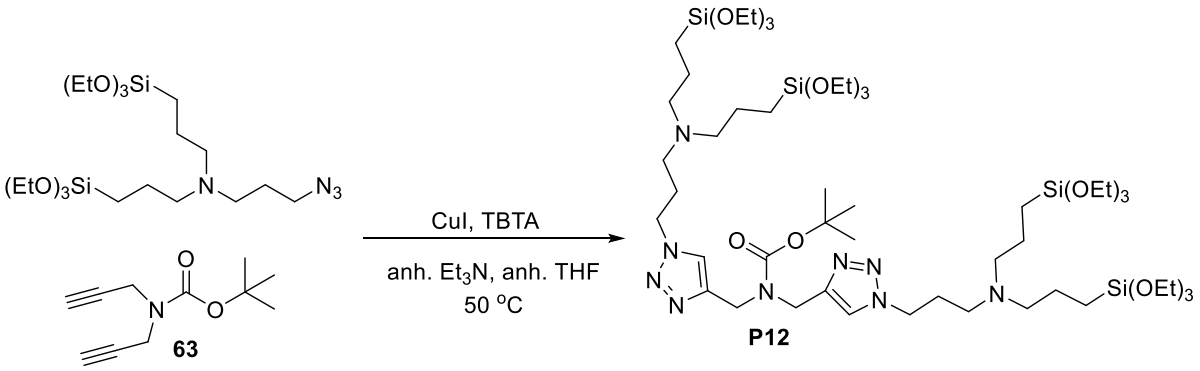

To a dry, 100 mL Schlenk flask equipped with a stir bar and under Argon atmosphere, CuI (7.60 mg, 0.04 mmol), TBTA (21.20 mg, 0.04 mmol) and anhydrous THF (20 mL) were added. The resulting mixture was stirred for 30 min, then 3-azido-*N*,*N*-bis(3-(triethoxysilyl)propyl)propan-1-amine (2.03 g, 4.0 mmol), *tert*-butyl di(prop-2-yn-1-yl)carbamate **63** (463.46 mg, 2.4 mmol) and anhydrous Et_3N (1.0 mL, 0.73 g/mL, 7.2 mmol) were added by using a syringe. The resulting mixture was stirred at 50 °C (Argon atmosphere) until *tert*-butyl di(prop-2-yn-1-yl)carbamate **63** was fully consumed (20 h, reaction monitored by TLC). Then, the solvent was partially evaporated under reduced pressure, the remaining solution was filtered through Whatman® membrane filters PTFE (pore size 0.2 μm, diam. 47 mm) and the filtrate was evaporated at reduced pressure to afford

the final product **P12** as colorless oil (2.33 g, 96% yield). **^{1}H NMR (360 MHz, $CDCl_3$) δ (ppm)**: 7.55 (s, 1H), 7.47 (s, 1H), 4.53 (s, 4H), 4.36 (t, *J* = 7.2 Hz, 4H), 3.81 (q, *J* = 7.2 Hz, 24H), 2.48-2.36 (m, 12H), 2.01 (t, *J* = 7.2 Hz, 4H), 1.52-1.46 (m, 17H), 1.21 (t, *J* = 7.2 Hz, 36H), 0.57 (t, *J* = 7.2 Hz, 8H); **^{13}C NMR (91 MHz, $CDCl_3$) δ (ppm)**: 155.2, 129.1, 128.0, 80.3, 58.3, 57.1, 56.8, 50.9, 48.5, 28.4, 26.8, 20.1, 18.3, 7.9. **IR (film)** 2972.7, 2926.8, 2883.2, 1695.4, 1455.6, 1389.7, 1164.0, 1072.8, 952.5, 770.3 cm^{-1}. **MS (ESI) m/z**: 1232.7, 1210.7, 816.5, 702.4, 605.9, 509.3, 438.3; **HRMS (ESI) m/z** $[M + Na]^+$ calcd for $C_{53}H_{111}N_9O_{14}Si_4Na$: 1232.7220, found: 1232.7195.

3.5.2.4 Synthesis of silylated precursor P13

3.5.2.4.1 Synthesis of but-3-en-1-yl methanesulfonate[67]

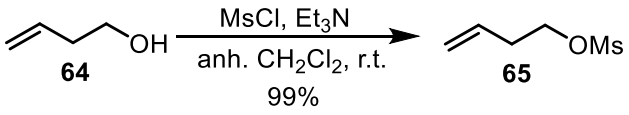

In a 250 mL Schlenk flask under nitrogen atmosphere were added but-3-en-1-ol **64** (8.0 mL, 0.843 g/mL, 93.50 mmol) dissolved in dry dichloromethane (100 mL) and dry triethylamine (5.0 mL, 0.73 g/ mL, 117 mmol). Then, the mixture was stirred with cooling (ice bath) over a period of 15 min. After this time, methanesulfonyl chloride (15.0 mL, 1.48 g/mL, 193.80 mmol) was added and the reaction mixture was stirred overnight at room temperature under argon atmosphere. Then, 100 mL of fresh dichloromethane were added to the crude and it was washed first with HCl 5 M (50 mL x 2) and then with saturated aqueous solution of Na_2CO_3 (50 mL x 2) and brine (50 mL x 2).The organic fraction was dried using anhydrous sodium sulphate and the solvent evaporated under vacuum to afford the final product **65** as yellow liquid (13.80 g, 99% yield). **^{1}H NMR (360 MHz, $CDCl_3$) δ (ppm)**: 5.84-5.73 (m, 1H), 5.21-5.14 (m, 2H), 4.27 (t, *J* = 7.2 Hz, 2H), 3.01 (s, 3H), 2.54-2.48 (m, 2H).

3.5.2.4.2 Synthesis of 3,5-bis(but-3-en-1-yloxy)benzaldehyde 67

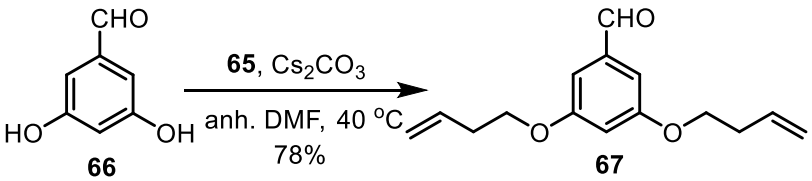

To a stirred mixture of 3,5-dihydroxybenzaldehyde **66** (1.38 g, 10.0 mmol) and cesium carbonate (13.03 g, 40.0 mmol) in anhydrous DMF (80 mL) was added an excess of but-3-en-

1-yl methanesulfonate **65** (4.50 g, 30.0 mmol). The reaction was stirred at 40 ºC under argon atmosphere until 3,5-dihydroxybenzaldehyde was fully consumed (TLC monitoring, 48 h). Then, 100 mL of water were added and the product was extracted using hexane (200 mL x 3). The organic phase was washed with 1 M NaOH solution to remove excess of but-3-en-1-yl methanesulfonate, dried with anhydrous sodium sulfate and the solvent was removed under vacuum to afford the final product **67** as yellow liquid (1.93 g, 78% yield). **^{1}H NMR (360 MHz, $CDCl_3$) δ (ppm)**: 9.89 (s, 1H), 7.00 (br s, 2H), 6.71 (br s, 1H), 5.93-5.84 (m, 2H), 5.20-5.11 (m, 4H), 4.05 (t, *J* = 7.2 Hz, 4H), 2.58-2.55 (m, 4H); **^{13}C NMR (91 MHz, $CDCl_3$) δ (ppm)**: 192.0, 160.5, 138.3, 134.1, 117.3, 108.1, 107.8, 67.6, 33.5. **IR (film):** 3078.9, 2980.0, 2876.7, 1697.7, 1592.4, 1452.6, 1295.6, 1296.0, 1165.9, 1065.9, 1065.1, 843.9, 676.0 cm^{-1}. **GC-MS (EI) m/z:** 246.2 [M^+], 192.1, 163.1, 150.1, 138.0, 121.1, 110.0, 91.1, 75.0, 65.1, 55.1; **HRMS (ESI) m/z** $[M + Na]^+$ calcd for $C_{15}H_{18}O_3Na$: 269.1148 , found: 269.1141.

3.5.2.4.3 Synthesis of 3,5-bis(but-3-en-1-yloxy)benzoic acid 68[68]

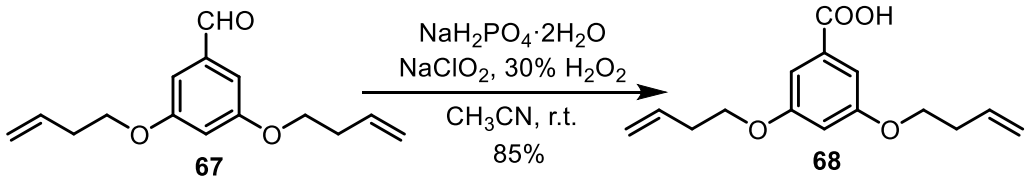

To a stirred solution of 3,5-bis(but-3-en-1-yloxy)benzaldehyde **67** (1.97 g, 8.0 mmol) in acetonitrile (12.0 mL) was added a solution of $NaH_2PO_4{\cdot}2H_2O$ (374.4 mg, 2.4 mmol) in water (5.0 mL) and 30% H_2O_2 (4.0 mL, 9.97 mol/L, 40.0 mmol). Finally, a solution of 80% purity $NaClO_2$ (1.27 g, 11.2 mmol) in water (10.0 mL) was added dropwise during 2 h to the stirred mixture at room temperature. Oxygen evolved from the solution was monitored until the end of the reaction with a bubbler connected to the flask. A small amount of Na_2SO_3 was added to destroy the unreacted HClO and H_2O_2. The mixture was acidified with 10% aqueous HCl, and the product was extracted using ethyl acetate (60 mL x 3). The organic phase was dried with anhydrous sodium sulfate and the solvent was removed under vacuum to afford a residue which was purified by a flash column chromatography through silica gel eluting with hexane/EtOAc = 2:1, obtaining the product **68** as a colorless solid (1.78 g, 85% yield). **^{1}H NMR (360 MHz, $CDCl_3$) δ (ppm)**: 7.25 (d, *J* = 3.6 Hz, 2H), 6.70 (br s, 1H), 5.94-5.85 (m, 2H), 5.21-5.11 (m, 4H), 4.05 (t, *J* = 7.2 Hz, 4H), 2.58-2.53 (m, 4H); **^{13}C NMR (91 MHz, $CDCl_3$) δ (ppm)**: 171.7, 160.0, 134.2, 130.9, 117.2, 108.4, 107.6, 67.5, 33.5.

3.5.2.4.4 Synthesis of *tert*-butyl 3,5-bis(but-3-en-1-yloxy)benzoate 69[82]

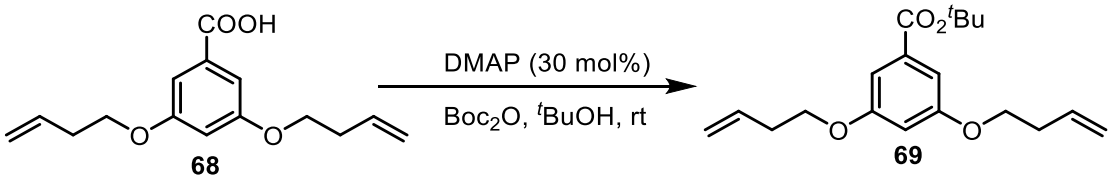

In a 10 mL round bottom flask, 3,5-bis(but-3-en-1-yloxy)benzoic acid **68** (1.31 g, 5.0 mmol), di-*tert*-butyl dicarbonate (2.18 g, 10.0 mmol) and 4-dimethylaminopyridine (183.3 mg, 1.5 mmol) were dissolved in 40 mL of *tert*-butanol. The reaction mixture was stirred at room temperature under argon atmosphere until 3,5-bis(but-3-en-1-yloxy)benzoic acid **68** was fully consumed (TLC monitoring, 48 h). Then, the solvent was removed under reduced pressure and the residue was purified by flash column chromatography through silica gel eluting with hexane/AcOEt = 15:1, obtaining the pure product **69** as colorless oil (1.38 g, 87% yield). **^{1}H NMR (360 MHz, $CDCl_3$) δ (ppm)**: 7.13 (d, J = 3.6 Hz, 2H), 6.62 (t, J = 3.6 Hz, 1H), 5.94-5.84 (m, 2H), 5.20-5.10 (m, 4H), 4.03 (t, J = 7.2 Hz, 4H), 2.56-2.53 (m, 4H), 1.58 (s, 9H); **^{13}C NMR (91 MHz, $CDCl_3$) δ (ppm)**: 165.5, 159.8, 134.3, 133.9, 117.1, 107.8, 105.9, 81.2, 67.4, 33.5, 28.2. **IR (film):** 3078.7, 2977.7, 1711.7, 1594.3, 1445.8, 1300.5, 1159.9, 1049.1, 915.6, 767.2 cm^{-1}. **GC-MS (EI) m/z:** 318.2 $[M]^+$, 262.1, 245.2, 208.1, 190.1, 166.1, 154.0, 136.0, 55.1; **HRMS (ESI) m/z** $[M + Na]^+$ calcd for $C_{19}H_{26}O_4Na$: 341.1723, found: 341.1707.

3.5.2.4.5 Synthesis of *tert*-butyl 3,5-bis(4-((3-(triethoxysilyl)propyl)thio)butoxy)benzoate, P13[71]

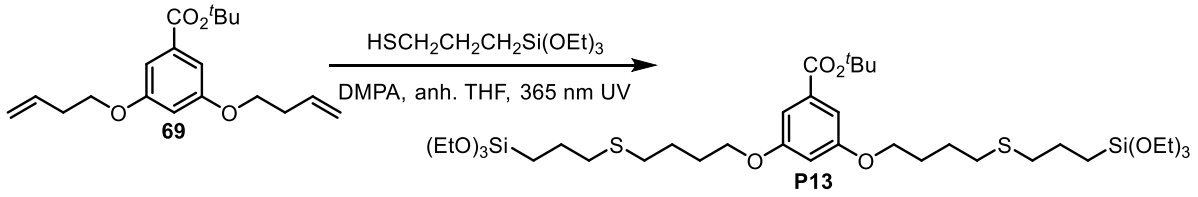

In a 50 mL Schlenk tube under nitrogen, *tert*-butyl 3,5-bis(but-3-en-1-yloxy)benzoate **69** (954.5 mg, 3.0 mmol) and 2,2-dimethoxy-1,2-diphenylethanone (DMPA) (153.8 mg, 0.6 mmol) were dissolved in anhydrous THF (12.0 mL). Then (3-mercaptopropyl)triethoxysilane (1.5 g, 6.3 mmol) was added and the stirred mixture was irradiated with a UV lamp at 365 nm

under argon atmosphere until *tert*-butyl 3,5-bis(but-3-en-1-yloxy)benzoate **69** was fully consumed (TLC monitoring, 16 h). Then, the solvent was removed under reduced pressure and the residue was purified by flash column chromatography through silica gel eluting with hexane/AcOEt = 10:1, obtaining the pure product **P13** as colorless oil (1.66 g, 70% yield). **^{1}H NMR (360 MHz, $CDCl_3$) δ (ppm)**: 7.09 (br s, 2H), 6.58 (br s, 1H), 3.97 (t, *J* = 7.2 Hz, 4H), 3.82 (q, *J* = 7.2 Hz, 12H), 2.56 (apparent q, *J* = 7.2 Hz, 8H), 1.88-1.76 (m, 4H), 1.74-1.70 (m, 8H), 1.57 (s, 9H), 1.21 (t, *J* = 7.2 Hz, 18H), 0.74 (t, *J* = 7.2 Hz, 4H); **^{13}C NMR (91 MHz, $CDCl_3$) δ (ppm)**: 165.6, 159.9, 133.8, 107.6, 105.7, 81.2, 67.6, 58.4, 35.1, 31.6, 28.4, 28.1, 26.2, 23.2, 18.3, 9.9. **IR (film):** 2972.2, 2925.1, 1713.7, 1594.6, 1445.3, 1389.1, 1326.1, 1248.8, 1161.9, 1074.2, 956.6, 768.1 cm^{-1}. **MS (ESI) m/z:** 817.4 $[M+Na]^+$, 749.4, 647.3, 425.3, 393.3; **HRMS (ESI) m/z** $[M + Na]^+$ calcd for $C_{37}H_{70}O_{10}S_2Si_2Na$: 817.3841, found: 817.3846.

3.5.2.5 Synthesis of silylated precursor P14

3.5.2.5.1 Synthesis of 3-(benzyloxy)propan-1-ol 71[72]

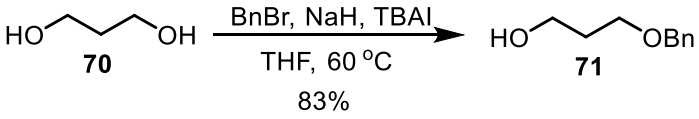

To a solution of propane-1,3-diol **70** (7.60 g, 100 mmol) in 200 mL of anhydrous THF was added NaH (4.40 g, 60% dispersion in mineral oil, 110 mmol) portionwise. The mixture was stirred at room temperature for 30 min, then benzyl bromide (18.90 g, 110 mmol) was added dropwise, followed by tetrabutylammonium iodide (7.40 g, 20 mmol) in one portion. The mixture was heated to 60 ºC and stirred overnight. After cooling, an equal volume of water was added, and the mixture was extracted with diethyl ether. The combined organic layer was washed with brine, dried over anhydrous Na_2SO_4, and filtrated. The solvent was evaporated, and the resulting residue was purified by flash column chromatography on silica gel with hexane/EtOAc = 5:1 to afford a yellow liquid (13.80 g, 83% yield). **^{1}H NMR (360 MHz, $CDCl_3$) δ (ppm)**: 7.38-7.28 (m, 5H), 4.53 (s, 2H), 3.80 (apparent q, *J* = 7.2 Hz, 2H), 3.67 (t, *J* = 7.2 Hz, 2H), 2.28 (t, *J* = 3.6 Hz, 1 H), 1.91-1.84 (m, 2H).

3.5.2.5.2 Synthesis of ((3-iodopropoxy)methyl)benzene 72[72]

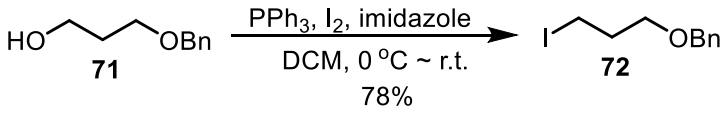

To a solution of 3-(benzyloxy)propan-1-ol **71** (9.30 g, 56.0 mmol) in 180 mL of CH_2Cl_2 was added PPh_3 (15.42 g, 58.8 mmol) and imidazole (4.57g, 61.6 mmol), followed by the addition of iodine portionwise (15.63 g, 61.6 mmol) at 0 ºC (ice bath). Then the reaction mixture was stirred at rt for 16 h and then quenched with aqueous Na_2SO_3 solution. The organic layer was separated and the aqueous layer was extracted with CH_2Cl_2. The combined organic layer was dried with Na_2SO_4 and filtered. The solvent was evaporated, the residue was purified by flash column chromatography through silica gel eluting with hexane, obtaining a colorless liquid (12.1 g, 78% yield). **^{1}H NMR (360 MHz, $CDCl_3$) δ (ppm)**: 7.38-7.27 (m, 5H), 4.52 (s, 2H), 3.54 (t, *J* = 7.2 Hz, 2H), 3.31 (t, *J* = 7.2 Hz, 2H), 2.13-2.06 (m, 2H).

3.5.2.5.3 Synthesis of 3,5-bis(3-(benzyloxy)propoxy)benzaldehyde 73

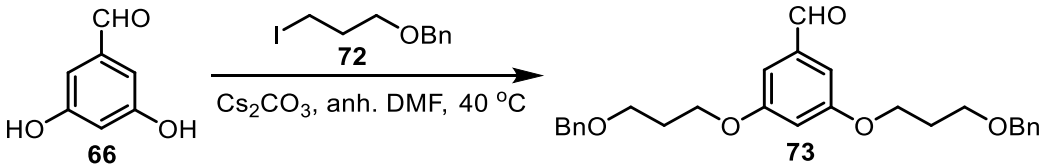

To a stirred solution of 3,5-dihydroxybenzaldehyde **66** (2.07 g, 15 mmol) and cesium carbonate (24.44 g, 75.0 mmol) in anhydrous DMF (120 mL) was added an excess of ((3-iodopropoxy)methyl)benzene **72** (10.35 g, 37.5 mmol). The reaction was stirred at 40 ºC under argon atmosphere until 3,5-dihydroxybenzaldehyde **66** was fully consumed (TLC monitoring, 41 h). Then, 60 mL H_2O were added and the product was extracted using EtOAc (80 mL x 3). The organic phase was washed with water (3 times), dried with anhydrous sodium sulfate and the solvent was removed under vacuum to afford the crude product as yellow liquid. The pure product was obtained by a flash column chromatography through silica gel eluting with hexane/EtOAc = 5:1, colorless oil (6.07 g, 93% yield). **^{1}H NMR (360 MHz, $CDCl_3$) δ (ppm)**: 9.88 (s, 1H), 7.33-7.27 (m, 10H), 7.00 (d, *J* = 3.6 Hz, 2H), 6.69 (t, *J* = 3.6 Hz, 1H), 4.53 (s, 4H), 4.12 (t, *J* = 7.2 Hz, 4H), 3.66 (t, *J* = 7.2 Hz, 4H), 2.13-2.05 (m, 4H); **^{13}C NMR (91 MHz, $CDCl_3$) δ (ppm)**: 192.1, 160.6, 151.8, 138.3, 128.4, 127.7, 127.6,

108.0, 107.7, 73.1, 66.6, 65.3, 29.6. **IR (film):** 3029.5, 2932.3, 1696.8, 1591.9, 1452.1, 1295.4, 1164.7, 1094.2, 734.2, 696.7 cm^{-1}. **ESI-MS m/z:** 457.2 $[M + Na]^+$, 306.9, 249.9, 181.1, 165.1, 141.1, 91.1; **HRMS (ESI) m/z** $[M + Na]^+$ calcd for $C_{27}H_{30}O_5Na$: 457.1985, found: 457.1984.

3.5.2.5.4 Synthesis of 3,5-bis(3-(benzyloxy)propoxy)benzoic acid 74[68]

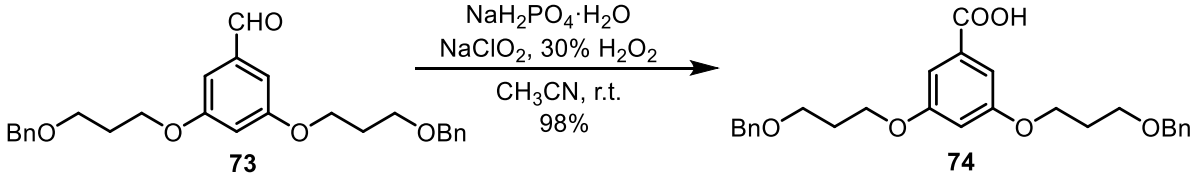

To a stirred solution of 3,5-bis(3-(benzyloxy)propoxy)benzaldehyde (3.70 g, 8.5 mmol) in acetonitrile (20 mL) was added a solution of $NaH_2PO_4 \cdot 2H_2O$ (358.0 mg, 2.30 mmol) in water (5.0 mL) and 30% H_2O_2 (1.1 mL, 9.97 mol/L, 10.97 mmol). Finally, a solution of 80% purity $NaClO_2$ (1.36 g, 12.0 mmol) in water (12 mL) was added dropwise during 2 h to the stirred mixture at room temperature. Oxygen evolved from the solution was monitored until the end of the reaction with a bubbler connected to the flask. A small amount of Na_2SO_3 was added to destroy the unreacted oxidant reagents. The reaction mixture was acidified with 10% aqueous HCl, and the product was extracted using ethyl acetate (80 mL x 3). The organic phase was dried with anhydrous sodium sulfate and the solvent was removed under vacuum to afford the crude product, which was purified by a flash column chromatography through silica gel eluting with hexane/EtOAc = 1:2, white solid (3.78 g, 99% yield). **^{1}H NMR (360 MHz, $CDCl_3$) δ (ppm)**: 7.32-7.24 (m, 12H), 6.67 (br s, 1H), 4.53 (s, 4H), 4.12 (t, J = 7.2 Hz, 4H), 3.67 (t, J = 7.2 Hz, 4H), 2.18-2.05 (m, 4H); **^{13}C NMR (91 MHz, $CDCl_3$) δ (ppm)**: 160.1, 152.7, 138.3, 129.8, 128.4, 127.7, 127.6, 108.3, 107.4, 73.1, 66.6, 65.2, 29.6. **IR (film):** 3651.4, 3024.9, 2861.2, 1686.4, 1593.5, 1445.7, 1393.4, 1297.5, 1169.4, 1091.7 cm^{-1}. **ESI-MS m/z:** 473.2 $[M + Na]^+$, 433.2, 283.1, 239.1, 181.1, 122.1; **HRMS (ESI): m/z** $[M + Na]^+$ calcd for $C_{27}H_{30}O_6Na$: 473.1935, found: 473.1937.

3.5.2.5.5 Synthesis of *tert*-butyl 3,5-bis(3-(benzyloxy)propoxy)benzoate 75[83]

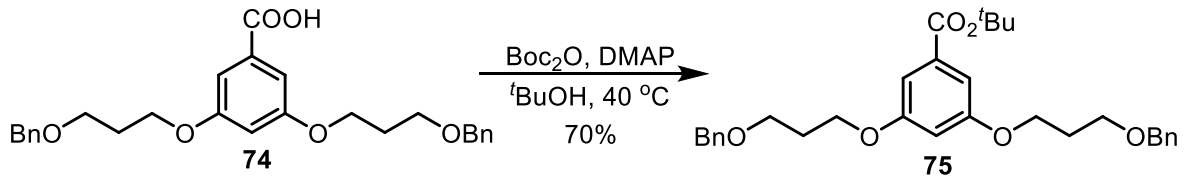

In a 10 mL round bottom flask, 3,5-bis(3-(benzyloxy)propoxy)benzoic acid **74** (5.40 g, 12.0 mmol) , di-*tert*-butyl dicarbonate (5.24 g, 24.0 mmol) and 4-dimethylaminopyridine (439.8 mg, 3.6 mmol) were dissolved in 80 mL of *tert*-butanol. The reaction mixture was stirred at 40 ºC under argon atmosphere until 3,5-bis(3-(benzyloxy)propoxy)benzoic acid **74** was fully consumed (TLC monitoring, 48 h). Then, the solvent was removed under reduced pressure and the residue was purified by flash column chromatography through silica gel eluting with hexane/AcOEt = 10:1, obtaining the pure product **75** as colorless oil (4.25 g, 70% yield). **^{1}H NMR (360 MHz, $CDCl_3$) δ (ppm)**: 7.33-7.12 (m, 10H), 7.13 (d, J = 3.6 Hz, 2H), 6.60 (t, J = 3.6 Hz, 1H), 4.52 (s, 4H), 4.09 (t, J = 7.2 Hz, 4H), 3.65 (t, J = 7.2 Hz, 4H), 2.10-2.04 (m, 4H), 1.58 (s, 9H); **^{13}C NMR (91 MHz, $CDCl_3$) δ (ppm)**: 165.6, 159.6, 138.4, 133.9, 128.4, 127.65, 127.60, 107.8, 105.8, 81.1, 73.1, 66.7, 65.1, 29.7, 28.2. **IR (film):** 3651.4, 2930.3, 2860.4, 1710.1, 1593.9, 1445.8, 1300.6, 1160.7, 1096.4, 731.9, 696.7 cm^{-1}. **ESI-MS m/z:** 529.3 $[M + Na]^+$, 451.3, 433.2, 283.1, 265.1, 181.1, 122.1; **HRMS (ESI): m/z** $[M + Na]^+$ calcd for $C_{31}H_{38}O_6Na$: 529.2561, found: 529.2555.

3.5.2.5.6 Synthesis of *tert*-butyl 3,5-bis(3-hydroxypropoxy)benzoate 76[84]

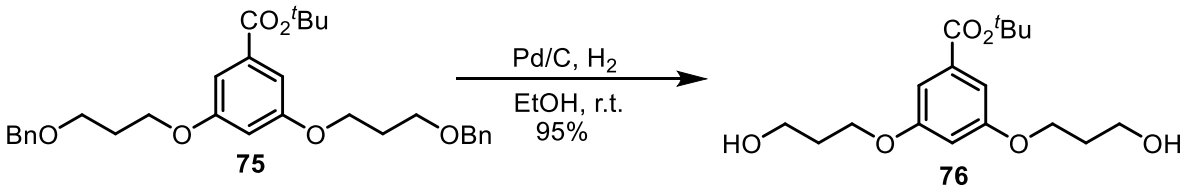

A mixture of *tert*-butyl 3,5-bis(3-(benzyloxy)propoxy)benzoate **75** (1.40 g, 2.77 mmol) and preequilibrated 10% Pd/C (0.308 g, 0.029 mmol Pd) in 20 mL of absolute ethanol was hydrogenated at room temperature and atmospheric pressure. When *tert*-butyl 3,5-bis(3-(benzyloxy)propoxy)benzoate **75** was fully consumed (TLC monitoring, 17 h), the mixture was filtered through celite® 545, and the filtrate was evaporated at reduced pressure to afford the crude product. The pure product was obtained after flash column chromatography through

silica gel eluting with hexane/EtOAc = 1:2, white solid (858 mg, 95% yield). **^{1}H NMR (360 MHz, $CDCl_3$) δ (ppm)**: 7.14 (d, *J* = 3.6 Hz, 2H), 6.62 (t, *J* = 3.6 Hz, 1H), 4.16-4.12 (m, 4H), 3.85 (t, *J* = 7.2 Hz, 4H), 2.07-2.01 (m, 4H), 1.58 (s, 9H); **^{13}C NMR (91 MHz, $CDCl_3$) δ (ppm)**: 165.4, 159.7, 134.0, 107.8, 105.8, 81.3, 65.9, 60.3, 31.9, 28.1. **IR (film):** 3274.5, 2967.9, 2870.6, 1705.7, 1595.1, 1447.7, 1349.7, 1299.2, 1169.9, 1058.6, 847.4, 767.4 cm^{-1}. **ESI-MS m/z:** 349.2 $[M + Na]^+$, 293.1, 271.1, 253.1, 195.1, 122.1**; HRMS (ESI): m/z** $[M + Na]^+$ calcd for $C_{17}H_{26}O_6Na$: 349.1622, found: 349.1618.

3.5.2.5.7 Synthesis of *tert*-butyl 3,5-bis((4,4-diethoxy-9-oxo-3,10-dioxa-8-aza-4-silatridecan-13-yl)oxy)benzoate, P14

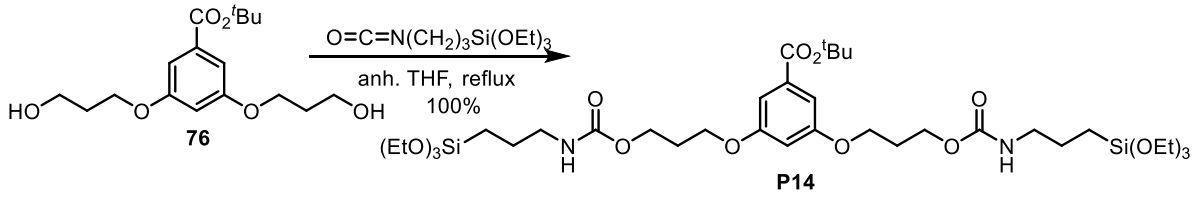

In a 100 mL Schlenk tube under nitrogen, *tert*-butyl 3,5-bis(3-hydroxypropoxy)benzoate **76** (1.96 g, 6.0 mmol) and 3-(isocyanatopropyl)triethoxysilane (7.42 g, 7.42 mL, 1.0 g/mL, 30.0 mmol) were dissolved in dry THF (20 mL). The mixture was stirred under reflux and argon atmosphere. After 17 hours, the starting material was fully consumed (TLC monitoring). Then, the solvent was removed under reduced pressure and the residue was purified by flash column chromatography through silica gel eluting with hexane/EtOAc = 2:1 to obtain the pure product **P14** as colorless oil (4.90 g, 100% yield). **^{1}H NMR (360 MHz, $CDCl_3$) δ (ppm)**: 7.12 (broad s, 2H), 6.59 (t, *J* = 3.6 Hz, 1H), 4.99 (br s, 2H), 4.22 (t, *J* = 7.2 Hz, 4H), 4.05 (t, *J* = 7.2 Hz, 4H), 3.81 (q, *J* = 7.2 Hz, 12H), 3.18 (q, *J* = 7.2 Hz, 4H), 2.09-2.04 (m, 4H), 1.72-1.61 (m, 4H), 1.57 (s, 9H), 1.21 (t, *J* = 7.2 Hz, 18H), 0.62 (t, *J* = 7.2 Hz, 4H); **^{13}C NMR (91 MHz, $CDCl_3$) δ (ppm)**: 165.5, 159.7, 156.5, 133.8, 107.7, 105.8, 81.2, 64.6, 61.3, 58.4, 43.4, 28.9, 28.1, 23.3, 18.3, 7.6. **IR (film):** 3343.6, 2972.7, 2927.5, 1708.6, 1595.9, 15527.2, 1242.3, 1163.0, 1071.9, 953.2, 767.1 cm^{-1}. **ESI-MS m/z:** 843.1 $[M + Na]^+$, 775.4, 729.3, 673.3; **HRMS (ESI): m/z** $[M + Na]^+$ calcd for $C_{37}H_{68}N_2O_{14}Si_2Na$: 843.4101, found: 843.4108.

3.5.2.6 Synthesis of silylated precursors P15 and P16

3.5.2.6.1 Synthesis of tri-*tert*-butyl 1,4,7,10-tetraazacyclododecane-1,4,7-tricarboxylate[73]

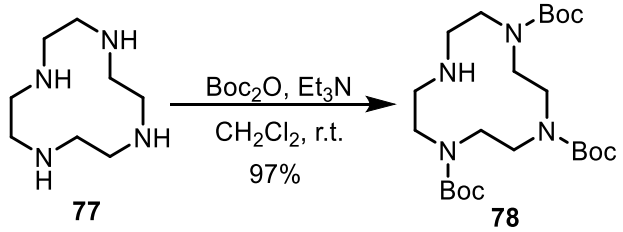

A solution of di-*tert*-butyl dicarbonate (2.28 g, 10.45 mmol) in anhydrous CH_2Cl_2 (60 mL) was added dropwise over 1 h to the solution of cyclen **77** (1.00 g, 5.81 mmol) and Et_3N (4.03 mL, 0.73 g/mL, 29.05 mmol), in CH_2Cl_2 (250 mL) under nitrogen atmosphere. After the addition, the mixture was cooled to 0 ºC. A second solution of Boc_2O (1.52 g, 6.97 mmol) in CH_2Cl_2 (60 mL) was added dropwise over 1 h. The solution was slowly warmed to room temperature and stirred for 18 h, washed with aqueous 1 M Na_2CO_3 (2 × 150 mL), dried with anhydrous Na_2SO_4, and concentrated under reduced pressure to obtain the crude product as a white solid, which was used in the next step without further purification (2.65 g, 97% yield)**.** **^{1}H NMR (360 MHz, $CDCl_3$) δ (ppm)**: 3.61 (br s, 4H), 3.39-3.27 (m, 8H), 2.84 (br s, 4H), 1.46 (br s, 9H), 1.44 (br s, 18H).

3.5.2.6.2 Synthesis of tri-*tert*-butyl 10-(prop-2-yn-1-yl)-1,4,7,10-tetraazacyclododecane-1,4,7-tricarboxylate 79[74]

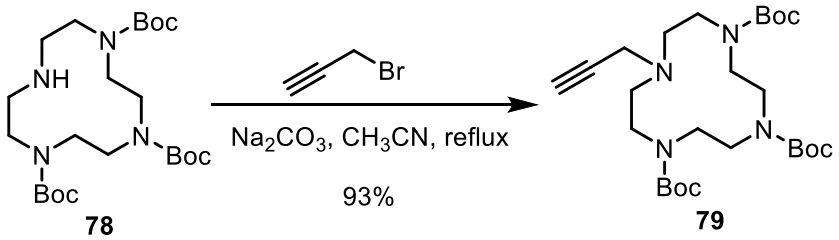

To a stirred solution of *tri*-boc cyclen **78** (2.36 g, 5.0 mmol) in CH_3CN (60 mL) was added Na_2CO_3 (1.06 g, 10.0 mmol) and propargyl bromide (80% in toluene, 0.89 g, 6.0 mmol). The mixture was heated at reflux for 16 h. The insoluble residues were separated by filtration and the solvent removed in vacuo. The residue was purified by flash column chromatography on silica gel with hexane/ EtOAc = 2:1 to afford a white solid (2.36 g, 93% yield). **^{1}H NMR (360 MHz, $CDCl_3$) δ (ppm)**: 3.51-3.30 (m, 14H), 2.78 (br s, 4H), 2.08 (br s, 1H), 1.46 (br s, 9H), 1.44 (br s, 18H).

3.5.2.6.3 Synthesis of tri-*tert*-butyl 10-((1-(2-(bis(3-(triethoxysilyl)propyl)amino)ethyl)-1*H*-1,2,3-triazol-4-yl)methyl)-1,4,7,10-tetraazacyclododecane-1,4,7-tricarboxylate, P15

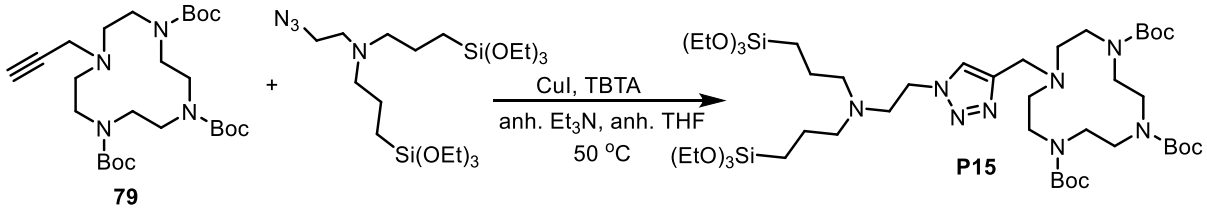

To a dry, 100 mL Schlenk flask equipped with a stir bar and under Argon atmosphere, CuI (7.60 mg, 0.04 mmol), TBTA (21.20 mg, 0.04 mmol) and anhydrous THF (20 mL) were added. The resulting mixture was stirred for 30 min, then tri-*tert*-butyl 10-(prop-2-yn-1-yl)-1,4,7,10-tetraazacyclododecane-1,4,7-tricarboxylate **79** (1.02 g, 2.0 mmol), *N*-(2-azidoethyl)-3-(triethoxysilyl)-*N*-(3-(triethoxysilyl)propyl)propan-1-amine (0.99 g, 2.0 mmol) and anhydrous Et_3N (1.0 mL, 0.73 g/mL 7.2 mmol) were added by using a syringe. The resulting mixture was stirred at 50 ºC (Argon atmosphere) until tri-*tert*-butyl 10-(prop-2-yn-1-yl)-1,4,7,10-tetraazacyclododecane-1,4,7-tricarboxylate was fully consumed (48 h, reaction monitored by TLC). Then, the solvent was evaporated under reduced pressure and anhydrous hot pentane was added to the residue to extract the bis-silylated product, this digestion with hot pentane was repeated several times and the pentane extracts were concentrated under reduced pressure to provide the pure product **P15** as colorless oil (1.87 g, 93% yield). **^{1}H NMR (360 MHz, $CDCl_3$) δ (ppm)**: 7.50 (s, 1H), 4.35 (t, *J* = 7.2 Hz, 2H), 3.89 (s, 2H), 3.81 (q, *J* = 7.2 Hz, 12H), 3.56 (br s, 4H), 3.36 (br s, 8H), 2.88 (t, *J* = 7.2 Hz, 2H), 2.69-2.62 (m, 4H), 2.46 (t, *J* = 7.2 Hz, 4H),1.46-1.43 (m, 27+4H), 1.21 (t, *J* = 7.2 Hz, 18H), 0.54 (t, *J* = 7.2 Hz, 4H); **^{13}C NMR (151 MHz, $CDCl_3$) δ (ppm)**: 156.3, 155.9, 155.5, 141.6, 123.8, 79.7, 79.5, 79.3, 58.5, 57.2, 54.4, 53.2, 50.2, 49.0, 47.8, 45.3, 28.9, 28.7, 28.6, 20.5, 18.5, 8.0. **IR (film):** 2972.7, 2927.5, 2883.9, 2811.6, 2097.6, 1685.9, 1458.1, 1412.6, 1364.2, 1248.7, 1157.1, 1074.7, 953.3, 771.2 cm^{-1}. **MS (ESI) m/z:** 1005.6 $[M + H]^+$, 713.4, 595.4, 403.3; **HRMS (ESI) m/z** $[M + Na]^+$ calcd for $C_{46}H_{92}N_8O_{12}Si_2Na$: 1027.6265, found: 1027.6233.

3.5.2.6.4 Synthesis of tri-*tert*-butyl 10-((1-(3-(bis(3-(triethoxysilyl)propyl)amino)propyl)-1*H*-1,2,3-triazol-4-yl)methyl)-1,4,7,10-tetraazacyclododecane-1,4,7-tricarboxylate, P16

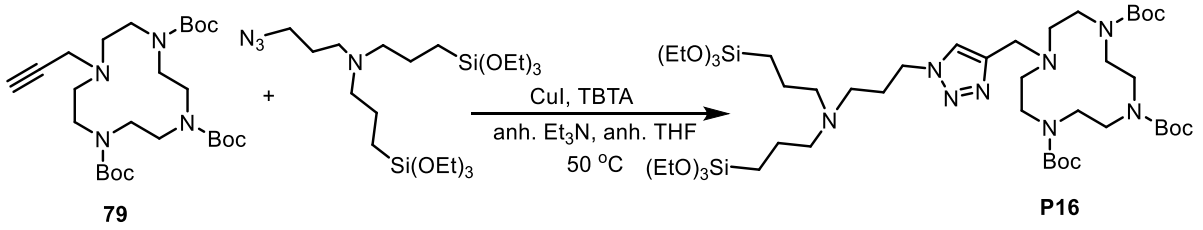

To a dry, 100 mL Schlenk flask equipped with a stir bar and under Argon atmosphere, CuI (7.60 mg, 0.04 mmol), TBTA (21.20 mg, 0.04 mmol) and anhydrous THF (20 mL) were added. The resulting mixture was stirred for 30 min, then tri-*tert*-butyl 10-(prop-2-yn-1-yl)-1,4,7,10-tetraazacyclododecane-1,4,7-tricarboxylate **79** (1.02 g, 2.0 mmol), 3-azido-*N*,*N*-bis(3-(triethoxysilyl)propyl)propan-1-amine (1.02 g, 2.0 mmol) and anhydrous Et_3N (1.0 mL, 0.73 g/mL 7.2 mmol) were added by using a syringe. The resulting mixture was stirred at 50 ºC (Argon atmosphere) until tri-*tert*-butyl 10-(prop-2-yn-1-yl)-1,4,7,10-tetraazacyclododecane-1,4,7-tricarboxylate was fully consumed (48 h, reaction monitored by TLC). Then, the solvent was evaporated under reduced pressure and hot anhydrous pentane was added to the residue to extract the bis-silylated product, this digestion with hot pentane was repeated several times and the pentane extracts were concentrated under reduced pressure to provide the pure product **P16** as colorless oil (1.80 g, 88% yield). **^{1}H NMR (360 MHz, $CDCl_3$) δ (ppm)**: 7.43 (s, 1H), 4.35 (t, *J* = 7.2 Hz, 2H), 3.89 (s, 2H), 3.83 (q, *J* = 7.2 Hz, 12H), 3.35 (br s, 4H), 3.35-3.31 (m, 8H), 2.69-2.61 (m, 4H), 2.43-2.37 (m, 6H), 2.00 (t, *J* = 7.2 Hz, 2H), 1.50-1.43 (m, 27+4H), 1.21 (t, *J* = 7.2 Hz, 18H), 0.56 (t, *J* = 7.2 Hz, 4H); **^{13}C NMR (151 MHz, $CDCl_3$) δ (ppm)**: 156.2, 155.7, 155.4, 141.7, 123.1, 79.5, 79.4, 79.2, 58.3, 57.2, 56.8, 54.4, 53.4, 53.1, 51.0, 50.8, 50.1, 49.7, 48.5, 48.2, 47.7, 28.7, 28.5, 28.4, 20.4, 20.2, 18.3, 8.0. **IR (film):** 2972.7, 2927.8, 2884.1, 2809.4, 2094.6, 1685.3, 1458.3, 1412.8, 1364.4, 1248.7, 1157.5, 1074.7, 953.8, 771.7, 702.1 cm^{-1}. **MS (ESI) m/z:** 1019.7 $[M + H]^+$, 509.3, 460.3, 410.3, 360.3; **HRMS (ESI) m/z** $[M + H]^+$ calcd for $C_{47}H_{95}N_8O_{12}Si_2$: 1019.6603, found: 1019.6559.

3.5.2.7 Attempted synthesis of disilylated precursors P17 and P18

3.5.2.7.1 Synthesis of 4,7,10-tris(2-(*tert*-butoxy)-2-oxoethyl)-1,4,7,10-tetraazacyclododecan-1-ium bromide 80[75]

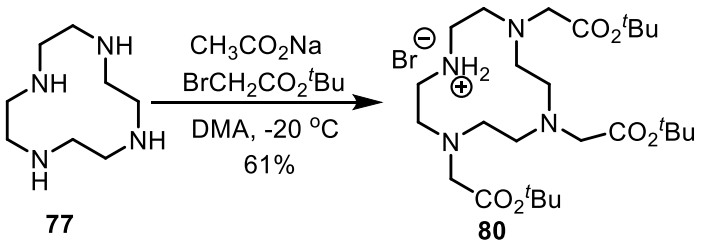

To a suspension of cyclen **77** (2.00 g, 11.62 mmol) and $CH_3CO_2Na \cdot 3H_2O$ (5.26 g, 38.4 mmol) in DMA (24 mL) at -20 °C was added dropwise a solution of *tert*-butyl bromoacetate (7.48 g, 38.4 mL, 96 mmol) in DMA (20 mL) over a period of 0.5 h. The reaction temperature was maintained at -20 °C during the addition, after which the reaction mixture was allowed to reach room temperature. After 24 h of vigorous stirring, the reaction mixture was poured into water (100 mL) to give a clear solution. Solid $NaHCO_3$ (5.05 g, 60.1 mmol) was added portion wise, the precipitate was collected by filtration and dissolved in $CHCl_3$ (80 mL). The solution was washed with water (60 mL), dried with anhydrous Na_2SO_4, filtered, and concentrated to about 10 mL. Diethyl ether was added, after which the final product **80** precipitated as a white solid, (4.2 g, 61% yield). **^{1}H NMR (360 MHz, $CDCl_3$) δ (ppm)**: 10.04 (br s, 2H), 3.37 (s, 4H), 3.29 (s, 2H), 3.09 (br s, 4H), 2.92-2.88 (m, 12H), 1.46 (s, 27H); **^{13}C NMR (91 MHz, $CDCl_3$) δ (ppm)**: 170.56, 81.66, 58.17, 51.30, 49.27, 47.52, 28.19.

3.5.2.7.2 Synthesis of tri-*tert*-butyl 2,2',2''-(10-(prop-2-yn-1-yl)-1,4,7,10-tetraazacyclododecane-1,4,7-triyl)triacetate 81[76]

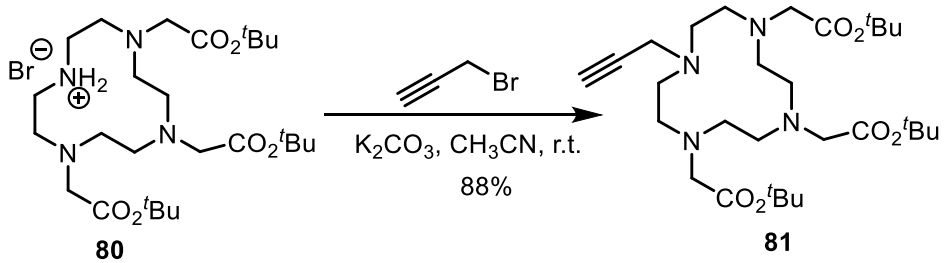

To a solution of hydrobromide **80** (4.19 g, 7.05 mmol) in acetonitrile (70 ml), was added potassium carbonate (1.95 g, 14.10 mmol) and the suspension was stirred for 30 min. The solution was placed in an ice-bath and propargyl bromide (80% in toluene, 1.05 g, 7.05 mmol)

was added dropwise. The ice-bath was removed, the reaction was allowed to reach room temperature and stirred overnight at room temperature. The inorganic solid was removed by filtration, and the solvent evaporated under reduced pressure. The resulting oil was dissolved in hot toluene and filtered to remove the inorganic residue. After evaporation of the solvent under reduced pressure the product **81** was obtained as a yellow oil (3.27 g, 88 %). **^{1}H NMR (360 MHz, $CDCl_3$) δ (ppm)**: 3.43 (d, *J* = 3.6 Hz, 2H), 3.28 (s, 6H), 2.82- 2.79 (m, 12H), 2.70- 2.67 (m, 4H), 2.14-2.13 (m, 1H), 1.45 (s, 27H); **^{13}C NMR (91 MHz, $CDCl_3$) δ (ppm)**: 171.12, 80.72, 79.31, 72.51, 56.78, 52.14, 51.80, 51.61, 43.08, 28.23.

3.5.3 Synthesis of 1,2-bis(triethoxysilyl)ethene (BTSE)[85-86]

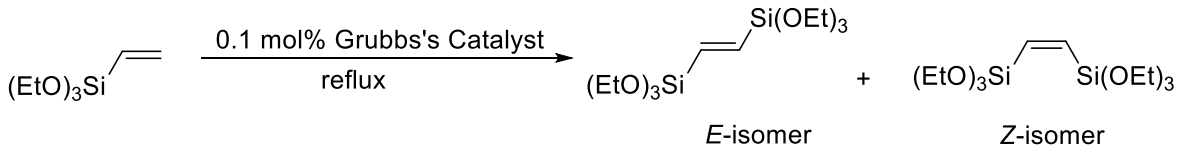

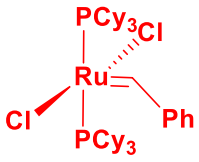

Grubbs Catalyst™ 1st Generation
100% (*E*)-BTSE

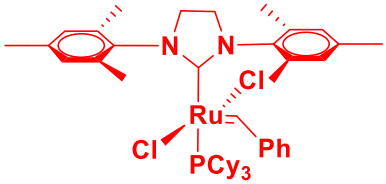

Grubbs Catalyst™ 2nd Generation
80% (*E*)-BTSE

Grubbs catalyst™ 2nd generation C848 (42.45 mg, 0.05 mmol) and vinyltriethoxysilane (VTES) (9.51 g, 50 mmol) were added to a Schlenk flask under argon. After the solution was stirred for one hour at room temperature and then refluxed for 24 h, unreacted VTES was distilled off. Subsequently, BTSE was vacuum distilled to give a clear colorless liquid (6.1 g, 69% yield, 3 mbar, 105 ºC). BTSE was identified by ^{1}HNMR as a diastereoisomeric mixture (80% E). **^{1}H NMR (360 MHz, $CDCl_3$) δ (ppm)**: 6.75 (s, 0.37 H, *Z*-isomer), 6.65 (s, 1.49 H, *E*-isomer), 3.84-3.79 (m, 12 H; *Z*- and *E*-isomer), 1.24-1.15 (m, 18 H; *Z*-and *E*-isomer).

Grubbs catalyst™ 1st generation C823 $(PCy_3)_2Cl_2Ru{=}CHPh$ (82.30 mg, 0.1 mmol) and vinyltriethoxysilane (VTES) (19.02 g, 100 mmol) were added to a Schlenk flask under argon. After the solution was stirred for one hour at room temperature and then refluxed for 24 h, unreacted VTES was distilled off. Subsequently, BTSE was vacuum distilled to give a clear colorless liquid (12.53 g, 71% yield, 4 mbar, 124 ºC). *E*-BTSE was identified by ^{1}HNMR as a diastereoisomerically pure product (100% *E*). **^{1}H NMR (360 MHz, $CDCl_3$) δ (ppm)**: 6.66 (s, 2 H; *E*-isomer), 3.83 (q, *J* = 7.2 Hz, 12 H), 1.23 (t, *J* = 7.2 Hz, 18 H).

3.5.4 Preparation of Periodic Mesoporous Organosilica Nanoparticles (PMO NPs)

3.5.4.1 Preparation of E or BTSE PMO NPs[79]

In an open 250 mL round bottom flask without reflux condenser was placed a solution of cetyltrimethylammonium bromide (CTAB, 250 mg, 0.686 mmol) in Mili-Q water (120 mL) and then 875 µL of 2 M NaOH was added (1.75 mmol of NaOH). The mixture was stirred at 1000 rpm at 80 °C for 50 min. Then, the stirring speed was enhanced to 1400 rpm and 1,2-bis(triethoxysilyl)ethene (BTSE, 800 µL, 2.29 mmol) was added rapidly under stirring. The condensation process was conducted for two hours at 80 °C. The suspension was cooled to room temperature while stirring and the NPs were collected by centrifugation (13500 rpm in 6*25 mL flasks tubes for 45 mins). The supernatant was removed and an aliquot of the solid was taken and was dried for FTIR. In order to remove the surfactant, 10 mL of an alcoholic solution of ammonium nitrate [NH_4NO_3, 6 g/L in 96% EtOH] was added to each tube. The six tubes were sonicated for 30 min at 50 °C, then cooled and centrifuged (30 min at 13500 rpm at 25 °C), the supernatant was discarded. This NH_4NO_3 washing was performed 3 times. Each solid in the tubes was washed successively with 96% ethanol, Mili-Q water, 96% ethanol using the same protocol (30 min at 50 °C sonication, centrifugation). The final product was dried for few hours under vacuum at room temperature. The **E PMO NPs** were obtained as white solid. At the same time, another aliquot of the solid was taken and was dried for FTIR. It was compared the IR of the sample before removal of surfactant and after removal to check whether the CH_2 bands of CTAB had completely disappeared.

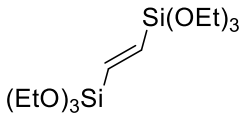

E80 (E/Z 80/20)
E100 (E/Z 100/0)

100% E PMO NPs： 232 mg. **^{13}C-CP-MAS NMR (75 MHz) δ (ppm)**: 146.30. **IR *v* (ATR) (cm^{-1})**: 3323.6, 1188.0, 1034.3, 925.1, 790.5. **Zeta Potential**: ζ = -32 mV, pH = 6.69. **DLS**: 1023.56 nm.

80% E PMO NPs： 267 mg. **Zeta Potential**: ζ = -26 mV, pH = 7.00. **DLS**: 977.50 nm.

3.5.4.2 Preparation of E-Pn 90/10 PMO NPs and E-Pn 75/25 PMO NPs

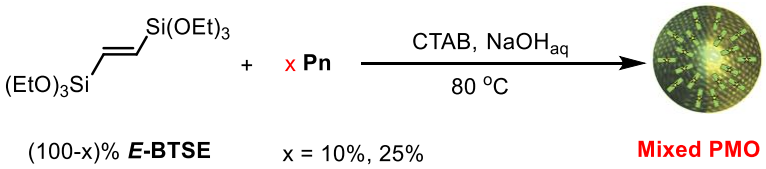

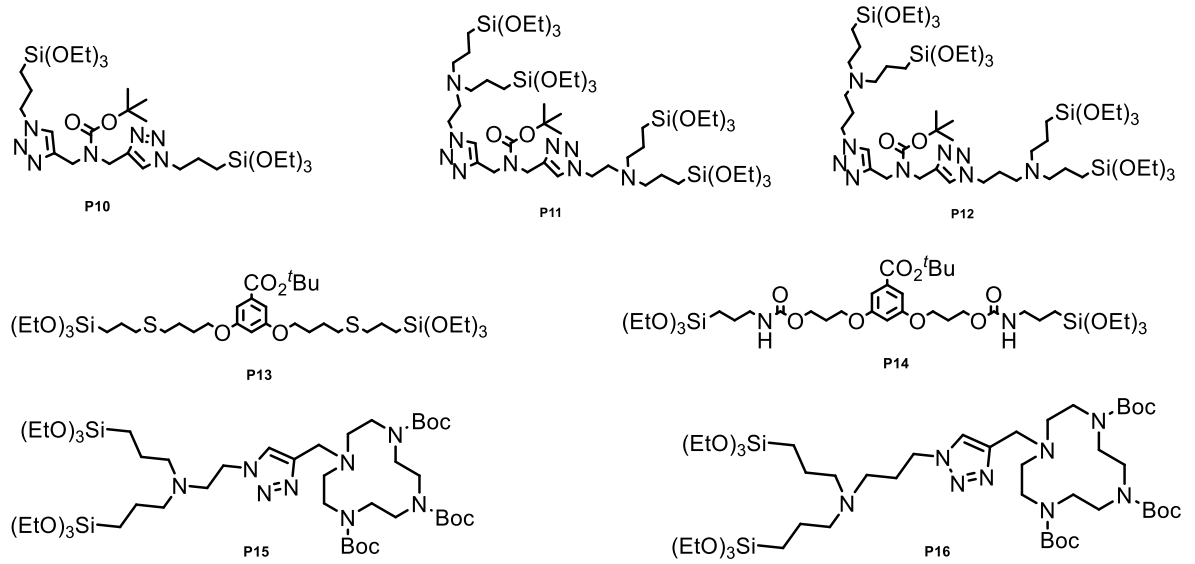

3.5.4.2.1 Preparation of E-Pn 90/10 PMO NPs

In an open 250 mL round bottom flask without reflux condenser was placed a solution of CTAB (250 mg, 0.686 mmol) in Mili-Q water (120 mL) and then 875 µL of 2 M NaOH was added (1.75 mmol of NaOH). The mixture was stirred at 1000 rpm at 80 °C for 50 min. Then, the stirring speed was enhanced to 1400 rpm and a mixture of 100% *E*-BTSE (704.34 mg, 2.00 mmol) with **Pn** (0.2 mmol) were added rapidly under stirring. The condensation process was conducted for two hours at 80 °C. Afterwards, the suspension was cooled to room temperature while stirring and the NPs were collected by centrifugation during 45 min at 13500 rpm. The samples were then extracted three times with a solution of NH_4NO_3 (6 g/L in 96% EtOH), and washed three times with 96% ethanol, Mili-Q water, 96% ethanol, respectively. Extraction and the following steps were identical as those described for **E PMO NPs**. The **E-Pn 90/10 PMO NPs** were obtained as white solid.

E-P10 90/10 PMO NPs: 247 mg. **^{13}C-CP-MAS NMR (75 MHz) δ (ppm)**: 155.6, 146.1, 123.8, 81.1, 57.9, 52.5, 28.2, 24.9, 17.4, 10.4. **IR ν (ATR) (cm^{-1})**: 3337.7, 1671.3, 1416.6, 1187.7, 1036.9, 927.3. **BET:** S_{BET} = 683 m^{2}g^{-1}, V_{pore} = 0.48 cm^{3}g^{-1}, $\emptyset_{pore}$ = 2.8 nm. **TGA** (air,

5 °C/min, 20-1000 °C) residual mass 78.17%. **Zeta Potential**: ζ = -29 mV, pH = 6.99. **DLS**: 447 nm.

E-P11 90/10 PMO NPs: 312 mg. **^{13}C-CP-MAS NMR (75 MHz) *δ* (ppm)**: 155.4, 146.0, 125.2, 81.0, 58.1, 52.8, 48.2, 28.5, 20.6, 10.8. **IR *ν* (ATR) (cm^{-1})**: 3322.9, 1673.0, 1412.0, 1187.7, 1036.2, 923.7, 187.9. **BET:** S_{BET} = 509 m^2g^{-1}, V_{pore} = 0.34 cm^3g^{-1}, $\emptyset_{pore}$ = 2.7 nm. **TGA** (air, 5 °C/min, 20-1000 °C) residual mass 75%. **Zeta Potential**: ζ = 33 mV, pH = 5.92. **DLS**: 800 nm.

E-P12 90/10 PMO NPs: 313 mg. **^{13}C-CP-MAS NMR (75 MHz) *δ* (ppm)**: 156.1, 146.1, 124.7, 81.0, 58.0, 48.0, 28.4, 18.5, 10.6. **IR *ν* (ATR) (cm^{-1})**: 3361.9, 1655.6, 1370.1, 1188.0, 1033.4, 924.1, 788.8. **BET:** S_{BET} = 505 m^2g^{-1}, V_{pore} = 0.66 cm^3g^{-1}, $\emptyset_{pore}$ = 2.8 nm. **TGA** (air, 5 °C/min, 20-1000 °C) residual mass 72%. **Zeta Potential**: ζ = 36 mV, pH = 5.44. **DLS**: 479 nm.

E-P13 90/10 PMO NPs: 332 mg. **^{13}C-CP-MAS NMR (75 MHz) *δ* (ppm)**: 164.9, 160.2, 146.3, 134.2, 107.5, 81.6, 68.3, 58.0, 33.1, 28.4, 24.2, 17.1, 12.6. **IR *ν* (ATR) (cm^{-1})**: 3311.8, 2975.4, 1692.3, 1596.5, 1449.9, 1187.3, 1033.1, 923.2, 788.5. **BET:** S_{BET} = 973 m^2g^{-1}, V_{pore} = 0.66 cm^3g^{-1}, $\emptyset_{pore}$ = 2.7 nm. **TGA** (air, 5 ^{o}C/min, 20-1000 ^{o}C) residual mass 77 %. **Zeta Potential**: ζ = -31 mV, pH = 6.80. **DLS**: 1122 nm.

E-P14 90/10 PMO NPs: 330 mg. **^{13}C-CP-MAS NMR (75 MHz) *δ* (ppm)**: 165.4, 160.0, 146.1, 133.8, 108.6, 80.9, 62.8, 58.0, 43.9, 28.2, 23.9, 17.3, 10.5. **IR *ν* (ATR) (cm^{-1})**: 3316.2, 1695.5, 1448.5, 1187.9, 1035.2, 923.1, 789.2. **BET:** S_{BET} = 696 m^2g^{-1}, V_{pore} = 0.37 cm^3g^{-1}, $\emptyset_{pore}$ = 2.1 nm. **TGA** (air, 5 ^{o}C/min, 20-1000 ^{o}C) residual mass 75%. **Zeta Potential**: ζ = -38 mV, pH = 6.72. **DLS**: 694 nm.

E-P15 90/10 PMO NPs: 332 mg. **^{13}C-CP-MAS NMR (75 MHz) *δ* (ppm)**: 155.9, 146.2, 124.6, 79.1, 58.0, 50.5, 28.8, 21.3, 11.4. **IR *ν* (ATR) (cm^{-1})**: 3334.8, 2976.5, 1673.8, 1416.7, 1187.2, 1038.5, 924.7, 790.1, 424.2. **BET:** S_{BET} = 513 m^2g^{-1}, V_{pore} = 0.36 cm^3g^{-1}, $\emptyset_{pore}$ = 2.8 nm. **TGA** (air, 5 ^{o}C/min, 20-1000 ^{o}C) residual mass 60%. **Zeta Potential**: ζ = 39 mV, pH = 6.66. **DLS**: 520 nm.

E-P16 90/10 PMO NPs: 297 mg. **^{13}C-CP-MAS NMR (75 MHz) *δ* (ppm)**: 156.3, 146.4, 124.8, 79.1, 58.1, 48.5, 28.7, 19.8, 27.2, 10.7. **IR *ν* (ATR) (cm^{-1})**: 3358.4, 2976.8, 1667.9,

1417.3, 1188.1, 1040.3, 924.6, 792.3, 423.8. **BET:** S_{BET} = 492 m^2g^{-1}, V_{pore} = 0.33 cm^3g^{-1}, $\emptyset_{pore}$ = 2.7 nm. **TGA** (air, 5 ^oC/min, 20-1000 ^oC) residual mass 68%. **Zeta Potential**: ζ = 34 mV, pH = 6.25. **DLS**: 621 nm.

3.5.4.2.2 Preparation of E-Pn75/25 PMO NPs

In an open 250 mL round bottom flask without reflux condenser was placed a solution of CTAB (250 mg, 0.686 mmol) in Mili-Q water (120 mL) and then 875 μL of 2 M NaOH was added (1.75 mmol of NaOH). The mixture was stirred at 1000 rpm at 80 °C for 50 min. Then, the stirring speed was enhanced to 1400 rpm and a mixture of 100% *E*-BTSE (581.09 mg, 1.65 mmol) with **Pn** (0.55 mmol) were added rapidly under stirring. The condensation process was conducted for two hours at 80 °C. Afterwards, the suspension was cooled to room temperature while stirring and the NPs were collected by centrifugation during 45 min at 13500 rpm. The samples were then extracted three times with a solution of NH_4NO_3 (6 g/L in 96% EtOH), and washed three times with 96% ethanol, Mili-Q water, 96% ethanol, respectively. Extraction and the following steps were identical as those described for **E PMO NPs**. The **E-Pn 75/25 PMO NPs** were obtained as white solids.

E-P10 75/25 PMO NPs: 315 mg. **^{13}C-CP-MAS NMR (75 MHz) δ (ppm)**: 156.1, 145.5, 123.6, 81.9, 57.7, 52.8, 28.3, 24.8, 17.9, 10.4. **IR ν (ATR) (cm^{-1})**: 3302.3, 1670.8, 1414.8, 1186.9, 1012.0, 926.6, 784.0. **TGA** (air, 5 °C/min, 20-1000 °C) residual mass 67%. **Zeta Potential**: ζ = -23 mV, pH = 7.34. **DLS**: 507 nm.

E-P11 75/25 PMO NPs: 536 mg. **^{13}C-CP-MAS NMR (75 MHz) δ (ppm)**: 155.7, 145.5, 125.3, 80.2, 57.8, 28.4, 21.7, 11.1. **IR ν (ATR) (cm^{-1})**: 3331.9, 1672.4, 1412.3, 1186.7, 1011.4, 923.1, 785.6. **TGA** (air, 5 °C/min, 20-1000 °C) residual mass 58%. **Zeta Potential**: ζ = 20 mV, pH = 6.25. **DLS**: 513 nm.

E-P12 75/25 PMO NPs: 644 mg. **^{13}C-CP-MAS NMR (75 MHz) δ (ppm)**: 1561.2, 146.1, 124.8, 81.7, 58.2, 48.8, 28.6, 19.8, 10.3. **IR ν (ATR) (cm^{-1})**: 3294.2, 1676.8, 1388.2, 1012.7, 923.4, 786.5. **TGA** (air, 5 °C/min, 20-1000 °C) residual mass 57%. **Zeta Potential**: ζ = 24 mV, pH = 4.85. **DLS**: 321 nm.

E-P13 75/25 PMO NPs: 334 mg. **^{13}C-CP-MAS NMR (75 MHz) δ (ppm)**: 165.3, 160.4, 146.4, 134.2, 107.1, 81.1, 68.3, 58.3, 33.8, 28.5, 17.6, 13.1. **IR ν (ATR) (cm^{-1})**: 3359.1,

1709.4, 1594.2, 1447.0, 1035.6, 924.5, 790.3. **BET:** S_{BET} = 259 m^2g^{-1}, V_{pore} = 0.17 cm^3g^{-1}, $\emptyset_{pore}$ = 2.6 nm. **TGA** (air, 5 ^oC/min, 20-1000 ^oC) residual mass 67%. **Zeta Potential**: ζ = -26 mV, pH = 9.07. **DLS**: 742 nm.

E-P14 75/25 PMO NPs: 420 mg. **^{13}C-CP-MAS NMR (75 MHz) *δ* (ppm)**: 166.3, 160.2, 158.2, 146.5, 134.0, 111.0, 105.2, 81.1, 63.8, 58.1, 43.6, 28.3, 24.2, 17.7, 10.6. **IR *ν* (ATR) (cm^{-1})**: 3340.1, 1692.2, 1447.3, 1188.5, 1035.8, 922.5, 791.1. **BET:** S_{BET} = 329 m^2g^{-1}, V_{pore} = 0.26 cm^3g^{-1}, $\emptyset_{pore}$ = 2.7 nm. **TGA** (air, 5 ^oC/min, 20-1000 ^oC) residual mass 63%. **Zeta Potential**: ζ = -42 mV, pH = 6.85. **DLS**: 562 nm.

E-P15 75/25 PMO NPs: 342 mg. **^{13}C-CP-MAS NMR (75 MHz) *δ* (ppm)**: 155.5, 146.2, 138.7, 125.2, 79.5, 57.6, 50.0, 40.4, 28.7, 20.9, 17.2, 10.8. **IR *ν* (ATR) (cm^{-1})**: 3359.9, 2933.4, 1670.8, 1416.0, 1038.5, 923.9, 791.1. **BET:** S_{BET} = 162 m^2g^{-1}, V_{pore} = 0.15 cm^3g^{-1}, $\emptyset_{pore}$ = 3.6 nm. **TGA** (air, 5 ^oC/min, 20-1000 ^oC) residual mass 53%. **Zeta Potential**: ζ = 33 mV, pH = 6.08. **DLS**: 639 nm.

E-P16 75/25 PMO NPs: 306 mg. **^{13}C-CP-MAS NMR 75 MHz) *δ* (ppm)**: 155.5, 145.9, 123.8, 79.3, 56.4, 47.9, 28.7, 19.4, 11.0. **IR *ν* (ATR) (cm^{-1})**: 3351.3, 2975.5, 1667.7, 1417.2, 1187.0, 1040.7, 928.1, 790.3, 424.3. **TGA** (air, 5 ^oC/min, 20-1000 ^oC) residual mass 55%. **Zeta Potential**: ζ = 41 mV, pH = 4.66. **DLS**: 463 nm.

3.5.4.3 Preparation of pure P12 PMO NPs and pure P16 PMO NPs

In an open 100 mL round bottom flask without reflux condenser was placed a solution of CTAB (125 mg, 0.34 mmol) in Mili-Q water (60 mL) and then 437 µL of 2 M NaOH was added. The mixture was stirred at 1000 rpm at 80 °C for 50 mins. Then, the stirring speed was enhanced to 1400 rpm and **P12** or **P16** (0.1 mmol) in absolute ethanol (1.0 mL) was added rapidly under stirring. The condensation process was conducted for 24 hours at 80 °C. Afterwards, the suspension was cooled to room temperature while stirring and the NPs were collected by centrifugation during 15 min at 20000 rpm. The samples were then extracted twice with a solution of NH_4NO_3 (6 g/L in EtOH), and washed three times with ethanol, Mili-Q water, ethanol, respectively. Extraction and the following steps were identical as those described for **E PMO NPs**. **Pure P12/P16 PMO NPs** were obtained as white solids.

Pure P12 PMO NPs: 43.7 mg. **IR *ν* (ATR) (cm^{-1})**: 3395.7, 2936.4, 1682.3, 1367.4, 1103.1, 1023.6, 783.8, 688.4. **BET:** S_{BET} = 186 m^2g^{-1}, V_{pore} = 0.26 cm^3g^{-1}, $\emptyset_{pore}$ = 5.6 nm. **Zeta Potential**: ζ = 11 mV, pH = 8.94. **DLS**: 269 nm.

Pure P16 PMO NPs: 48.0 mg. **^{13}C-CP-MAS NMR 75 MHz *δ* (ppm)**: 146.1, 123.7, 57.6, 49.2, 28.6, 23.6, 11.8. **IR *ν* (ATR) (cm^{-1})**: 3420.6, 2975.1, 1682.2, 1458.7, 1249.7, 1152.5, 1029.6, 772.4. **BET:** S_{BET} = 20 m^2g^{-1}, non-porous NPs. **Zeta Potential**: ζ = 24 mV, pH = 7.08. **DLS**: 217nm.

3.5.5 HIFU stimulation experiment with E-Pn PMO NPs

Nanoparticles were resuspended in PBS (pH 5.5) at a concentration of 10 mg/mL in an eppendorf tube. The tube was submitted to an ultrasound field from a focused 1 MHz probe (Precision Acoustics, UK) driven by a signal generator (Agilent 33220a, France) and RF power amplifier (ADECE, France). The transducer was placed in a custom made 3 axis motorized positioning system to be able to send ultrasound accurately on the eppendorf tube at the focus of the probe. Degassed water was applied between the transducer and the eppendorf tube. Peak negative pressure of 1.0, 1.4 and 1.6 MPa in continuous mode were used in this study. Ultrasound stimulation time was set to 15 seconds. The transducer was calibrated using an HGL-200 PVDF bullet type hydrophone (Onda, Sunnyvale, CA), at the focus distance of the transducer.

3.5.6 Laboratory assay for the removal of Boc group from E-Pn PMO NPs

The corresponding **E-Pn PMO NPs** (50 mg) were added to distilled water (10 mL) (pH adjusted to 7, 5, 3 or 1), the mixture was heated quickly to 80 or 100 ^oC and stirred at this temperature for 30 min. Then the **PMO NPs** were collected by centrifugation, washed with EtOH and dried for FTIR. The IR spectra of the samples before and after the treatment were compared to check if the Boc group was removed. In some cases, also the ^{13}C NMR CP MAS spectra were checked.

3.6 References

1. E. Maloney, J. H. Hwang, *Int. J. Hyperthermia* **2015**, *31*, 302.
2. P. E. Huber, J. W. Jenne, R. Rastert, I. Simiantonakis, H. P. Sinn, H. J. Strittmatter, D. von Fournier, M. F. Wannenmacher, J. Debus, *Cancer Res.* **2001**, *61*, 8441.
3. J. E. Kennedy, GR. ter Haar, D. Cranston, *British Journal of Radiology* **2003**, *76*, 590.
4. J. E. Kennedy, *Nat. Rev. Cancer* **2005**, *5*, 321.
5. A. C. Schmitz, D. Gianfelice, B. L. Daniel, W. Mali, M. van den Bosch, *Eur. Radiol*. **2008**, *18*, 1431.
6. K. Hynynen, *Ultrasonics* **2010**, *50*, 221.
7. E. Warmt, T. R. Kiessling, R. Stange, A. W. Fritsch, M. Zink, J. A. Kas, *New J. Phys.* **2014**, *16*, 073009.
8. V. Y. T. Cheung, *Best Pract. Res. Clin. Obstet. Gynaecol.* **2018**, *46*, 74e83.
9. S. A. Quadri, M. Waqas, I. Khan, M. A. Khan, S. S. Suriya, M. Farooqui, B. Fiani, *Neurosurg. Focus* **2018**, *44*, E16.
10. M. Manzano, M. Vallet-Regí, *Chem. Commun.* **2019**, *55*, 2731.
11. A. L. S. Marques, M. P. Andres, R. M. Kho, M. S. Abrão, *J. Minim. Invasive. Gynecol.* **2019**, DOI: 10.1016/j.jmig.2019.07.029
12. D. B. Rodrigues, P. R. Stauffer, D. Vrba, M. D. Hurwitz, *Int. J. Hyperth.* **2015**, *31*, 260.
13. T. R. Wang, R. Dallapiazza, W. J. Elias, *Int. J. Hyperth.* **2015**, *31*, 285.
14. M. Brown, P. Farquhar-Smith, J. Williams, G. R. ter Haar, N. de Souza, *Br. J. Anaesthesia* **2015**, *115*, 520.
15. O. Al-Bataineh, J. Jenne, P. Huber, *Cancer Treat. Rev.* **2012**, *38*, 346.
16. I. A. Shehata Elhelf, H. Albahar, U. Shah, A. Oto, E. Cressman, M. Almekkawy, *Diagn. Interv. Imaging.* **2018**, *99*, 349.
17. G. Ter Haar, C. Coussios, *Int. J. Hyperthermia* **2007**, *23*, 89.
18. X. Qian, X. Han, Y. Chen, *Biomaterials* **2017**, *142*, 13.
19. H. Gruell, S. Langereis, *J. Control. Release* **2012**, *161*, 317.
20. M. Ba, H. Long, X. Zhang, Y. Tang, Y. Wu, S. Wang, Z. Yan, B. Zhang, S. Cui, *Int. J. Gynecol Cancer* **2016**, *26*, 1571.
21. N. Zhang, X. Cai, W. Gao, R. Wang, C. Xu, Y. Yao, L. Hao, D. Sheng, H. Chen, Z. Wang, Y. Zheng, *Theranostics* **2016**, *6*, 404.
22. A. Sathaworawong, R. Wanitphakdeedecha, *J. Cosmet Dermatol* **2018**, *17*, 162.
23. C. Yang, Y. Li, M. Du, Z. Chen, Recent advances in ultrasound-triggered therapy. *J. Drug Target.* **2019**, *27*, 33.
24. N. Blum, A. Yildirim, R. Chattaraj, A. Goodwin, *Theranostics* **2017**, *7*, 694.
25. Y. You, Z. Wang, H. Ran, Y. Zheng, D. Wang, J. Xu, Z. Wang, Y. Chen, P. Li, *Nanoscale* **2016**, *8*, 4324.
26. J. W. Huang, J. S. Xu, R. X. Xu, *Biomaterials* **2010**, *31*,1278;
27. X. Wang, H. Chen, Y. Chen, M. Ma, K. Zhang, F. Li, Y. Zheng, D. Zeng, Q. Wang, J. Shi, *Adv. Mater.* **2012**, *24*, 785.
28. J. A. Feshitan, F. Vlachos, S. R. Sirsi, E. E. Konofagou, M. A. Borden, *Biomaterials* **2012**, *33*, 247.

29. J. R. McLaughlan, D. M. J. Cowell, S. Freear, *Phys. Med. Biol.* **2018**, *63*, 015004.
30. D. B. Thimiri Govinda Rak, N. A. Khan, *Micro Nano Lett.* **2018**, *13*, 292.
31. G. Canavese, A. Ancona, L. Racca, M. Canta, B. Dumontel, F. Barbaresco, T. Limongi, V. Cauda, *Chem. Eng. J.* **2018**, *340*, 155.
32. G. Bruno, G. Canavese, X. Liu, C. S. Filgueira, A. Sacco, D. Demarchi, M. Ferrari, A. Grattoni, *Nanoscale* **2016**, *8*, 18718.
33. Y. Zhou, X. Han, X. Jing, Y. Chen, *Adv. Healthcare Mater.* **2017**, *6*, 1700646.
34. X. Q. Qian, X. X. Han, Y. Chen, *Biomaterials* **2017**, *142*, 13.
35. N. T. Blum, G. M. Gyorkos, S. J. Narowetz, E. N. Mueller, A. P. Goodwin, *ACS Appl. Mater. Interfaces* **2019**, *11*, 36324.
36. Y. Zhou, Z. Wang, Y. Chen, H. Shen, Z. Luo, A. Li, Q. Wang, H. Ran, P. Li, W. Song, Z. Yang, H. Chen, Z. Wang, G. Lu, Y. Zheng, *Adv. Mater.* **2013**, *25*, 4123.
37. X. Zhang, Y. Zheng, Z. Wang, S. Huang, Y. Chen, W. Jiang, H. Zhang, M. Ding, Q. Li, X. Xiao, X. Luo, Z. Wang, H. Qi, *Biomaterials* **2014**, *35*, 5148.
38. H. S. Min, S. Son, D. G. You, T. W. Lee, J. Lee, S. Lee, J. Y. Yhee, J. Lee, M. H. Han, J. H. Park, S. H. Kim, K. Choi, K. Park, K. Kim, I. C. Kwon, *Biomaterials* **2016**, *108*, 57.
39. T. Z. Liu, N. Zhang, Z. G. Wang, M. Y. Wu, Y. Chen, M. Ma, H. R. Chen, J. L. Shi, *ACS Nano* **2017**, *11*, 9093.
40. A. Yildirim, R. Chattaraj, T. Blum Nicholas, D. Shi, K. Kumar, P. Goodwin Andrew, *Adv. Healthcare Mater.* **2017**, *6*, 1700514.
41. A. Yildirim, D. Shi, S. Roy, N. T. Blum, R. Chattaraj, J. N. Cha, A. P. Goodwin, *ACS Appl. Mater. Interfaces* **2018**, *10*, 36786.
42. C. Bera, S. B. Devarakonda, V. Kumar, A. K. Ganguli, R. K. Banerjee, *Phys. Chem. Chem. Phys.* **2017**, *19*, 19075.
43. S. Ahmad Reza Dibaji, M.F. Al-Rjoub, M.R. Myers, R.K. Banerjee, *J. Nanotechnol. Eng. Med.* **2014**, *4*, 040902.
44. G. Canavese, A. Ancona, L. Racca, M. Canta, B. Dumontel, F. Barbaresco, T. Limongi, V. Cauda, *Chem. Eng. J.* **2018**, *340*, 155.
45. X. Qian, W. Wang, W. Kong, Y. Chen, *RSC Adv.* **2014**, *4*, 17950.
46. B. E. Oeffinger, M. A. Wheatley, *Ultrasonics* **2004**, *42*, 343.
47. H. Hu, H. Zhou, J. Du, Z. Q. Wang, L. An, H. Yang, F. H. Li, H. X. Wu, S. P. Yang, *J. Mater. Chem.* **2011**, *21*, 6576.
48. H. P. Martinez, Y. Kono, S. L. Blair, S. Sandoval, J. Wang-Rodriguez, R. F. Mattrey, A. C. Kummel, W. C. Trogler, *MedChemComm* **2010**, *1*, 266.
49. X. Qian, W. Wang, W. Kong, Y. Chen, *J. Nanomater.* **2014**, 972475, DOI: 10.1155/2014/972475.
50. M. Wu, Y. Chen, L. Zhang, X. Li, X. Cai, Y. Du, L. Zhang, J. Shi, *J. Mater. Chem. B*, **2015**, *3*, 766.
51. Y. Chen, Q. Meng, M. Wu, S. Wang, P. Xu, H. Chen, Y. Li, L. Zhang, L. Wang, J. Shi, *J. Am. Chem. Soc.* **2014**, *136*, 16326.

52. V. H. Rawal, M. P. Cava, *Tetrahedron Lett.***1985**, *26*, 6141.
53. S. S. Bhawal, R. A. Patil, D. W. Armstrong, *RSC Adv.* **2015**, *5*, 95854.
54. A. R. Bogdan, M. Charaschanya, A. W. Dombrowski, Y. Wang, S. W. Djuric, O*rg. Lett.* **2016**, *18*, 1732.
55. B. Li, R. Z. Li, P. Dorff, J. C. McWillams, R. M. Guinn,S. M. Guinness, L. Han, K. Wang, S. Yu, *J. Org. Chem.* **2019**, *84*, 4846.
56. C. Zinelaabidine, O. Souad, J. Zoubir, B. Malika, A. Nour-Eddine, *Int. J. Chem. (Toronto, ON, Can.)* **2012**, *4*, 73.
57. J. Wang, Y.L. Liang, J. Qu, *Chem. Commun.* **2009**, 5144.
58. V. Dugas, Y. Chevalier, *Langmuir* **2011**, *27*, 14188.
59. K. P. Cole, J. H. Park, *Bull. Korean Chem. Soc.* **2009**, *30*, 230.
60. S. Torii, H. Tanaka, M. Taniguchi, Y. Kameyama, *J. Org. Chem.* **1991**, *56*, 3633.
61. P. Strazzolini, N. Misuri, P. Polese, *Tetrahedron Lett.* **2005**, *46*, 2075.
62. V. V. Rostovtsev, L. G. Green, V. V. Fokin, K. B. Sharpless, *Angew. Chem. Int. Ed*. **2002**, *41*, 2596.
63. M. Meldal, C. W. Tornøe, *Chem. Rev*. **2008**, *108*, 2952.
64. J. Wu, F. Fang, W. Y. Lu, J. L. Hou, C. Li, Z. Q. Wu, X. K. Jiang, Z. T. Li, Y. H. Yu, *J. Org. Chem.,* **2007**, *72*, 2897.
65. K. Bürglová, N. Moitra, J. Hodacová, X. Cattoën, M. Wong Chi Man, *J. Org. Chem.* **2011**, *76*, 7326.
66. C. Gascó, Universitat Autònoma de Barcelona, Master thesis, **2015**.
67. X. Hu, K. T. Nguyen, V. C. Jiang, D. Lofland, H. E. Moser, D. Pei, *J. Med. Chem.,* **2004**, *47*, 4941.
68. E. Dalcanale, *J. Org. Chem.* **1986**, *51*, 567.
69. J. Ezquerra, C. Pedregal, A. Rubio, B. Yruretagoyena, A. Escribano, F. Sánchez-Ferrando, *Tetrahedron* **1993**, *49*, 8665.
70. H. Suzuki, A. Ishigami, A. Orimoto, A. Matsuyama, S. Handa, N. Maruyama, Y. Yokoyama, H. Okuno, M. Nakakoshi, *Chem. Pharm. Bull.* **2012**, *60*, 1164.
71. K. L. Killops, L. M. Campos, C. J. Hawker, *J. Am. Chem. Soc.* **2008**, *130*, 5062.
72. F. G. Sun, M. Li, Z. H. Gu, *Org. Chem. Front.,* **2016**, *3*, 309.
73. S. Hwang, W. Cha and M. E. Meyerhoff, *Angew. Chem. Int. Ed.* **2006**, *45*, 2745.
74. K. Jobe, C. H. Brennan, M. Motevalli, S. M. Goldup, M. Watkinson, *Chem. Commun.* **2011**, *47*, 6036
75. B. Jagadish, G. L. Brickert-Albrecht, G. S. Nichol, E. A. Mash, N. Raghunand, *Tetrahedron Lett.* **2011**, *52*, 2058.
76. A. K. R Junker, M. Tropiano, S. Faulkner, T. J. Sørensen, *Inorg. Chem.* **2016**, *55*, 12299.
77. S. Díez-González, *Catal. Sci. Technol.* **2011**, *1*, 166.
78. J. G. Croissant, X. Cattoën, M.W.C. Man, J.O. Durand, N.M. Khashab, *Nanoscale* **2015**, *7*, 20318.
79. J. Croissant, X. Cattën, M. W. C. Man, A. Gallud, L. Raehm, P. Trens, M. Maynadier, J.-O. Durand, *Adv. Mater.* **2014**, *26*, 6174.
80. F. Macleod, S. Lang, J. A. Murphy, *Synlett*, **2010**, *4*, 529.
81. K. Bürglová, A. Noureddine, J. Hodacová, G. Toquer, X. Cattoën, M. Wong Chi Man, *Chem. Eur. J.* **2014**, *20*, 10371.

82. K. Takeda, A. Akiyama, H. Nakamura, S. Takizawa, Y. Mizuno, H. Takayanagi, Y. Harigaya, *Synthesis*, **1994**, *10*, 1063.
83. K. Takeda, A. Akiyama, H. Nakamura, S. Takizawa, Y. Mizuno, H. Takayanagi, Y. Harigaya, *Synthesis* **1994**, *10*, 1063.
84. C. H. Heathcock, R. Ratcliffe, *J. Am. Chem. Soc.* **1971**, *93*, 1746.
85. C. Vercaemst, M. Ide, P. V. Wiper, J. T. A. Jones, Y. Z. Khimyak, F. Verpoort, P. V. Der Voort, *Chem. Mater*. **2009**, *21*, 5792.
86. B. Marciniec, H. Maciejewski, J.Gulinski, L. Rzejak, *J. Organomet. Chem.* **1989**, *362*, 273.
87. B. Li, R. Li, P. Dorff, J. C. McWilliams, R. M. Guinn,; SM. Guinness, L. Han, K. Wang, S. Yu, *J. Org. Chem.* **2019**, *84*, 4846.
88. A. Feinle, S. Flaig, M. Puchberger, U. Schubert, N. Hüsing, *Chem. Commun.* **2015**, *51*, 2339.
89. S. S. Park, MH. Jung, Y. S. Lee, J. H. Bae, S. H. Kim, C. S. Ha, *Mater. Design* **2019**, *184*, 108187.
90. M. Xie, H. Shi, K. Ma, H. J. Shen, B. Li, S. Shen, X. S. Wang, Y. Jin, *J. Colloid Interface Sci.* **2013**, *395*, 306.
91. S. Dutta, H. M. Kao, K. C. W. Wu, *APL Materials* **2014**, *2*, 113314.

CHAPTER 4

ANTI-INFLAMMATORY SILICA NANOPARTICLES AND COTTON FABRICS WITH POTENTIAL TOPICAL MEDICAL APPLICATIONS

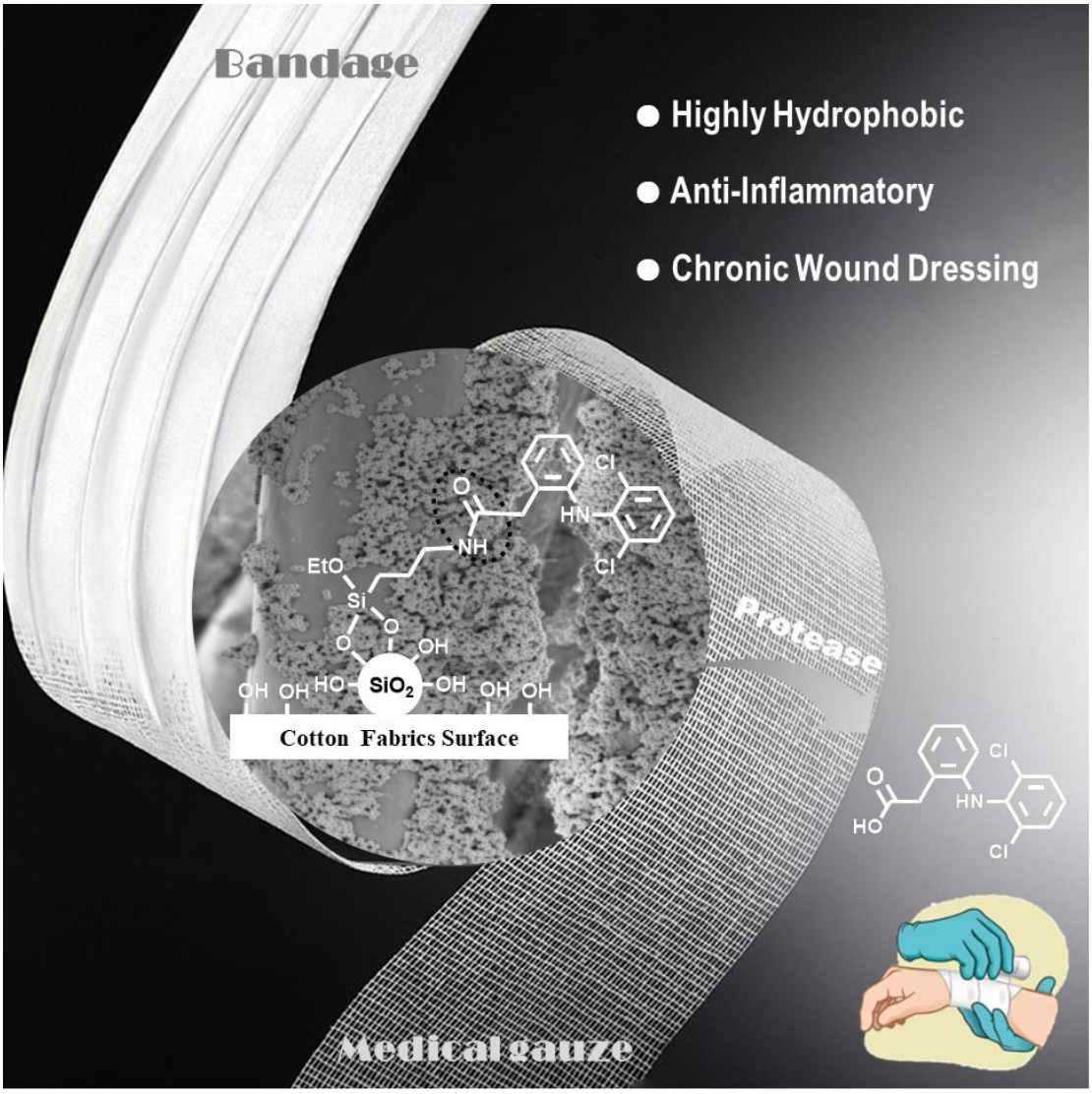

H. Li, A. Granados,* E. Fernández,* R. Pleixats,* A. Vallribera,* Anti-inflammatory cotton fabrics and silica nanoparticles with potential topical medical applications. *ACS Appl. Mater. Interfaces* **2020**, DOI: 10.1021/acsami.0c06629

CHAPTER 4

ANTI-INFLAMMATORY SILICA NANOPARTICLES AND COTTON FABRICS WITH POTENTIAL TOPICAL MEDICAL APPLICATIONS

4.1 Introduction

In recent years, some industrial companies have focused their research on the development of functional finishing for textile materials with high-added value and applications in different areas. The interest for antibacterial activity, ultraviolet protection, self-cleaning, and wrinkle-free properties has been rapidly increasing.[1-4] Cotton cellulose fibers are the most important in the apparel industry, since cotton-made clothes are the most comfortable garments. In addition, cellulose is a natural, low cost biodegradable material and the chemical and physical properties of cotton involve not only strength and elasticity, but also water affinity and permeability. Furthermore, functionalized cotton fabrics have also been envisaged for medical purposes. Recent strategies have focused on anti-inflammatory properties related to the acceleration of wound healing. In fact, wound dressings research has been set by the insights on wound healing process and by patient's demand. High expectations arise regarding the wound dressing, which must accelerate cicatrisation. In this context, Gedanken's group synthesized tannic acid nanoparticles, which were embedded into cotton fabric and presented inhibitory effect on myeloperoxidase from human leukocytes.[5] Moreover, biopolymers such as chitosan and sodium alginate mixtures were prepared and used for coating by pad-dry technique. Their healing ability was positively estimated using the carrageenan-induced rats paw oedema test.[6] Functionalization of gauzes with liposomes entrapping anti-inflammatory drugs has also been described as a strategy to improve wound healing.[7-8] Very recently, in 2019, the group of Pinho has reported a cotton textile functionalized with cyclodextrin-hydroxypropyl methyl cellulose-based hydrogel capable to encapsulate and release gallic acid with anti-inflammatory capacity.[9]

On the other hand, nanoscale biomaterials have been largely examined as agents for therapeutic and diagnostic (i.e., theranostic) applications.[10] Amongst them, silica-based nanoparticles (either dense or mesoporous) have deserved great attention as a biocompatible form of silica.[11-14] Particularly, mesoporous silica nanoparticles (MSNs)[15] present significant advantages for biomedical applications[16-20] due to their exclusive physicochemical properties (high surface area, tunable pore size, pore volume and hydrophilicity, good colloidal stability,

enriched surface silanol groups) and facile surface modifications. In the past decade, they have exhibited high potential as stimuli-responsive drug delivery vehicles for targeted cancer treatment and as bioimaging devices.[21-26] The uptake of the drug and the controlled release upon an appropriate stimulus (pH, light, temperature, enzymes), takes place through the mesopores of the surface-modified MSNs with adjustable pore sizes and morphologies. Mou and Yang have prepared positive-charge functionalized MSNs for pH-stimuli responsive oral drug delivery of sulfasalazine (an anti-inflammatory anionic prodrug used for inflammatory bowel disease) targeting at intestine.[27] Surface modification of ordered mesoporous SBA-15 nanoparticles with (3-aminopropyl)triethoxysilane has been found to significantly increase the loading of non-steroidal anti-inflammatory drugs (NSAID) and decrease their rate of delivery.[28-29] Periodic mesoporous ionosilica nanoparticles with ammonium walls can also be used as carrier vehicles for anionic drugs such as sodium diclofenac and are efficient in inhibiting lipopolysaccharides-induced inflammation.[30] Betamethasone, a synthetic anti-inflammatory corticosteroid, has been loaded via post-impregnation on MSNs (SBA-15-NH_2). Treatment of cotton fabric with the loaded-MSNs and the bacteriostatic polysaccharide chitosan afforded functional textiles with antibacterial activity, whose drug delivery properties have been described.[31]

It should be mentioned that in almost all the numerous studies on MSNs for drug delivery, the cargo is physically adsorbed into the pores and rarely covalently bound to the nanoparticles. Nevertheless, Kleitz and Qiao have designed a promising bacterial azo-reductase-responsive delivery system in which the prodrug sulfasalazine is covalently anchored to the surface of MCM-48 mesoporous silica nanospheres. The release of both 5-aminosalicylic acid and sulfapyridine is triggered by the reduction of the azo group of the prodrug by the bacterial enzymes commonly found in the colon.[32] As an alternative to the drug encapsulation, dense hybrid silica nanoparticles containing the antimicrobial triclosan covalently linked to the ceramic matrix through carbamate functions have also been reported.[33] Such hybrid nanoparticles proved to be active against common bacterial pathogens such as *E. coli* (Gram-negative) and *S. aureus* (Gram-positive). On the other hand, Khashab's group proposed in 2016 a new strategy for drug delivery based on the biodegradation of drug-encapsulated MSNs with oxamide functions incorporated into the pore walls, in the presence of trypsin model proteins.[34]

On the other hand, as the group has long experience in carrying out sol-gel processes for the preparation of hybrid silicas[35-49] and in the coating of surfaces,[50-56] especially textiles,[50-55] we envisioned the covalent anchoring of anti-inflammatory agents on silica nanoparticles. The functionalized non-porous or mesoporous silica nanoparticles would be dispersed on cotton textiles. We expect that the cotton fabrics which coated by drug-functionalized silica nanoparticles have potential topical applications in medical textiles (bandages, gauzes or strips). The presence of functionalized silica nanoparticles in wound dressings would increase the roughness of the surface of the fabric and, consequently, its hydrophobicity and durability.[57-60] This is advantageous for keeping dry the gauze and wound, acting as a barrier to the microorganisms and helping the rapid wound healing. Hydrophobic cotton with anti-inflamatory drug can not only be useful to cover a simple bruise in order to let it dry, but also for more important and extensive burning lesions, in order to avoid that the exudative fluid that contains proteins gets stuck to the cotton gauze.

The repairing effect of anti-inflammatory drugs on human tissues can only take place if the drug is released from the fabric matrix and comes into direct contact with the cells involved in the inflammatory response in the wounded area. During inflammation, a large number of leukocytes leave the blood vessels and are recruited to the wounded area (chemotaxis), locally activating metabolic processes. The result is an increased phagocytic activity, a rise in the release of proteases, peroxidases and oxygen reactive species, which contribute to the cleavage and elimination of external agents.[61]

As proteases are capable of hydrolysing amide bonds found in peptides and proteins, one interesting proposal would be the connection of the drug to the linker by an amide functional group. A good choice as anti-inflammatory agents would be salicylic acid, (*S*)-ibuprofen and diclofenac, the most common and worldwide known non-steroidal anti-inflammatory drugs (NSAIDs) containing a carboxyl group in the molecule.

Salicylic acid is a phytochemical with beneficial effects on human well-being. It is a phenolic compound present in various plants, where it has a vital role in protection against pathogenic agents. Natural sources include fruits, vegetables and spices.[62] Ibuprofen and diclofenac, two of the most used non-steroidal anti-inflammatory drugs, are widely used as anti-inflammatory and analgesic agents for the treatment of arthritis, sprains and strains, gout, migraine, dental pain, and pain after surgical operations. They can ease pain and reduce inflammation.[63] (*S*)-Ibuprofen can also be used to relieve cold and 'flu-like' symptoms including high temperature

(fever).[64] The most famous and defined effect of these drugs is inhibition of prostaglandin synthesis. They have anti-inflammatory effects by blocking the effect of cyclooxygenase (COX) enzymes. Some prostaglandins are produced at sites of injury or damage, and cause pain and inflammation. However, when the production of COX enzymes is blocked, less prostaglandins are produced, which means that pain and inflammation are relieved.[63]

The main actions of diclofenac are summarized in **Figure 4.1**. As mentioned before, diclofenac anti-inflammatory effects are mainly related to its ability to inhibit cyclooxygenase (COX), an enzyme involved in the generation of several inflammatory mediators from arachidonic acid. Diclofenac has also been reported to inhibit other enzymes such as phospholipase A2 (PLA-2) (which would result in lower free arachidonic acid availability) or 5-lipooxygenase (5-Lox) (which would result in a decrease in the production of proinflammatory leukotrienes). These and other reported actions of diclofenac have been linked to its anti-inflammatory effects.[65]

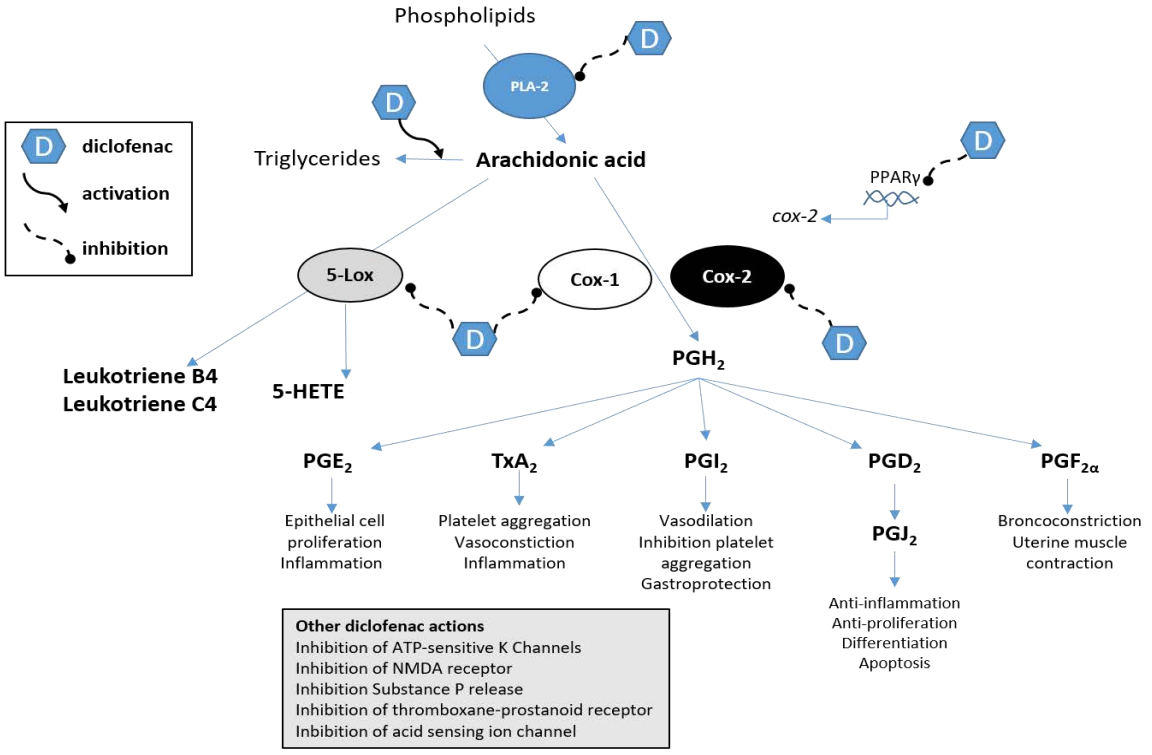

Figure 4.1 Main actions of diclofenac

We undertook this project in collaboration with Prof. Adelina Vallribera and Dr. Albert Granados (from our group in *Departament de Química*, UAB) and Prof. Ester Fernández (*Departament de Biologia Cel·lular, Fisiologia i Immunologi*a and *Institut de Neurociències*, UAB). Dr. Albert Granados had previously described the covalent attachment of the three

carboxyl-containing non-steroidal anti-inflammatory drugs (NSAIDs) (salicylic acid, ibuprofen and diclofenac) directly onto cotton fabric surfaces (**Figure 4.2**). It had been shown that these textiles with anti-inflammatory properties were capable of releasing the drug when the fabric was in the presence of the protease cathepsin G or leukocytes obtained from rat blood.[66]

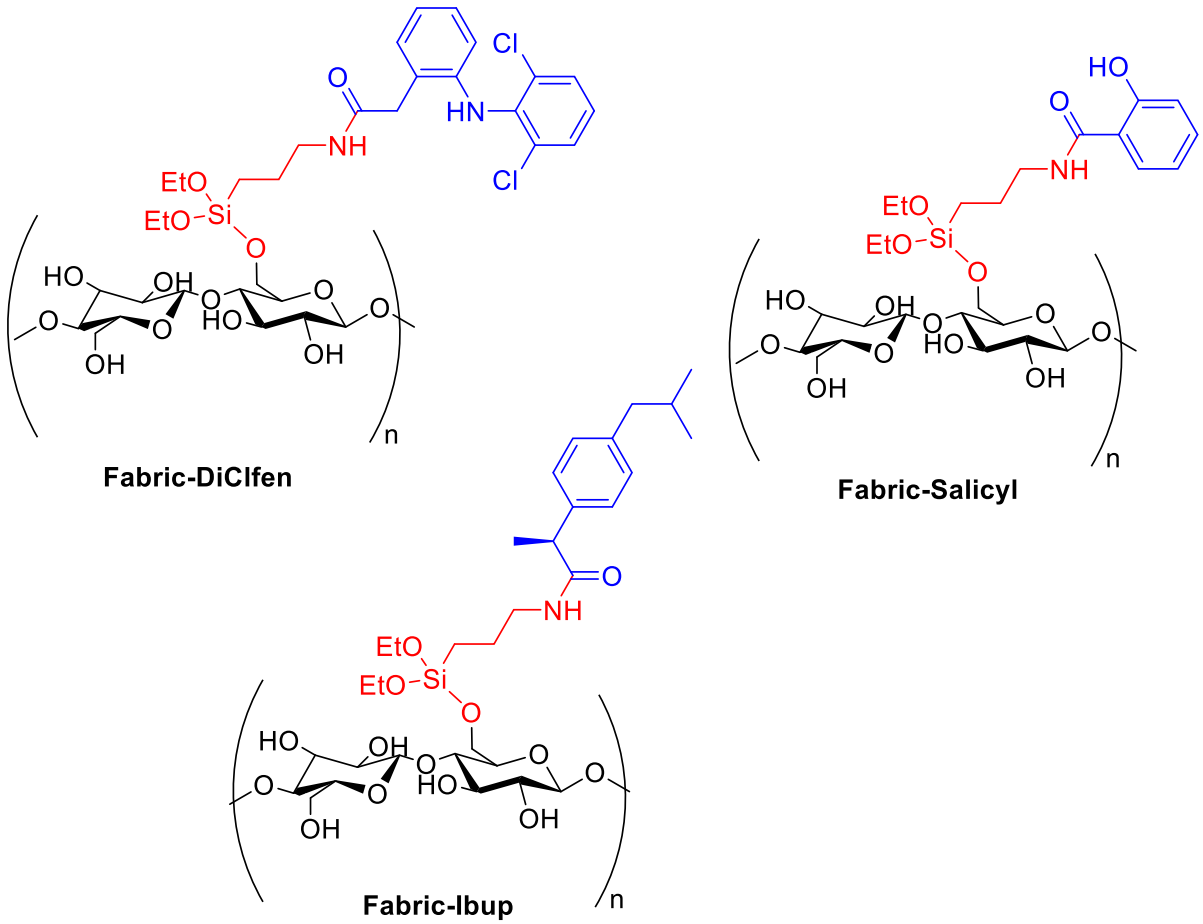

Figure 4.2 Schematic representation of cotton fabrics covalently modified with anti-inflammatory drugs.

4.2 Objectives

Following the precedents mentioned in the introduction and our general interest on medical applications of functionalized silica nanoparticles, our objectives in this part of the thesis were:

a) The preparation and characterization of new silica nanoparticles covalently functionalized with carboxyl-containing anti-inflammatory drugs (salicylic acid **82**, ibuprofen **83** and diclofenac **84**) through amide bonds (**Figure 4.3**). These nanomaterials would be prepared by post-grafting and sol-gel co-condensation methodologies.

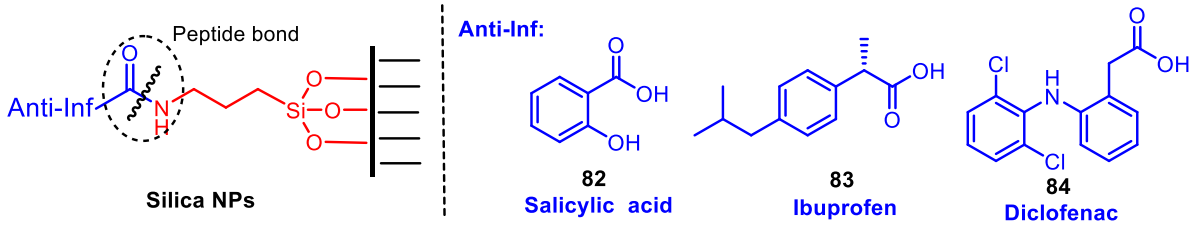

Figure 4.3 Silica nanoparticles covalently functionalized with non-steroidal anti-inflammatory drugs

b) The preparation and characterization of cotton fabrics loaded with these functionalized silica nanoparticles by dip-coating (**Figure 4.4**). The presence of functionalized silica nanoparticles would increase the roughness of the surface of the fabric and, consequently, its hydrophobicity.

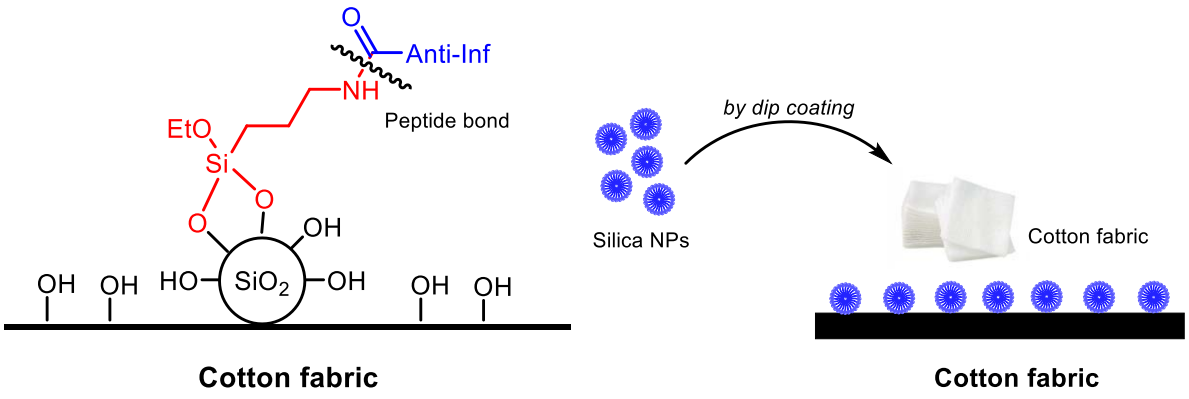

Figure 4.4 Cotton fabrics coated with silica nanoparticles functionalized with anti-inflammatory drugs

c) The treatment of functionalized nanoparticles and coated cotton fabrics with model proteases and leukocytes from animal origin, which should result in the *in situ* release of the anti-inflammatory drug by the selective enzymatic cleavage of the amide bond. Topical cutaneous applications in wound dressings and cream formulations for the acceleration of wound healing were envisaged.

4.3 Results and Discussion

In this part, we describe the preparation of silica nanoparticles covalently functionalized with carboxyl-containing non-steroidal anti-inflammatory drugs through amide bonds, which will be cleaved by proteases to release the drugs *in situ*. Moreover, we report the loading of cotton fabrics with these functionalized silica nanoparticles by one-step-coating. We envisage potential topical applications in cutaneous chronic wounds.

4.3.1 Synthesis of silylated derivatives of anti-inflammatory drugs

Following the procedure previously described by Dr. Albert Granados, the desired commercial anti-inflammatory agent (salicylic acid **82**, ibuprofen **83** or diclofenac **84**) was mixed with *N,N'*-dicyclohexylcarbodiimide (DCC, 1 equiv.), 4-(dimethylamino)pyridine (DMAP, 5 mol%) and 3-(triethoxysilyl)propylamine **85** (1.2 equiv) in CH_2Cl_2 at room temperature overnight, affording the silylated precursors **P19-P21**, respectively, with excellent yields (90-94%) after chromatographic separation.[66] These classical conditions gave excellent performance and the silylated derivatives showed unusual good stability towards moisture (**Scheme 4.1**).

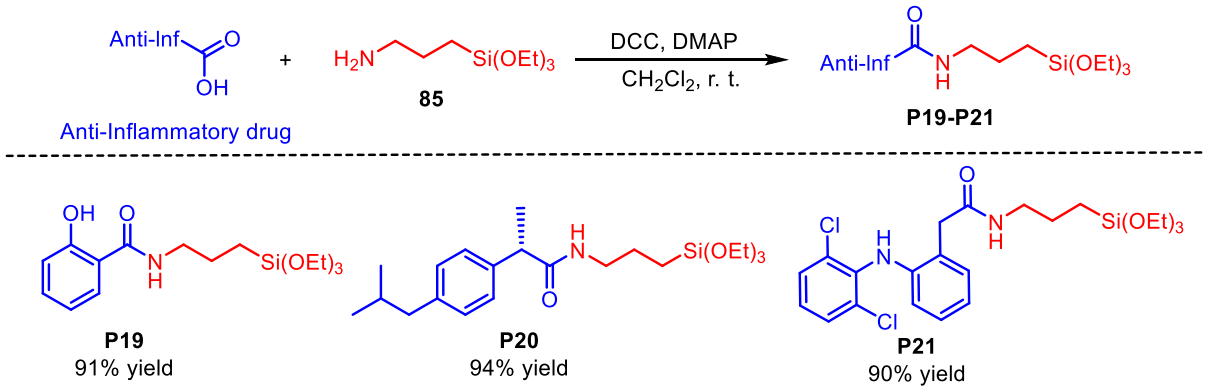

Scheme 4.1 Coupling reaction of anti-inflammatory agents with 3-(triethoxysilyl)propylamine.

This is a classic amidation reaction, in which DCC is used for the purpose of activating the carbonyl of the carboxylic acid with a better leaving group. Carbonyl electrophilia was improved by making the nucleophilic attack by the amine and the release of the leaving group much more effective. The mechanism of the reaction is as follows (**Scheme 4.2**).

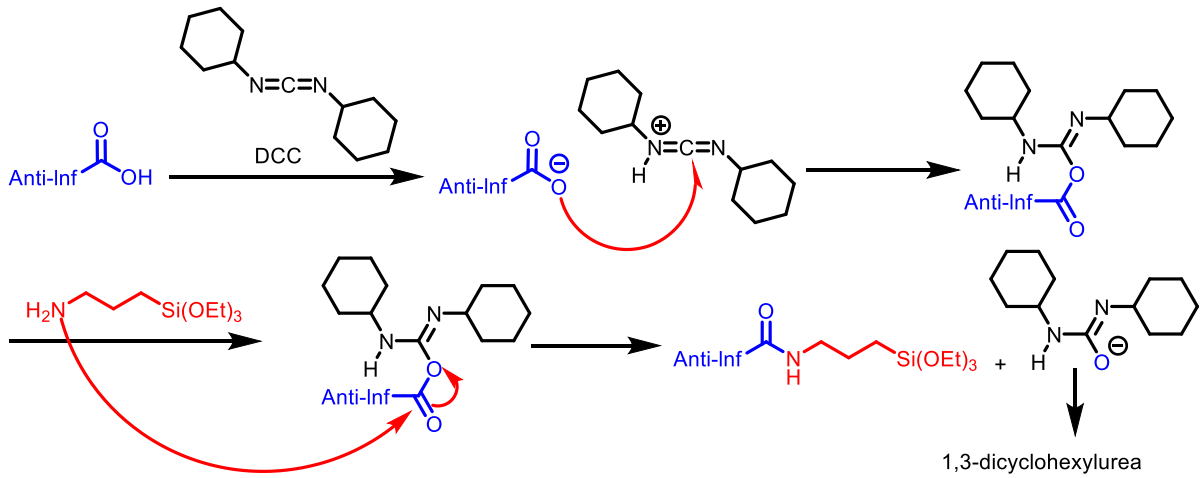

Scheme 4.2 Peptide bond formation mechanism mediated by DCC

4.3.2 Preparation of silica nanoparticles functionalized with anti-inflammatory drugs

From the silylated anti-inflammatory precursors **P19-P21**, we turned to the covalent anchoring of the drugs to silica nanoparticles. Different types of functionalized silica nanoparticles were prepared by grafting on MSNs of MCM-41 type[67] and **M0**[68] and by sol-gel co-condensation methodologies (**Scheme 4.3**) (for the synthesis of MCM-41 and **M0** NPs, see **Chapter 2 Scheme 2.15**). Specifically, $\mathbf{M_I}$ and $\mathbf{M_{II}}$ were synthesized by anchoring the precursors to MSNs MCM-41 and **M0**, respectively, under standard conditions, in refluxing toluene for 24 h. Materials $\mathbf{M_{III}}$ were obtained by co-condensation of precursors **P19-P21** with tetraethyl orthosilicate (TEOS) using cetyltrimethylammonium bromide (CTAB) as template in an aqueous buffer solution of pH 7 from mixtures with the molar ratios CTAB : TEOS : **Pn** : H_2O = 5 : 40 : 2 : 30000 (n = 19-21).[69] The final solution was stirred at room temperature for 12 h and then the nanoparticles were collected by centrifugation (13500 rpm) at room temperature. The surfactant was removed from the obtained solid by treatment with an ethanolic solution of NH_4NO_3 and then the resulting material was washed successively with ethanol, Mili-Q water and ethanol. Materials $\mathbf{M_{IV}}$ were prepared by co-condensation of precursors **P19-P21** with TEOS using a 28% aqueous ammonia solution in ethanol with the molar ratios TEOS : **Pn** : EtOH : NH_3 : H_2O = 100: 5 : 8587: 889 : 2160.[57] The mixed solution was stirred at room temperature for 12 h and then the nanoparticles were collected by centrifugation (13500 rpm) at room temperature and washed with ethanol until neutral pH was reached.

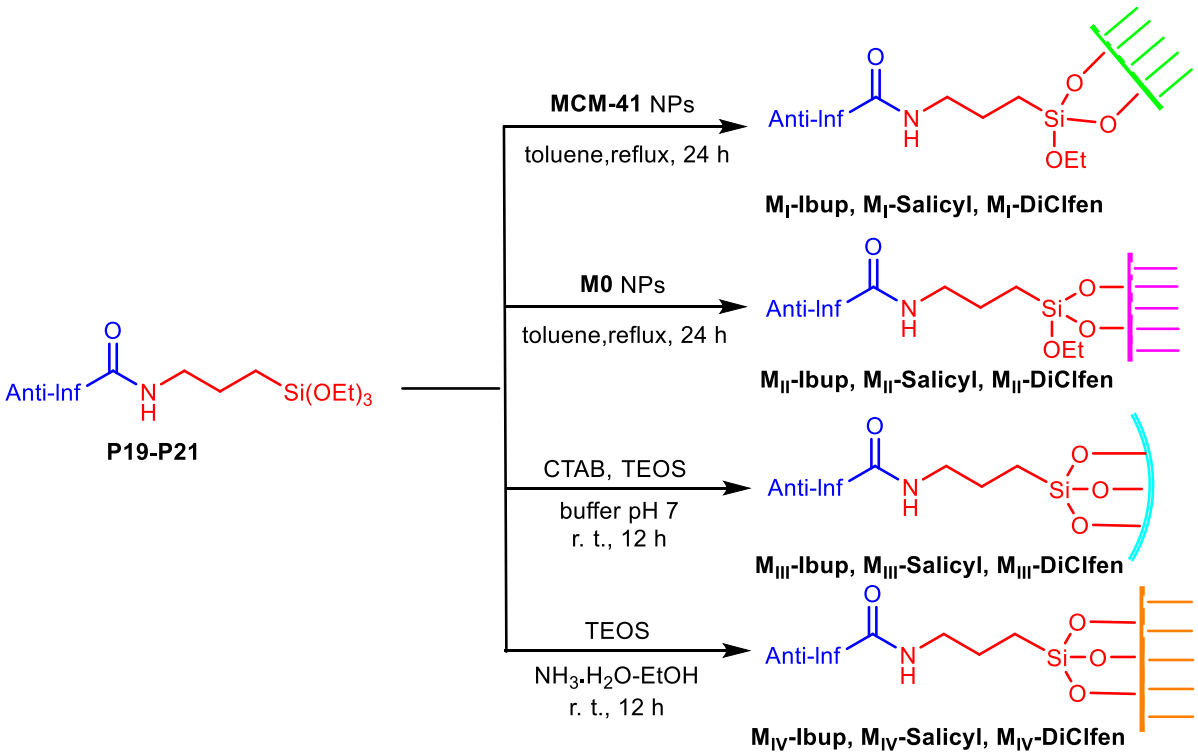

Scheme 4.3 Preparation of silica nanoparticles functionalized with anti-inflammatory drugs.

4.3.3 Characterization of silica nanoparticles functionalized with anti-inflammatory drugs

The modified silica nanoparticles **M_I-M_{IV}** were characterized by elemental analysis, ^{13}C and ^{29}Si CP MAS solid state NMR, Transmission Electron Microscopy (TEM), Scanning Electron Microscopy (SEM), nitrogen-sorption measurements, Dynamic Light Scattering (DLS), zeta-potential and Infrared Spectroscopy (IR).

It is well known that salicylic acid exhibits fluorescence in the visible range when it is irradiated at 365 nm. Similarly, the silylated precursor **P19** exhibit the same property. Thus, all four kinds of silica nanoparticles (**M_I-Salicyl**, **M_{II}-Salicyl**, **M_{III}-Salicyl**, **M_{IV}-Salicyl**) prepared from **82** also display blue fluorescence under UV-Vis light (**Figure 4.5**). Conversely, ibuprofen and diclofenac functionalized silica nanoparticles did not exhibit fluorescence.

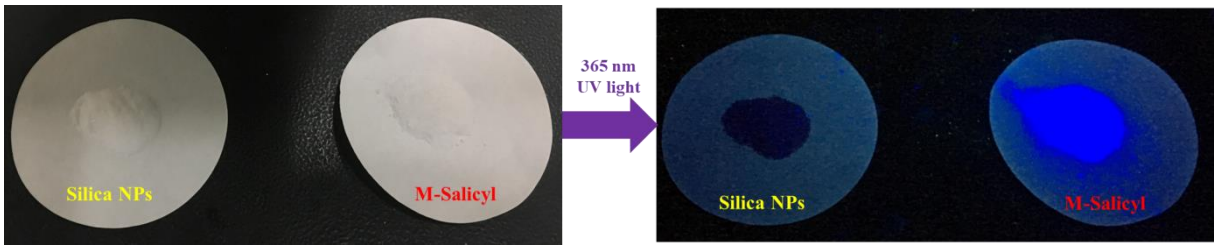

Figure 4.5 The fluorescence of the salicylic acid functionalized silica nanoparticles (**M-Salicyl**)

Here, we only focus on the characterization of the diclofenac modified silica nanoparticles **M-DiClfen**. The characterization data of the other functionalized nanoparticles is presented in the experimental ***Section* 4.5.3**. In **Table 4.1** we gather some physical data of diclofenac modified silica nanoparticles.

Table 4.1 Some physical data of **M-DiClfen**.

Material	S_{BET} (m^2g^{-1})	V_{pore} (cm^3g^{-1}) [a]	$Ø_{pore}$ (nm) [b]	Drug loading ($mmolg^{-1}$) [d]	Particle size		Zeta potential (mV)
					TEM	DLS [e]	
M_I-DiClfen	771	0.37	2.6	0.65	145 ± 51	283	-30
M_{II}-DiClfen	256	0.18	1.9 [c]	0.49	76 ± 5	135	-15
M_{III}-DiClfen	662	0.47	2.2	0.22	45 ± 4	169	-30
M_{IV}-DiClfen	9	0.007	nd [f]	0.26	360 ± 25	424	-50

[a] Determined from the uptake at saturation at $p/p^0 = 0.8$; [b] Determined by NLDFT (desorption); [c] Determined by BJH (desorption); [d] Calculated from the N elemental analysis; [e] Hydrodynamic diameters; [f] Non-porous material. Not determined.

These silica NPs were first investigated by electron microscopies (TEM and SEM) to confirm their nanometric size and features (**Figure 4.6**). **M_I-DiClfen,** obtained from MCM-41 type NPs by grafting, preserve the initial rod-like morphology with lengths about 145 ± 51 nm. The TEM images display the typical parallel channels throughout the rods. **M_{II}-DiClfen,** obtained by grafting to **M0**, also preserved the initial spherical morphology, with diameters around 76 ± 5 nm. The TEM images clearly indicate the presence of pores, though they are not as organized as in MCM-41. Interestingly, the synthesis of **M_{III}-DiClfen** by co-condensation of TEOS with 5 mol% of silylated diclofenac **P21** yielded small spherical NPs uniform in size (45 ± 4 nm), with similar porosity as for **M0**, as seen by TEM. **M_{IV}-DiClfen,** prepared by co-condensation in the absence of template, appeared as non-porous dense spherical nanoparticles with a narrow size distribution and an average diameter of 360 ± 25 nm. The hydrodynamic diameters measured by DLS were in good accordance with the TEM size of the corresponding dried particles, if we consider the likely adsorption of water molecules onto the nanoparticle surface (**Table 4.1**). The TEM statistical particle size distribution and DLS of **M_{IV}-DiClfen** is depicted as an example in **Figure 4.7**.

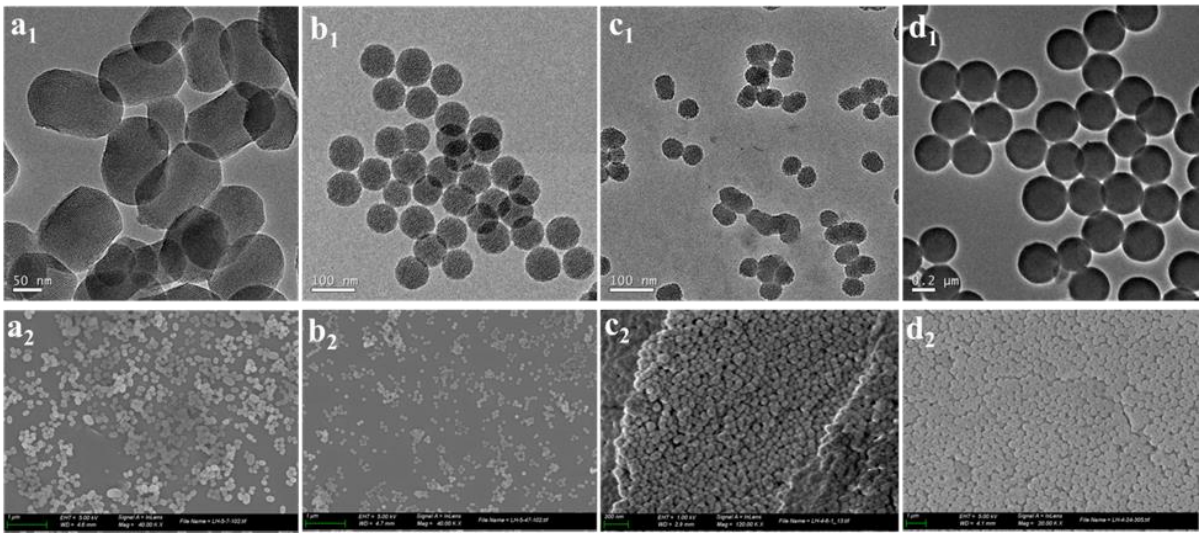

Figure 4.6 TEM and SEM images of diclofenac-functionalized silica nanoparticles: TEM (a_1) and SEM (a_2) of **M_I-DiClfen**, TEM (b_1) and SEM (b_2) of **M_{II}-DiClfen**, TEM (c_1) and SEM (c_2) of **M_{III}-DiClfen**, TEM (d_1) and SEM (d_2) of **M_{IV}-DiClfen.**

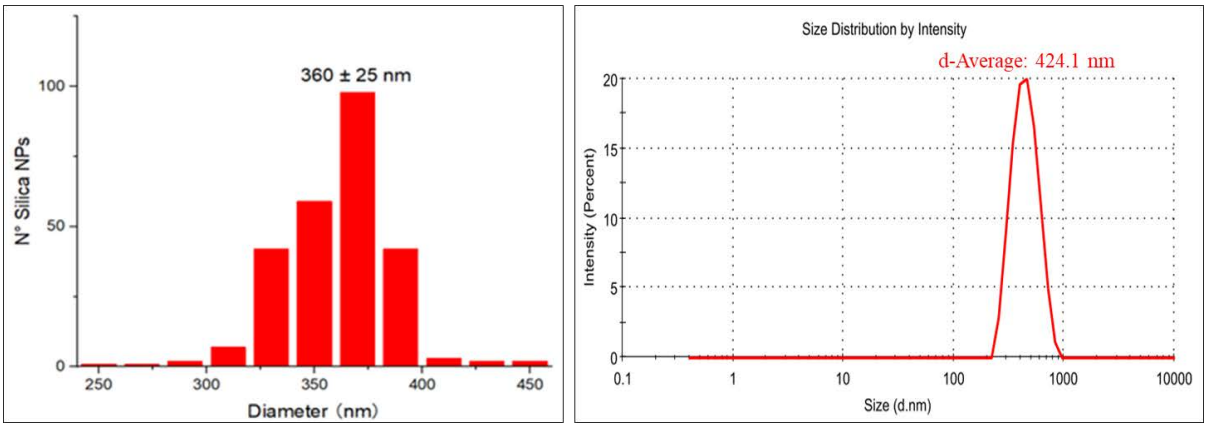

Figure 4.7 TEM statistical size distribution and DLS of **M4-DiClfen**

N_2-sorption experiments confirmed the porosity of the nanoparticles **M-DiClfen** (**Figure 4.8** and **Table 4.1**). As is usually observed, the surface area and pore volume for **M_I-DiClfen** and **M_{II}-DiClfen**, derived from grafting, were significantly reduced with respect to the parent MSNs (see **Chapter 2**, **Table 2.3**), and the pore diameter was slightly decreased. **M_{III}-DiClfen** obtained by co-condensation in the presence of template exhibited a significant surface area of 662 m^2g^{-1} and a pore volume of 0.47 cm^3g^{-1}. All of them displayed isotherms typical of mesoporous materials, whereas **M_{IV}-DiClfen**, synthesized without surfactant, was non-porous as expected.

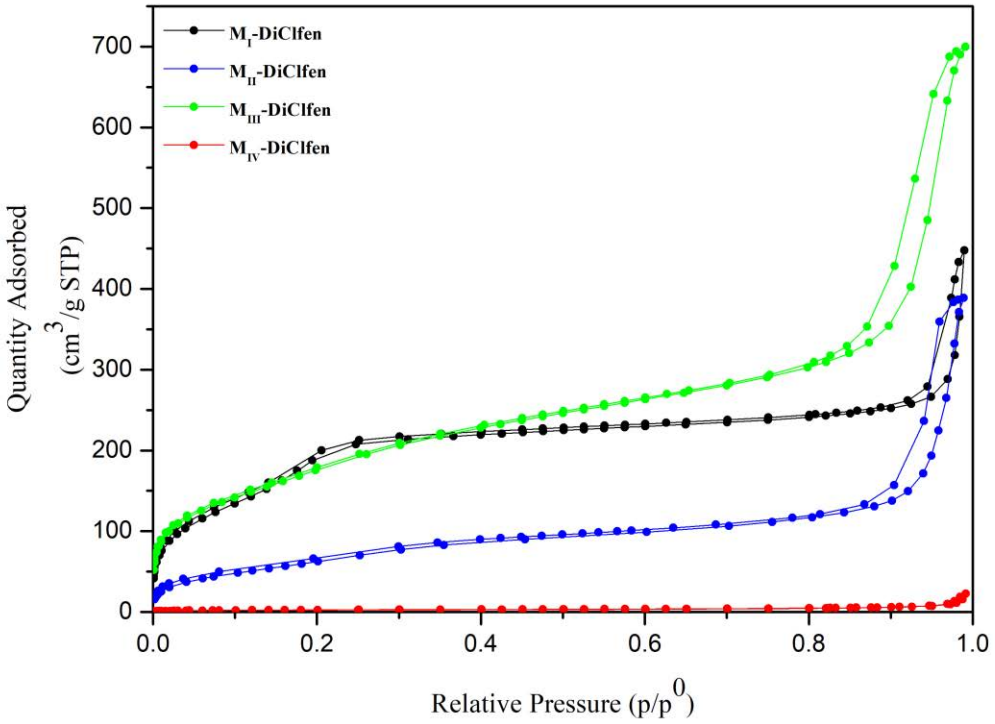

Figure 4.8 N_2-sorption isotherms of **M_I-DiClfen**, **M_{II}-DiClfen**, **M_{III}-DiClfen** and **M_{IV}-DiClfen**.

The drug loading of different silica nanoparticles was deduced from the nitrogen elemental analysis (**Table 4.1**).

The dispersibility of the NPs was checked in Mili-Q water and they were moderately aggregated after dispersion at 1 mg/mL. The modified silica NPs exhibited negative values from -15 to -50 mV, which are due to residual deprotonated silanol groups (isoelectric point of *ca* 3.5 for silica) with some modulation from the functionalization with the drug (**Table 4.1**). The highly negative zeta potential means that the particles display good stability in suspension. The observation of negative values indicates that there is no protonation of the weakly basic diarylamino group present in **M-DiClfen** nanomaterials.

The presence of the organic moiety in the modified nanoparticles was ensured by the solid state ^{29}Si and ^{13}C NMR spectra. For example, the ^{29}Si CP MAS NMR spectrum of **M_{III}-DiClfen** showed two groups of chemical shifts: T units from -59 to -67 ppm derived from the organosilane **P21**, and Q units ranging from -93 to -112 ppm resulting from TEOS (**Figure 4.9**, top). The presence of T signals indicated that the integrity of the Si-C bond was maintained during the formation of the nanomaterials, which was also confirmed by the ^{13}C CP MAS NMR spectrum with the signal at 10 ppm (**Figure 4.9**, bottom). The superposition of the ^{13}C-NMR spectrum of **P21** in solution and that of **M_{III}-DiClfen** in the solid state shows

a good similarity between the two spectra, supporting thereby the integrity of the organic framework. For the functionalized nanoparticles **M_{III}-DiClfen**, the ^{29}Si CP MAS NMR spectrum exhibits mostly T^2 and T^3 environments (not T^1), which confirms the strong anchoring of the organic moiety within the silica network by two or three Si-O-Si linkages. This is also the case for **M_{II}-DiClfen** and **M_{IV}-DiClfen**. However, whereas for the functionalized nanoparticles derived from co-condensation procedures (**M_{III}-DiClfen** and **M_{IV}-DiClfen**) the intensity of T^3 signals are higher than those of T^2, for **M_{II}-DiClfen** derived from grafting, T^2 is more intense than T^3 (see experimental ***Section* 4.5.3**).

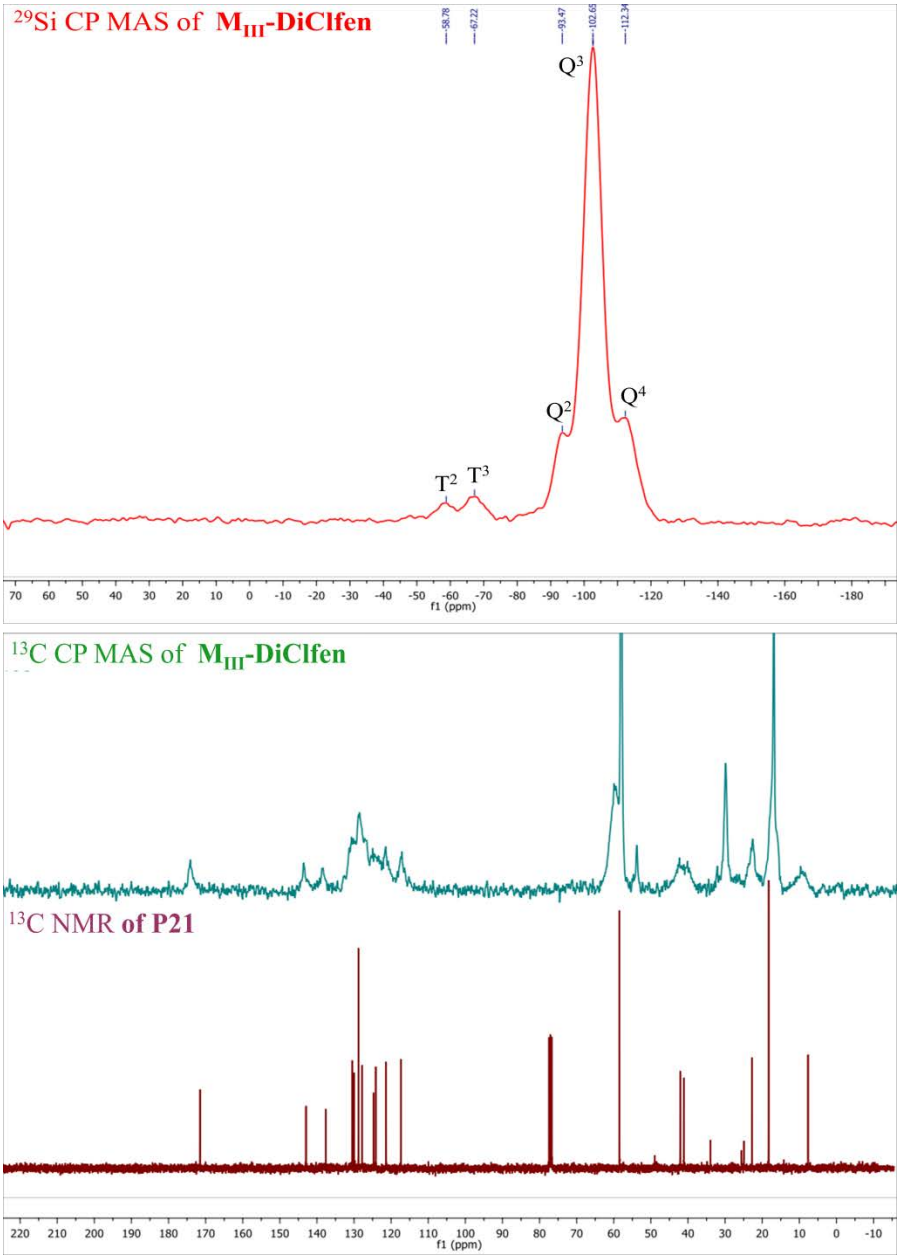

Figure 4.9 ^{29}Si CP MAS NMR spectrum of **M_{III}-DiClfen** (top); ^{13}C CP MAS NMR spectrum of **M_{III}-DiClfen** and ^{13}C NMR spectrum of **P21** (bottom).

4.3.4 Preparation and characterization of cotton fabrics loaded with drug-functionalized silica nanoparticles

With the drug-functionalized silica nanoparticles in hand, we turned to the loading of cotton fabrics with these nanoparticles. Preliminary essays using methods such as dip-coating,[60] or padding[70] with solutions of previously synthesized and isolated anti-inflammatory modified silica nanoparticles (**M_I-Anti-Inf**, **M_{II}-Anti-Inf** and **M_{III}-Anti-Inf)** did not give the desired hydrophobicity for the textiles. The cotton fabrics which were coated with these silica nanoparticles were hydrophilic. In order to improve the hydrophobicity of coated cotton fabrics, three strategies were adopted.

1) First we tried to improve the hydrophobicity of cotton fabrics by modifying its surface with some hydrophobic organic molecules. For example, a piece of **M_{III}.Salicyl** coated cotton fabrics was immersed in 1 vol.% of a fluorinated alkyl silane (FAS) in toluene. Finally, the contact angle (CA) of the cotton was 141.4 °. Interestingly, the cotton fabric changed from hydrophilic to highly hydrophobic.

2) Then, we tried to improve the hydrophobicity by capping the free silanol groups on the silica nanoparticle surface. Thus, **M_{III}-DiClfen** was treated with TMSBr in the presence of Et_3N in toluene at room temperature for 24 h, the capped nanoparticles were isolated by centrifugation, and washed successively with toluene, methanol, Et_2O and acetone (**Scheme 4.4**). These new nanoparticles **M_{III}-DiClfen-TMS** were dispersed in ethanol (0.5 wt.%), a piece of cleaned cotton fabric was immersed in the as-prepared coating solution and ultrasonicated for 30 min at room temperature. Finally, the coated cotton was dried at 110 °C in an oven for 60 min. In this way, the CA of the resulting cotton fabric was 143.3 °.

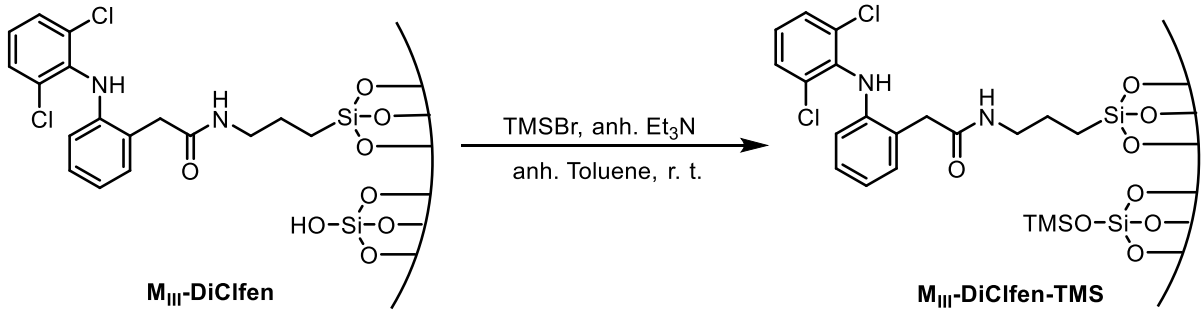

Scheme 4.4 Preparation of **M_{III}-DiClfen-TMS**

3) Finally, we tried to improve the hydrophobicity of cotton fabrics by adding certain amounts of fluorinated alkyl silanes (FAS) of two different lengths, namely (1*H*,1*H*,2*H*,2*H*-nonafluorohexyl)triethoxysilane (**FAS-3**)[70] and (1*H*,1*H*,2*H*,2*H*-tridecafluorooctyl)triethoxysilane (**FAS-5**)[71] in the co-condensation process, leading to **M_{III}-Salicyl**-x**FAS-n** (x = 0.5 or 1.0; n = 3 or 5). Then, a piece of cotton was loaded with these nanoparticles by the procedure described in the second method. As shown in **Scheme 4.5**, these hydrophobic nanoparticles were obtained by co-condensation of precursor **P19** with TEOS using CTAB as template in an aqueous buffer solution of pH 7.[69] When the molar ratios of reagents were CTAB : TEOS : **P19** : **FAS-3** : H_2O = 5 : 40 : 2 : 2 : 30000, **M_{III}-Salicyl**-0.5 **FAS-3** was obtained, and the CA of the coated cotton was 111.8 °**. M_{III}-Salicyl-0.5 FAS-5** was also prepared under the same conditions using the longer chain fluorinated reagent **FAS-5**, and the CA of the corresponding coated cotton was 126.3 °. An increase of the amount of **FAS-5** (molar ratios CTAB : TEOS : **P19** : **FAS-5** : H_2O = 5 : 40 : 2 : 1 : 30000) gave **M_{III}-Salicyl-1.0 FAS-5**. The CA of the corresponding coated fabric did not increase significantly (128.8 °).

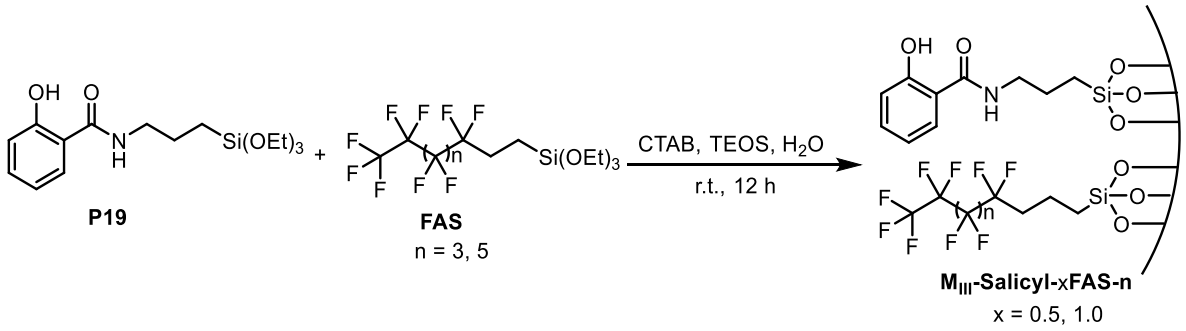

Scheme 4.5 Preparation of **M_{III}-Salicyl**-x**FAS-n** (x = 0.5 or 1.0; n = 3 or 5)

However, we finally discarded these three approaches. In the third approach, the fabrics were not highly hydrophobic. In the first and second described approaches, we certainly obtained highly hydrophobic textiles, but we had some problems when performing the treatment with proteases to release the drug (difficulties in wetting the textile in the buffer solution).

Lin and co-workers had described the preparation of fluoro-containing silica nanoparticles by one-step coating method for generation of surface superhydrophobicity.[57] Thus, we finally chose to prepare cotton fabrics loaded with drug-functionalized silica nanoparticles by this one-step coating method depicted in **Scheme 4.6**. The coating solutions were obtained by co-hydrolysis of TEOS with organosilanes **P19-P21** (molar ratio 10:0.5) in aqueous ammonia in

ethanol under stirring. Without any isolation and purification, the resulting milky solution was ultrasonicated for 30 min to produce a homogeneous suspension in which a piece of cotton textile was immersed, and the whole system was ultrasonicated for half an hour. Then, the cotton textile was removed from the solution and washed with distilled water several times, then dried at 120 °C for one hour. In this way, the textiles loaded with drug-functionalized nanoparticles **Fabric-M_{IV}-Anti-Inf** were obtained**.** The measured water contact angle (CA) was 140.5 ° for the fabric loaded with **M_{IV}-DiClfen** by this one-step coating. When the immersion process of the textile on the coating solution, sonication, removal and drying was repeated until three times, the contact angle achieved a value of 141.8 ° (**Figure 4.10**).

Thus, we had achieved hydrophobicity, even in the absence of fluorinated reagents, by covering the surface of the cotton piece with the functionalized silica nanoparticles by this one-step coating method.

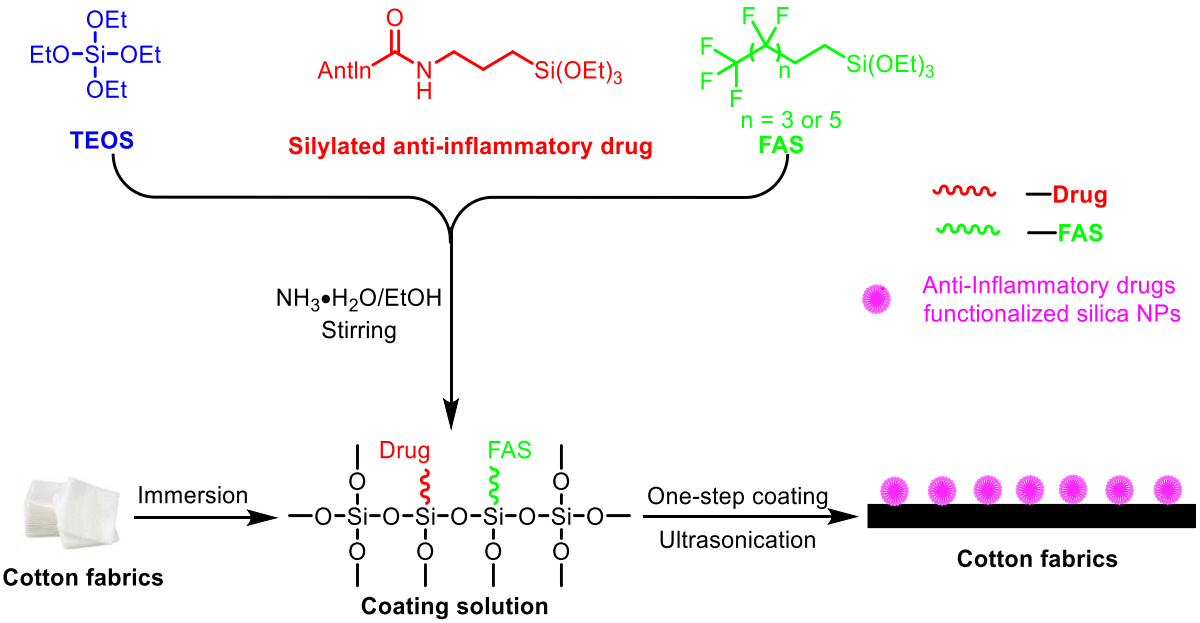

Scheme 4.6 Schematic illustration of the silica sol preparation and coating procedure for highly hydrophobic cotton fabrics.

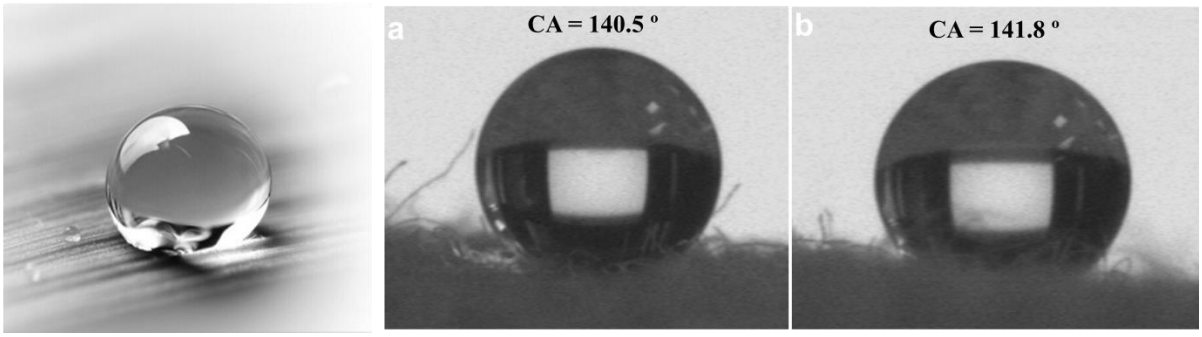

Figure 4.10 Pictures of water drops on the fabrics treated with **M_{IV}-DiClfen** (**Fabric-M_{IV}-DiClfen**).

In an attempt to increase this hydrophobicity, several textiles were also prepared by this one-step coating method by adding certain amounts of fluorinated alkyl silanes (FAS) of two different lengths, **FAS-3**[70] and **FAS-5**[71] in the co-hydrolysis process. With the silylated diclofenac derivative **P21** as a model and keeping constant the molar ratio of TEOS:**P21** at 10:0.5, we have examined the influence of the amount of added **FAS-3** (x mmol) on the hydrophobicity of the resulting fabrics (**Table 4.2**). Indeed, with x = 0.25, a higher water contact angle of 148 ° was found, but a further increase on the amount of added **FAS-3** did not give significant improvements (entries 3-5 of **Table 4.2** and **Figure 4.11a**). Interestingly, a superhydrophobic fabric (entry 6 of **Table 4.2**, CA of 156 °, **Figure 4.11b**) was obtained by using **FAS-5** with the longer fluorinated chain (x = 0.25) (**Fabric-M_{IV}-DiClfen-0.25 FAS-5**).

Table 4.2 Some data of **Fabric-M4-DiClfen-x FAS-n**

Entry	FAS [a]		CA (°) [b]	EDX [c]					
	n	**x** (mmol)		C	O	Si	N	Cl	F
1	3	0	141	43.49	41.08	11.18	0.86	3.38	-
2	3	0.25	148	30.97	37.92	19.60	1.28	3.66	6.57
3	3	0.50	147	32.33	37.78	21.12	0.72	1.28	6.66
4	3	0.75	147	41.35	41.39	9.78	0.63	1.21	5.63
5	3	1.00	148	42.14	32.90	18.31	0.52	1.45	4.67
6	5	0.25	156	41.76	37.01	13.76	0.89	2.93	3.64

[a] Molar ratio TEOS:**P21**:FAS = 10:0.5:x. [b] The hydrophobic tests performed were the measurement of the contact angle of a water droplet (4 μL) deposited on top of each fabric; [c] EDX was taken on a SEM Zeiss Merlin with and INCA detector from Oxford Instruments.

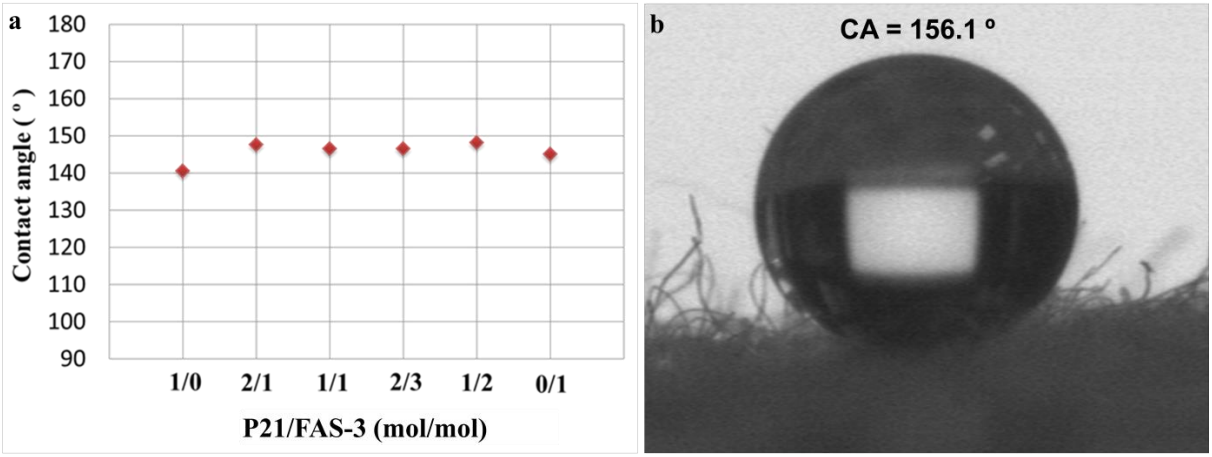

Figure 4.11 a) Influence of **P21/FAS-3** ratio in the hydrolysis reaction on the resulting water contact angles of the coated cotton fabrics (TEOS:Drug = 20:1, mol/mol). b) Water contact angle of the cotton coated with **M_{IV}-DiClfen-0.25 FAS (n = 5) (Fabric-M_{IV}-DiClfen-0.25 FAS-5).**

Some data of cotton fabrics prepared by one-step coating with **M_{IV}-DiClfen** and FAS (**Fabric-M_{IV}-DiClfen-x FAS-n**) and the corresponding functionalized silica nanoparticles (**M_{IV}-DiClfen-x FAS-n**) are summarized in **Table 4.2** and **Table 4.3**, respectively.

Table 4.3 Some physical data of **M4-DiClfen-x FAS-n**

Material	S_{BET} (m^2g^{-1})	V_{pore} (cm^3g^{-1}) [a]	$Ø_{pore}$ (nm) [b]	Drug loading ($mmolg^{-1}$) [c]	Particle size [d]	Zeta potential (mV)
M_{IV}-DiClfen-0.25 FAS-3	334	0.189	2.3	0.121	167	-41
M_{IV}-DiClfen-0.50 FAS-3	336	0.193	2.3	0.104	183	-42
M_{IV}-DiClfen-0.75 FAS-3	348	0.199	2.3	0.221	312	-36
M_{IV}-DiClfen-1.00 FAS-3	374	0.255	2.7	0.096	403	-37
M_{IV}-DiClfen-0.25 FAS-5	286	0.142	2.0	0.319	229	-48

[a] Determined from the uptake at saturation at $p/p^0 = 0.8$; [b] Determined by BJH (adsorption); [c] Calculated from the N elemental analysis; [d] Hydrodynamic diameters, determined by DLS.

From the amount of fluorine (EDX) in the fabrics (entries 2-6 of **Table 4.2**) and the obtained loading of the drug derivative in the nanoparticles when increasing amounts of FAS were used (**Table 4.3**), we can infer that the fluorinated silane is not completely co-condensed, probably due to the lower solubility in the medium. This fact is more pronounced with the longer chain fluorinated silane (compare entries 2 and 6 of **Table 2**). This is the result of FAS acting as template.[72] Thus, contrary to the non-porous **M_{IV}-DiClfen (Table 4.1)**, the

functionalized nanoparticles **M_{IV}-DiClfen-x FAS-n** show some porosity (from 286 to 374 m^2g^{-1}, **Table 4.3**). The corresponding N_2-sorption isotherms are shown in **Figure 4.12**. The nanoparticles have hydrodynamic diameters (DLS) from 167 to 403 nm and high negative zeta potential values, indicative of stability (**Table 4.3**).

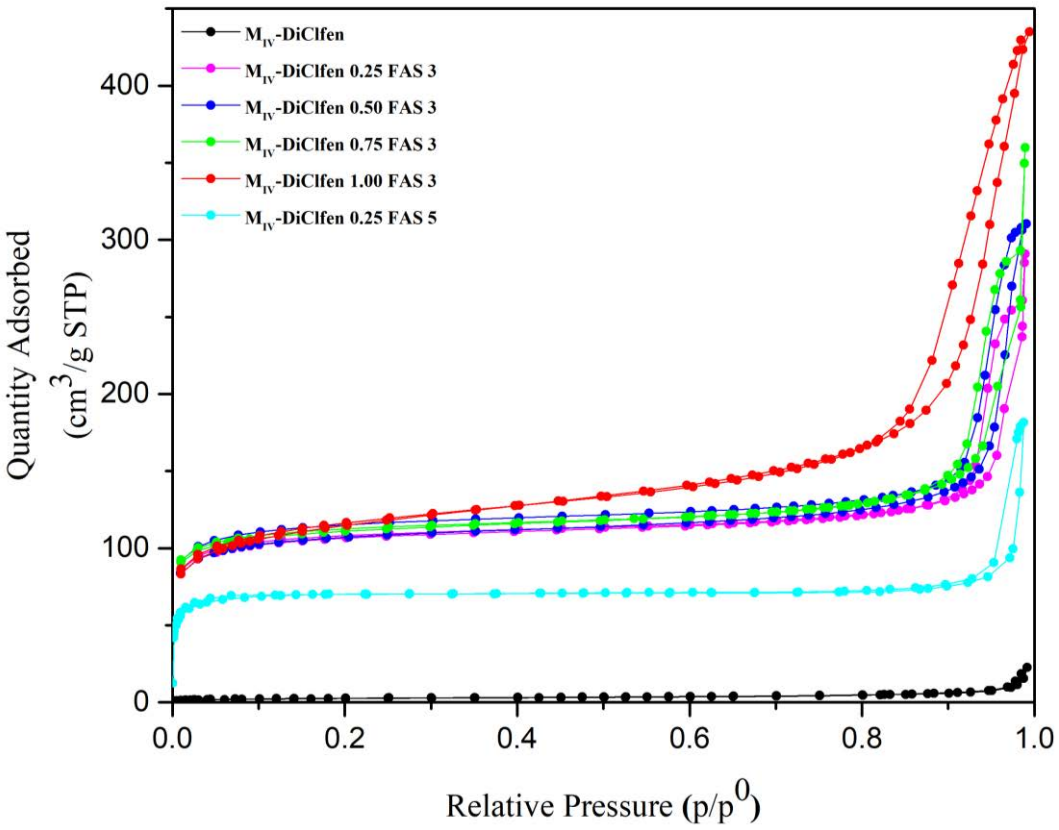

Figure 4.12 N_2-sorption isotherms of **M4-DiClfen-x FAS-n**

The presence of abundant silica nanoparticles on the surface of cotton fabric loaded with **M_{IV}-DiClfen** by one-step coating was clearly observed by SEM (**Figure 4.13**). The chemical composition of the surface of the fabrics was analyzed by EDX. As expected, in all cotton fabrics the EDX analysis showed peaks for the elements C, O, N, Cl, together with F when FAS was used (entries 2-6, **Table 4.2** and ***Section* 4.5.5**). As an example, we display the EDX spectrum (**Figure 4.14**) and the corresponding element mapping (**Figure 4.15**) of **Fabric-M_{IV}-DiClfen**. The peaks corresponding to silicon, chlorine and nitrogen clearly indicate the presence of the diclofenac-modified silica nanoparticles coating.

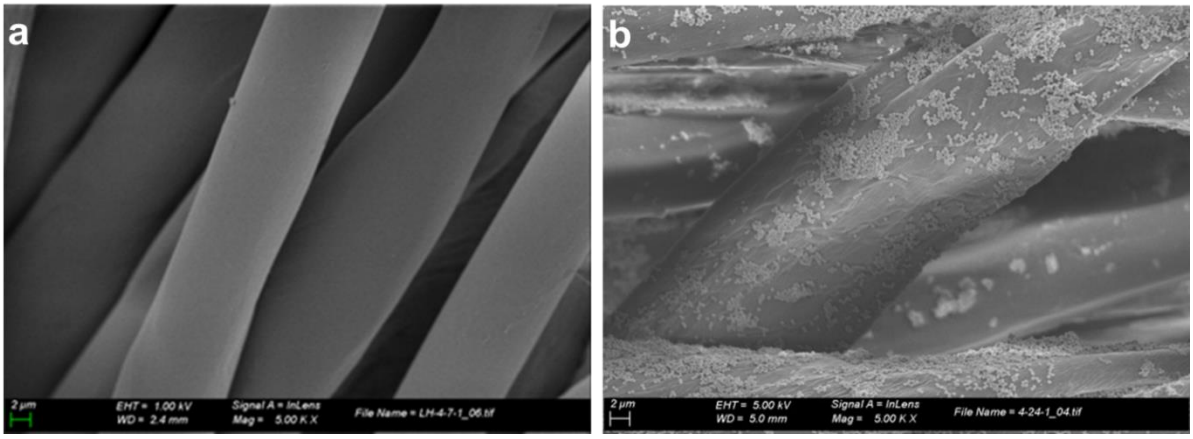

Figure 4.13 SEM images of a) uncoated cotton fabric and b) coated cotton fabric **Fabric-M_{IV}-DiClfen**

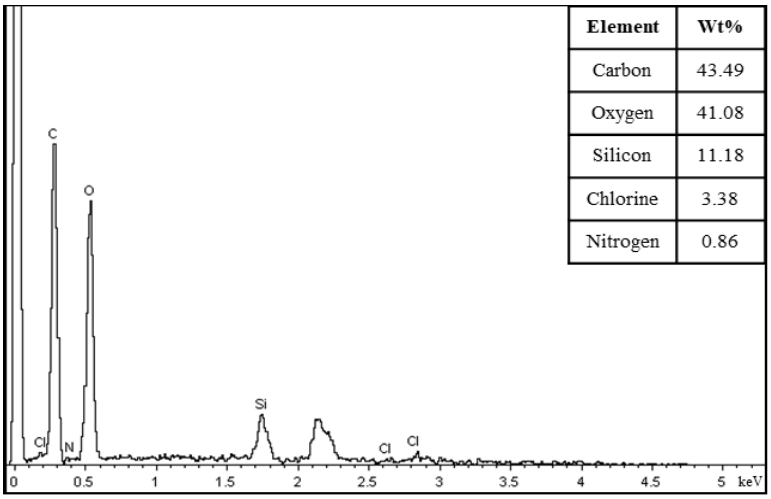

Element	Wt%
Carbon	43.49
Oxygen	41.08
Silicon	11.18
Chlorine	3.38
Nitrogen	0.86

Figure 4.14 EDX spectrum of the coated cotton fabric **Fabric-M4-DiClfen**

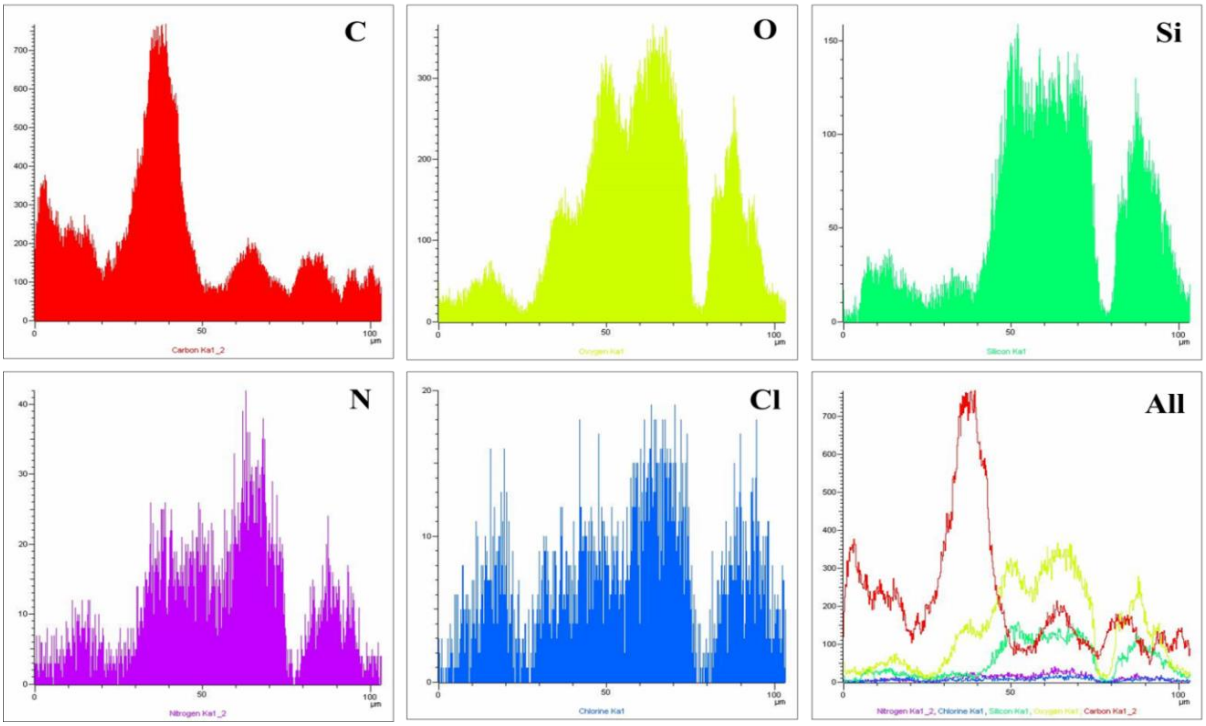

Figure 4.15 Corresponding element mapping of the coated cotton fabric **Fabric-M_{IV}-DiClfen**

The SEM image, EDX spectrum and the corresponding element mapping of the superhydrophobic **Fabric-M_{IV}-DiClfen-0.25 FAS-5** are presented in **Figure 4.16** and **Figure 4.17.**

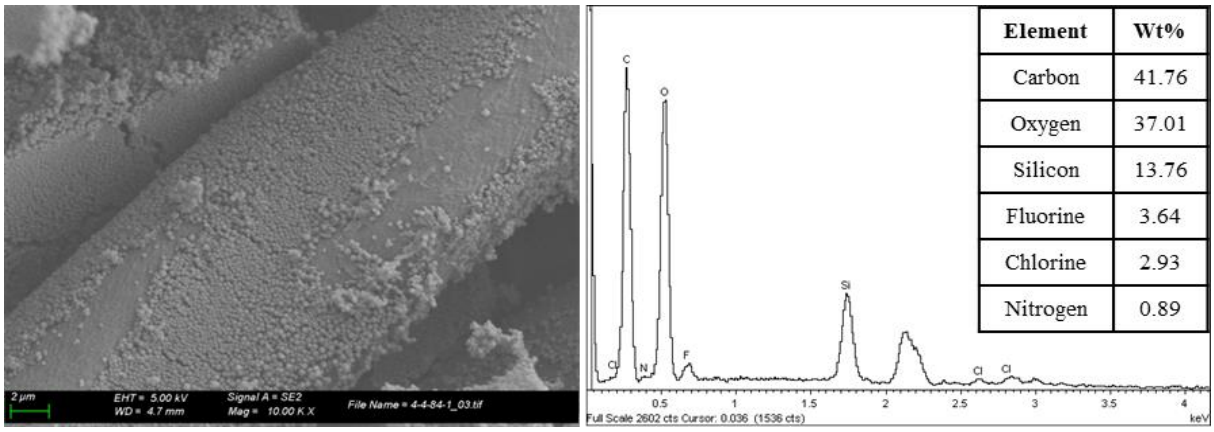

Element	Wt%
Carbon	41.76
Oxygen	37.01
Silicon	13.76
Fluorine	3.64
Chlorine	2.93
Nitrogen	0.89

Figure 4.16 SEM image and EDX spectrum of coated cotton fabrics **Fabric-M_{IV}-DiClfen-0.25 FAS-5**

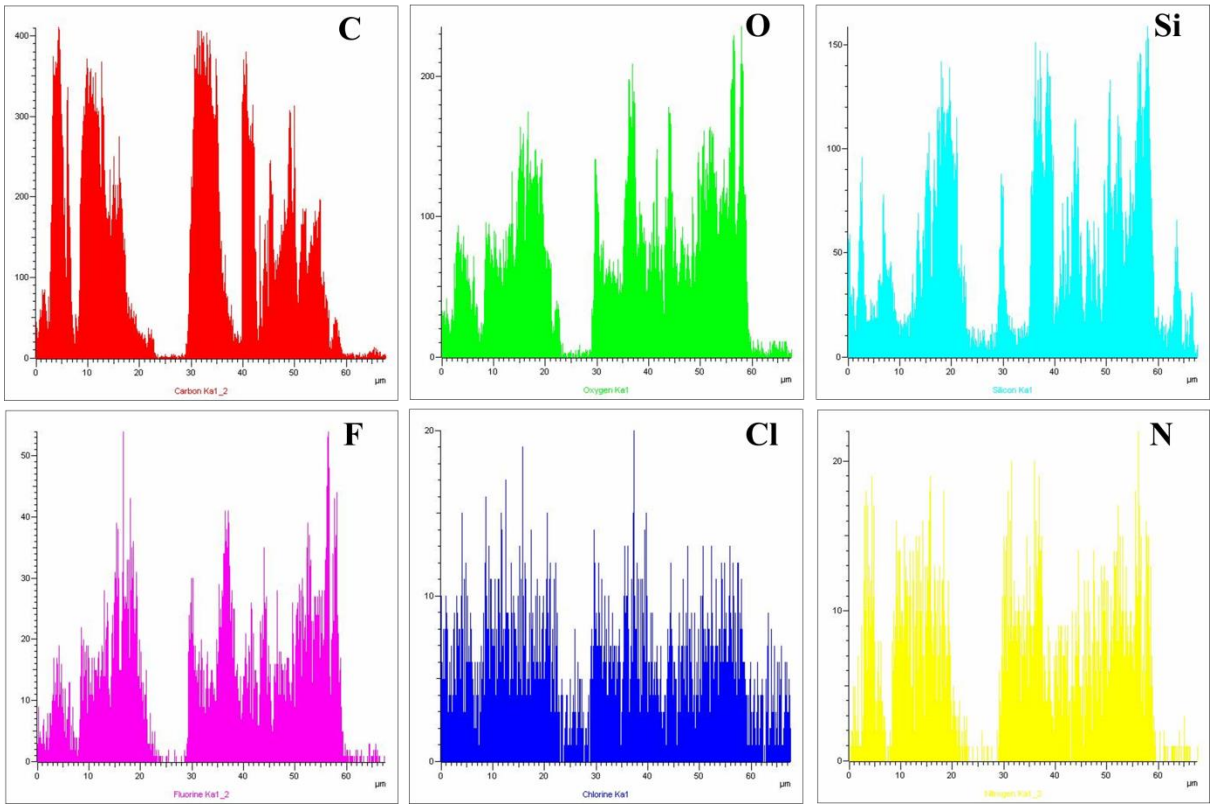

Figure 4.17 EDX corresponding element mapping of coated cotton fabrics **Fabric-M_{IV}-DiClfen-0.25 FAS-5**

This elemental composition is corroborated by XPS (**Figure 4.18**) and Fourier-Transform Infrared Spectroscopy (FTIR) (**Figure 4.19**). The spectrum of uncoated fabric exhibited absorptions due to O-H stretching at around 3333 cm^{-1}, C-H stretching at 2900 cm^{-1} and C-O-C stretching at 1018-1100 and 1099 cm^{-1}, all of them consistent with those of typical

cellulose.[73-74] In addition of these signals, in the IR spectrum of the coated cotton appeared a new absorption at 795 cm^{-1} corresponding to Si-C stretching. The typical absorption due to Si-O-Si moiety characteristic of silica nanoparticles, which should appear at 1100-1000 cm^{-1} region, was overlapped by the C-O absorption of cellulose.[70, 75] The intensity of the peaks at this region increases and becomes higher than in uncoated cotton fabrics, indicating the presence of Si-O-Si bond on the coating surface. These results confirmed the successful coating of the cotton cellulose with modified silica nanoparticles.

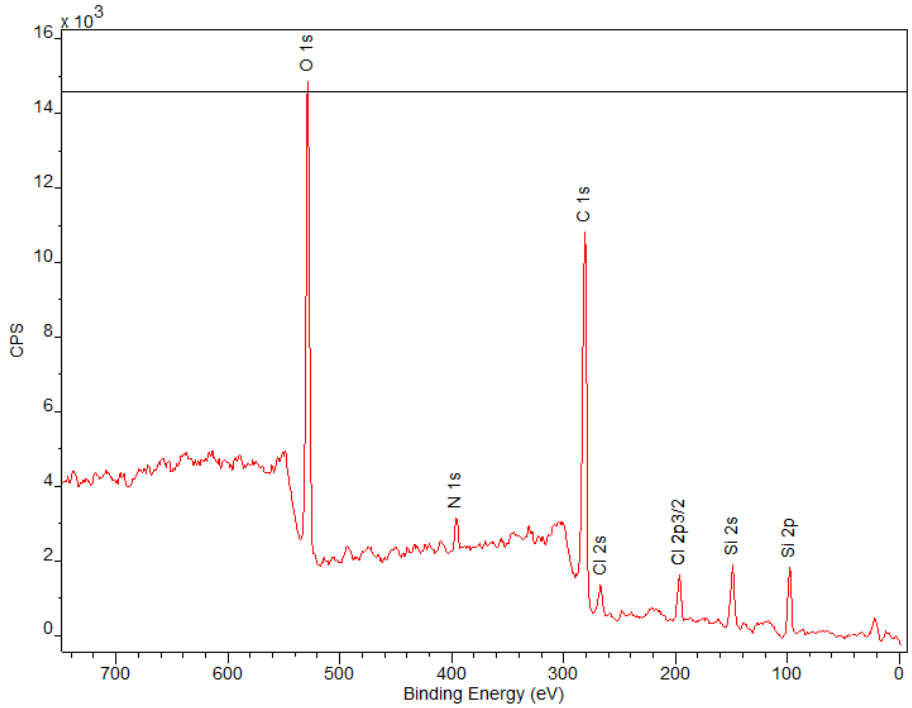

Figure 4.18 XPS spectrum of coated cotton fabric **Fabric-M_{IV}-DiClfen**

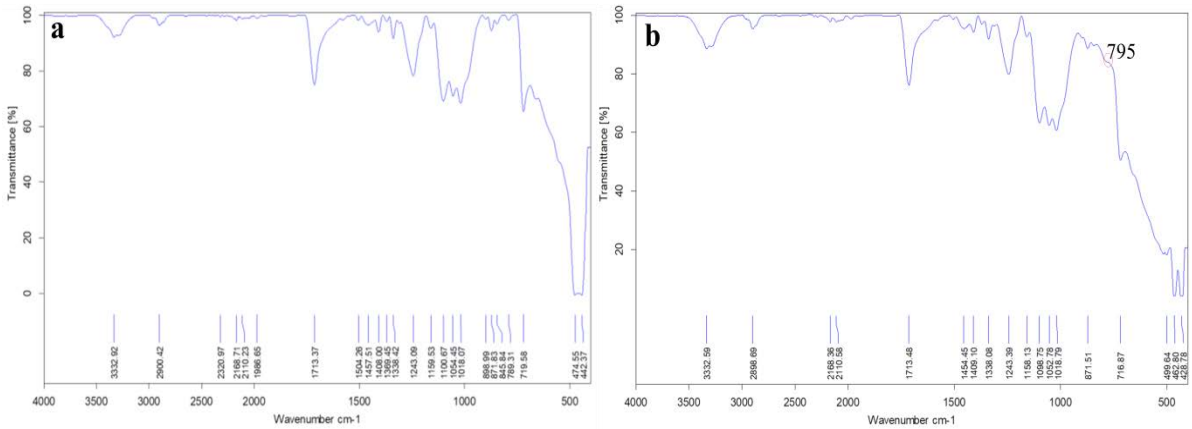

Figure 4.19 FTIR spectra of a) uncoated cotton fabrics b) coated cotton fabrics **Fabric-M4-DiClfen**

4.3.5 Release of anti-inflammatory drugs from the functionalized silica nanoparticles and coated cotton fabrics by selective cleavage of amide bond with proteases

As we have pointed out, the repairing effect of inflammation in human tissues can only take place if the drug is detached from the silica nanoparticles or cotton fabrics and comes into direct contact with the damaged area. Thus, we have studied the release of the drug from functionalized silica nanoparticles and the coated cotton fabrics assaying proteases, such as papain and proteinase K. We also used leukocytes from animal origin (**Scheme 4.7**).

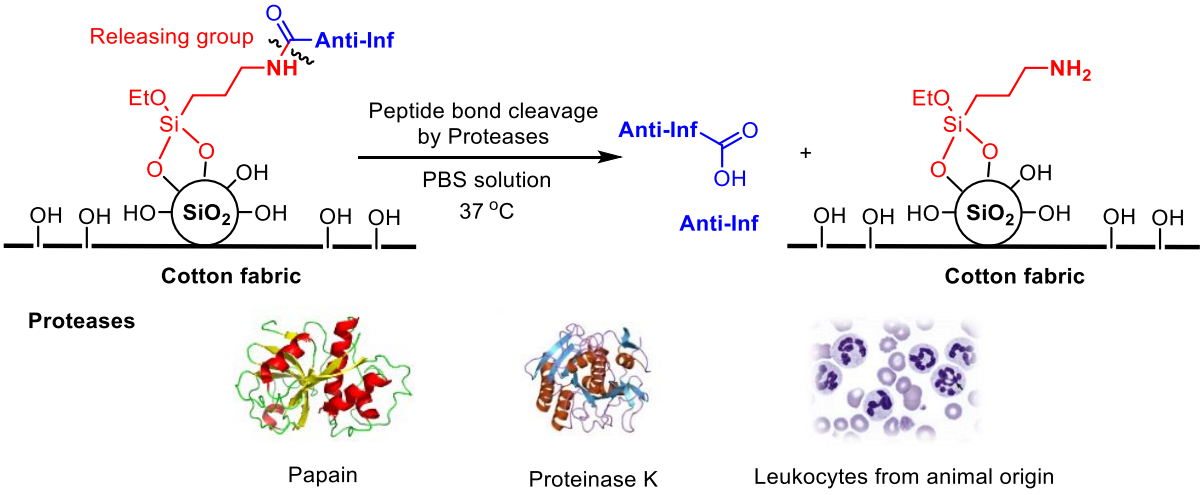

Scheme 4.7 Release of anti-inflammatory drug by enzymatic cleavage of amide bond

The experiments were performed in PBS buffer (pH = 7.4) at 37 °C under stirring. After removal of the coated textile pieces or separation of the nanoparticles by centrifugation, the solutions were extracted with dichloromethane and analyzed by GC-MS, the release of the anti-inflammatory drug being confirmed (**Figure 4.20**).

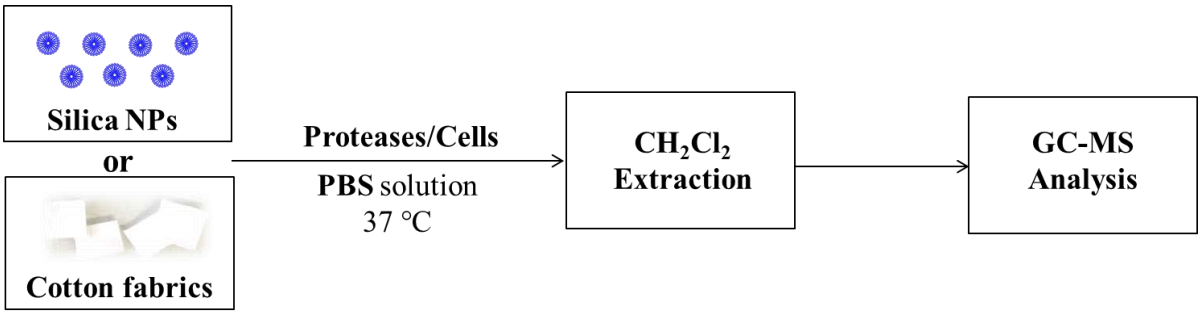

Figure 4.20 Anti-inflammatory drug release experiment

Some silica NPs functionalized with salicylic acid, ibuprofen and diclofenac, **Fabric-M_{IV}-DiClfen** and **Fabric-M_{IV}-DiClfen-0.25 FAS-5** were tested. Blank experiments were also performed to assure the need of the presence of the drug and the enzyme for the detection of the anti-inflammatory agent (**Table 4.4**).

Table 4.4 All the experiments of drug release

Entry	Material type	Sample	Proteases	Time h	GC-MS Analysis Anti-inflmmatory drug Yes (√), No (×)	Note
1	Silica NPs	**MCM-41 NPs**	-	48	×	Blank exp.
2	Silica NPs	**MCM-41 NPs**	Papain	48	×	Blank exp.
3	Silica NPs	**MCM-41 NPs**	Proteinase K	48	×	Blank exp.
4	Silica NPs	**MCM-41 NPs**	Cells	48	×	Blank exp.
5	Silica NPs	**M_{IV}-No Drug**	-	48	×	Blank exp.
6	Silica NPs	**M_{IV}-No Drug**	Cells	48	×	Blank exp.
7	Silica NPs	**M_{I}-DiClfen**	Papain	48	√	
8	Silica NPs	**M_{I}-DiClfen**	Papain	12	√	
9	Silica NPs	**M_{I}-DiClfen**	Papain	1	√	
10	Silica NPs	**M_{II}-DiClfen**	Papain	48	√	
11	Silica NPs	**M_{III}-DiClfen**	Papain	48	√	
12	Silica NPs	**M_{IV}-DiClfen**	Papain	48	√	
13	Silica NPs	**M_{IV}-DiClfen**	Proteinase K	48	√	
14	Silica NPs	**M_{IV}-DiClfen**	Cells	24	√	
15	Silica NPs	**M_{I}-Ibup**	Papain	48	√	
16	Silica NPs	**M_{II}-Ibup**	Papain	48	√	
17	Silica NPs	**M_{III}-Ibup**	Papain	48	√	
18	Silica NPs	**M_{IV}-Ibup**	Papain	48	√	
19	Silica NPs	**M_{IV}-Ibup**	Proteinase K	48	√	
20	Silica NPs	**M_{IV}-Ibup**	-	48	×	Blank exp.
21	Silica NPs	**M_{IV}-DiClfen-FAS (n = 5)**	Papain	48	√	
22	Cotton fabrics	**Fabric-M_{IV}-DiClfen**	-	48	×	Blank exp.
23	Cotton fabrics	**Fabric -M_{IV}-No Drug**	Cells	24	×	Blank exp.
24	Cotton fabrics	**Fabric -M_{IV}-No Drug**	-	48	×	Blank exp.
25	Cotton fabrics	**Clean Cotton fabrics**	Papain	48	×	Blank exp.
26	Cotton fabrics	**Clean Cotton fabrics**	Cells	24	×	Blank exp.
27	Cotton fabrics	**Fabric -M_{IV}-DiClfen**	Papain	48	√	
28	Cotton fabrics	**Fabric-M_{IV}-DiClfen**	Proteinase K	48	√	
29	Cotton fabrics	**Fabric -M_{IV}-DiClfen**	Cells	24	√	
30	Cotton fabrics	**Fabric-M_{IV}-DiClfen-FAS n = 5**	Proteinase K	48	√	

As an example, we show in **Figure 4.21** the results of the experiments with **M_{IV}-DiClfen** and **Fabric-M_{IV}-DiClfen**.

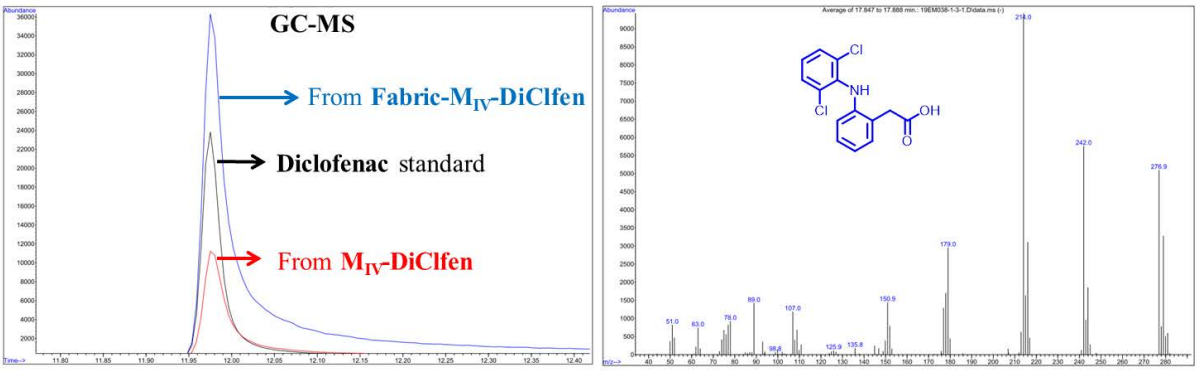

Figure 4.21 The GC-MS for the experiment of **M_{IV}-DiClfen** and **Fabric- M_{IV}-DiClfen**

From the SEM images of **Fabric-M_{IV}-DiClfen**, we can confirm that the silica nanoparticles remain on the surface of the cotton fabrics after the protease treatment, only the anti-inflammatory drugs being released (**Figure 4.22**).

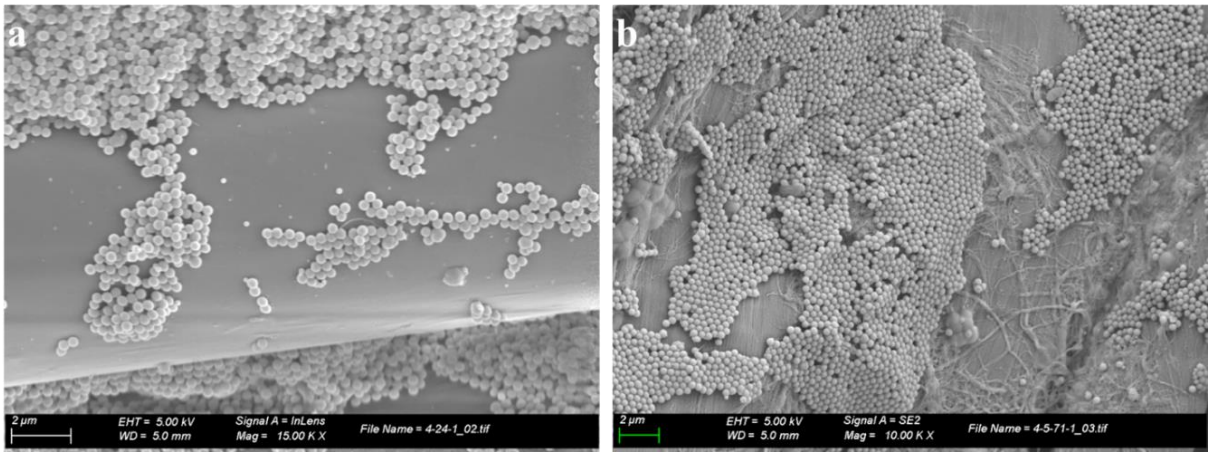

Figure 4.22 SEM images of **Fabric-M_{IV}-DiClfen**: a) before the protease treatment, b) after the treatment with proteinase K.

By Gas Chromatography-Mass Spectrometry (GC-MS), we had been able to detect easily in a qualitative way the released drug from silica nanoparticles and coated cotton fabrics after the protease treatment. We selected **M_{IV}-DiClfen**, **M_{IV}-DiClfen-1.0 FAS-3** and **Fabric- M_{IV}-DiClfen** for the quantitative study of the drug release by using the UV-Vis technique (absorption of diclofenac at 276 nm, in acetonitrile). The calibration curve (**Figure 4.23**) of diclofenac was provided by Dr. Albert Granados.

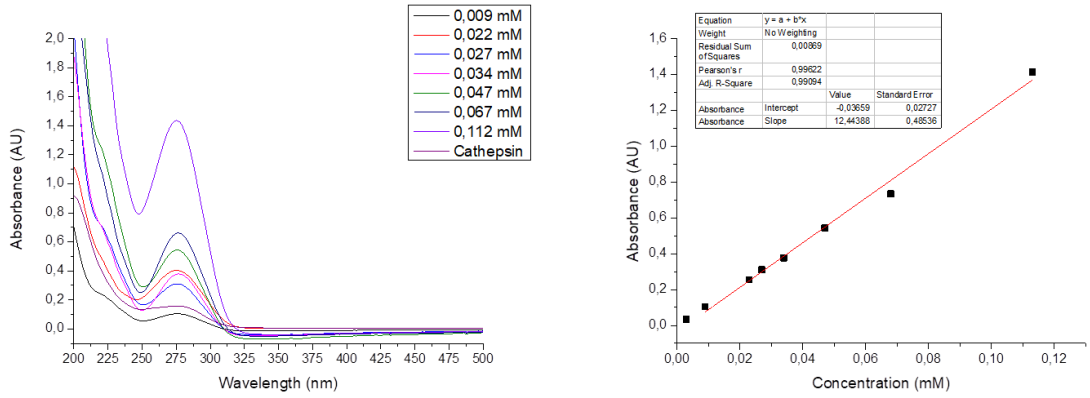

Figure 4.23 A calibration curve of diclofenac

The drug loading of the cotton fabric coated with **M_{IV}-DiClfen** was determined by gravimetric analysis. A textile piece (3 × 3 cm) of **Fabric-M_{IV}-DiClfen** has gained 51 mg of weight after coating. As already mentioned (**Scheme 4.6**), it was prepared by one-step coating procedure through co-hydrolysis of TEOS and **P21** (molar ratio 10:1) in aqueous ammonia/ethanol. This increase of weight corresponds to the **M_{IV}-DiClfen** coating. From the N elemental analysis, the corresponding drug loading of the isolated **M_{IV}-DiClfen** was deduced to be 0.44 mmol·g^{-1}. Therefore, the diclofenac loading on the coated cotton textile **Fabric- M_{IV}-DiClfen** was 2.22 × 10^{-2} mmol. A second piece of **Fabric-M_{IV}-DiClfen** prepared by the same procedure had a loading of 1.72 × 10^{-2} mmol diclofenac.

Then, **M_{IV}-DiClfen** (TEOS:**P21** of 20:1 in entries 1-4 and 10:1 in entries 9-15 of **Table 4.5**), **M_{IV}-DiClfen-1.0 FAS-3** (TEOS:**P21**:FAS of 20:1:2; entries 5-8 of **Table 4.5**) and three pieces of **Fabric-M_{IV}-DiClfen** (entries 16-18 of **Table 4.5**) were treated with several proteases (papain, proteinase K, trypsin and leukocytes of animal origin) for the quantification of the drug release by using the UV-Vis technique. The experiments were performed in PBS buffer (pH = 7.4) at 37 °C under stirring with an orbital shaker. After removal of the coated textile pieces or separation of the nanoparticles, the solutions were extracted with dichloromethane, then the solvent was removed under vacuum. The residue was dissolved in acetonitrile and the solution was analyzed by UV-Vis.

Table 4.5 The diclofenac release with different proteases

Entry	Material	TEOS:P21:FAS[a]	Protease[b]	Time (h)	% release[c]
1	**M_{IV}-DiClfen**	20:1:0	Proteinase K	24	7.3%
2	**M_{IV}-DiClfen**	20:1:0	Papain	24	10.3%
3	**M_{IV}-DiClfen**	20:1:0	Trypsin	24	20.5%
4	**M_{IV}-DiClfen**	20:1:0	Cells[d]	24	7.7%
5	**M_{IV}-DiClfen-1.0 FAS-3**	20:1:2	Proteinase K	24	7.4%
6	**M_{IV}-DiClfen-1.0 FAS-3**	20:1:2	Papain	24	13.0%
7	**M_{IV}-DiClfen-1.0 FAS-3**	20:1:2	Trypsin	24	10.5%
8	**M_{IV}-DiClfen-1.0 FAS-3**	20:1:2	Cells[d]	24	9.1%
9	**M_{IV}-DiClfen**	10:1:0	Proteinase K	24	14.8%
10	**M_{IV}-DiClfen**	10:1:0	Papain	24	19.1%
11	**M_{IV}-DiClfen**	10:1:0	Trypsin	24	24.4%
12	**M_{IV}-DiClfen**	10:1:0	Trypsin	4	22.3%
13	**M_{IV}-DiClfen**	10:1:0	Trypsin	2	16.4%
14	**M_{IV}-DiClfen**	10:1:0	Trypsin	1	15.6%
15	**M_{IV}-DiClfen**	10:1:0	Cells[d]	24	9.3%
16	**Fabric-M_{IV}-DiClfen**[e]	10:1:0	Proteinase K	24	14.9%
17	**Fabric-M_{IV}-DiClfen**[f]	10:1:0	Trypsin	24	10.3%
18	**Fabric-M_{IV}-DiClfen**[g]	10:1:0	Cells[g]	24	31.5%

[a] The molar ratio of TEOS:P21:FAS for the preparation of materials; [b] The protease working concentration 0.1 mM; [c] Determined by UV analysis; [d] 4×10^6 cells from rat whole blood in 1 mL PBS; [e] The drug loading is 2.22×10^{-2} mmol; [f] The drug loading is 1.72×10^{-2} mmol; [g] The fabric was prepared as follows: **M_{IV}-DiClfen** was dispersed in ethanol-ammonia solution, then a piece of cotton fabric was dip-coated,and ultrasonicated for 30 minutes. The cotton fabric was washed with distilled water and dried in the oven for 1 h. The drug loading is 0.43×10^{-2} mmol, the experiment was carried out with 16×10^6 cells in 5 mL PBS.

As shown in **Table 4.5**, the amount of diclofenac released from functionalized silica nanoparticles **M_{IV}-DiClfen**, **M_{IV}-DiClfen-1.0 FAS-3** and coated cotton **Fabric-M_{IV}-DiClfen** with different proteases was relatively low (7.3% - 24.4%). The activity was found somehow dependent on the protease used. Interestingly, the presence of FAS has, in general, no deleterious effect on the drug release from silica nanoparticles (compare entries 1-4 with

entries 5-8 in **Table 4.5**). When the amount of **P21** was increased during the coating process (from TEOS:**P21** = 20:1 to TEOS:**P21** = 10:1) the corresponding percentage of release was also increased (compare entries 1-3 with entries 9-11 in **Table 4.5**). A release dynamic experiment performed with **M_{IV}-DiClfen** (TEOS:**P21** = 10:1) with trypsin at different reaction times (1, 2, 4 and 24 h) (entries 11-14 of **Table 4.5**), showed that about 64% of the total drug release occurred in the first hour (from 15.6% after one hour to 24.4 % after 24 h). For the **Fabric-M_{IV}-DiClfen**, the values of released diclofenac after 24 h range from 14.9% with proteinase K to 10.3% with trypsin (entries 16-17 in **Table 4.5**). Additionally, a special piece of **Fabric-M_{IV}-DiClfen** with a relatively low drug loading (0.43×10^{-2} mmol), was prepared as follows: the previously prepared **M_{IV}-DiClfen** was dispersed in 28% ethanol-ammonia solution, and then the cotton fabric was immersed in the solution and ultrasonicated for 30 min. The value of released diclofenac after 24 h with leukocytes from rat blood was 31.5% (entry 18, **Table 4.5**).

Diclofenac causes a 80% inhibition of COX-2 at 0.23 micromolar.[76] COX-2 is induced by the presence of inflammatory stimuli and is responsible for the generation of large amounts of a number of arachidonic acid derivatives, most of them exhibiting proinflammatory effects. So the blockade of COX-2 activity is considered to be the main mechanism justifying the antiinflammatory effects of diclofenac. Although in our studies we have not achieved the total release of diclofenac present in the nanoparticles and fabrics, this 0.23 micromolar concentration means, with the volumes used, a release of about 0.23×10^{-6} to 1.15×10^{-6} mmol (0.07×10^{-3} to 0.34×10^{-3} mg) of diclofenac, a threshold that is achieved in both functionalized silica nanoparticles **M_{IV}-DiClfen**, **M_{IV}-DiClfen-1.0 FAS-3** and cotton textiles **Fabric-M4-DiClfen.**

4.4 Conclusions

We have performed the covalent attachment of three carboxyl-containing non-steroidal anti-inflammatory drugs (NSAIDs) on mesoporous and non-porous silica nanoparticles through an amide functional group. We have used grafting and co-condensation procedures for the preparation of modified silica nanoparticles of different size. Salicylic acid, (*S*)-ibuprofen and diclofenac are the Food and Drug Administration (FDA)-approved anti-inflammatory agents selected. Furthermore, cotton fabrics have been coated with silica nanoparticles functionalized with such anti-inflammatory drugs by one-step procedure, which results in an increased roughness of the surface and provides hydrophobicity to the modified fabrics. This property is enhanced by the addition of a certain amount of fluorinated alkyl silane (FAS) in the co-condensation process to form the coating solution. The characterization of the functionalized nanoparticles and cotton textiles has been accomplished by microscopic and spectroscopic techniques. We have demonstrated that the corresponding anti-inflammatory drug is released *in situ* by the selective enzymatic cleavage of the amide bond in the presence of model proteases and leukocytes obtained from rat blood (detection by GC-MS and quantification by UV-Vis). The percentages of drug release were lower from diclofenac-functionalized silica nanoparticles and from fabrics coated with these nanoparticles than from fabrics covalently modified with the same drug (studies performed by Dr. Albert Granados). In any case, the amounts were enough for anti-inflammatory activity. High expectations arise for topical cutaneous applications in dressings intended to treat chronic wounds. The hydrophobicity would be advantageous for keeping the dressing and the wound dry. Alternatively, it would avoid that the cotton gauze gets stuck to the injured area in the case of more important lesions caused by burns. Moreover, anti-inflammatory functionalized silica nanoparticles can find applications for ointment and cream topical formulations.

4.5 Experimental section

4.5.1 General information

The information of NMR, IR, MS, elemental analysis, TEM, the surface areas and *p*-XRD is given in ***Section* 2.2.5.1**.

Scanning electron microscopy (SEM), **energy-dispersive X-ray spectroscopy** (EDX) and element linescans mapping were performed on a SEM Zeiss Merlin with and INCA detector from Oxford Instruments. Microscopic investigations of the specimens were carried out using a ZEISS MERLIN scanning electron microscope (SEM). The specimens were mounted on conductive carbon adhesive tabs and images were taken after the specimens had been sputter-coated (K550X EMITECH) with a very thin layer of gold. To determine the elemental composition of the fabric surface, an INCA energy-dispersive X-ray (EDX) detector from Oxford Instruments was used. Electron microscopy belongs to *Servei de Microscòpia* of UAB.

Dynamic light scattering (DLS) and **zeta potential measurements** have been performed by the ICTS "NANBIOSIS", more specifically by the Biomaterial Processing and Nanostructuring Unit (U6), Unit of the CIBER in Bioengineering, Biomaterials & Nanomedicine (CIBER-BBN) located at the *Institute of Materials Science of Barcelona* (ICMAB-CSIC). These analyses were performed on a Zetasizer Nano ZS (Malvern Instruments) with 8 mg of silica NPs in 8 mL Mili-Q water, the pH of the solution was measured by CRISON pH METER Basic 20.

Contact angle (CA) measurements: the hydrophobic tests performed were the measurement of the contact angle of a water droplet (4 μL) deposited on top of each fabric. These experiments were carried out at ICMAB installations with a Contact Angle Measuring System DSA 100 from KRÜSS, which is located in a physico-chemical laboratory (humidity and temperature control).

X-ray photoelectron spectroscopy (XPS) was performed at *Catalan Institute of Nanoscience and Nanotechnology* (ICN2) with a SPECS PHOIBOS 150 hemispherical analyzer (SPECS GmbH, Berlin, Germany), at room temperature, in a base pressure of 5×10^{-10} mbar using monochromatic Al Kalpha radiation (1486.74 eV) as excitation source.

UV-Vis absorption spectroscopy was recorded with an UV-Vis 8453 spectrophotometer, Hewlett-Packard ("Diode-Array") at 200-600 nm (absorption peak of diclofenac at 276 nm, in acetonitrile).

Others: When required, experiments were carried out with standard high vacuum and Schlenk techniques. Chromatographic purifications were performed under N_2 pressure using 230-400 mesh silica gel (flash chromatography). Dry toluene was purchased from Merck. Dry dichloromethane was from solvent processing equipment (PureSolv, Innovative Technology).

The proteases used in the experiments reported in this manuscript were proteinase K (50.7 units/mg), papain (20 units/mg), cathepsin G (60 units/mg) and trypsin (≥10,000 BAEE units/mg protein) (purchased from Sigma Chem). All of them have similar molecular weight (20-30 kDa) and are active in a quite wide pH range, including the physiological pH (7.4). Whereas papain is obtained from papaya, trypsin is obtained from bovine pancreas, proteinase K is of bacterial origin.

Whole blood was obtained from Sprague-Dawley rats of the university animal facility. The rats were exsanguinated as end-point procedure under anesthesia (ketamine-xylazine (80/20 mg / kg i.p.), a total of 15 mL of blood was collected with heparinized syringes. The pooled blood was diluted 1: 1 with physiological saline and centrifuged at 500 g at room temperature for 30 minutes on a percoll gradient. The layer containing leukocytes was collected, re-suspended in 50 mL cold PBS and centrifuged again at 500 g for 10 minutes. The supernatant was discarded and the pellet was incubated with lysis buffer to eliminate any residual red blood cells. The cells were washed with 50 mL cold PBS, centrifuged again and the resulting pellet was re-suspended in a small volume of PBS. The cells were then counted in a Neubauer chamber and the volume of the suspension was corrected to get the desired number of leukocytes.

4.5.2 General procedure for the preparation of P19-P21

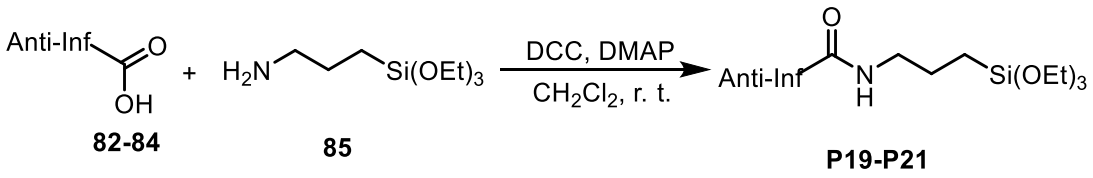

The corresponding anti-inflammatory drug (1 mmol) was placed in a Schlenk under argon atmosphere. Then, DMAP (6 mg, 5 mol %), DCC (206 mg, 1 mmol) and dry dichloromethane (5 mL) were added and the solution was stirred until homogenization. Then 3-(triethoxysilyl)propan-1-amine (266 mg, 1.2 mmol) was introduced by syringe. The reaction was allowed to proceed under stirring at room temperature until completion (TLC monitoring). The crude mixture was poured into water and extracted with dichloromethane. The combined organic phase was washed with brine, dried with anhydrous sodium sulphate and evaporated under vacuum. The residue was purified by silica gel column chromatography to afford the desired silylated derivative.

2-Hydroxy-*N*-(3-(triethoxysilyl)propyl)benzamide, P19[1]

Eluent mixture: hexane/ethyl acetate 9:1. Colorless oil, 91% yield. **^{1}H NMR (360 MHz, $CDCl_3$) δ** (ppm): 0.72 (t, *J* = 7.0 Hz, 2H), 1.24 (t, *J* = 7.0 Hz, 9H), 1.78 (m, 2H), 3.47 (apparent q, *J* = 7.2 Hz, 2H), 3.82 (q, *J* = 7.0 Hz, 6H), 5.62 (br s, 1H), 6.83 (m, 1H), 6.90 (br s, 1H), 6.98 (d, *J* = 8.3 Hz, 1H), 7.38 (m, 2H). **^{13}C NMR (91 MHz, $CDCl_3$) δ (ppm)**: 169.9, 161.3, 133.8, 125.6, 118.5, 118.2, 114.5, 58.4, 41.7, 22.6, 18.1, 7.7. **IR (ATR) ν (cm^{-1})**: 3377.8, 2927.7, 1734.3, 1640.0, 1539.3, 1364.1, 1071.6, 950.9, 750.9, 445.0.

(*S*)-2-(4-Isobutylphenyl)-*N*-(3-(triethoxysilyl)propyl)propanamide, P20.

Eluent mixture: hexane/ethyl acetate 3:1. White solid, 94% yield. **^{1}H NMR (400 MHz, $CDCl_3$) δ (ppm)**: 0.51 (t, *J* = 6.6 Hz, 2H), 0.90 (d, *J* = 6.4 Hz, 6H), 1.18 (t, *J* = 7.0 Hz, 9H), 1.53 (m, 5H), 1.85 (m, 1H), 2.45 (d, *J* = 7.2 Hz, 2H), 3.18 (apparent q, J = 6.4 Hz, 2H), 3.51 (q, *J* = 7.2 Hz, 1H), 3.77 (q, *J* = 7.0 Hz, 6H), 5.62 (br s, 1H), 7.10 (d, *J* = 8.0 Hz, 2H), 7.19 (d, *J* = 8.0 Hz, 2H). **^{13}C NMR (101 MHz, $CDCl_3$) δ (ppm)**: 174.3, 140.6, 138.8, 129.5, 127.3, 58.36, 46.8, 45.0, 41.8, 30.2, 22.8, 22.4, 18.5, 18.3, 7.5. **IR (ATR) ν (cm^{-1})**: 3293.8, 2926.1, 1644.2, 1546.0, 1387.4, 1074.7, 952.9, 762.0, 456.3. **HRMS (ESI) m/z** $[M + Na]^+$ calcd for $C_{22}H_{39}NO_4SiNa$: 432.2542, found: 432.2541.

2-(2-((2,6-Dichlorophenyl)amino)phenyl)-*N*-(3-(triethoxysilyl)propyl)acetamide, **P21.**

Eluent mixture: hexane/ethyl acetate 4:1. White solid, 90% yield. **^{1}H NMR (360 MHz, $CDCl_3$) δ (ppm)**: 0.61 (t, *J* = 7.0 Hz, 2H), 1.22 (t, *J* = 7.0 Hz, 9H), 1.63 (m, 2H), 3.27 (apparent q, *J* = 6.5 Hz, 2H), 3.67 (s, 2H), 3.81 (q, *J* = 7.0 Hz, 6H), 6.22 (br s, 1H), 6.51 (d, *J* = 8.0 Hz, 1H), 6.91 (t, *J* = 7.3 Hz, 1H), 6.98 (t, *J* = 8.0 Hz, 1H), 7.10 (d, *J* = 8.0, 1H), 7.16 (d, *J* = 7.3 Hz, 1H), 7.34 (d, *J* = 8.0 Hz, 2H), 7.51 (s, 1H). **^{13}C NMR (91 MHz, $CDCl_3$) δ (ppm)**: 171.5, 143.0, 137.6, 130.5, 130.0, 128.8, 127.8, 124.8, 124.2, 121.4, 117.4, 58.5, 42.1, 41.2, 22.7, 18.3, 7.6. **IR (ATR) ν** (cm^{-1}): 3280.2, 2926.6, 1729.3, 1619.2, 1564.7, 1445.8, 1076.0, 952.0, 746.8, 449.8. **HRMS (ESI) m/z** $[M + Na]^+$ calcd for $C_{23}H_{32}Cl_2N_2O_4SiNa$: 521.1401, found: 521.1409.

4.5.3 Preparation of silica nanoparticles functionalized with anti-inflammatory drugs

4.5.3.1 Preparation of functionalized mesoporous silica nanoparticles by grafting to MCM-41 NPs

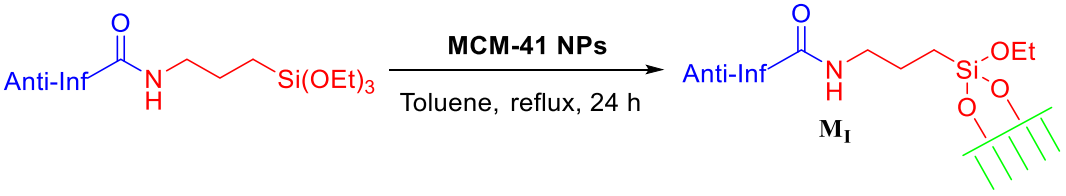

In a 100 mL round bottom flask equipped with a Dean-Stark apparatus, the corresponding silylated anti-inflammatory derivative (**P19-P21**) (0.15 mmol) and mesostructured silica nanoparticles **MCM-41 NPs** (180 mg, 3.0 mmol) were refluxed in dry toluene (30 mL) for 24 h. Then the suspension was centrifuged (13500 rpm at 25 °C for 45 min). The solid was washed successively with ethanol (3 × 20 mL), acetone (2 × 20 mL) and CH_2Cl_2 (2 × 20) (30 min at 50 °C under sonication, 30 min for centrifugation), then dried under vacuum and finally crushed to give the grafted material as a white solid.

M_I-Salicyl. **EA**: 0.70% N, 12.00% C, 2.41% H (0.50 mmol/g material). **^{13}C-CP-MAS NMR (100.6 Hz) δ (ppm)**: 171, 160, 133, 127, 118, 117, 115, 58, 42, 22, 16, 9. **IR *ν* (ATR) (cm^{-1})**: 3375.8, 2978.2, 1637.8, 1043.9, 962.0, 794.9. **DLS**: 544.2 nm, **Zeta Potential**: ζ = -25.1 mV, pH = 7.25.

M_I-Ibup. **EA**: 0.97% N, 19.13% C, 3.09% H (0.69 mmol/g material). **IR *ν* (ATR) (cm^{-1})**: 3337.9, 2975.1, 1648.8, 1034.5, 803.3, 645.5. **DLS**: 224.7 nm, **Zeta Potential**: ζ = -29.2 mV, pH = 7.18.

M_I-DiClfen. **EA**: 1.83% N, 18.85% C, 2.33% H (0.65 mmol/g material). **^{13}C-CP-MAS NMR (100.6 Hz) *δ* (ppm)**: 174, 138, 129, 128, 59, 43, 29, 16, 9. **IR *ν* (ATR) (cm^{-1})**: 3331.4, 2978.9, 1643.8, 1041.8, 813.2, 648.4. **BET**: S_{BET} = 771 m^2/g, V_{pore} = 0.37 cm^3g^{-1}, $\emptyset_{pore}$ = 2.2 nm. DLS: 282.6 nm, Zeta Potential: ζ = -29.8 mV, pH = 7.26.

4.5.3.2 Preparation of functionalized mesoporous silica nanoparticles by grafting to M0 NPs

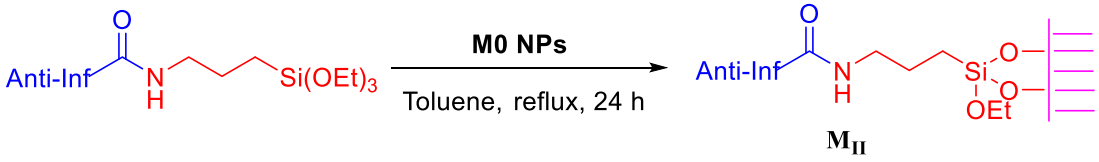

M_{II}

In a 100 mL round bottom flask equipped with a Dean-Stark apparatus, the corresponding silylated anti-inflammatory derivative (**P19-P21**) (0.15 mmol) and mesostructured silica nanoparticles **M0 NPs** (180 mg, 3.0 mmol) were refluxed in dry toluene (30 mL) for 24 h. Then the suspension was centrifuged (13500 rpm at 25 °C for 45 min). The solid was washed successively with ethanol (3 × 20 mL), acetone (2 × 20 mL) and CH_2Cl_2 (2 × 20) (30 min at 50 °C under sonication, 30 min for centrifugation), then dried under vacuum and finally crushed to give the grafted material as a white solid.

M_{II}-Salicyl. **EA**: 1.30% N, 13.57% C, 2.28% H (0.93 mmol/g material). **IR *ν* (ATR) (cm^{-1})**: 3364.3, 2926.8, 1638.3, 1043.6, 809.9, 650.0. **DLS**: 158.9 nm, **Zeta Potential**: ζ = -26.3 mV, pH = 7.30.

M_{II}-Ibup. **EA**: 0.96% N, 15.45% C, 2.76% H (0.69 mmol /g material). **IR *ν* (ATR) (cm^{-1})**: 3319.6, 2926.5, 1646.8, 1042.8, 801.7, 649.7. **DLS**: 518.4 nm, **Zeta Potential**: ζ = -4.44 mV, pH = 7.26.

M_{II}-DiClfen. **EA**: 1.37% N, 14.62% C, 2.37% H (0.49 mmol/g material). **IR *ν* (ATR) (cm^{-1})**: 3337.5, 2926.3, 1643.1, 1042.2, 812.1, 649.4. **^{13}C-CP-MAS NMR (100.6 Hz) *δ* (ppm)**: 174,

138, 131, 129,125, 60, 40, 23, 16, 9. **^{29}Si-CP-MAS NMR (79.5 MHz) δ (ppm)**: -60 (T^2), -68 (T^3), -93 (Q^2), -103 (Q^3), -113 (Q^4). **DLS**: 135.0 nm, **Zeta Potential**: ζ = -15.4 mV, pH = 7.10. **BET**: S_{BET} = 332 m^2g^{-1}, V_{pore} = 0.18 cm^3g^{-1}, $\emptyset_{pore}$ = 1.9 nm.

4.5.3.3 Preparation of functionalized mesoporous silica nanoparticles by co-condensation method in buffer solution

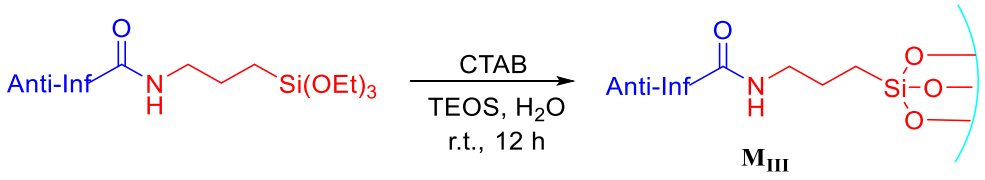

M_{III}

The functionalized **MSNs** were synthesized in an aqueous buffer solution of pH 7 from a mixture with the following molar ratios: CTAB:TEOS:**Pn**:H_2O = 5:40:2:30000 (n = 19-21). Initially, CTAB (455.5 mg, 1.25 mmol) was dissolved in the buffer solution [prepared from KH_2PO_4 (428.8 mg, 3.15 mmol) and NaOH (72.5 mg, 1.81 mmol) in H_2O (135 mL, 7500 mmol)], under vigorous stirring (1200 rpm) and heating at 95 ºC. When the solution became homogeneous, a mixture of TEOS (2.08 g, 10 mmol) and the corresponding silylated anti-inflammatory derivative (**P19-P21**) (0.5 mmol) was added slowly. The reaction mixture was maintained for 12 hours under stirring (1200 rpm) at room temperature. The NPs were collected by centrifugation (13500 rpm at 25 °C for 45 mins). In order to remove the surfactant, 20 mL of an alcoholic solution of ammonium nitrate [NH_4NO_3, 6 g/L in 96% EtOH] was added to each tube, sonicated for 30 min at 50 °C, then cooled and centrifuged (30 min at 13500 rpm at 25 °C), the supernatant was discarded. This NH_4NO_3 washing was performed 3 times. Each solid in the tubes was washed successively with 96% ethanol, Mili-Q water and 96% ethanol using the same protocol (sonication for 30 min at 50 °C, then centrifugation). The final white solid was dried for few hours under vacuum at room temperature.

M_{III}-Salicyl. **EA**: 0.72% N, 10.31% C, 2.07% H (0.51 mmol/g material). **^{13}C-CP-MAS NMR (100.6 Hz) δ (ppm)**: 170, 160, 132, 127, 118, 117, 115, 59, 57, 41, 29, 22, 17, 16, 9. **IR ν (ATR) (cm^{-1})**: 3385.0, 2980.2, 1637.1, 1052.3, 960.7, 795.8. **DLS**: 261.8 nm, **Zeta Potential**: ζ = -27.1 mV, pH = 7.35.

M_{III}-Ibup. **EA**: 0.80% N, 14.06% C, 3.67% H (0.57 mmol/g material). **^{13}C-CP-MAS NMR (100.6 Hz) δ (ppm):** 177, 140, 129, 127, 58, 46, 45, 42, 30, 21, 17, 9. **IR ν (ATR) (cm^{-1})**: 3369.6, 2974.6, 1632.5, 1044.4, 957.5, 796.0. **DLS**: 181.4 nm, **Zeta Potential**: ζ = -35.1 mV, pH = 7.51.

M_{III}-DiClfen. **EA**: 0.62% N, 9.40% C, 2.19% H (0.22 mmol/g material). **^{13}C-CP-MAS NMR (100.6 Hz) δ (ppm)**: 174, 144, 138, 130, 129, 128, 127, 125, 124, 121, 117, 58, 42, 40, 23, 17, 10. **^{29}Si-CP-MAS NMR (79.5 MHz) δ (ppm)**: -58 (T^2), -66 (T^3), -93 (Q^2), -103 (Q^3), -113 (Q^4). IR ν (ATR) (cm^{-1}): 3387.3, 2977.8, 1639.0, 1048.9, 960.7, 795.4. **DLS**: 168.6 nm, **Zeta Potential**: ζ = -30.0 mV, pH = 7.56. **BET**: S_{BET} = 256 m^{2}g^{-1}, V_{pore} = 0.47 cm^{3}g^{-1}, $\emptyset_{pore}$ = 2.2 nm.

4.5.3.4 Preparation of functionalized silica nanoparticles by co-condensation method in ammonia solution

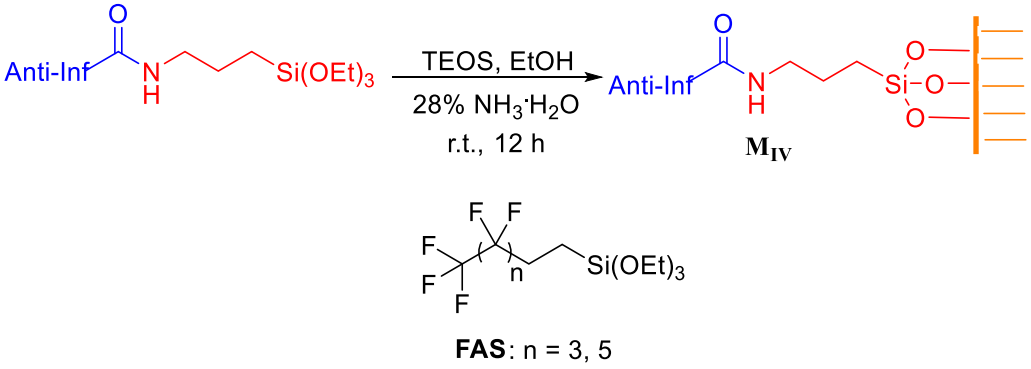

TEOS (2.08 g, 10.0 mmol) and the corresponding silylated anti-inflammatory derivative (**P19-P21**) (0.5 mmol) and, in some cases, the corresponding FAS (x mmol) were dissolved in absolute EtOH (25 mL). Then, an ammonium hydroxide-ethanol solution was added (6 mL of 28% $NH_3{\cdot}H_2O$ in 25 mL EtOH). The mixture was magnetically stirred intensively (1400 rpm) at room temperature for 12 hours. The functionalized nanoparticles were collected by centrifugation (12000 rpm for 10 mins) and washed with ethanol until neutral pH was reached. Then, the obtained white solid was washed successively with Mili-Q water and 96% ethanol, and was dried under vacuum for several hours.

M_{IV}-No drug. **IR ν (ATR) (cm^{-1})**: 3652.7, 2982.8, 1625.1, 1454.9, 1035.3, 788.3, 489.2, 458.2. **DLS**: 400.9 nm, **Zeta Potential**: ζ = -55.2 mV, pH = 9.40.

M_{IV}-Salicyl. **EA**: 1.28% N, 6.02% C, 2.13% H (0.91 mmol/g material). **^{13}C-CP-MAS NMR (100.6 Hz) δ (ppm)**: 170, 160, 134, 128, 120, 117, 114, 58, 42, 24, 18, 9. **IR ν (ATR) (cm^{-1})**: 3324.5, 2978.9, 1599.6, 1033.0, 800.5, 648.9. **DLS** and **Zeta Potential** were not determined (aggregated nanoparticles).

M_{IV}-Ibup. **EA**: 0.67% N, 2.36% C, 1.84% H (0.48 mmol/g material). **^{13}C-CP-MAS NMR (100.6 Hz) δ (ppm)**: 176, 140, 138, 129, 128, 59, 47, 45, 30, 22, 17, 8. **IR ν (ATR) (cm^{-1})**: 3324.1, 2980.1, 1629.7, 1453.8, 1039.1, 796.7, 649.9. **DLS**: 410.9 nm, **Zeta Potential**: ζ = -52.4 mV, pH = 9.42.

M_{IV}-DiClfen. **EA**: 0.74% N, 5.99% C, 1.71% H (0.26 mmol/g material). **^{13}C-CP-MAS NMR (100.6 Hz) δ (ppm)**: 174, 144, 139, 129, 59, 42, 23, 17, 8. **^{29}S-CP-MAS NMR (79.5 MHz) δ (ppm)**: -60 (T^2), -68 (T^3), -95 (Q^2), -103 (Q^3), -113 (Q^4). IR ν (ATR) (cm^{-1}): 3324.4, 2982.8, 1637.4, 1037.6, 806.4, 648.0. **DLS**: 424.1 nm, **Zeta Potential**: ζ = -50.0 mV, pH = 9.01. **BET**: S_{BET} = 9 m^{2}g^{-1}, V_{pore} = 0.007 cm^{3}g^{-1}, $\emptyset_{pore}$ = - nm (not porous).

M_{IV}-DiClfen-0.25 FAS (n = 3), **EA**: 0.34% N, 7.24% C, 1.78% H (0.12 mmol diclofenac derivative/g material). **IR ν (ATR) (cm^{-1})**: 3400.0, 2980.7, 1633.5, 1037.3, 804.6, 646.8. **DLS**: 168.8 nm, **Zeta Potential**: ζ = -41.0 mV, pH = 8.77. **BET**: S_{BET} = 334 m^{2}g^{-1}, V_{pore} = 0.189 cm^{3}g^{-1}, $\emptyset_{pore}$ = 2.3nm.

M_{IV}-DiClfen-0.50 FAS (n = 3), **EA**: 0.29% N, 7.12% C, 1.79% H (0.10 mmol diclofenac derivative/g material). **IR ν (ATR) (cm^{-1})**: 3338.3, 2980.3, 1633.3, 1037.8, 806.6, 646.2. **DLS**: 183.2 nm, **Zeta Potential**: ζ = -41.8 mV, pH = 8.43. **BET**: S_{BET} = 336 m^{2}g^{-1}, V_{pore} = 0.193 cm^{3}g^{-1}, $\emptyset_{pore}$ = 2.3 nm.

M_{IV}-DiClfen-0.75 FAS (n = 3), **EA**: 0.62% N, 7.60% C, 1.75% H (0.22 mmol diclofenac derivative/g material). **IR ν (ATR) (cm^{-1})**: 3309.6, 2980.6, 1632.8, 1038.8, 797.2, 647.7. **DLS**: 312.3 nm, **Zeta Potential**: ζ = -36.1 mV, pH = 9.59. **BET**: S_{BET} = 348 m^{2}g^{-1}, V_{pore} = 0.199 cm^{3}g^{-1}, $\emptyset_{pore}$ = 2.3 nm.

M_{IV}-DiClfen-1.00 FAS (n = 3). **EA**: 0.27% N, 8.40% C, 1.51% H (0.10 mmol diclofenac derivative/g material). **IR ν (ATR) (cm^{-1})**: 3417.9, 2981.2, 1634.7, 1041.3, 814.1, 645.7. **DLS**: 402.8 nm, **Zeta Potential**: ζ = -36.6 mV, pH = 8.96. **BET**: S_{BET} = 374 m^{2}g^{-1}, V_{pore} = 0.255 cm^{3}g^{-1}, $\emptyset_{pore}$ = 2.7 nm.

M_{IV}-DiClfen-0.25 FAS (n = 5), **EA**: 0.89% N, 7.19 % C, 1.80 % H (0.32 mmol diclofenac derivative/g material). **IR *ν* (ATR) (cm^{-1})**: 3304.1, 2979.0, 1633.6, 1033.2, 800.7, 647.7. **DLS**: 229.0 nm, **Zeta Potential**: ζ = -47.7 mV, pH = 8.70. **BET**: S_{BET} = 286 m^2g^{-1}, V_{pore} = 0.142 cm^3g^{-1}, $\emptyset_{pore}$ = 2.0 nm.

4.5.3.5 Preparation of M_{III}-DiClfen-TMS

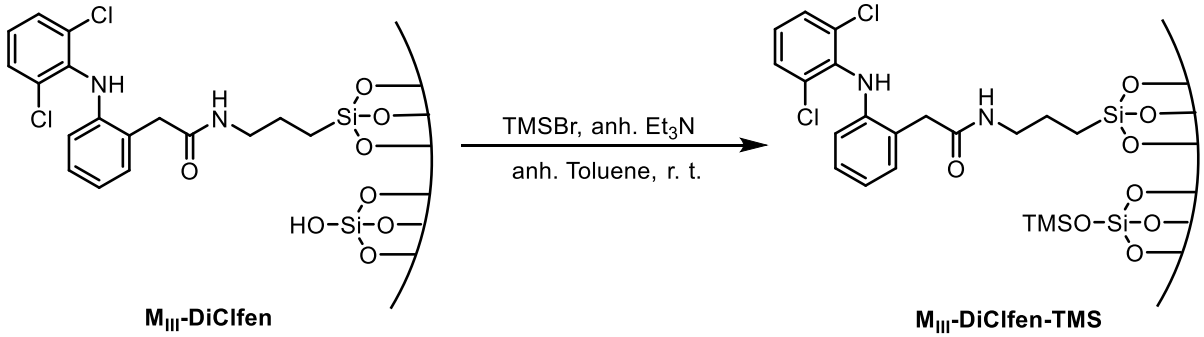

In a 50 mL Schlenk tube under nitrogen, **M_{III}-DiClfen** (250 mg) was added and degassed for 30 min. After this time, anhydrous toluene (15 mL), trimethylsilyl bromide (0.5 mL, 1.16 g/cm^3, 3.79 mmol) and anhydrous Et_3N (0.5 mL, 0.727 g/cm^3 , 3.49 mmol) were added and the mixture was stirred at room temperature for 24 h. Then, the material was filtered and washed with toluene (3 × 15 mL), methanol (3 × 15 mL), Et_2O (3 × 15 mL) and acetone (3 × 10 mL) to afford **M_{III}-DiClfen-TMS** as a white powder (0.249 g). **EA**: 0.49% N, 11.88% C, 2.47% H (0.18 mmol drug/g material).

4.5.3.6 Preparation of M_{III}-Salicyl-x FAS-n (x = 0.5 or 1.0; n = 3 or 5)

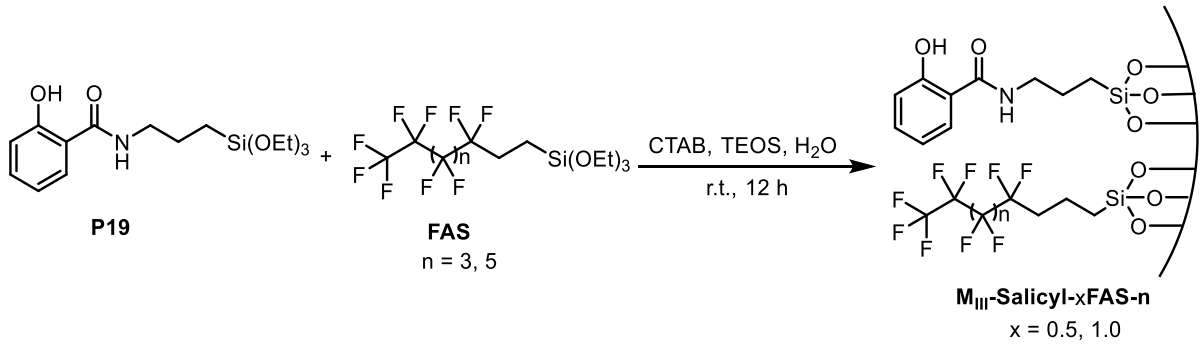

MSNs were synthesized in an aqueous buffer solution of pH 7 from a mixture with the following molar ratios: CTAB:TEOS:**P19:**FAS:H_2O = 5:40:**2**:x:3000. Initially, CTAB (455.5 mg, 1.25 mmol) were dissolved in the buffer solution, prepared from KH_2PO_4 (428.8 mg,

3.15 mmol) and NaOH (72.5 mg, 1.81 mmol) in H_2O (135 mL, 7500 mmol), under vigorous stirring and heating at 95 ºC. When the solution became homogeneous, a mixture of TEOS (2.08 g, 10 mmol), **P19** (170.74 mg, 0.5 mmol) and **FAS** was added slowly. The reaction was maintained for 12 hours under stirring at room temperature. The NPs were collected by centrifugation (13500 rpm at 25 °C for 45 mins). In order to remove the surfactant, 20 mL of an alcoholic solution of ammonium nitrate [NH_4NO_3, 6 g/L in 96% EtOH] was added to each tube, sonicated for 30 min at 50 °C, then cooled and centrifuged (10 min at 12000 rpm at 25 °C), the supernatant was discarded. This NH_4NO_3 washing was performed 3 times. Each solid in the tubes was washed successively with 96% ethanol, Mili-Q water, 96% ethanol using the same protocol (30 min at 50 °C sonication, centrifugation). The final product was dried for few hours under vacuum at room temperature. The **M_{III}-Salicyl-xFAS-n** were obtained as white solids. **EA** (for **M_{III}-Salicyl-0.5 FAS-3**): 0.84% N, 9.84% C, 1.68% H (0.49 mmol drug/g material).

4.5.4 General procedure for the preparation of hydrophobic cotton fabrics coated with functionalized silica nanoparticles

A dip coating solution was prepared by adding **M-Anti-Inf** in absolute ethanol. Then, a piece of the clean cotton textile (3 × 3 cm) was immersed in the as-prepared coating solution and ultrasonicated for 30 min at room temperature. Finally, the coated sample was dried at 120 °C in an oven for 60 min. The resulting textile was not hydrophobic (**CA** < 90 °). In order to obtain hydrophobicity, the cotton was immersed in 1 vol.% of $CF_3(CF_2)_3(CH_2)_2Si(OEt)_3$ (FAS) in toluene and ultrasonicated for 30 min at room temperature. Then the cotton was dried at 120 °C in an oven for 60 min. Finally, the cotton pieces were rinsed with toluene and dried (**CA** > 110 °).

4.5.5 General procedure for the one-step coating of cotton fabrics with anti-inflammatory silica nanoparticles (Fabric-M_{IV}-Anti-inflammatory-x FAS-n)

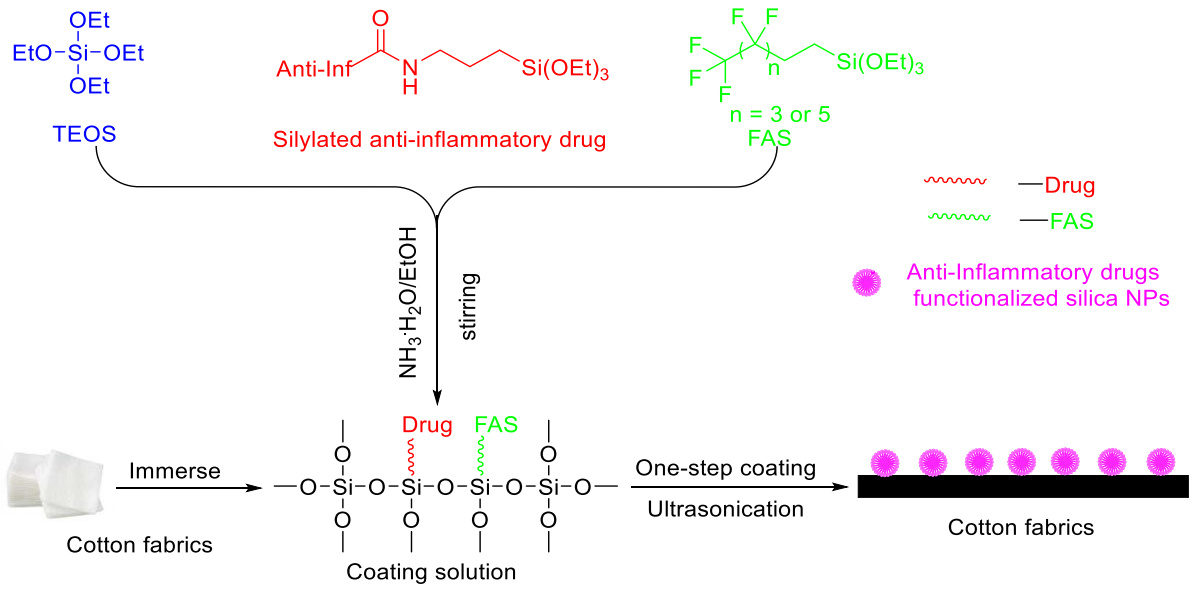

TEOS (2.08 g, 10.0 mmol), the corresponding silylated anti-inflammatory derivative (**P19-P21**) (0.5 mmol) and, in some cases, the corresponding FAS (x mmol) were dissolved in absolute EtOH (25 mL). Then, an ammonium hydroxide-ethanol solution (6 mL of 28% $NH_3{\cdot}H_2O$ in 25 mL EtOH) was added. The mixture was magnetically stirred intensively (1400 rpm) at room temperature for 12 hours. The resulting milky mixture was then ultrasonicated for 30 min to produce a homogenous suspension prior to the coating on the fabric. Then, a piece of clean cotton textile (3 × 3 cm) was immersed in the as-prepared coating solution and the whole system was ultrasonicated for 30 min. The coated cotton textile was first washed with distilled water several times and then dried at 120 °C in an oven for 60 min.

Fabric-M_{IV}-No Drug. **IR *ν* (ATR) (cm^{-1})**: 3333.9, 2898.6, 1713.8, 1453.2, 1238.9, 1054.2, 720.3, 455.5.

Fabric- M_{IV}-Salicyl. **CA** = 138.4°. **IR *ν* (ATR) (cm^{-1})**: 3334.3, 2888.0, 1712.8, 1452.6, 1338.7, 1050.3, 719.0, 438.3. **EDX**: 40.62% C, 43.22% O, 15.75% Si, 0.40% N.

Fabric- M_{IV}-Ibup. **CA** = 138.6°. **IR *ν* (ATR) (cm^{-1})**: 3336.0, 2902.3, 1712.7, 1407.9, 1338.5, 1241.9, 1053.6, 718.7, 482.9. **EDX**: 50.73% C, 45.97% O, 3.65% Si, 0.36% N.

Fabric-M_{IV}-DiClfen. **CA** = 140.5°. **IR** ***ν*** **(ATR) (cm^{-1})**: 3332.6, 2898.7, 1713.5, 1454.5, 1338.1, 1158.1, 1052.8, 716.9, 462.8. **EDX**: 43.49% C, 41.08% O, 11.18% Si, 0.86% N, 3.38% Cl.

Fabric-M_{IV}-DiClfen-0.25 FAS-3. **CA** = 147.6°. **IR** ***ν*** **(ATR) (cm^{-1})**: 3332.9, 2897.9, 1712.7, 1452.8, 1232.7, 1653.4, 468.9. **EDX**: 30.97% C, 37.92% O, 19.60% Si, 1.28% N, 3.66% Cl, 6.57% F.

Fabric-M_{IV}-DiClfen-0.50 FAS-3. **CA** = 146.5°. **IR** ***ν*** **(ATR) (cm^{-1})**: 3330.3, 2897.4, 1712.0, 1408.0, 1051.7, 460.0. **EDX**: 32.33% C, 37.78% O, 21.12% Si, 0.72% N, 1.38% Cl, 6.66% F.

Fabric-M_{IV}-DiClfen-0.75 FAS-3. **CA** = 146.5°. **IR** ***ν*** **(ATR) (cm^{-1})**: 3334.7, 2898.3, 1712.3, 1452.4, 1239.1, 1053.2, 483.8. **EDX**: 41.35% C, 41.39% O, 9.78% Si, 0.63% N, 1.21% Cl, 5.63% F.

Fabric-M_{IV}-DiClfen-1.00 FAS-3. **CA** = 148.2°. **IR** ***ν*** **(ATR) (cm^{-1})**: 3332.5, 2898.0, 1713.5, 1408.2, 1018.4, 475.9. **EDX**: 42.14% C, 32.90% O, 18.31% Si, 0.52% N, 1.45% Cl, 4.67% F.

Fabric-M_{IV}-DiClfen-0.25 FAS-5. CA = 156.1°. **IR** ***ν*** **(ATR) (cm^{-1})**: 3334.8, 2900.0, 1712.1, 1454.5, 1055.9, 720.6, 466.7. **EDX**: 41.76% C, 37.01% O, 13.76% Si, 0.89% N, 2.93% Cl, 3.64% F.

4.5.6 Drug release procedures

4.5.6.1 Treatment of anti-inflammatory functionalized silica nanoparticles with proteases (GC-analysis).

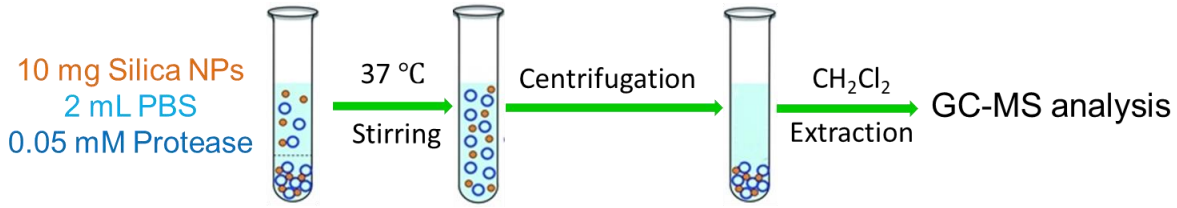

The corresponding functionalized silica nanoparticles (10 mg) were dispersed in phosphate-buffered saline (PBS) (2.0 mL) in a centrifuge tube, the corresponding protease was added and the mixture was gently stirred at 37 °C for the given time. The final concentration of protease was 0.05 M. Then, the sample was centrifuged and the supernatant was extracted with dichloromethane (1 mL × 2). The corresponding anti-inflammatory released drug was detected by GC-MS analysis of the combined extracts.

4.5.6.2 Treatment of anti-inflammatory functionalized silica nanoparticles with leukocytes from animal origin (GC-analysis).

The corresponding functionalized silica nanoparticles (35 mg) were dispersed in phosphate-buffered saline (PBS) (2.0 mL) in an eppendorf tube, leukocytes from animal origin (2×10^6 cells) were added and the mixture was gently stirred at 37 ^{o}C for 24 h. Then, the sample was centrifuged and the supernatant was extracted with dichloromethane (1 mL × 2). The corresponding anti-inflammatory released drug was detected by GC-MS analysis of the combined extracts.

4.5.6.3 Treatment of cotton fabrics coated with anti-inflammatory functionalized silica nanoparticles with proteases (GC-analysis).

The corresponding cotton fabrics (a piece of 3 × 3 cm cut in four pieces) were dispersed in phosphate-buffered saline (PBS) (4.0 mL) in a tube, the corresponding protease was added and the mixture was gently stirred at 37 ℃ for 48 h. The final concentration of protease was 0.05 mM. Then, after removal of the cotton pieces, the supernatant was extracted with dichloromethane (1 mL × 2). The corresponding anti-inflammatory released drug was detected by GC-MS analysis of the combined extracts.

4.5.6.4 Treatment of cotton fabrics coated with anti-inflammatory functionalized silica nanoparticles with leukocytes from animal origin (GC-analysis).

The corresponding cotton fabrics were dispersed in phosphate-buffered saline (PBS) (2.5 mL) in a tube, leucocytes of animal origin (4×10^6 cells) were added and the mixture was gently stirred at 37 ^{o}C for 24 h. Then, after removal of the cotton pieces, the supernatant was extracted with dichloromethane (1 mL × 2). The corresponding anti-inflammatory released drug was detected by GC-MS analysis of the combined extracts.

4.5.6.5 Treatment of anti-inflammatory functionalized silica nanoparticles with proteases for quantitative analysis by UV-Vis.

The corresponding functionalized silica nanoparticles (10 mg) were dispersed in phosphate-buffered saline (PBS) (1.0 mL) in an *eppendorf* vial, the corresponding protease was added, and the mixture was gently stirred at 37 °C for the given time (orbital shaker). The final concentration of protease was 0.1 mM. Then, the sample was centrifuged, and the supernatant

was extracted with dichloromethane (10 × 3 mL). The solvent was removed under vacuum from the combined organic phases. The residue was dissolved in acetonitrile and the solution was analyzed by UV-Vis.

4.5.6.6 Treatment of anti-inflammatory functionalized silica nanoparticles with leukocytes from animal origin for quantitative analysis by UV-Vis.

The corresponding functionalized silica nanoparticles (10 mg) were dispersed in phosphate-buffered saline (PBS) (1.0 mL) in an *eppendorf* vial, leukocytes from animal origin (4×10^6 cells) were added and the mixture was gently stirred at 37 °C for 24 h (orbital shaker). Then, the sample was centrifuged, and the supernatant was extracted with dichloromethane (10 × 3 mL). The solvent was removed under vacuum from the combined organic phases. The residue was dissolved in acetonitrile and the solution was analyzed by UV-Vis.

4.5.6.7 Treatment of cotton fabrics coated with anti-inflammatory functionalized silica nanoparticles with proteases for quantitative analysis by UV-Vis.

A piece of **Fabric-M4-DiClfen** (3 × 3 cm) were cut into small pieces and dispersed in phosphate-buffered saline (PBS) (5.0 mL) in a tube, the corresponding protease was added, and the mixture was gently stirred at 37 °C for 24 h (orbital shaker). The final concentration of protease was 0.1 mM. Then, after removal of the cotton pieces, the supernatant was extracted with dichloromethane (20 × 3 mL). The solvent was removed under vacuum from the combined organic phases. The residue was dissolved in acetonitrile and the solution was analyzed by UV-Vis.

4.5.6.8 Treatment of cotton fabrics coated with anti-inflammatory functionalized silica nanoparticles with leukocytes from animal origin for quantitative analysis by UV-Vis.

A piece of **Fabric-M4-DiClfen** (3 × 3 cm) (0.43×10^{-2} mmol diclofenac) was cut into small pieces and dispersed in phosphate-buffered saline (PBS) (5.0 mL) in a tube, leukocytes from animal origin (16×10^6 cells) were added and the mixture was gently stirred at 37 °C for 24 h (orbital shaker). Then, the sample was centrifuged, and the supernatant was extracted with dichloromethane (20 × 3 mL). The solvent was removed under vacuum from the combined organic phases. The residue was dissolved in acetonitrile and the solution was analyzed by UV-Vis.

4.6 References

1. M. Miraftab, *Wound care materials: an overview in Medical and Healthcare Textiles*, Eds: S. C. Anand, J. F. Kennedy, M. Miraftab, S. Rajendran, Ed Woodhead, **2010**, pp.193.
2. B. Simoncic, B. Tomsic, *Text. Res. J.* **2010**, *80*, 1721.
3. C. H. Dong, P. S. He, Z. Lu, S. G. Wang, S. Y. Sui, J. Liu, L. Zang, P. Zhu, *J. Therm. Anal. Calorim.* **2018**, *131*, 1079.
4. A. A. A. Salama, R. M. Kotb, R. N. Shaker, *J. Chem. Pharm. Res.* **2015**, *7*, 181.
5. I. Perelshteina, E. Rudermana, A. Franceskob, M. M. Fernandes, T. Tzanov, A. Gedankena, *Ultrasonic Sonochemistry* **2014**, *21*, 1916.
6. R. M. Kotb, N. A. A. Elsayed, A. A. A. Salama, *J. Chem. Pharm. Res.* **2014**, *6*, 900.
7. H. Ferreira, T. Matamá, R. Silva, C. Silva, A. C. Gomes, A. Cavaco-Paulo, *React. Funct. Polym.* **2013**, *73*, 1328.
8. H. Ferreira, R. Silva, T. Matamé, C. Silva, A. C. Gomes, A. Cavaco-Paulo, *J. Liposome Res.* **2016**, *26*, 269.
9. Pinho, E; R. C. Calhelha, I. C. F. R. Ferreira, G. Soares, *Polym. Adv. Technol.* **2019**, *30*, 863.
10. H. Huang, J. F. Lowell, *Adv. Funct. Mater.* **2017**, *27*, 1603524.
11. D. Tarn, C. E. Ashley, M. Xue, E. C. Carnes, J. I. Zink, C. J. Brinker, *Acc. Chem. Res.* **2013**, *46*, 792.
12. F. Tang, L. Li, D. Chen, *Adv. Mater.* **2012**, *24*, 1504.
13. D. Ni, D. Jiang, E. B. Ehlerding, P. Huang, W. Cai, *Acc. Chem. Res.* **2018**, *51*, 778.
14. J. G. Croissant, X. Cattoën, M. Wong Chi Man, J. O. Durand, N. M. Khashab, *Nanoscale* **2015**, *7*, 20318.
15. S. H. Wu, C. Y. Mou, H. P. Lin, *Chem. Soc. Rev.* **2013**, *42*, 3862.
16. Z. Li, J. C. Barnes, A. Bosoy, J. F. Stoddart, J. I. Zink, *Chem. Soc. Rev.* **2012**, *41*, 2590.
17. N. Z. Knezevic, J. -O. Durand, *ChemPlusChem* **2015**, *80*, 26.
18. Y. Feng, N. Panwar, D. J. H. Tng, S. C. Tjin, K. Wang, K. T. Yong, *Coord. Chem. Rev.* **2016**, *319*, 86.
19. T. L. Nguyen, Y. Choi, J. Kim, *Adv. Mater.* **2018**, 1803953.
20. J. G. Croissant, Y. Fatieiev, A. Almalik, N. M. Khashab, *Adv. Healthcare Mater.* **2018**, *7*, 1700831.
21. C. Argyo, V. Weiss, C. Bräuchle, T. Bein, *Chem. Mater.* **2014**, *26*, 435.
22. N. Z. Knezevic, J. -O. Durand, *Nanoscale* **2015**, *7*, 2199.
23. S. Giret, M. Wong Chi Man, C. Carcel, *Chem. Eur. J.* **2015**, *21*, 13850.
24. J. H. Zhu, Y. M. Niu, Y. Li, Y. X. Gong, H. H. Shi, Q. Huo, Y. Liu, Q. W. Xu, *Mater. Chem. B* **2017**, *5*, 1339.
25. M. Vallet-Regí, M. Colilla, I. Izquierdo-Barba, M. Manzano, *Molecules* **2018**, *23*, 47.
26. W. Chen, C. A. Glackin, M. A. Horwitz, J. I. Zink, *Acc. Chem. Res.* **2019**, *52*, 1531.
27. C. H. Lee, L. W. Lo, C. Y. Mou, C. S. Yang, *Adv. Funct. Mater.* **2008**, *18*, 3283.
28. E. Ahmadi, N. Dehghannejad, S. Hashemikia, M. Ghasemnejad, H. Tabebordbar, *Drug Deliv.* **2014**, *21*, 164.
29. M. Mohammadzadeh, M. S. Nourbakhsh, E. Khodaverdi, F. Hadizadeh, S. O. Malayeri, *Chem. Biol. Drug Des.* **2016**, *88*, 370.
30. R. Bouchal, M. Daurat, M. Gary-Bobo, A. Da Silva, L. Lesaffre, D. Aggad, A. Godefroy, P. Dieudonné, C. Charnay, J. -O. Durand, *ACS Appl. Mater. Interfaces* **2017**, *9*, 32018.
31. S. Hashemikia, N. Hemmatinejad, E. Ahmadi, M. Montazer, *Drug Deliv.* **2016**, *23*, 2946.

32. A. Popat, B. P. Ross, J. Liu, S. Jambhrunkarm, F. Kleitz, S. Z. Qiao, *Angew. Chem. Int. Ed.* **2012**, *51*, 12486.
33. I. Makarovsky, Y. Boguslavsky, M. Alesker, J. Lellouche, E. Banin, J.-P. Lellouche, *Adv. Funct. Mater.* **2011**, *21*, 4295.
34. J. G. Croissant, Y. Fatieiev, K. Julfakyan, J. Lu, A. H. Emwas, D. H. Anjum, H. Omar, F. Tamanoi, J. I. Zink, N. M. Khashab, *Chem. Eur. J.* **2016**, *22*, 14806.
35. X. Elias, R. Pleixats, M. Wong Chi Man, J. J. E. Moreau, *Adv. Synth. Catal.* **2007**, *349*, 1701.
36. M. Trilla, R. Pleixats, M. Wong Chi Man, C. Bied, J. J. E. Moreau, *Adv. Synth. Catal.* **2008**, *350*, 577.
37. S. Niembro, A. Shafir, A. Vallribera, R. Alibés, *Org. Lett.* **2008**, *10*, 3215.
38. R. Bernini, S. Cacchi, G. Fabrizi, G. Forte, S. Niembro, F. Petrucci, R. Pleixats, A. Prastaro, R. M. Sebastián, R. Soler, M. Tristany, A. Vallribera, *Org. Lett.* **2008**, *10*, 561.
39. R. Bernini, S. Cacchi, G. Fabrizi, G. Forte, F. Petrucci, A. Prastaro, S. Niembro, A. Shafir, A. Vallribera, *Org. Biomol. Chem.* **2009**, *7*, 2270.
40. R. Bernini, S. Cacchi, G. Fabrizi, S. Niembro, A. Prastaro, A. Shafir, A. Vallribera, *ChemSusChem* **2009**, *2*, 1036.
41. M. Trilla, R. Pleixats, M. Wong Chi Man, C. Bied, *Green Chem.* **2009**, *11*, 1815.
42. R. Bernini, S. Cacchi, G. Fabrizi, G. Forte, F. Petrucci, A. Prastaro, S. Niembro, A. Shafir, A. Vallribera, *Green Chem.* **2010**, *12*, 150.
43. A. Boffi, S. Cacchi, P. Ceci, R. Cirilli, G. Fabrizi, A. Prastaro, S. Niembro, A. Shafir, A. Vallribera, *ChemCatChem* **2011**, *3*, 347.
44. A. Monge-Marcet, X. Cattoën, D. A. Alonso, C. Nájera, M. Wong Chi Man, R. Pleixats, *Green Chem.* **2012**, *14*, 1601.
45. G. Borja, A. Monge-Marcet, R. Pleixats, T. Parella, X. Cattoën, M. Wong Chi Man, *Eur. J. Org. Chem.* **2012**, *19*, 3625.
46. S. Niembro, S. Donnici, A. Shafir, A. Vallribera, M. L. Buil, M. A. Esteruelas, C. Larramona, *New J. Chem.* **2013**, *37*, 278.
47. M. Fernández, M. Ferré, A. Pla-Quintana, T. Parella, R. Pleixats, A. Roglans, *Eur. J. Org. Chem.* **2014**, *28*, 6242.
48. M. Ferré, X. Cattoën, M. Wong Chi Man, R. Pleixats, *ChemCatChem* **2016**, *8*, 2824.
49. M. Ferré, R. Pleixats, M. Wong Chi Man, X. Cattoën, *Green Chem.* **2016**, *18*, 881.
50. R. Soler, J. Salabert, R. M. Sebastián, A. Vallribera, N. Roma, S. Ricart, E. Molins, *Chem. Commun.* **2011**, *47*, 2889.
51. J. Salabert, R. M. Sebastián, A. Vallribera, *Chem. Commun.* **2015**, *51*, 14251.
52. A. M. Montagut, E. Gálvez, A. Shafir, R. M. Sebastián, A. Vallribera, *Chem. Eur. J.* **2017**, *23*, 3810.
53. A. M. Montagut, A. Vallribera, R. M. Sebastián, E. Alarcón, *Fabrics Functionalized with Pharmacologically Active Substances.* United Kingdom Patent No. 17039815-9, **2017**.
54. A. M. Montagut, A. Granados, A. Ballesteros, R. Pleixats, M. Llagostera, P. Cortés, R. M. Sebastián, A. Vallribera, *Tetrahedron* **2019**, *75*, 102.
55. A. M. Montagut, A. Granados, C. Lazurko, A. El-Khoury, E. J. Suuronen, E. I. Alarcon, R. M. Sebastián, A. Vallribera, *Cellulose* **2019**, *26*, 7495.

56. A. Granados, A. Vallribera, *Dyes and Pigments* **2019**, *170*, 107597.
57. H. Wang, J. Fang, T. Cheng, J. Ding, L. Qu, L. Dai, X. Wang, T. Lin, *Chem. Commun*. **2008**, *7*, 877.
58. C. H. Xue, S. T. Jia, J. Zhang, L. Q. Tian, *Thin Solid Films* **2009**, *517*, 4593.
59. T. J. Athauda, R. R. Ozer, *Cellulose* **2012**, *19*, 1031.
60. J. Zhang, B. Li, L. Wu, A. Wang, *Chem. Commun.* **2013**, *49*, 11509.
61. L. Cañedo-Dorantes, M. Cañedo-Ayala, *Int. J. Inflam.* **2019**, 3706315. DOI: 10.1155/2019/3706315.
62. P. Randjelović, S.Veljković , N. Stojiljković , D. Sokolović, I. Ilić, D. Laketić, D. Randjelović, N. Randjelović. *Acta Facultatis Medicae Naissensis* **2015**, *32*, 259.
63. S. L. Collins, R. A. Moore, H. J. McQuay, P. J. Wiffen, *Eur. J. Pain*, **1998,** *2*, 285.
64. M. A. Lomaga, *Therapeutic formulations for the treatment of cold and flu-like symptoms*, United States Patent, No. US20160045465A1, **2016**.
65. T. J. Gan, *Curr. Med. Res. Opin*. **2010**, *26*, 1715.
66. A. Granados, *PhD thesis*, Universitat Autònoma de Barcelona, **2018**.
67. C. Théron, A. Gallud, C. Carcel, M. Gary-Bobo, M. Maynadier, M. Garcia, J. Lu, F. Tamanoi, J. I. Zink, M. Wong Chi Man, *Chem. Eur. J.* **2014**, *20*, 9372.
68. H. Li, M. Pérez-Trujillo, X. Cattoën, R. Pleixats, *ACS Sustainable Chem. Eng.* **2019**, *7*, 14815.
69. Q. J. He, X. Z. Cui, F. M. Cui, L. M. Guo, J. L. Shi, *Microporous Mesoporous Mater.* **2009**, *117*, 609.
70. C. H. Xue, S. T. Jia, J. Zhang, L. Q. Tian, H. Z. Chen, M. Wang, *Sci. Technol. Adv. Mater.* **2008**, *9*, 035008.
71. H. X. Wang, J. Ding, Y. H. Xue, X. G. Wang, T. Lin, *J. Mater. Res.* **2010**, *25*, 1336.
72. Y. Han, J. Y. Ying, *Angew. Chem. Int. Ed.* **2005**, *44*, 288.
73. C. D. Zhang, L. M. Price, W. H. Daly, *Biomacromolecules* **2006**, *7*, 139.
74. Z. T. Liu, Y. Yang, L. L. Zhang, P. Sun, Z. W. Liu, J. Lu, H. P. Xiong, Y. D. Peng, S. W. Tang, *Carbohydr. Polym.* **2008**, *71*, 18.
75. M. E. Yazdnshenas, M. Shateri-Khalilabad, *Ind. Eng. Chem. Res.* **2013**, *52*, 12846.
76. T. D. Warner, F. Giuliano, I. Vojnovic, A. Bukasa, J. A. Mitchell, J. R. Vane, *Proc. Natl. Acad. Sci. USA.* **1999**, *96*, 7563.

CHAPTER 5

FUNCTIONALIZED MAGNETIC MESOPOROUS SILICA NANOPARTICLES FOR RARE EARTH ELEMENT RECOVERY FROM WASTEWATER

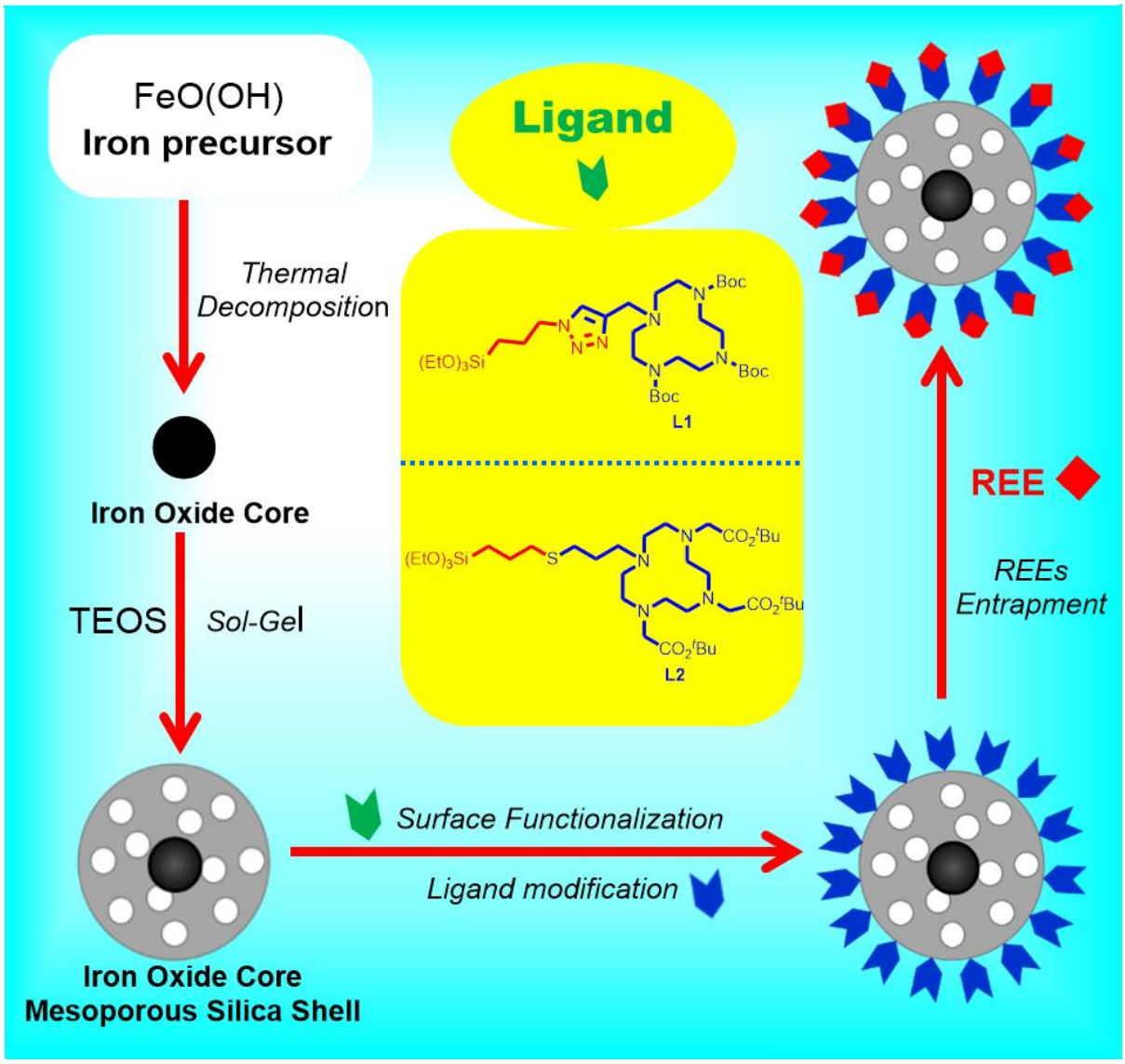

H. Li, M. Menard, G. Seisenbaeva, R. Pleixats,* J. -O. Durand,* Functionalization of iron oxide core-shell silica nanoparticles for heavy rare earth elements recovery from wastewater. In preparation, **2020**.

CHAPTER 5

FUNCTIONALIZED MAGNETIC MESOPOROUS SILICA NANOPARTICLES FOR RARE EARTH ELEMENT RECOVERY FROM WASTEWATER

5.1 Introduction

Rare earth elements (REEs) are the collective name for 17 chemically similar metallic elements which include Scandium (Sc), Yttrium (Y) and the 15 lanthanide elements: Lanthanum (La), Cerium (Ce), Praseodymium (Pr), Neodymium (Nd), Promethium (Pm), Samarium (Sm), Europium (Eu), Gadolinium (Gd), Terbium (Tb), Dysprosium (Dy), Holmium (Ho), Erbium (Er), Thulium (Tm), Ytterbium (Yb), and Lutetium (Lu). They were defined by the International Union of Applied and Pure Chemistry (IUPAC) in 2005.[1-3] All these metals have many similar properties, and that often causes them to be found together in geologic deposits. They are also referred to as "rare earth oxides".[4] They are usually divided into the light rare earth element (LREE) and the heavy rare earth element (HREE). La, Ce, Pr, Nd, Pm, Sm are referred to as LREEs, while HREEs include metal elements from Eu to Lu, and Y.[5-6] Scandium, as the lightest REE, is not similar to either the LREEs or the HREEs; therefore, Sc constitutes a class by itself.[7] Dy, Nd, Tb, Eu and Y are considered the most economically critical REEs, with regard to their low natural abundance and high demands for the production. All the REEs are arranged with respect to supply risk, importance to green energy, and economic importance in the medium term up to the year 2025 (**Figure 5.1**).[8-14] Although the REEs have similar electron configurations, their distinctive physical and chemical properties make them widely used in many technologies,[15] as they can provide chemical, catalytic, electrical, magnetic, and optical properties to the end-products they are used in. The REEs are essential raw materials for a wide range of applications, including metallurgy (metal refining and metal alloying), catalysts in the automotive and the petro-chemical industry, colouring of glass/ceramics, phosphors (LEDs, compact fluorescent lamps, flat panel displays), lasers, rechargeable solid state batteries (Ni-MH), optical fiber and others. Additionally, REEs are vital elements in emerging technologies such as solid state fuel cells, superconductors, magnetic cooling, hydrogen storage and high performance permanent magnets. HREEs are crucial in a variety of high-tech applications ranging from wind-turbines and hybrid cars to HD drives and cell phone speakers and microphones.[13-19] These applications are dependent on the availability of rare earth elements (REEs), considered as

the "vitamins" of modern industry, due to their crucial role in the development of new cutting-edge technologies.[13]

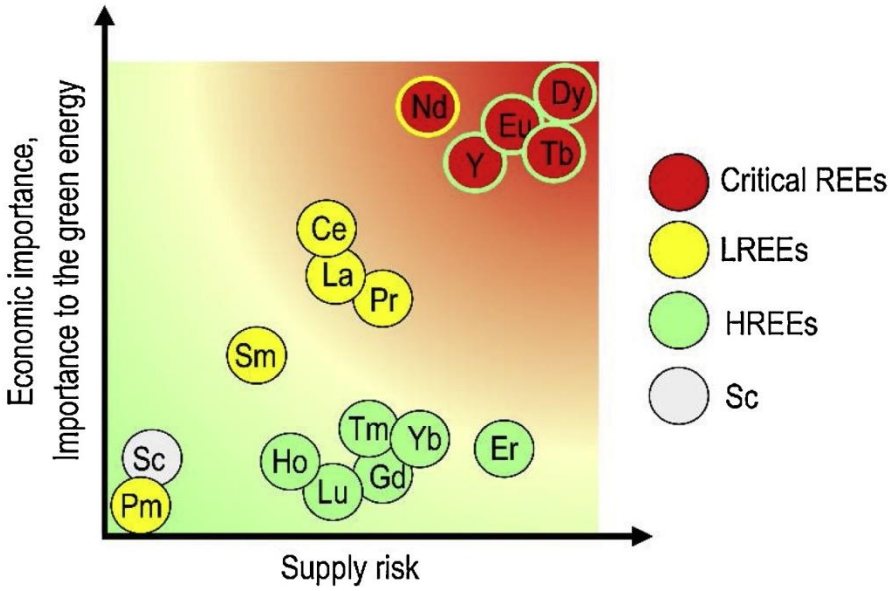

Figure 5.1 Critical assessment of rare earth elements (REEs) in the medium term (2015-2025). Reproduction with permission of Elsevier.[13]

Today, with the increasing demand for high-end products, such as electric vehicles, high-performance home appliances, computers and smartphones, the demand for REEs, as their essential raw materials, will greatly increase. On the other hand, their supply is effectively restricted to only a few large mining districts.[11,20] The largest mining fields of ores like bastnäsite, monazite, and xenotime, containing primarily REEs, are in the Asian states.[21] Among them, China has the most abundant REE reserves.[22-24] According to the literature, the total world REE reserves were estimated to be around 120 million tons in 2018 and the world demand for REEs in 2018 was about 142 thousand tons.[21] It seems to be sufficient for hundreds of years of global demand.[25] However, individual countries may still deal with supply problems because of a severe REEs production monopoly and complicated production technologies, plagued by environmental risks.[26] For this reason, the balance between supply and demand of individual REEs is becoming a major problem for manufacturers and consumers of these elements in many countries.[27] To mitigate this problem, other options, alternative to the primary supply of REEs from mined ores, are steadily gaining importance. In this context, an increasingly promising alternative is offered by the secondary supply of REEs based on recycling and waste management technologies. Since recycling and waste management are key factors of a circular economy, their enhancement to improve the supply

of these critical raw materials is a very attractive option.[9,28] Moreover, mountains of e-waste rich in REEs are indeed growing across the globe, if this waste could be turned into a valuable resource, this will both protect human health and enlarge the planet's increasingly strained REE resources.

High demand and limited resources of REEs, combined with potential environmental problems, enforce the development of innovative low-cost techniques and materials to recover REEs from electronic waste and wastewaters. As we have mentioned in **Chapter 1** (*Section* 1.7), magnetic nanoparticles (MNPs) offer the attractive possibility of magnetic separation of nanomaterials and excellent potential reuse without loss of efficiency. The most frequently used magnetic nanomaterials for rare earth elements (REEs) adsorption are based on magnetite (Fe_3O_4),[29-41] maghemite (γ-Fe_2O_3)[42-46] and zerovalent iron (Fe^0).[47-48] Among all iron oxide nanoparticles, maghemite nanoparticles have the best chemical stability along with satisfactory magnetic properties.[15] In order to assure good selectivity and the possibility of magnetic separation, the magnetic core-shell nanoparticles were developed.[49-50] The core-shell nanoparticles can offer the following possible advantages: (i) the use of the core as a support allows the obtention of the specific surface (shell) nano-architecture in terms of porosity and surface area; (ii) the synergism between the shell and the core enabling to achieve higher RE^{3+} adsorption efficiency, yield and selectivity; (iii) the mobility of nanoparticles can enhance the treatment ability and facilitate nanoparticle's recycling after pollutant treatment with an introduced external magnetic field.[50-52]

In recent years, various magnetic core-shell NPs were synthesized for the adsorption of various RE^{3+} from aqueous solutions. In 2012, Wang and colleagues synthesized humic acid-coated Fe_3O_4 magnetic nanoparticles (**Fe_3O_4@HA MNPs**) for Eu^{3+} adsorption, which can remove 99% of Eu(III) in aqueous solution at pH 8.5.[34] In 2013, Wang *et al*. synthesized a new functionalized Fe_3O_4@shell nanoparticles (**Fe_3O_4@SiO_2-Cl(P507) NPs**) for La^{3+} adsorption, in which the shell of silica was modified with (3-chloropropyl)triethoxysilane (CPTS) functionalized with 2-ethylhexyl phosphonic acid mono-2-ethylhexyl ester (P507).[35] In 2014, K. Binnemans *et al.* prepared a core-shell Fe_3O_4@SiO_2 nanoparticles (**Fe_3O_4@SiO_2(TMS-EDTA) NPs**) with the *N*-[(3-trimethoxysilyl)propyl]ethylenediamine triacetic acid (TMS-EDTA) functionalized silica shell for Nd^{3+} adsorption.[36] In 2015, C. Basualto *et al.* synthesized the superparamagnetic magnetite nanoparticles (**Fe_3O_4@OA NPs**) for La^{3+}, Ce^{3+}, Pr^{3+} and Nd^{3+} adsorption. The synthesized nanoparticles were coated with

oleic acid and then functionalized with three organophosphorus extractants (OA), namely di(2-ethylhexyl)phosphoric acid (D2EHPA), bis(2,4,4-trimethylpentyl)phosphinic acid (CYANEX 272), and (2,4,4-trimethylpentyl)dithiophosphinic acid (CYANEX 301).[37] In 2016, S. N. Almeida and H. E. Toma demonstrated a successful nanohydrometallurgical separation of Nd and La by using superparamagnetic nanoparticles (**Fe_3O_4@SiO_2(EAPS/DTPA) NPs**), in which the silica shell was functionalized with ethylenediaminepropylsilane (EAPS) and diethylenetriaminepentaacetic acid (DTPA), as complexing agents.[38] In 2017, Yan *et al*. prepared a magnetic bio-adsorbent: **Fe_3O_4-C_{18}@chitosan-DETA NPs** for Dy^{3+}, Nd^{3+} and Er^{3+} adsorption. The NPs were prepared from an octadecyltriethoxysilane (C18) modified Fe_3O_4 core, and the shell was synthesized from the modified chitosan with sodium tripolyphosphate and functionalized with epichlorohydrin and diethylenetriamine (DETA).[39] In 2018, Li and colleagues prepared a novel magnetic mesoporous silica nanoparticles (**Fe_3O_4@mSiO_2-DODGA**) with Fe_3O_4 NPs as the core and the nanocomposite of mesoporous silica and *N*,*N*-dioctyl diglycolamide as the shell for efficiently adsorbing and recycling REEs.[40] Last year, novel adsorbents for La^{3+}, Pr^{3+} and Nd^{3+} based on functionalized magnetite nanoparticles were synthetized by C. Basualto and co-workers. In that case, three organophosphorus extractants-CYANEX 272 (**Fe_3O_4@OA(C272) NPs**), CYANEX 301 (**Fe_3O_4@OA(C301) NPs**) or D2EHPA (**Fe_3O_4@OA(D2PA) NPs**) were used to functionalize oleic acid coated Fe_3O_4 NPs.[41] All the above examples used Fe_3O_4 as the core and the shells were from various materials. Some magnetic core-shell nanoparticles using γ-Fe_2O_3 as a core have also been described. In 2018, Wang *et al.* synthesized NPs with a γ-Fe_2O_3 core and silica shell, functionalized by N-[(3-trimethoxysilyl)propyl]ethylenediaminetriacetic acid trisodium salt (**γ-Fe_2O_3@SiO_2(RCOONa) NPs**) and by sodium 3-(trihydroxysilyl)propyl methylphosphonate (**γ-Fe_2O_3@SiO_2($R_1R_2PO_3Na$) NPs**) for separation of Sm^{3+} from a dilute aqueous solution.[46] In 2019, novel magnetic nanoparticles (**γ-Fe_2O_3-NH_4OH@SiO_2(APTMS) NPs**) formed from magnetic γ-Fe_2O_3 core, stabilized electrostatically in basic media NH_4OH, doped with SiO_2 shell and functionalized with (3-aminopropyl)trimethoxysilane (APTMS) were prepared by T. Kegl and colleagues in order to adsorb Tb^{3+},[44] and Dy^{3+},[45] from aqueous solution. Zhang *et al*. synthesized magnetic nanoparticles (**Fe^0@SiO_2@PA/SiO_2(DTPA) NPs**) with Fe^0 NPs acting as the core and the shell consisting of two layers. The first silica layer was obtained using tetraethoxysilane (TEOS) as precursor, and the second layer was a composite of poly(allylamine) hydrochloride (PA) and silica, using tetramethoxysilane (TMOS) as precursor. The obtained NPs were functionalized by diethylenetriaminepentaacetic acid

(DTPA) for La^{3+}, Ce^{3+}, Pr^{3+}, Nd^{3+}, Sm^{3+}, Tb^{3+}, Eu^{3+}, Gd^{3+}, Ho^{3+}, and Dy^{3+} adsorption.[48] Besides, Iftekhar *et al.* synthesized NPs with a Zr core and a shell from xanthan gum and Zn-Al nanocomposite for Sc^{3+}, Nd^{3+}, Tm^{3+}, and Yb^{3+} adsorption.[53]

Adsorption is an effective, economical, simple and ecofriendly technique to remove REEs from wastewater, but in order to recover the REEs, desorption and separation of RE^{3+} from the adsorbents are very important for the reusability of REEs and adsorbents. Generally, desorption of RE^{3+} from adsorbents with a high affinity for an adsorbate requires a high concentration of acid (such as HCl,[54] HNO_3,[53] or H_2SO_4,[55]) and/or chelating agents.[56]

According to the available research data, the functionalized nanomaterials (NMs) previously mentioned showed a great adsorption capacity for RE^{3+} and can be easily reused for further adsorption. Moreover, the adsorption/desorption cycles do not significantly reduce the amount of adsorbed RE^{3+}.[14] In **Figure 5.2** we summarize the total recovery route of REEs and NMs from wastewater.[56] In general, it involves the following steps: adsorption of RE^{3+} on NM surfaces, separation of NMs∩RE^{3+} from wastewater, desorption of RE^{3+} from NMs, separation of RE^{3+} from NMs, and regeneration of both REEs and NMs. After removing the REEs from wastewater, further conventional wastewater treatment can be applied.[14]

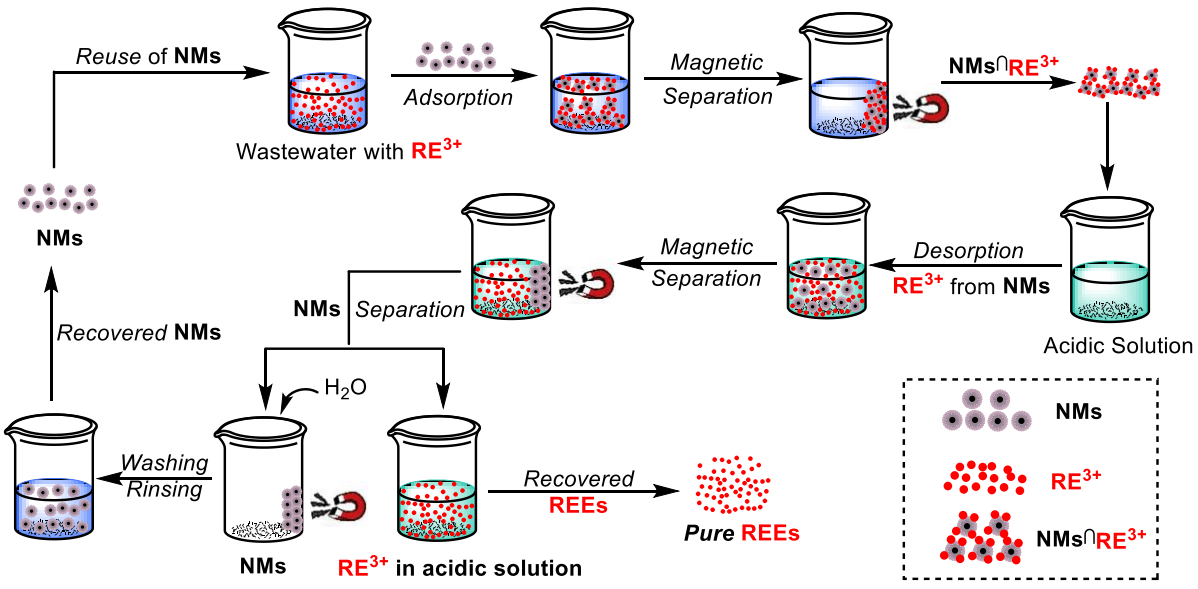

Figure 5.2 Recovery route of REEs and NMs. Reproduction with permission from Elsevier[14]

The adsorbents should contain precisely selected functional ligands according to the Pearson's hard-soft acid base (HSAB) theory (-SH, $-NH_2$, -P=O, -COOH, etc.), which will have a high tendency to remove REE's metal ions. This theory can predict the selectivity of

metal ions for donor ligands. Hard acids and bases tend to have a smaller ionic radius, a high oxidation state and weak polarizability, while soft acids and bases tend to have a large ionic radius, a low oxidation state and strong polarizability. Hard acids (Na^+, K^+, Mg^{2+}, Ca^{2+}, Cr^{3+}, Al^{3+}, Ga^{3+}, Co^{3+}, Fe^{3+}) react preferentially with hard bases (carbonates, sulphates, carboxylates, nitrates, alcohols, amines, phosphates, ethers, H_2O, OH^-, NH_3, hydrazines), and soft acids (Cu^+, Au^+, Ag^+, Hg^{2+}, Hg^+, Cd^{2+}) with soft bases (phenyl groups, thiols, ethylenes, thioethers, cyanides, H_2S).[57-58] Rare earth ions (RE^{3+}), such as scandium (Sc^{3+}), yttrium(Y^{3+}), lanthanum (La^{3+}), cerium (Ce^{3+}), praseodymium (Pr^{3+}), neodymium (Nd^{3+}), promethium (Pm^{3+}), samarium (Sm^{3+}), europium(Eu^{3+}), gadolinium (Gd^{3+}), terbium (Tb^{3+}), dysprosium (Dy^{3+}), holmium (Ho^{3+}), erbium (Er^{3+}), thulium (Tm3+), ytterbium (Yb^{3+}) and lutetium (Lu^{3+}) are classified as hard acids and present strong affinity for charged ligands or neutral O- and N-donors, as indicated by a wide number of articles concerning the formation of their complexes in solution.[59-61] On the basis of HSAB theory, RE^{3+} react preferentially with carbonates, sulphates, carboxylates, nitrates, alcohols, amines, phosphates, ethers, H_2O, OH^-, NH_3 and hydrazine.

The recycling of REEs is not easy and challenges are at every level. These elements are present in small amounts in tiny electronic parts of gadgets such as mobile phones or in some materials (such as in touch screens). They are evenly distributed and difficult to extract. Moreover, the isolation and purification of individual REE is challenging due to their chemical similarities. In order to develop other sources of REEs and reduce the environmental impact of their isolation, there is a clear-cut need for new technologies that reduce the cost of industrial-scale REEs recycling.

In this context, we will focus in this chapter on the development of functionalized magnetic nanoparticles (MNPs), which are easy to remove by using external magnetic field, as a novel approach for REEs recycling from aqueous solutions (wastewaters) after pre-processing technology. Moreover, this approach for the recovery of REEs from the wastewater can potentially provide a better source for pure form of REE. The expected results will cover the field of research and development of novel adsorbent nanomaterials for recycling of RE metal ions in order to improve REE selectivity and recycling rate, and to achieve a sustainable growth. Indeed, there is a great social demand for more sustainable society that force the industries to reuse waste as a feedstock and that stimulate changes in the existing laws in the direction of providing incentives for recycling.

5.2 Objectives

This project has been developed on the frame of the European MetRecycle project, which contributes to the Strategic Implementation Plan of the European Innovation partnership on the recycling of raw materials. It deals with a novel strategic approach using advanced nanotechnology to achieve selective, efficient recycling process of REEs, with the focus on the HREE.

The ultimate goal of our work has been the design and synthesis of several novel adsorbents for the specific and selective recovery of different rare earth elements (REEs) from wastewater.

The adsorbents chosen were functionalized magnetic core-shell silica nanoparticles. In **Figure 5.3** we present in a schematic form the route to be followed for the obtention of the nanomaterials for REEs entrapment (**Figure 5.3A&B**) and the proposed silylated cyclen-based ligands **L1-L2** for the functionalization of the nanoparticles (Figure 5.3**C**). The *tert*-butoxycarbonyl groups from **L1** and *tert*-butyl groups from **L2** would be removed after the preparation of the materials in order to have new nanomaterials with amino and carboxyl groups, respectively. Finally, studies of adsorption/desorption of rare earth ions in aqueous solutions will be performed with these functionalized magnetic core-shell nanoparticles containing coordinating groups.

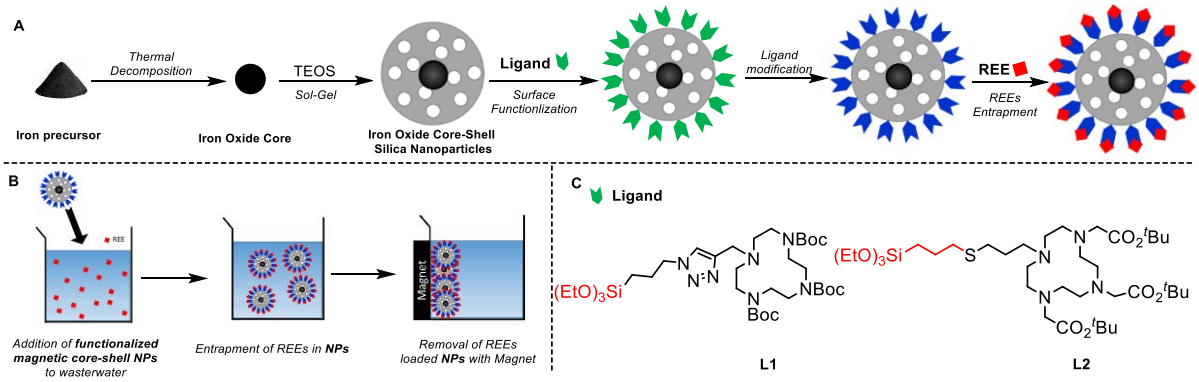

Figure 5.3 A) Schematic route for the preparation of functionalized magnetic core-shell silica nanoparticles for REEs recovery from wastewater B) Principle of REEs removal by magnetic core-shell nanoparticles. C) Proposed silylated ligands for the functionalization of the nanoparticles

5.3 Results and discussion

This part of the thesis was mainly carried out in a four-month stay at the *Institute Charles Gerhardt Montpellier* (ICGM, France) under the guidance of Dr. Jean-Olivier Durand (preparation and characterization of the nanomaterials). The adsorption/desorption experiments of rare earth ions with the nanomaterials will be performed by the group of Prof. Gulaim Seisenbaeva (Swedish University of Agricultural Sciences, Sweden).

5.3.1 Synthesis of silylated cyclen-based ligands L1 and L2

Based on the work previously reported in **Chapter 3**, the ligand **L1** was first synthesized in quantitative yield by a copper-catalyzed alkyne-azide cycloaddition reaction (CuAAC)[62-63] of the alkyne **79** (see ***Section* 3.3.1.3**) with commercial (3-azidopropyl)triethoxysilane **10** under anhydrous conditions, using $CuBr(PPh_3)_3$ as catalyst in dry THF at 60 °C (**Scheme 5.1**).

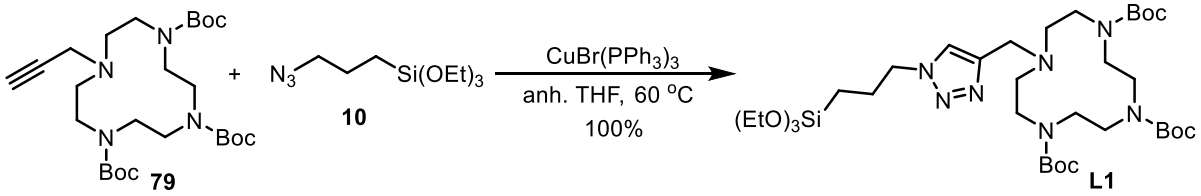

Scheme 5.1 Synthesis of **L1**

On the other hand, we envisaged ligand **L2** to be obtained through a thiol-alkene click reaction between the suitable alkene and (3-mercaptopropyl)triethoxysilane. The synthesis of **L2** is summarized in **Scheme 5.2**. The commercial cyclen **77** was treated with three equivalents of *tert*-butyl 2-bromoacetate in the presence of sodium acetate to afford compound **80**,[64] which was reacted with allyl bromide in acetonitrile at room temperature in the presence of potassium carbonate to give **86**[65] in an overall 60% yield from **77**. The alkene **86** and (3-mercaptopropyl)triethoxysilane were irradiated at 365 nm using 2,2-dimethoxy-1,2-diphenylethanone (DMPA) as initiator, and the desired ligand **L2** was obtained in quantitative yield.

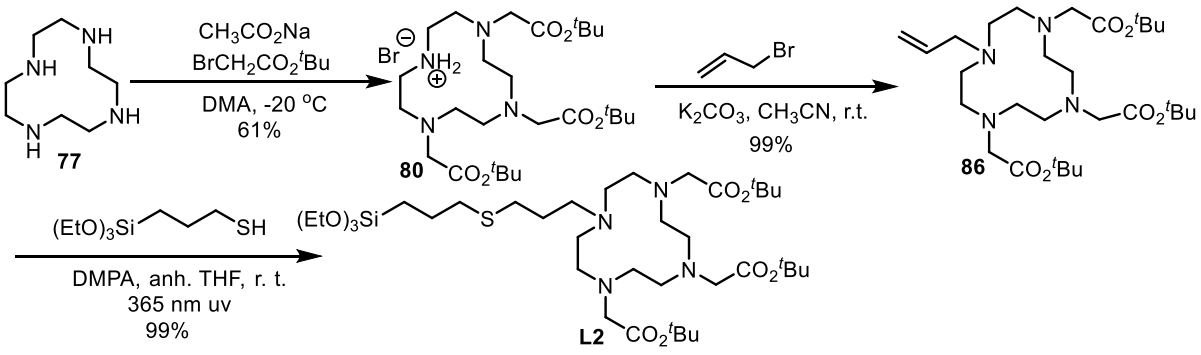

Scheme 5.2 Synthesis of **L2**

5.3.2 Preparation and characterization of magnetic core-shell silica nanoparticles

As shown in **Scheme 5.3**, magnetic core-shell silica nanoparticles were prepared in two steps. First, we established a suitable protocol, inspired from the literature data, to synthesize spherical, monodispersed in size, iron oxide nanocrystals (**Fe_3O_4 NCs**). The **Fe_3O_4 NCs** were synthesized via thermal decomposition at 340 °C of hydrated iron oxide (FeO(OH)), using *n*-docosane as the solvent (boiling point 368 °C) and oleic acid as both reducing agent and nanocrystals stabilizer. The synthesized **Fe_3O_4 NCs** were washed with Et_2O and EtOH, and then dispersed in chloroform and stabilized by the addition of oleylamine.[66] The resulting **Fe_3O_4 NCs** were monodisperse and spherical with a size of 21 ± 2 nm (see TEM images in **Figure 5.4**, **a1-a3**).

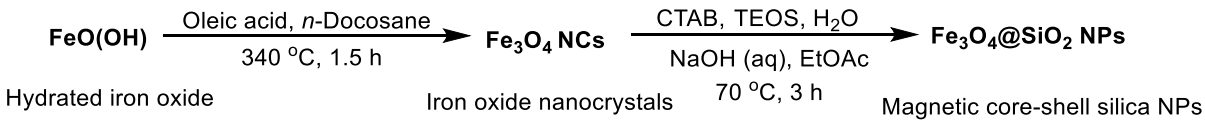

Scheme 5.3 Preparation of magnetic core shell silica nanoparticles

Then, the silica shell was built at the surface of the **Fe_3O_4 NCs** by surfactant (CTAB) mediated base-catalyzed so-gel process with TEOS as silica source according to a procedure adapted from that described by M. Ménard *et al*.[67] Surfactant removal was achieved by washing with a nitrate ammonium-ethanol solution (6 g/L). The as-prepared **Fe_3O_4@SiO_2 NPs** core-shell sample was a black powder and TEM images (**Figure 5.4**, **b1-b3**) showed the presence of monodisperse and regular silica spheres with radial mesostructures encapsulating 22 nm spherical **Fe_3O_4 NCs**. The core-shell NPs have an overall diameter of 124 ± 6 nm by TEM, which was in agreement with the average hydrodynamic diameter (183 nm) of the nanoparticles determined by DLS (**Figure 5.5a**). The zeta potential of **Fe_3O_4@SiO_2 NPs** was determined in water and the negative zeta potential value agreed with the presence of deprotonated silanol groups ($Si\text{-}O^-$) at the surface of the NPs (**Figure 5.5b**).

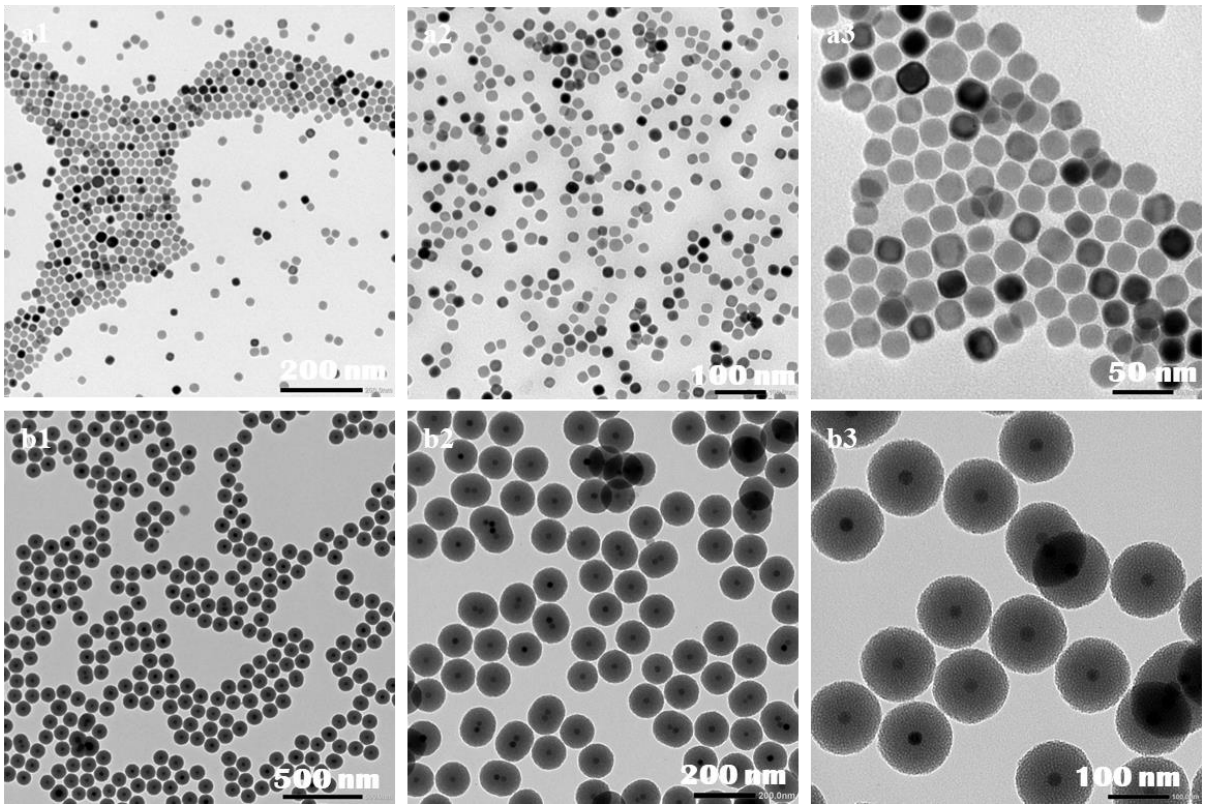

Figure 5.4 TEM images of a1-a3) **Fe_3O_4 NCs** and b1-b3) **Fe_3O_4@SiO_2 NPs** at different magnification

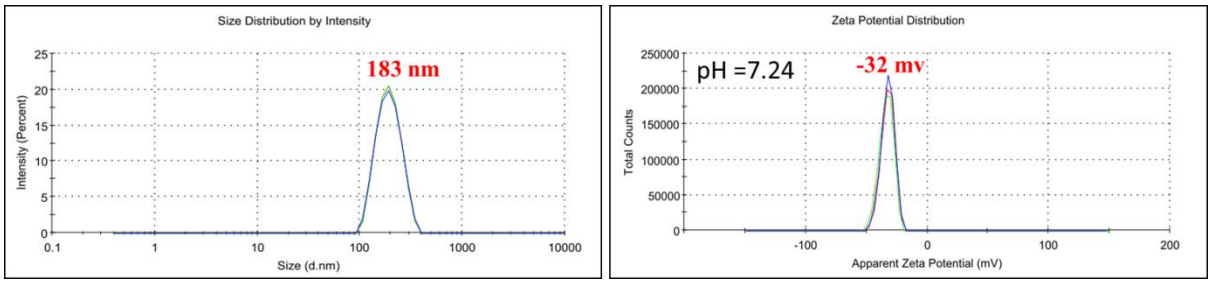

Figure 5.5 a) DLS size distribution of **Fe_3O_4@SiO_2 NPs**, b) Zeta potential of **Fe_3O_4@SiO_2 NPs**

FTIR spectrum of **Fe_3O_4@SiO_2 NPs** (**Figure 5.6**) proved the presence of SiO_2 framework with characteristic peaks around 1060 and 795, 961.5 cm^{-1} that correspond to asymmetric stretching vibration of Si-O-H bonds (γ_{as}Si-O-H) and scissoring (bending) of Si-H bonds (γ_sSi-O-Si).

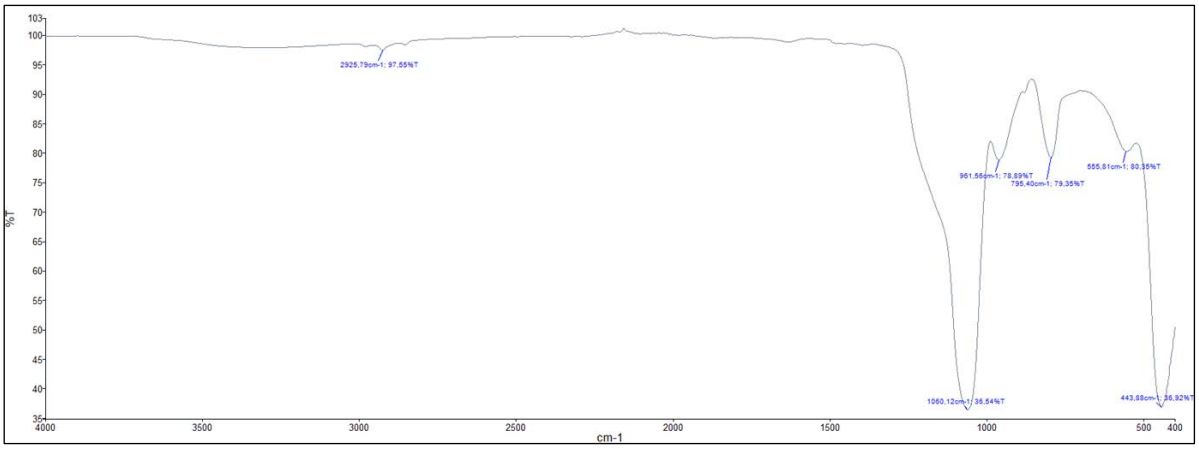

Figure 5.6 FTIR spectrum of **Fe_3O_4@SiO_2 NPs**

TGA analysis was performed for **Fe_3O_4@SiO_2 NPs** core-shell nanoparticles (**Figure 5.7**). The first loss of mass of 4.48% was attributed to the water remaining in the system despite freeze-drying. Then, the other mass losses of 2.46 % and 6.63% (ca. 9.09% in total) by further heating to 800 °C are related to the transformations $Fe_3O_4 \rightarrow Fe_2O_3 \rightarrow 2$ FeO. The transformation of maghemite (Fe_3O_4) into hematite (Fe_2O_3) is an irreversible reaction, while the FeO phase is a metastable phase, which returns to hematite as soon as the sample is cooled back.[68]

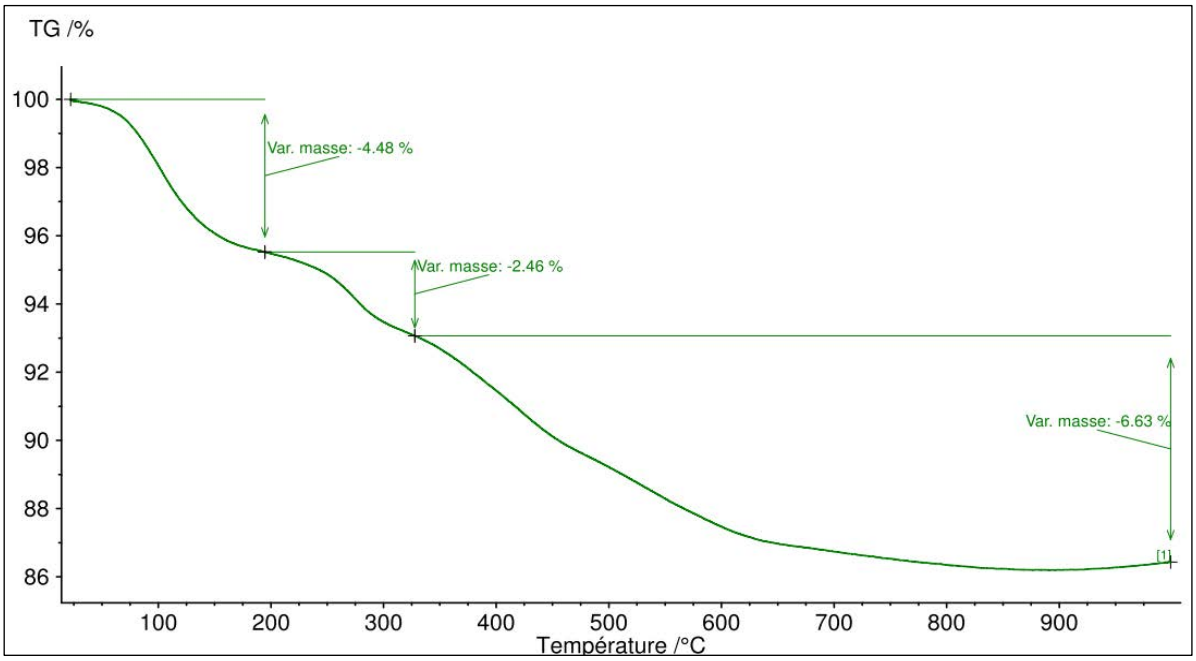

Figure 5.7 TGA of **Fe_3O_4@SiO_2 NPs**

N_2 isotherm sorption analysis (BET) for **Fe_3O_4@SiO_2 NPs** provided a *type IV* isotherm typical for mesoporous materials (see **Figure 5.14** later on). However, the hysteresis and the main part of the adsorption was due to porosity derived from the interstitial voids between the

NPs in the dry powder. The porosity inside the individual nanoparticles as they will be dispersed in solution should be deduced from the part of the isotherm up to $p/p^o = 0.8$ (determination of pore volume). The BET analysis gives specific surface area of 75 m^2/g which is quite low for a mesoporous material and the t-plot analysis shows that there is external surface and micropores. It is difficult to extract a pore diameter for microporous samples from N_2 sorption. However, as mentioned before, the mesoporosity was visible in the TEM images. Perhaps the surface of the pores is blocked by a layer of microporous silica at 78 K.

5.3.3 Preparation and characterization of functionalized magnetic core-shell silica nanoparticles

In this section, we describe first how two different silylated cyclen ligands (**L1** and **L2**) were used to modify the surface of **Fe_3O_4@SiO_2 NPs** by post-grafting methods. We initially investigated different grafting conditions with ligand **L2**. Specifically, the ligand **L2** (x mmol; x= 0.1 or 0.2) was added to the mixture of **Fe_3O_4@SiO_2 NPs** (100 mg) in the corresponding solvent (toluene or DMF) (10 mL) with 500 µL H_2O and 25 µL Et_3N as catalysts. Each mixture was sonicated for 2 h and then heated at the corresponding temperature for 24 h. After that, the mixture was cooled to room temperature, then centrifuged and washed successively with H_2O, ethanol and acetone. The as-prepared modified nanoparticles were dried under vacuum, and finally crushed to give the grafted materials **Fe_3O_4@SiO_2 NPs-Ln-I** as black powders. We summarize the results of surface grafting with **ligand L2** in the different conditions in **Table 5.1** and **Figure 5.8**. When this process was performed in toluene at 135 °C with 0.1 mmol of **L2** per 100 mg of **Fe_3O_4@SiO_2 NPs**, FTIR spectrum showed that almost no ligand was grafted on the surface of core-shell nanoparticles (**Figure 5.8, Table 5.1**, entry 1). When the solvent was changed to DMF and the temperature was 90 ºC, it was obvious from the IR spectrum that **L2** was grafted to **Fe_3O_4@SiO_2 NPs**, because the adsorption at 1653-1657 cm^{-1} corresponds to the carbonyl group (C=O) of **L2** (**Table 5.1**, entry 2). With DMF as solvent, the temperature was increased to 120 and 130 ºC (**Table 5.1**, entries 3 and 4). Additional experiments were performed in DMF at 120 ºC in the absence of water (**Table 5.1**, entry 5) and with 0.2 mmol of **L2**/100 mg of parent nanoparticles (**Table 5.1**, entry 6). In order to compare the ligand loading on the surface of **Fe_3O_4@SiO_2 NPs**, TGA was performed on the corresponding functionalized nanoparticles, because the differences in the total mass loss are mainly due to the amount of ligand grafted to the surface.

From the results of **Table 5.1**, the best conditions were established as follows: in DMF at 120 °C with 2 mmol **L2**/g parent nanoparticles, using an appropriate amount of water and a small amount of Et_3N as catalyst.

Table 5.1 Investigation of surface grafting with ligand **L2**

Entry	Reaction conditions [a]			γ(C=O) 1653-1657 cm^{-1} [c]	TGA[d]
	Solvent	Temperature (°C)	Ligand (mmol/g)[b]		
1	Toluene	135	1	×	nd[e]
2	DMF	90	1	√	18.1%
3	DMF	120	1	√	18.2%
4	DMF	130	1	√	17.7%
5 [f]	DMF	120	1	√	17.0%
6	DMF	120	2	√	20.8%

[a] Post-grafting conditions. [b] Ligand amount per g **Fe_3O_4@SiO_2 NPs**. [c] determined by FTIR. [d] Loss mass, TGA with a heating rate of 5 °C/min from 25 to 1000 °C. [e] Not determined. [f] Without H_2O as catalyst.

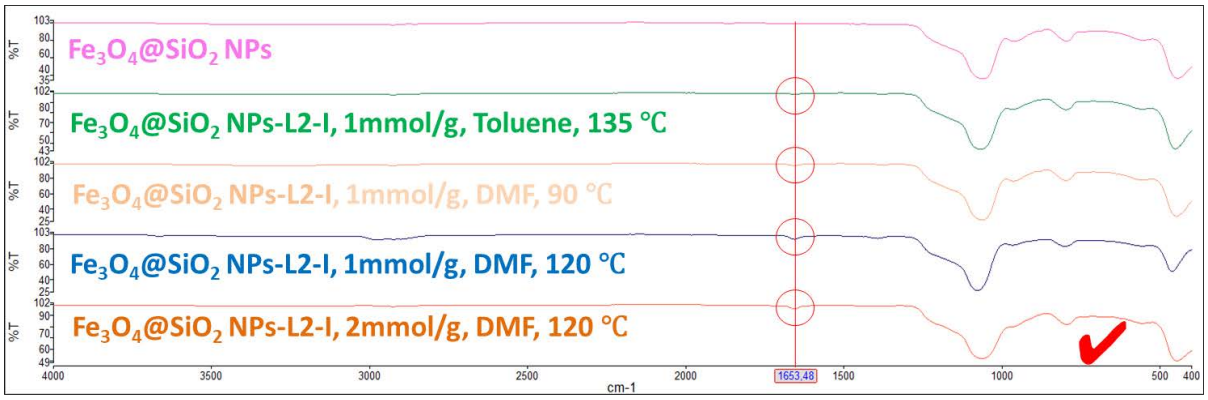

Figure 5.8 FTIR of **Fe_3O_4@SiO_2 NPs-L2-I** prepared in different conditions

Under the optimal conditions, **L1** and **L2** were grafted onto the surface of **Fe_3O_4@SiO_2 NPs** and the functionalized nanomaterials **Fe_3O_4@SiO_2 NPs-Ln-I** (n = 1, 2) were obtained (**Figure 5.9**).

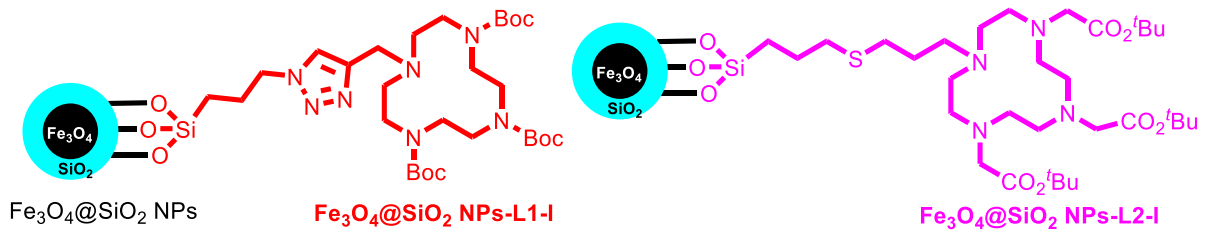

Figure 5.9 The structure of **Fe_3O_4@SiO_2 NPs -L1-I** and **Fe_3O_4@SiO_2 NPs -L2-I**

Then, the Boc group and ^{t}Bu group should be removed from the obtained materials in order to have free amine and carboxyl groups to coordinate to the REEs. For that purpose, the nanomaterials **Fe_3O_4@SiO_2 NPs-Ln-I** (n = 1, 2) were treated with a 5:1 TFA/CH_2Cl_2 solution under stirring at room temperature for 1 hour. Then the final nanoparticles **Fe_3O_4@SiO_2 NPs-Ln-II** (n = 1, 2) (**Figure 5.10**) were collected by centrifugation.

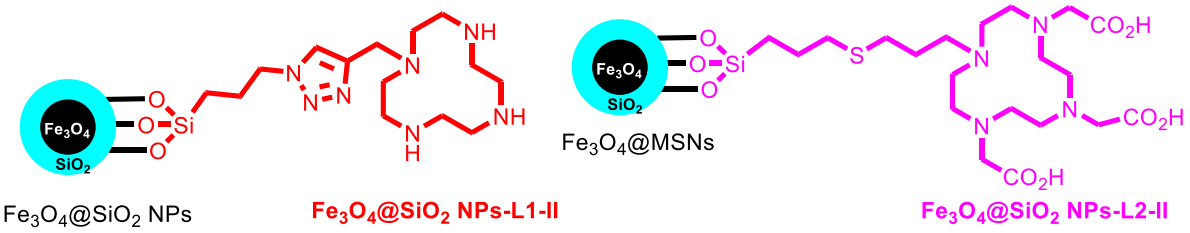

Figure 5.10 The structure of **Fe_3O_4@SiO_2 NPs-L1-II** and **Fe_3O_4@SiO_2 NPs-L2-II**

The functionalized nanoparticles were characterized by FTIR, DLS, zeta potential, N_2-adsorption analysis, TGA and elemental analysis. Some physical data are given in **Table 5.2**

Table 5.2 Some data of functionalized magnetic core-shell mesoporous silica nanoparticles

Material	N_2-sorption measurements[a]			Particle size (nm)[c]	Zeta potential		Ligand loading	
	S_{BET} (m^2g^{-1})	V_{pore} (cm^3g^{-1})	Ø $_{pore}$ (nm)[b]		pH	(mV)	EA mmol·g^{-1}[d]	TGA wt%[e]
Fe_3O_4@SiO_2 NPs	75	0.05	17.1	183	7.24	-32	-	-
Fe_3O_4@SiO_2 NPs-L1-I	41	0.03	30.5	216	6.85	-6	nd[f]	5.31%
Fe_3O_4@SiO_2 NPs-L1-II	nd	nd	nd	nd	6.99	39	0.15	4.34%
Fe_3O_4@SiO_2 NPs-L2-I	65	0.05	26.9	237	6.75	-14	nd	7.76%
Fe_3O_4@SiO_2 NPs-L2-II	nd	nd	nd	nd	6.65	-36	0.18	7.19%

[a] Determined from the uptake at saturation at p/p° = 0.8. It includes external surface and micropores surface. [b] Diameter determined by BJH, it refers to interparticles porosity. Also, micropores of < 2 nm. [c] Hydrodynamic diameters from DLS. [d] EA: elemental analysis, experimental value of N content. [e] Determined by mass loss with TGA (a heating rate of 5 ºC/min from 30 to 800 ºC). [f] Not determined.

First, FTIR were recorded for **Fe_3O_4@SiO_2 NPs-Ln-I** (n = 1, 2) (**Figure 5.11**). The appearance of the C=O absorption at 1657-1658 cm^{-1} supported the grafting of ligand on the surface of the core-shell parent nanoparticles.

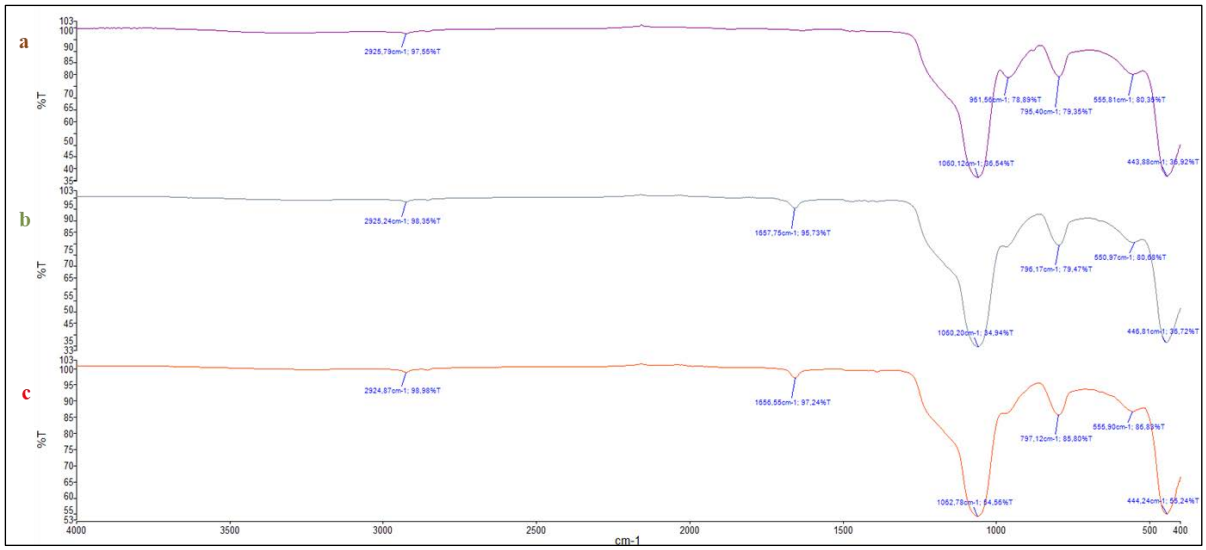

Figure 5.11 FTIR of a) **Fe_3O_4@SiO_2 NPs**, b) **Fe_3O_4@SiO_2 NPs-L1-I** and **Fe_3O_4@SiO_2 NPs-L2-I**

The size monodispersity of the NPs in ethanol was confirmed by DLS measurements. The hydrodynamic diameters of **Fe_3O_4@SiO_2 NPs-L1-I** and **Fe_3O_4@SiO_2 NPs-L2-I** were 216 nm and 237 nm, respectively (**Figure 5.12**).

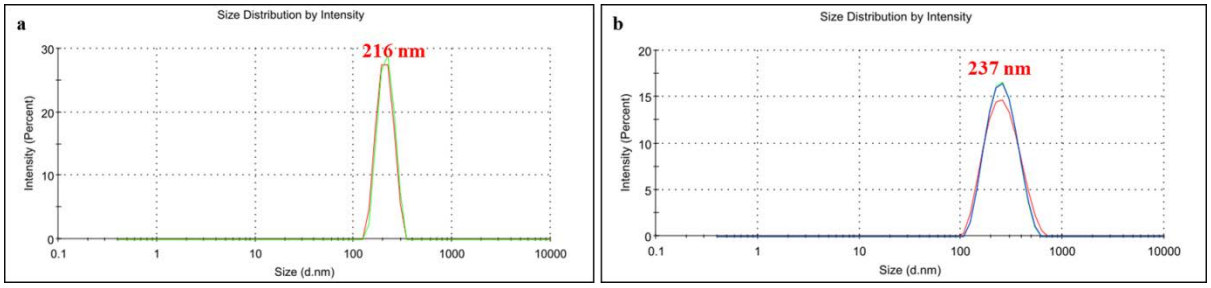

Figure 5.12 DLS of a) **Fe_3O_4@SiO_2 NPs-L1-I** and b) **Fe_3O_4@SiO_2 NPs-L2-I**

Zeta potentials were also measured by using DLS technique (**Figure 5.13**). The NPs were dispersed in distilled water at 1 mg/mL. Compared with **Fe_3O_4@SiO_2 NPs** (ζ = -32 mV, **Figure 5.6b**), the absolute values of ζ-potential for **Fe_3O_4@SiO_2 NPs-Ln-I** (n = 1, 2) are lower (-6 and -13.9 mV, **Figure 5.13**, **a1** and **b1**). This confirms that the silica coating process was effective since the charge surface properties are changed. Conversely, after the removal of Boc and ^{t}Bu groups, the zeta potential of corresponding nanoparticles **Fe_3O_4@SiO_2 NPs-Ln-II** (n = 1, 2) increase again (39 and -36 mV, **Figure 5.13 a2** and **b2**). The ζ potential of **Fe_3O_4@SiO_2 NPs-L1-II** was more negative because of carboxylate functions, **Fe_3O_4@SiO_2 NPs-L2-II** was more positive because of the amino groups liberated upon BOC cleavage, and these amino groups were protonated at this pH.

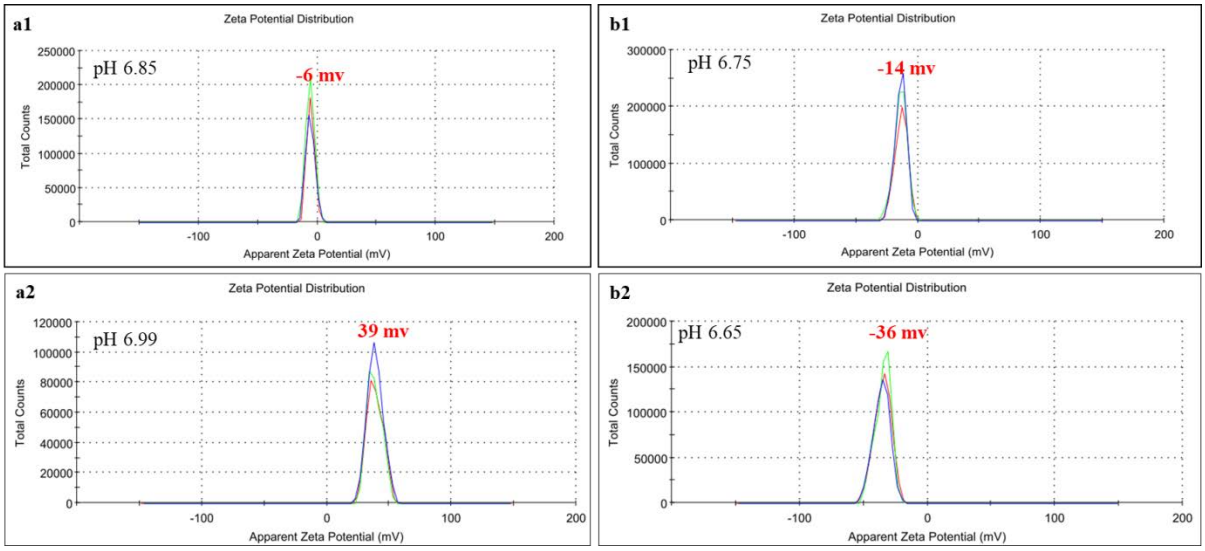

Figure 5.13 Zeta potential of a1) **Fe_3O_4@SiO_2 NPs-L1-I**, a2) **Fe_3O_4@SiO_2 NPs-L1-II** and b1) **Fe_3O_4@SiO_2 NPs-L2-I**, b2) **Fe_3O_4@SiO_2 NPs-L2-II**

The BET analysis gives type IV isotherms with specific surface area of 41 m^2/g for **Fe_3O_4@SiO_2 NPs-L1-I** and 65 m^2/g **Fe_3O_4@SiO_2 NPs-L2-I**. (**Figure 5.14, Table 5.2**). As we mentioned before, maybe the surface of the pores of magnetic core-shell silica nanoparticles is blocked by a layer of microporous silica at 78 K, the pore size given in **Table 5.2** is the interparticles porosity.

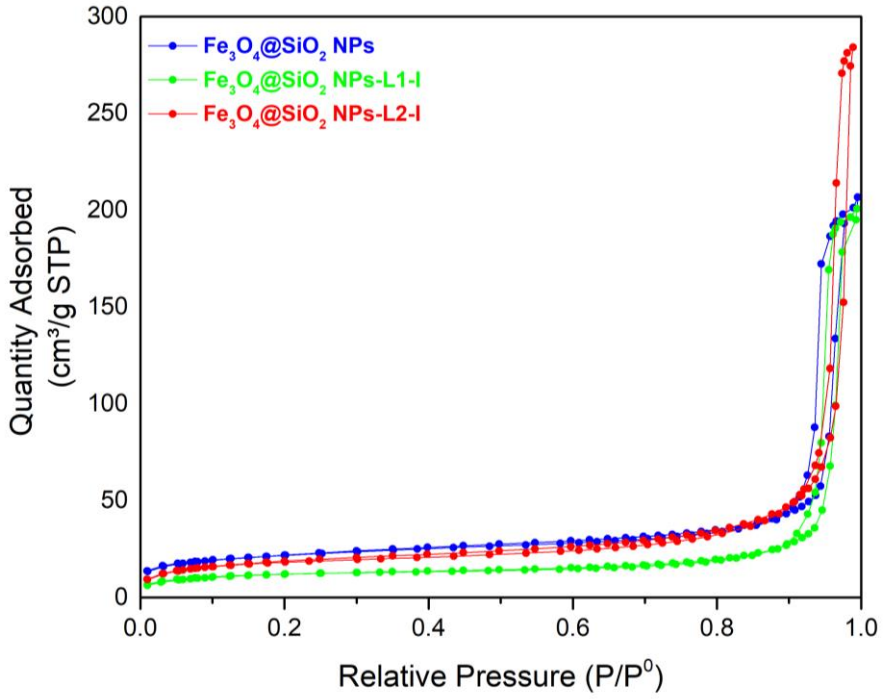

Figure 5.14 N_2-adsorption- desorption analysis of **Fe_3O_4@SiO_2 NPs** and **Fe_3O_4@SiO_2 NPs-Ln-I** (n = 1, 2)

According to the literature, the mass loss observed while heating functionalized magnetic NPs up to 200 °C, usually corresponds to evaporation of absorbed moisture. Further heating up to 800 ºC causes additional mass losses due to phase changes, cracking of residual surface species, decomposition of SiO_2 shell and decomposition/removal of used functional groups.[68-70] TGA analyses of the nanomaterials were performed in order to quantify the amount of the ligand layer with respect to the inorganic core-shell (**Figure 5.15**). We observed in all cases a first mass loss of approximately 1.3-1.8% by heating up to 120 °C due to absorbed moisture, which was also present in the parent non-functionalized core-shell nanoparticles. Compared with the mass loss observed for **Fe_3O_4@SiO_2 NPs** (ca. 9.09%) between 120 and 800 °C (**Figure 5.7**), the increased mass loss in functionalized nanoparticles refers to the amount of surface grafted ligand. The results were the following: **Fe_3O_4@SiO_2 NPs-L1-I**, total mass loss of 14.44%, 5.35% of the nanomaterial corresponds to the ligand (**Figure 5.15 a1**); **Fe_3O_4@SiO_2 NPs-L1-II**, total mass loss of 13.43%; 4.34% of ligand (**Figure 5.15 a2**); **Fe_3O_4@SiO_2 NPs-L2-I**, total mass loss of 16.85%; 7.76% of ligand (**Figure 5.15 b1**); **Fe_3O_4@SiO_2 NPs-L2-II**, total mass loss of 16.28%, 7.19% of ligand (**Figure 5.15 b2**).

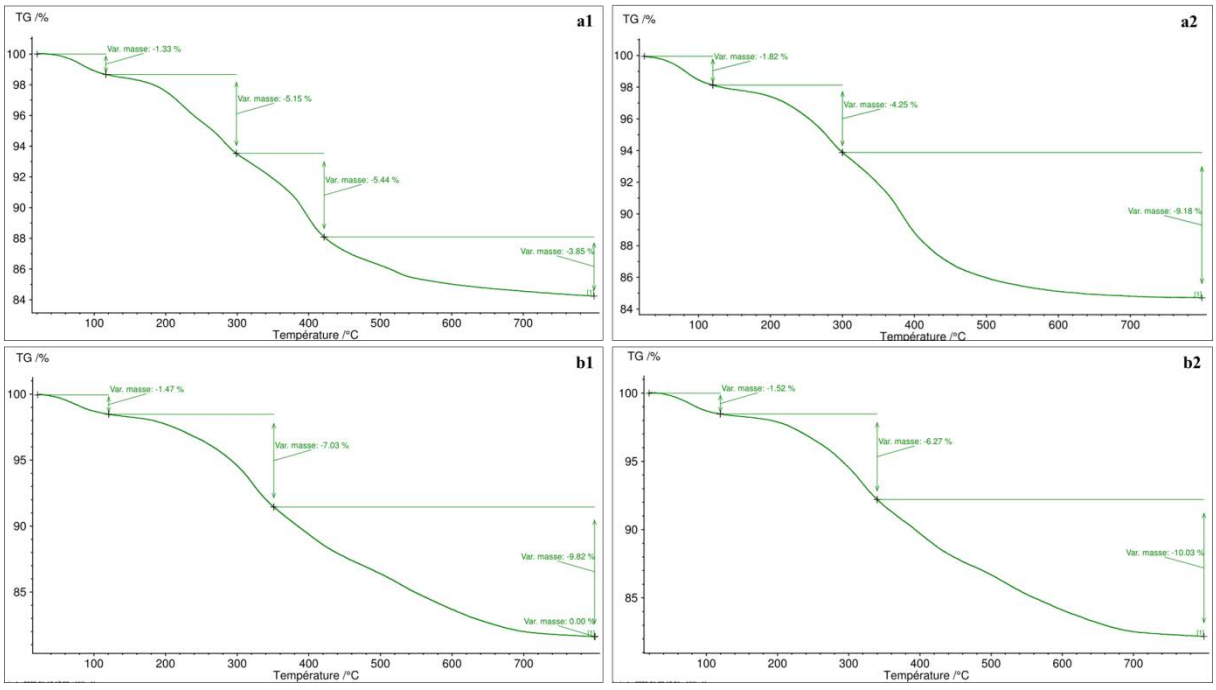

Figure 5.15 TGA analysis of a1) **Fe_3O_4@SiO_2 NPs-L1-I**, a2) **Fe_3O_4@SiO_2 NPs-L1-II** and b1) **Fe_3O_4@SiO_2 NPs-L2-I**, b2) **Fe_3O_4@SiO_2 NPs-L2-II**

Elemental analysis of the functionalized nanoparticles was performed in order to obtain a more precise ligand loading on the surface of **Fe_3O_4@SiO_2 NPs** core-shell composites by the

determination of the content of N. The results obtained from elemental analysis for **Fe_3O_4@SiO_2 NPs-L1-II** (1.46% N, 0.15 mmol ligand/g, 5.26wt%) and for **Fe_3O_4@SiO_2 NPs-L2-II** (1.01% N, 0.18 mmol ligand/g, 8.92wt%) are in accordance with those obtained from TGA analysis.

5.3.4 Adsorption/desorption of heavy metals from aqueous solutions with functionalized magnetic core-shell silica nanoparticles

As we mentioned in the introduction, REEs are used for their specific properties which make them difficult to replace. The recycling of REEs from electronic waste, specifically permanent NdFeB and SmCo magnets as well as NiMH batteries, become economically interesting and should provide a secondary supply of these elements, but they are mixed with other metals (Fe, Ni, Co, …). Thus, in order to recycle the REEs, we must be able to separate them from transition metals, such as Ni and Co, therefore to find a good extractant of these transition metal to purify REEs is quite important.

The prepared magnetic core-shell silica nanoparticles were first studied in the adsorption of Ni^{2+} and Co^{2+} from aqueous solutions at room temperature. The adsorption/desorption experiments of functionalized magnetic core-shell silica nanoparticles are in course at the laboratory of Prof Gulaim Seisenbaeva in Sweden. We present here the first results.

5.3.4.1 Adsorption of transition metal cations (Ni and Co) from aqueous solutions with functionalized magnetic core-shell silica nanoparticles

Adsorption of Ni^{2+} and Co^{2+} by four magnetic nanoparticles was studied, namely **Fe_3O_4@SiO_2 NPs, Fe_3O_4@SiO_2 NPs-L1-II**, **Fe_3O_4@SiO_2 NPs-L2-II** and **Fe_3O_4@SiO_2 NPs-DTPA**. The nanomaterial **Fe_3O_4@SiO_2 NPs-DTPA** was provided by Dr. Mathilde Ménard as the control sample. They were studied in batch experiments at room temperature, where the uptake of these metal cations was evaluated in relation to initial metal concentration and contact time. For isotherm experiments stock solutions of Ni^{2+} and Co^{2+} (50 mM) were prepared using nitrate salts and the final concentrations were adjusted by dilution with milli-q water (varying between 0.5-25 mM). Samples (10 mg) of magnetic nanoparticles (**MNPs**) were mixed with 10 mL of metal cation solution in plastic tubes of 50 mL and put on a shaker for 24 hours. After each experiment, **MNPs** were centrifuged (7000 g) for 10 min and an aliquot (1 mL) was separated to determine the metal concentration in the

remaining solution. The samples were first diluted 5-10 times (depending on the initial metal concentration) and titrated afterwards with EDTA using xylenol orange as an indicator. For each sample the titrations were repeated 3 times, and the average concentration was calculated.

The uptake of metal cation by the magnetic nanoparticles was calculated according to this equation:

$Up=(C_o-C_e)*V/m$

Where: C_o is the initial metal concentration which was also measured by titration

C_e is the equilibrium metal concentration

V is the metal solution volume which was kept constant

m is the NPs weight.

All the magnetic nanoparticles showed similar maximum adsorption capacity (varying between 1-2.16 mmol/g), **Fe_3O_4@SiO_2 NPs** having the lowest capacity for both heavy metals (**Table 5.3**). For both heavy metals, adsorption isotherms were best fit with Langmuir curves, having higher correlation coefficients compared to Freundlich model (**Figure 5.16**).

Table 5.3 Average maximum adsorption capacity for each magnetic nanoadsorbent and heavy metal (mmol/g)

Entry	Sample	Ni	Co
1	**Fe_3O_4@SiO_2 NPs**	1.00	1.00
2	**Fe_3O_4@SiO_2 NPs-L1-II**	2.13	2.00
3	**Fe_3O_4@SiO_2 NPs-L2-II**	1.16	1.33
4	**Fe_3O_4@SiO_2 NPs-DTPA**	2.16	1.44

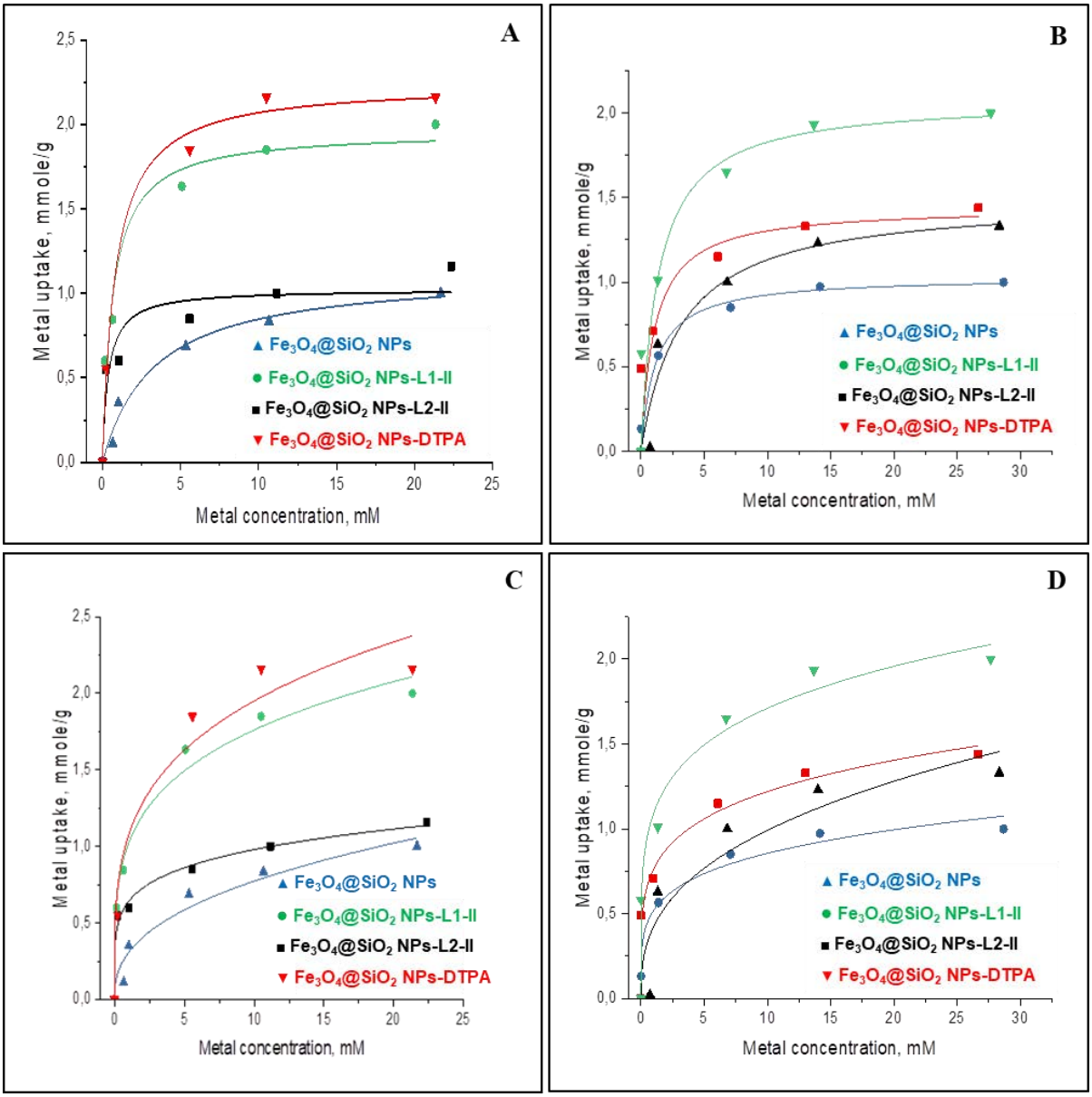

Figure 5.16 Metal adsorption isotherms A, B) Langmuir isotherms for Ni^{2+} and Co^{2+}, respectively; C, D) Freundlich isotherms for Ni^{2+} and Co^{2+}, respectively

For kinetic tests, the magnetic nanoadsorbents (20 mg) were mixed with 20 mL of metal cation solutions (with 10 mM initial metal concentration) and the uptake was measured after set interval of times. For that purpose, an aliquot of 1 mL was separated, diluted 10 times and the remaining metal concentration was evaluated by titration with EDTA and xylenol orange (**Figure 5.17**). The results showed fast uptake at the first 1-2 hours of metal interaction with magnetic nanoparticles, reaching over 70% of the total capacity. Slower uptake was found after these 2 hours and the equilibrium was reached after 5-6 hours.

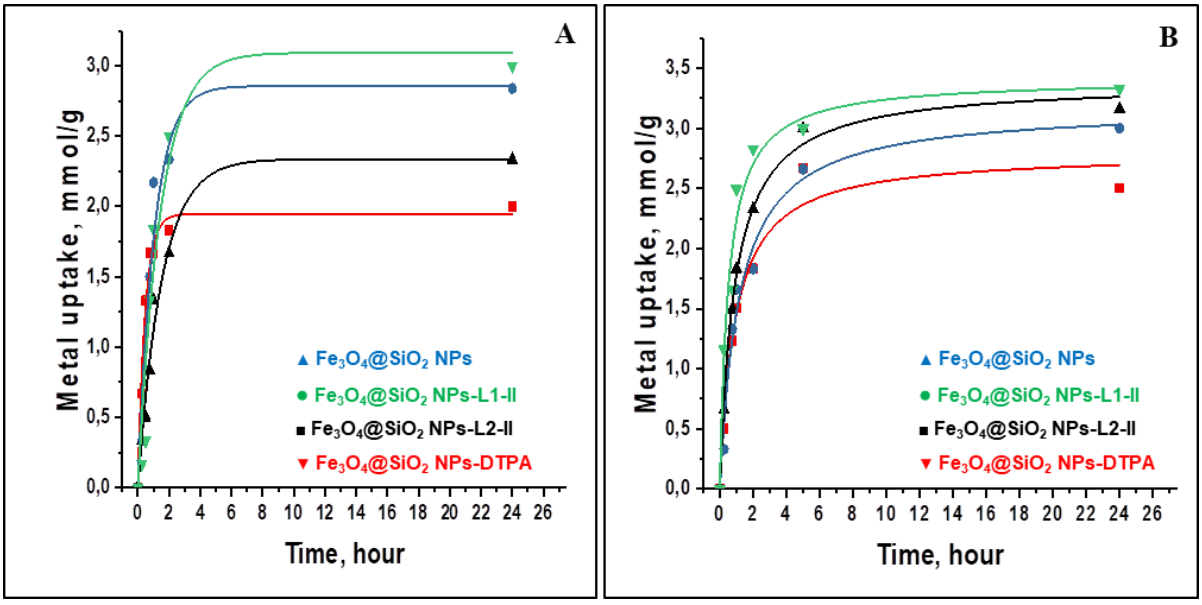

Figure 5.17 Adsorption kinetics of two heavy metals for A) Cobalt, B) Nickel

5.3.4.2 Adsorption/desorption of rare earth ions from aqueous solutions with functionalized magnetic core-shell silica nanoparticles

Due to the sudden worldwide explosion of COVID-19, the research work of some laboratories has been stopped, the other adsorption/desorption experiments of magnetic nanomaterials have also been interrupted temporarily.

5.4 Conclusions

In summary, we have synthesized two silylated cyclen-based ligands presenting *N*-Boc (**L1**) or *tert*-butyl esters groups (**L2**). Then two new functionalized magnetic core-shell nanoparticles **Fe_3O_4@SiO_2 NPs-L1-I** and **Fe_3O_4@SiO_2 NPs-L2-I** have been prepared by a post grafting method consisting of the reaction of **Fe_3O_4@SiO_2 NPs** with the corresponding ligand **Ln** in DMF at 120 °C in the presence of H_2O and Et_3N as catalysts. These nanomaterials were characterized by FTIR, TGA, TEM, BET, DLS, and zeta potential. The TEM images show the mesoporosity of magnetic core-shell silica nanoparticles. The nitrogen sorption analysis reveals low surface areas, a porosity derived mostly from interparticles voids, with the presence of microporous material. Probably the surface of the pores is blocked by a layer of microporous silica at 78 K.

The Boc and *tert*-butyl groups were removed from the materials by treatment with a 5:1 TFA/CH_2Cl_2 solution at room temperature to obtain new functionalized magnetic core-shell nanoparticles **Fe_3O_4@SiO_2 NPs-L1-II** and **Fe_3O_4@SiO_2 NPs-L2-II** containing amino and carboxyl groups, respectively. The efficient removal of Boc and ^{t}Bu groups has been confirmed by zeta potential and TGA analyses.

These magnetic nanomaterials **Fe_3O_4@SiO_2 NPs-Ln-II** (n = 1, 2) have been tested as nanoadsorbents of transition metal cations (Ni^{2+} and Co^{2+}) in aqueous solutions at room temperature. Both nanomaterials showed good maximum adsorption capacities (varying between 1.16-2.13 mmol/g), similar or even better than the model **Fe_3O_4@SiO_2 NPs-DTPA,** specially **Fe_3O_4@SiO_2 NPs-L1-II.**

Unfortunately, the emergence of the **COVID-19** interrupted the experiments of adsorption/ desorption of the rare earth metal ions from aqueous solutions.

5.5 Experimental section

5.5.1 General information

The information corresponding to NMR, MS and elemental analysis is given in ***Section* 2.2.5.1**. The information corresponding to DLS, zeta potential and the nitrogen-sorption measurements (BET surface area, pore size, pore volume) is given in ***Section* 3.5.1**.

From *Institut Charles Gerhardt Montpellier* (France), FTIR, TEM and TGA analyses were performed:

FTIR spectra were recorded in the 4000-400 cm^{-1} range using 32 scans at a nominal resolution of 4 cm^{-1} with a Perkin Elmer 100 FT spectrophotometer equipped with an ATR unit.

TEM images were recorded with JEOL 1200 EXII microscope (JEOL Europe SAS, Croissy Sur Seine, France). For the purpose of TEM analysis, the sample particles were dispersed in ethanol and then dropped onto copper grids covered with porous carbon films.

TGA analyses were performed with a thermal analyser STA 409 Luxx® (Netzsch) in the range 25-800 °C by a heating speed of 5 °C/min.

Materials: Cyclen (CAS 294-90-6, Fluorochem), di-*tert*-butyl dicarbonate (CAS 24424-99-5, Sigma Aldrich), allyl bromide (CAS 106-95-6, Sigma Aldrich), propargyl bromide (CAS 106-96-7, Fluorochem), (3-mercaptopropyl)triethoxysilane (CAS 4420-74-0, Sigma Aldrich), (3-azidopropyl)triethoxysilane (CAS 83315-69-9, Abcr GmbH), iron oxide (CAS 20344-49-4, Sigma Aldrich), oleic acid (CAS 112-80-1, Sigma Aldrich), *n*-docosane (CAS 629-97-0, Acros), oleylamine (CAS 112-90-3, Acros), tetraethyl orthosilicate TEOS (CAS 78-10-4, Sigma Aldrich), cetyltrimethylammonium bromide CTAB (CAS 57-09-0, Sigma Aldrich), pentane (CAS 109-66-0, Fisher), chloroform (CAS 67-66-3, Sigma Aldrich), trifluoroacetic acid (CAS 76-05-1, Fluorochem), triethylamine (CAS 121-44-8, Merck), dichloromethane (CAS 76-09-2, Carlo Erba), ethyl acetate (CAS 141-78-6, VWR), ethanol and acetone (Honeywell).

5.5.2 Synthesis of silylated cyclen-based ligands L1 and L2

5.5.2.1 Synthesis of tri-*tert*-butyl 10-((1-(3-(triethoxysilyl)propyl)-1*H*-1,2,3-triazol-4-yl)methyl)-1,4,7,10-tetraazacyclododecane-1,4,7-tricarboxylate

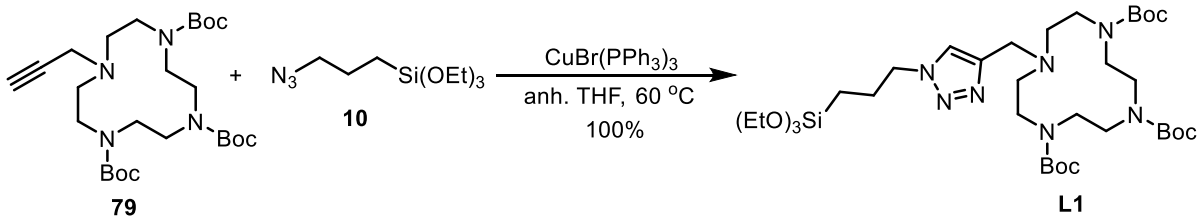

To a dry, 100 mL Schlenk flask equipped with a stir bar and under Argon atmosphere, tri-*tert*-butyl 10-(prop-2-yn-1-yl)-1,4,7,10-tetraazacyclododecane-1,4,7-tricarboxylate **79** (763.5 mg, 1.50 mmol), $CuBr(PPh_3)_3$ (69.5 mg, 0.075 mmol) and anhydrous THF (15 mL) were added. Then, (3-azidopropyl)triethoxysilane **10** (380.9 mg, 1.54 mmol) was added by using a syringe. The resulting mixture was stirred at 60 ºC (Argon atmosphere) for 48 h. Then, the solvent was evaporated under reduced pressure and the crude product was obtained as colorless solid (1.16 g, 100% yield) without any purification. **^{1}H NMR (360 MHz, $CDCl_3$) δ (ppm)**: 7.69-7.64 (m, 1H), 4.32 (t, *J* = 7.2 Hz, 2H), 3.90 (s, 2H), 3.82 (q, *J* = 7.2 Hz, 6H), 3.55 (s, 4H), 3.36 (br s, 8H), 2.80-2.62 (m, 4H), 2.04-1.96 (m, 2H), 1.46-1.43 (m, 27H), 1.21 (t, *J* = 7.2 Hz, 9H), 0.58 (t, *J* = 7.2 Hz, 2H). **IR *v* (ATR) (cm^{-1})**: 2971.9, 2926.3, 1682.4, 1457.9, 1391.0, 1153.8, 1074.3, 943.0, 643.0. **MS (ESI)** m/z: 279.1, 473.3, 721.4, 730.5, 758.5; **HRMS (ESI)** m/z $[M + H]^+$ calcd for $C_{35}H_{67}N_7O_9Si$: 758.4842, found: 758.4835.

5.5.2.2 Synthesis of tri-*tert*-butyl 2,2',2''-(10-allyl-1,4,7,10-tetraazacyclododecane-1,4,7-triyl)triacetate

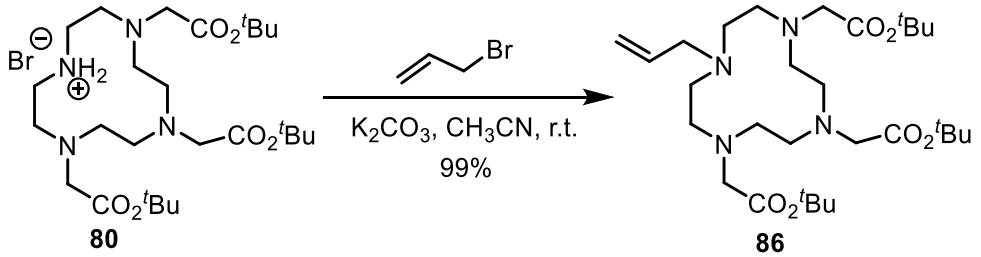

To a solution of hydrobromide **80** (2.51 g, 4.22 mmol) in acetonitrile (40 ml), potassium carbonate (1.46 g, 10.56 mmol) was added and the suspension was stirred for 30 min at room temperature. The mixture was placed in an ice-bath and allyl bromide (511.1 mg, 4.22 mmol)

was added dropwise. The ice-bath was removed, and the reaction mixture was allowed to reach room temperature and stirred overnight at room temperature. The inorganic solid was removed by filtration, and the solvent evaporated under reduced pressure. The resulting oil was dissolved in hot toluene and filtered to remove the inorganic residue. After evaporation of the solvent under reduced pressure the product was obtained as a yellow oil (2.32 g, 99 %). **^{1}H NMR (360 MHz,** $CDCl_3$) δ (ppm): 5.91-5.83 (m, 1H), 5.18-5.09 (m, 2H), 3.28- 3.31 (m, 6H), 3.06 (d, J = 3.6 Hz, 2H), 2.83 (s, 12H), 2.62 (t, J = 7.2 Hz, 4H), 1.45 (s, 27H). **^{13}C NMR (91 MHz, $CDCl_3$) δ (ppm):** 171.2, 136.1, 117.2, 80.7, 59.0, 56.7, 56.3, 52.1, 51.9, 51.7, 28.2. **MS (ESI) m/z**: 387.2, 443.3, 499.3, 553.4, 555.4; **HRMS (ESI) m/z** $[M]^+$ calcd for $C_{29}H_{54}N_4O_6$: 554.4146, found: 554.4099.

5.5.2.3 Synthesis of tri-*tert*-butyl 2,2',2''-(10-(3-((3-(triethoxysilyl)propyl)thio)propyl)-1,4,7,10-tetraazacyclododecane-1,4,7-triyl)triacetate

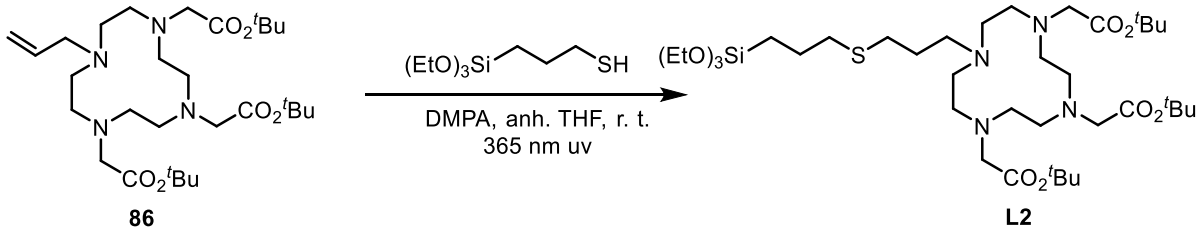

In a 50 mL Schlenk tube under nitrogen, tri-*tert*-butyl 2,2',2''-(10-allyl-1,4,7,10-tetraazacyclododecane-1,4,7-triyl)triacetate **86** (554.8 mg, 2.06 mmol) and 2,2-dimethoxy-1,2-diphenylethanone (105.3 mg, 0.41 mmol) were dissolved in anhydrous THF (10.0 mL). Then (3-mercaptopropyl)triethoxysilane (489.9 g, 2.06 mmol) was added and the stirred mixture was irradiated with a UV lamp at 365 nm under argon atmosphere for 72 h. Then, the solvent was removed under reduced pressure and the desired product **L2** was obtained as yellow oil (1.62 g, 99% yield)**. ^{1}H NMR (360 MHz, $CDCl_3$) δ (ppm)**: 3.93-3.79 (m, 6H), 3.77-3.73 (m, 2H), 3.55-3.00 (m, 8H), 2.82-2.54 (m, 18H), 1.87-1.86 (m, 2H), 1.85-1.71 (m, 2H), 1.46 (s, 27H), 1.25-1.21 (m, 9H), 0.74 (t, J = 7.2 Hz, 2H). **IR ν (ATR) (cm^{-1})**: 2974.3, 1721.8, 1454.6, 1366.6, 1251.0, 1147.1, 1102.9, 956.8, 782.8, 474.5. **MS (ESI)** m/z: 403.3, 459.3, 486.3, 515.4, 516.4, 534.4, 555.4, 621.4, 661.5, 793.5; **HRMS (ESI)** m/z $[M]^+$ calcd for $C_{38}H_{76}N_4O_9SSi$: 793.5175, found: 793.5150.

5.5.3 Preparation of functionalized magnetic core-shell silica nanoparticles

5.5.3.1 Preparation of Fe_3O_4 NCs (Fe_3O_4 nanocrystals)

A mixture of hydrated iron oxide (FeO(OH), 180 mg), oleic acid (3.2 g), and *n*-docosane (5.0 g) was prepared in a 100 mL two neck round bottom flask and stirred under vacuum at 100 °C for 30 minutes. Then, the mixture was heated at 100 °C under argon atmosphere for another 30 min and, after that time, the temperature was increased to 340 °C. As soon as the mixture reached 340 °C, the reaction was conducted for 1 h 30 min. The solution was cooled down during 1 h without stirring. The resulting black solid was dissolved in pentane (15 mL), mixed with an ether/ethanol solution (30 mL, 2:1 v:v), and centrifugated 10 minutes at 20000 rpm. The organic black solution was removed and the solid NCs were redispersed in pentane (2 mL), washed with the ether/ethanol solution (30 mL, 2:1 v:v) and then centrifugated. Finally, an ether/ethanol solution (30 mL, 1:1 v:v) was used to wash the sample again. The supernatant was removed and the **Fe_3O_4 NCs** were stored in chloroform (15 mL) and stabilized by addition of oleylamine (200 µL).

5.5.3.2 Preparation of Fe_3O_4@SiO_2 NPs

Cetyltrimethylammonium bromide (2.0 g, CTAB) was dissolved in distilled water (250 mL), the mixture was stirred at 70 °C during 45 minutes at 1000 rpm in a 1.0 L flat bottom flask. Then the mixture was cooled down to 40 °C, **Fe_3O_4 NCs** dispersed in chloroform (5 mL of the solution obtained in 5.5.3.1) were added to the mixture and the solution was stirred at this temperature for 30 min, and then at 70 °C for 40 min to stabilize the NCs in the micelles. Finally, distilled water (300 mL) was added to the solution, followed by the addition of sodium hydroxide (300 µL of a 2 M aqueous solution), tetraethoxysilane (7.5 mL, TEOS) and ethyl acetate (12.5 mL, EtOAc), and the condensation process was conducted for 3 h at 70 ºC under stirring (700 rpm). Afterwards, the solution was cooled at room temperature while stirring; fractions were gathered in polypropylene tubes and collected by centrifugation during 15 minutes at 20000 rpm. Each sample was then extracted four times with an alcoholic solution of ammonium nitrate (6 g/L), and washed successively with ethanol, acetone, and ethanol. Each extraction and washing involved a sonication step of 15 minutes in order to remove the CTAB surfactant. The as-prepared material was dried under an air flow for few hours. **IR *ν* (ATR) (cm^{-1})**: 2979.6, 1067.8, 963.6, 797.2, 451.3. **BET:** S_{BET} = 75 m^2g^{-1}, V_{pore} = 0.05 cm^3g^{-1}, interparticles porosity = 17.1 nm. **TGA** (air, 5 °C/min, 20-800 °C) loss mass 14.0%. **Zeta Potential**: ζ = -32 mV, pH = 7.24. **DLS**: 183 nm.

5.5.3.3 Preparation of Fe_3O_4@SiO_2 NPs-Ln-I

In a 50 mL round-bottom flask equipped with a Dean-Stark apparatus, ligand **Ln** (0.1 mmol), **Fe_3O_4@SiO_2 NPs** (100 mg), H_2O (500 μL) and Et_3N (25 μL) were sonicated for 2 h, and then the mixture was heated in DMF at 120 ºC (10 mL) for 24 h. After this time, the suspension was centrifugated (20000 rpm at 25 °C for 15 min). The solid was washed successively with H_2O (2 × 30 mL), ethanol (2 × 30 mL) and acetone (2 × 30 mL) (sonication for 10 min, 10 min for centrifugation), dried under vacuum, and finally crushed to give the grafted material **Fe_3O_4@SiO_2 NPs-Ln-I** as black solid.

Fe_3O_4@SiO_2 NPs-L1-I: IR *ν* (ATR) (cm^{-1}): 2925.2, 2854.4, 1657.8, 1060.2, 966.4, 796.2, 551.0, 446.8. **BET:** S_{BET} = 41 m^2g^{-1}, V_{pore} = 0.03 cm^3g^{-1}, interparticles porosity = 30.5 nm. **TGA** (air, 5 °C/min, 20-800 °C) loss mass 15.8%. **Zeta Potential**: ζ = -6 mV, pH = 6.85. **DLS**: 216 nm.

Fe_3O_4@SiO_2 NPs-L2-I: **IR *ν* (ATR) (cm^{-1})**: 2924.9, 2852.8, 1656.6, 1062.8, 967.2, 797.1, 555.9, 444.2. **BET:** S_{BET} = 65 m^2g^{-1}, V_{pore} = 0.05 cm^3g^{-1}, interparticles porosity = 26.9 nm **TGA** (air, 5 °C/min, 20-800 °C) loss mass 15.8%. **Zeta Potential**: ζ = -14 mV, pH = 6.75. **DLS**: 237 nm.

5.5.3.4 Preparation of Fe_3O_4@SiO_2 NPs-Ln-II

The **Fe_3O_4@SiO_2 NPs-Ln-I** were dissolved in TFA/CH_2Cl_2 (5:1) solution, the mixture was stirred at room temperature for 60 minutes. Then the NPs were collected by centrifugation (20000 rpm at 25 °C for 10 min). The material **Fe_3O_4@SiO_2 NPs-L1-II** was washed successively with EtOH (2 × 30 mL), saturated $NaHCO_3$ solution (2 × 30 mL), distilled water (2 × 30 mL), acetone (2 × 30 mL) and EtOH (2 × 30 mL)**.** The material **Fe_3O_4@SiO_2 NPs-L2-II** was washed successively with EtOH (2 × 30 mL), acetone (2 × 30 mL) and EtOH (2 × 30 mL). Finally, the new materials **Fe_3O_4@SiO_2 NPs-Ln-II** were dried under vacuum for several hours.

Fe_3O_4@SiO_2 NPs-L1-II: **IR *ν* (ATR) (cm^{-1})**: 2925.4, 2852.8, 1656.2, 1081.3, 966.9, 797.3, 553.8, 447.5. **TGA** (air, 5 °C/min, 20-800 °C) loss mass 15.3%. **Zeta Potential**: ζ = 39 mV, pH = 6.99. **Elemental analysis:** 7.33%C, 1.63%H, 1.46% N.

Fe_3O_4@SiO_2 NPs-L2-II: **IR *ν* (ATR) (cm^{-1})**: 2925.1, 2855.4, 1658.0, 1063.4, 964.7, 797.4, 554.8, 450.7. **TGA** (air, 5 °C/min, 20-800 °C) loss mass 17.8%. **Zeta Potential**: ζ = -36 mV, pH = 6.65. **Elemental analysis:** 9.05%C, 1.84%H, 1.01% N, 1.76%S.

5.6 References

1. IUPAC: *Nomenclature of inorganic chemistry* - IUPAC *recommendations 2005.* Cambridge, UK: International Union of Applied and Pure Chemistry (IUPAC), **2005**.
2. J. M. Klinger, *Extr. Ind. Soc.* **2015**, *2*, 572.
3. A. Tsamis, M. Coyne, *Recovery of Rare Earths from Electronic Wastes: An Opportunity for High-Tech SMEs*; Centre for Strategy and Evaluation Services LLP: Brussels, Belgium, **2015**.
4. European Rare Earths Competency Network (ERECON). *Strengthening the European Rare Earths Supply-Chain Challenges and Policy Options*; European Comission: Brussels, Belgium, **2014**.
5. Z. M. Migaszewski, A. Gałuszka, *Crit. Rev. Environ. Sci. Technol.* **2015**, *45*, 429.
6. K. M. Goodenough, F. Wall, D. Merriman, *Nat. Resour. Res.* **2018**, *27*, 201.
7. D. A. Atwood, *The Rare Earth Elements. Fundamentals and Applications.* John Wiley & Sons, West Sussex, **2012**.
8. K. Binnemans, P. T. Jones, B. Blanpain, T. van Gerven, Y. Yang, A. Walton, M. Buchert, *J. Clean. Prod.* **2013**, *51*, 1
9. A. Golev, M. Scott, P. D. Erskine, S. H. Ali, G. R. Ballantyne, *Resour. Policy* **2014**, *41*, 52.
10. N. T. Nassar, X. Due, T. E. Graedel, *J. Ind. Ecol.* **2015**, *19*, 1044.
11. T. Dutta, K. H. Kim, M. Uchimiya, E. E. Kwon, B. H. Jeon, A. Deep, S.T. Yun, *Environ. Res.* **2016**, *150*, 182.
12. R. S. Pell, F. Wall, X. Yan, G. Bailey, *Resour. Policy* **2019**, *62*, 472.
13. C. E. D. Cardoso, J. C. Almedia, C. B. Lopes, T. Trindade, C. Vale, E. Pereira, *Nanomaterials* **2019**, *9*, 814.
14. T. Kegl, A. Košak, A. Lobnik, Z. Novak, A. K. Kralj, I. Ban, *J. Hazard. Mater.* **2020**, *386*, 121632.
15. R. M. Izatt, S. R. Izatt, R. L. Bruening, N. E. Izatt, B. A. Moyer, *Chem. Soc. Rev.* **2014**, *43*, 2451.
16. X. Li, F. Zhang, D. Zhao, *Nano Today* **2013**, *8*, 643.
17. F. Sadri, A. M. Nazari, A. Ghahreman, *J. Rare Earth* **2017**, *35*, 739.
18. Y. Zhang, W. Wei, G. K. Das, T. T. Y. Tan, *J. Photochem. Photobiol. C: Photochem. Rev.* **2014**, *20*, 71.
19. P. Zhang, L. Zhang, J. Tang, *Dalton Trans.* **2015**, *44*, 3923.
20. A. R. Chakhmouradlan, F. Wall, *Elements* **2012**, *8*, 333.
21. N. A. Manchen, B. Sprecher, G. Bailey, J. Ge, A. Tukker, *Resour. Conserv. Recy.* **2019**, *142*, 101.
22. L. Shen, N. Wu, S. Zhong, L. Gao, *J. Resour. Ecol.* **2017**, *8*, 213.
23. S. Zhang, *Int. Bus. Manage.* **2013**, *6*, 21.
24. B. Zhou, Z. Li, Y. Zhao, C. Zhang, Y. Wei, *Gospod. Surowcami Min.* **2016**, *32*, 29.
25. B. Zhou, Z. Li, C. Chen, *Minerals* **2017**, *7*, 203.
26. K. Binnemans, P. T. Jones, T. Müller, L. Yurramendi, *J. Sustain. Metall.* **2018**, *4*, 126.
27. K. Binnemans, P. T. Jones, *J. Sustain. Metall.* **2015**, *1*, 29.
28. N. Haque, A. Hughes, S. Lim, C. Vernon, *Resources* **2014**, *3*, 614.
29. D. Dupont, W. Brullot, M. Bloemen, T. Verbiest, K. Binnemans, *ACS Appl. Mater. Interfaces* **2014**, *6*, 4980.
30. C. Gok, J. Radioanal. *Nucl. Chem.* **2014**, *301*, 641.
31. R. M. Ashour, A.F. Abdel-Magied, A. A. Abdel-Khalek, O. S. Helaly, M. M. Ali, *J. Environ. Chem. Eng.* **2016**, *4*, 3114.

32. R. M. Ashour, A. Abdel-Khalek, M. M. Ali, F. Abdel-Magied, *Chem. Technol.: Indian J.* **2016**, *11*, 100.
33. R. M. Ashour, R. El-Sayed, A. F. Abdel Magied, A. A. Abdel Khalek, M. M. Ali, K. Forberg, A. Uheida, M. Muhammed, J. Dutta, *Chem. Eng. J.* **2017**, *327*, 286.
34. S. Yang, P. Zong, X. Ren, Q. Wang, X. Wang, *ACS Appl. Mater. Interfaces* **2012**, *4*, 6891.
35. D. Wu, Y. Sun, Q. Wang, *J. Hazard. Mater.* **2013**, *260*, 409.
36. D. Dupont, J. Luyten, M. Bloemen, T. Verbiest, K. Binnemans, *Ind. Eng. Chem. Res.* **2014**, *53*, 15222.
37. C. Basualto, J. Gaete, L. Molina, F. Valenzuela, C. Yañez, J. F. Marco, *Sci. Technol. Adv. Mater.* **2015**, *16*, 035010.
38. S. N. Almeida, H. E. Toma, *Hydrometallurgy* **2016**, *161*, 22.
39. E. Liu, X. Zheng, X. Xu, F. Zhang, E. Liu, Y. Wang, C. Li, Y. Yan, *New J. Chem.* **2017**, *41*, 7739.
40. J. Li, A. Gong, F. Li, L. Qiu, W. Zhang, G. Gao, Y. Liu, J. Li, *RSC Adv.* **2018**, *8*, 39149.
41. L. Molina, J. Gaete, I. Alfaro, V. Ide, F. Valenzuela, J. Paada, C. Basualto, *J. Mol. Liq.* **2019**, *275*, 178.
42. A. Miraoui, M. A. Didi, D. Villemin, J. Radioanal. *Nucl. Chem.* **2016**, *307*, 963.
43. Y. J. Zhang, Z. M. Zhang, S. C. Xu, L. M. Yu, Y. Z. Long, Q. W. Tang, *RSC Adv.* **2016**, *6*, 6623.
44. T. Kegl, A. Košak, A. Lobnik, I. Ban, *Materials* **2019**, *12*, 1294.
45. T. Kegl, I. Ban, A. Lobnik, A. Košak, *J. Hazard. Mater.* **2019**, *378*, 120764.
46. Y. Wang, H. Katepalli, T. Gu, T.A. Hatton, Y. Wang, *Langmuir* **2018**, *34*, 2674.
47. S. U. Yesiller, A. E. Eroğlu, T. Shahwan, *J. Ind. Eng. Chem.* **2013**, *19*, 898.
48. H. Zhang, R.G. McDowell, L.R. Martin, Y. Qiang, *ACS Appl. Mater. Interfaces* **2016**, *8*, 9523.
49. S. Banerjee, N. P. Kumar, A. Srinivas, S. Roy, *J. Hazard. Mater.* **2019**, *375*, 216.
50. M. B. Gawande, A. Goswami, T. Asefa, H. Guo, A. V. Biradar, D. L. Peng, R. Zboril, R. S. Varma, *Chem. Soc. Rev.* **2015**, *44*, 7540.
51. S. Wei, Q. Wang, J. Zhu, L. Sun, H. Lin, Z. Guo, *Nanoscale* ***2011***, ***3***, 4474.
52. H. L. Ding, Y. X. Zhang, S. Wang, J. M. Xu, S. C. Xu, G. H. Li, *Chem. Mater.* **2012**, *24*, 4572.
53. S. Iftekhar, V. Srivastava, S.B. Hammouda, M. Sillanpää, *Carbohydr. Polym.* **2018**, *194*, 274.
54. A. A. Galhoum, M. G. Mahfouz, S.T. Abdel-Rehem, N. A. Gomaa, A. A. Atia, T. Vincent, E. Guibal, *Cellulose* **2015**, *22*, 2589.
55. J. F. Gargari, H. S. Kalal, A. Shakeri, A. Khnachi, *J. Colloid Interface Sci.* **2017**, *505*, 745.
56. T. Ogata, H. Narita, M. Zanaka, *Hydrometallurgy* **2015**, *152*, 178.
57. J. Lemire, J. J. Harrison, R. J. Turner, *Nat. Rev. Microbiol.* **2013**, *11*, 371.
58. M. Saito, S. Kawaharasaki, K. Ito, S. Yamada, K. Hayamizu, S. Seki, *RSC Adv.* **2017**, *7*, 14528.
59. P. D. Bernardo, A. Melchior, M. Tolazzi, P. L. Zanonato, *Coord. Chem. Rev.* **2012**, *256*, 328.
60. A. M. Fedosseev, M. S. Grigoriev, N. A. Budantseva, D. Guillaumont, C. L. Naour, E. Simoni, C. D. Auwer, P. Moisy, *Comptes Rendus Chim.* **2010**, *13*, 839.
61. P. J. Panak, A. Geist, *Chem. Rev.* **2013**, *113*, 1199.
62. V. V. Rostovtsev, L. G. Green, V. V. Fokin, K. B. Sharpless, *Angew. Chem. Int. Ed*. **2002**, *41*, 2596.
63. M. Meldal, C. W. Tornøe, *Chem. Rev*. **2008**, *108*, 2952.
64. B. Jagadish, G. L. Brickert-Albrecht, G. S. Nichol, E. A. Mash, N. Raghunand, *Tetrahedron Lett.* **2011**, *52*, 2058.
65. A. K. R Junker, M. Tropiano, S. Faulkner, T. J. Sørensen, *Inorg. Chem.* **2016**, *55*, 12299.

66. S. Dib, M. Boufatit, S. Chelouaou, F. Sadi-Hassaine, J. Croissant, L. Long, L. Raehm, C. Charnay, J. -O. Durand, *RSC Adv.* **2014**, *4*, 24838.
67. M. Ménard, F. Meyer, C. Affolter-Zbaraszczuk, M. Rabineau, A. Adam, P. D. Ramirez, S. Bégin-Colin, D. Mertz, *Nanotechnology* **2019**, *30*,174001.
68. M. Aliahmad, N. N. Maghaddan, *Materials Science-Poland*, **2013**, *31*, 264.
69. S. Yoon, *J. Magnetics* **2014**, *19*, 323.
70. S. D. Topel, E. P. Legaria, C. Tiseanu, J. Rocha, J. M. Nedelec, V. G. Kessler, G. A. Seisenbaeva, *J. Nanopart. Res.* **2014**, *16*, 2783.

CHAPTER 6

CONCLUSIONS AND OUTLOOK

CHAPTER 6

CONCLUSIONS AND OUTLOOK

Nanotechnology is rapidly sweeping through all vital fields of science and technology such as electronics, aerospace, defense, medicine and catalysis. This involves the design, synthesis, characterization, and application of materials and devices on the nanometer scale. At the nanoscale, physical, chemical, and biological properties differ from the properties of individual atoms and molecules of bulk matter. Specifically, the design and development of silica-based nanomaterials have captivated the attention of several researchers worldwide. The applications of organosilicas were still limited by the lack of control on the morphology and particle size. The ability to control both the size and morphology of the material and to obtain nano-sized silica particles broadened the spectrum of applications of mesoporous organosilicas and/or improved their performances. This doctoral thesis has been mainly focused on the elaboration of functionalized silica-based nanoparticles for various applications in catalysis, nanomedicine and rare earth metal recovery.

We have presented an introduction to different types of silica nanoparticles, such as mesoporous silica nanoparticles (MSNs), mesoporous organosilica nanoparticles (MONs), periodic mesoporous organosilica nanoparticles (PMO NPs) and magnetic core-shell silica nanoparticles, from definition to synthesis, characterization and applications. Although remarkable efforts have been made on the preparation and application of novel organosilica NPs, better control of size, shape, porosity, and significant improvements in their physicochemical properties remains yet a major challenge in order to broaden the scope of applications (**Chapter 1**).

We have prepared and fully characterized mesoporous silica nanoparticles derived from mono- and bis-silylated proline-valinol amides by both post-grafting and co-condensation methods. We have evaluated the activity of these nanomaterials as recyclable catalysts in the asymmetric aldol reaction. The best organocatalysts are those derived from the monosilylated precursor, observing good diastereo- and enantiomeric ratios with a simple and environmentally friendly optimized protocol (water, 0 °C, absence of cocatalyst). The nanocatalyst was easily recovered by centrifugation and recycled up to six runs without loss of activity and selectivity. The use of organosilica nanoparticles reduces the problems of

diffusion and low reaction rates encountered with bulk organosilicas. To the best of our knowledge, this is the first report on the obtention of functionalized mesoporous silica nanoparticles by co-condensation procedures with a chiral precursor of a certain structural complexity and the first report of asymmetric induction on the direct aldol reaction achieved by chiral organocatalysts based on mesoporous silica nanoparticles (**Chapter 2**). *These promising results open the way to the future design and development of more recyclable organocatalysts based on silica nanoparticles for other useful asymmetric organic reactions.*

We have performed some studies aimed to the use of organosilica nanoparticles as recyclable catalytic systems for the asymmetric fluorination and trifluoromethylation reactions. Unfortunately, we did not succeed in our purposes. *Thus, the design of other recyclable catalysts for the enantioselective α-fluorination or α-trifluoromethylation of carbonyl compounds remains a challenge for the future, as this is a subject barely explored* (**Chapter 2**).

A series of mixed periodic mesoporous organosilica nanoparticles (mixed PMO NPs) possessing Boc and t*ert*-butyl ester groups have been prepared and fully characterized as potential HIFU (High Intensity Focused Ultrasound) responsive agents. In addition, two pure PMO NPs have also been synthesized without any other source of silica. All these nanomaterials were expected to release CO_2 and/or isobutene from the temperature-sensitive COO^tBu group (Boc group) under HIFU stimulation. We have found that the Boc group in these nanomaterials was more stable than expected, as no decomposition of this group occurred before 120 °C by thermogravimetric analysis (TGA). The Boc group could not be removed under HIFU conditions at 80 ºC, requiring the addition of acid. *But the concept is nevertheless promising for future contrast agents for HIFU based theraphies. Precursors with more electrophilic Boc groups and the introduction of carboxylic acid functions in PMO NPs can be considered. On the other hand, the mixed PMO NPs bearing acidic and coordinating carboxyl groups resulting from the tert-butyl ester hydrolysis would be very relevant for potential applications in catalysis or in nanomedicine for pH-triggered drug delivery* (**Chapter 3**).

We have performed the covalent attachment of three carboxyl-containing non-steroidal anti-inflammatory drugs (NSAIDs) (salicylic acid, (*S*)-ibuprofen and diclofenac) on mesoporous and non-porous silica nanoparticles through an amide functional group by using both grafting and co-condensation procedures. Moreover, the one-step coating of cotton fabrics with silica

nanoparticles functionalized with such anti-inflammatory agents has been found to increase the roughness of the surface, providing hydrophobicity to the modified fabrics. This property has been enhanced by the addition of fluorinated alkyl silanes (FAS) in the co-condensation process to form the coating solution. Characterization of the functionalized nanoparticles and coated cotton textiles has been accomplished by microscopic and spectroscopic techniques. The treatment of anti-inflammatory functionalized nanoparticles and coated cotton fabrics with model proteases and leukocytes from rat blood have resulted in the *in situ* release of the drug by the selective enzymatic cleavage of the amide bond (detection by GC-MS and quantification by UV-Vis). Topical cutaneous applications in wound dressings and cream formulations for the acceleration of wound healing are envisaged (**Chapter 4**). *Extension of this work to the covalent functionalization of silica nanoparticles with microbicides and with antifungals for the obtention of modified cotton fabrics can be envisaged.*

We have synthesized and characterized two new functionalized magnetic core-shell mesoporous silica nanoparticles as novel adsorbents for the specific and selective recovery of different rare earth elements (REEs) from wastewater. These nanomaterials contain cyclen-based ligands with coordinating amino and/or carboxyl groups. These magnetic nanomaterials have been tested as nanoadsorbents of transition metal cations (Ni^{2+} and Co^{2+}) in aqueous solutions. Both nanomaterials showed good adsorption capacities. *They will be tested soon in the adsorption/desorption of REs ions (specifically RE^{3+}) for their removal and recovery from aqueous solutions* (**Chapter 5**).

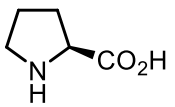

1

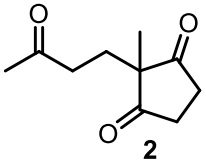

2

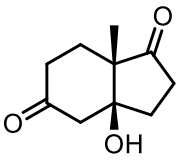

3

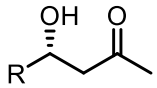

4a 4-NO_2-Ph, **4b** 2-naphthyl
4c Ph, **4d** ^{i}Pr, **4e** ^{t}Bu, **4f** ^{i}PrCH$_2$

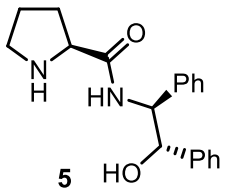

5

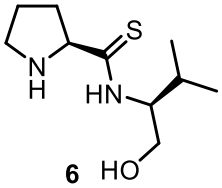

6

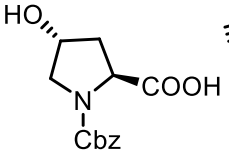

7

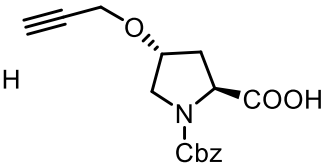

8

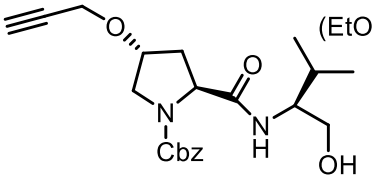

9

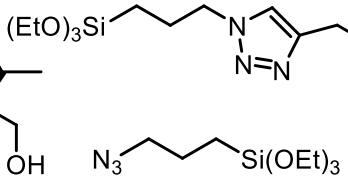

10

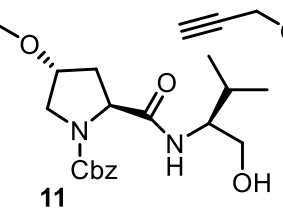

11

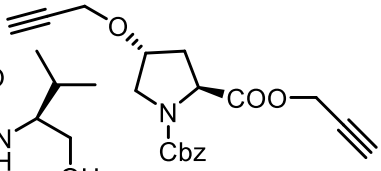

12

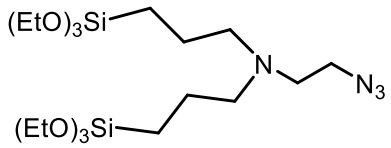

13

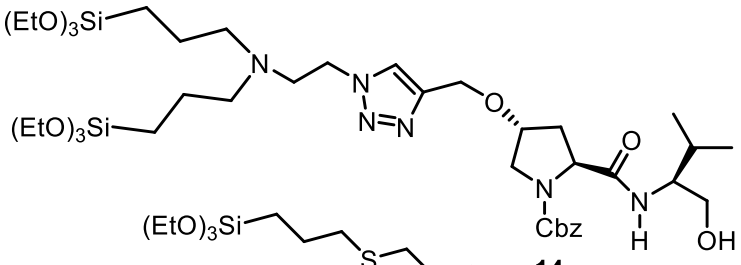

14

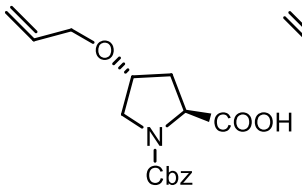

15

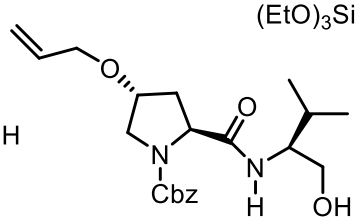

16

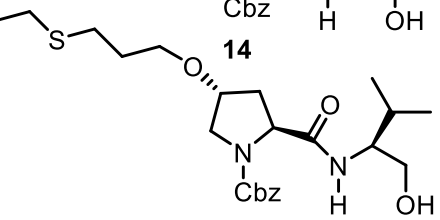

17

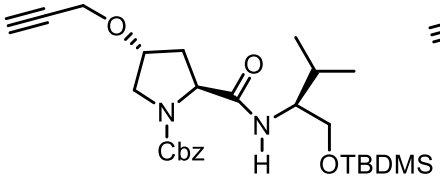

18

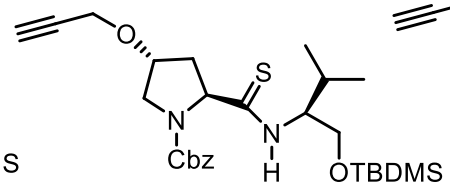

19

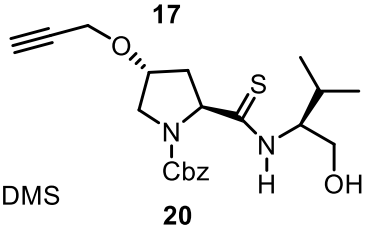

20

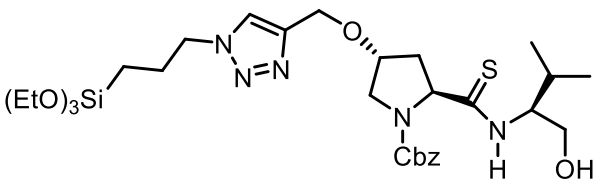

21

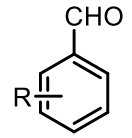

22a: R = 4-NO_2
22b: R = 2-NO_2
22c: R = 2,4-NO_2
22d: R = 4-Cl
22e: R = 4-F
22f: R = 4-Br
22g: R = 2-Cl
22h: R = 2,4-Cl
22i: R = 4-CF_3

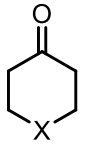

23a: X = CH_2
23d: X = O

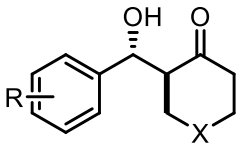

24xy
x = a, d ; y = a-i

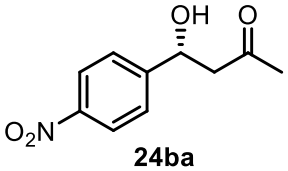

24ba

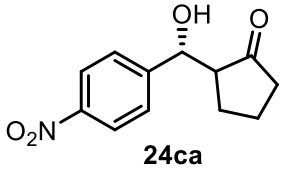

24ca

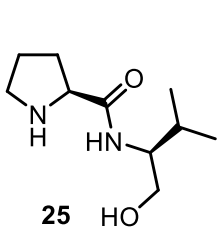

25

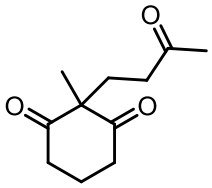

26

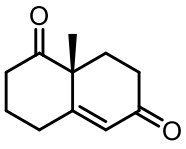

27

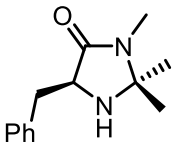

28

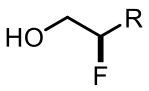

29

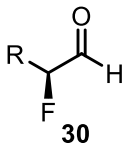

30

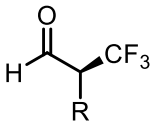

31

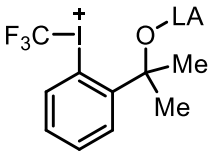

32

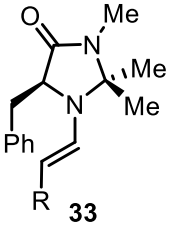

33

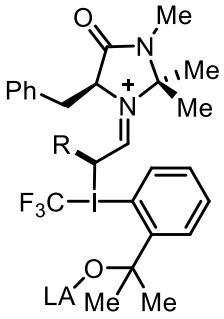

34

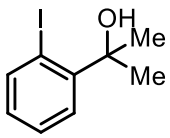

35

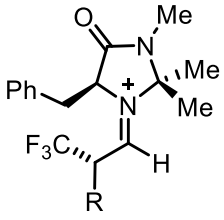

36

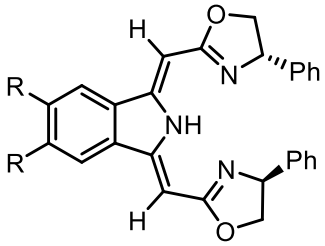

37

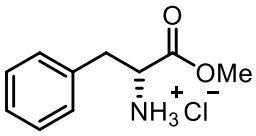

38

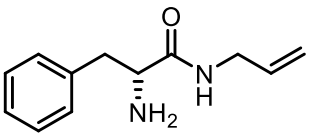

39

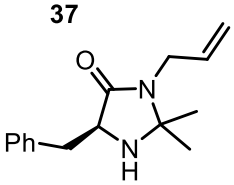

40

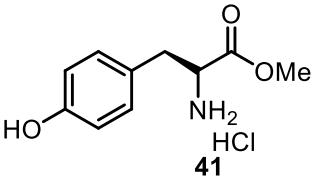

41

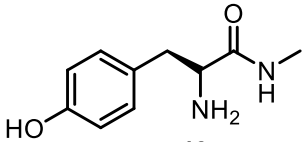

42

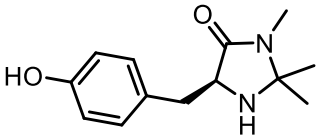

43

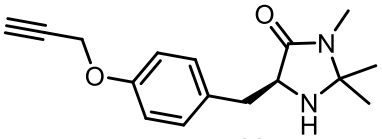

44

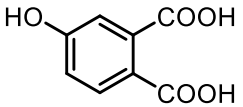

45

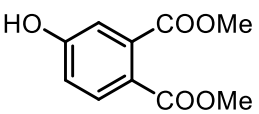

46

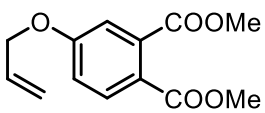

47

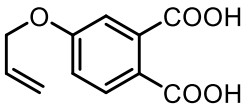

48

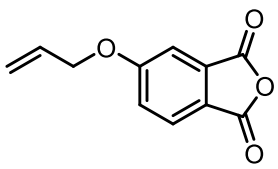

49

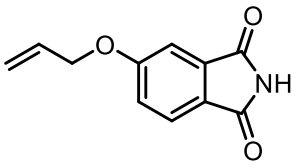

50

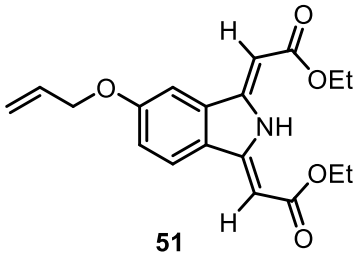

51

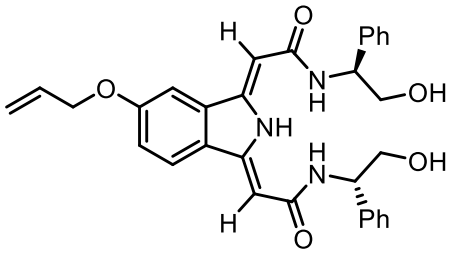

52

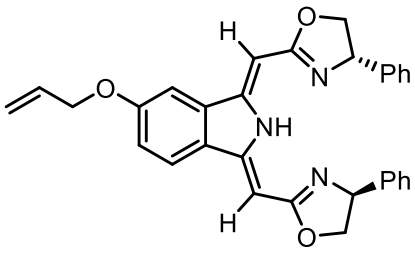

53

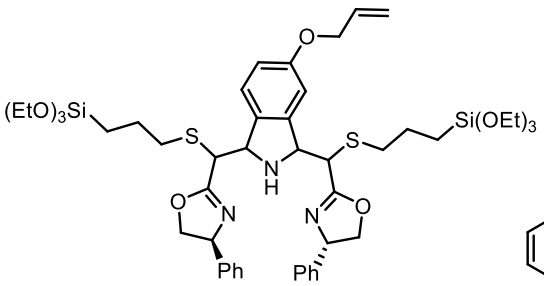

54

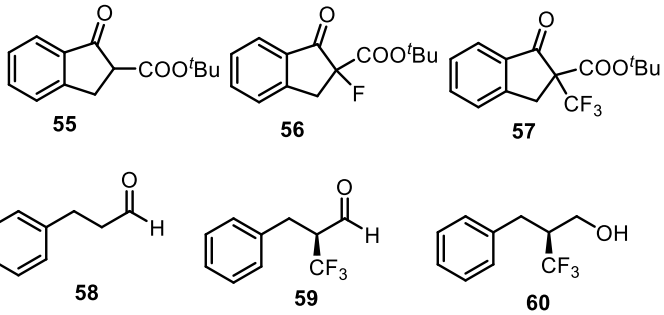

55 **56** **57** **58** **59** **60**

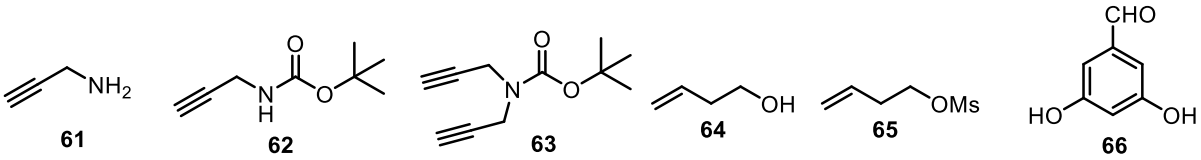

61 **62** **63** **64** **65** **66**

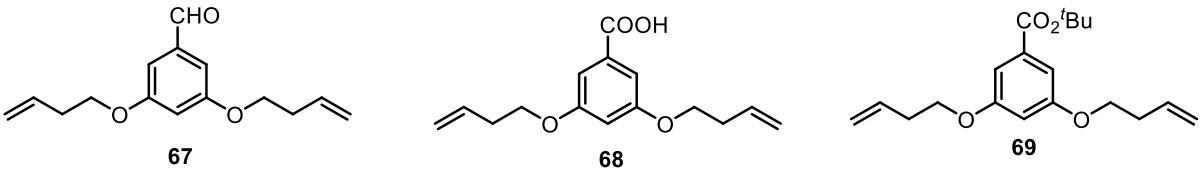

67 **68** **69**

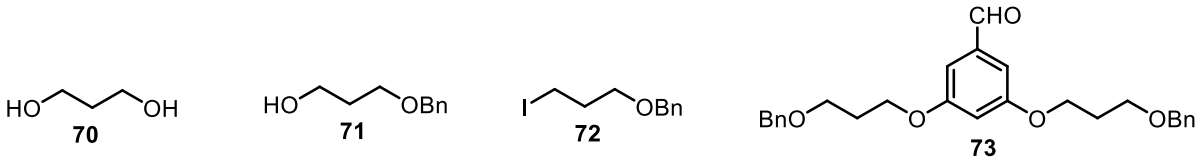

70 **71** **72** **73**

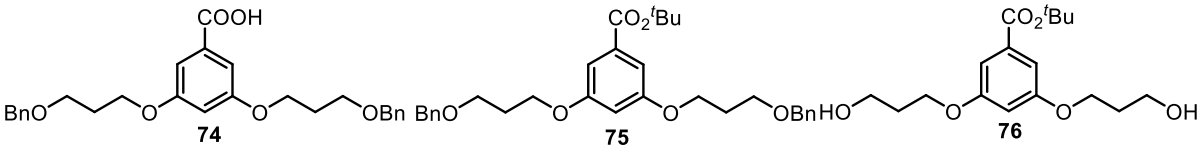

74 **75** **76**

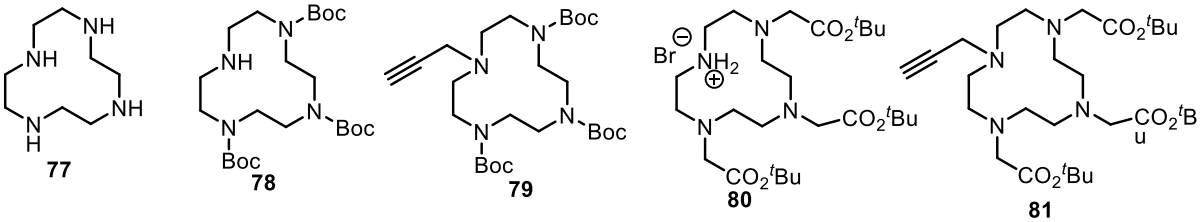

77 **78** **79** **80** **81**

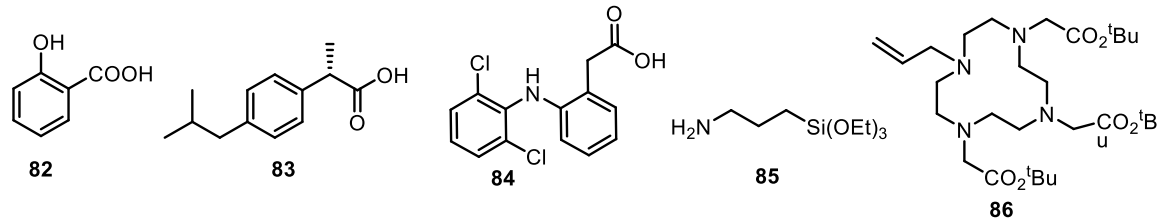

82 **83** **84** **85** **86**

Formula index

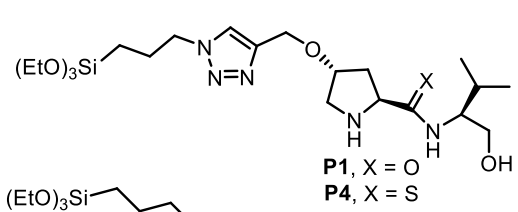

P1, X = O
P4, X = S

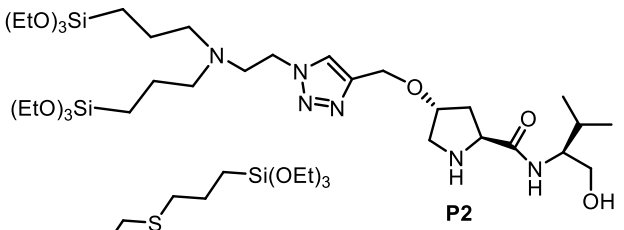

P2

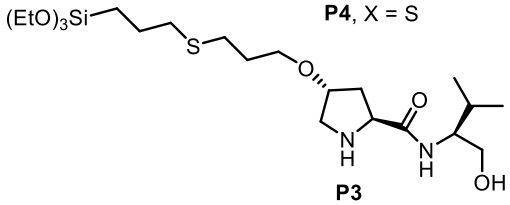

P3

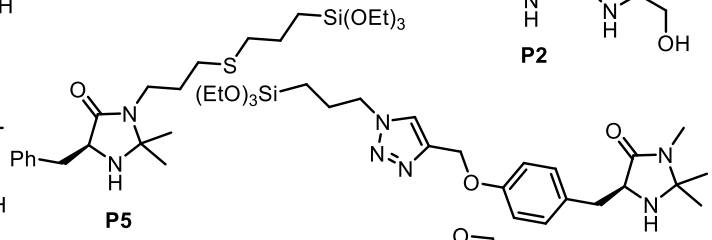

P5

P6

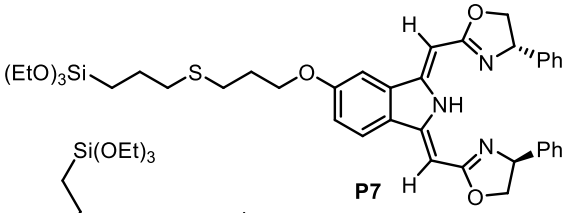

P7

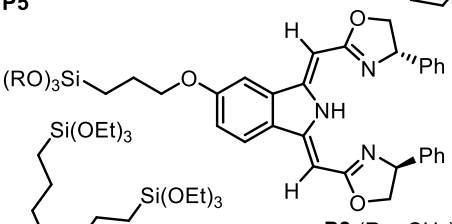

P8 (R = CH_3)
P9 (R = Et)

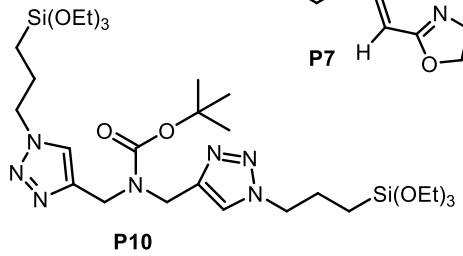

P10

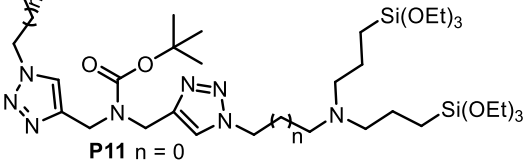

P11 n = 0
P12 n = 1

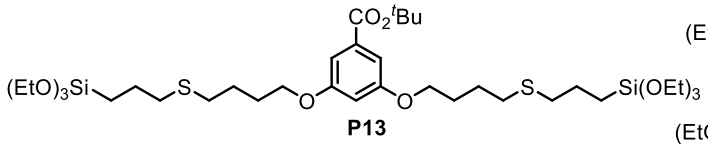

P13

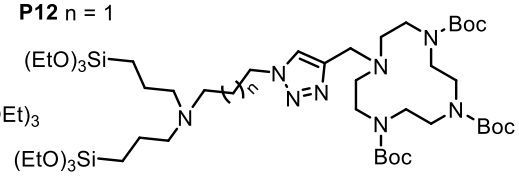

P15 n = 0
P16 n = 1

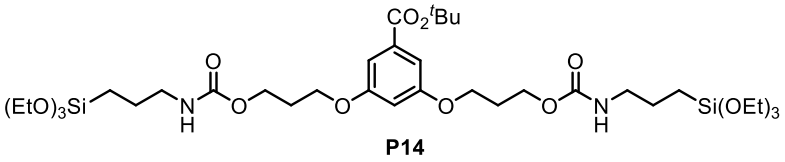

P14

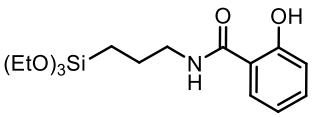

P19

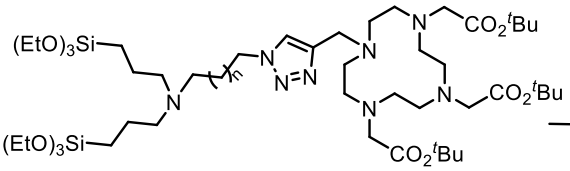

P17 n = 0
P18 n = 1

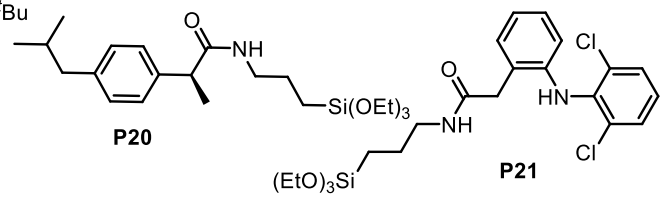

P20

P21

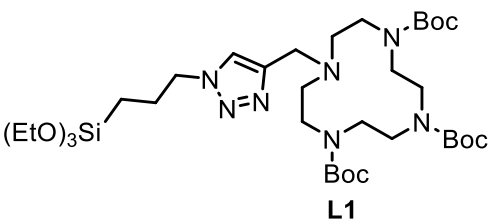

L1

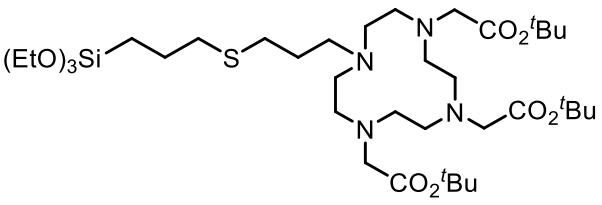

L2

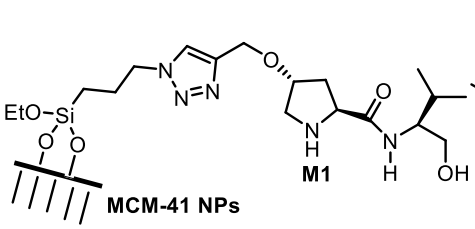

M1

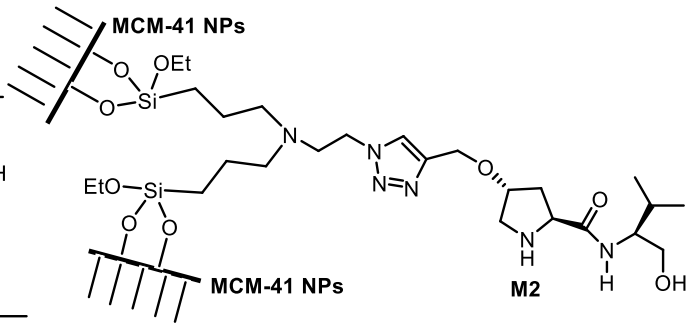

M2

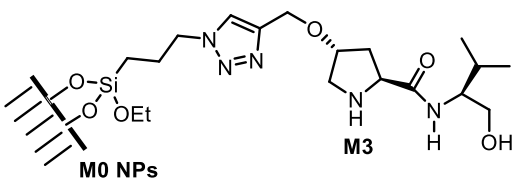

M3

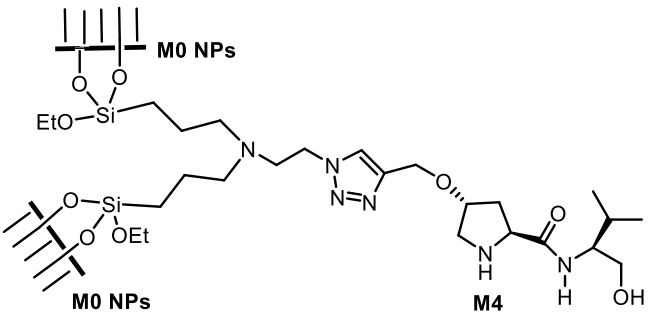

M4

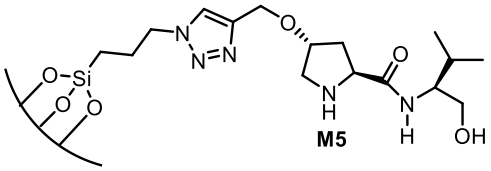

M5

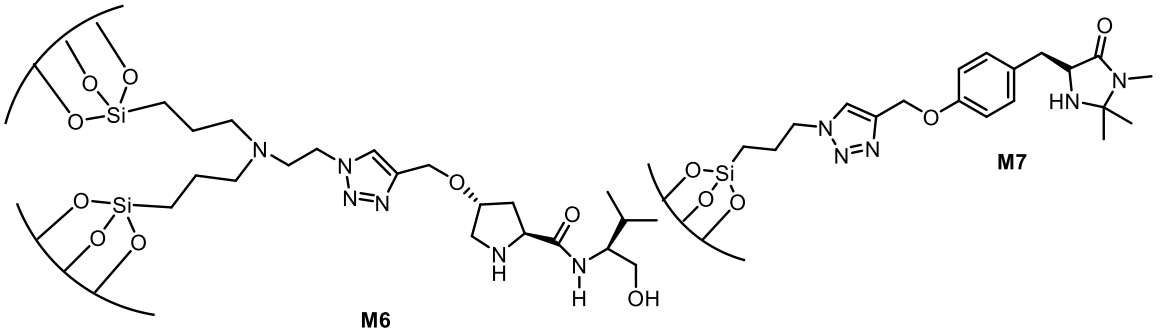

M6

M7

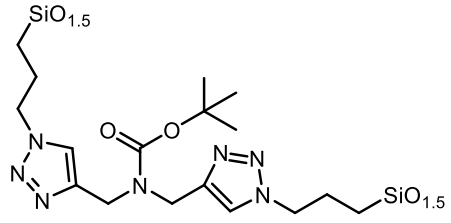

E-P10 (100-x)/x PMO NPs
x = 10, 25

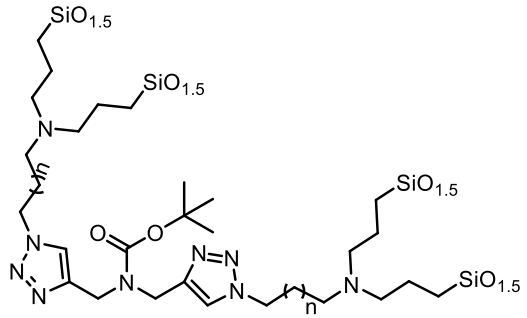

E-P11 (100-x)/x PMO NPs n = 0
E-P12 (100-x)/x PMO NPs n = 1
x = 10, 25

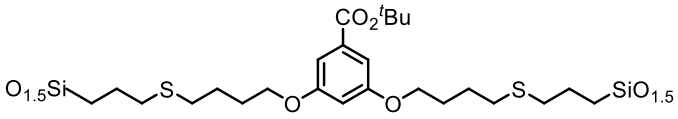

E-P13 (100-x)/x PMO NPs
x = 10, 25

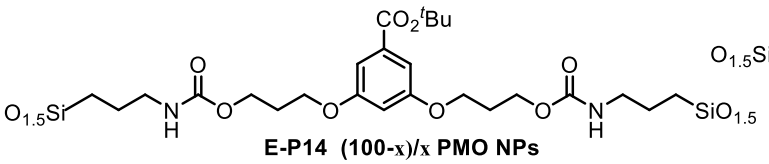

E-P14 (100-x)/x PMO NPs
x = 10, 25

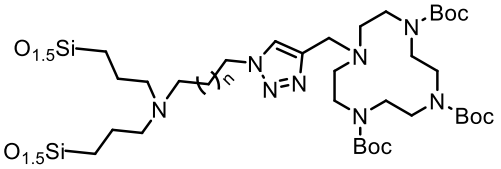

E-P15 (100-x)/x PMO NPs n = 0
E-P16 (100-x)/x PMO NPs n = 1
x = 10, 25

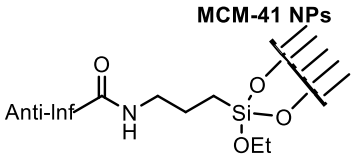

M_I-Ibup, M_I-Salicyl, M_I-DiClfen

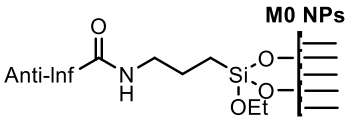

M_{II}-Ibup, M_{II}-Salicyl, M_{II}-DiClfen

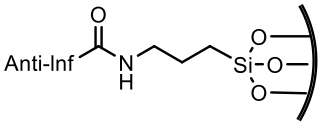

M_{III}-Ibup, M_{III}-Salicyl, M_{III}-DiClfen

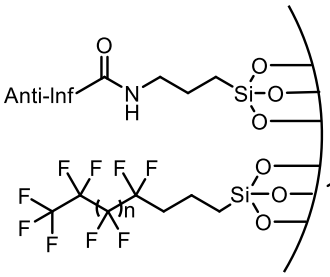

M_{III}-Anti-Inf-x**FAS**-n

x = 0.5, 1.0
n = 3, 5

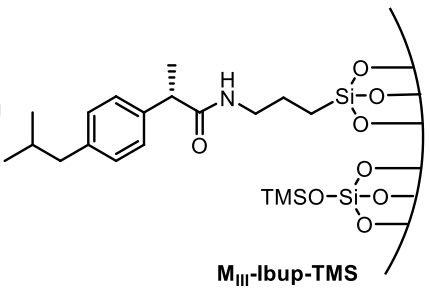

M_{III}-Ibup-TMS

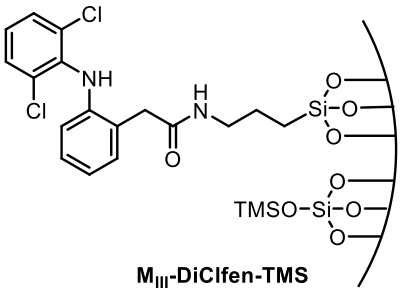

M_{III}-DiClfen-TMS

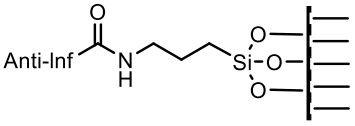

M_{IV}-Ibup, M_{IV}-Salicyl, M_{IV}-DiClfen

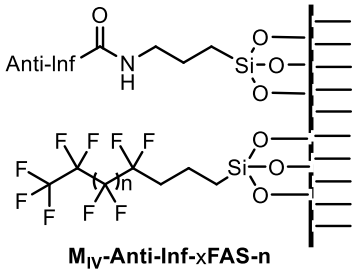

M_{IV}-Anti-Inf-x**FAS**-n

x = 0.25, 0.5, 0.75, 1.0
n = 3, 5

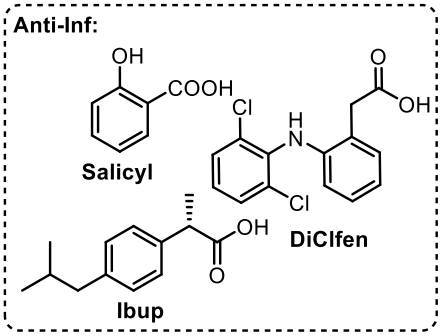

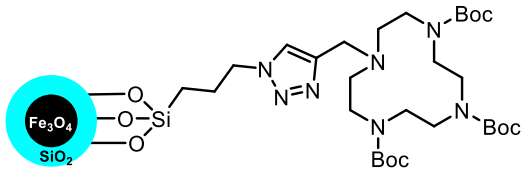

Fe_3O_4@SiO_2 NPs

Fe_3O_4@SiO_2 NPs-L1-I

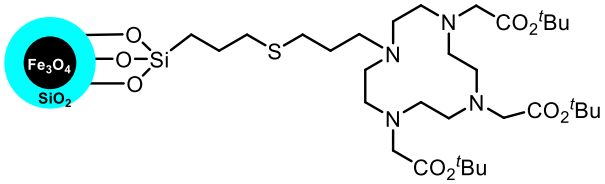

Fe_3O_4@SiO_2 NPs-L2-I

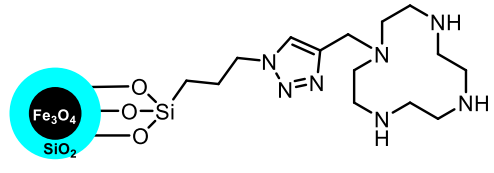

Fe_3O_4@SiO_2 NPs

Fe_3O_4@SiO_2 NPs-L1-II

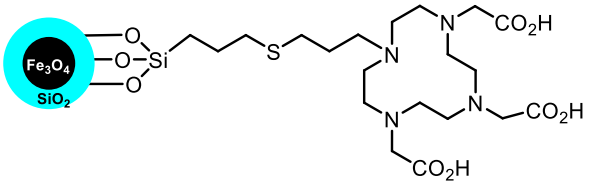

Fe_3O_4@SiO_2 NPs-L2-II

PhD in Chemistry, Doctoral School
Department of Chemistry, Faculty of Science
Universitat Autònoma de Barcelona
08193-Cerdanyola del Vallès, Barcelona, Spain
2016/09/23-2020/07/31

Functionalized Silica Nanoparticles for Catalysis, Nanomedicine and Rare Earth Metal Recycling

Hao Li

Ingénierie Moléculaire et Nano-Objets
Institut Charles Gerhardt Montpellier UMR 5253
Université Montpellier, France
2017/10/01-2017/10/30 and 2019/10/01-2020/01/31